UC Berkeley
UC Berkeley Electronic Theses and Dissertations

Title
Chemistry and Physics of Graphite in Fluoride Salt Reactors

Permalink
https://escholarship.org/uc/item/0xz1s5jx

Author
Vergari, Lorenzo

Publication Date
2023

Peer reviewed|Thesis/dissertation

Chemistry and Physics of Graphite in Fluoride Salt Reactors

By

Lorenzo Vergari

A dissertation submitted in partial satisfaction of the

requirements for the degree of

Doctor of Philosophy

in

Engineering – Nuclear Engineering

in the

Graduate Division

of the

University of California, Berkeley

Committee in charge:

Professor Raluca O. Scarlat, Chair
Professor Massimiliano Fratoni
Professor Per F. Peterson
Professor Digby D. Macdonald
Professor Van Carey

Summer 2023

Abstract

Chemistry and Physics of Graphite in Fluoride Salt Reactors

by

Lorenzo Vergari

Doctor of Philosophy in Engineering – Nuclear Engineering

University of California, Berkeley

Professor Raluca O. Scarlat, Chair

Graphite is a ubiquitous material in nuclear engineering. Within Generation IV designs, graphite serves as a reflector or fuel element material in Fluoride-Salt-Cooled High-Temperature Reactors (FHRs), Molten Salt Reactors (MSRs), and High-Temperature Gas Reactors (HTGRs). Graphite versatility in nuclear systems stems from its unique combination of mechanical, thermal, chemical, and neutronic properties. These properties are influenced by operational parameters like temperature, radiation, and chemical environment. In FHRs and MSRs, graphite can interact with the salt through multiple mechanisms, including salt-infiltration in graphite pores, chemical reactions with salt constituents, and tribo-chemical wear. The goal of this Ph.D. dissertation is to investigate mechanisms of interaction of fluoride salts with graphite in FHRs and assess their impact on salt reactor engineering.

Chemical interactions between the salt and graphite are studied by exposing a graphite sample to $2LiF-BeF_2$ (FLiBe) salt and to the cover gas above the salt at 700°C for 240 hours. Chemical and microstructural characterization of the samples highlights formation of two types of C-F bonds upon exposure, with different degrees and mechanisms of fluorination upon salt and gas exposure.

Infiltration of salt in graphite pores is examined by reviewing literature on infiltration and its effect and by studying salt wetting on graphite. Contact angles for salt on graphite are measured under variable conditions of graphite surface finish and salt chemistry, and used to predict salt infiltration.

Wear and friction of graphite-graphite contacts at conditions relevant to pebble-bed FHR operation is studied through tribology experiments in argon and in FLiBe. Characterization via SEM/EDS, polarized light microscopy, and Raman spectroscopy is employed to seek a mechanistic understanding. Different mechanisms of lubrication are observed in the tests: in argon, graphite is observed to self-lubricate by forming a tribo-film that remains stable at high temperature in argon; in FLiBe, boundary lubrication is observed and postulated to be associated with C-F bond formation at graphite crystallite edges.

1

The interactions between graphite and tritium are studied. Tritium production rates in FHRs are quantified to be three orders of magnitude larger compared to light water reactors. A literature review is performed to investigate the thermodynamics and kinetics of the hydrogen-graphite interaction; the findings are employed to develop an improved model for hydrogen uptake and transport in graphite, which is used to extract tritium transport parameters from experimental studies.

The experiments conducted in this dissertation indicate that the presence of the salt impacts graphite engineering performance in the reactor and after discharge in multiple ways, from providing increased lubrication to impacting graphite surface chemistry. As a further development, exploration of other areas where the salt could have an effect, including evolution of oxidation and graphite reactive sites upon neutron irradiation, in the presence of salt-exposure, is recommended.

To freedom of thought and expression

Table of contents

List of figures

List of tables

Acknowledgments

As my experience at Berkeley comes to an end, it is now time to acknowledge with heartfelt gratitude the group of people that have accompanied me on this journey.

First, I would like to express my gratitude to my advisor, Dr. Raluca O. Scarlat. Dr. Scarlat, you are a role model. Your passion, dedication, resourcefulness, and sense of ethics have taught me what being a Berkeley Engineer means. I wish to thank the members of my Ph.D. dissertation committee, Dr. Massimiliano Fratoni, Dr. Per Peterson, Dr. Digby Macdonald, and Dr. Van Carey for their support and mentorship over the years. As an aspiring professor, I see all of you as examples to follow.

I am thankful to all the friends, colleagues, mentors, and mentees that helped me shape this research. A big thank you goes to past and present members of the SALT group for making Etcheverry Hall a more colorful ~~prison~~ home: Haley, Sasha, Ryan, Christian, Michael, Nathanael, Maksim, Maximilien, Sara, Niv, Randall, Riccardo, Amit, Zach, Jimmy, Xin Hui, Nyah, Dominic, Richa, Alan, and Colton. I am also thankful to my friends and colleagues at Kairos Power, and especially to Dr. Meric de Bellefon and Jake Quincey – you taught me a lot.

I am thankful to the nuclear friends that accompanied me day by day and night by night on this path and in particular the Cragmont crew: Yves, Carla, Jaewon, Andrew, Max, and (honoris causa) Matthew.

Finally, I wish to express my profound gratitude to my family. Mum and Dad: grazie per essere sempre vicini, anche a 9000 km di distanza. Stefano: I am more than excited to celebrate the success that awaits you. Lisa: thanks for your continuous support and the uncountable moments of joy that you gifted me in these years; everything is better when we are together.

1 Introduction

Graphite is a ubiquitous material in nuclear engineering. Among Generation IV designs, graphite serves as a reflector or fuel element material in Fluoride-Salt-Cooled High-Temperature Reactors (FHRs), Molten Salt Reactors (MSRs), and High-Temperature Gas Reactors (HTGRs). Graphite versatility in nuclear systems stems from its unique combination of mechanical, thermal, chemical, and neutronic properties. Among the most important attributes of graphite is its ability to maintain structural integrity at very high temperatures compared to metals, which provides major benefits for reactor safety. The properties of graphite are influenced by operational parameters like temperature (e.g., graphite and coolant temperature profiles, temperature gradients), mechanical conditions (e.g., loads, load cycles, deformations), radiation (e.g., fluence, dpa, neutron spectrum), and chemical environment (e.g., chemical compatibility with coolants and cover gas, chemical interactions in accident scenarios).

In FHRs and MSRs, graphite can interact with the salt through multiple mechanisms, including chemical reactions with salt constituents, physical infiltration of salt in graphite pores, and tribo-chemical wear against other components. The aim of this dissertation is to investigate physical and chemical mechanisms of interactions of fluoride salts with graphite and assess their impact on reactor operation, safety, and waste management. The key elements discussed in this thesis are introduced in the following subsections.

1.1   Reactors employing molten fluoride salts

Molten fluoride salts are employed in two thermal-spectrum, high-temperature reactor designs: Molten Salt Reactors (MSRs) and Fluoride-Salt-Cooled High-Temperature Reactors (FHRs) (Scarlat and Andreades 2017; Yoshioka and Kinoshita 2017).

MSRs are liquid-fueled reactors that employ a fissile-containing salt mixture as a fuel salt. In MSRs, thermal energy is generated by fission within the fuel salt and transferred to a secondary (fuel-less) salt through a heat exchanger. The fuel salts used in these reactors are typically ternary or quaternary mixtures, with enriched uranium fluoride as the primary fissile material. Often, MSRs salts may include thorium fluoride as a fertile element (Serp et al. 2014). In these reactors, nuclear graphite is employed as a moderator and reflector.

Although MSRs are considered a Generation IV design, early prototypes of MSRs have been built and operated more than 50 years ago. The first example of an MSR in history is the Aircraft Reactor Experiment (ARE), which operated over a period of four days in 1954 (MacPherson 1985). The first MSR operating over an extended period of time is the Molten Salt Reactor Experiment (MSRE), a 7.4 MWth reactor built and operated at Oak Ridge National laboratory that ran between 1965 and 1969 using a fuel salt nominally composed of LiF, BeF_2, ZrF_4, UF_4 and ThF_4.

Compared to MSRs, FHRs have a relatively short history, with the first FHR paper being published in 2003 (Forsberg et al. 2003). FHRs are solid-fueled reactors using fluoride salts as a coolant. The fuel for FHRs is in the form of tristructural-isotropic coated (TRISO) particles, embedded in prismatic assemblies or spherical graphite matrix pebbles (PB-FHRs). The coolant salt

investigated for most FHR designs is FLiBe, the eutectic mixture of LiF (enriched in Li-7) and BeF_2. In addition to graphite matrix being used as a fuel element, nuclear graphite is used as the material for reflector pebbles and for the reflector (Andreades et al. 2016).

1.2   Graphite

Graphite is a crystalline form of carbon, both available in nature and manufactured artificially. Most commercial applications, including nuclear, use mixtures of natural and synthetic graphite instead of natural graphite because of the higher control that can be exerted in terms of physical properties and chemical purity.

While most types of commercial graphite are produced starting from needle coke, which yields anisotropic thermal and electrical properties (Ragan and Marsh 1983), graphite for nuclear applications is manufactured using isotropic coke, such as petroleum coke or coal tar pitch, or ground graphite as a filler (Burchell et al. 2007), to ensure isotropy of thermal and mechanical properties, and of irradiation-induced dimensional changes (Burchell et al. 2007). The raw materials used as a filler are calcined at temperatures between 900 °C and 1300 °C, crushed, ground and milled (Kelly 1981; Zhou et al. 2017). The filler particles are then blended with binders (usually coal tar pitches) in order to increase adhesion of the raw powder. The resulting mix is formed by extrusion molding or isostatic compression, yielding the *green artifact* (Bonal et al. 2009)*.* The choice forming technique impacts the orientation of the crystallite and the response to irradiation (Haag et al. 1990). The artifact is then baked (at 1000 °C) and can be impregnated (up to six times) to increase its density. For *nuclear graphite*, which is employed as reflector and/or moderator in HTGRs, FHRs, and MSRs, the final step is graphitization, which occurs at 2500 °C -2800 °C (Kelly 1981). For *graphite matrix*, which is employed for TRISO-containing fuel pebbles in HTGRs and PB-FHRs, graphitization is replaced by carbonization up to 1000 °C (Yeo et al. 2018) to preserve the integrity of the fuel. For both nuclear graphite and graphite matrix, graphitization is not complete. As a result, amorphous carbon regions, agglomerations of small particles in spherical shape (rosettes), voids, and nanosized graphite crystallites with amorphous carbon exist alongside well-graphitized regions (Wen et al. 2008). As a result of the manufacturing process and the heterogeneity of the raw materials, nuclear graphite and graphite matrix will have intra-grain and inter-grain heterogeneity, with regions that contain more graphitized carbon, and regions of less graphitized carbon. The mechanical and thermal properties of graphite depend on the choice of the filler, the filler particle size, the choice of the binding agents and the graphitization temperature (Kelly 1981). Graphite for nuclear applications is also manufactured with particular care to limit the concentration of neutron absorbers such as boron and lithium.

As a result of the manufacturing processes, graphite materials are composed of grains that can span from ten microns to millimeter-scale (Burchell et al. 2007). The size of the graphite grains depends primarily on the grain size of the petroleum coke, coal tar pitch, or graphite flake used as a raw material. The maximum size of graphite grain is often used as metric to classify graphite grades (Table 1.1).

Table 1.1: Classification of graphite according to ASTM D8075-16 standard (ASTM International 2016)

Graphite type	Maximum grain size (μm)
Microfine	<1
Ultrafine	1–10
Superfine	10–50
Fine	50–100
Medium	100–4000
Coarse	>4000

In-between grains there are pores on the order of microns to tens of microns. In this thesis, this porosity is referred to as microporosity, using the classification from (Mays 2007). The microporosity depends on raw materials and on the manufacturing process, which may include one, several or no impregnation steps for the purpose of densification and porosity reduction. The homogeneity of the microporosity within the graphite compact will depend on the specifics of the graphite manufacturing process, and any surface machining or other finishing treatments.

Each graphite grain is composed of crystallites that are on the order of tens of nanometers (Atsumi et al. 1996; Chi and Kim 2008; Li et al. 2007; Mironov et al. 2012; Wu et al. 2020a; Zheng et al. 2014). The population of graphite crystallites is expected to span a certain size distribution, which usually is assumed to be Gaussian, but could be bimodal, or multi-modal (Wu et al. 2020a). Orientation of the crystallites is impacted by the green artifact forming process. For nuclear graphites, forming by isostatic compression is preferred to extrusion molding, as it preserves the random ordering of the crystallites (Li et al. 2016; Shen et al. 2021). In-between the crystallites there is nanoporosity, which consists of pores in the order of nanometers to tens of nanometers.

The distribution of pore size might significantly change from one graphite type to another (Table 1.2). The total porosity (α_T) can be classified according to its permeability by fluids at room temperature as open porosity (α_O) or closed porosity (α_C). The fraction of the total porosity that is attributed to closed porosity will vary across graphite grades; in the examples included in a recent review of nuclear graphite porosity, some graphite grades present predominantly open porosity (e.g. IG-110), others present predominantly closed porosity (e.g. NBG-18) (Lee et al. 2020). Each experimental technique for probing porosity has a different sensitivity to pore size and type of pore (i.e., closed, open or total).

Table 1.2: Graphite grades discussed in this dissertation

Graphite grade	Manufacturer	Type	Reference
IG-110	Toyo Tanso Co.	Superfine	(Delmore et al. 2018; Gallego et al. 2020; He et al. 2014a, 2015b; Tang et al. 2017; Zhang et al. 2018a, 2016)
A3 graphite matrix	nonproprietary	Fine	(Delmore et al. 2018; Hoinkis et al. 1986)
NBG-17	SGL Carbon Group	Medium fine	(Gallego et al. 2020; He et al. 2015; Tang et al. 2017)
NBG-18	SGL Carbon Group	Medium coarse	(Gallego et al. 2020; He et al. 2015; Tang et al. 2017)
CGB	Union Carbide	Medium fine	(Grimes 1964 pp. 38–42)
UGG-1 (ultrafine graphite grain)	nonproprietary	Ultrafine	(Lian et al. 2016)
R-8710	SGL Carbon Group	Ultrafine	(Lian et al. 2016)
ETU-10	Ibiden	Superfine	(Gallego et al. 2020)
GCMB	UCAR Ltd	n.a.	(Hacker et al. 2000)
PGA	Anglo Great Lakes Ltd or British Acheson Electrodes Ltd	Medium	(Hacker et al. 2000)
G347A	Tokai Carbon	Superfine [a]	(Contescu et al. 2019)
Gilsocarbon	nonproprietary	n.a.	(Jones et al. 2020)
2020	Mersen USA	Superfine	(He et al. 2015)
G2	Non specified (He et al. 2014b)	Superfine	(He et al. 2015)
2114	Mersen USA	Superfine	(Gallego et al. 2020; He et al. 2015)
G1	Non specified (He et al. 2014b)	Superfine	(He et al. 2015)
AXF-5Q	POCO Graphite Inc.	Ultrafine	(He et al. 2015)
ZXF-5Q	POCO Graphite Inc.	Microfine	(He et al. 2015)
POCO TM	POCO Graphite Inc.	Superfine	(Gallego et al. 2020; He et al. 2015)
UGG-2 (ultrafine graphite grain)	nonproprietary	Ultrafine	(Lian et al. 2016)
NPIG (nanopore isotropic graphite)	nonproprietary	Ultrafine	(Song et al. 2014)
NG-CT-10	FangDa Carbon New Material	Fine	(Zhang et al. 2018a)
NG-CT-50	FangDa Carbon New Material	Ultrafine	(Tang et al. 2017)
NBG-25	SGL Carbon Group	Fine	(Gallego et al. 2020)
PCEA	GrafTech International	Medium fine	(Gallego et al. 2020)
PGX	GrafTech International	Medium fine	(Gallego et al. 2020)
AGOT (Acheson graphite ordinary temperature)	National Carbon	n.a.	(Grimes 1964 pp. 38–42)

[a] Manufacturer data, http://schunk-tokai.pl/en/wp-content/uploads/New-G347.pdf

Each crystallite nominally has hexagonal packing structure, which consists of ABAB-stacked graphene layers. The crystallographic parameters that describe each crystallite are in-plane lattice spacing ("a"), which is the carbon-to-carbon atom distance, and out of plane lattice spacing ("c"), which is the graphene-layer-to-graphene-layer spacing. The size of the crystallite is characterized by in-plane crystallite size ("L_a"), which represents the extent of the continuous graphene layers, and out-of-plane crystallite size ("L_c"), which represents the continuous stacking of graphene layers. Rhombohedral and turbostratic crystallites can also be present in graphite. Rhombohedral structures consist of ABCABC stacking. Turbostratic crystallites consists of unaligned stacked planes. Stacking faults also occur with a certain frequency. The fractions of crystally ordered and disordered structures in graphite can be probed by Raman spectroscopy and X-ray diffraction (Li et al. 2007; Pimenta et al. 2007).

The edge of each graphene sheet can have two types of structural configurations: zigzag and armchair (Figure 1.1). While carbon atoms in the interior of graphite crystallites have sp^2 electronic configuration, carbon atoms at the edge may have sp^3 configuration. These atoms represent sites

of higher energy than carbon atoms in the interior of the crystallite. Other types of defects can also exist in the interior of the graphene planes and inter-graphene plane. In the rest of this thesis, such sites of higher energy are referred to as reactive carbon sites (RCS).
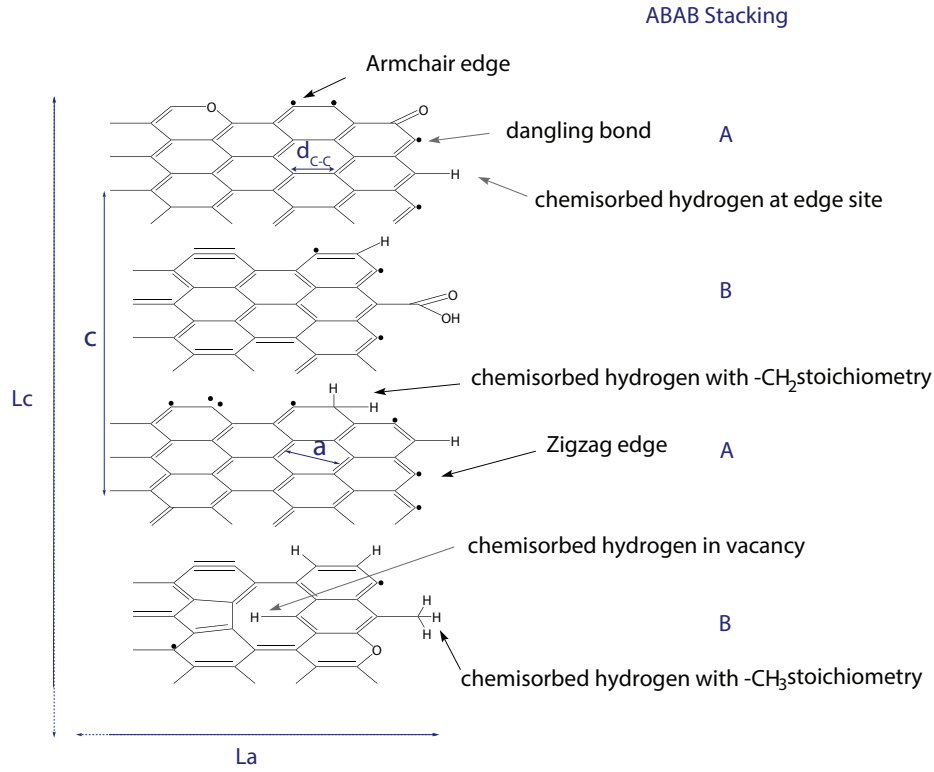
a = 2.46 Å   c = 6.71 Å d_{C-C} = 1.42 Å   (for perfectly graphitized graphite)

Crystallite Density = 2.269 g/cm³   (Zemann, 1969)

L_a, L_c ~ 10's to 100's nm

C_{edge}/C_{total} = 0.15 (nm³)/ a c L_c

C_{edge}/C_{total} + C_{bulk}/C_{total} = 1   (Wu et al., 2020)

Figure 1.1: The graphite lattice, microstructural parameters, representative chemical functional groups at RCS shown at vacancy and edge sites, and example hydrogen atoms chemisorbed at RCS showing -CH, -CH₂ and -CH₃ stoichiometry.

The presence of defects and porosity is such that the actual density of both natural and artificial graphite is lower than the crystallite density. The ratio of the actual density (bulk density) of a graphite sample to its crystallite density can be used as a definition of total porosity in such a sample. The crystallite density of a defect-free graphite with ABAB stacking can be computed, from its lattice parameters, as Equation 1.1 (Zemann 1965):

$$\rho_{cryst} = \frac{M_C\ N_{cell}}{\frac{\sqrt{3}}{2}\ a^2 c\ N_{Av}}$$

1.1

where, in addition to the lattice parameters a and c, M_C is the carbon molar mass, N_{cell} is the number of atoms in the elemental cell (4) and N_{Av} is Avogadro's number. The defect-less hexagonal graphite (a= 2.46 Å, c=6.71 Å) has a crystallite density of 2.269 g/cm^3 (Zemann 1965). In the case of ABCABC stacking, the elemental cell comprehends four consecutive layers instead of three (so that its lattice parameter c is 3/2 of that for hexagonal graphite) but includes $N_{cell} = 6$ atoms, so that the crystallite density is unchanged. Turbostratic carbon does not have a stacking order across layers and the distance between two adjacent is larger (> 0.342 nm) (Pimenta et al. 2007), leading to a lower density (less than 2.225 g/cm^3).

Neutron irradiation of graphite in a nuclear reactor causes changes in microstructure with an impact on RCS density and porosity distribution. As a fast neutron collides with the crystal lattice, it displaces one or more lattice atoms (primary knock-on atoms). The minimum neutron energy required to produce a displacement increases with temperature and is between 24 eV and 60 eV (Burchell 1997; Kelly 1981). Through the collision, the primary knock-on atoms may receive an energy that is sufficient to recoil on other atoms and displace them, starting a collisional cascade, with a final number of displacements per atom (dpa) on the order of 10^2 (Telling and Heggie 2007). Displaced atoms leave a lattice vacancy and an interstitial carbon atom, the so-called Frenkel pair. The displaced atoms can diffuse between the two planes and recombine with vacancies or coalesce in-between the planes. The coalesced atoms form a cluster that may be destroyed by collisions with fast neutrons or displaced atoms, or they may grow to form a new graphite plane. The formation of new planes causes crystallite growth in the direction perpendicular to the basal plane (c direction). Adjacent vacancies coalesce parallel to the basal plane, forming sinks for other vacancies and causing a shrinkage parallel to the basal plane (a direction). The shrinkage and growth rates in the a and c direction decrease with increasing graphitization temperature. In the early phases of irradiation, the expansion in the c direction is accommodated by existing cracks, formed during manufacture, and the contraction in the a direction is the only visible effect. The presence of preferential orientations of the crystallites can lead to an overall directional shrinking of the graphite. Forming by isostatic compression instead of extrusion molding helps preserving the random orientation (Li et al. 2016; Shen et al. 2021). With increasing neutron fluence (i.e. with a longer irradiation or a higher neutron flux), available cracks are closed and incompatibility of the two dimensional changes leads to the generation of new porosity (Contescu et al. 2019) and the shrinkage rate is counterbalanced (*turnaround*) (Burchell 1997). The dpa at which turnaround occurs depends on graphite type and reduces with higher irradiation temperatures. In the case of IG-110U graphite at 600 °C, the turnaround is around 15 dpa (Ishiyama et al. 1996). Further irradiation causes an increase in the swelling rate, due to both the new porosity and the c direction expansion, until fracture of the graphite (Burchell and Snead 2007). Neutron irradiation also causes changes in graphite thermo-physical and mechanical properties such as thermal conductivity, coefficient of thermal expansion, electrical resistivity, elastic modulus, and tensile strength. Finally, graphite creep can occur at lower temperatures in presence of irradiation (Burchell 1997). The reader is referred to (Kelly 1981) and (Telling and Heggie 2007) for additional detail on irradiation damage, and to (Burchell 1997) and references therein for changes to thermo-physical and mechanical properties.

In summary, graphite is a porous material composed of micron-sized grains and micro-pores; the graphite grains are comprised of nanometer-sized crystallites and nano-pores. Graphite for nuclear applications is manufactured with particular care to preserve a random orientation of the crystallites, ensure isotropy of thermal, mechanical and irradiation properties, and achieve low concentration of neutron poisons. Nominally, crystallites have hexagonal packing structure consisting of ABAB-stacked graphene layers; the edges of the graphene layers as well as defects within the graphene layers create opportunities for RCS. Irradiation of graphite leads to changes in microstructure and porosity and introduces additional RCS.

1.3 Structure of the dissertation

The scope of this dissertation is to investigate physical and chemical mechanisms of interactions of fluoride salts with graphite and assess their impact on graphite engineering during reactor operation and waste management. This investigation is conducted by a combination of literature review, experiments, and computation. Literature review and computational work are conducted to generate results applicable to MSRs and FHRs. Experimental work is performed at conditions of relevance to FHRs. In the experiments, both nuclear graphite and graphite matrix are investigated. Salts used in this study include FLiBe and FLiNaK. FLiBe is a $LiF-BeF_2$ mixture employed as a coolant in FHRs. FLiNaK is a LiF-NaF-KF mixture often used as a non-beryllium-containing surrogate of FLiBe in experiments. FLiNaK have comparable thermodynamic properties but differences in chemical and electronic behavior (Langford et al. 2022; Williams et al. 2006). As such, experiments in FLiNaK may not yield results directly applicable to FLiBe but help develop proof-of-principle methodologies that can be further applied to FLiBe.

This thesis is organized in four chapters, with the first two chapters focusing on the interactions, and the last two chapters presenting two topics of engineering relevance for graphite in a salt-containing reactor.

Chapter 2: Chemical Interactions of Graphite and Molten Fluoride Salts

Thermodynamics suggests that graphite is inert when exposed to fluoride salts. Recent experimental studies, however, indicate formation of carbon-fluorine bonds upon graphite exposure to FLiBe and FLiNaK. This chapter presents an experiment in which graphite is exposed to FLiBe and to the cover gas above the salt at 700°C for 240 hours. Chemical and microstructural characterization of the samples is performed to investigate the interaction and provide a mechanistic description.

Chapter 3: Infiltration of Salt in Graphite Pores

During the MSRE, resistance to salt infiltration was a key criterion used to inform the choice of graphite grade for use in the reactor. This chapter offers a review of the phenomenology of salt infiltration in graphite and presents a parametric study for FLiNaK wetting on graphite which helps quantify how salt and graphite properties impact infiltration.

Chapter 4: Graphite-Graphite Tribology

In a PB-FHR, graphite pebbles will roll and slide against each other and surrounding structures. Quantifying friction and wear in pebble-pebble and pebble-structure contacts is necessary to predict pebble flow and degradation in the core. In this chapter, two graphite-graphite tribology experiments, relevant to dry sliding in argon and lubricated sliding in FLiBe are presented.

Chapter 5: Tritium Uptake by Graphite

Tritium management is important for FHRs and MSRs, since large amounts of tritium are produced by neutron irradiation of the lithium and beryllium contained in the salts and tritium solubility in the salt is limited (Forsberg et al. 2017b). Graphite has shown to have a chemical affinity for tritium and has been proposed as a vector to remove tritium from FHRs. This chapter focuses on quantifying tritium production rates in FHRs and MSRs, reviewing graphite-tritium interaction chemistry, and modeling hydrogen isotope transport in graphite.

2 Chemical Interactions of Graphite and Molten Fluoride Salts

Graphite components are present in the cores of FHRs and MSRs with large surface areas exposed to molten salts (Andreades et al. 2016; Serp et al. 2014). For example, the core of the Mark-I PB-FHR contains 68,000 m^2 graphite surface (580,000 graphite pebbles) in 12 m^3 of FLiBe salt (Andreades et al. 2014), corresponding to a graphite surface area to salt volume ratio of 800 m^{-1}; the Molten Salt Breeder Reactor (MSBR) design had 330 m^2 of graphite moderator surface area in 2.3 m^3 of fuel salt (Kasten 1969), corresponding to a graphite surface area to salt volume ratio of 140 m^{-1}. During PB-FHR operations, graphite pebbles and reflectors are exposed to both molten 2LiF-BeF$_2$ (FLiBe) and to the cover gas above the salt (e.g., in the defueling chute) for durations of tens of days to tens of years. Characterizing the chemical and microstructural changes of graphite caused by salt-graphite interactions with salt is relevant to assessing the performance of graphite during reactor operation and to predicting graphite conditions upon its discharge from the reactor. In particular, it is of relevance to understanding when graphite-salt chemical interactions impact graphite capacity to uptake tritium (Chapter 5), understanding resistance to molten salt infiltration and oxidation (Chapter 3), and understanding evolution of tribological properties (Chapter 4).

During the MSRE, exposure to fuel salt (nominally composed of LiF, BeF$_2$, ZrF$_4$, and UF$_4$ and ThF$_4$ but also containing UF$_3$, fission products, and transuranics because of operation (Haubenreich and Engel 1970)) for 2.5 years was concluded to lead to "no attack by salt," citing no change in surface finish, and no development of cracks (Haubenreich and Engel 1970). This is not a surprising engineering observation, given that for infinite, defect-free, graphite, chemical oxidation by FLiBe or by MSRE fuel salt at a UF$_4$/UF$_3$ redox potential ratio of 10-100 (corresponding to 10^{-43} to 10^{-45} Pa F$_2$ partial pressure, i.e. 710 to 740 kJ/mol fluorine potential (Zhang et al. 2018b)) is not thermodynamically favorable. For example, C + 2F$_2$ = CF$_4$ has $\Delta G_f = $ - 400 kJ/mol F$_2$ at 600 °C (Wu et al. 2018a), so, at the MSRE fluorine potential, a partial pressure of 10^{-18} to 10^{-21} Pa of CF$_4$ would be expected, indicating a negligible reaction progression from an engineering perspective.

Nevertheless, graphite does fluorinate at high fluorine potential (e.g., under 1 atm F$_2$ or HF gas), and highly fluorinated graphite is broadly synthesized and studied (Gupta et al. 2003; Hamwi et al. 1988; Nakajima et al. 1999; Touhara et al. 1987). Similarly, fluorination of graphite oxide with fluorine gas is known to occur as well (Nakajima et al. 1988a; b; Nakajima and Matsuo 1994). These are both scenarios of high heterogeneous atom content (e.g., units to tens of percent F or O atoms) in the graphite. For MSR and FHR applications, very low fluorine potentials producing low heterogeneous atom content (> 100 ppm) are of interest. There is previous evidence of fluorination of graphite upon exposure to both FLiBe and LiF-NaF-KF (FLiNaK) molten fluoride salt. In (Yang et al. 2012), formation of C-F bonds replacing pre-existing C-H bonds in nuclear graphite (IG-110, Toyo Tanso Co. Ltd.) exposed to FLiNaK at 500°C for 16 hours by x-ray near edge absorption spectroscopy (XANES) was observed. (Wu et al. 2018a) showed evidence of fluorination of IG-110 after exposure to molten FLiBe at 700 °C for 12 hours, based on glow discharge mass spectroscopy (GDMS) that indicated higher penetration in the sample for fluorine compared to

beryllium and lithium, and x-ray photoelectron spectroscopy (XPS) that showed signal for fluorine-bound carbon. Unfortunately, while XPS can allow for interpretation of the type and abundance of chemical bonds on the graphite surface, graphite samples observed in (Wu et al. 2018a) had low fluorination levels, and the C 1s peak cannot be easily deconvoluted for interpretation.

This work seeks to advance the mechanistic description of surface fluorination of graphite by FLiBe, in order to better postulate the engineering relevance of this phenomenon. This study performs a FLiBe-exposure at 700 °C over an extended time period (240 hours), seeking to achieve a higher level of surface fluorination, thus enabling XPS analysis for interpretation and quantification of carbon-hetero-atom species on the salt-exposed graphite surface. Identifying the possible species formed and consumed and their respective concentrations and characterizing the behavior in the cover gas phase as well as the liquid phase, is helpful towards developing a mechanistic description of the phenomenon. Since graphite is a porous material, it is possible that salt-graphite reactions occur at the liquid-solid interface and via the gas phase as an intermediary. Therefore, to understand the role of the salt-graphite interface towards facilitating these fluorination reactions, this study exposes graphite to molten salt, and to the cover gas immediately above the salt and compares the degree of fluorination and types of functional groups that appear on the graphite surface. If this week-long experiment achieves higher levels of fluorination than previously reported in day-long exposures, that indicates engineering relevance of the kinetics of this reaction, and further motivates the need for a mechanistic description of fluorination reaction and transport pathways. Samples are characterized by surface and depth profiling XPS, SEM/EDS, and Raman spectroscopy, to describe the chemical and microstructural evolution of the graphite surface.

2.1 Experimental

2.1.1 Materials

Three IG-110 graphite samples are used in this study. One sample is kept as a reference, one sample is exposed to liquid FLiBe, and one sample is exposed to the cover gas above the salt. IG-110 nuclear graphite was provided by Dr. Will Windes from Idaho National Laboratory (INL). Table 2.1 summarizes IG-110 properties,

Table 2.2 includes a description of the samples. Hydrofluorinated FLiBe ($2.07\pm0.11:1$ LiF:BeF$_2$) is used in this study (Carotti et al. 2018; Kelleher 2013; Kelleher et al. 2015; Vidrio et al. 2022). The same salt batch and graphite source block were used as in (Wu et al. 2018a), which lists the major constituents and minor constituents in FLiBe, and the impurities in graphite.

Table 2.1. Properties of IG-110 nuclear graphite, as reported by the manufacturer unless otherwise specified.

Manufacturer	Toyo Tanso
Fabrication Process	Cold Isostatic Pressing
Bulk Density (g/cm^3)	1.77
Open Porosity	14-18% (Yamashina and Hino 1989)
Total Porosity	22%
Average Grain Size (μm)	20
Average Pore Size (μm) (Yamashina and Hino 1989)	3

Table 2.2: Graphite Sample Description

Sample ID	Exposure Type	Sample Preparation	Dimensions (cm)
IG_REF	Reference	Machined with a low-speed saw, polished with 1200 grit SiC paper, sonicated DI water, and degassed in vacuum (in alumina boat in tube furnace) at 1500 °C, 12 hours	L: 1 x H: 1 x W: 0.3
IG_L	Liquid FLiBe	Preparation as reference. Exposed to molten FLiBe at 700 °C, 240 hours in positive-pressure Ar glovebox (<1 ppm O_2 and H_2O); three hours cooling to room temperature in cover gas above FLiBe.	L: 1 x H: 1 x W: 0.3
IG_G	Cover gas above FLiBe	Preparation as reference. Exposed to cover gas above FLiBe at 700 °C, 240 hours in positive-pressure Ar glovebox (<1 ppm O_2 and H_2O); three hours cooling to room temperature in cover gas above FLiBe.	L: 1 x H: 1 x W: 0.3

2.1.2 Sample preparation

IG-110 samples are machined into 1 cm x 1 cm x 0.3 cm solid samples with a low-speed diamond saw, polished with 1200 grit SiC, and then ultrasonically cleaned with deionized (DI) water for five minutes. The samples are first dried and then degassed with under vacuum in an alumina boat at 1500 °C for twelve hours. Test and reference samples are cooled inside the furnace under vacuum and then stored inside the Ar glovebox before the experiment. The sample weight of all samples before and after vacuum heat treatment is measured with a QUINTIX224-1S Sartorius analytical balance with built-in internal calibration (220g range, 0.0001g readability/repeatability) outside the glovebox. Sample weight change due to vacuum baking is measured for each sample and averages to 0.08(2) %; the errors are calculated by integrating instrumental error and measurement error.

2.1.3 Salt-exposure

The apparatus used in this experiment is an evolution of the experimental apparatus described in (Wu et al. 2018a). The set-up consists of a crucible, crucible lid, central rod, and sample-holding rods, to which the samples are connected (Figure 2.1). To prevent the introduction of metallic impurities or products of metal corrosion in the experimental apparatus, no metallic components

are used for the experiment. The crucible and central rod are made from a block of IG-110 graphite provided by Dr. Will Windes at INL. The sample holder rods are made of 2 mm-diameter, 100 mm long type 2 glassy carbon (Alfa Aesar, part 038010-DM). Sample holder rods are located both above and below the salt free surface, to expose graphite samples to both the liquid FLiBe and the cover gas above it.
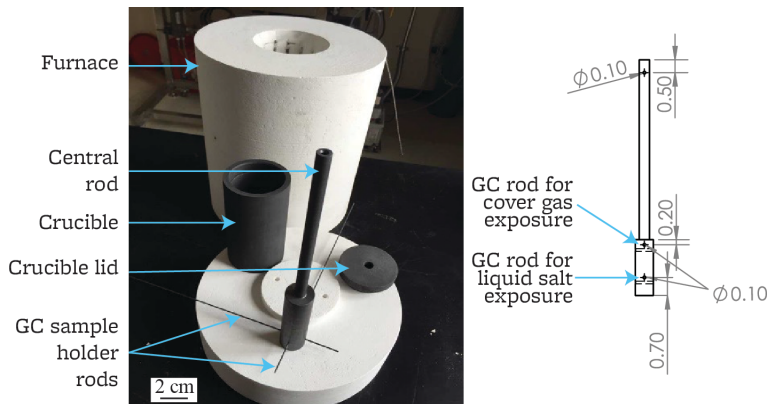
Figure 2.1: Experimental apparatus for salt-exposure of graphite samples. Salt-wetted graphite area to salt volume ratio = 50 m⁻¹. Drawing units are cm.

The experimental apparatus is set inside a vertical furnace, and the experiment is performed inside an inert argon atmosphere glovebox (LC Technologies), O_2 < 1ppm and H_2O < 1 ppm, operated in slight positive pressure. The samples are exposed at a temperature of 700 °C for 240 hours, as measured by an ungrounded Type K thermocouple (Omega, part KMQXL-040U-12) and read with a data acquisition model (National Instrument, part cRIO-9067) running LabVIEW 2018. At the end of the experiment, the test samples are raised a few centimeters above the salt level while at 700 °C; the entire set-up is cooled to room temperature over the course of three hours. Test samples are subsequently removed from the central rod and stored inside the argon glovebox.

2.1.4   Sample Characterization

Before characterization, samples are sonicated in DI water for two minutes. Characterization with SEM, EDS, and XPS are conducted at University of Wisconsin Madison (UWM). The samples are then packaged according to OSHA standard for beryllium safety (OSHA 29 CFR 1910.1024), and shipped to University of California Berkeley (UCB), where they are stored in argon atmosphere and characterized via SEM/EDS and Raman spectroscopy.

2.1.4.1.   SEM/EDS

SEM imaging at is performed at UWM using a Zeiss LEO 1530 at an accelerating voltage of 3 to 5 kV and at UCB using a Thermo Fisher Scios 2 with an accelerating voltage of 20 kV and a current of 0.40 nA. Beryllium safety handling procedure are described in Section 2.1.5. SEM has a scanning depth of 5 μm (Ul-Hamid 2018). EDS maps are acquired with Scios 2 at the same voltage and current and analyzed on AZtec 2.1 (Oxford Instruments). The depth probed by SEM/EDS in graphite at 20 kV voltage is estimated to 5 μm (Ul-Hamid 2018). Additional EDS data, collected at UW Madison (UWM) at an accelerating voltage of 10 kV, are included as Supplementary Information (Figure 7.1).

2.1.4.2. XPS

XPS spectra are recorded using a Thermal Scientific K-alpha spectrometer with a monochromatic Al Kα (1486.6 eV) excitation source. Beryllium safety handling procedure are described in Section 2.1.5. Survey XPS spectra are acquired at 0.5 eV energy step size and 1.00 eV narrow scans. High resolution XPS spectra are recorded at 12 keV nominal operating voltage, with a 400 µm spot size and 50 eV pass energy with 100 scans. XPS depth profiling is performed on the samples exposed to liquid FLiBe. Each depth-profiling step is composed of 2 keV monoatomic Ar^+ ions sputtering for 120 seconds followed by high-resolution acquisition of C 1s, O 1s, and F 1s spectra. Nine depth-profiling steps are performed. Each step is estimated to remove a thickness corresponding to approximately 10 nm: argon sputtering size is estimated to five times the X-ray spot size (400 µm); assuming an Ar+ current I =1 µA, the flux of Ar ions on the surface is calculated as: $\emptyset = I/e/A = 1 \ 10^{15}$ Ar/s-cm^2, where e is the electron charge and A is the sputtering area. Considering a C-C planar bond length $l_{C\text{-}C}$= 0.142 nm (Bernal 1924), the area of a 2D carbon hexagonal cell is $A_c = 1.5\sqrt{3} \ l_{C-C}^2$; with two full atoms in each hexagon, the surface density of carbon atoms is $S_C = 2/A_c = 3.85 \ 10^{15}$ at C/cm^2; assuming an Ar sputtering yield ξ= 1 (Philipps et al. 1982), a 120s depth profiling step leads to the removal of N= 120 ξ ø /S_C = 31 monolayers of carbon atoms; considering a graphite interplanar distance of 0.335 nm (Bernal 1924), one sputtering step removes a thickness of approximately 10 nm.

Charging effects are corrected on all spectra using the non-functionalized sp^2 carbon C at 284.3 eV as an internal reference. Peak analysis is performed using SDP v9.0 fitting software from XPS International. Recorded spectra are smoothed using 5 points Gaussian smoothing and baseline-subtracted with a Shirley baseline before peak-fitting. Fitting of the O 1s and F 1s peaks is performed using symmetric 80% Gaussian - 20% Lorentzian peaks (Leung et al. 1999; Tressaud et al. 1996).

2.1.4.3. Raman Spectroscopy

Raman spectra are recorded at Lawrence Berkeley National Laboratory (LBNL) using a Horiba LabRam HR confocal Raman microscope with a 532 nm laser source and an optical magnification of 50x. Beryllium safety handling procedure are described in Section 2.1.5. The slit size is set to 200 nm and Raman spectra are collected in the 1000–3000 cm^{-1} wavenumber range. The depth probed by the laser source is estimated at 30–60 nm, and the sampling diameter is in the order of one micron (Compagnini et al. 1997; Scharf and Singer 2003). Five spectra are acquired per sample and fitted using Lorentzian functions on OriginPro 2021b. Crystallite parameters are estimated using the correlations provided in (Cançado et al. 2008; Maslova et al. 2012; Tuinstra and Koenig 1970). Statistical analysis of crystallite parameters is performed using two-sample t-tests.

2.1.5 Beryllium safety

Gloveboxes, fume-hoods, and personal protective equipment are used to provide protection from respiratory and dermal exposure to beryllium. Beryllium contamination in the laboratory is monitored by swipes of laboratory surfaces and air monitoring in the laboratory that houses the gloveboxes. The experimental work at UWM is performed from November 2018 to June 2019 during which 29 surface swipes are analyzed. Any detection of beryllium above the detection limit of 0.025 µg/100 cm^2 (five swipe samples with detectable Be) is followed by cleaning and

decontamination procedures. The housekeeping goal for the laboratory in which this work was performed was 0.2 μg/100 cm^2 (the free-release limit); it was exceed three times and was followed by cleaning of laboratory floor and surfaces and procedure updates for moving samples between glovebox and fume-hood work. The DOE-recommended house-keeping limit of 3 μg/100 cm^2 was not exceeded in any of these instances. Before characterization, samples are sonicated in DI water for two minutes. Characterization of the samples with SEM/EDS, XPS, and Raman is performed after reviewing handling protocols with instrument managers. PPE used during characterization include double-layered disposable gloves (exchanged at every contact with the sample) and lab coats. Sample stubs and stages used during characterization are wiped clean with water or ethanol after each use.

2.2 Results

2.2.1 SEM/ EDS analysis

Figure 2.2 shows SEM micrographs for the reference sample and the two exposed samples. SEM (sampling depth ~5 μm (Ul-Hamid 2018)) of the samples show sub-micron-sized pits and few-micron-sized flakes on the graphite surface. The pits are attributed to the use of an oxide-containing (alumina) boat while pre-baking the samples in a vacuum at 1500 °C; appearances of a pitted surface with holes of tens of micron diameter and of micron-sized flakes were previously observed upon oxidation of nuclear graphites IG-110 and NBG-18 in dry air at 1100 °C and above (Lee et al. 2014). EDS of the exposed samples shows a signal from oxygen (Figure 2.3), but oxygen presence is not of relevance to post-salt exposure conditions because samples are washed in water post salt-exposure, and oxygen can also adsorb onto the surface while the samples are handled in air during characterization.

Spheres of 1 to 4 μm diameter are observed inside of the pores of the liquid FLiBe-exposed sample and spheres of 1 to 2 μm diameter are observed in the pores of the cover gas-exposed sample. At the location of the spheres, EDS (sampling depth ~5 μm (Ul-Hamid 2018)) shows signal from fluorine (Figure 2.3) and no signal from carbon. Since Li and Be are not detectable by EDS, it is postulated that the spheres may be composed of BeF_2 and/or LiF. A point spectrum of one of the spherical particles is included as Supplementary Information (Figure 7.1).
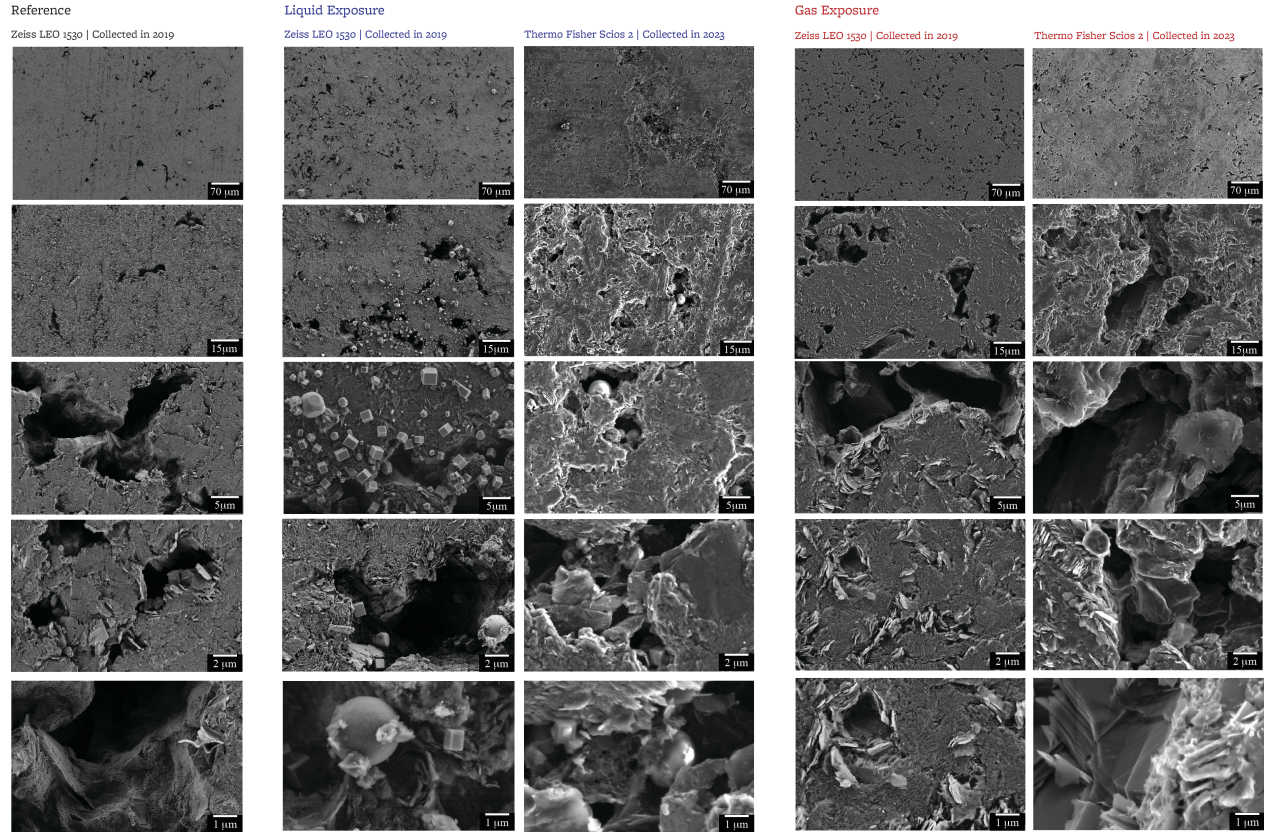
Notes: Zeiss LEO 1530 micrographs collected at UWM after sonicating in DI water for two minutes. Thermo Fisher Scios 2 micrographs collected at UCB. SEM/EDS, XPS, and Raman characterization have led to repeated taping and untaping of the sample surfaces before characterization of the samples of UCB.

Figure 2.2: SEM micrographs of reference and exposed IG-110 samples. For each sample, micrographs are collected at up to two locations and may not be representative of the overall sample. Additional images provided as in Mendeley Data repository linked in Supplementary Information.
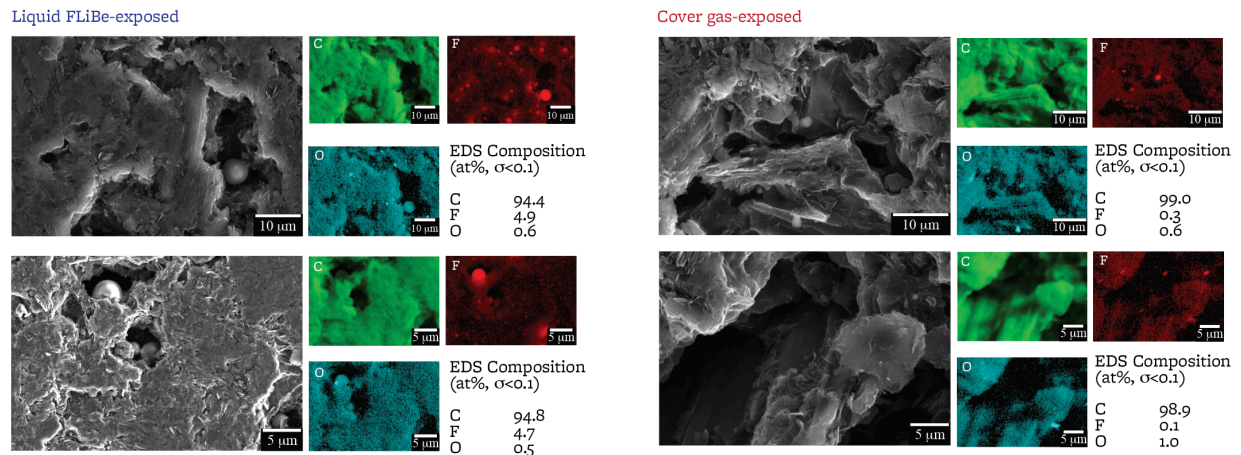
Atomic compositions are area averages over the area covered by the corresponding SEM images.

Figure 2.3: EDS of exposed IG-110 samples. Scans acquired at locations where spherical particles are observed and may not be representative of overall sample. Additional spectra provided as in Mendeley Data repository linked in Supplementary Information.

2.2.2　XPS surface analysis

XPS spectra (sampling depth: 2-12 nm (Lesiak et al. 2018; Shinotsuka et al. 2015), sampling diameter: 400 µm) are collected at two locations on each sample to investigate the chemical composition on the surface of the graphite samples. The XPS surveys of the three samples are shown in Figure 2.4**.** The surveys are consistent with published XPS spectra for IG-110 (Choi et al. 2011; Lee et al. 2014; Lei et al. 2019; Wu et al. 2018a; Zhang et al. 2023), which show a strong C 1s peak and smaller peaks associated to O 1s (Choi et al. 2011; Lee et al. 2014; Wu et al. 2018a; Zhang et al. 2023) and F 1s (Wu et al. 2018a). The presence of F 1s and F KLL peaks on the exposed samples indicates appearance of fluorine species on graphite surface upon exposure to both liquid FLiBe and the cover gas above it. XPS survey of the samples show the presence of small amounts of Na 1s (Lei et al. 2019), Sr 1s (Zhang et al. 2023), S, N, and Ca. Full survey results are compiled in Mendeley Data repository linked in Supplementary Information.

XPS Composition (at%)

	Reference	Liquid-exposed	Gas-exposed
C	93.6(1.9)	98.2(3)	96.9(1.5)
F	-	1.4(2)	0.26(6)
O	5.4(1.4)	0.39(5)	2.37(1.0)
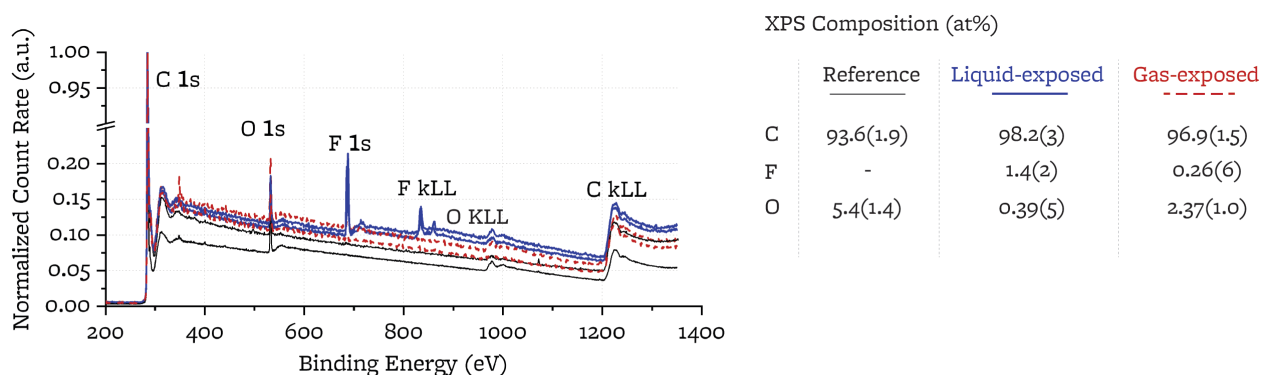
Notes
Two points are surveyed per sample. Surveys normalized to C 1s count rate intensity. XPS composition in Table calculated from high resolution scans. XPS surveys report concentrations < 1 s.d. for N, Ca, Na, S (included in Supplementary Information)

Figure 2.4: XPS survey of reference and exposed IG-110 samples.

2.2.2.1.　C 1s peaks

High-resolution C 1s peaks for two points on each sample are shown in Figure 2.5. All spectra are normalized to the same maximum intensity and same peak maximum location of 284.3 eV. The C 1s peak is fitted with one asymmetric sub-peak (peak C sp^2)) and seven symmetric sub-peaks C_1 to C_7.

Three of the symmetric sub-peaks (C_1, C_2, C_7) are assigned to carbon atoms, consistently with literature on carbon XPS analysis. The remaining four sub-peaks (C_3, C_4, C_5, C_6) are in the region 285.5-289, which has been previously associated to oxygen-containing carbon functional groups (OC) and fluorine-containing carbon functional groups (FC). Interpretation of the sub-peaks in this region is ambiguous, as many possible assignments have been proposed in literature. For example, (Crassous et al. 2009) assigns a peak at 285 eV to C-CO groups, while (Larciprete et al. 2012) assigns a peak at 285 to C-O ether bonds. As another example, a peak at approximately 288 eV can be attributed to semi-ionic C-F bonds (Crassous et al. 2009; Nansé et al. 1997; Touhara and Okino 2000; Tressaud et al. 1996; Yun et al. 2007) or C=O double bonds (Blyth et al. 2000;

Crassous et al. 2009; Larciprete et al. 2012; Yumitori 2000). Because of this ambiguity, an individual interpretation for sub-peaks C_3-C_6 is not proposed, but they are collectively assigned to OC and FC groups. This issue is further discussed in Section 2.3.1, with an example showing how peak fitting of a spectrum does not lead to univocal results.
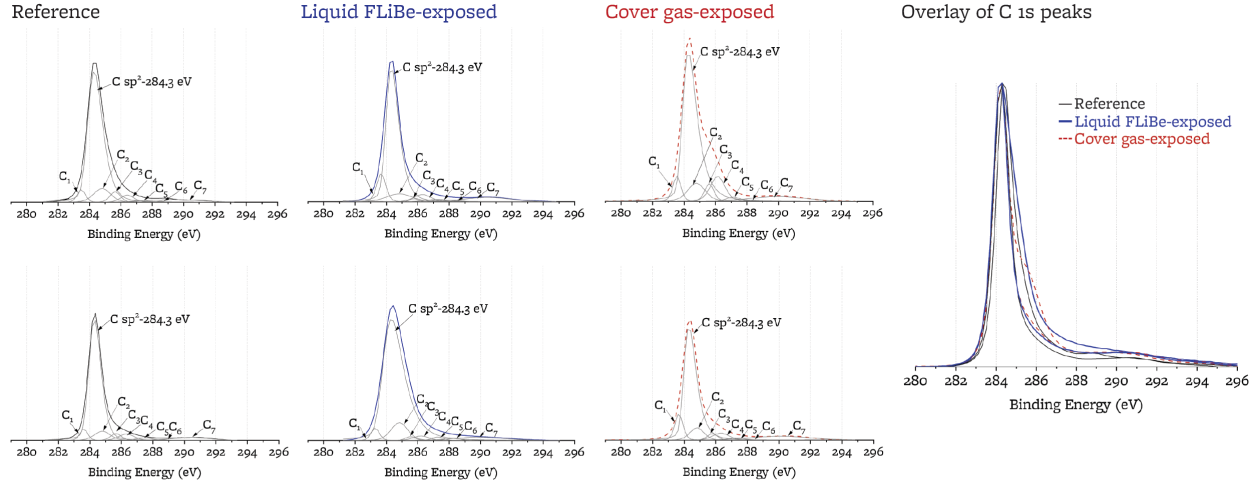
Notes
5-point Gaussian smoothing applied on all spectra. Two points are analyzed per sample. Peaks in overlay normalized to respective C 1s count rate intensities.

Figure 2.5: XPS C 1s peaks for reference and exposed IG-110 samples. Peak-fitting parameters in Table 2.3.

Table 2.3: XPS C 1s peak fitting parameters for spectra in Figure 2.5. Rows are ordered by type of peak assignment.

C 1s Sub-Peak	BE (eV) | FWHM (eV) Area (%), relative to the total C 1s peak area [first assignment | second assignment]						C 1s Sub-Peak Interpretation	
	Reference sample		Liquid FLiBe-exposed		Cover gas-exposed			
	Point1	Point 2	Point 1	Point 2	Point 1	Point 2		
C sp²	284.3 | 1.1 73.7%	284.3 | 0.9 72.3%	284.3 | 0.9 66.1%	284.3 | 1.5 78.1%	284.3 | 1.1 63.1%	284.3 | 0.9 63.6%	sp²	(Blume et al. 2015; Larciprete et al. 2012)
C_1	283.5 | 0.6 3.7%	283.6 | 0.6 4.3%	283.7 | 0.7 9.5%	283.3 | 0.6 3.0%	283.5 | 0.6 5.5%	283.7 | 0.6 9.3%	Point defects	(Barinov et al. 2009; Blume et al. 2015; Larciprete et al. 2012)
C_2	284.8 | 1.3 8.6%	284.8 | 1.2 7.1%	284.8 | 1.9 7.6%	284.8 | 1.3 8.8%	284.8 | 1.3 8.6%	284.8 | 1.0 7.5%	sp³	(Blume et al. 2015; Larciprete et al. 2012; Theodosiou et al. 2020)
C_7	289.4 | 3.9 5.1%	290.4 | 2.8 5.5%	290.5 | 3.5 7.7%	289.9 | 3.7 4.8%	290.0 | 3.8 6.8%	290.1 | 4.5 10.0%	π- π*	(Blyth et al. 2000; Larciprete et al. 2012; Theodosiou et al. 2020)
C_3	285.7 | 0.8 3.6%	285.6 | 0.8 4.0%	285.8 | 0.6 1.0%	285.5 | 0.7 1.1%	285.6 | 0.7 4.4%	285.8 | 0.7 2.8%		
C_4	286.3 | 1.1 4.8%	286.4 | 1.0 3.5%	286.3 | 1.3 4.6%	286.2 | 1.1 2.1%	286.1 | 1.1 9.9%	286.3 | 1.2 5.0%	OC and FC groups	(Asanov et al. 1998; Blyth et al. 2000; Crassous et al. 2009; Larciprete et al. 2009, 2012a; Nansé et al. 1997; Sato et al. 2004; Touhara and Okino 2000; Tressaud et al. 1996; Yumitori 2000; Yun et al. 2007)
C_5	287.4 | 1.2 2.0%	287.2 | 1.5 1.1%	287.2 | 1.8 2.0%	287.3 | 0.9 1.1%	287.1 | 0.9 1.5%	287.3 | 1.3 1.6%		
C_6	288.6 | 0.7 0.3%	288.5 | 0.5 0.3%	288.0 | 1.8 1.4%	288.2 | 1.0 0.9%	288.1 | 0.8 0.3%	288.1 | 1.3 0.2%		
$\dfrac{A_{C_{sp2}} + A_{C7}}{A_{C2}}$	9.2	10.9	9.8	9.5	8.1	9.8	sp²/ sp³ ratio	

2.2.2.2. O 1s peaks

High-resolution O 1s peaks for two points on each sample are shown in Figure 2.6. All spectra are normalized to their respective C 1s maximum intensity and to C 1s peak location of 284.3 eV. Unlike C 1s spectra, O 1s peaks contain a limited number of sub-peaks that can be separated from

each other during peak-fitting. Following (Larciprete et al. 2012), the O 1s peak is fitted with four symmetric sub-peaks O_1 to O_4. The assignment of each sub-peak is reported in Table 2.4, alongside to Ω, which quantifies total amount of C-bound oxygen atoms relative to total number of carbon atoms, calculated as Equation 2.1:

$$\Omega = \frac{A_{O\,1s}/SF_O}{A_{C1s}/SF_C} \qquad\qquad 2.1$$

where SF_O and SF_C are oxygen and carbon sensitivity factors (SF_O=2.9, SF_C=1 in SDP v9.0).
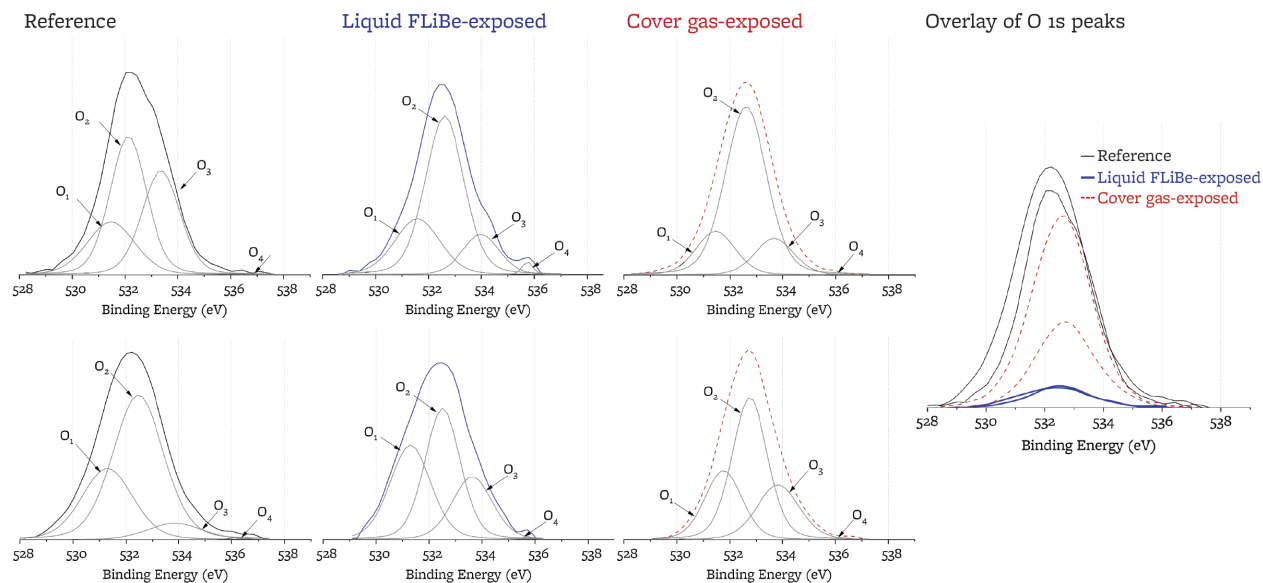
Notes
5-point Gaussian smoothing applied on all spectra. Two points are analyzed per sample. Peaks in overlay normalized to respective C 1s count rate intensities.

Figure 2.6: XPS O 1s peaks for reference and exposed IG-110. Peak-fitting parameters in Table 2.4.

Table 2.4: XPS O 1s peak fitting parameters for spectra in Figure 2.6. Rows are ordered by type of peak assignment.

O 1s Sub-Peak	BE (eV) | FWHM (eV) Area (%), relative to the total C 1s peak area						O 1s Sub-Peak Interpretation	
	Reference sample		Liquid FLiBe-exposed sample		Cover gas-exposed sample			
	Point 1	Point 2	Point 1	Point 2	Point 1	Point 2		
O_1	531.5 | 2.1 21.8%	531.4 | 2.2 30.3%	531.6 | 2.0 24.5%	531.3 | 1.8 35.0%	531.5 | 1.7 16.9%	531.8 | 1.6 25.8%	C=O	(Larciprete et al. 2012)
O_2	532.1 | 1.6 43.7%	532.5 | 2.3 61.7%	532.6 | 1.7 59.7%	532.5 | 1.6 42.3%	532.6 | 1.9 69.1%	532.8 | 1.6 50.8%	C-O in epoxy structure	(Larciprete et al. 2012)
O_3	533.4 | 1.7 34.2%	533.9 | 2.4 7.6%	534.0 | 1.6 14.4%	533.6 | 1.8 22.7%	533.7 | 1.7 14.0%	533.8 | 1.9 23.4%	C-O in ether structure	(Larciprete et al. 2012)
O_4	536.2 | 1.1 0.3%	536.3 | 1.0 0.4%	535.7 | 0.5 1.4%	535.7 | 0.5 0.3%	535.8 | 0.5 0.1%	536.6 | 0.5 0.1%	O-C=O	(Larciprete et al. 2012)
Ω	4.5%	6.9%	0.4%	0.4%	3.2%	1.7%	at% of carbon-bound oxygen relative to total number of carbon atoms	

Note: Area percentages are relative to the total O 1s peak area for each sample.

2.2.2.3. F 1s peaks

High-resolution F 1s peaks for two points on each sample are shown in Figure 2.7. All spectra are normalized to their respective C 1s intensity and to C 1s peak location of 284.3 eV. The F 1s peak is fitted with five symmetric sub-peaks F_1 to F_5. The sub-peaks are summarized in Table 2.5; low energy peaks are assigned to salt species LiF and BeF_2 and higher energy peaks are attributed to CF bonding.

The relative abundance of BeF_2 to LiF can be computed from the area ratio of peaks F_1 and F_2, with correction for the stoichiometric ratio of fluorine atoms bound to Li and Be. In liquid FLiBe, BeF_2:LiF is nominally 0.5, and the corresponding F_2:F_1 peak ratio would be 1. In gas phase in equilibrium with FLiBe at 700°C, the equilibrium BeF_2:LiF ratio is 10^7 at 700 °C and the BeF_2:$LiBeF_3$ vapor phase ratio is 11 at 700 °C and 16 at 460 °C. If F_1 is attributable to $LiBeF_3$, then the corresponding F_2:F_1 ratio for condensed (quenched) gas phase would be 8 at 700 °C and 11 at 460 °C (correcting for the fluorine stoichiometry) (Olander et al. 2002; Smith et al. 2020). For the liquid exposed sample, the observed F_2:F_1 peak ratio is 2.2(8); this value being above unity indicates that some amount of gas-transport into the surface porosity may be occurring. For the gas-exposed sample, the observed F_2:F_1 peak ratio is 20(17), much higher than for the liquid-exposed sample, as expected (Olander et al. 2002).

The peaks at higher energy are attributed to carbon-fluorine bonds, and their relative areas vary across the spectra. Sub-peak F_3, is attributed to semi-ionic carbon-fluorine bonds (Sato et al. 2004; Tressaud et al. 1996; Yun et al. 2007; Zhou et al. 2014). Sub-peak F_4 is attributed to covalent carbon-fluorine bonds (Nansé et al. 1997; Yun et al. 2007; Zhou et al. 2014). Both sub-peak F_3 and sub-peak F_4 have a large FWHM (>1.7 eV), suggesting that they may be in turn composed of sub-peaks associated to different bonds. Further peak-fitting of F_3 and F_4 is not conducted to avoid over-fitting. An additional peak at high binding energy, sub-peak F_5, is required for the fitting of the spectra of the sample exposed to gas above the salt, and it is attributed to covalent C-F bonds in CF_2 and CF_3 groups.
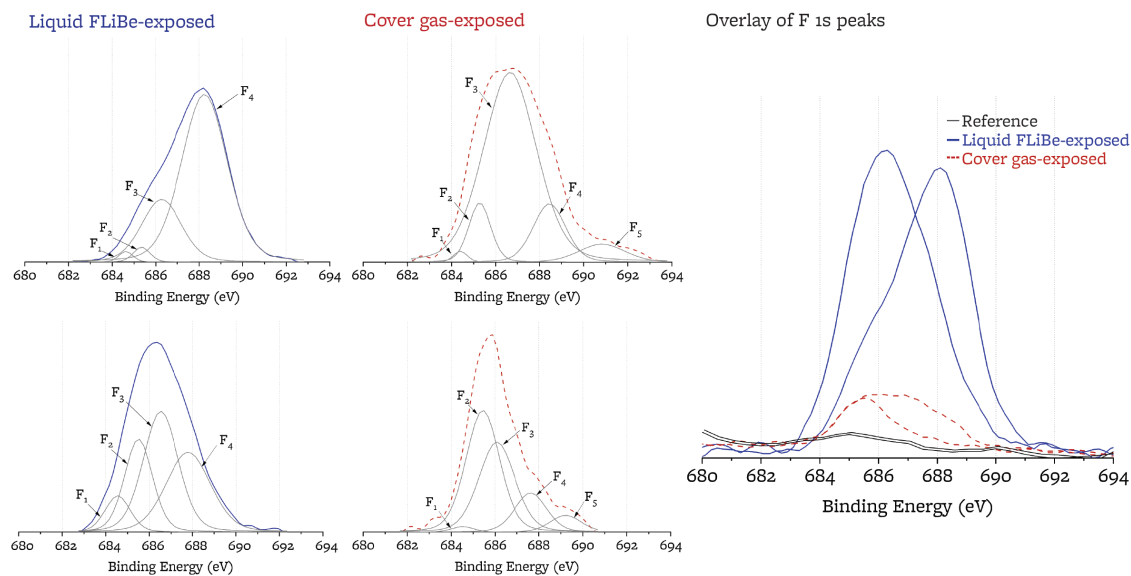
Liquid FLiBe-exposed   **Cover gas-exposed**   Overlay of F 1s peaks

Notes

5-point Gaussian smoothing applied on all spectra. Two points are analyzed per sample. Peak-fitting not performed for reference sample because of low F 1s signal. Peaks in overlay normalized to respective C 1s count rate intensities.

Figure 2.7: XPS F 1s peaks for reference and exposed IG-110 samples. Peak-fitting parameters in Table 2.5.

Table 2.5: XPS F 1s peak fitting parameters for spectra in Figure 2.7. Rows are ordered by type of peak assignment.

SF 1s Sub-Peak	BE (eV) | FWHM (eV) Area (%), relative to the total F 1s peak area				F 1s Sub-Peak Interpretation	
	Liquid FLiBe-exposed sample		Cover gas-exposed sample			
	Point 1	Point 2	Point 1	Point 2		
F_1	684.6 | 0.8 1.4%	684.5 | 1.4 8.1%	684.5 | 0.7 1.1%	684.5 | 1.2 1.3%	**LiF** or **LiBeF₃**	(Beamson and Briggs 1992; Cui et al. 2023; Darapaneni et al. 2022; Yang et al. 2016) hypothesized
F_2	685.3 | 0.9 2.3%	685.5 | 1.5 22.9%	685.4 | 1.2 9.1%	685.4 | 1.8 44.3%	**BeF₂**	(C.D. Wagner, W.M. Riggs, L.E. Davis, J.F. Moulder 1995; Murch and Thorn 1980)
F_3	686.3 | 2.2 23.6%	686.5 | 1.9 37.5%	686.8 | 2.9 70.8%	686.1 | 1.9 35.2%	**Semi-ionic C-F bonds**	(Asanov et al. 1998; Nansé et al. 1997; Sato et al. 2004; Tressaud et al. 1996; Yun et al. 2007)
F_4	688.2 | 2.5 72.6%	687.8 | 2.4 31.6%	688.6 | 1.7 13.3%	687.6 | 1.7 13.5%	**Covalent C-F bonds**	(Clark et al. 1973; Nansé et al. 1997; Yun et al. 2007)
F_5	-	-	690.9 | 2.5 5.8%	689.2 | 1.7 5.7%	**Covalent C-F bonds in CF2, CF3 groups**	(Yun et al. 2007)
F_2/F_1	1.7	2.8	8.5	33.2	Corresponding to (2 BeF₂)/LiF or (2 BeF₂)/ (3 LiBeF₃) Liquid: expect 1 or 0.67 Vapor space: expect 12 or 8 at 700 °C	
$\dfrac{A_{F1s}/SF_F}{A_{C1s}/SF_C}$	1.6%	1.2%	0.3%	0.2%	at% of fluorine relative to total number of carbon atoms	
Φ	1.6%	0.8%	0.3%	0.1%	Degree of fluorination	
$\dfrac{A_{F3}}{A_{F3}+A_{F4}+A_{F5}}$	24.5%	54.2%	78.8%	64.8%	% Semi-ionic F of CF in F 1s	

20

To assess the extent of fluorination, the *degree of fluorination* ϕ is defined (Equation 2.2), which quantifies total amount of C-bound fluorine atoms (F_C) relative to total number of carbon atoms:

$$\Phi = \frac{(A_{F3} + A_{F4} + A_{F5})/SF_F}{A_{C1s}/SF_C} \qquad 2.2$$

where SF_F is fluorine sensitivity factor (SF_F = 4.43 provided by SDP v9.0). Averaging over the two spectra of each sample, the sample exposed to liquid FLiBe has ϕ_{liq} = 1.2(5)%, while the sample exposed to the cover gas has ϕ_{gas} = 0.2(1)% (6 times lower). The comparison suggests that surface fluorination occurs to a larger extent in the sample exposed to molten FLiBe than in the cover gas. In both samples, fluorination occurs by formation of both semi-ionic and covalent C-F bonds. Semi-ionic bonds are bonds that involve sp^2-hybridized carbon atoms in the graphene planes and intercalated fluorine atoms without disrupting the planarity of the graphene planes, i.e., preserving the sp^2 hybridization of the carbon atoms (Mallouk et al. 1997). Covalent bonds involve sp^3 hybridized carbon atoms and can occur at crystallite edges (Krawietz and Haw 1998).

For the sample exposed to the liquid salt, one of the two points shows predominantly signal from semi-ionic bonds, while the other shows predominantly signal from covalent bonds. Averaging across the two points, covalent bonds are prevalent over semi-ionic with a ratio of 1.5:1 of covalent bonds to semi-ionic bonds. Semi-ionic bonds are the prevalent type of bonds for both points of the sample exposed to the cover gas above the salt, with a ratio of approximately 1:2.5 of covalent bonds to semi-ionic bonds.

2.2.2.4. *C KLL peak and D-parameter*

In literature, it is common to estimate the ratio of sp^2 to sp^3 bound carbon atoms by peak-fitting C 1s peaks and calculating the ratios of areas of peaks associated to sp^2 to sp^3 bound carbon atoms (Blume et al. 2015; Díaz et al. 1996; Jackson and Nuzzo 1995; Lascovich et al. 1991; Leung et al. 1999; Theodosiou et al. 2020). Due to the possible presence of C-F and C-O bonds, peak fitting of the C1s peak can be ambiguous. The D parameter, i.e. the difference between the maxima and minima of the first derivative of the C KLL spectra (Mizokawa et al. 1987; Theodosiou et al. 2020), has been shown to correlate linearly with the sp^2 content (Mizokawa et al. 1987) and is therefore an independent metric for the sp^2 to sp^3 ratio that removes the ambiguity from peak-fitting. The D-parameters are calculated after 3-points adjacent averaging for all C KLL peaks (Lesiak et al. 2018) and plotted in Figure 2.8 against the sp^2 to sp^3 ratio from C 1s peak fitting. (Lesiak et al. 2018) reports that the D-parameter is influenced by oxygen content. Plotting the D-parameter against the oxygen content, a correlation between the two is not observed for the present samples, providing confidence that the D-parameter is a good indicator of sp^2/sp^3 content for the present samples (Figure 2.8).

The calculated D-parameters and sp^2 / sp^3 ratios (Figure 2.8) show large intra-sample variability for both the reference and exposed samples. This variability may reflect heterogeneity of sp^2 and sp^3 carbon content across locations of the sample (e.g., filler, binder, pore edge) and does not allow to conclude whether a change in sp^2 and sp^3 content takes place with exposure.

Figure 2.8: Example of D parameter calculation from C KLL peak and correlation of D parameter with sp²/sp³ ratio from C 1s peak and oxygen content from O 1s area.
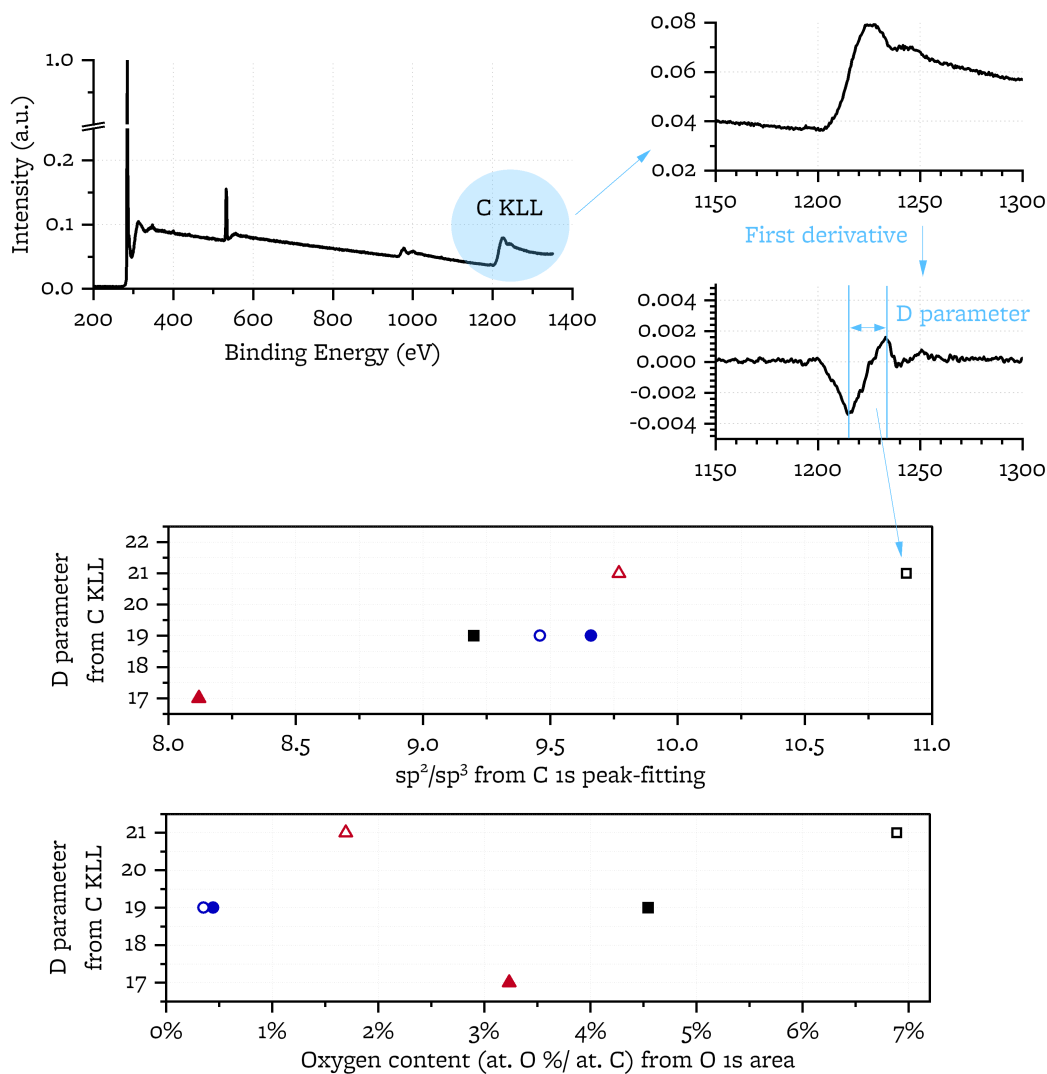
Notes:
Reference sample datapoints in **black** squares, liquid FLiBe-exposed sample datapoints in **blue** circles, gas-exposed sample datapoints in **red** triangles. Full and empty symbols refer to two points on each sample. Oxygen content calculated as in Equation 1.

2.2.3 Depth profiling

Argon ion sputtering is used to acquire XPS F 1s and C 1s peaks at ten different depths from the surface. Depth D9 is estimated at less than 100 nm. Figure 2.9 shows the C 1s and F 1s peaks at the different depths for two points on the sample exposed to liquid salt for 240h. The C 1s peaks do not display differences in peak profile or shape at increasing depth from the surface. The F1 s peaks for both points show a change in shape with an increase in relative intensity at binding energies of 686-687 eV (attributed to semi-ionic C-F bonds), and a decrease in relative intensity at binding energies of 688-689 eV (attributed to covalent C-F bonds). Full peak-fitting parameters are included in Mendeley Data repository linked in Supplementary Information.
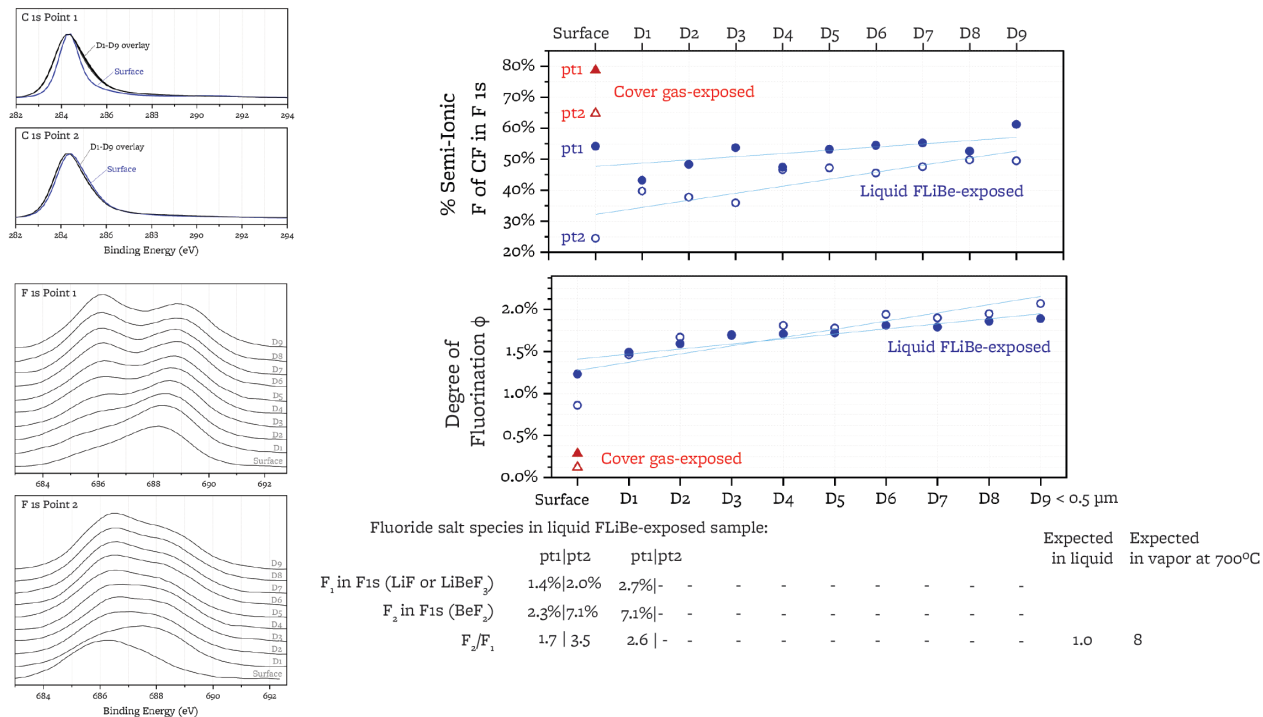
Figure 2.9: XPS depth profiling of the liquid FLiBe-exposed IG-110 sample.

Fluoride salt species in liquid FLiBe-exposed sample:

	Surface pt1|pt2	D1 pt1|pt2	D2	D3	D4	D5	D6	D7	D8	D9 < 0.5 µm	Expected in liquid	Expected in vapor at 700°C
F_1 in F1s (LiF or LiBeF$_3$)	1.4%|2.0%	2.7%|-	-	-	-	-	-	-	-	-		
F_2 in F1s (BeF$_2$)	2.3%|7.1%	7.1%|-	-	-	-	-	-	-	-	-		
F_2/F_1	1.7 | 3.5	2.6 | -	-	-	-	-	-	-	-	-	1.0	8

The ratio of the F 1s area associated to C-F bonds to the C 1s area suggests a slight increase fluorination parameter Φ from 1.2(5)% F_C/C at the surface to 2.0(1)% F_C/C at depth D9 (Figure 2.9). Peak-fitting of the F 1s peaks suggests an increase of the semi-ionic character of the C-F bonds with depth. Averaging across the two points sampled on the surface of the salt-exposed sample, 40% of the carbon-bound fluorine atoms on the surface are involved in semi-ionic bonds. At depth D9, the percentage increases to 55%.

Signals for LiF and BeF$_2$ are visible on the surface for one point and on the surface and at depth D1 for the other point. This indicates that FLiBe penetration in the sample is limited to the region sputtered in the first step. The F$_2$:F$_1$ ratio is calculated in the range of 1.7 to 3.5, which is closest to liquid FLiBe (1 expected value for liquid phase), but nevertheless more abundant in BeF$_2$ than liquid FLiBe, as observed for FLiBe vapor species (8 expected value for vapor phase at 700°C, and 11 at 460 °C).

2.2.4 Raman analysis

Raman spectra (sampling depth: approximately 120 nm (Scharf and Singer 2003), sampling diameter: approximately 1 µm (Wu et al. 2020a) with 532 nm laser source) are collected at five points on each sample and displayed in Figure 2.10. The location of the peaks composing the spectra is consistent with previous results for nuclear graphite. Raman spectra for IG-110 were included in (Wu et al. 2018b, 2020a; b; Zheng et al. 2014) and show narrow D, G, and D' bands at approximately 1350 cm^{-1}, 1580 cm^{-1}, and 1610 cm^{-1} wavenumbers in the first order spectrum

and T+D, G', and D'+D band at approximately 2450 cm^{-1}, 2700 cm^{-1}, and 2950 cm^{-1} wavenumbers in the second order spectrum.

Upon exposure, multiple features of the Raman spectra are shown to change: both the intensity of the D band and full width half maximum (FWHM) of the G band increase; the intensity between the D and the G band does not fall below 0.1, leading to the appearing of a bridge; the intensity of the G' band decreases.

Peak-parameters of the D, G, and G' bands are used to estimate graphite crystallite parameters L_a and L_c, according to the correlations in (Cançado et al. 2008; Maslova et al. 2012; Tuinstra and Koenig 1970) and as shown in previous studies that used Raman spectroscopy to characterize graphite (Vergari et al. 2023b; Wu et al. 2018b, 2020d) (Table 2.6). Raman analysis suggests an increase of the I(D)/I(G) ratio and a broadening of the full width half maximum (FWHM) of the G band, which correlate to a statistically significant decrease of the basal crystallite parameter L_a (Cançado et al. 2008; Maslova et al. 2012; Tuinstra and Koenig 1970). The crystallite parameter L_a decreases more in the salt-exposed sample than in the gas-exposed sample (respectively 50% and 40% decrease vs reference). The intensity of the G' band decreases with exposure, but the peak decomposition between the G'2D and the two G'3D peaks does not change significantly for either sample, yielding a degree of stacking order R and a crystallite parameter L_c statistically unchanged with exposure to either liquid salt or to the cover gas above it (Table 2.6). Overall, this suggests that exposure to the liquid salt and the gas above yield the same type of microstructural changes and that these changes are higher upon liquid exposure.

Raman Spectra
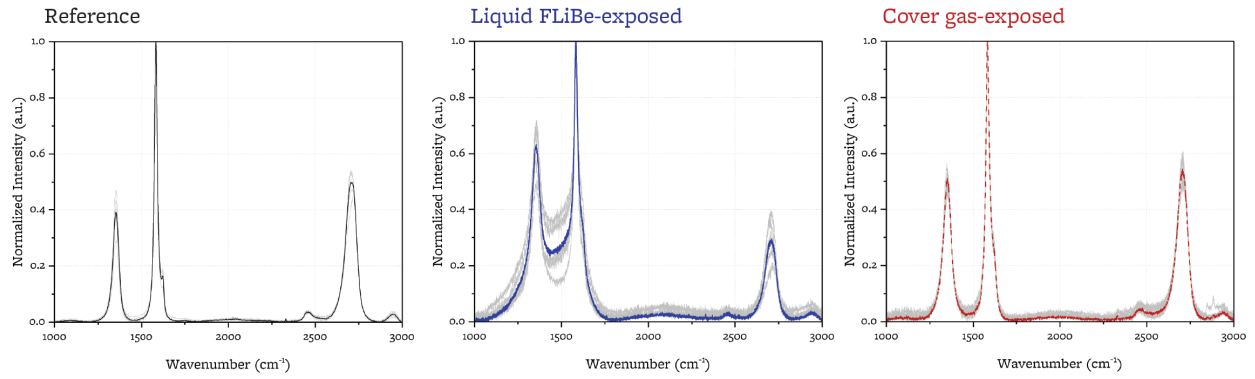
Peak-Fitting Examples
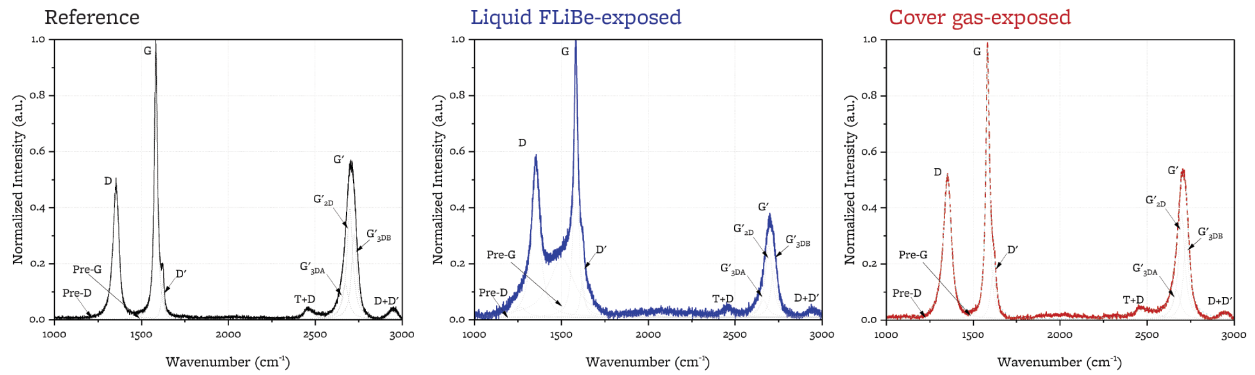
Notes
Top row: spectra collected on five points of each sample (gray lines) and averages for each sample.
Bottom row: example peak-fitted spectra for each sample.

Figure 2.10: Raman spectra for reference and exposed IG-110 samples.

Table 2.6: Raman figures of merits and crystallite microstructural parameters (calculated from Raman spectra in Figure 2.10).

	Reference	Liquid FLiBe-exposed	Cover gas-exposed
I(D)/I(G)	0.41(6)	**0.68(12)**	**0.54(4)**
≠ Reference Sample (p-value)		0.001	0.002
Cover gas-exposed ≠ Liquid FLiBe-exposed (p-value)			0.03
FWHM(D) (cm^{-1})	36 (1)	**67(7)**	**50(2)**
≠ Reference Sample (p-value)		<0.001	<0.001
Cover gas-exposed ≠ Liquid FLiBe-exposed (p-value)			0.001
FWHM(G) (cm^{-1})	20(1)	**29(3)**	**24(2)**
≠ Reference Sample (p-value)		<0.001	0.001
Cover gas-exposed ≠ Liquid FLiBe-exposed (p-value)			0.02
A(G') *% to total spectrum area*	43(1)%	**14(5)%**	**35(1)%**
≠ Reference Sample (p-value)		<0.001	<0.001
Cover gas-exposed ≠ Liquid FLiBe-exposed (p-value)			<0.001
Degree of stacking order R (Cançado et al. 2008) *from G' peak decomposition in G'2D and G'3DB*	47(8)%	41(10)%	41(6)%
≠ Reference Sample (p-value)		0.34	0.19
Cover gas-exposed ≠ Liquid FLiBe-exposed (p-value)			0.88
c (nm) (Cançado et al. 2008) *from G' peak decomposition in G'2D and G'3DB*	0.6768(9)	0.6774(11)	0.6775(7)
≠ Reference Sample (p-value)		0.34	0.19
Cover gas-exposed ≠ Liquid FLiBe-exposed (p-value)			0.88
L_a (nm) (Tuinstra and Koenig 1970) *from D/G Area ratios*	27(4)	**13(2)**	**18(1)**
≠ Reference Sample (p-value)		<0.001	<0.001
Cover gas-exposed ≠ Liquid FLiBe-exposed (p-value)			0.001
L_a (nm) (Maslova et al. 2012)*from FWHM(G)*	68(10)	**30(7)**	**43(6)**
≠ Reference Sample (p-value)		<0.001	<0.001
Cover gas-exposed ≠ Liquid FLiBe-exposed (p-value)			0.014
L_c (nm) (Cançado et al. 2008) *from G' peak decomposition in G'2D and G'3D$_B$*	27(3)	26(2)	26(1)
≠ Reference Sample (p-value)		0.37	0.18
Cover gas-exposed ≠ Liquid FLiBe-exposed (p-value)			0.76

Note: values in bold indicate a significant difference (p<0.05). Raman sampling depth: approximately 120 nm (Scharf and Singer 2003), sampling diameter: approximately 1 µm (Wu et al. 2020a)

2.3   Discussion

2.3.1   Interpretation of XPS parameters sensitive to fluorination
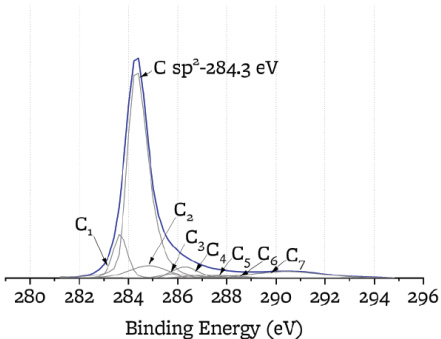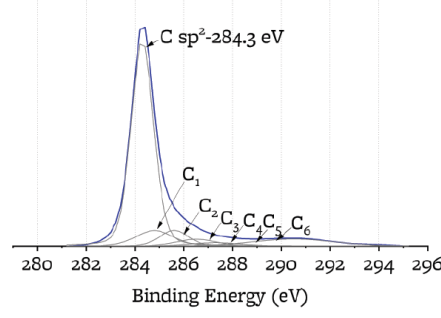
The nature of the chemical interaction between FLiBe and nuclear graphite is reflected in multiple features of XPS and Raman spectra, with some of them being more effective than others in characterizing the interaction.

The XPS survey scanning the full BE range is helpful to identify what chemical species in addition to carbon are present on the surface of the sample. This information can help restrict the candidate attributions of the C 1s sub-peaks, in the case this is peak fitted.

The C 1s XPS peaks contain information about the chemical nature of the carbon atoms at the surface of the sample and can indicate the presence of fluorine-carbon bonds, for example by sub-peaks in the 285 to 289 eV range, between the main sp^2, sp^3 peaks and the π- π* peak. Nevertheless, peak-fitting of C 1s peak is complex, since, in addition to the main C sp^2 sub-peak, it comprehends multiple low-intensity sub-peaks that can be attributed to either C-F or C-O bonds or other types of defects (Crassous et al. 2009; Nansé et al. 1997). As a result, peak-fitting of the C 1s for species at sub 1% concentration may not be univocal or reproducible by other researchers performing similar analysis on the same data. An example showing this issue is included in Table 2.7, where two possible ways of peak fitting and interpreting C 1s spectrum for the same sample are illustrated,

26

which lead to 1 and 7 for the semi-ionic C-F to covalent C-F ratio, and 10 and 9 for the sp^2/sp^3 ratio. Thus, characterization of C-O and C-F bonds in graphite is based on O1s and F1s peak-fitting, and characterization of sp^2/sp^3 ratio is based on the D parameter from the C KLL peak. For the F1s peak, salt residuals (LiF, BeF$_2$, LiBeF$_3$, Li$_2$BeF$_4$) would lead to peaks at 684-685 eV binding energy (Beamson and Briggs 1992; C.D. Wagner, W.M. Riggs, L.E. Davis, J.F. Moulder 1995; Murch and Thorn 1980) and C-F bonds lead to peaks above 686 eV (Asanov et al. 1998; Nansé et al. 1997; Sato et al. 2004; Tressaud et al. 1996; Yun et al. 2007), with semi-ionic C-F at 686-687 eV and covalent C-F above 687 eV.

Table 2.7: Examples of peak-fitting results for C 1s peak of liquid-FLiBe exposed sample

Fit 1
8 sub-peaks
χ^2= 6.4
C sp² asimmetry : 17%

C sp²-284.3 eV

Sub-Peak	BE (eV) | FWHM (eV) Area (%)	Sub-Peak Interpretation	
C sp²	284.3 | 0.9 66.1%	sp²	(Blume et al. 2015; Larciprete et al. 2012)
C$_1$	283.7 | 0.7 9.5%	Point defects	(Barinov et al. 2009; Blume et al. 2015; Larciprete et al. 2012)
C$_2$	284.8 | 1.9 7.6%	sp³	(Blume et al. 2015; Larciprete et al. 2012; Theodosiou et al. 2020)
C$_7$	290.5 | 3.5 7.7%	π- π*	(Blyth et al. 2000; Larciprete et al. 2012; Theodosiou et al. 2020)
C$_3$	285.8 | 0.6 1.0%	C-O-C ether	(Larciprete et al. 2012)
C$_4$	286.3 | 1.3 4.6%	C-O-C epoxy and/or C-CF$_n$	(Crassous et al. 2009; Larciprete et al. 2012; Yumitori 2000) (Crassous et al. 2009)
C$_5$	287.2 | 1.8 2.0%	C=O and/or semi-ionic C-F	(Blyth et al. 2000; Crassous et al. 2009; Larciprete et al. 2012; Yumitori 2000) (Crassous et al. 2009; Nansé et al. 1997; Touhara and Okino 2000; Tressaud et al. 1996; Yun et al. 2007)
C$_6$	288.0 | 1.8 1.4%	O-C=O and/or covalent C-F	(Blyth et al. 2000; Crassous et al. 2009; Larciprete et al. 2009, 2012a; Yumitori 2000) (Crassous et al. 2009; Nansé et al. 1997; Touhara and Okino 2000; Tressaud et al. 1996)

Fit 2
7 sub-peaks
χ^2= 7.3
C sp² asimmetry : 5%

C sp²-284.3 eV

Sub-Peak	BE (eV) | FWHM (eV) Area (%)	Sub-Peak Interpretation	
C sp²	284.3 | 1.1 68.8%	sp²	(Blume et al. 2015; Larciprete et al. 2012)
C$_1$	284.8 | 1.8 8.7%	sp³	(Blume et al. 2015; Larciprete et al. 2012; Theodosiou et al. 2020)
C$_6$	290.5 | 4.0 8.7%	π- π*	(Blyth et al. 2000; Larciprete et al. 2012; Theodosiou et al. 2020)
C$_2$	285.6 | 1.4 6.8%	C-CO	(Blyth et al. 2000; Crassous et al. 2009)
C$_3$	286.5 | 1.9 4.1%	C-O and/or C-CF$_n$	(Crassous et al. 2009; Larciprete et al. 2009; Yumitori 2000) (Crassous et al. 2009)
C$_4$	287.3 | 2.5 2.6%	C=O and/or semi-ionic C-F	(Blyth et al. 2000; Crassous et al. 2009; Larciprete et al. 2012; Yumitori 2000) (Crassous et al. 2009; Nansé et al. 1997; Touhara and Okino 2000; Tressaud et al. 1996; Yun et al. 2007)
C$_5$	288.7 | 2.6 0.4%	O-C=O and/or covalent C-F	(Blyth et al. 2000; Crassous et al. 2009; Larciprete et al. 2009, 2012a; Yumitori 2000) (Crassous et al. 2009; Nansé et al. 1997; Touhara and Okino 2000; Tressaud et al. 1996)

Notes: Spectra collected on liquid FLiBe-exposed sample. 5-point Gaussian smoothing applied on both spectra

2.3.2 Interpretation of Raman parameters sensitive to fluorination

Raman spectra have been widely used to extract information on the microstructural parameters of graphite at depth up to a few nm (Cançado et al. 2008; Vergari et al. 2023a; Wu et al. 2020a). Studies using Raman spectroscopy to characterize fluorinated graphite samples have indicated multiple changes (tabulated in Table 2.8) consistent with a loss of crystal order in the graphite. These changes have been observed both for samples containing semi-ionic -CF (Nakajima et al. 1999; Robinson et al. 2010; Wu et al. 2018a) and samples containing covalent C-F (Gupta et al. 2003; Nakajima et al. 1999; Wu et al. 2018a) , produced in gas-phase reactions (Gupta et al. 2003; Nakajima et al. 1999; Robinson et al. 2010) and liquid phase reactions in molten salts (Tian et al. 2017 p. 201; Wu et al. 2018a). Raman spectra indicate a higher content of surface defects after salt-exposure that appear as a consequence of graphite-fluorination processes. It is noted that similar Raman features appear in graphite not exposed to fluorine but used in experiments involving high-temperature tribological experiments (Chapter 4), ball milling (Niwase et al. 1995; Welham et al. 2003), and irradiation (Ammar et al. 2015; Nakamura et al. 1990) (Table 2.9).

Table 2.8: Summary of XPS and Raman observations in graphite fluorination studies

Sample Type	Fluorinating agent	Temperature	Exposure duration	Degree of fluorination ϕ	XPS observations	Raman observation	XRD observations	Reference
Natural graphite powder	F_2	80°C -520°C	2 min – 10 min	up to 18%	T < 150°C : F 1s shows peak for semi-ionic CF; T > 150°C : F 1s shows peak for covalent CF	Increase in I(D)(/I(G), FWHM(D), FWHM(G), FWHM (2G). Decrease in I(G').	T < 150°C : decrease in crystallite size along c axis L_c; T > 150°C : no change in crystallite size along c axis L_c	(Nakajima et al. 1999)
Graphene films	XeF_2	Room temperature	up to 300 s	up to 25%	F 1s main peaks attributed to semi-ionic CF	Increase in I(D)(/I(G), FWHM(D), and FWHM(G).	N/A	(Robinson et al. 2010)
Graphite	F_2, K_2NiF_6, and $KAgF_2$	Room temperature, 380°C, 515°C	1 min – 2 weeks	5% to 94%	N/A	Increase in I(D)(/I(G), FWHM(D), and FWHM(G). Appearance of shoulder between D and G bands.	Room temperature and T = 380°C: increase in measured interplanar distance. T = 515°C: loss of crystal structure.	(Gupta et al. 2003)
Nuclear graphite IG-110	Liquid FLiBe	700°C	12 h	<0.1 %	F 1s shows peaks for semi-ionic CF and covalent CF. % semi-ionic CF > % covalent CF	Increase in I(D)/I(G). FWHM(D), FWHM(G). Decrease in I(G') and A(G'). Appearance of shoulder between D and G bands.	Increase in measured interplanar distance c.	(Wu et al. 2018a)
Nuclear graphite IG-110	Liquid FLiBe	700°C	240 h	1.2(5) %	F 1s shows peaks for semi-ionic CF and covalent CF. % semi-ionic CF < % covalent CF	Increase in I(D)/I(G). FWHM(D), FWHM(G). Decrease in I(G') and A(G'). Appearance of shoulder between D and G bands.	N/A	This study
Nuclear graphite IG-110	Cover gas above FLiBe	700°C	240 h	0.20(12) %	F 1s shows peaks for semi-ionic CF and covalent CF. % semi-ionic CF > % covalent CF	Same changes as for liquid-FLiBe-exposed but to a smaller degree.	N/A	This study

Table 2.9: Examples of graphite surface modification studies that do not involve fluorination and exhibit defects probed by Raman spectroscopy similar to those observed in fluorination.

Experiment Type	Temperature	Atmosphere and duration	Sample Type	Raman observation	Reference
Graphite-on-graphite wear testing	600 °C	Ar gas, 1 h	Nuclear graphite ET-10	Increase in I(D)/I(G), FWHM(D), FWHM(G). Decrease in I(G') and A(G'). Appearance of shoulder between D and G bands.	(Vergari et al. 2023a; b) Chapter 4
Stainless steel and agate ball milling	Room temperature	Ar gas, up to 5000 h	Graphite powder	Increase in I(D)/I(G), FWHM(D), FWHM(G). Appearance of shoulder between D and G bands. Loss of D and G band distinction after 1000's h milling.	(Niwase et al. 1995)
Stainless steel ball milling	Room temperature	Vacuum, 1000 h	Graphite powder	Increase in I(D)/I(G), FWHM(D), FWHM(G). Appearance of shoulder between D and G bands.	(Welham et al. 2003)
Electron beam irradiation	Room temperature	Ar gas, 5s	Isotropic graphite T-6P	Decrease in I(D)/I(G). Increase in FWHM(G).	(Nakamura et al. 1990)
$^{37}Cl^+$ ion beam irradiation	Room temperature - 600°C	N/A	Nuclear graphite	Increase in I(D)/I(G), FWHM(D), FWHM(G). Decrease in I(G') and A(G'). Appearance of shoulder between D and G bands and disappearance of D and G band at increasingly high fluences. Changes more pronounced at low temperatures and high fluences.	(Ammar et al. 2015)

2.3.3   Time-dependence of chemical and microstructural changes

To investigate time-evolution of graphite exposed to molten FLiBe, the 240-hour exposure from this study is compared with the 12-hour exposure from (Wu et al. 2018a) (Table 2.10). XPS and Raman spectra from (Wu et al. 2018a) are re-analyzed to be methodologically consistent with the new data presented here, since some of the peak fitting parameters used in (Wu et al. 2018a) (e.g., number and shape of XPS and Raman peaks, Raman constraints) differ from those used here; all re-analyzed results are included in the Mendeley Data repository linked in Supplementary Information. The fluorine content on the graphite exposed to liquid salt for 12h is lower than that on the graphite exposed for 240h by a factor of 7. With longer exposure, the F 1s spectrum shifts towards higher binding energies, indicating a higher relative amount of covalent C-F as opposed to semi-ionic C-F (Figure 2.11). This leads to the conclusion that the kinetics of covalent C-F formation is slower than that of semi-ionic C-F formation. Surface microstructural changes as characterized by Raman are similar between the 12 hour and the 240-hour exposure. The oxygen content after the 12h exposure is lower than in the reference sample, and it remains more than double the oxygen content after 240 hours. The sum of oxygen and fluorine content after exposure is lower than the oxygen content of the non-exposed reference samples. These observations indicate that (i) fluorination occurs over a timescale longer than tens of hours, (ii) oxygen content decrease has a different time-constant than fluorination (iii) intercalation fluorine species occurs before formation of covalent C-F bonds; and (iv) surface microstructural changes occur within 12 hours of liquid exposure. Further studies are needed to establish the relationships among chemical and surface microstructural modifications in graphite upon exposure to molten salt and the cover gas above it, to confirm the formation of covalent and semi-ionic C-F, and to developing a mechanistic description for the formation of covalent and semi-ionic C-F with exposure to salt and to the cover-gas above the salt.
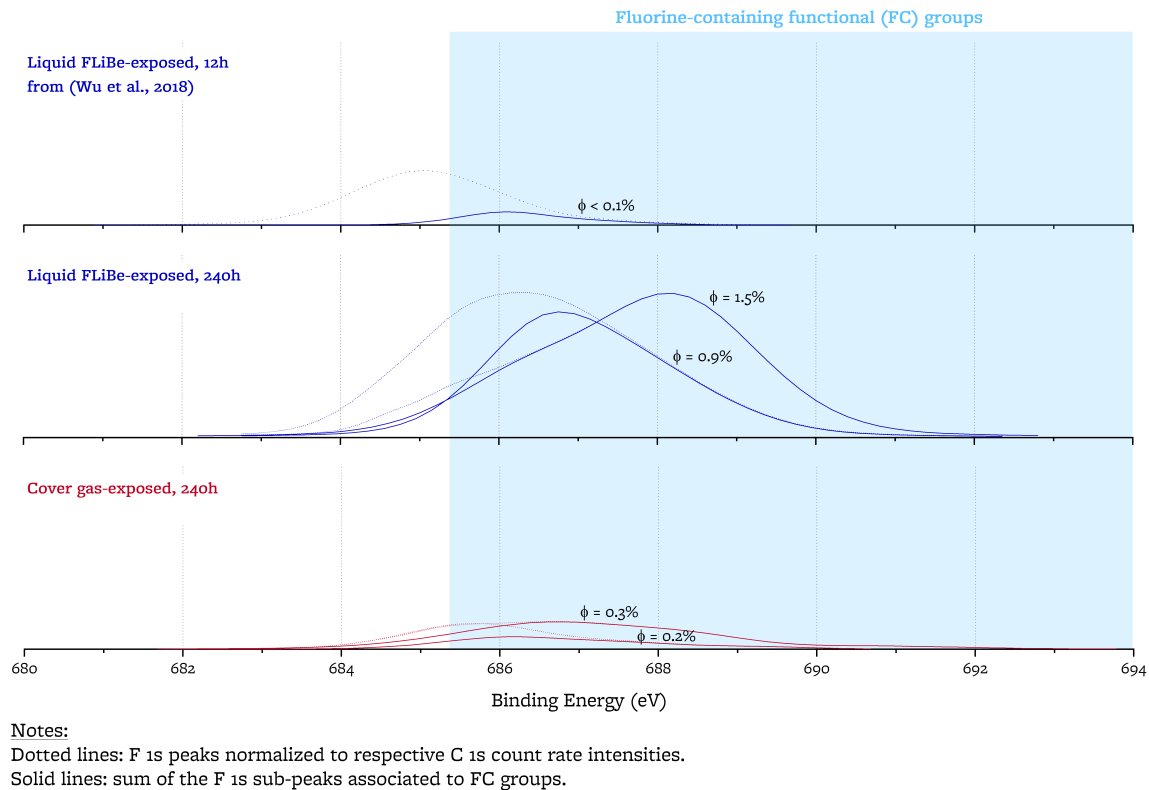
Figure 2.11: Comparison of the F 1s XPS spectra of the sample exposed to liquid FLiBe for 12 hours in (Wu et al. 2018a) and the samples exposed to liquid FLiBe and the cover gas above it for 240 hours and presented in this study.

Notes:
Dotted lines: F 1s peaks normalized to respective C 1s count rate intensities.
Solid lines: sum of the F 1s sub-peaks associated to FC groups.

Table 2.10: Summary of comparative metrics of graphite surface modifications upon exposure to FLiBe at 700 °C.

	Depth of sampling (nm) [1]		Reference	Liquid FLiBe-exposed, 12h (Wu et al. 2018a)	Liquid FLiBe-exposed, 240h	Cover gas-exposed, 240h
XPS, Sampling diameter = 400 µm		n =	2	1	2	2
Survey	2-12	O (at. %)	5.4(1.4)	1.0	0.39(5)	2.37(11)
		F (at. %)	-	0.2	1.4(2)	0.27(7)
		C (at. %)	93.6(1.9)	98.2	98.2(3)	96.9(1.5)
O 1s	8	Ω (CO/C at. %)	5.7(1.7)	1.0	0.40(6)	2.5(1.1)
		BeF$_2$/LiF area ratio (corrected by stoichiometry)	-	1.3	1.1(4)	10(9)
F 1s	7	F (at. %)	-	0.3	1.4(2)	0.27(7)
		ϕ (CF/C at. %)	-	<0.1	1.2(5)	0.20(12)
		%SI (Semi-ionic F/CF at.%)	-	74	39(21)	72(10)
		$\phi_{semi-ionic}$ (CF/C at. %)		<0.07	0.5(3)	0.14(8)
		$\phi_{covalent}$ (CF/C at. %)		<0.03	0.7(3)	0.06(8)
C 1s		sp^2/sp^3 from C 1s	10.1(1.2)	9.6	9.7(2)	9.0(1.2)
C KLL	3	D parameter (indicative of sp^2/sp^3)	20 (1)	19	19 (-)	19 (2)
Raman, Sampling diameter = 1 µm (Wu et al. 2020a)		n =	5	5	5	5
	120	I(D)/I(G)	0.41(6)	0.60(17)	0.68(12)	0.54(4)
		FWHM(D)	36.4(1.0)	81(25)	66(7)	50(2)
		FWHM(G)	20.4(0.8)	29(5)	29(3)	24.1(1.7)
		A(G')	43.2(1.0)	14(2)	15(5)	35.1(1.2)
		Degree of Graphitization (%)	47(8)	33(16)	41(10)	41(6)
		c (nm) (Cançado et al. 2008)	0.6768(9)	0.6784(18)	0.6774(11)	0.6775(7)
		L$_a$ (nm) (Tuinstra and Koenig 1970)	27(4)	13(3)	13(2)	17.6(6)
		L$_c$ (nm) (Cançado et al. 2008)	27(3)	25(4)	26(2)	25.6(1.4)
Data Analysis [2]						
Semi-ionic F		C$_{bulk}$/C$_{total}$ (%)	96.6(5)	93.0(1.6)	93.0(1.1)	94.8(1.8)
		Semi-Ionic C-F/ C$_{bulk}$ (%)	-	0.08(1)	0.5(3)	0.15(2)
Covalent CF		C$_{edge}$/C$_{total}$ (%)	3.4(5)	7.0(1.6)	7.0(1.1)	5.2(1.8)
		Covalent C-F/ C$_{edge}$ (%) [3]	-	0.37(9)	10.4(3.9)	1.1(5)
		C-O/ C$_{edge}$ (%) [3]	160(50)	14(3)	5.7(1.2)	50(30)
		(Covalent C-F + C-O)/ C$_{edge}$(%) [3]	160(50)	15(3)	16(4)	50(30)
		$\phi_{covalent}$ + Ω (C at. %)	5.7	1.0	1.1	2.56

Notes:
(1) XPS [36,37] and Raman [31] sampling depth defined as the depth from which 99% of the signal is originated
(2) Cbulk = Ctotal – Cedge and Cedge/Ctotal = (0.15 nm^3)/ (c*a*La) from Eq. 15 of [70], with a=0.246 µm from XRD in (Wu et al. 2020a) and c and L$_a$ from Raman.
(3) Since one or multiple F atoms can be bound to a common C atom, the % CF and % CO occupancy of the edge atoms on graphite crystallite surfaces can be smaller than the Covalent C-F/ Cedge ratio

Figure 2.12 displays the C-F depth profile computed based on the GDMS depth profiling from Ref (Wu et al. 2018a) (12 hour liquid FLiBe exposure), showing that ϕ is in agreement with F1s ϕ for this sample. ϕ increases with depth, followed by a decrease past one µm of depth. This initial increase in ϕ with depth is also seen in the XPS depth profiling (limited to up to 100nm of depth) for the 240-hour liquid-exposed sample. The mechanism that leads to lower ϕ at the surface will need further investigation; it may be explained by differences in transport properties of different C-F species and differences among kinetics of formation and of conversion among the different types of C-F.

Calculations based on: GDMS Li, Be, and F depth profiling data.
F calibration is based on calibrated wppm for Be and Li,
assuming the following parameters that were determined by F 1s XPS:
(1) surface F is predominantly LiF and BeF_2 (2) BeF_2: LiF=1.4:1.
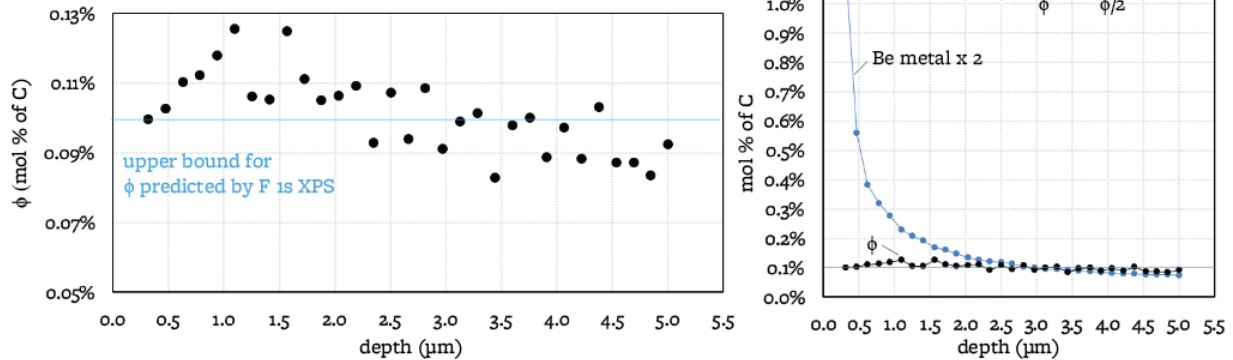
Figure 2.12. ϕ and Be metal depth profiling calculated from GDMS data from IG-110 sample with 12-hour exposure to liquid FLiBe (Wu et al. 2018a).

From GDMS depth profiling, it is observed a Be metal concentration that is initially above corresponding C-F concentration that would be produced by the reaction:

$$BeF_2\,(salt) + 2C\,(graphite) \leftrightarrow 2C - F\,(graphite) + Be\,(metal)$$
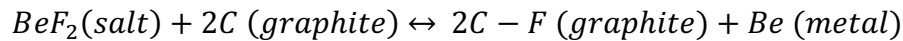
Thus, it is postulated that this reaction occurs at the salt-graphite interface and is followed by transport of Be metal and C-F into the graphite, and that Be metal progression into the graphite appears to be slower than C-F progression into the graphite. The SEM/EDS observation (Figure 2.2) of sparse F-containing spherical particles (attributed to BeF_2 and LiF) in the graphite pores below the surface and not only on the surface may suggest that the reaction may also occurring in the pore space in first microns below the surface. Integrating the total content of Be metal and approximating the C-F concentration profile as a square wave, one would deduce C-F presence to a depth of > 10 µm at a ϕ content of 0.07% for the 12-hour liquid FLiBe exposure.

2.3.4   Comparison between liquid-phase and gas-phase exposure

SEM/EDS shows localized fluorine-rich regions (at the microns to sub-micron length scale) and XPS F 1s spectra (400 µm sampling diameter) show C-F bond formation in both cover-gas exposed and liquid-FLiBe exposed graphite samples. Fluorination occurs to a larger extent in the sample exposed to liquid FLiBe than to the cover gas: $\phi_{liq} = 1.2(5)\%$, $\phi_{gas} = 0.2(1)\%$ (Table 2.10).

Two types of CF bonds are observed in the F 1s peak: covalent C-F and semi-ionic C-F. Covalent C-F bonds are hypothesized to form at crystallite edges (similarly to how oxygen has been shown to bind at crystallite edges (Markin et al. 1997; Otake and Jenkins 1993; Pan and Yang 1992)), in alignment with no measurable changes in sp^2/sp^3 ratio (based on XPS C 1s and C KLL); however, the standard deviations on sp^2/sp^3 are greater than 10%, so if any changes were to occur they would not be distinguishable. The occupancy of covalent C-F bonds on carbon edge sites is observed to be up to 10% (correcting for the fact that C_{edge}/C_{total} increases after salt exposure, see Table 2.10). Raman spectroscopy suggests a decreased basal crystallite size L_a, and thus a corresponding increase in carbon edge sites available for hosting covalent C-F bonds without increasing the sp^3 content.

33

C-O bond removal is also observed by O1s XPS, with liquid-exposed having more removal of C-O bonds than the gas-exposed sample (Table 2.10). Since it C:O and C:F stoichiometry is not a priori known, one cannot precisely say if sites of oxygen removal from C-O bonds correspond in magnitude to the density of sites of C-F formation (Table 2.10); as an order of magnitude, however, it is possible to compare remaining C-O + C-F to initial C-O on the reference sample: for the cover-gas sample this value is within two standard deviations of the reference sample, for the liquid-exposed samples, this value is a factor of ten lower (more than two standard deviations away from the reference sample) and interestingly it is the same value for the 12h and the 240h exposures, except that the short exposure has predominantly C-O and the long exposure has predominantly C-F. With only one data point it is hard to draw conclusions about the role of C-O removal in the formation of C-F bonds, but future studies are warranted to further probe this question, by salt-exposure of graphite with different levels of C-O content, and by O 1s XPS depth profiling along with F 1s depth profiling.

Semi-ionic C-F is hypothesized to occur as intercalates between the graphene planes. The abundance of semi-ionic F/C_{bulk} is observed to be up to 0.5% (correcting for the fact that C_{bulk}/C_{total} decreases after salt exposure, see Table 2.10). Fluorine intercalates would be expected to increase the graphene layer spacing, as measured by Raman and XRD, however, at 0.5% intercalate content, these changes would be on the order of 0.007Å (assuming 4.7Å graphene layer spacing for semi-ionic F intercalates, as reported by (Nakajima 2001)); this change would be three times smaller than one standard deviation of the inter-layer spacing determined from Raman and same order of magnitude as one standard deviation of the value determined by XRD, thus not observable by the techniques employed here. Nevertheless, surface microstructural changes as probed by Raman are indicative of a partial loss of crystallinity as have been observed upon intercalation of fluorine species between graphene planes (Gupta et al. 2003; Nakajima et al. 1999; Robinson et al. 2010), and the changes are more pronounced in the liquid FLiBe-exposed sample than the cover-gas-exposed sample (Table 2.6). Future studies are needed to verify the presence of semi-ionic C-F (e.g. by EPR or solid-state ^{19}F NMR (Chingas et al. 1985; Panich et al. 2001)), to understand the degree to which such a low concentration of C-F would have an impact on irradiation behavior or macroscopic surface properties of the graphite, and to assess whether the fluorine on spent fuel pebbles could be mobilized by gamma radiation while in storage and cause corrosion of the containers (Toth and Felker 1990).

Surface heterogeneity in C-F formation in seen in SEM/EDS and the variability among XPS points. Further studies are needed to understand the length scales of the fluorination heterogeneity, and to understand if it is linked to initial heterogeneity of the graphite surface, or if it is a manifestation of the stochastic nature of the surface fluorination process.

It is postulated that C-F form by different mechanisms in the liquid phase than in the cover gas of the molten salt. Covalent C-F is predominant in the sample exposed to liquid salt, and semi-ionic C-F is predominant in the sample exposed to the cover gas; the XPS depth-profiling of the liquid-exposed sample shows lower %SI and lower ϕ across the sampled depth than for the cover-gas exposed sample (Figure 2.9). Nevertheless, there is evidence of C-F progression into the salt-exposed sample without progression of salt species or Be metal species (except for the sporadic observation with SEM/EDS of spherical particles attributed to LiF and BeF_2 in the graphite pores close to the surface). Depth profiling (by GDMS and XPS) of the liquid FLiBe-exposed samples

indicates presence of C-F beyond the sample surface (Figure 2.9 and Figure 2.12), a slight increase in %SI with depth, no detectable salt species beyond the first XPS sputtering step, and a shallower depth progression of the hypothesized Be metal than the depth progression of the C-F content. However, since %SI and ϕ remain very different between cover-gas exposed sample and the depth-profiling results on the liquid-exposed sample, *it is postulated that the dominant mechanism of surface fluorination in the liquid occurs at the liquid-solid interface, followed by transport of the reaction products into the depth of the graphite.* The transport of fluorination products into the graphite depth can occur by diffusion along the surface of crystallites, diffusion through the graphite bulk, or diffusion via gas-phase intermediaries. Future studies are needed to better elucidate the reaction mechanisms and transport mechanisms at the graphite surface, and to define the corresponding time scales and spatial scales of relevance for these mechanisms.

2.3.5   Other sample parameters impacting salt-graphite interaction.

In addition to IG-110 polished samples, data is also collected on un-polished samples (as machined). The observations discussed above for gas vs. liquid phase exposure remain the same across this broader set of samples. Data for all samples is available in the Mendeley Data repository linked in Supplementary Information.

Table 2.11: Parameters impacting surface fluorination of graphite by exposure to molten FLiBe at 700 °C.

		Exposure Duration			Exposure Type			Graphite Surface Finish		
		12h (n=1)	240h (n=2)	Observations	Liquid FLiBe (n=4)	Cover Gas (n=4)	Observations	Polished (n=4)	Machined (n=2)	Observations
XPS metrics (sample size indicated in each column)	$\Delta\Omega$ (vs ref. sample)	4.76%	5.32(6)%	Longer exposure leads to higher ϕ, ϕ_{SI} and ϕ_{cov} lower %SI.	5.32(6)%[1]	3.3(1.1)%[1]	Lower %SI with liquid exposure.	4.3(1.3)%	No reference	Large standard deviations prevent from comparison
	LiF/BeF$_2$ (=2 in FLiBe)	0.8	1.0(4)		0.7(4)	0.3(2)		0.6(5)	0.47(12)	
	ϕ	0.05%	1.2(5)%		0.9(5)%	0.26(9)%		0.7(6)%	0.40(17)%	
	% SI = Semi-ionic F of CF in F 1s	76%	39(21)%		27(19)%	42(19)%		56(23)%	30(23)%	
	$\phi_{SI} = \%SI * \phi$	0.04%	0.42(6)%		0.2(2)%	0.15(8)%		0.29(17)%	0.10(7)%	
	$\phi_C = (1 - \%SI) * \phi$	0.01%	0.8(6)%		0.6(4) %	0.11(7)%		0.4(5)%	0.3(2)%	
Raman metrics (n=5)	I(D)/I(G)	0.60(17)	0.68(12)	Surface microstructural changes appear insensitive to exposure time	0.53(15)	0.43(8)	Surface microstructural changes are more pronounced with liquid exposure	0.68(12)	0.35(11)	Surface microstructural changes upon salt exposure are more pronounced with polished graphite
	FWHM(D)	81(25)	66(7)		56(10)	49(8)		58(7)	47(10)	
	FWHM(G)	29(5)	29(3)		26(4)	22(2)		27(4)	22(2)	
	A(G')	14(2)	15(5)		28(5)	39(5)		25(5)	42(5)	
	Degree of Graphitization (%)	33(16)	41(10)		43(12)%	44(15)%		41(11)	45(15)	
	c (nm) (Cançado et al. 2008)	0.6784(18)	0.6774(11)		0.6773(13)	0.6772(17)		0.6775(12)	0.6770(17)	
	L$_a$ (nm) (Tuinstra and Koenig 1970)	13(3)	13(2)		20(5)	23(11)		15(2)	28(12)	
	L$_c$ (nm) (Cançado et al. 2008)	25(4)	26(2)		26(3)	27(4)		26(3)	27(4)	
Samples		One sample (polished and exposed to liquid FLiBe) considered for each exposure duration.			Two samples (one polished, one machined) considered for each exposure type. All samples are exposed for 240 hours.			Two samples (one exposed to liquid FLiBe, one exposed to the cover gas) considered for each graphite surface finish type. All samples are exposed for 240 hours.		

Notes: [1] Calculated only on polished samples, as machined reference not available.

2.3.6 Engineering relevance on graphite performance in the reactor

The study of the effect of the long-term exposure of nuclear graphite to FLiBe at high temperature is motivated by the usage of graphite components in MSRs and FHRs. In Table 2.12, the engineering relevance of chemical and microstructural changes at the surface of the salt and cover-gas exposed graphite is discussed for graphite used in nuclear reactors that employ molten salt.

Table 2.12: Postulated impact of surface fluorination of graphite

Application	Relevance to reactor operation and waste management	Expected changes	Overall effect
Wear and Friction in salt-lubricated environment	Integrity of fuel elements , dust generation, residence time in core (He et al. 2023; Vergari et al. 2023a)	• Decrease in L_a and oxygen release (decrease in $\Delta\Omega$) cause increase in number of edge sites available to C-C bonding • Formation of covalent C-F leads to passivation of edge sites	Since $\Delta\Omega > \phi_C$, a net increase in edge sites available for C-C bonding is expected. This is predicted to favor formation of lubricating tribo-film (Chapter 4) (unless presence of salt impacts film stability (He et al. 2023)), decreasing wear and friction
Uptake of hydrogen isotopes	Tritium uptake and desorption during reactor operation; tritium activity in spent fuel (Forsberg et al. 2020; Vergari and Scarlat 2021b)	• Decrease in L_a and oxygen release (decrease in $\Delta\Omega$) cause increase in number of edge sites available for C-H bonding • Formation of covalent C-F leads to passivation of edge sites (unavailable to hydrogen)	Oxygen-containing chemical groups are inaccessible to hydrogen until oxygen is released (Otake and Jenkins 1993; Pan and Yang 1992; Vergari and Scarlat 2021c). Since $\Delta\Omega > \phi_C$, a net increase in edge sites available for C-H bonding is observed. This is expected to favor tritium uptake (unless newly formed C-H are promptly replaced by C-F bonds, as shown in FLiNaK for pre-existing C-H bonds (Yang et al. 2012))
Graphite Oxidation	Chronic oxidation due to oxide impurities and acute oxidation during licensing base events.	• Decrease in L_a increases number of edge sites. • Formation of semi-ionic C-F can increase interlayer spacing	Increase in number of edge sites causing increase in reactivity towards oxygen (Contescu et al. 2012). Increase in interlayer distance can create pathway for oxygen inside graphite crystallites, otherwise inaccessible (Chapter 5), further favoring oxidation.
Salt infiltration	Changes to pebble buoyancy, impacts to heat transfer and mechanical properties, carry-over of salt into spent fuel storage (Vergari et al. 2022).	• Graphite anodes fluorinated in molten salt have been reported to lead to be less wetted by fluoride salts (Haverkamp 2012)	Higher contact angle after fluorination would lead to a higher differential pressure required for salt-infiltration into graphite.

2.4 Conclusion

In reactors that employ graphite components and molten fluoride salts, characterizing the chemical and microstructural changes of graphite caused by salt-graphite interactions is relevant to assessing the performance of graphite during reactor operation and to predicting graphite conditions upon its discharge from the reactor. In this study, the chemical and microstructural changes that occur to nuclear graphite upon exposure to FLiBe salt for 240h at 700°C are investigated, focusing on both samples exposed to the liquid FLiBe, and samples exposed to the cover gas above molten salt. Characterization of the samples is performed using SEM/EDS, surface XPS, depth profiling XPS, and Raman spectroscopy, and prior GDMS depth profiling data is re-analyzed.

Overall, this study advances the understanding of FLiBe-graphite interactions in MSRs and FHRs and provides evidence of graphite fluorination upon exposure to the salt. It identifies presence of both semi-ionic and covalent C-F bonds formation on the surface, to differing degrees in the salt-exposed and cover-gas-exposed samples. It also concludes that C-F bonds form by different mechanisms in the liquid phase than in the cover gas of the molten salt. C-F formation is accompanied by surface microstructural changes and removal of C-O groups. Further studies are needed to establish the relationships among chemical and surface microstructural modifications in graphite upon exposure to molten salt and the cover gas above it, to confirm the formation of covalent and semi-ionic C-F, to develop a mechanistic description for the formation of covalent and semi-ionic C-F with exposure to salt and to the cover-gas above the salt, and to develop a prediction of the of the relevance of these surface modifications to graphite engineering.

2.5 Acknowledgement

3 Infiltration of Molten Fluoride Salts in Graphite

During the MSRE, resistance to salt infiltration was one of the criteria used to inform the choice of graphite grade for use in the reactor (Haubenreich and Engel 1970). However, graphite infiltration studies from the MSRE program apply only tangentially to the FHR, since the MSRE salt differs from the FHR salt in composition, physicochemical properties, and operational conditions. The twofold goal of this chapter is to define under which conditions graphite used in FHRs is infiltrated by fluoride salts and identify the impact of salt infiltration in graphite in an FHR.
This goal is pursued in two steps: first, literature on salt infiltration is reviewed and used to discuss its engineering effects in the FHR; second, a study of salt wetting on graphite is performed to identify what variables affect wetting and parametrically predict infiltration in an FHR.

3.1 Phenomenology of Infiltration and Engineering Considerations for Reactor Operation and Waste Disposal

In the 1960's and 1970's, the MSRE and Molten Salt Breeder Reactor (MSBR) programs at ORNL started investigating the effects of salt infiltration into graphite in MSRs (MacPherson 1985). Resistance to salt infiltration was one criterion used to inform the choice of graphite grade for use in the MSRE (Haubenreich and Engel 1970). Fuel salt infiltration into graphite was considered detrimental because of its effect on fuel inventory change during reactor operation; graphite degradation by fission product collision and decay, neutron irradiation and thermal cycling (Briggs et al. 1963; Lee et al. 2020; Rosenthal et al. 1972). Salt infiltrating the graphite might also carry gas fission products, including the strong neutron poison ^{135}Xe, into the pores, which could increase neutron absorptions in the graphite and diminish the neutron moderation effect (Rosenthal et al. 1972 p. 175). For these reasons, MSRE designers set a 0.5 % design limit to the volume of salt that could infiltrate graphite, and CGB graphite was selected as the moderator. Infiltration up to 2 vol. % was considered tolerable, and infiltration above 4 vol. % was considered unacceptable for reactor control (Briggs 1964b p. 255).

The MSRE-era concerns about salt infiltration remain for new-generation MSRs and, in part, for FHRs, since FHR salt does not contain fissile material (Scarlat and Andreades 2017; Yoshioka and Kinoshita 2017). More broadly, graphite infiltration studies from the MSRE program apply only tangentially to the FHR, since the MSRE salt differs from the FHR salt in composition, physicochemical properties, and operational conditions. In the FHR, the fuel is encapsulated in TRISO particles dispersed inside graphite matrix pebbles or prismatic elements, and infiltration of the salt to the TRISO particles may not be tolerated during operation. Moreover, infiltration of the salt will impact the management and disposal of the fuel forms and the reflector after their removal from the core. Presence of salt residuals in the pores of the graphite waste would change mechanical (Zhang et al. 2018a), radiological (Toth and Felker 1990), and chemical properties (Forsberg and Peterson 2015) of the waste and potentially require additional decontamination steps (Forsberg and Peterson 2015; Riley et al. 2018; Vergari and Fratoni 2021).

These differences make FHR-specific salt-infiltration research necessary, and several research groups have started conducting experiments more directly applicable to the FHR (Gallego et al. 2020; He et al. 2015; Lian et al. 2016; Zhong et al. 2017). Within this research, most of the effort up to date has been on measuring infiltration extent in graphite under a variety of conditions, but only limited understanding exists about what the infiltration effects for reactor operation and waste processing would be. In this chapter, predictions of graphite infiltration are provided based on graphite pore size distribution, the surface tension of the salt, the contact angle between the graphite and the salt, complement them with compiled results from fluoride salt-infiltration experiments, and the conditions that change the parameters of relevance to salt infiltration are investigated. These results are discussed with respect to the infiltration limits defined for the MSRE, and a hypothesis is presented for properties that may be impacted by infiltration and for which future studies are needed to support entire life-cycle consideration, from reactor operations to disposal, for graphite matrix and nuclear graphite for fuel elements and reflectors in FHRs.

3.1.1   Salt Infiltration into Graphite

This section describes salt infiltration into graphite and identifies the variables that most significantly affect the extent and the kinetics of salt infiltration. Molten salt must flow into graphite open pores to infiltrate graphite. Diffusion, another mechanism by which constituents of the salts can enter graphite, is not classified as infiltration, and is therefore not discussed in this chapter. Diffusion of gas and salt constituents in graphite is discussed in (Compere et al. 1975; Lee et al. 2020).

The infiltration of a liquid substance into a cylindrical pore of diameter d occurs when the pressure difference ΔP between the liquid P_{liquid} and the gas in the pore P_{pore} reaches the value prescribed by the Washburn equation (Washburn 1921):

$$\Delta P = P_{liquid} - P_{pore} = -4\gamma\cos\theta/d \qquad\qquad 3.1$$

where θ is the contact angle, γ is the liquid–gas surface tension (usually simply referred to as surface tension), and d is the pore diameter. Therefore, the contact angle, surface tension, and pore diameters are the three parameters that dictate the pressure at which salt infiltrates graphite. These values are compiled in Table 3.1, and they are each discussed in the next three subsections.

Table 3.1: Contact angle measurements of fluoride salts on graphite via sessile drop method. Results are grouped by study and ordered by magnitude of contact angle within each study. Studies are ordered chronologically.

Molten salt	Graphite grade	Average pore diameter (μm) [a]	Temperature (°C)	Atmosphere	Graphite preparation	Contact angle (deg.)	Reference
CsF	CGB	0.2	700	Helium	Not discussed	41 ± 2	(Grimes 1964 pp. 38–42)
FLiNaK		0.2	500–720			90 ± 4	
LiF-NaF (60:40 mol)		0.2	700–800			120 ± 4	
LiF-BeF₂-ZrF₄-ThF₄-UF₄ (70:23:5:1:1 mol)		0.2	500–800			140 ± 8	
FLiBe		0.2	500–800			147 ± 12	
FLiNaK	NBG-18	12	n.a.	Argon (H₂O < 1ppm, O₂ < 1ppm)	Degassing (details not reported) and 1200-grit polishing	135	(He et al. 2015)
FLiNaK	IG-110	3.9	n.a.	Not reported	Not discussed	140 ± 10	(Lian et al. 2016)
	UGG-1	0.5				140 ± 10	
FLiNaK	IG-110	3.9	450–600	Argon (H₂O < 1ppm, O₂ < 1ppm)	Degassing at 700°C for 3 h in argon	95–170	(Delmore et al. 2018)
FLiBe	IG-110	3.9				110–160	
FLiBe	A3	0.8 [d]				110–150	

[a] From (Gallego et al. 2020), when not noted otherwise
[b] From (Wu 2019)

3.1.1.1.   Pressure

Depending on its location in the reactor, graphite may be subjected to different pressures of salt. Graphite at the top of the reactor will be subjected to the cover gas pressure, whereas graphite deeper in the reactor experiences higher pressure caused by static and dynamic fluid forces. Using the case of the Mark-I PB-FHR as a reference with a 12 m tall reactor vessel and a pressure drop in the primary coolant circuit up to 3 m of head (Andreades et al. 2016), graphite in the core would experience (absolute) pressures ranging from 100 kPa at the top of the core and immediately upstream of the pump to 400 kPa at the bottom of the core and immediately downstream of the pump. Graphite in a reactor with taller vessels would be subjected to even higher pressures (e.g., 500 kPa for a 19 m tall core, similar to the ORNL 2012 Advanced High Temperature Reactor (AHTR) design (Varma et al. 2012)).

3.1.1.2.   Contact angle

The contact angle θ is the angle formed by the tangent to the liquid–gas interface and the solid–liquid interface. The equilibrium contact angle is the result of a balance between adhesive forces of the two materials (the liquid and the solid) and cohesive forces within the liquid (at the liquid–vapor interface). Small contact angles (θ < 90°) indicate a tendency of the liquid to adhere to the solid surface (the liquid *wets* the solid); large contact angles (θ > 90°) indicate that cohesive forces prevail over adhesive forces (the liquid *does not wet* the solid) (Figure 3.1) (Rideal 1931).
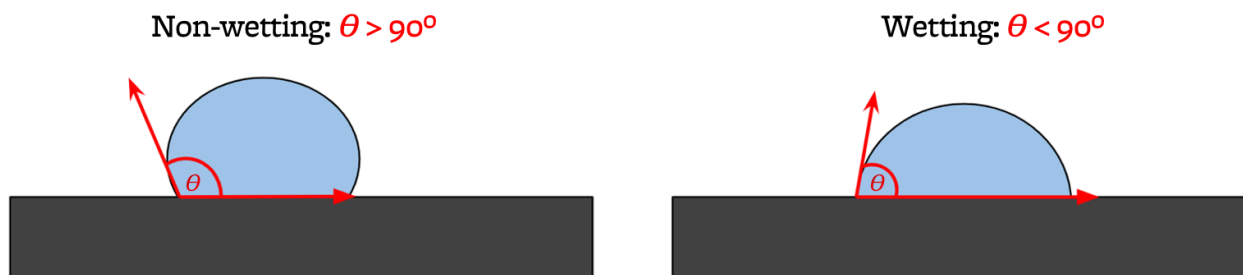
Figure 3.1: Sessile droplets with low and high contact angles.

Table 3.1 lists contact angles measured using the sessile drop method. This method involves placing a small piece of the solid salt on top of graphite in a furnace to measure the contact angle at various temperatures. At its melting point, the salt coalesces and forms droplets. The angle formed by the droplet with the graphite surface is the contact angle of interest (Eustathopoulos et al. 2005). The studies listed in Table 3.1 and Table 3.2 explore the dependence of contact angle and surface tension on salts (Delmore et al. 2018; Grimes 1964 pp. 38–42) and on graphite grade (Gallego et al. 2020; Lian et al. 2016; Song et al. 2014; Tang et al. 2017).

In all studies (except for the case of CsF), contact angles between graphite and fluoride salts are above 90°, indicating that graphite is not wetted. The contact angle shows variability across fluorides salts and dependence on the graphite grade.

The dependence on the fluoride salts can be observed in the MSRE data (Grimes 1964 pp. 38–42) for FLiNaK, FLiBe, and the MSRE fuel salt that were tested on CGB graphite. The contact angle varies by more than 50° across these fluorides. FLiNaK is shown to have a lower contact angle than FLiBe, suggesting that infiltration experiments with FLiNaK would be conservatively bounding for FLiBe.

For a given fluoride salt, the contact angle shows a limited variability across graphite grades. The FLiNaK contact angles on IG-110 and UGG-1 (Lian et al. 2016), on NBG-18 (He et al. 2015), and as-manufactured IG-110 falls within a 20° interval. The values estimated during the MSRE for CGB graphite vary by at least 40°. FLiBe contact angle varies over an interval of 35° on A3 matrix and on IG-110 (Delmore et al. 2018). The variability could be imputed to the heterogeneity of the surface finish, inaccuracies in the image digitalization and parameter extraction, and variations in the environmental conditions (e.g., the degassing or adsorption of moisture or oxygen (Delmore et al. 2018; Eustathopoulos et al. 2005; Lian et al. 2016)) or in the chemistry of the salt.

3.1.1.3. *Surface tension*

The liquid–gas surface tension is defined as the force per unit length required to expand the liquid surface area. Several experimental methods are available for measuring surface tension (Ebnesajjad 2011), but only the sessile drop method and the maximum bubble pressure method have been used for molten fluorides. In the sessile drop method, surface tension is estimated based on the size and the shape of the droplets, and several equations have been developed for correlating surface tension and geometrical parameters (Hutzler et al. 2018; Worthington 1881; Ziesing 1953). In the maximum bubble pressure method, a small-diameter tube is immersed in the liquid, and the surface tension is calculated from the maximum pressure necessary to form a bubble at the end of the tube (Mysels 1990). Table 3.2 lists the experimental values for surface tension of FLiBe,

FLiNaK, and the MSRE fuel salt. In two of the studies, measurements were taken over a temperature interval, and linear correlations for the temperature dependence of surface tension were developed.

The surface tension is sometimes considered a liquid property, but it is an interaction property that depends on gas atmosphere and potentially on the properties of the solid substrate in sessile droplet setups and the tube in the maximum-bubble-pressure method. Although liquid and solid properties are usually documented in contact angle experiments, Table 3.2 shows that the atmospheric conditions during the test are sometimes not reported and may account for some of the observed variability in contact angle measurements (Chau et al. 2009).

One of the studies in Table 3.2, an MSRE-era report (Grimes 1964 pp. 38–42), reports the surface tension and the contact angle over CGB graphite for five types of salts (measured via sessile drop method), highlighting a negative linear correlation between the cosine of the graphite contact angle and the surface tension (Grimes 1964 pp. 38–42). However, if the results on FLiBe (Lian et al. 2016) are considered, then the linear correlation becomes less evident. This linear correlation would differ from the Young–Laplace equation (Young 1802), which postulates an inverse proportionality between contact angle and liquid–gas surface tension.

Table 3.2: Surface tension measurements of molten fluoride salts of applications in nuclear energy.

Molten Salt	Method	Temperature (°C)	Atmosphere	Surface tension (N/m)	Notes	Reference
LiF-BeF$_2$-UF4	Maximum bubble pressure method	460–750	Not reported	0.19–0.17 (±5%)	Developed correlation for surface tension as a linear function of temperature	(Macpherson 1958)
FLiNaK	Sessile drop method	Not reported	Not reported	0.16 ± 0.01	Uncertainties and experimental procedure not reported	(Lian et al. 2016)
LiF-BeF$_2$ (variable composition)	Maximum bubble pressure method	500–970	Argon	0.15–0.2 (errors between −10% and +30%)	Measurements performed using mixtures with LiF molar fraction from 0.33 to 1	(Yajima et al. 1982)
CsF	Sessile drop method	700	Helium	0.107	Uncertainties and experimental procedure not reported	(Grimes 1964 pp. 38–42)
FLiNaK		500–720		0.184		
LiF-NaF (60:40 mol)		700–800		0.220		
LiF-BeF$_2$-ZrF$_4$-ThF$_4$-UF$_4$ (70:23:5:1:1 mol)		500–800		0.230		
FLiBe		500–800		0.230		
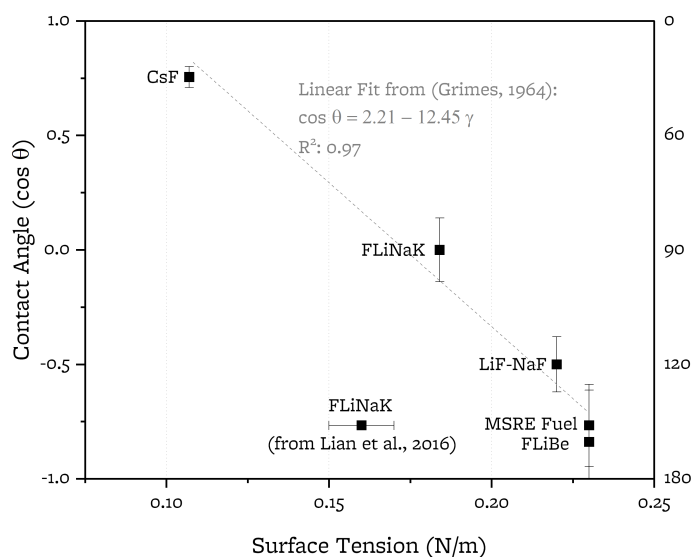
Figure 3.2: Contact angle and surface tension for fluoride salts on graphite; studies compiled in Table 3.1 and Table 3.2. (Macpherson 1958), (Lian et al. 2016), (Yajima et al. 1982)

3.1.1.4. *Pore size distribution*

A factor that causes variations in infiltration behavior across graphite grades is the pore size distribution in graphite. Table 3.1 lists the average pore diameter of graphite grades used in salt infiltration experiments, and Figure 3.3 shows the pore size distribution of the graphite grades described in the literature (Gallego et al. 2020). At low pressures, the molten salt does not infiltrate graphite. As the salt pressure increases, the salt will infiltrate progressively smaller pores until all open pores are filled. As a result, infiltration occurs at an interval of pressures that directly depends on the pore-size distribution.

A technique to investigate pore size distribution in graphite is mercury porosimetry (MP). In this technique, graphite is exposed to an increasing pressure of mercury, which progressively occupies the pore volume. Because mercury does not wet graphite, mercury does not infiltrate graphite pores at zero pressure. As the pressure increases, pores of increasingly smaller size are infiltrated, and the infiltrated volume is recorded. Knowledge of mercury contact angle on graphite and surface tension allows Eq. 3.1 to link the distribution of infiltrated mercury to the pore size distribution. Mercury is liquid at room temperature, and measurements are made at room temperature.

MP results indicate a correlation between graphite grain size and its porosity distribution. Fine-grained graphites (e.g., ZXF-5Q, AXF-5Q, POCO-TM, ETU-10, 2114, IG-110, NBG-25) are characterized by a narrow distribution of pore size (width of about 1–5 μm). Accordingly, MP studies of ultrafine- to fine-grained graphites show no infiltration below a threshold pressure and a steep increase in the intruded volume beyond that pressure (Figure 3.4). Medium- and coarse-grained graphite (e.g., CGB, PGX, NBG-18, NBG-17, PCEA) have wider porosity distribution, so

their infiltration curves in Figure 3.4 are less steep and span a larger pressure interval (Gallego et al. 2020).
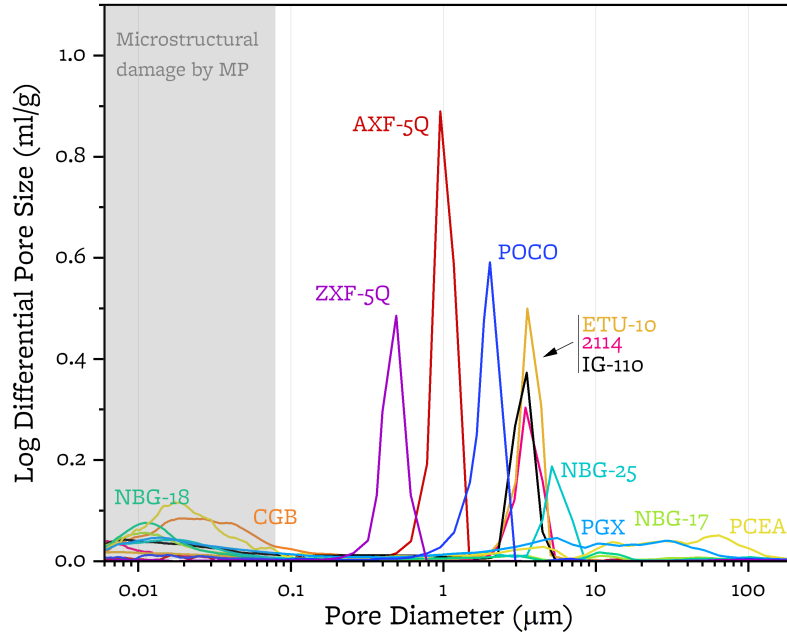
Figure 3.3: Pore size distribution for several graphite grades. The area at low pore sizes corresponds to the region in which the porosimetry introduces structural damage to the graphite, connecting open pores and creating new porosity. Data from (Gallego et al. 2020).

In addition to being technique for pore size analysis, MP has also been used as a tool to predict salt infiltration behavior. Using Eq. 3.1 the infiltration pressure distribution with two different liquids (e.g., mercury and salt) on a sample with a given pore size distribution can be written as

$$\Delta P_{salt} = \Delta P_{Hg} \frac{\gamma_{salt} \cos\theta_{salt}}{\gamma_{Hg} \cos\theta_{Hg}} \qquad 3.2$$

where γ_{salt}, ΔP_{salt}, and θ_{salt} are the surface tension, the infiltration pressure, and the contact angle with the salt, and γ_{Hg}, ΔP_{Hg}, and θ_{Hg} are the corresponding terms for mercury.

The relationship between MP and salt infiltration studies motivated MP studies on several graphite grades (Figure 3.4) and calculations of corresponding FLiNaK infiltration behavior (Gallego et al. 2020).
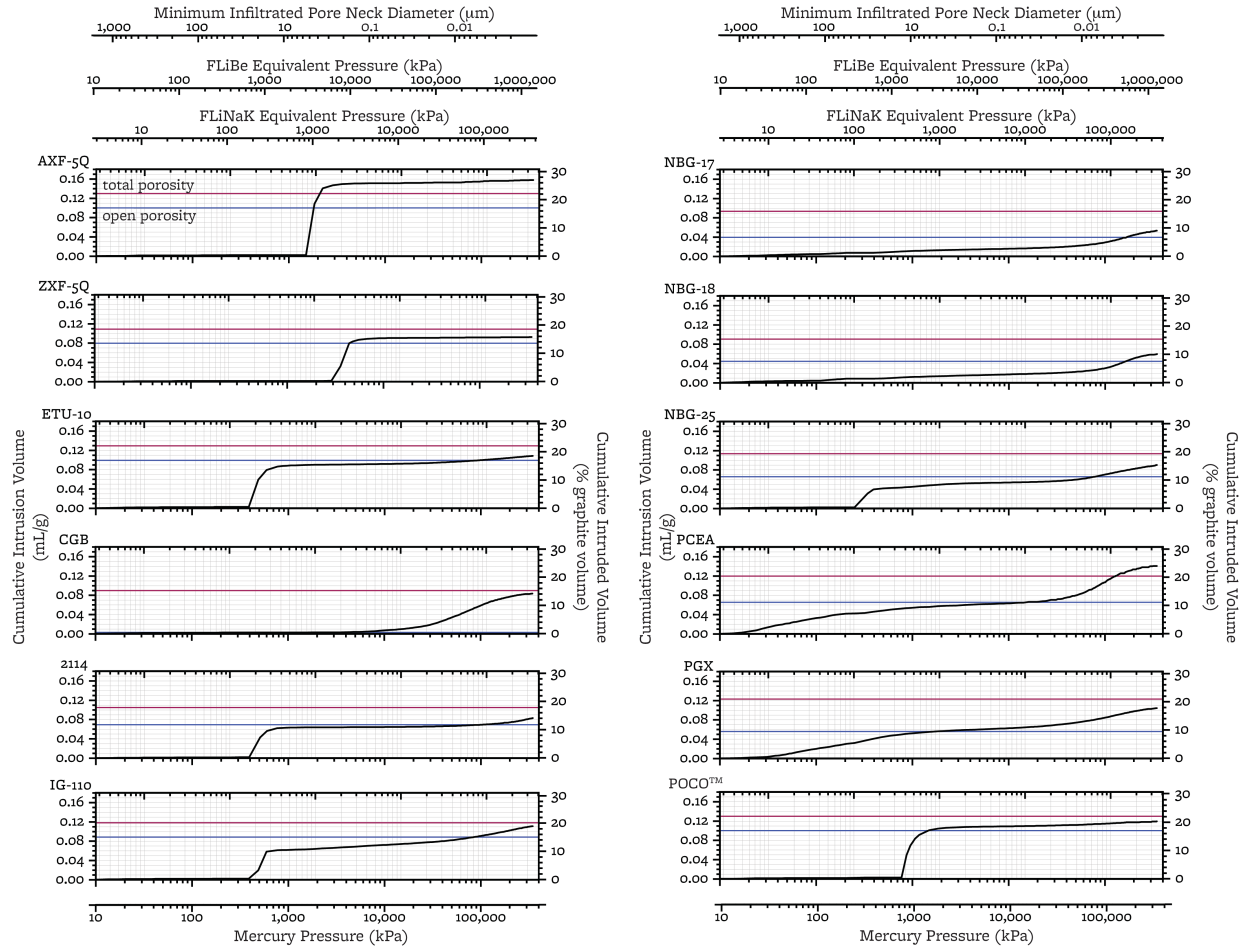
Figure 3.4: Mercury porosimetry curves of several graphite grades. Data from (Gallego et al. 2020).

The maximum amount of mercury expected to infiltrate in graphite corresponds to the volume of the open pores. Nevertheless, all graphite grades in Figure 3.4 reach volumes of intruded mercury beyond their open porosity. Three potential reasons for this behavior exist. The first reason is simply that the reported values of open porosity are incorrect, which seems the case for ZXF-5Q and AXF-5Q because the intruded volume seems to plateau at high pressures. A second reason applies to those graphite grades whose infiltration curves become steeper at pressures around 70,000 kPa (e.g., 2114 and NBG-17). In this case, the intruded volume increases because of the structural damage caused by high pressure (~70 MPa in MP), in excess of graphite mechanical strength, which opens the path to closed porosity (Baker and Morris 1971; Dickinson and Shore 1968; Jones et al. 2018). This topic will be further discussed in Section 3.1.3.2. A third reason could be the biased quantification of total graphite pore volume. Variability in the predicted pore volume among different techniques arises from pore connectivity (open porosity vs. closed

46

porosity), scale at which porosity is probed, and the type of averaging (volume-averaging vs. surface- averaging).

3.1.1.5.   *Extent of salt infiltration*

In addition to predicting infiltration curves with MP, they can be obtained directly via salts infiltration studies. The American Society for Testing and Measurements (ASTM International) outlined the procedure for molten salt infiltration studies in the ASTM standard D8091-12 (ASTM International 2016). Several groups have performed direct salt infiltration studies, measuring the weight change and the volume of infiltrated salt (Figure 3.5, Table 3.3) (Gallego et al. 2020; He et al. 2015; Lian et al. 2016; Song et al. 2014; Tang et al. 2017; Zhang et al. 2016; Zhong et al. 2017). Figure 3.5 shows the percentage of graphite volume that infiltrated by FLiBe and FLiNaK salt at a given salt pressure. The salt pressure is a design parameter of the reactor, and it can vary across different MSR and FHR designs. As discussed in Section 3.1.1.1, pressures of $100 - 500$ kPa can be of relevance for several MSR and FHR designs. In the MSRE, 0.5 vol % salt infiltration into graphite was the design goal, and 4 vol % and above was deemed unacceptable for reactor control (Briggs 1964b p. 255). Figure 3.5 makes the simplifying assumptions that a 4% percentage infiltrated volume is considered inacceptable for every MSR design (as it was for the MSRE) and that the contact angle and surface tension of the salt used in MSRs are comparable to those of the salt used in experiments (FLiBe and FLiNaK). Under these assumptions, most of the nuclear graphite grades would be infiltrated to inacceptable extents when exposed to the salt pressures of interest. ZXF-5Q, UGG-2, NG-CT-50, and G2 would be the only grades shown in Figure 3.5 that satisfy the requirements. For FHRs, infiltration limits have not been set yet.

Table 3.3: Studies of fluoride salt infiltration into graphite. Infiltration data shown in Figure 3.5.

Molten salt	Graphite grade	Average pore diameter (μm) [a]	Temperature (°C)	Atmosphere	Sample treatment before experiment	Sample Geometry	Salt absolute pressure (kPa)	Infiltration Duration (hours)	Reference
FLiNaK	IG-110	1.84[c]	n.a.	Argon	Not discussed	Ø70mm x 40 mm cylinders	100–10,000	n.a.	(Song et al. 2014)
	NPIG	0.069[c]							
FLiNaK	2020	n.a.	650	Argon	Samples are degassed but details are not provided	Ø12.7mm x 20mm cylinders	150-10,000	20 and 100	(He et al. 2014b, 2015b)
	2114	3.5							
	IG-110	3.9							
	NBG-18	12							
	G1	n.a.							
	G2	n.a.							
FLiNaK	IG-110	3.9	n.a.	No explicit mention of atmospheric composition	n.a.	Ø150mm x 150mm cylinders	100–500	n.a.	(Lian et al. 2016)
	UGG-1	0.5							
FLiNaK	ZXF-5Q	n.a.	n.a.	Argon	Sonicated in DI water and acetone and degassed in vacuum at 120 °C for 5h.	Ø12.7mm x 20mm cylinders	100-500	12	(Zhang et al. 2016)
FLiBe	IG-110	3.9	700	Argon (H₂O < 1ppm, O₂ < 1ppm)	Samples are degassed but details are not provided	Ø10mm x 20mm cylinders	100-1,000	20	(Tang et al. 2017)
	NG-CT-50	n.a.							
	NG-CT-10	2[d]							
	NBG-18	12							
FLiBe[b]	MCMB	0.096	700	Argon	Degassed in vacuum at 150 °C for 2h	Ø10mm x 5mm cylinders	100-650	20	(Zhong et al. 2017)
	A3	0.76							
FLiNaK	IG-110	3.9	700	Argon (H₂O < 1ppm, O₂ < 1ppm)	Degassing at 700°C for 1 h in argon	Ø10mm x 20mm cylinders	100-1,000	20	(Zhang et al. 2018a)
	NG-CT-10	2[d]							
FLiNaK	IG-110	2.06[e]	650	Argon	Sonicated in DI water and acetone and degassed in vacuum at 100 °C for 2h.	Ø10mm x 20mm cylinders	100-500	24	(He et al. 2018)
	SiC-coated IG-110	0.01[e]							
FLiNaK	IG-110	3.9	750	Argon	Degassing at 1200°C for 8 h in vacuum	Ø10mm x 22mm cylinders	798	12	(Gallego et al. 2020)
	2114	3.5							
	ETU-10[f]	3.6							
	NBG-25	5.1							
	PCEA	64							
	NBG-18	12							

Notes:

[a] From (Gallego et al. 2020), when not noted otherwise.

[b] Study not included in Figure 3.5 because infiltration results not included in the original study

[c] From (Song et al. 2014).

[d] Most probable pore size from mercury porosimetry (Zhang et al. 2018a).

[e] Median pore size from mercury porosimetry (He et al. 2018).

[f] ETU-10 is the purified version of ET-10.

The weight change and infiltrated salt volume (the latter often reported as a ratio to the graphite volume) are two useful metrics to quantify how much salt infiltrates graphite, but they do not directly indicate what fraction of graphite porosity is occupied by salt. This information is better communicated by the *D* parameters introduced by ASTM, which quantify the ratio of the weight

change relatively to the mass of salt that would entirely occupy the open porosity (D_0) and the total porosity (D_1), as shown in the following equations:

$$D_0 = \frac{m_{post} - m_{pre}}{\rho_{salt} V_0} \qquad\qquad 3.3$$

$$D_1 = \frac{m_{post} - m_{pre}}{\rho_{salt} V_t} \qquad\qquad 3.4$$

where m_{pre} and m_{post} are the graphite sample mass pre- and post-infiltration, ρ_{salt} is the salt density, V_0 is the volume of open pores, and V_t is the volume of open and total pores. The D_0 parameter can be calculated as a ratio of the infiltrated volume (as a percentage to the graphite volume) $V_\%$ and the open porosity α_0 as shown in Equation 3.5. Similarly, the D_1 parameter is calculated as a ratio of $V_\%$ and the total porosity α.

$$D_0 = V_\% / \alpha_o \qquad\qquad 3.5$$

Figure 3.5 shows the infiltrated volume and D_0 parameter for the salt infiltration studies available in literature.
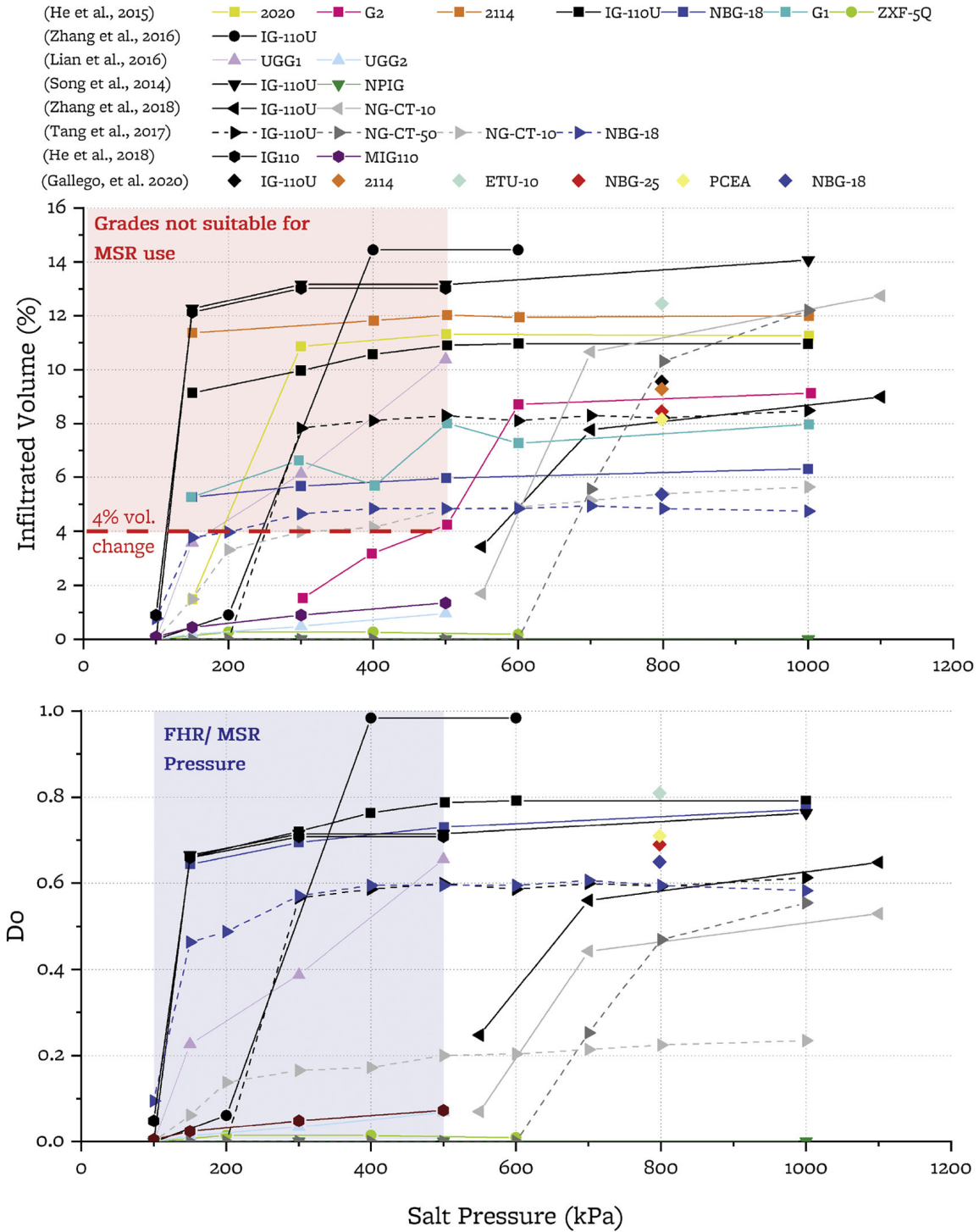
Note: Solid lines indicate studies with FLiNaK, dashed lines indicate studies with FLiBe.

Do parameters calculated using Equation 5 with ρ_{FLiBe} = 1940 kg/m³, ρ_{FLiNaK}=2020 kg/m³ (Williams et al., 2006) and α from Figure 4.

Figure 3.5: Fluoride salt intrusion as a function of absolute salt pressure. Studies listed in Table 3.3. Data from (Gallego et al. 2020; He et al. 2015; Lian et al. 2016; Song et al. 2014; Tang et al. 2017; Zhang et al. 2018a, 2016).

Figure 3.5 shows that for all graphite grades except G1 (the trend for G1 is not discussed in all sources (He et al. 2015)), the infiltrated volume and the D0 parameter increase monotonically with pressure. Some graphite grades, particularly IG-110, are used in more than one study. At a given pressure and for a given graphite grade, the infiltrated volume and the D0 parameter may vary by more than 75%. The variations are smaller (less than 40%) at pressures on the order of megapascals. Because samples that have a larger surface-to-volume ratio would offer a larger pore surface to the molten salt, differences across studies could be ascribed, at least in part, to the shape and the size of the graphite samples, which are not specified by the ASTM procedure.

Another noteworthy cause of the dispersion of the results could be the variability of contact angles and surface tensions across studies. To quantify their effect, it is useful to look at the example of IG-110. Figure 3.6 shows the cumulative pore size distribution of IG-110 (which is the integral form of the pore distribution of Figure 3.3). The fraction of pores that would be infiltrated by FLiNaK at 300 kPa is overlaid on the figure. This is shown for three combinations of contact angle and surface tension from Table 3.1. A variability in infiltrated volume of up to 1.4% (corresponding to 10% of the overall open porosity measured by MP) is observed by using different combinations of the surface tension and the contact angle in Table 3.1. Because the slope of the cumulative open porosity distribution is not constant, the variability of contact angles and surface tension may affect the result, depending on the infiltration pressure (higher pressure would shift the dotted vertical curves to the left, lower pressures to the right).
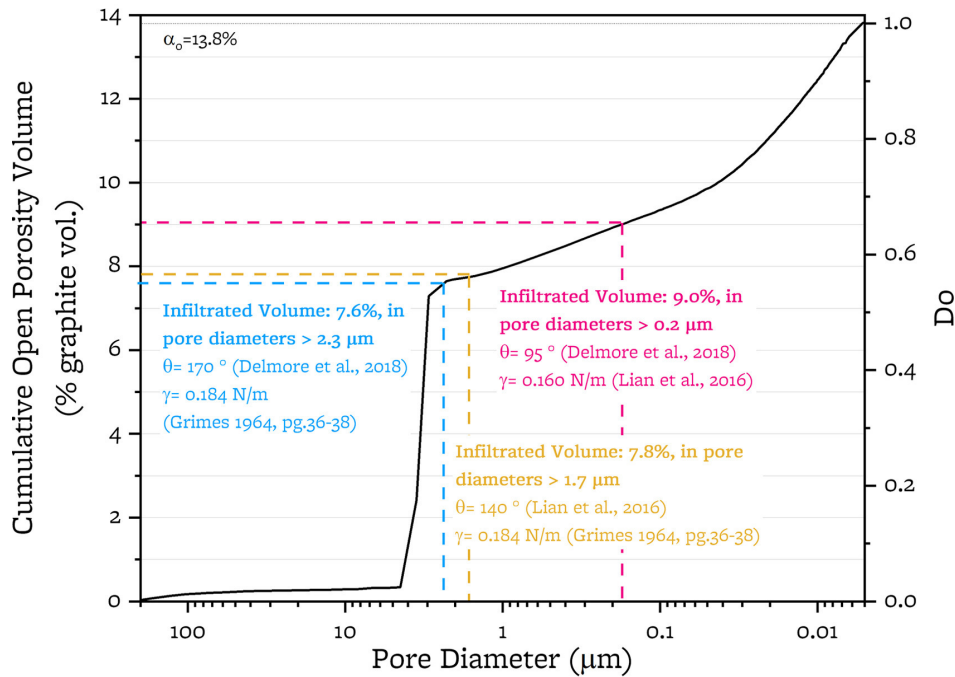
Graphite grade: IG-110U, Open Porosity: 13.8%, Salt: FLiNaK, Salt Absolute Pressure: 300 kPa.
Cumulative pore size distribution from (Gallego et al., 2020)

Figure 3.6: Prediction of volume of infiltrated FLiNaK in IG-110 graphite at 300 kPa for various contact angles and surface tensions. The cases in magenta and orange represent the extreme combinations of surface tensions and contact angles, the case in orange is intermediate.

51

Of the available infiltration studies, only one used FLiBe (Tang et al. 2017). Three of the grades used in the study (NBG-18, IG-110, NG-CT-50) are also used in other studies with FLiNaK. In the case of NBG-18, experimental points with FLiBe are within a 15% range from points with FLiNaK. For the other two graphite grades, the variations are larger. For all three grades, infiltration with FLiBe seems to be less pronounced than with FLiNaK. This observation is aligned with predictions using Eq. (1) with the contact angles and the surface tension for FLiBe (Grimes 1964 pp. 38–42) and FLiNaK (Lian et al. 2016) of Table 3.1. Using these data, the FLiBe pressure required to infiltrate a pore of a given size is 56% larger that the corresponding FLiNaK pressure. However, because large variabilities exist in contact angles, surface tensions, and experimental pressures, a definitive comparison cannot be performed.

In summary, the pressure required for salt infiltration into graphite is determined by the salt contact angle on graphite, the surface tension, and the graphite porosity (Eq. 3.1). Fluoride salts used in reactor applications do not wet graphite. Contact angle measurements vary across salts, depend on the atmosphere, and may also change depending on the graphite grades. The lower and upper experimental estimates for contact angles of fluoride salts differ by 80°, corresponding to a 2.4% change in predicted infiltrated salt volume. Surface tension is inversely proportional to contact angles, and its estimate varies by as much as 0.7 N/m in experiments (Table 3.1). Each graphite grade has its proper pore size distribution. Fine-grained graphite grades are characterized by narrow distributions; coarse-grained graphite have broader distributions (Figure 3.3). The combination of these factors influences the amount of salt that can infiltrate at any given pressure, which is generally expressed in the form of infiltrated volume, weight change, or by the D parameters (Figure 3.5). Once a limit to the maximum acceptable infiltration volume is established, the results of experimental studies can be used to identify grades that would satisfy the requirement. Only a handful of graphite grades would satisfy the 4 vol % limit for reactor control set in the MSRE. Salt infiltration experiments present large variability: for a given graphite grade, salt, and pressure, the infiltrated volume may change by as much as 75%. Infiltration experiments and estimates for contact angles and surface tensions indicate that FLiBe infiltrates graphite less than FLiNaK: the FLiBe pressure required to infiltrate a pore of a given size is 56% larger that the corresponding FLiNaK pressure.

3.1.1.6. *Kinetics of salt infiltration*

The kinetics of penetration have been correlated with properties of the liquid and wetting parameters by means of the *penetrability* parameter v^* (Washburn 1921):

$$v^* = \frac{\gamma}{\eta}\frac{cos\theta}{2} \qquad\qquad 3.6$$

where η is the dynamic viscosity. The penetrability has the same units as velocity and is defined as the distance that the liquid would penetrate in a capillary tube of unit radius in unit time, when flowing without added pressure. Because the cosine of the contact angle is negative for non-wetting salts, their penetrability is negative, and the parameter is not meaningful for non-wetting fluids. However, the functional form of the penetrability suggests that salts with a larger surface tension to viscosity ratio might have a faster kinetics of penetration. As a result, FLiBe (η = 0.009 Pa·s at 600°C (Ambrosek et al. 2009), γ = 0.23 N/m (Grimes 1964)) is expected to have a slower kinetics of penetration than FLiNaK (η = 0.005 Pa·s at 600°C (Williams et al. 2006), γ=0.18 N/m (Grimes 1964)).

The time required for infiltrated salt to reach equilibrium in the graphite might vary depending on the size and shape of the graphite samples. Not all salt infiltration studies report their infiltration times (Table 3.3). Studies that report times use graphite samples of similar size and shape (cylinders of 10-12.7 mm diameter and 5 - 22 mm height) and use salt infiltration times in the order of few tens of hours (Table 3.3). Among these, one study explores two different infiltration times (20h and 100h) (He et al. 2015) finding that 20h was sufficient time to allow the molten salt to infiltrate five different grades (IG-110, 2114, NBG-18, G1, and G2) of graphite (He et al. 2015). Allowing the salt to contact the graphite for an additional 80 h results in a less than 8% increase in salt infiltration for all grades of graphite tested, as measured by weight gain (He et al. 2015).

An infiltration time below 10 h may not be sufficient to allow for a complete equilibration even in thin samples (Vacik et al. 2001). (Vacik et al. 2001) measures lithium concentration as a function of depth after exposing 2mm thick samples of pyrolytic carbon and glassy carbon—two of the coatings proposed to decrease infiltration into graphite (Lee et al. 2020)—to molten FLiNaK for 1, 5, and 10 h. The study found that lithium concentration increased by a factor of about five after between 1 and 5 h of salt exposure and by a further factor of about five after between 5 and 10 h, as measured by thermal neutron depth profiling. This study also concluded that, based on the shape of the measured lithium depth profiles, a Fickian diffusion process was not responsible for the majority of lithium found within the graphite; therefore, diffusion of the salt into graphite is a subdominant process to salt infiltration into the graphite's pores (Vacik et al. 2001).

While these results suggest that few tens of hours may be a sufficient infiltration time to observe equilibrium infiltration for graphite samples of few mm to few tens of mm dimensions, graphite components in use in MSRs and FHRs are larger in size and may need longer time for equilibration. Infiltration studies using test specimens of variable size and shape are recommended to explore the time dependence of infiltration. Furthermore, it is of importance to observe whether infiltration rate is pressure-dependent and determine low salt pressures lead to slow infiltration rates.

3.1.2   Reactor effects impacting salt infiltration.

Most of the experiments presented in Section 3.1.1 aim to understand salt infiltration into graphite at prescribed temperatures and atmospheres and try to minimize the external phenomena that can disrupt these conditions. However, nuclear reactor environments include external phenomena that can influence the infiltration behavior in both normal operation and accident scenarios. Section 3.1.2 explores how irradiation and ingress of air or moisture can affect salt infiltration.

3.1.2.1.   Effect of neutron irradiation on infiltration

Irradiation introduces dimensional changes in graphite, causing shrinking for low fluences and swelling after turnaround (Burchell and Snead 2007). Graphite shrinking could lead to a change in open porosity. The porosity change may affect the amount of salt that can infiltrate graphite. If the shrinkage is isotropic, then the linear shrinkage will be proportional and the total porosity will remain constant, while the dimensions of pores will decrease proportionately, shifting the distributions of Figure 3.3 to the left. This will lead to a decrease of the percentage of infiltrated porosity at any infiltration pressure. If the shrinkage in anisotropic, pre-turnaround irradiation may lead to disappearance of porosity, which can impact salt infiltration. This change occurs only if the porosity that disappears because of shrinking has a sufficiently large diameter. For a given salt pressure, the minimum pore diameter that can be infiltrated by salt is calculated according to Eq.

3.1. Using the conservative value of 500 kPa for the pressure of MSRs and FHRs, a salt contact angle of 110° (corresponding to the lowest bound estimate for FLiBe), and a surface tension of 0.230 N/m (Grimes 1964 pp. 38–42), salt infiltrates pores of diameter larger than 0.6 μm. If graphite shrinking only leads to the shrinking of pores with a diameter smaller than that, then it does not affect the salt infiltration behavior. Similarly, graphite swelling can lead to an increase of the pore size and/or to the formation of new porosity. An isotropic swelling will lead to an increase of the percentage of porosity that is infiltrated at any pressure level. If new porosity is created, this will impact the amount of salt that infiltrates graphite only if the diameter of the newly created pores is smaller than 0.6 μm.

Density Functional Theory (DFT) calculations and N_2 adsorption, which probe for porosity in the nanometer to hundreds of nanometers scale (*nanoporosity*), have shown the appearance of new porosity for both pre- and post-turnaround fluences (Contescu et al. 2019; Hoinkis et al. 1986). The infiltration pressure that corresponds to this new porosity is on the order of 1–16 MPa, exceeding the pressure to which graphite is subjected in MSRs and FHRs (Table 3.4). The appearance of new porosity is not reported at and beyond the micron scale (*microporosity*). Instead, an MP study of Gilsocarbon graphite has shown that pre-turnaround fluences leads to a 2% decrease in pore volume, and that the porosity decrease is not limited to pores of one size but occurs uniformly for pores with diameters between 0.002 and 20 μm (Jones et al. 2020). This result suggests that pre-turnaround irradiation creates porosity only at the nanometer scale to accommodate the changes in the crystallite parameters and causes a bulk shrinkage of graphite, thereby decreasing the pore volumes accessible to salt. This finding is supported by scanning electron microscopy (SEM) of irradiated IG-110 graphite from (Huang et al. 2019). The SEM images show the appearance of new sub-micrometer sized pores but an overall decrease in total pore volume at both pre- and post-turnaround irradiation levels.

Table 3.4: Graphite porosity created by neutron irradiation and corresponding infiltration pressure. In the illustration, upward arrows indicate an increase of porosity, downward arrows a decrease. The techniques employed in the studies are shown beside the arrows.

	Pre-Turnaround	Post-Turnaround	
Nano-Porosity	↑ N_2 adsorption (Hoinkis et al., 1986) DFT (Contescu et al., 2019)	↑ DFT (Contescu et al., 2019)	
Micro-Porosity	↓ SEM (Huang et al., 2019) MP (Jones, Matthews & Laudone, 2020)	↓ SEM (Huang et al., 2019)	→ Less salt infiltration

Graphite grade	Average pore size (µm)	Neutron damage (dpa)	Irradiation condition vs. turnaround	Method of porosity estimation	Change in pore volume	Scale of new porosity (µm)	Minimum required pressure to infiltrate new porosity* (MPa)	Reference
A3	0.9 (Wang et al. 2020)	6.6–7.1	Pre-turnaround	N_2 adsorption	n.a.	<0.02	15.7	(Hoinkis et al. 1986)
G347A	Not reported	9–30	Pre- and post-turnaround	N_2 adsorption, DFT	n.a.	<0.35	0.9	(Contescu et al. 2019)
Gilsocarbon	Not reported	7	Pre-turnaround	MP	−3%	No new porosity	-	(Jones et al. 2020)
IG-110	3.9 (Gallego et al. 2020)	9.24–21	Pre- and post-turnaround	SEM	−5% at 9.24 dpa, −11% at 21 dpa	<0.5	0.6	(Huang et al. 2019)

* Assuming contact angle of 110° and surface tension of 0.230 N/m (Grimes 1964 pp. 38–42).

Irradiation might also affect salt infiltration in a way that does not involve porosity change. Laser microscopy measurements show that irradiation leads to an increase in surface roughness (up to 400% increase at 20 dpa) (Huang et al. 2019). Because the contact angle of the salt on graphite may depend on the surface finish, this added roughness may affect the wetting behavior of the salt. Future studies of salt-contact angles with variable surface finish would enable estimating the magnitude and the direction of this effect.

Only one study provides a direct comparison of the infiltration behavior of irradiated and unirradiated graphite (Huang and Tang 2018). In the study, IG-110 graphite is irradiated with Xe ions to a fluence of 2.4×10^{15} ions/cm^2, corresponding to a peak of 4.4 dpa[a]. Ion irradiation is preferred to neutron irradiation to avoid neutron activation and to produce damage faster. After irradiation at room temperature, the graphite sample and an unirradiated control are annealed at 700°C for 2 h and then immersed in FLiBe at 700°C at a pressure of 300 kPa for 20 h. The immersion leads to a weight gain of 7.9% for the control and of 8.2% for the irradiated sample (i.e., a difference of less than 0.4%). The increase is too small to be significant, considering that

---

[a] Corresponding to neutron fluence of $1.1 \ 10^{15}$ n/cm^2, as calculated using dpa/fluence conversion factor in (Campbell et al. 2016)

the microstructure of the two samples might have been slightly different before irradiation, but these data do not show an appreciable reduction of porosity with irradiation.

In summary, both pre- and post-turnaround irradiation studies show creation of porosity in the sub-micrometer scale and an overall reduction of the total graphite porosity by a few percent. Because a salt at the FHR/MSR pressures can infiltrate only pores larger than 0.6 µm, irradiation is expected to decrease the total volume of salt that infiltrates graphite. Irradiation might also change the contact angle of graphite by increasing the surface's roughness, but this is an effect that has yet to be investigated. Overall, experimental salt infiltration studies on irradiated graphite do not show appreciable changes in weight gain with irradiation.

3.1.2.2. *Effect of air and water vapor on infiltration*

The effects of high-temperature oxygen or water vapor on salt infiltration are partly discussed in MSRE reports. The contact angle of the fluoride salts on graphite is influenced by the presence of water vapor in the atmosphere (Grimes 1964 pp. 38–42). The introduction of 10 ppm of water vapor into flowing helium reduced the contact angle of the MSRE fuel solvent over CGB graphite from 150° to 20°. The same change from non-wetting to wetting behavior occurred after replacing the fuel solvent with FLiBe or CGB graphite with AGOT or pyrolytic graphite. In these cases, the formation of a scum-oxide layer over the salt drop was observed, and the graphite was wet by the oxide ring. The water vapor concentration required for these changes in wettability and the speed at which they occur depend on the fluoride salt. Both the MSRE fuel solvent and FLiBe start to wet graphite at water vapor concentrations of 10 ppm, but the oxide shell over the drop forms in about 1 h for the MSRE fuel and 10 h for FLiBe. This phenomenon is less pronounced for FLiNaK, in which the contact angle only changed by 10° after exposure to an atmosphere containing 1000 ppm of water vapor. With a 20º wetting angle, pores of all sizes, even nanopores, will be impregnated by the salt. Using Equation 3.6 with a 20° contact angle and with FLiBe surface tension and viscosity, the predicted penetrability is 12 m/s. This large penetrability indicates that the salt would rapidly impregnate the pores following an event leading to the build-up of a moisture concentration   in   the   reactor   atmosphere. The different behavior between FLiBe and FLiNaK could be attributed to the absence of BeF_2, a slower hydrolysis, and the solubility of the oxide (Grimes 1964 pp. 38–42). Unlike water vapor, the presence of oxygen gas (in concentrations up to 400 ppm) was not found to affect the wetting behavior of FLiBe and the MSRE fuel salt (Grimes 1964 pp. 38–42).

Accidental ingress of air and water vapor, as well as the presence of ppm-level concentrations of air and water vapor in the reactor core could also cause oxidation of the graphite (acute in the first case, chronic in the second), leading to an increase in graphite porosity that could result in a larger infiltration volume. Studies of acute (Luo et al. 2005a; Wang et al. 2012; Xiaowei et al. 2004) and chronic (Contescu et al. 2014, 2018a; Contescu and Mee 2016) graphite oxidation are available for gas environments , but not for salt-based systems. In the case of acute oxidation in gas environments, using IG-110 graphite as a reference, oxidation rates are in the order of 10^{-6} s^{-1} at 700 °C (e.g. 0.4% porosity change in 1 hour) (Xiaowei et al. 2004). For chronic oxidation, (Contescu and Mee 2016) reports oxidation rates for moisture concentrations of up to 200 ppm at temperatures of 800 °C and above (for IG-110, oxidation rate is 10^{-9} at 800 °C, leading to a 0.1% porosity increase in a day of operation under these conditions).

If graphite oxidation in the salt occurs comparably to oxidation in gas environments, it would lead to the generation of open porosity with diameters in the order of hundreds of μm (Wang et al. 2012), which would be then infiltrated by the salt.
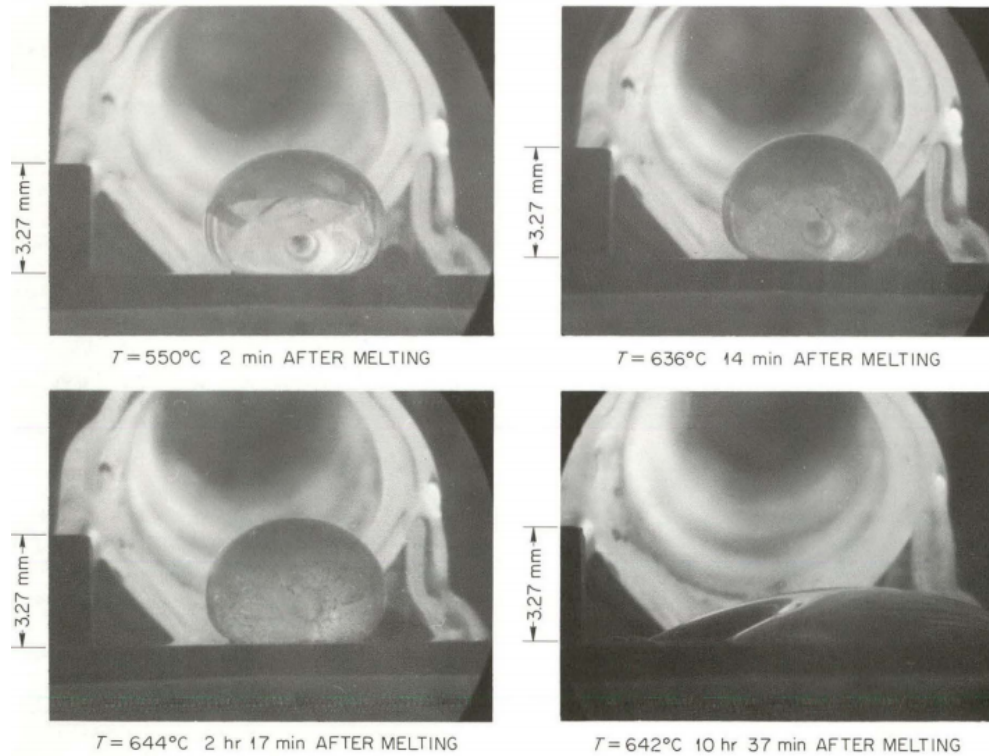
Figure 3.7: FLiBe droplets on CGB graphite in presence of 10 ppm water vapor in helium flow for different elapsed time after melting. The formation of the oxide layer makes the FLiBe droplet progressively more opaque and ultimately makes it wet graphite after around 10 ppm (Grimes 1964 pp. 38–42).

In summary, MSRE studies show that the presence of moisture in the ppm range in the cover gas is sufficient to change the wetting behavior of FLiBe from non-wetting to wetting. This change would allow salt to infiltrate graphite open porosity even at low pressure, affecting the mechanical, thermal, and neutronic properties of graphite. This change does not occur in FLiNaK or with oxygen instead of water. In addition to the change on the wetting behavior, air and moisture could lead to chronic oxidation of the graphite, leading to the generation of hundreds-of-micron sized pores, which would be subject to infiltration at reactor pressures.

3.1.3   Effects of salt infiltration on graphite Properties

Graphite components in MSRs and FHRs must sustain thousands of hours of operation while maintaining their functional properties. Therefore, they must resist environments with phenomena such as irradiation, oxidation, temperature gradients, and mechanical forces. Salt infiltration might affect graphite performance under such conditions. The effects of salt infiltration on nuclear graphite microstructure, mechanical, thermo-physical, neutronic, and functional properties are discussed in this section.

3.1.3.1. Pore Breakdown

As introduced in Section 3.1.1, salt infiltration at high pressures introduces damages to the graphite microstructure, causing the mechanical breakdown of pores into larger cavities (He et al. 2013; Lian et al. 2016; Song et al. 2014). This phenomenon is observed experimentally in infiltration studies at very high salt pressures when the graphite weight-gain rate starts to increase again after having plateaued. This effect differs for various grades of nuclear graphite with different pore sizes, as shown in Figure 3.4, but the required pressures are always on the order of 10 MPa or more. Because the operating pressures of FHRs and MSRs are below these values by several orders of magnitude, infiltration-driven mechanical breakdown of pores is not expected to occur.

As discussed in Section 3.1.2, changes to graphite porosity occur under neutron irradiation and could occur because of chronic oxidation. The change in pore size distribution produces a change in the mechanical properties (Marsden et al. 2016; Olasov et al. 2019). It is not known if irradiation under applied pressure could change the irradiation evolution of porosity, or it this would be of relevance to surface properties (such as thermal contact resistance), or to bulk mechanical properties. Changes in porosity and surface roughness could impact the amount of salt that carries along with the graphite at discharge from the core and could affect the decontamination strategies for removal of salt from the graphite. Removal of salt from the graphite is especially necessary for fuel elements, since solidified fluoride salt undergoes gamma radiolysis when the temperature drops below 150°C (Toth and Felker 1990). Removal of salt is also of importance for performance in a disposal repository, both for fuel and non-fuel graphite, and changes in porosity may change the effectiveness of salt-clean-up techniques for the graphite surface.

3.1.3.2. Tensile and Compressive Strength

The effect of salt infiltration on graphite mechanical properties has been explored (Zhang et al. 2018a). In the study, IG-110, and NG-CT-10 samples were exposed to a pressure of up to 1 MPa of FLiNaK at 700°C. After infiltration, the samples were cooled to room temperature, loaded into the uniaxial stress testing device, reheated to 700°C to remelt the infiltrated salt, and subjected to either tensile or compressive strength testing (Zhang et al. 2018a). As shown in Figure 3.8, infiltration leads to a decrease in the high temperature compressive and tensile strength of both graphite grades. The decrease is approximately linear with infiltration pressure. Interpolating the trend for IG-110 to Mark-I PB-FHR conditions, graphite is expected to undergo a 10% and 3% decrease in compressive and tensile strength, respectively.
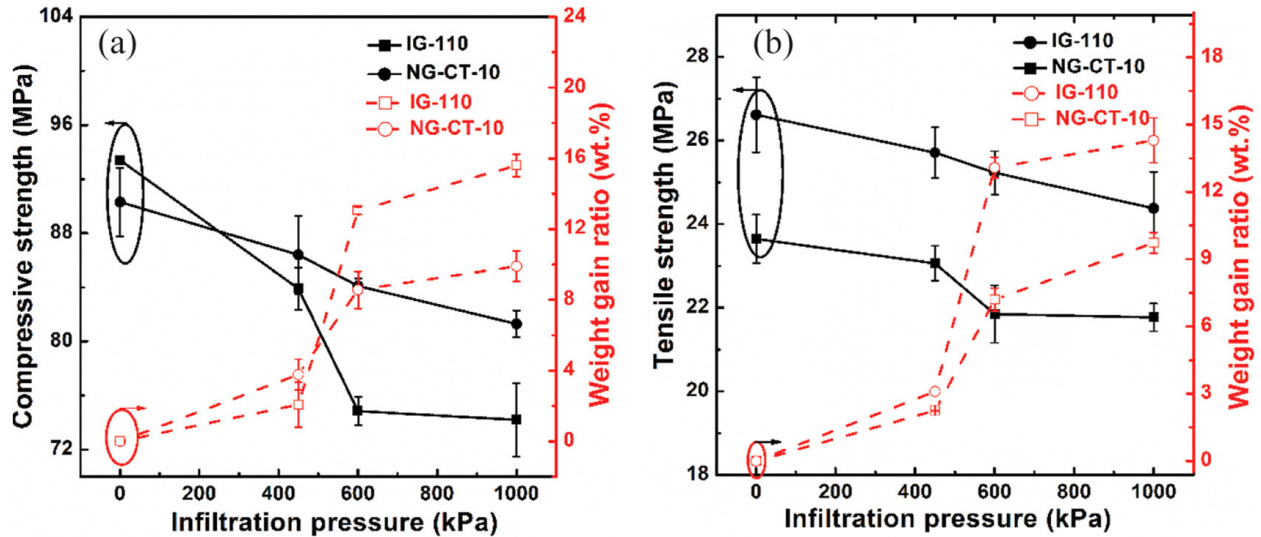
Figure 3.8: The influence of FLiNaK infiltration on the high-temperature (a) compressive strength and (b) tensile strength of graphite grades IG-110 and NG-CT-10 (Zhang et al. 2018a).

(Zhang et al. 2018a) also provides evidence of mechanical damage of infiltrated graphite upon thermal cycling and salt freeze-thaw cycles. High temperature (700 °C) compressive strength tests are performed on virgin graphite and samples that underwent one thermal cycle after salt-infiltration (i.e., infiltrated with salt at high temperature, cooled down to room temperature and then reheated to 700 °C). Fracture analysis of the graphite samples failed in the tests shows that virgin and salt-infiltrated samples have a different orientation of the fracture lines, indicating a change of the mechanism of fracture from shear fracture to longitudinal fracture. This change is attributed to the thermal stress while re-heating of the infiltrated samples due to the dissimilar coefficient of thermal expansion (CTE) for graphite and salt, which causes a tensile stress on graphite pores (Zhang et al. 2018a). FLiBe has a CTE of 2.13×10^{-4} K^{-1} over the 450°C–600°C interval, whereas nuclear graphite has a CTE of 7×10^{-6} K^{-1} over the 200°C–600°C interval (Hacker et al. 2000) (Vidrio 2019).

Unlike (Zhang et al. 2018a), whose results suggest that thermal cycling may lead to damage of thermally-cycled infiltrated graphite, MSRE-era studies report no effect of thermal cycles on infiltrated graphite integrity. As discussed in (Briggs et al. 1963), CGB graphite samples were infiltrated by MSRE fuel salt at a gauge pressure of 1 kPa (unknown temperature) and underwent 100 freeze-thaw cycles between 200°C and 700°C. (Briggs et al. 1963) reports no. change in the number and size of graphite cracks after cycling (investigation method is not reported). Additional studies on thermal cycling of infiltrated graphite, involving pressures higher than the 1 kPa used in (Briggs et al. 1963) and mechanical testing, are recommended to quantify the extent of damage, if any, and its dependence on the number of cycles.

3.1.3.3. Heat Transfer

Salt infiltration in graphite pores might change the thermal conductivity of graphite components in FHRs and MSRs, thereby affecting the heat transfer behavior in the reactor. The effect of infiltration on graphite thermal conductivity has not been explored in literature, but some predictions can be made based on the thermal conductivity of salt, graphite, and the cover gas (which is assumed to be argon). The thermal conductivity of FLiBe (1.0 W/mK, (Williams et al. 2006)) is larger than that of argon (0.016 W/mK, (Engineering ToolBox 2003)). As a result, if the salt were to infiltrate the pores, replacing the argon in them, the effective thermal conductivity would increase. There are several computational models for the thermal conductivity of porous materials (e.g. parallel and series models, Maxwell-Eucken model (Gong et al. 2014)). A study investigating graphite thermal conductivity change upon oxidation shows that the thermal conductivity decreases linearly with the increase of open porosity (Matsuo 1980). This observation suggests that graphite can be modeled as a system in which heat conduction occurs in parallel across the graphite and across the pores. With this model, the effective heat conduction for the non-infiltrated graphite $k_{0\%}$ can be modeled as

$$k_{0\%} = \alpha k_{Ar} + (1 - \alpha)k_c \qquad\qquad 3.7$$

where k_{Ar} and k_c are the thermal conductivity of argon and carbon, and α is graphite porosity (as a percentage of the volume). If the graphite is infiltrated, then the thermal conductivity would change:

$$k_{V\%} = k_{V\%} + V\%(k_{Salt} - k_{Ar}) \qquad\qquad 3.8$$

where V% is the fraction of the graphite volume occupied by the salt, and k_{Salt} is the salt thermal conductivity. Using this model for thermal conductivity of the infiltrated graphite, the change in thermal conductivity is negligible, even at high infiltrated volumes. For example, considering IG-110 graphite as a reference, the effective thermal conductivity would increase from 120 W/mK[b] in the non-infiltrated case to 120.1 W/mK when the salt occupies 10% of the graphite volume. The predicted change depends on the specific correlation used for computing the effective thermal conductivity of a porous media. Experimental measurements of thermal conductivity of infiltrated and non-infiltrated graphite are required to confirm that the changes are negligible.

The effect on thermal contact resistance, however, might be of relevance. Salt infiltration may change solid-to-solid thermal contact resistance and graphite-to-salt thermal contact resistance. For heat transfer in a pebble bed, pebble-to-pebble thermal contact resistance could of relevance in the response to reactivity transients, in terms of thermal response of the fuel elements to power transients (Fratoni and Greenspan 2011), and resilience to fuel hot-spots (Asakuma et al. 2016). For heat transfer from the pebble fuel to molten salt, the graphite-salt thermal contact resistance could be of relevance, and it would likely be influenced by salt intrusion (Fieberg and Kneer 2008; Wang et al. 2016).

3.1.3.4. Neutronics

The presence of salt in graphite pores could influence pebble motion in the core, thereby impacting the discharge burnup. In PB-FHRs, pebbles are cyclically inserted at the bottom of the core and

---

[b] Data from manufacturer available at https://www.toyotanso.com/Products/catalog.en.full.pdf

extracted at the top after rising through the core height. The upwards motion is made possible by buoyancy, as the pebbles are less dense than the salt. Since infiltration of salt in the pores will lead to a change in the pebble density, it may impact the pebble motion, increasing the time each pebble spend in the core at each cycle. The increased residence time in the core may impact the burnup at discharge and reduce the number of cycles each pebble will undergo.

In addition to this, since the salt has different scattering and absorption cross sections from graphite, infiltration may lead to a change in the neutron spectrum. The change would be more impactful for MSRs, because of the presence of fission products in the salt. Previous studies of graphite infiltrations in the MSRE were concerned with the presence of ^{135}Xe in graphite pores. Xenon-135 is a strong neutron poison fission product (Rosenthal and Briggs 1968) that remains dissolved in the MSR fuel salt. Salt infiltration into graphite pores would introduce ^{135}Xe in the moderator and allow it to diffuse deeper into the graphite, leading to an increase in the neutron absorption and a worsening of graphite moderation (Rosenthal et al. 1972 p. 175). The effect of ^{135}Xe on graphite moderation can be reduced by 80% by sparging the xenon from the salt (Rosenthal et al. 1972 p. 175). To date, no study has evaluated the effects of salt infiltration on the PB-FHR neutronics, which could derive from the change in pebble buoyancy and the counteracting effects of increased neutron moderation and absorption.

3.1.3.5. *Chemical Reactions*

As discussed in Section 2, when graphite is exposed to fluoride salts, such as FLiBe or FLiNaK, at high temperature, fluorine present in the salt can react with the carbon atoms in graphite. The reactions occur at the crystallite edges and lead to the formation of C–F bonds and an increase in the available reactive carbon sites (RCSs). These reactions can occur on the graphite surface if salt does not infiltrate graphite (Compere et al. 1975; Lee et al. 2020), but they may occur within the bulk of the sample if the salt reaches it by infiltrating graphite porosity (Compere et al. 1975; Lee et al. 2020). In these conditions, the increase of RCSs would not only be limited to the graphite surface and may cause larger trapping term and change the effectiveness of graphite as a tritium scavenger in the core. To substantiate these hypotheses, direct studies of the graphite–molten salt–hydrogen system are needed.

Graphite oxidation can occur when oxygen gas or water vapor are present in the atmosphere. The kinetics of oxidation increase with temperature, and the oxidation process is rate-limited by chemical reactions, pore diffusion, or mass transport depending on the temperature interval (Xiaowei et al. 2004). In the nuclear engineering field, oxidation of graphite has been extensively studied in the context of HTGRs (Kane et al. 2017a; Windes et al. 2014; Xiaowei et al. 2004) and GCRs (Marsden et al. 2020; Standring 1966). In these reactors, graphite oxidation could be chronic because of oxygen and moisture in the coolant, or it could take place in accident scenarios during fuel handling (HTGRs only) and upon entrance of oxygen or water vapor in the core. A study on graphite oxidation in helium shows that at a temperature of 800°C and steam partial pressures of 1–10 Pa, oxidation rates are on the order of 10^{-9} s^{-1}. At this rate, about 100 days are sufficient to cause a weight loss of 1% of graphite (Contescu et al. 2018). The weight loss corresponds to an increase in graphite porosity by the same amount. If the new porosity is produced uniformly at all scales, then the infiltrated volume of salt would increase by the same amount. Graphite oxidation in reactors that employ molten salts has not yet received wide attention, and it is unclear whether the presence of fluoride salts accelerates or decelerates graphite oxidation. The coal community

has dedicated some attention to the study of graphite oxidation in molten sodium carbonates and sulfates. This research has shown that sodium alkali metal molten salts have a catalytic effect in coal gasification (i.e., graphite oxidation is faster when the graphite is immersed in the salt (Dunks et al. 1980, 1982; McKee and Chatterji 1975; Stelman 1976)). For example, oxidation rates at 900°C have been shown to increase roughly by a factor of 40 when graphite is immersed in a lithium carbonate salt (McKee and Chatterji 1975). If similar behaviors were confirmed in fluoride salts, then a few days would be sufficient to introduce macroscopic oxidation changes in graphite. Therefore, graphite oxidation studies in HTGRs and GCRs could underestimate oxidation effects in MSRs and FHRs. As a result, the increase in salt infiltration might be more pronounced than the 1% in 100 days estimated previously. As in the case of tritium management, the infiltration of salt in graphite would increase the surface area of contact between the salt and graphite, which could increase the catalytic effect, if one is present. Similarly, porosity introduced by chronic oxidation may increase salt infiltration, as discussed in Section 3.1.2.2. The consequences of salt-mediated oxidation that would need to be considered include performance of graphite and fuel matrix material as a waste form (i.e., changes in dissolution rate in a repository).

3.1.4   Conclusions

Graphite infiltration studies from the MSRE and MSBR programs apply only partially to FHRs, since the MSRE salt greatly differs from the FHR salt in composition, physicochemical properties, and operational conditions. In the FHR, infiltration of the salt has an impact on reactor operation and on the management and disposal of graphite components after their removal from the core.

Infiltration in FHRs can be predicted from the graphite porosity, the salt contact angle on graphite, and the surface tension (Eq. 3.1), parameters that vary greatly across graphite grades, salt chemistry, and operational conditions. Using the conservative value of 500 kPa for the pressure of MSRs and FHRs, a salt contact angle of 110° (lowest bound estimate for FLiBe), and a surface tension of 0.230 N/m (Grimes 1964 pp. 38–42), salt infiltrates pores of diameter larger than 0.6 μm. Comparing this result with the pore size distribution of graphite grade suggests that few graphite grades would satisfy the 4 vol % limit set in the MSRE; even fewer would satisfy the 0.5 vol % design target (Briggs 1964b p. 255). This is also confirmed in direct salt infiltration studies (Figure 3.5) and indicates that the most graphite grades would be unsuitable for MSRs at these conditions but not necessarily for FHRs, for which infiltration limits have not yet been defined.

To define infiltration limits for FHRs, it is necessary to evaluate the effect of salt infiltration on graphite properties and quantify its impact on reactor safety and graphite waste management. Current literature suggests that infiltration worsens graphite's mechanical properties (up to −25% in compressive strength and −10% in tensile strength) and may affect the extent of graphite–salt reactivity, which in turn affects tritium uptake and oxidation resistance. A quantification of the effects on graphite neutronics, heat transfer, and performance in safety transients is absent in the literature. Providing a quantitative assessment of these effects and their implications to reactor operation and waste management would be needed to establish infiltration limits in the development of graphite reflectors and fuel elements for FHRs and MSRs.

3.1.5   Acknowledgement

disposal" authored by L. Vergari, M. Nelson, A. Droster, C. Contescu, N. Gallego, R.O. Scarlat and published *Journal of Nuclear Materials*. The co-authors of the original manuscript have been informed of the inclusion in this dissertation.

The authors contribution to the original manuscript are as follows:

LV: Conceptualization, Formal analysis, Data curation, Writing – original draft, Visualization, Project administration. **MN**: Conceptualization, Formal analysis, Data curation, Writing – original draft. **AD**: Conceptualization, Formal analysis, Data curation, Writing – original draft. **CC**: Investigation, Writing – review & editing. **NG**: Investigation, Writing – review & editing. **ROS**: Validation, Writing – review & editing, Resources, Supervision, Funding acquisition.

3.2 Predicting Infiltration Through Wetting: Parametric Study of Molten Fluoride Salts Wetting Behavior on Graphite.

Methods to predict salt infiltration can help nuclear reactor designers select graphite grades that are resistant to infiltration at the salt pressure and operational conditions of interest. The Washburn equation (Washburn 1921), introduced in Section 3.1, is a helpful tool to predict the pressure dependence of salt infiltration in graphite.

Among the terms that enter the Washburn equation, salt pressure and graphite pore distributions are well characterized, while contact angle (CA) and surface tension (ST) are not. Only few studies measure CA and ST for molten salts (Delmore et al. 2018; Grimes 1964; Lian et al. 2016; Zhang et al. 2018a), and they do not discuss the dependence of these factors on experimental conditions such as salt chemistry, graphite microstructure and surface finish, as well as the reactor environment. Variations in liquid composition, substrate structure (composition, orientation, and surface roughness) as well as environment (inert gas, temperature, pressure) have been observed to have an impact on CAs and ST on droplets of water (Ghasemi and Ward 2010), oils (ZISMAN 1964), molten alloys (König and Keck 1983) , nanofluids (Prajitno et al. 2016) and chlorides (Stepanov 2018) on various substrates, but there is a lack of research on the effects of these variables for fluoride salts on graphite.

This study seeks to explore the variability in the CA of fluoride salts on graphite upon changes to graphite conditions (microstructure, pre-treatment, and surface finish) and salt compositions to infer the effect of these variables on wetting behavior. As opposed to using a contact angle goniometer to measure droplet edges, an image-processing python script is employed to approximate CA and volume, allowing for higher-throughput analysis. The reference salt used in this study is FLiNaK, a mixture of LiF, NaF, and KF. FLiNaK is not a candidate salt for MSR or FHR operation but is often used as a surrogate for FLiBe (the salt used in FHRs) to avoid beryllium toxicity. The methodology developed in this work will be applied to FLiBe and other Be containing salts in the near feature.

3.2.1 Methods

3.2.1.1. Materials

3.2.1.1.1. Graphite

Samples of two nuclear graphite grades are used in this study: ET-10 and IG-110. Table 3.5 describes the properties of the used grades. To explore the effect of graphite preparation on contact angle, samples are selectively baked to degas adsorbed oxygen and moisture, polished to achieve a smooth finish, and/or sanded with coarse grit sandpaper to achieve a rougher finish. Sample baking is performed at 600 °C for 6 hours in argon. Sample polishing is performed by grinding with 1200 grit SiC and polishing with 9 μm diamond particle suspension. Sample sanding is performed using 120 grit SiC for about two minutes per surface. Ra roughness is measured using a Mahr SD26 profilometer with a 2 μm radius tip over a traversing length of 5.60 mm. The reported roughness values correspond to the standard deviations of these Ra data. Table 3.6 provides the preparation conditions of all samples.

Table 3.5: Graphite source materials

Graphite	Type	Producer	Average Grain Diameter	Open Porosity
ET-10 [1]	Isostatically Molded Nuclear Graphite	Ibiden	d = 15 µm	15%
IG-110 [2]	Isostatically Molded Nuclear Graphite	Toyo Tanso	d = 20 µm	22%
Notes:				
[1] Manufacturer data, available at https://www.fgm.ibiden.co.jp/multilanguage/english/list.html				
[2] Manufacturer data, available at https://www.toyotanso.com/Products/Special_graphite/data.html				

Table 3.6: Graphite Sample matrix

		Baking Treatment	
		As Received	Baked
Surface Finish Treatment	As Received	IG-110	IG-110/ET-10
	Polished	-	IG-110/ ET-10
	Roughened	-	ET-10

3.2.1.1.2. Salt

Experiments are conducted using LiF-NaF-KF (46.5-11.5-42 mol %, FLiNaK) salt. Unlike $2LiF$-BeF_2 (FLiBe), FLiNaK is not currently being investigated for use in FHRs and MSRs, but it is largely employed as a surrogate for FLiBe to avoid beryllium toxicity. FLiNaK use as a FLiBe surrogate is motivated by their similarity in melting point and low vapor pressure at the temperature of interests, as shown in (Williams et al. 2006). The FLiNaK used in this experiment is prepared at Oak Ridge National Laboratory (ORNL). FLiNaK is used as received and after the addition of known amounts CrF_3 and FeF_3 (from 100 wppm to 10,000 wppm). For tests involving as received FLiNaK, salt samples are in the form of frozen pills with masses of 100 to 1000 mg. For tests involving FLiNaK doped with FeF_3 and CrF_3, salt samples are prepared by crushing frozen FLiNaK pellets with a mortar and mixing them with the chosen amount of CrF_3 and FeF_3 powder (Sigma Aldrich, purity 99.9%). Using a furnace, the powders are then heated in a graphite mold at 500°C for 30 minutes and then cooled for 30 minutes to obtain frozen salt pills with similar shapes. Details on the chemicals used in this study are included in Table 3.6. The mold has been prepared by drilling holes of about 5 mm diameter and depth in a graphite block outside the glovebox. The mold was then baked at 600°C for 4 hours in the glovebox to remove oxygen.
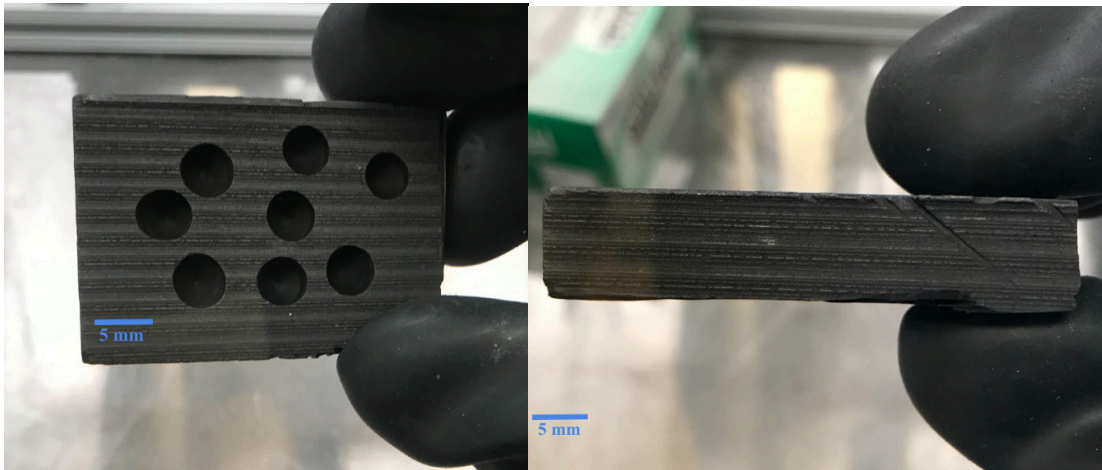
Figure 3.9: Pictures of the graphite mold

Table 3.7: Chemicals used in the study

Chemical	Origin/ CAS number	Details
FLiNaK	Oak Ridge National Laboratory	-
CrF_3	Millipore Sigma/ 7788-97-8	99.99% purity
FeF_3	Millipore Sigma/ 7783-50-8	-
FLiNaK from corrosion experiment	SALT lab at UC Berkeley	Sampled from a SS316L corrosion experiment using FLiNaK + 5 wt.% FeF_3

3.2.1.2. *Sessile Drop Method*

The contact angle of FLiNaK on graphite is measured using the sessile drop method. In this shape-analysis method a droplet of the liquid of interest is molten on the substrate and contact angle can be estimated from the droplet's shape (Morel 1966). Figure 3.10 illustrates the experimental setup used for the sessile drop method.
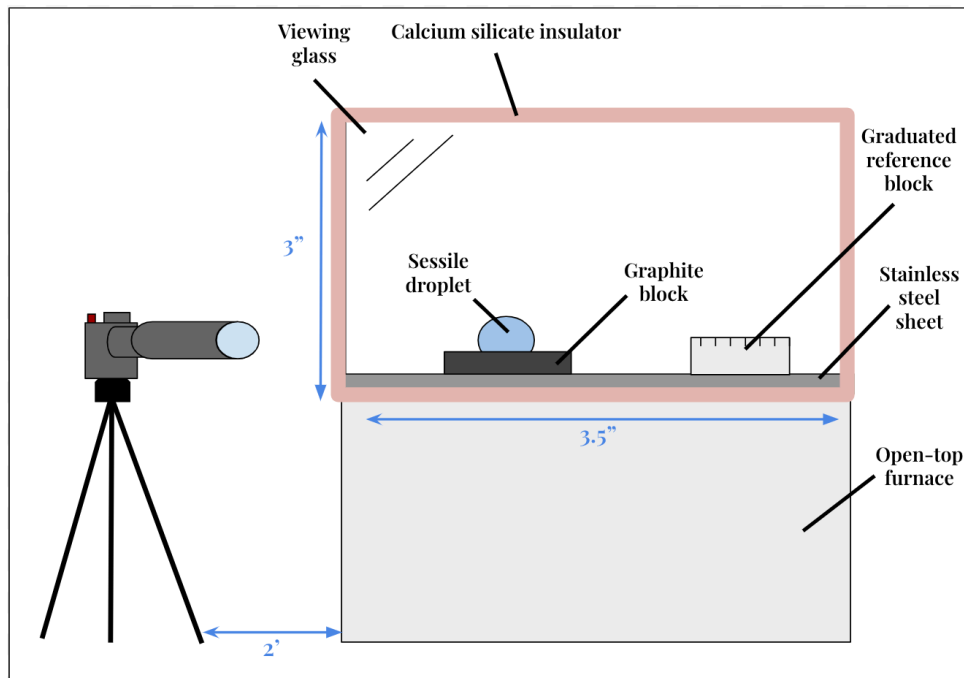
Figure 3.10: Illustration of the experimental apparatus (not to scale, glovebox not shown)

In an inert argon (O_2 < 1ppm, H_2O < 1ppm) glovebox (LC Technology), an open-top furnace (Omega CRFC-16/115-A) is placed on insulating blocks and capped with a grated stainless-steel plate. A calcium silicate cage with an adjustable display window is placed onto the grated steel to allow for thermal insulation. Graphite samples are positioned individually or in pairs into the cage and the salt samples are loaded onto their surface. A reference graduated block serving as a scalebar is introduced at approximately the same distance from the window as the salt samples. A type-N grounded thermocouple (Omega NMQXL-040G-12) is inserted into the cage to measure the system's temperature, and the furnace is controlled to heat up to 550º C using a data acquisition module (National Instrument, part cRIO-9067) running LabVIEW 2018. A high-resolution camera (Canon Rebel SL3) is equipped with a 150mm lens (Irix 150 mm f/2.8 Macro Drangonfly) and mounted on a tripod outside of the glovebox. The camera is used in manual mode, with a low shutter speed and a high aperture (1/10 s and f/10), and ISO is adjusted per experiment. Observations and notes during the experiment are recorded on a e-Lab notebook.

3.2.1.3. *Image Analysis*

The raw images are transferred to a computer and are processed on Adobe Photoshop. Processing involves rotating the image so that the droplet-solid edge is parallel to the horizontal, masking the droplet to create a contrast with the foreground, and cropping the image to reduce the file dimension. The masking of the droplet is performed to avoid surrounding noise from being analyzed as part of the droplet.
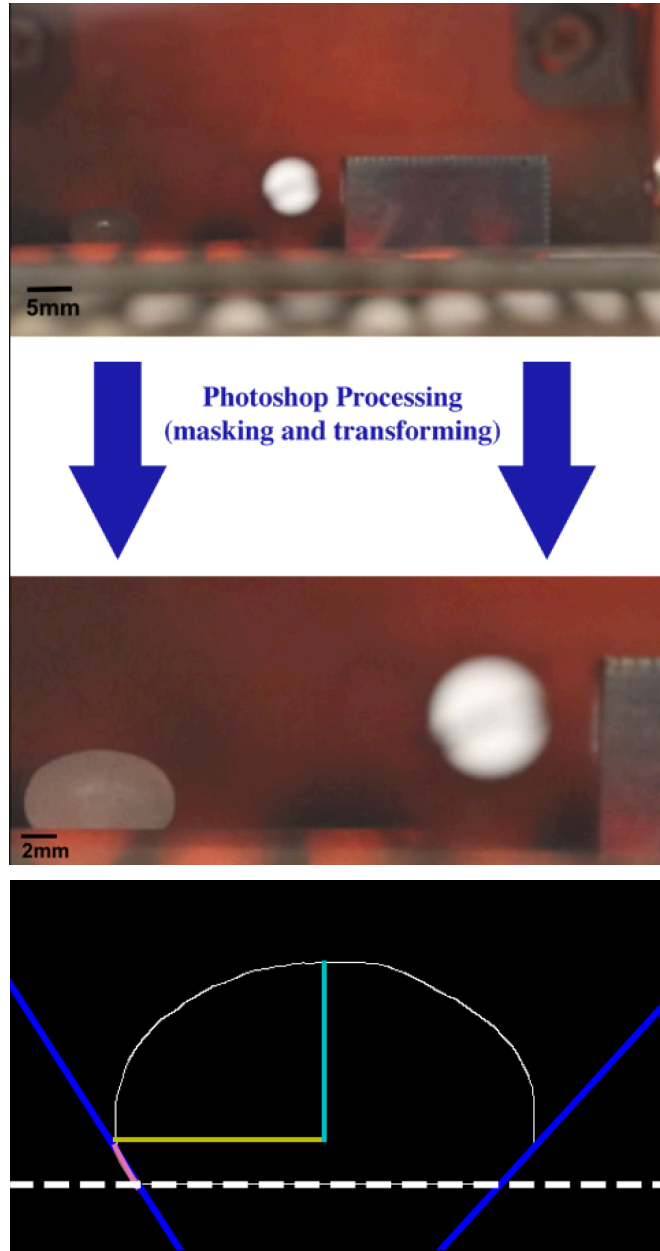
Figure 3.11: (Top) An example of a Photoshop processing with FLiNaK on an IG-110 sample. (Bottom) Computed lengths and slopes of droplet outline: the yellow and teal segments correspond to horizontal and vertical maximum radii, respectively, and the dark blue lines are the slopes used to calculate contact angle.

These processed images are next loaded in Python to extract relevant geometric parameters of the droplet, which are outlined in Figure 3.11. A Python script employing a graphical user interface (GUI) is written to identify the droplet outline using intensity thresholding, allowing the user to adjust pixel inclusion conditions to control the specificity of the outline.

Using the known scale of the reference graduated block in the image, these pixel-values are converted to centimeters, and physical features of the droplet are computed assuming spherical

68

symmetry of the droplet. Sample information such as graphite grade, graphite pretreatment conditions, temperature, salt mass, and salt mixture are specified manually. The script identifies the left and right CAs of the droplet by collecting twenty pixels from each edge, fitting them to a third-degree polynomial, calculating the derivatives at the contact points, and then taking the arctangents to estimate the CA. The degree of the polynomial and number of fitting points are kept uniform throughout all data acquisitions and are selected as the lowest numbers that yield consistent estimates in repeatability runs (Figure 7.2, Figure 7.3 in Supplementary Information). Statistical comparisons across different experiments are performed using t-tests at 5% significance level. The CA for each salt-graphite run is calculated by averaging the left and right edge angles for each image and taking the mean of these averages over all images corresponding to that run (i.e., the salt, graphite grade and treatments), with standard deviations calculated from all angles of each run.

3.2.1.4. *Software Calibration*

A water droplet is used to provide a benchmark of computed contact angles, testing the accuracy of the analysis script. The calibration experiment is conducted using the lower measuring plate of a modular compact rheometer (702e space multiDrive Anton Paar) at 22°C in air atmosphere.
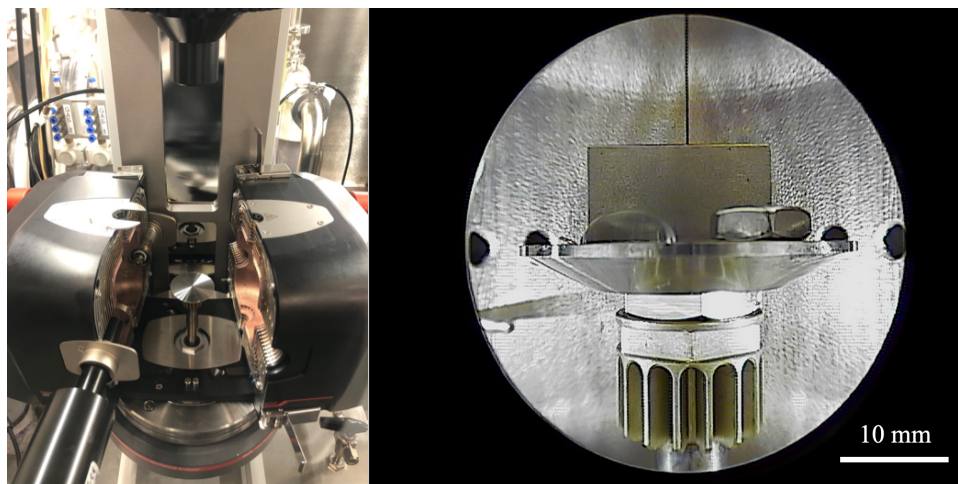
Figure 3.12: Pictures of the lower measuring plate of the AntonPaar modular compact rheometer (left) and of the water droplet taken with the DigiEye 600 camera (right)

A water droplet of 125 µl is placed on the plate with a pipette. The lower measuring plate is made of 316L stainless steel and has a diameter of 40 mm. Average roughness of the plate is measured by using the same method as for the graphite samples.

Picture is taken with a DigiEye 600 camera (Anton Paar). A nut from which diameter has been measured (9.37 mm) is placed next to the droplet, at the same distance from the camera, to provide a reference. Results obtained are compared with sessile drop data available in literature (Table 3.8).

Table 3.8: Comparison of calculated contact angle of water on 316L stainless steel with literature

Volume of the droplet (μL)	Average roughness Ra (μm)	Contact Angle (°)	Source
3	0.1-0.5	65.59	(Chimezie and Srinivas Gurram 2016)
	0.2-0.4	73.04	
	0.1-0.3	71.8	
	0.5-0.6	82.24	
15	0.72	60.8 + 2.8	(Bueno 2005)
N/A	0.6 - 0.8	74.4 - 87.0	(Arifvianto et al. 2011)
125	0.52 ± 0.06	68.2 ± 0.9	This study

The result from our study is within the 20° range from the different values reported in references and for contact angle of water on 316L stainless steel of similar roughness. While it has been demonstrated that droplet size has no significant impact on the value of contact angle for volume in the microliter range (1-10 μL) on smooth surface (Drelich 1997), it is important to highlight that the values obtained in our study is measured on a much larger droplet than in literature (Volume ~100x bigger).

3.2.2   Results

Compiled results are included in Table 3.9. Example images of the droplets during the experiments are shown in Figure 3.13 for FLiNaK + metal fluorides and in Figure 3.14 for pure FLiNaK.

Table 3.9: Summary of the measurements (ordered by increasing contact angle), at 550 to 650 °C

Graphite				Droplet						
			Average roughness Ra (μm)	Mass (mg)		Volume at 650°C (μL)	Solute		Contact Angle (°)	Frozen Contact Angle (°)
Grade	Baking	Surface finish		Before	After		CrF3 (Cr ppm)	FeF3 (Fe ppm)		
IG-110	Baked	Polished	0.67 ± 0.06	255	255	125	0	0	120.8 ± 1.9	113.5 ± 1.45 (n=2)
ET-10	Baked	Polished	N/A	506	N/A	247	0	0	122.2 ± 2.6	99.8 ± 4.8 (n=1)
IG-110	Baked	Polished	0.67 ± 0.06	136	N/A	67	0	0	127.2 ± 1.0	113.9 ± 0.8 (n=2)
IG-110	Baked	Polished	0.67 ± 0.06	66	N/A	32	0	0	128.0 ± 12.1	115.9 ± 0.4 (n=2)
IG-110	Baked	Polished	0.67 ± 0.06	932	N/A	460	0	0	128.5 ± 1.6	118.8 ± 9.3 (n=1)
ET-10	Baked	Roughened	3.3 ± 0.3	151	151	73	$(7.3 \pm 0.5) \times 10^1$	0	128.9 ± 1.7	119.9 ± 7.8 (n=1)
IG-110	Non baked	As received	1.3 ± 0.3	786	N/A	380	0	0	132.1 ± 6.2	109.9 ± 4.0 (n=1)
ET-10	Baked	As received	1.7 ± 0.2	1011	N/A	490	0	0	133.2 ± 4.1	117.6 ± 4.7 (n=4)
ET-10	Baked	Polished	N/A	N/A	N/A	N/A	N/A	N/A	135.3 ± 4.0	120.9 ± 2.7 (n=2)
ET-10	Baked	Roughened	3.3 ± 0.3	94	N/A	46	0	$(5.1 \pm 0.7) \times 10^1$	137.2 ± 2.8	N/A
ET-10	Baked	Roughened	3.3 ± 0.3	169	N/A	83	0	0	138.2 ± 2.5	N/A
ET-10	Baked	Roughened	3.3 ± 0.3	141	141	69	$(7.5 \pm 0.5) \times 10^2$	0	139.5 ± 4.9	104.1 ± 4.4 (n=1)
ET-10	Baked	Roughened	3.3 ± 0.3	154	N/A	75	0	$(4.8 \pm 0.4) \times 10^2$	142.6 ± 7.8	N/A
ET-10	Baked	Roughened	3.3 ± 0.3	179	179	88	$(7.5 \pm 0.5) \times 10^3$	0	143.4 ± 4.5	106.2 ± 4.7 (n=1)
IG-110	Baked	As received	1.07 ± 0.09	691	N/A	338	0	0	144.0 ± 1.6	N/A
ET-10	Baked	Roughened	3.3 ± 0.3	196	N/A	96	0	$(4.9 \pm 0.4) \times 10^3$	144.3 ± 7.5	N/A
Details of averaging and error calculation			Average and standard deviation over five runs	Mass measurement uncertainty σ(m)= 1mg		Volume is estimated by using the density of FLiNaK (Gallagher et al. 2022)	Dilution of CrF3/ FeF3 in FLiNaK. Error propagation from mass measurement uncertainty		Average and standard deviation over five images on left and right contact angle	Average and standard deviation over (n) image on left and right contact angle

71
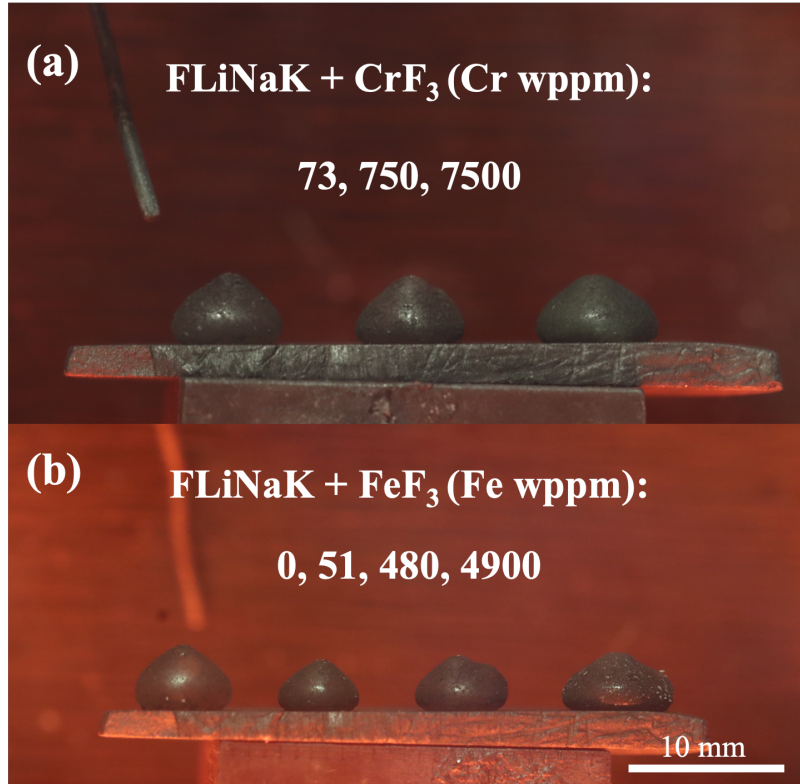
Figure 3.13: Molten FLiNaK droplets containing corrosion products on baked and roughened ET-10. See Table 3.9 for uncertainties on wppms.
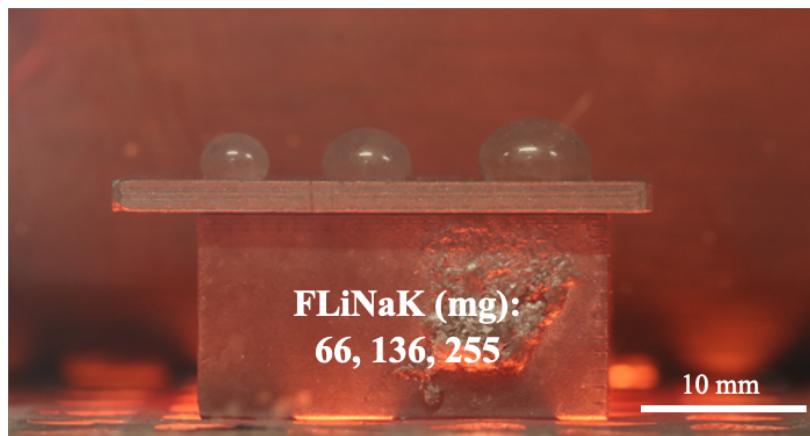
Figure 3.14: Molten FLiNaK droplets of different size on baked and polished IG-110. See Table 3.9 for uncertainties on wppms.

3.2.2.1. *Sources of Uncertainty*

In this work, the total uncertainty (T) is quantified as the standard deviation of CAs from each set of droplet-graphite images (approximately five images per set). The total uncertainty is plotted in the figures of the following sections by means of bidirectional error bars. Two distinct contributions are recognized in the total uncertainty: the measurement uncertainty (M) and the analysis uncertainty (A). Measurement uncertainty arises from changes in photography conditions

(e.g., noise around the edges, glare from glovebox glass, tilt of surface, and imperfect focus of the camera). Analysis uncertainty (A) arises from the image post-processing and in analysis steps, which depend on the user masking the droplets and computing the contact angles.

A procedure is defined to separate the contribution of analysis and measurement uncertainties. A photograph is independently analyzed by three co-authors (Table 3.10), and the analysis uncertainty is estimated as the standard deviation between the six angles of each system. The measurement uncertainty is then calculated as the difference (in quadrature) of the total uncertainty and the analysis uncertainty. This procedure is applied to two different photographs to observe variability.

Table 3.10: Uncertainty calculations for two example cases

Graphite Sample	Molten Salt	Contact Angle	Total Uncertainty	Analysis Uncertainty	Measurement Uncertainty
IG-110 B & P	FLiNaK	127.7º	5.7º (4.5%)	4.9º (3.8%)	3.0º (2.3%)
ET-10 B & R	FLiNaK + 750 wppm FeF_3	154.5º	4.4º (3.1%)	3.8º (2.5%)	2.3º (1.5%)

As shown in Table 3.10, the analysis uncertainty is the main source of uncertainty in both cases. Expecting these sample cases to be representative for the entire dataset of images, it is concluded that the analysis drives the total uncertainty in all sets of data.

The analysis uncertainty can be decreased by examining a larger number of images so that inaccurate masks or angle approximations are less weighted in computing the average CA. The measurement uncertainty is inherent to the image collection process and can be reduced by improving the image collection process in terms of lighting, focus, and positioning of the camera and the graphite-droplet system. Regardless, the low total uncertainties show that there is high repeatability of results if the photography conditions are controlled so that edges are easily distinguishable from the background.

3.2.3 Discussion

3.2.3.1. *Comparison with literature*

Limited reports of FLiNaK contact angle on graphite are available on literature (Section 3.1). Reported data often lack information on graphite preparation treatment or error quantification. Table 3.11 displays the FLiNaK contact angle data measured in this study alongside literature results. Results in (He et al. 2014b), (Lian et al. 2016) and the current study are distributed within a 20° window. As previous results do not report the mass of the droplets used for contact angle measurement, it is not possible to infer whether part of the spread of the results stems from droplet size effects.

Table 3.11: Comparison of measured FLiNaK contact angles with literature, as reviewed in Section 3.1

Graphite Grade	Baking Treatment	Surface Finish Treatment	Temperature (°C)	Contact Angle	Reference
CGB	N/A	N/A	500-720	90±4°	(Grimes 1964)
IG-110	6h at 600°C	9 μm diamond particle suspension polishing	600-650	121±2°	This study
ET-10	6h at 600°C	9 μm diamond particle suspension polishing	600-650	122±3°	
ET-10	6h at 600°C	120 grit SiC grinding	600-650	138±3°	
IG-110	As received	As received	600-650	132±6°	
ET-10	6h at 600°C	As received	600-650	133±4°	
NBG-18	N/A	1200 grit SiC polishing	N/A	135°	(He et al. 2014b)
UGG-1	N/A	N/A	N/A	140±10°	(Lian et al. 2016)
IG-110	N/A	N/A	N/A	140±10°	(Lian et al. 2016)
IG-110	6h at 600°C	As received	600-650	144±2°	This study
IG-110	3h at 700°C	N/A	450-600	95-170°	(Delmore et al. 2018)

3.2.3.2. *Drop-shape analysis of frozen droplets*

After melting and upon solidification, droplets condense in size and adopt a slightly different shape, causing a decrease in contact angle; the contact angles of frozen FLiNaK are included in Table 3.9. In every case the frozen droplets have a lower angle than the molten states, but this varies depending on graphite preparation and salt composition. For instance, there is a 2° difference between molten and frozen FLiNaK on baked and polished IG-110, whereas baked and roughened ET-10 sees a 37° decrease in angle with a CrF_3-FLiNaK mixture. The varying inequalities between different graphite-salt conditions suggest that the contact angle of frozen sessile droplets is not representative of the molten droplets and should not be used for drop shape analysis.

3.2.3.3. Size effect
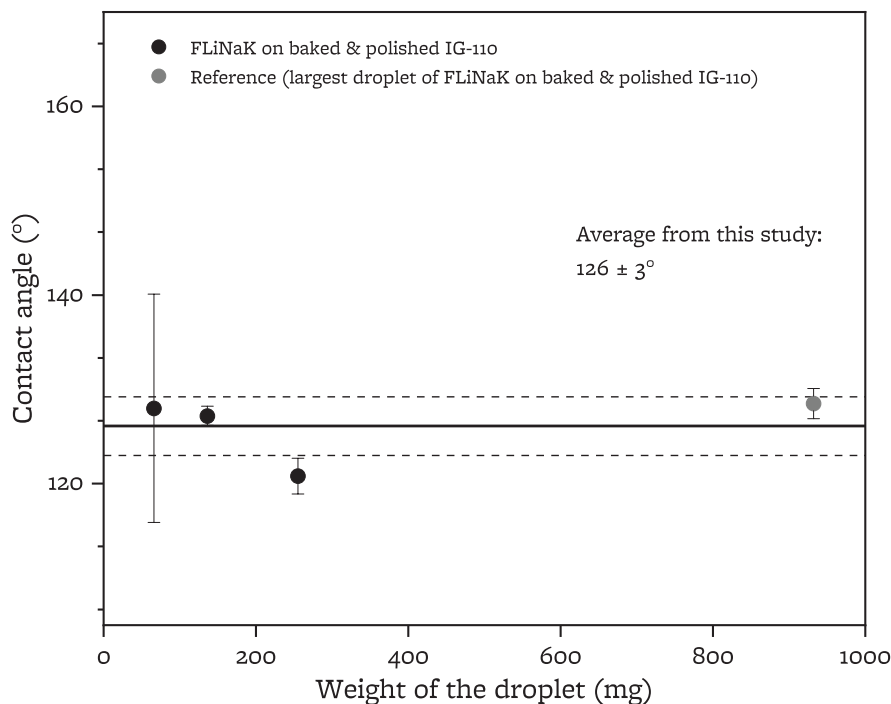
Note: To convert from droplet mass in mg to droplet in volume in μL,
divide by 1.97 (Sohal et al., 2010)

Figure 3.15: Effect of size on contact angle.

Literature on contact angle of various liquids has shown that for certain liquid-solid systems, the sessile contact angle manifests size dependence for droplets below a critical size, depending on both the liquid and the solid (Drelich et al. 1993, 1996; Good and Koo 1979; Ponter and Boyes 1972). For example, (Good and Koo 1979) shows size dependence for water on PMMA (critical radius ~ 0.4 cm) and for ethylene glycol on PTFE (critical radius ~ 0.5 cm), but not for decane on PTFE. (Drelich et al. 1996) observes that size dependence may depend on roughness, by showing no size dependence for water on as-received PTFE and size dependence for water on roughened PTFE.

Figure 3.15 plots the contact angle of FLiNaK on baked and polished IG-110 as a function of droplet size. Our data, collected over a mass interval spanning to less than 100 mg to above 1 g, corresponding to approximately 0.2 cm to 0.6 cm droplet radii, indicates that contact angle is not size dependent within this interval. Additional measurements for smaller droplet size and on rougher substrate are required to confirm the absence of size-dependence for the FLiNaK-graphite system.

3.2.3.4. Graphite Treatment
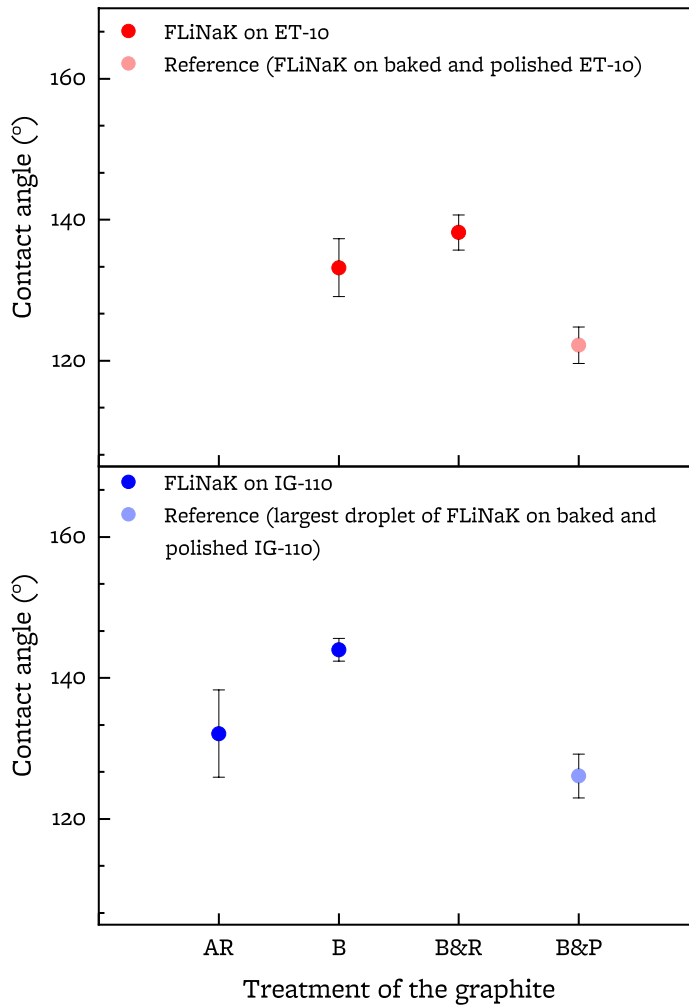
Figure 3.16: Effect of graphite treatment on contact angle (AR: As Received, B: Baked, B&R: Baked & Roughened, B&P: Baked & Polished).

Graphite components from MSRs and FHRs are subject to wear with use. This is especially the case for pebble-bed reactors where fuel-containing graphite pebbles are moving and sliding on surrounding materials. Graphite wear can lead to the formation of a smoother surface (He et al. 2023; Vergari et al. 2023a). For instance, tribology testing of ET-10 in Argon at 600°C (Section 4.1) leads to the decrease in Ra roughness from 1.2-1.9 µm to 0.3-0.4 µm (Table 4.4). Similarly testing of ET-10 in FLiBe + 1 wt.% Be at 600 °C (Section 4.2) decreases Ra roughness from 1.4 µm to 0.7 µm (Table 4.7). From Figure 3.16, it can be observed that polishing the graphite result in smaller contact angle and thus increased wetting. Thus, since wear leads to a polishing effect, it may decrease the resistance to infiltration.

On the contrary, irradiation of graphite causes roughening of its surface. (Huang et al. 2019) shows an increase in Rms roughness from 0.1 µm to 0.4 µm after 20 dpa Argon ion irradiation. Contact angle of pure FLiNaK is plotted against the average roughness of the graphite substrate in Figure 3.17. A simple model proposed by (Kim et al. 2016) postulates that roughness may impact

wetting only when the droplet size is less than 40 times than the characteristic scale of the surface roughness. In our study, the smallest droplet weights 66 mg and has a diameter equal to ~ 4 mm (Figure 3.14). The maximum average roughness of the graphite samples considered in this study is equal to 3.3 μm and is thus more than 1000 times smaller than the droplet diameter, suggesting that an effect of roughness should not be seen. This expectation aligns with what is observed with ET-10 (change in contact angle lower than one standard deviation as roughness changes from 1.7 μm Ra to 3.3 μm Ra), but not with IG-110, which undergoes a statistically significant change in contact angle (p-value <0.001 , full p-values available in Mendeley Data repository linked in Supplementary Information) as roughness varies from 1.1 μm Ra to 0.7 μm Ra. Overall, these observations suggest that the impact of roughness may be depending on the specific roughness interval or may change depending on the grade. As discussed in Section 2, fluorination is observed upon long term exposure of the graphite to salt. The chemical interaction may be impacting wetting to different extents depending on the roughness. Further exploration is needed to generate a mechanistic description of wetting.
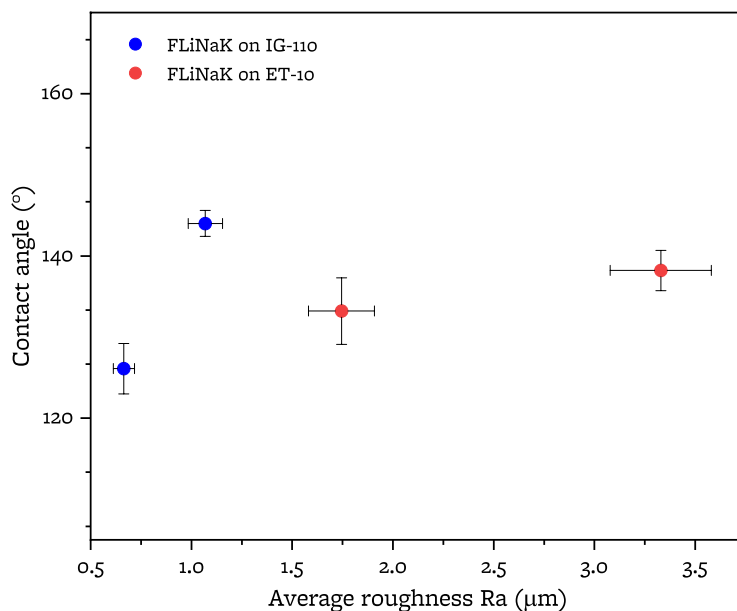
Note: Datapoints collected on baked IG-110, baked and polished IG-110
(largest FLiNaK droplet), baked ET-10, and baked and roughened ET-10

Figure 3.17: Effect of graphite roughness on contact angle.

3.2.3.5. Salt composition
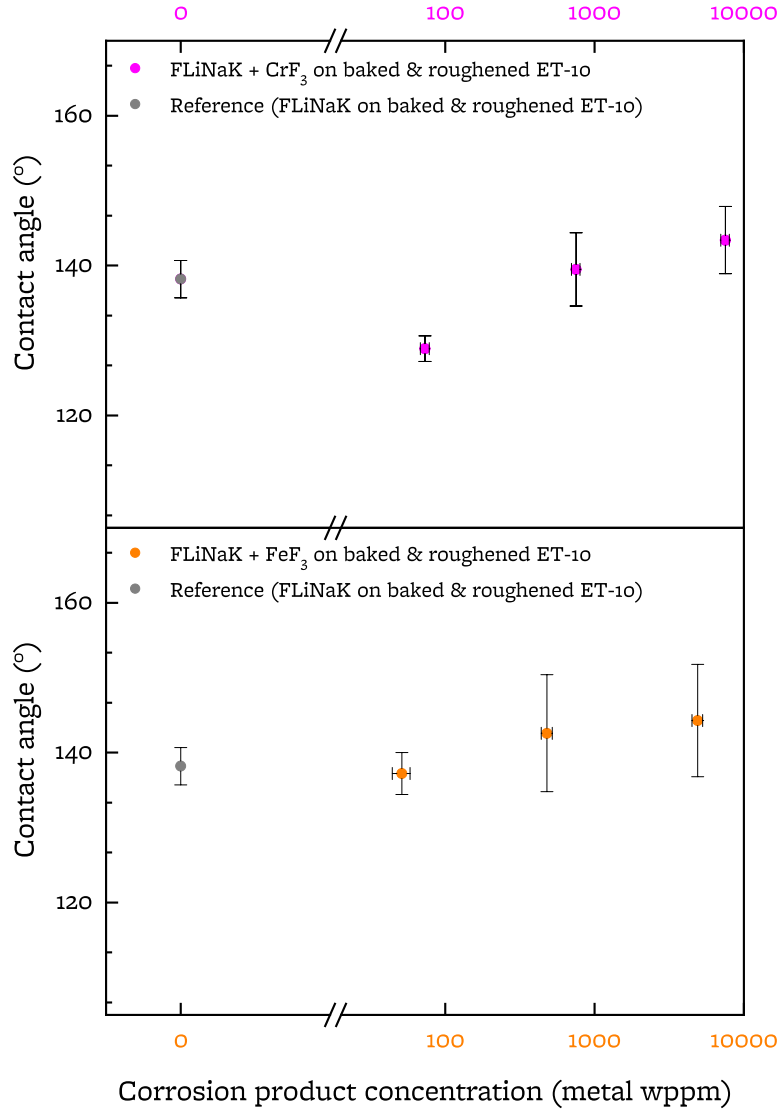
Figure 3.18: Effect of corrosion product addition on contact angle.

The equilibrium concentration of Cr and Fe ions dissolved in the salt will depend on the redox potential chosen for the reactor operation (Zhang et al. 2018b). It has been observed that the valence state of Cr is dependent on the salt in which it is dissolved: while Cr^{2+} is favored in FLiBe, Cr^{3+} is favored in FLiNaK (Liu et al. 2020). In the MSRE, the target redox potential was set in the range 0.9-1.1V vs Be^{2+}/Be ^{c} (Baes 1974). At this redox potential and assuming SS 316L internals, the equilibrium concentration of Cr^{2+} in the salt would be in the range of 0.1 ppm - 1000 ppm, with the lower values corresponding to lower redo potentials and lower temperature (600 °C) and the higher values corresponding to higher redox potential and higher temperatures (700 °C). Gen IV

---

^{c} Corresponding to $10 < x_{UF4}/_{UF3} < 100$, as converted in (Vergari et al. 2022b).

reactors employing molten salt reactors may target different redox potentials than the MSRE, leading to larger or lower concentrations of transition metals in the salt.

In this study, a statistically significant decrease in contact angle is observed upon addition of 73 wppm Cr^{3+} (corresponding to 100 wppm CrF_3). No statistically significant change in wetting behavior occurs when adding CrF_3 in larger amounts. It is interesting to note that solubility limit for Cr^{3+} in FLiNaK is estimated to 2,000 wppm at 600°C in (Yin et al. 2018) and 600 wppm at 530°C in (Zakharova et al. 2020). It is possible that two of the three droplets had Cr^{3+} concentrations above solubility limit, and that the lack of a significant changes in wetting is due to a phase separation of the chromium. This is not expected for the droplet with the lowest Cr^{3+} concentration selected in this study, as the concentration is expected to be eight to thirty times lower than the solubility limit. No statistically significant change is observed upon addition of FeF_3 in any amount.

Overall, this suggests that compositional changes may impact the wetting on graphite, and that changes will be impacted by type and amount of the impurity. The results observed in FLiNaK may vary from those in FLiBe but suggest that higher wetting may be observed at chromium compositions comparable to what is expected during reactor operation. It is therefore recommended to conduct infiltration tests using salt compositions that are representative of the reactor salt.

If similar results are assumed in FLiBe, one can draw conclusions on the relevance of these wetting changes for Gen IV reactors. Under these assumptions, a reactor operated within the MSRE target redox potential window may experience changes in wetting driven by corrosion product concentration, as the Fe and Cr content will be in the order of tens of wppm. Further measurements in FLiBe at lower corrosion product concentration (units to few tens of wppm) are required to quantify the effect for FHRs where a tight redox control is applied.

3.2.3.6.   *Benchmarking: using the Washburn equation to predict infiltration*

As discussed in Section 3.1, the Washburn equation (Eq. 1) constitutes a useful tool to predict the volume of infiltrated salt in graphite components in FHRs and MSRs without running a direct infiltration study. If mercury porosimetry data are available, the Washburn equation can be used to convert the mercury pressure necessary to infiltrate a pore of diameter d to the corresponding salt infiltration pressure, according to Eq. 3.9, and pore size distribution can be plotted against the salt pressure to generate an infiltration curve.

$$k = \frac{\Delta P_{Hg}(d)}{\Delta P_{salt}(d)} = \frac{\gamma_{Hg} \cos(\theta_{Hg})}{\gamma_{salt} \cos(\theta_{salt})} \qquad\qquad 3.9$$

Infiltration predictions using the Washburn equation have been tested against direct infiltration data in work by two groups investigating FLiNaK infiltration in graphite. In (He et al. 2015), nuclear graphite samples of six grades (including IG-110) are infiltrated with FLiNaK at absolute pressures up to 1100 kPa (temperature: 650°C, duration: 100h). The infiltrated volumes are recorded and plotted against salt pressure. The salt pressures are compared to the pressure of mercury required to infiltrate the same volume, and the ratio $k = \frac{\Delta P_{Hg}(d)}{\Delta P_{salt}(d)}$ is calculated to 3.6-3.8 depending on the graphite grade. As shown in Equation *3.9*, this ratio depends on the wetting

parameters of the salt and the mercury. Table 3.12 reports literature values for the wetting parameters of mercury and graphite and for the surface tension of FLiNaK. Using these values in Equation *3.9* one can extract bounding values for the contact angle of FLiNaK on these graphite grades. Contact angle for FLiNaK on baked ET-10 and IG-110 are within the calculated bounds, suggesting that the Washburn equation predicts accurately the salt infiltrated volumes measured in this study.

In (Gallego et al. 2020, 2021b), nuclear graphite samples of seven grades (including IG110 and ET10) are infiltrated with FLiNaK at absolute pressures in the interval 500-798 kPa (temperature: 750°C, duration: 12h). The FLiNaK infiltrated volumes are reported alongside mercury porosimetry data, so that the parameter k can be calculated. Apart from one grade (NBG-18), the values of k calculated in this study are larger than 0.5, which is the minimum value that allows for a $\cos(\theta_{salt}) > -1$ (see input values in Table 3.12. Noting that the experiment in (He et al. 2015) has a duration of 100 hours while the experiments in (Gallego et al. 2020, 2021b) last for 12 hours, it could be hypothesized that the systematic overestimation of the values of k in (Gallego et al. 2020, 2021b) may indicate that the equilibrium infiltration volumes had not been attained at 12 hours of equilibration, thus providing insight into infiltration kinetics. This hypothesis is consistent with the discussion on infiltration kinetics presented in Section 3.1.1.6, where it is shown that equilibration times of 10 hours have previously resulted in partial infiltrations.

Table 3.12: Calculation of FLiNaK contact angle from direct infiltration experiments.

Wetting Parameters for Eq. 3.9

	Min	Max
Mercury ST, γ_{Hg} (N/m)	0.420 (Kemball 1946)	0.485 (Kemball 1946)
Mercury CA, θ_{Hg} (°)	150 (Awasthi et al. 1996)	156 (Awasthi et al. 1996)
FLiNaK ST, γ_{FLiNaK} (N/m)	0.150 (Lian et al. 2016)	0.184 (Grimes 1964)

Calculation of FLiNaK contact angle from infiltration studies using Eq. 3.9

Study Reference	Equilibration Time	Infiltration Pressure Range	Graphite Grades	Measured $k = \dfrac{\Delta P_{Hg}(d)}{\Delta P_{salt}(d)}$	Calculated FLiNaK contact angle (Eq. 3.9)
(He et al. 2015)	100 h	150-1000 kPa	6 grades, including IG-110	3.6 - 3.8	121°-145°
(Gallego et al. 2020, 2021b)	12 h	500-700 kPa	7 grades, including IG-110 and ET-10	0.01 for NBG-18 > 0. 7 for all other grades	91°-92° for NBG-18 >180° for all other grades

3.2.3.7. Engineering significance of the contact angle variability

In Figure 3.19 mercury porosimetry results for ET-10 and IG-110 from Section 3.1 are used with the contact angles measured in this study to generate an infiltration curve.
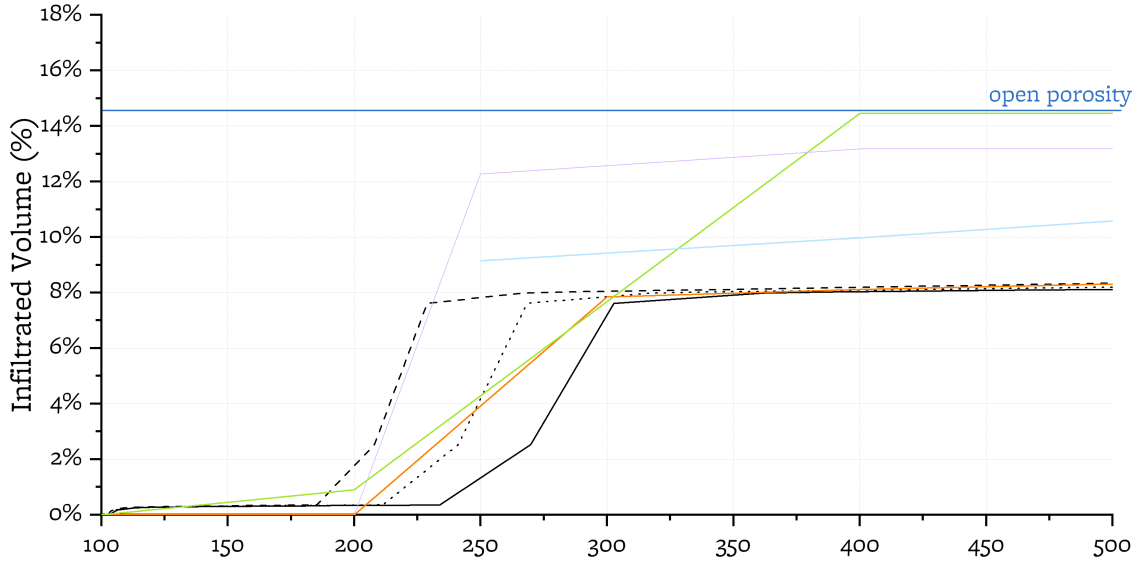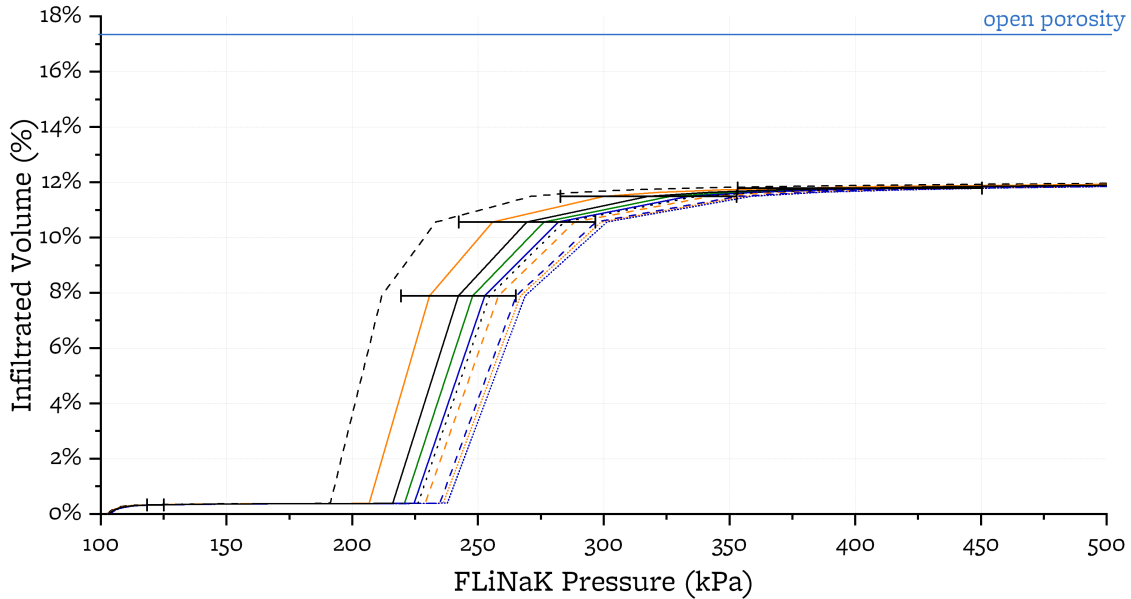
Input parameters: γ_{Hg}=0.485 N/m, θ_{Hg}=156°, γ_{Hg}=0.184 N/m (Table 3.12), and graphite porosity from (Gallego et al., 2020). Vacuum is assumed in graphite pores before infilration. Error bars drawn on one curve and representing variability of contact angle (Table 3.9) and input parameters.

Figure 3.19: Infiltrated volume percentage for the samples of graphite explored in this study.

In building Figure 3.19, the surface tension is assumed constant and equal to 0.184 N/m (Grimes 1964). For one of the curves, error bars are drawn to account for the variability in FLiNaK contact angle (Table 3.9), in FLiNaK surface tension, and in mercury wetting parameters (Table 3.12).

Data Figure 3.19 is limited to the pressure interval of relevance for FHRs and MSRs. These curves illustrate how the contact angle changes caused by graphite surface finish and salt chemistry (discussed in earlier section) impact the volume infiltrated at a given pressure.

An important take-away from Figure 3.19 is that changes to the contact angle will impact differently the infiltrated volume at different pressures because the graphite grades studied have a narrow porosity distribution. Because the porosity distribution of IG-110 and ET-10 is narrow, the impact on infiltrated volume is maximized at pressures at which pores of size close to the average pore start getting infiltrated. At these pressures, infiltrated volume can change by a factor of five depending on the salt chemistry and the graphite surface finish. Conversely, at lower or higher pressures, infiltrated volumes are not impacted by these parameters. This observation suggests that phenomena that change graphite's surface finish (irradiation, wear) and salt composition (corrosion) will be relevant for infiltration in reactors that operate at pressures in the proximity of the minimum pressure in which the average diameter is infiltrated.

3.2.4   Conclusion

This work presents a parametric study for contact angle of fluoride salts on graphite based on the sessile drop method. The data are collected for FLiNaK on nuclear graphite as a proof-of-principle before FLiBe testing. Contact angles are measured with pure FLiNaK and upon addition of known concentrations of CrF_3 and FeF_3 on graphite of controlled surface finish and microstructure conditions. The measurements indicate statistically significant variations of contact angle upon graphite baking, polishing, and additions of CrF_3. Further work will examine the effect of reducing agents and oxide content on wetting behavior, with confirmatory work needed to corroborate these trends in FLiBe.

In addition to contact angle, the script approximates droplet volume assuming a spherical symmetry, and from this the density can be calculated given a mass. Surface tension calculation was attempted during analysis but was unsuccessful using pre-existing equations for surface tension from drop-shape analysis (Worthington 1881; Ziesing 1953), possibly due to inherent sources of error when calculating sessile droplet surface tension (Sangiorgi et al. 1982). Development of more robust methods of surface tension analysis are currently being investigated.

3.2.5   Acknowledgement

This chapter contains material included in the manuscript *"Contact angle of molten fluoride salts on graphite: a parametric study"* authored by L. Vergari, Z. Falkowski, X.H. Ooi, M. Denis, R.D. Hayes, R.O. Scarlat in preparation for submission to *Journal of Nuclear Materials*. The co-authors of the original manuscript have been informed of the inclusion in this dissertation.

The authors contribution to the original manuscript are as follows:

LV: Conceptualization, Methodology, Software, Formal analysis, Investigation, Data curation, Visualization, Writing – original draft, Supervision. **ZF**: Validation, Formal analysis, Investigation, Data curation, Visualization, Writing – original draft. **XHO:** Software, Formal analysis, Investigation. **MD:** Validation, Investigation, Data curation, Visualization, Writing – original

draft. **RH:** Methodology, Writing – review & editing. **ROS**: Conceptualization, Visualization, Writing – review & editing, Supervision, Funding acquisition.

4 Graphite-Graphite Tribology in Fluoride Salt Reactors

In a PB-FHR, graphite pebbles will roll and slide against each other and surrounding structures. Quantifying friction and wear in pebble-pebble and pebble-structure contacts is necessary to predict pebble flow and degradation in the core. In this chapter, two graphite-graphite tribology experiments are presented. The first experiment (conducted in collaboration with Kairos Power) investigates graphite friction and wear in argon at room temperature and high temperature. The second experiment investigates graphite-graphite tribology in FLiBe and assesses the effect of salt temperature and salt composition on friction and wear.

4.1   Graphite Tribology in Argon: Self-lubrication at High Temperature

During online refueling and operation of pebble-bed reactors like the PB-FHR and the HTGR, fuel pebbles are continuously circulating through pebble handling systems and the core. In both HTGRs and PB-FHRs, pebbles will roll and slide against each other and against structural component surfaces. In HTGRs, the sliding will occur in helium atmosphere. In PB-FHRs, instead, the sliding will occur both in the fluoride salt and in regions in the reactor where the pebbles are not covered in salt, hence they are exposed to the cover gas, typically argon.

The dust generated during sliding can be a radiological hazard and contribute to the source term. For example, the dust may contain C-14, a radioactive isotope generated in FHR and HTGR cores by irradiation of graphite. The dust may also contain tritium. In FHRs, H-3 is generated by neutron irradiation of the lithium and beryllium salt and can undergo uptake into graphite (Chapter 5). In HTGRs, H-3 is created by irradiation of lithium impurities in the graphite and also by irradiation of the helium coolant from where it can transport into the graphite (Xie et al. 2018). Dust may be transported by the coolant and deposited on the heat exchangers, changing the heat transfer performance of the system, and out from the primary coolant circuit, where it can lead to a dose to plant workers or a radioactive dose release to the environment.

Friction will change the velocity and the trajectory of the moving graphite spheres, and the residence time of pebbles in the reactor (Rycroft et al. 2006). This may impact the distribution of fuel burnup in the core, in turn affecting the power distribution in the reactor core. As a result, characterizing the wear and friction behavior of pebbles as they roll and slide against structural component surfaces and against each other is important for modeling of the core behavior and for prediction of the contribution of the graphite dust to the radiological source term.

Due to the widespread use of graphite across industries, graphite friction behavior has been studied extensively since the mid-20th century. The variability of the results is wide, with graphite friction coefficients spanning from less than 0.1 to above 0.9 (Luo et al. 2010). This large variability indicates that graphite friction and wear are highly dependent on experimental parameters, such as the mating materials, sample preparation, the temperature, the environment, and the presence of lubricants among others. Of the studies investigating graphite-graphite friction, only few (Hiruta et al. 2013; Li and Sheehan 1981; Luo et al. 2005b; Xiaowei et al. 2006) use nuclear graphite and none uses carbon matrix – a carbonaceous material that does not undergo high temperature graphitization and is used for reflectors and fuel elements in HTGRs and PB-FHRs (Pappano et al. 2008; Yeo et al. 2018). The sample preparation is not uniform across studies in terms of baking (e.g., no degassing (Luo et al. 2005b), degassing at 200 °C (Hiruta et al. 2013), and degassing at

400 °C (Li and Sheehan 1981)). A few studies explore the dependence of the coefficient of friction on temperature and discuss the temperature-dependent mechanisms, yielding contradictory results (Hiruta et al. 2013; Li and Sheehan 1981; Luo et al. 2005b; Stansfield 1969). Most of the available studies involve the measurement of graphite friction in vacuum (Bowden and Young 1951; Savage 1948), air (Blau and Martin 1994; Li and Sheehan 1981; Spreadborough 1962) , or reactive environments (Lancaster and Pritchard 1981; Zaidi et al. 1991) with only a subset investigating graphite tribology in inert environments (Hiruta et al. 2013; Li and Sheehan 1981; Luo et al. 2005a; Stansfield 1969; Stempflé and Von Stebut 2006; Zaidi et al. 1990). To date, only one research group has studied graphite sliding in argon (Robert et al. 1995; Zaidi et al. 1990) and no peer reviewed literature on graphite friction in molten fluoride salts is available.

Kairos Power and the SALT group at the University of California, Berkeley have collaborated in a set of graphite tribology experiments to generate friction and wear results representative of the pebbles rubbing against each other and against the reflector in a PB-FHR and to understand the underlying mechanisms. This chapter presents and discusses the results of the graphite tribology experiments in argon, relevant to graphite-graphite friction in the PB-FHR handling systems and in the core cover space. This chapter reports the wear rates and friction coefficients at two temperatures in argon: room temperature (RT) and 600 °C (HT). The argon environment and the temperature of 600 °C used in this study are selected to be representative of the non-salt wetted regions of the Kairos Power FHR (KP-FHR) core, which operates between 550°C and 650°C (Kairos Power LLC 2018). In addition to being representative to the KP-FHR, a temperature of 600°C is included within the core temperature interval for most HTGRs and PB-FHRs, including Xe-100 (Mulder and Boyes 2020), HTR-PM (Zhang et al. 2009), and the Mark-I PB-FHR (Andreades et al. 2016). The tests at 600°C are compared to tests at room temperature in the same gaseous environment to investigate whether the friction coefficients and wear behaviors observe a temperature dependence, or if results from room temperature tests can be considered representative of the high temperature conditions.

Tribological testing is accompanied by the characterization of the graphite surfaces via digital microscopy (DM), polarized light microscopy, scanning electron microscopy (SEM), Raman spectroscopy, and X-ray diffraction (XRD, included in a Data in Brief article (Vergari et al. 2023b)) , which allows to formulate a mechanistic description for graphite friction and wear mechanisms in Ar inert gas and their temperature dependence.

4.1.1 Methods

4.1.1.1. Materials

The experiments presented in this work are performed with ET-10 nuclear graphite. Several grades of nuclear graphite are being considered for use in nuclear reactors, and nuclear codes such as ASME do not prescribe a specific grade. ET-10 is an isostatically molded graphite manufactured by Ibiden and selected by Kairos Power for the KP-FHR. The properties of ET-10 are included in Table 4.1. The samples are machined from ET-10 billets into 4-cm diameter spheres and 15-cm diameter disks. After manufacturing, the spheres are sonicated in acetone and the disks are wiped with an acetone-wetted cloth. Prior to the tests, the sphere and disk samples are degassed at 600 °C for 4 hours in argon atmosphere to remove any adsorbed oxygen and moisture.

Table 4.1: Characteristics of ET-10 graphite

Graphite Type	Nuclear Graphite
Fabrication Process	Isostatic Molding
Density	1.75 g/cm^3
Open Porosity	15%
Total Porosity	23%
Average Grain Size	15 μm

Manufacturer data at https://www.fgm.ibiden.co.jp/multilanguage/english/list.html

4.1.1.2. Tribology Measurements

The experiments are performed using a pin-on-disk tribometer. In pin-on-disk setups, the pin and the disk are in relative rotatory motion. In the performed experiment, the pin is static, and the disk rotates at a constant speed. An illustration of the experimental apparatus is shown in Figure 4.1. To reproduce the geometry of a PB-FHR pebble, the pin used in the experiments consists of a 4-cm diameter graphite sphere. ET-10 is used as the material of the spheres and the disks in all tests. The wear track diameter varies among tests, between 2 and 8 cm. The tribometer disk is located inside a cup that can be heated inductively for high-temperature testing. The tribometer is hosted in an inert environment glovebox (Ar, <1ppm O_2, <1ppm H_2O). During a test, the load cell measures the friction force F and the coefficient of friction μ is calculated as the ratio of the friction force F and the load L. The load of the pin and the speed of the disk relative to the pin are user defined. The load cell has an uncertainty of 0.3 N. Calibration of the load cell is performed at the beginning of the experimental campaign using NIST calibrated loads as per the manufacturer's instruction. The sliding distance is calculated from time (uncertainty of 0.001 min), the rotational velocity (uncertainty of 0.1 rpm) and the distance of the pin from the center of the disk (uncertainty of 0.01 mm). The temperature is measured by one type K thermocouple (Omega) placed in contact with the disk at the beginning and the conclusion of the tests in the vicinity of the radial locations of the pebble; the thermal gradient in the radial direction was not quantified; at high temperature, temperature uncertainty due to thermal gradients in the instrument is assumed to be +/- 10 °C. The radial location of the pebble varies among tests, such that new wear tracks are generated on the disk, with every test. The thermocouples are calibrated by the vendor, and temperature measurements are not otherwise calibrated. Temperatures are observed to vary +/-10 °C in the high temperature tests.

Specific wear rates are calculated according to the ASTM G99.17 Standard test method for wear testing with a Pin-on-Disk apparatus (ASTM International 2017). Based on the standard, the wear volume V_{wear} can be calculated from the size of the wear spot on the pin (the pebble, in this case) according to Equation 4.1:

$$V_{wear} = \pi d^4 / 32D \qquad\qquad 4.1$$

Where d and D are the wear spot and pebble diameters, respectively. The specific wear rate k is calculated from the wear volume according to Equation 4.2:

$$k = \frac{V_{wear}\rho}{lL} \qquad\qquad 4.2$$

Where ρ is the graphite density, l is the sliding distance, and L is the load. The wear spot diameter is measured using a digital microscope at a 50X magnification. Five wear spot diameter measurements are taken for each spot and the spot is assumed circular in shape; the uncertainty on the wear rate is estimated by propagating the uncertainty of the wear spot diameter (ASTM

86

International 2017). The assumption of negligible wearing of the disk in the calculation of the wear rates is verified, as indicated by microscopy of the worn disk, which show that the wear tracks are deposited on top of the disk surface (Figure 7.4 in Supplementary Information).
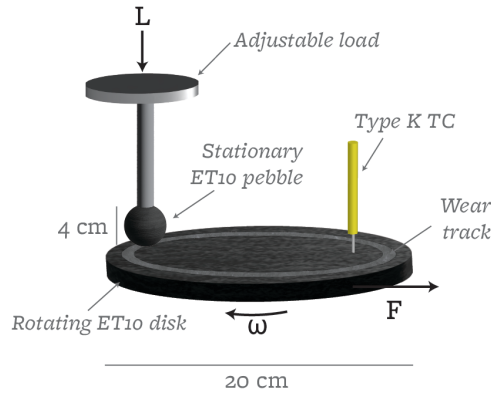
Figure 4.1: Tribology apparatus for high-temperature measurements in an argon glovebox.

Wear spots and tracks are generated on multiple pebbles and disks (or sides of the same disk). Table 4.2 provides a list of the IDs for the control samples (Pebble Ref, Disk Ref), wear spots on the disk (WS) and wear tracks on the disk (WT) studied.

Table 4.2: Sample Matrix. Applied load is 50.000(1) N for all runs [a].

RunID	Translational Speed (m/s)	Rotational Speed (rpm)	Radial Location (cm)	Rotational Frequency on Wear Track (1/m)	Tribology Testing Temperature (°C)	ID for Wear Spot (WS) on Graphite Pebble	ID for Corresponding Wear Track (WT) on Graphite Disk
-	no wear (reference)	-	-		-	Pebble Ref	-
-	no wear (reference)	-	-		-	-	Disk Ref
1	0.14996(6)	35.8(1)	4.000(1)	3.98	21	WS1	WT1
2	0.15017(8)	71.7(1)	2.000(1)	7.96	26	WS2	WT2
3	0.15009(7)	63.7(1)	2.250(1)	7.07	17	WS3	WT3
4	0.15017(6)	47.8(1)	3.000(1)	5.31	601	WS4	WT4
5	0.15006(15)	143.3(1)	1.000(1)	15.92	603	WS5	WT5
6	0.14998(6)	33.7(1)	4.250(1)	3.74	597	WP6	WT6
7	0.14991(6)	40.9(1)	3.500(1)	4.55	600	WS7	WT7

[a] uncertainty on applied load accounts for weight and counter-weight uncertainty; other errors not accounted could include friction in the vertical sections of the tribometer arm, and the load cell zero-ing.

4.1.1.3. *Characterization Techniques*

4.1.1.3.1. *Microscopy*

Digital microscopies and profilometry of the samples are generated using a Keyence digital microscope VHX-6000 with brightfield coaxial illumination. Roughness is measured using the digital microscope as the arithmetical mean height over a surface of approximately 0.1 mm^2. The microscope's built-in correction for spherical geometry is used to image the pebble. Images of the wear spots used for wear rate calculations were taken in an inert environment using a Dino-Lite

Digital Microscope Premier (50x magnification). Polarized light images are acquired on a Nikon Eclipse LV100NL optical microscope. A sensitive-tint retardation plate (Nikon POL λ) is used to introduce color contrast based on the texture orientation. Scanning electron microscopy (SEM) of the samples is performed using a Scios 2 dual beam SEM/FIB. Both the wear spot and the non-wear surface are imaged. In all SEM microscopies, a voltage of 20 kV and a current of 12 pA are used.

4.1.1.3.2. Raman Spectroscopy

The Raman spectra of the wear spots and the surrounding regions are collected using a Horiba LabRam HR confocal Raman microscope with a 532 nm laser source and an optical magnification of 50x. The slit size is set to 200 cm and Raman spectra are collected in the 0-3000 cm^{-1} wavenumber range. The depth probed by the laser source is estimated at 30-60 nm, and the sampling diameter is in the order of one micron (Compagnini et al. 1997; Scharf and Singer 2003). The individual spectra are fitted using Lorentzian functions on OriginPro 2021b and the crystallite parameters are estimated using the correlations provided in (Cançado et al. 2008; Maslova et al. 2012; Tuinstra and Koenig 1970). Statistical analysis of the crystallite parameters is performed using a two-sample t-test.

4.1.2 Results

4.1.2.1. Friction Coefficients and Wear Rates

Table 4.3 provides the experimental conditions for each of the tribology runs, and the results for average and max coefficient of friction (COF) and the specific wear rate. Average COFs and specific wear rates are generally reported in graphite tribology literature and used to as metrics for comparison across studies (Luo et al. 2010). Max COFs are not reported as often, but could be useful for engineering applications, as they would help establish a conservative estimate of the friction performance of the components.

Figure 4.2 shows the COFs as a function of sliding distance, for each of the runs described in Table 4.3.

Table 4.3: Coefficients of friction and specific wear rates. Pin on disk measurements. Pin material: ET-10, 4-sphere. Disk material: ET-10 disk, 1 – 4 cm diameter wear track.

Run ID	Track Circumference	Ambient Temperature[1]	Sliding Distance	# Track Cycles	Average COF[2]	Max COF[3]	COF at end of run[4]	Specific Wear Rate[5]
	(cm)	(°C)	(m)		(-)	(-)		(ug/ Nm)
1	25.132(6)	21	159.3(5)	633	0.62(18)	0.82(0.6)	0.77(2)	0.138(6)
2	12.566(6)	26	149.1(2)	1186	0.47(9)	0.79(0.6)	0.53(7)	0.71(5)
3	14.137(6)	17	99.2(2)	701	0.55(13)	0.76(0.6)	0.66(3)	0.286(17)
Average for room temperature:		21(5)[1,5]			0.55(14)		0.65(12)	0.4(3)
4	18.850(6)	601 (10)	149.4(4)	792	0.35(3)	0.61(6)	0.36(4)	0.104(11)
5	6.283(6)	603 (10)	148.2(2)	2358	0.31(3)	0.58(6)	0.31(2)	0.030(1)
6	26.704(6)	597 (10)	149.6(5)	560	0.35(7)	0.76(6)	0.32(5)	0.063(4)
7	21.991(6)	600 (10)	149.5(4)	680	0.32(4)	0.59(6)	0.32(8)	0.051 (5)
Average for high temperature runs:		600 (10)[1,5]			0.33(5)		0.33(2)	0.06(3)

[1]The temperature at the contact point is estimated from the COF (Eqn. 2) at 285 °C for RT and 720 °C for HT (see Section 4.1.3.2.3).
[2]Average and standard deviation over the entire sliding distance.
[3]Uncertainty reported based on load cell accuracy (0.3 N) and load (50 N).
[4]Average and uncertainty over the last 100 data points (0.07 m)
[5] Uncertainty propagated from wear spot diameter measurement.

The coefficient of friction and the specific wear rates are higher in inert atmosphere, room temperature tests. The average COF in room temperature tests is 0.55(14), while all the high temperature tests result in an average COF of 0.33(5). The specific wear rate is 0.4(3) ug/Nm for room-temperature wear in inert argon conditions and 0.06(3) ug/Nm at high temperature. Thus, the COF decreases by a factor of 1.5 and the wear rates decrease by a factor of 6.7, for high temperature vs. low temperature.

Repeatability of the COF results is demonstrated by three runs at room temperature (1, 2, 3) and four runs at high temperature (4, 5, 6, 7). A fresh region on the pebbles and disks is used for each run. Average COFs are within one standard deviation of each other for all room temperature, and high temperature runs, respectively.

Specific wear rates have a larger spot-to-spot variability, changing by as much as a factor of three across both high temperature and room temperature tests. The three wear rate data points at RT appear to correlate with increased number of rotational cycles, and do not appear to correlate with sliding distance. The four wear rates at HT are a factor of seven lower than at RT and they do not appear to correlate with number of rotational cycles, nor with sliding distance.
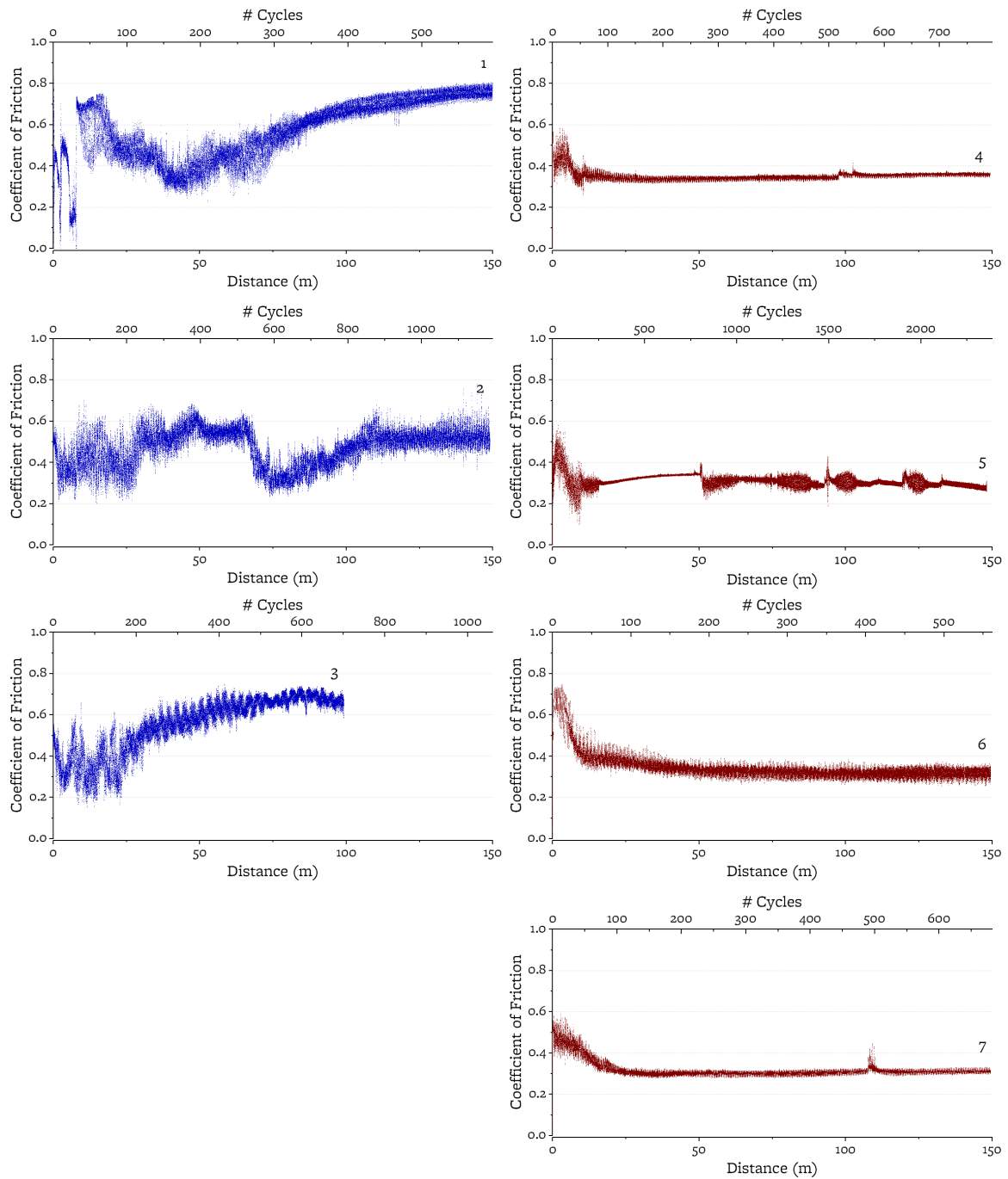
Figure 4.2: Coefficient of friction as function of sliding distance and disk rotational cycles. Left column: RT. Right-column: HT. See run details in Table 4.3.

The behavior of the coefficient of friction is consistent across runs at the same temperature. In all tests, COFs do not have a smooth behavior but oscillate. The amplitude of the oscillations is larger in room temperature tests (0.1- 0.2) than in high temperature tests (<0.05). The frequency of rotation of the spinning disc is between 4 and 16 m^{-1} depending on the test; frequency analysis of the data shows more oscillations in the RT COF than in the HT COF, at frequencies that do not

match this inherent frequency of the instrument. The room temperature COF does not reach a steady-state value during the 150 m sliding distances tested: it shows a decreasing trend starting from the first meters and up to 40-50 m of sliding, and an increasing trend thereafter. Conversely, the high temperature COF converges to a steady-state value after the running in period of 10-30 m of sliding distance. The COF behavior during the running-in period is emphasized in when the sliding distance is plotted on a logarithmic scale (Figure A2 provided in Appendix).

To check reversibility between low-temperature and high-temperature friction, two sequences of runs are performed at progressively higher temperature (Sequence 1) and progressively lower temperatures (Sequence 2) maintaining the same wear spot-wear track couple within each sequence (Figure 4.3). Within both sequences, the room-temperature and 600°C COFs are within one standard deviation of previously measured average COFs (Table 4.3). For both sequences, the average COF shows inverse dependence on temperature. Some hysteresis is observed for measurements at the intermediate temperatures of 200 and 400 °C: the amplitude of oscillation and the averaged COFs at 200 and 400 °C are larger when starting the wear spot at room temperature than when starting the wear spot at 600 °C.

(a) Sequence 1: Increasing Temperature

T	20 °C	200 °C	400 °C	600 °C
Avg. COF:	0.55±0.13	0.57±0.05	0.46±0.03	0.30±0.01

(b) Sequence 2: Decreasing Temperature

T	600 °C	400 °C	200 °C	20 °C
Avg. COF:	0.32±0.06	0.34±0.05	0.42±0.03	0.67±0.10
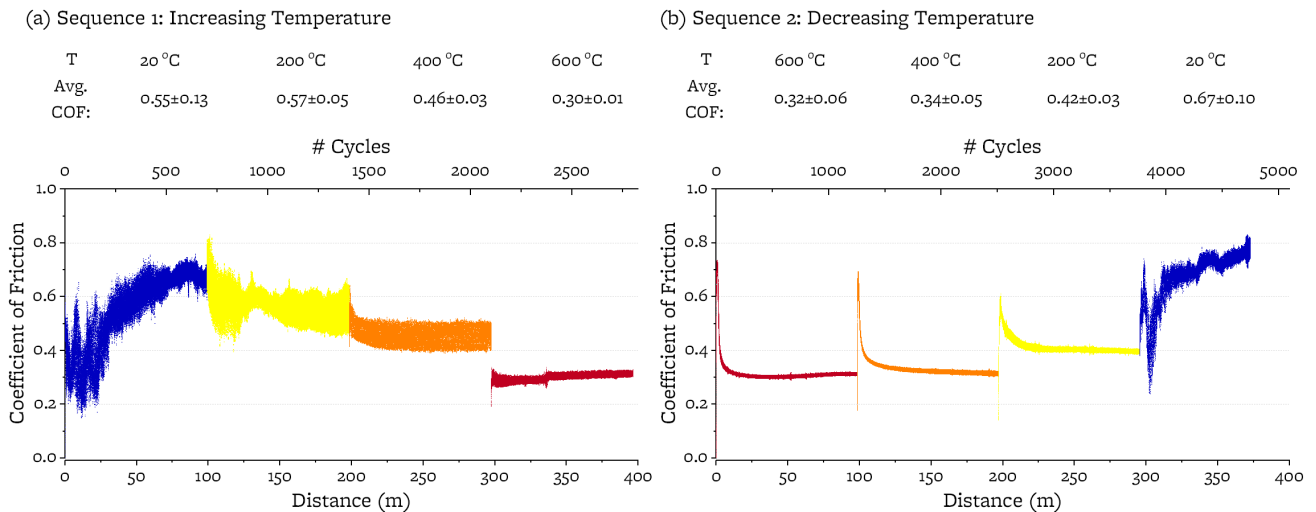
Figure 4.3: Coefficient of friction temperature hysteresis. The same wear-spot-wear-track contact is maintained within each sequence.

4.1.2.2. *Wear Marks: Digital Microscopy, SEM, and Polarized Light Microscopy*

Figure 4.4 shows the microscopy for the wear spots and the wear tracks. The HT wear spot is smaller in diameter than the RT wear spot (5.3 mm vs 3.4 mm), corresponding to lower wear rate at HT (as per Equation 1), and appears bright under coaxial light. The RT wear spot exhibits some shallow wear grooves and appears darker under coaxial light. As shown in SEM images, the 600 °C wear spot is characterized by a smooth texture over most of its surface, intertwined by abrasion grooves along the direction of sliding, 100-200 um width (see also Figure 4.6 and Figure 4.7). The RT wear spot shows a patchwork of smooth and rough regions (of similar texture to the nominal graphite surface). The bottom of the abrasion groves presents high roughness (see Table 4.4). The rough regions appear dark under coaxial illumination and polychromatic under polarized light. The polychromatic appearance under polarized light indicates high variation in crystallite orientation. The smooth regions appear shiny under coaxial illumination and monochromatic under polarized

light. The monochromatic appearance under polarized light indicates uniform orientation of the crystallites.

Pebble Ref	WS1 (21°C)	WS4 (601°C)

Digital Microscopy

SEM

Polarized Light Microscopy

Disk Ref	WT1 (21°C)	WT4 (601°C)

Digital Microscopy

Polarized Light Microscopy
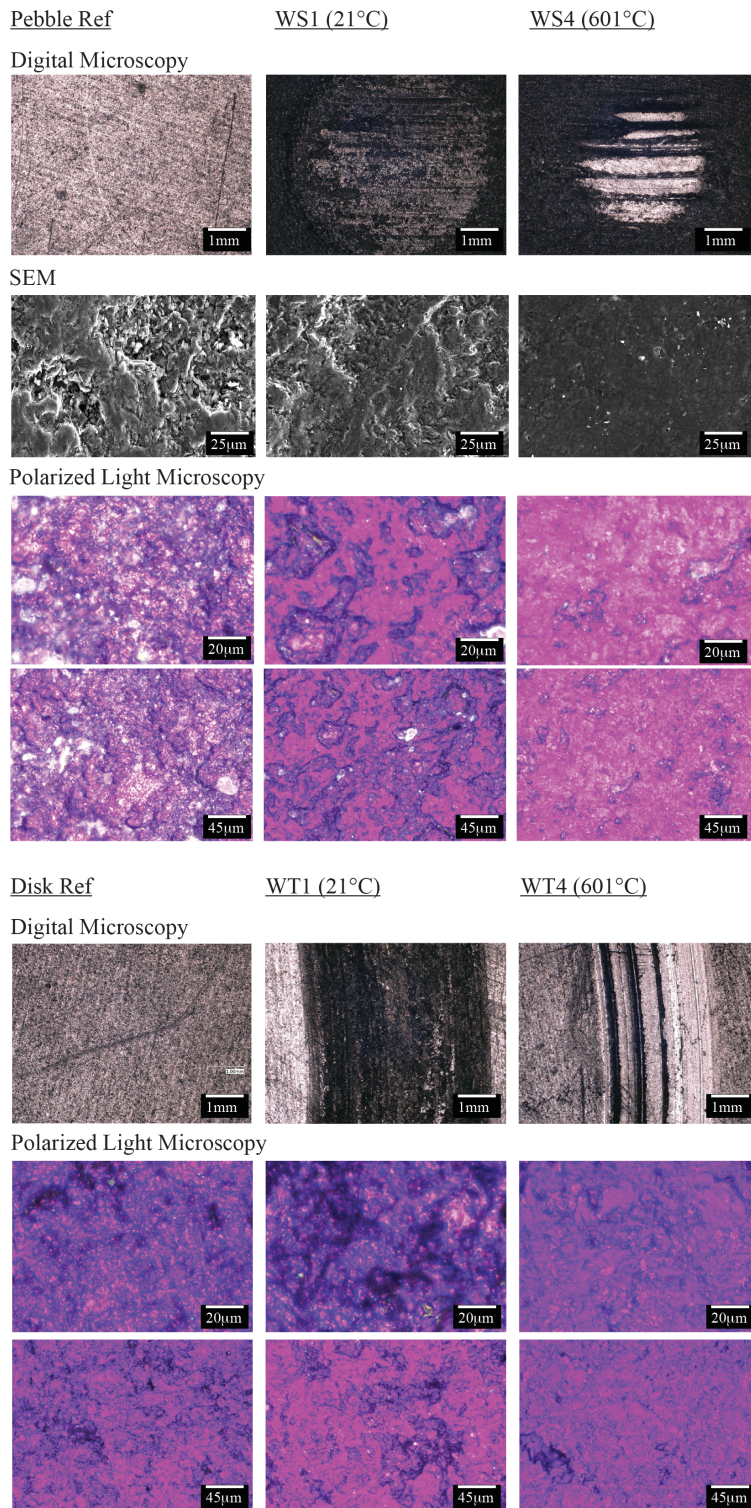
Figure 4.4: Microscopy of wear spots and wear tracks.

In the case of adhesion and two-body abrasions, one of the mating surfaces would have asperities, rather than grooves. In the case of three-body-abrasion by entrained debris, matching groves are formed on the two wear surfaces (Li 2017). Figure 4.5 shows matching patterns on the wear spot and wear track. The dark regions correspond to matching grooves in the disk and the pebble, indicating three-body abrasion at 600 °C. A smaller degree of three-body abrasion is observed at RT, with shallower grooves at RT. The RT patterns also show asperities that may be indicative of adhesion and two-body abrasion.
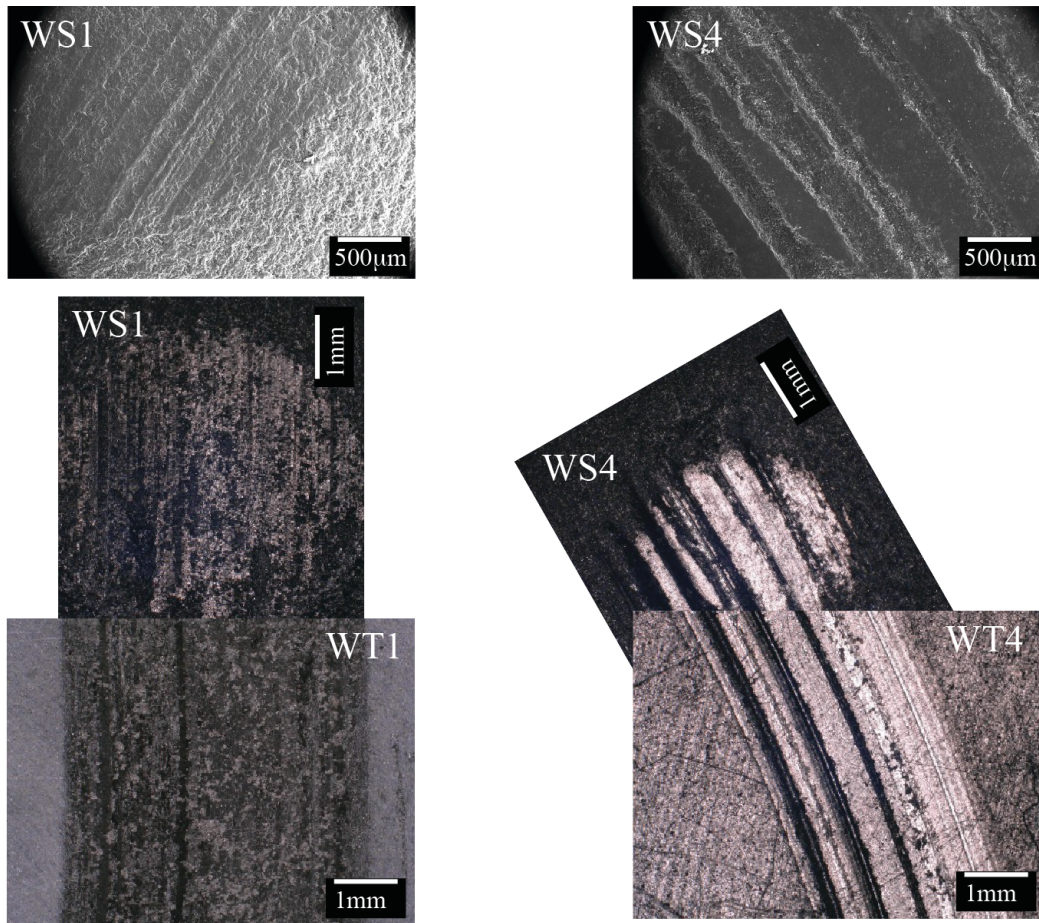
Figure 4.5: SEM showing the abrasion grooves on the wear spots and juxtaposition of digital microscopies of wear spots and corresponding wear tracks.

4.1.2.3. *Profilometry by digital microscopy*

Profilometry (Figure 4.6) is used to estimate surface roughness and morphological features of the wear marks. As shown in Figure 4.6, the smooth regions of the wear marks (which correspond to the bright regions under coaxial light and the monochromatic regions under polarized light) overlay the rest of the surface. Since these regions are not present in the reference samples and do not match the nominal surface, they are referred as *tribo-film* in the rest of this chapter. The bottoms of the abrasion grooves and of the gaps in the tribo-film show morphological features comparable to the nominal surface (dark under coaxial light, polychromatic under polarized light, with roughness Ra >0.5 μm). Table 4.4 provides a comparison of the morphological features of

the smooth film and nominal surface, for RT and HT wear marks. An estimate of the upper bound thickness of the tribo-film is performed through profilometry, as the difference between the elevation of the tribo-film surface and of the bottom of the gaps or grooves. This leads to an upper bound estimate because the gaps and grooves may extend below the nominal surface, but the same approach is taken across all samples to provide a consistent comparison. With this methodology the tribo-film thickness is up to 10 μm for RT wear spot, up to 50 μm for HT wear spot, and up to 20 μm for both the RT and the HT wear tracks.
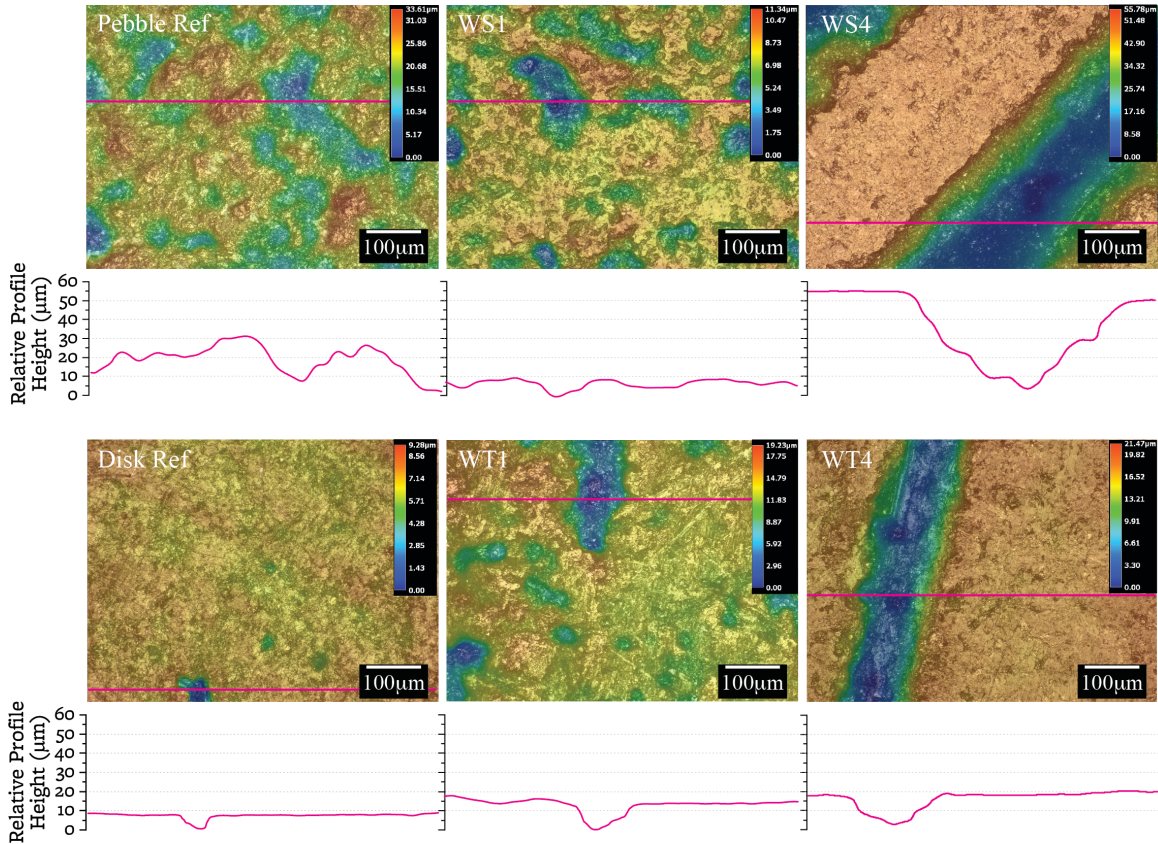
Figure 4.6: Profilometry of the non-worn samples, the wear spots, and the wear tracks. The relative height profile is reported along the purple line on the elevation map.

Table 4.4: Tribo-film characteristics: surface-coverage, roughness, and thickness

	Pebble Pebble Ref	WS1	WS4	Disk Disk Ref	WT1	WT4
Temperature of wear Size of wear spot (mm)	-	RT 5.3 (higher wear rate) Patchy with large gaps (100 um diameter)	600 °C 3.4 (lower wear rate) Uniform,	-	RT	600 °C
Description of wear surfaces	-	and shallow grooves.	with grooves (50-200 um width)	-	Patchy with some gaps (20 um diameter) and shallow grooves	Uniform with few gaps (1-20 um) and grooves (50-200 um width)
Surface Roughness Sa (um) Non-film (nominal surface): patches	1.9	1.2		1.2	3.6	
Non-film (nominal surface): Bottom of groove			1.3			4.2
Film	-	0.3	0.3	-	0.4	0.3
Surface open pore depth (um)	<30	-	-	<10	-	-
Film Thickness (um)	-	1-10	20-50	-	10-20	10-20

Roughness measured using the digital microscope as the arithmetical mean height over a surface of approximately 0.1 mm^2. Corresponding images provided in Data in Brief article (Vergari et al. 2023b).

4.1.2.4. *Debris: SEM Characterization*

Figure 4.7 shows the SEM images of the debris collected on the disk during room temperature and high temperature sliding. A much smaller amount of debris is produced at high temperature, the wear rate being seven times lower than at room temperature. The debris is composed of small isometric particles (1-10 um) and larger platelet-like debris (20-200 um). The smaller particles have been attributed to abrasion and adhesion processes (Luo et al. 2005b; Robert et al. 1995; Savage 1948) and they are of comparable size between room temperature and high-temperature sliding. The platelet-like debris is smooth on the surface and is larger in room temperature testing as compared to the debris from high-temperature testing. The size of the gaps in the film patches at room temperature is of comparable size with the RT debris platelets, indicating that tribo-film fracture could be the source of the platelet debris (Williams et al. 1997). Due to the platelet shape, this debris can be attributed to fatigue wear (Clark and Lancaster 1963; Luo et al. 2005b; Robert et al. 1995), in addition to film fracture (Yen 1995). The widths of the HT abrasion grooves are of comparable size to the HT debris platelet, indicating that the grooves could be caused by entrapped platelet debris.
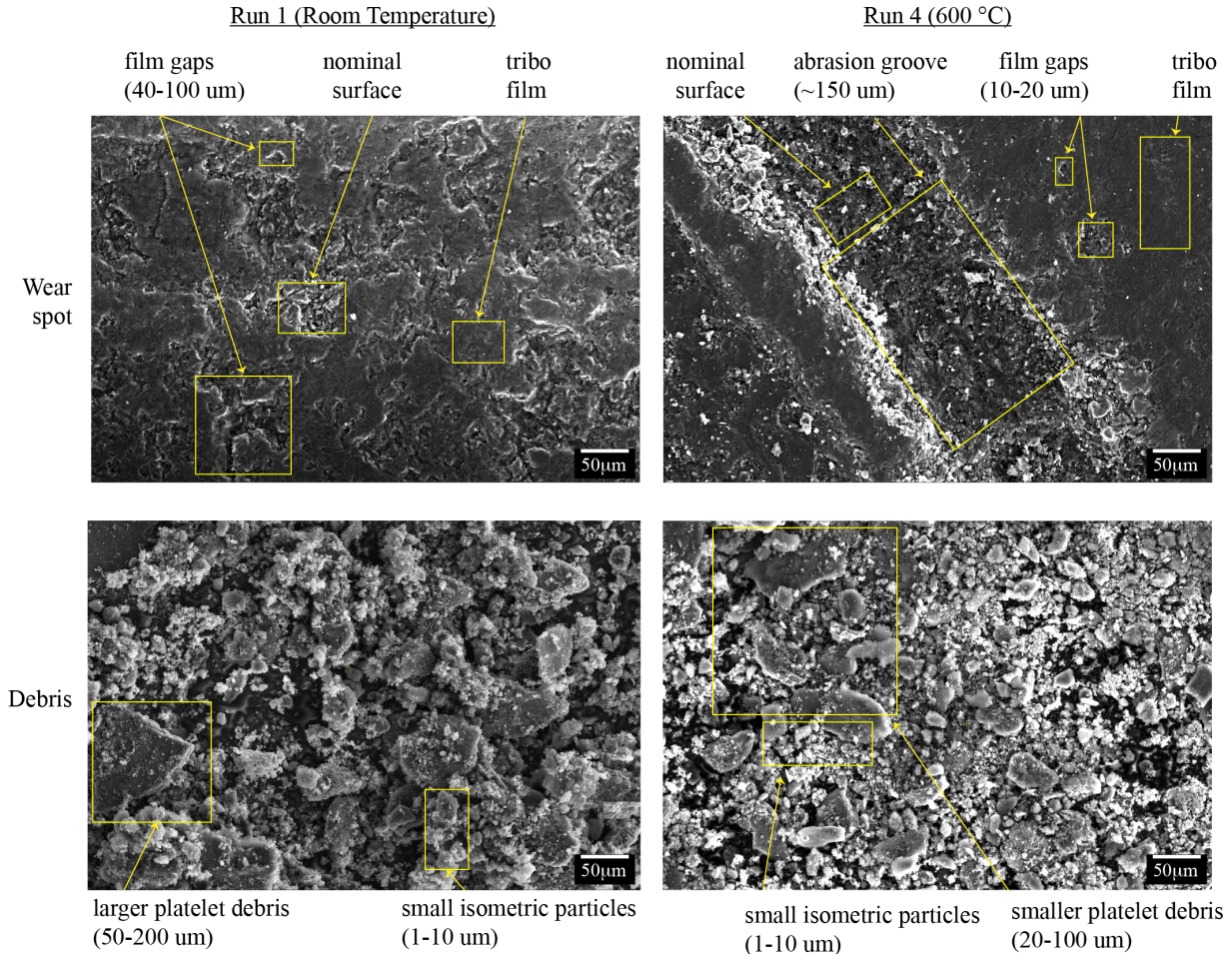
Figure 4.7: SEM images showing debris and wear spots at RT and HT.

As shown in (Luo et al. 2004) for IG-11 nuclear graphite tested in He at room temperature, size distribution of the debris generated in graphite-graphite sliding depends on the applied load. A quantitative analysis of the debris size dependence on the contact pressure is beyond the goal of this chapter. Nonetheless, performing such analysis in high temperature argon would be of relevance for the FHR, as the total debris surface area depends on debris size distribution and will impact dust transport in the core (Sun et al. 2020) and adsorption of gaseous species (Lam et al. 2018; Vergari and Scarlat 2021a).

4.1.2.5. *Raman Spectroscopy*

Raman spectra are acquired on 20 points of reference sample, 20 points on each wear spot, and on 10 points of each wear track. Each spectrum shows the characteristic peaks for nuclear graphite. Figure 4.8 shows an example of peak fitting and peak assignment applied to all other spectra. Raman spectra for single crystal graphite present a single band in the first order spectrum at 1575 cm^{-1} (G band) and the second-order G' band at 2700 cm^{-1}. The spectra for polycrystalline graphite include additional bands activated by the presence of defects, most importantly the D band (1350 cm^{-1}) and the D' band (1610 cm^{-1}) in the first-order spectrum, the D+D' band (2950 cm-1), the D+D" (2453 cm^{-1}) in the second-order spectrum (Tuinstra and Koenig 1970). The shape of the G' band is affected by the presence of turbostratic phase in graphite. For a perfectly crystallized

96

graphite, the G' band can be fitted with two Lorentzian at approximately 2670 cm^{-1} and 2720 cm^{-1} (G'_3DA and G'_3DB, respectively). For non-graphitized carbon, the G' band is fitted by a single peak around 2700 cm^{–1} (G'_2D) (Cançado et al. 2008). When turbostratic and graphitized regions coexist, as in commercially available nuclear graphite, all three peaks are present. Peak parameters from the Raman spectra are used to estimate crystallite parameters and microstructural properties: the crystallite dimension in the basal (La) direction computed from the two empirical correlations developed by (Tuinstra and Koenig 1970) and (Maslova et al. 2012); and the crystallite dimension in the axial direction (Lc) computed using the correlation developed by (Cançado et al. 2008).
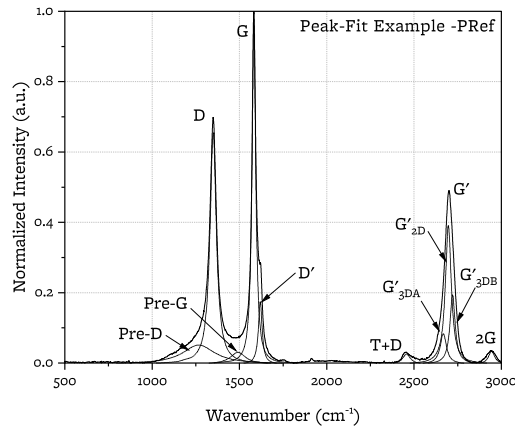
Figure 4.8. Raman peak-fitting example. From Pebble Ref sample.

Figure 4.9 shows the Raman spectra (sampling area of ~1 um) on the wear spots and tracks normalized by the G band intensity. Two classes of spectra are observed on the *tribo-film (*the smooth regions on the surface of the wear marks, as presented in Section 3.3) and on *nominal-surface* regions (bottom of grooves and gaps and non-worn regions). For spectra acquired on the *nominal surface*, the D and the G band are clearly separated (i.e., the intensity drops to 0.3 or less between the two peaks) and the intensity of the D band is less than 60% of the G band intensity. Spectra acquired on the *tribo-film* present a shoulder between the D and the G peak, and a larger relative intensity of the D band is between 80% and 90% of the G band. The presence of a peak between the D and G peak has been reported by (Ferrari and Robertson 2000) and correlated to an amorphization of the structure. Table 4.5 shows that crystallites of the *tribo-film* have about half the *La* parameter of crystallites on the *nominal-surface* (based on FWHM of the G peak), and generally no change in *Lc* (based on area decomposition of the G' peak). The wear track obtained at high temperature manifests a small but statistically significant 2% increase in *Tribo-film* crystallite axial size Lc vs. the reference (see Table 4.5).
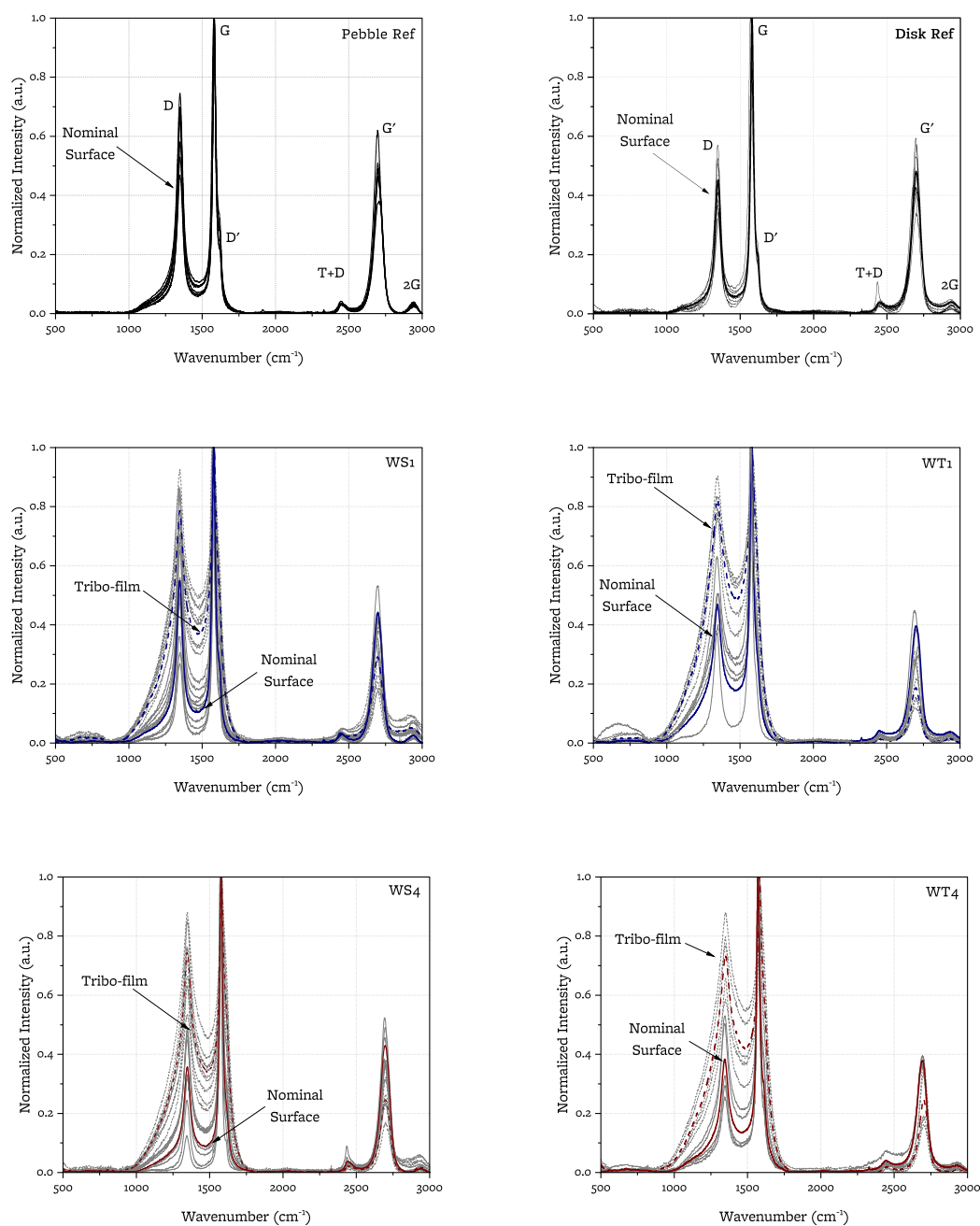
Figure 4.9: Raman spectra of the wear samples. The average spectra are displayed with thick lines. Nominal surface: solid lines. Tribo-film: dashed lines.

Table 4.5: Crystallite microstructural parameters calculated from Raman spectra. Statistically significant differences: La is smaller by a factor of two for the *Tribo-Film* vs. the *Nominal-Surfaces* for all samples, and Lc is 2% larger for the Tribo-film on the HT wear track vs. the Disk Ref.

Test Sample	Reference Pebble Ref	Disk Ref	20 °C tests Pebble: WS1		Disk: WT1		600 °C tests Pebble: WS4		Disk: WT4	
Location on sample (N=number of sampled points)	Nominal Surface (N=10)	Nominal Surface (N=10)	Nominal Surface (N=10)	Tribo-film (N=10)	Nominal Surface (N=5)	Tribo-film (N=5)	Nominal Surface (N=10)	Tribo-film (N=10)	Nominal Surface (N=5)	Tribo-film (N=5)
La (nm) (Tuinstra and Koenig 1970) *from D/G Area ratios*	25.6 ±4.6	18.0 ±2.3	20.5±7.0	10.7 ±2.3	16.2 ±8.3	9.0 ±2.2	31.1 ±6.3	11.2 ±2.3	23.0 ±7.0	8.0 ±1.8
≠ Nominal-Surface on Pebble Ref (p-value)		<0.001	0.07	<0.001			0.33	<0.001		
≠ Nominal-Surface on Disk Ref (p-value)					0.66	<0.001			0.19	<0.001
La (nm) (Maslova et al. 2012) *from FWHM(G)*	12.6 ±1.5	13.5 ±1.1	11.7±1.4	5.4 ±3.4	6.6 ±3.2	4.4 ±1.2	10.6 ±1.9	5.3 ±1.4	7.6 ±1.1	4.0 ±1.0
≠ Nominal-Surface on Pebble Ref (p-value)		0.145	0.17	<0.001			0.02	<0.001		
≠ Nominal-Surface on Disk Ref (p-value)					0.01	<0.001			<0.001	<0.001
Lc (nm) (Cançado et al. 2008) *from G' peak decomposition in G'2D and G'3DB*	24.2 ±1.1	24.5 ±0.9	25.3±1.2	23.3 ±1.9	25.3 ±3.0	26.0 ±2.3	25.4 ±1.6	24.4 ±2.0	25.5 ±1.2	26.9 ±0.8
≠ Nominal-Surface on Pebble Ref (p-value)		0.52	0.06	0.22			0.11	0.78		
≠ Nominal-Surface on Disk Ref (p-value)					0.58	0.27			0.15	<0.001

Note: highlighted entries indicative of significative differences at p-value of 0.01

4.1.3   Discussion

4.1.3.1.   *Prior studies of graphite friction and wear*

Graphite friction and wear behavior have a strong dependence on the environment in which sliding takes place. Starting from the early studies by Savage (Savage 1948), it has been shown that graphite has a high COF in vacuum (0.8-0.9), while it can achieve lower COFs (as low as 0.1) when a partial pressure of water (Savage 1948; Zaidi et al. 1990), oxygen (Yen 1996; Zaidi et al. 1990), or hydrogen (Zaidi et al. 1989; Zaidi et al. 1990) is present in the environment. In absence of these gasses, the COF and the wear rate is high because of the adhesion of dangling bonds (i.e. unsatisfied valence electrons) at the edges of graphite crystallites of the two mating components (Deacon and Goodman 1958; Lancaster and Pritchard 1981). Studies by synchrotron XRD and thermal desorption spectroscopy indicate that the lubricating effect of water, oxygen, and hydrogen is due to their adsorption to graphite's dangling bonds, which are thus passivated (Rietsch et al. 2013; Yen et al. 2004). In these reactive environments, graphite-graphite friction switches from a low COF to a high COF regime upon increasing the velocity beyond a critical value, depending on the specific gas. As such critical velocity is reached, the temperature increase at asperity contacts due to frictional heating is sufficient to cause desorption of adsorbed species from initially passivated graphite edge sites (Lancaster and Pritchard 1981; Yen 1995; Yen et al. 1997). However, this behavior occurs when graphite sliding occurs in a reactive environment (e.g. in air) in which environment species can be adsorbed and graphite edge sites can be passivated, but does not occur

in inert environment where graphite edge sites are not passivated in the first place (e.g. in N_2 or Ar) (Deacon and Goodman 1958; Yen et al. 1997).

In helium, graphite dangling bonds are not passivated, but the COF is still lower than in vacuum (Hiruta et al. 2013; Li and Sheehan 1981; Luo et al. 2005b; Robert et al. 1995; Stansfield 1969; Zaidi et al. 1991). The decrease in friction in the presence of inert gases vs. vacuum occurs because graphite crystallites, which are originally in random orientation, are reoriented along the direction of sliding by the inert atoms under pressure exerted by the normal load (Robert et al. 1995; Zaidi et al. 1995).

Based on the state of the surface and of the debris after the sliding, previous studies of graphite sliding in inert environments have interpreted the wear mechanisms as adhesive wear (Hiruta et al. 2013; Luo et al. 2005b) abrasive wear (Li and Sheehan 1981; Luo et al. 2005b) and fatigue wear (Luo et al. 2005b; Robert et al. 1995):

- Adhesive wear is reported as the main wear mechanism for graphite-graphite sliding in helium at 400 °C in (Luo et al. 2005b) and at 750 °C in (Hiruta et al. 2013), based on SEM of the wear spot. Adhesion occurs due to the chemical interaction of the dangling bonds at the edge of the crystallites at the sliding interface. After adhesive wear, the surface appears rough and presents tears left behind by material being peeled off by the mating component. The debris generated by adhesion of graphite is small and has a rough texture (Luo et al. 2005b).
- Abrasive wear is reported for room temperature graphite-graphite sliding in argon (Robert et al. 1995) (based on OM and BET adsorption of the debris) and in helium (Luo et al. 2005b) (based on SEM of the wear spots). Abrasion wear occurs due to ploughing effect of asperities of one of the components (2-body-abrasion) or entrained debris (3-body-abrasion) (Li 2017). As a result of abrasion, grooves are visible on the graphite surface. The debris generated by abrasion is finely divided (Robert et al. 1995). In brittle materials like graphite, abrasion can be accompanied by the presence of cracks perpendicular to the grooves.
- Fatigue wear has been reported for room temperature graphite-graphite sliding in argon (Robert et al. 1995) and helium (Hiruta et al. 2013) (based on OM and BET adsorption of the debris) and as a main wear mechanism for graphite at 200 °C in helium (based on SEM of wear spots) [11]. Fatigue wear has also been reported for graphite-steel sliding in air, in correspondence to the appearance of a low roughness graphite film on the graphite surface (Clark and Lancaster 1963; Williams et al. 1997). With the exception of these studies, fatigue wear has not been reported in graphite tribology, but is characteristic of metal-metal wear (Berthier et al. 1989; Challen et al. 1986; Zhang et al. 2021). Fatigue wear occurs by the formation and propagation of cracks under load cycles, which ultimately leads to the detachment of platelet-like debris (Clark and Lancaster 1963; Williams et al. 1997).

Only a small number of studies (summarized in Table 4.6) have explored the influence of temperature in graphite-graphite friction and wear in inert environment (helium). The results are conflicting. Two studies, (Li and Sheehan 1981; Stansfield 1969), show a decrease of the wear rates and/or the coefficient of friction with increasing temperature. Two other studies (Hiruta et al. 2013; Luo et al. 2005b) show the opposite trend. In all these studies, the low wear behavior is accompanied by the appearance of a reflective and smooth surface on the graphite. This smooth surface has been attributed to the presence of a lubricious film (Hiruta et al. 2013) or to fatigue wear (Luo et al. 2005b). The high wear behavior is characterized by a dark, grooved surface, with a larger diameter of the wear spots and wear scars than for the lower wear behavior. The rougher texture of the surface is indicative of adhesion wear.

Table 4.6: Coefficients of friction and specific wear rates in temperature-dependent studies of graphite friction in inert atmosphere. Listed in chronological order.

Graphite Type	Mating Material	Environment	Degassing pre-treatment	Temperature (°C)	Sliding Distance (m)	Sliding Velocity (m/s)	Normal Load (N)	COF (-)	Wear Rate (ug/Nm)	Wear Mechanisms	Study
PGX, ATJ, MHLM, H-359, H-205	PGX, ATJ, MHLM, H-359, H-205	Helium (2 ppm H2O)	Outgassing at 400 °C leads to surge transient in friction. Not present when outgassed at 800 °C	25, 400, 800	ATJ -ATJ: 6.25 (see (Stansfield 1969) for other couples)	0.002	80	ATJ -ATJ (see (Stansfield 1969) for other couples) At steady state 25°C: 0.35 400°C: 0.4 800°C: 0.3	ATJ -ATJ (see (Stansfield 1969) for other couples) 25°C: 290 400°C: 36 800°C: 29	Not discussed	(Stansfield 1969)
POCO AXF-5Q	POCO AXF-5Q	Commercial Helium (4-5 ppm O2, 1-2 ppm H2O) HTGR Helium (120 ppm H2, 10-20 ppm CH4 and CO2, 4-5 ppm O2, 1-2 ppm H2O)	Specimen degassed and exposed to air before experiment. Fine debris and slip-stick observed at 800°C. Friction decrease ascribed to oxygen adsorption.	25, 450, 800	3.39 -4.48	$7\ 10^{-6}$	100	HTGR Helium: 25°C: 0.65 450°C: 0.05 800°C: 0.15 Commercial helium: 25°C: 0.55 450°C: 0.05 800°C: 0.20	HTGR Helium: 25°C: 3.5 450°C: n.a. 800°C: n.a.	Not discussed	(Li and Sheehan 1981)
IG-11	IG-11	Helium	Graphite used in the study is not degassed prior to the experiments. Debris of average diameter of 2-3 um observed at all temp.	20, 100, 200, 300, 400	700	0.04	30	20°C: 0.150 100°C: n.a. 200°C: n.a. 300°C: n.a. 400°C: 0.336	20°C: 0.0006 100°C: 0.0013 200°C: 0.0012 300°C: 0.0012 400°C: 0.0014	20°C: Abrasive wear 200°C: Fatigue wear 400°C: Adhesive wear	(Luo et al. 2005b)
IG-11	IG-11	Helium	Specimens degassed to 200 °C for one hour. Debris above 200 um appears above 200 °C.	20, 200, 400, 600, 750	1008	0.08	20	n.a.	20°C: 0.04 200°C: 8 400°C: 4 600°C: 3 750°C: 2	Not discussed systematically, but high temperature results attributed to adhesive wear	(Hiruta et al. 2013)
ET-10	ET-10	Argon (<0.1 ppm O₂, <0.1 ppm H₂O). Detected up to 10 ppm O2 during high temperature tests	Degassing at 600 °C for 6 hours.	20 and 600	100-150	0.15	50	20°C: 0.55 600°C:0.33	20°C: 0.38 600°C: 0.06	20°C: Adhesive wear, abrasive wear, and crystallite fracture 600°C: Abrasive wear and crystallite fracture	This study

Notes:
Wear rates in (Luo et al. 2005b) comprehensive of both mating specimens and calculated from weight change.

4.1.3.2. Importance of degassing for high-temperature testing

Different degassing strategies are applied in high-temperature tribology studies for graphite (see Table 4.6 for a summary of experimental conditions for previously published studies). The results cannot be directly compared among the different studies, as the presence of oxygen or water in the graphite at the time of testing might have strongly influenced the results (Lancaster 1990; Stemplé et al. 2002). Of the two studies that report lower wear at room temperature, (Luo et al. 2005b) does not perform any outgassing of the graphite, and (Hiruta et al. 2013) only performs outgassing at 200 °C for one hour. In both cases, the moisture originally adsorbed to the graphite might not be entirely released prior to the experiment. Using thermal desorption spectroscopy on nuclear graphite, (Hirohata et al. 1994) shows that H_2O has a main desorption peak around 300 °C and a weaker one at 550 °C. By measuring gas release upon degassing isotropic graphite in-vacuo, (Arun Prakash et al. 2008) detects moisture release up to 300 °C (no oxygen was detected in the study). If the adsorbed moisture has not been fully removed, it will have a lubricious effect in the graphite-graphite sliding, as documented by (Zaidi et al. 1990). This effect will be noticeable at room temperature but will not be present when the temperature is increased above the moisture desorption temperature. It is concluded that (Hiruta et al. 2013; Luo et al. 2005b) do not perform sufficient degassing to remove the adsorbed moisture and show a lower coefficient of friction at room temperature. In contrast, (Li and Sheehan 1981; Stansfield 1969) perform degassing above 400 °C of the graphite before the tests; based on (Arun Prakash et al. 2008; Hirohata et al. 1994), this should be sufficient to desorb most of the desorbed moisture and all the adsorbed oxygen, and therefore the room temperature and high temperature tests are expected to have a comparable moisture and oxygen content. Thus, the low friction observed by (Hiruta et al. 2013; Luo et al. 2005b) at room temperature is attributable to the lubricating effect of adsorbed moisture, low friction is expected at high temperature as reported by (Li and Sheehan 1981; Stansfield 1969) and degassing is identified as important for this present study.

In our study, all graphite samples at are degassed 600 °C in an argon atmosphere for four hours to fully remove the adsorbed moisture and oxygen, and *a lower COF and lower wear rate are observed at 600 °C in Ar than at RT in Ar, thus reconciling and explaining the contradiction that previously existed in the literature.*

Despite the experiments being performed in a controlled atmosphere glovebox and the graphite being degassed to remove all the contained moisture and oxygen prior to the experiment, limited increases (from <0.1 ppm to a few ppm) of the oxygen content in the glovebox were detected during the high temperature testing (no moisture was observed). The source of the detected oxygen is expected to be the ceramic material used as insulation for the high temperature tests. When heated up, the insulation material desorbs oxygen. The oxygen might in principle react with the dangling bonds at the edge of the crystallites, passivating them and making them less reactive to the surface of the mating counterpart, causing a lower COF and wear rate at high-temperature than at room temperature (Zaidi et al. 1990). To test this possible effect, a sequence of runs at progressively lower temperatures, from 600 °C to 20 °C was performed (Figure 4.3). Since the passivation of graphite dangling bonds by oxygen has a negative Gibbs' free energy (Kane et al. 2017), bound oxygen would not desorb as the temperature decreases, and the coefficient of friction would remain small. The runs show an increase in friction as the temperature is lowered, ultimately going back to the COF observed in other room temperature tests thus refuting the possibility of oxygen effects at higher temperature. This test shows that *the decreased COF and wear rate at high temperature is not caused by passivation of the dangling bonds by few-ppm oxygen in the Ar*

cover gas. Additional testing of this hypothesis could be performed via X-ray Photoelectron Spectroscopy (XPS) analysis of the wear spot to verify the absence of C-O bonds on the high-temperature wear spot.

4.1.3.2.1.   Wear Mechanisms at Room Temperature and High Temperature

At room temperature, the wear marks and debris show signs that have been attributed to adhesive, abrasive, and fatigue wear in previous literature. The presence of rough regions on the wear spot and isometric debris is indicative of adhesive wear (Luo et al. 2005b); the grooves on the wear marks are attributable to three-body abrasive wear (Li 2017); the patchy smooth regions on the wear marks and the platelet-like debris are indicative of tribo-film fracture (Yen 1995) and similar features have been previously also assigned to fatigue wear (Clark and Lancaster 1963; Williams et al. 1997) (Figure 4.10).

At HT, the wear spots are covered by a continuous and smooth tribo-film, intertwined by deep abrasion grooves. The absence of a rough texture on the wear marks indicates that adhesion is not a main mechanism, as adhesion would lead to roughening (Luo et al. 2005b). Three-body abrasion continues to be present at HT, as documented by the grooves. Fracture of the tribo-film produces smooth, platelet-like debris (too large and too smooth to be from the nominal graphite surface) and leads to occasional gaps in the smooth film (of comparable size with the platelet debris).
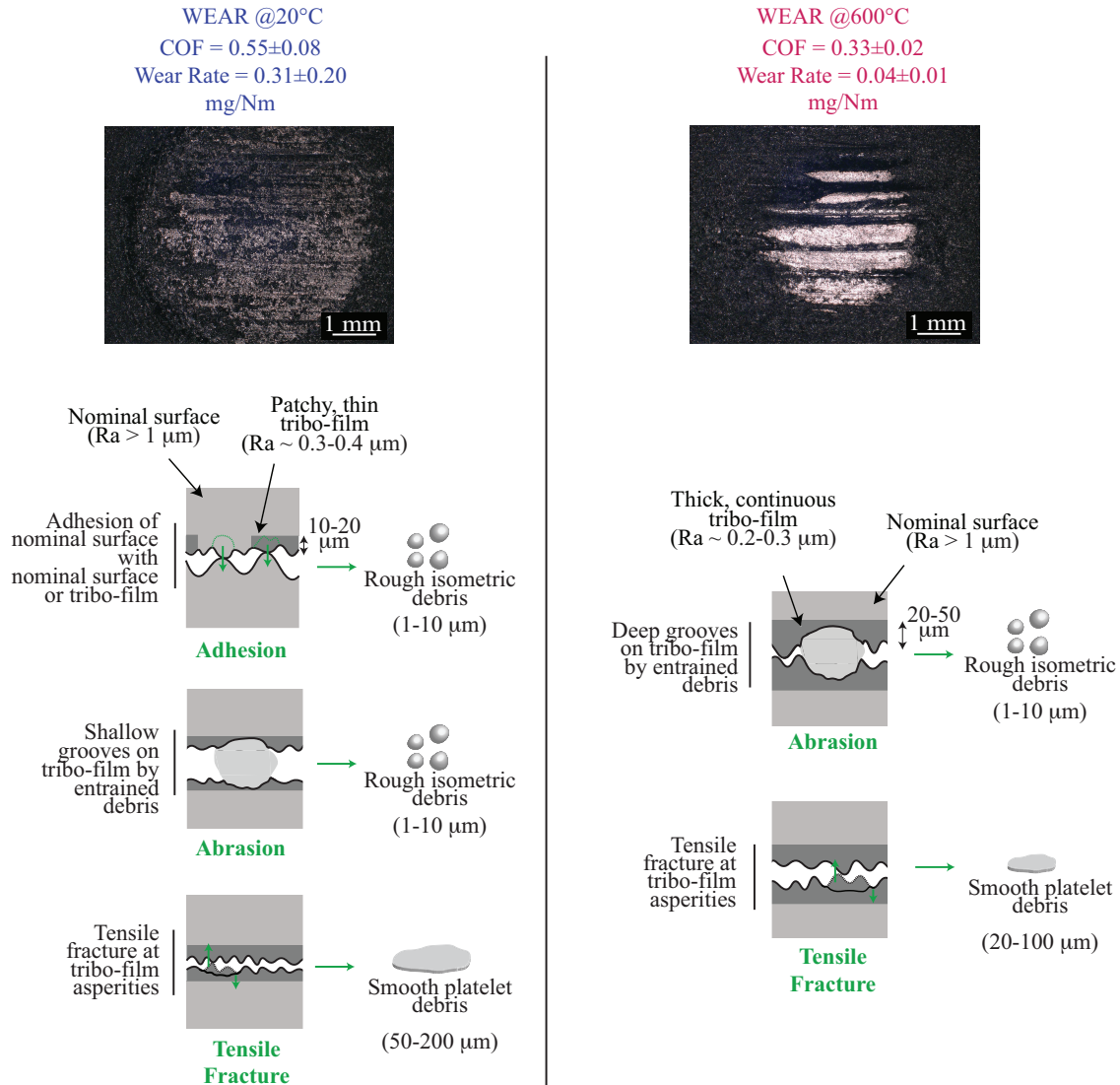
Figure 4.10: Wear mechanisms at RT and HT

4.1.3.2.2. *Graphite Self-Lubrication*

At both room and high temperature, a tribo-film is visible on the surface of the wear marks. The tribo-film is discontinuous and thin at room temperature – in which high wear, high friction, and slip-stick are observed, and is continuous and thicker at high temperature – for which low wear and friction are observed. *It is concluded that the film that forms at the wear spot has a lubricating role.* At HT, a more continuous film forms, thus resulting in lower friction coefficient and wear than at RT.

The film has different coverage of the surface but otherwise has the same characteristics at HT and RT: DM shows flat shiny regions, SEM shows flat regions, polarized microscopy shows uniform crystallite orientation, profilometry shows low roughness, and Raman is similar between the film

regions formed at RT and those formed at HT. The non-film areas on the wear spot have characteristics that are similar to the surface of the graphite before wear: Raman spectra and hence crystallite size and surface defect density are similar, roughness is similar, and appearance under SEM is similar. *This suggests that the film formation mechanism is the same at room temperature and high temperature.*

The appearance of a lubricious carbon film upon graphite-graphite sliding has been previously observed at room temperature in both inert (nitrogen gas) (Lancaster 1990) and reactive (moist air) conditions (Clark and Lancaster 1963; Lancaster 1990; Williams et al. 1997). Using atomic force microscopy (AFM) and transmission electron microscopy (TEM), (Lancaster 1990; Stempflé et al. 2002) showed that the film is composed of graphite crystallites, removed from the original location via basal cleavage (in most air) or fracture perpendicular to the basal planes (in nitrogen). *In this study, the tribo-film is observed not only at room temperature, but also at high temperature.*

Raman spectroscopy (Table 4.5) shows that the crystallites forming the tribo-film have different size that crystallites in the nominal surface: crystallites on the film have a smaller basal width (crystallite parameter La) and the same thickness (crystallite parameter Lc) than crystallites in the nominal surfaces. This suggests that the film is composed of crystallite fracturing perpendicularly to the basal planes and not cleaving along the basal planes, consistently with previous results of graphite sliding against steel in inert environments (Stempflé et al. 2002). Polarized microscopy shows that while crystallites in the nominal surface have a distribution of orientations, crystallites in the film region have a uniform orientation, i.e., they are aligned. Overall, this indicates that *the film is composed of aligned crystallites fractured perpendicularly to the basal planes (*Figure 4.11*).*
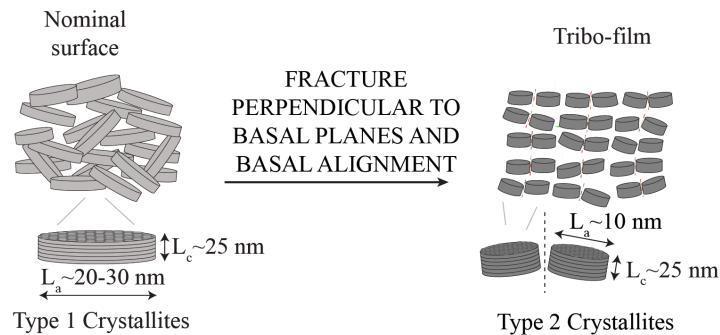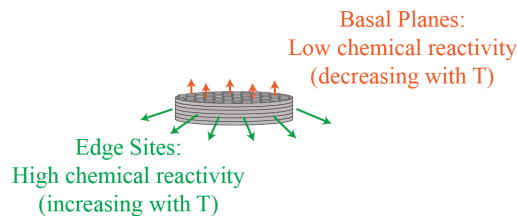
Figure 4.11: **Crystallite fracture and anisotropy of chemical reactivity leading to crystallite alignment in the tribo-film.**

Raman spectroscopy and polarized light microscopy yield similar results at room temperature and high temperature, suggesting that *the tribo-film forming mechanism is the same at the two temperatures*. However, digital and electron microscopies of the wear spots show a different degree of cohesion of the tribo-film at room temperature and high temperature.

The smooth texture of the film suggests that it does not wear by adhesion. Since graphite adhesion is driven by the interaction of dangling bonds at the edge of graphite crystallites and not by the interaction of the basal planes, the *film crystallites are oriented with their basal planes parallel to the sliding surface* and that the film acts as a *lubricant by decreasing the adhesion between the two sliding counterparts*.

At both temperatures, the wear debris that is generated is comprised of smooth platelet-like particles and rough small isotropic particles. The platelet-like particles fit the description of the debris observed in (Luo et al. 2005b) and attributed to fatigue wear, but could also be the result of tribo-film fracture (Williams et al. 1997; Yen 1995). Their smooth surface and the presence of gaps on the tribo-film indicate that they are detached from the film, i.e., the *tribo-film wears by fracture under mechanical load*. The larger diameter of the platelet-like debris at room temperature compared to high temperature is compatible with the larger gaps in the surface of the room temperature film. The debris generated by wear remains entrained between objects and causes the abrasion grooves visible on the wear spots and tracks. As measured by nano-indentation testing in (Clark and Lancaster 1963), the tribo-film is characterized by a lower hardness that the bulk surface. As shown in (Bowden et al. 1951; Rabinowicz et al. 1961), abrasive wear is linearly correlated to the inverse of hardness. This suggests that the tribo-film is more subject to abrasive wear than the nominal surface. Thus, the deep groves in the high temperature tests with *Nominal-surface* crystallites at the bottom of the grove (as observed by Raman) are attributed to groves in the tribo-film and the depth of the grooves is assumed indicative of the thickness of the tribo-film. Similarly, the shallow grooves at RT are attributed to a thin tribo-film layer at RT.

4.1.3.2.3.   *Temperature dependence of the tribo-film and of graphite self-lubrication*

The following description of wear and friction is formulated: at both room temperature and high temperature, adhesion and abrasion occur in the initial phases of sliding, leading to the fracture of crystallites perpendicularly to the basal planes. The fractured crystallites align along their basal planes leading to the appearance of a tribo-film. The increased resistance to adhesion and fracture at high temperature allows the film to grow and remain compact under sliding, thereby providing lubrication. The continuity of the tribo-film is only interrupted by deep (up to 50 µm) abrasion grooves. Abrasion of the tribo-film occurs at a higher rate than abrasion of the nominal surface due to the lower hardness of the film than of the nominal surface (Clark and Lancaster 1963). At room temperature, the resistance to fracture and adhesive wear is lower and the film is continuously locally fractured and reformed, leading to a patchy texture. The alternation of film destruction and reformation phases leads to oscillations of the COF: a decrease when a new layer of film is formed at the sliding interface, and an increase when the film is destroyed, and a new surface is exposed to adhesion forces.

The mechanism leading to the formation of the tribo-film consists in the fracture of the crystallites perpendicularly to the basal planes and the orientation of the fractured crystallites so that their basal planes face the sliding interface, as shown by Raman spectroscopy and polarized light microscopy. At high temperature, the film on the wear spot surface is thicker and more continuous. The observation of a thicker and more continuous film at high temperature compared to room

temperature could be attributed to either an increased tendency of film-formation or to an increase in the resistance to the film-fracturing mechanisms.

4.1.3.2.3.1. *Mechanical considerations*

Contact mechanics (for example, Hertz (Hertz 1899)and the Greenwood-Williamson models (Greenwood and Tripp 1970; Williamson and Greenwood 1966)) shows that the contact area between sliding asperities is partly under compressive stress (in the central region and at the front of the asperity) and partly under tensile stress (at the back of the asperity), and that also shear stress acts below the surface (Popov 2017) (tensile/ compressive stress schematically illustrated in Figure 4.12). As shown in the von Mises plots in (Luo et al. 2010), since graphite's tensile strength is more than five times lower than its compressive strength (Taylor et al. 1967) and two times lower than its shear strength (Kelly 1981), the first regions where graphite can fracture are those under tension. (Albers 2009) shows that graphite tensile strength increases linearly by up to 60% over the 25 °C-1600 °C temperature range, while (Malmstrom et al. 1951) shows more than linear increase in tensile strength up to 2500 °C. The tensile strength of the surface and the carbon film may be different from the bulk, but assuming that the temperature trends for the tensile strength apply also to the tribo-film, *the larger tensile strength at HT would lower the tendency of the film to be fractured, compared to the RT case*, and therefore promote its stability.
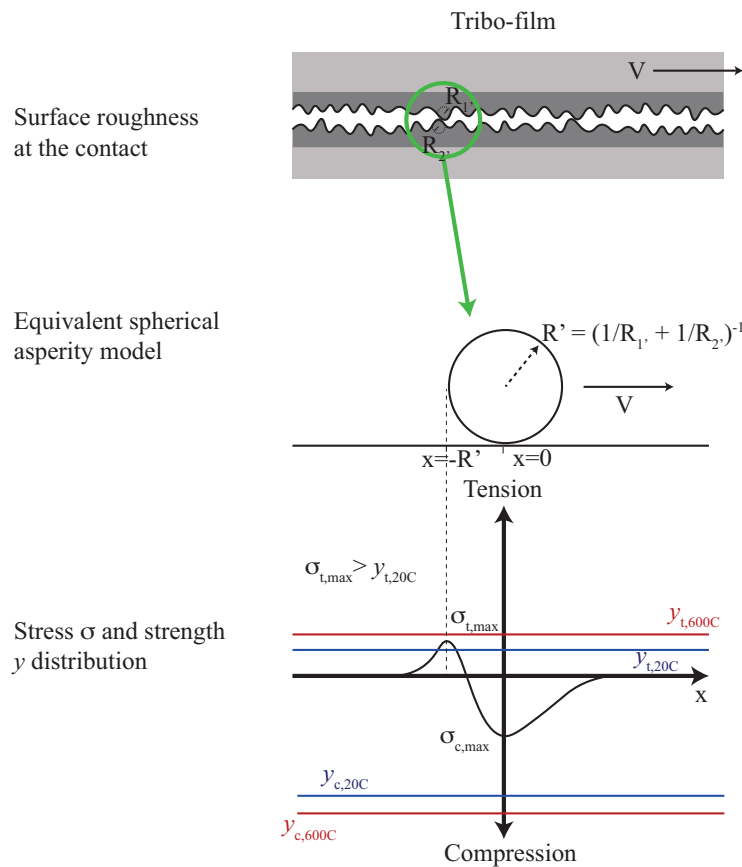
Figure 4.12: Stress and strength at asperity contacts. Stress distribution plotted qualitatively according to Hertz contact mechanics in presence of friction (Popov 2017).

In previous literature, fatigue wear has been identified as the wear mechanism when a tribo-film forms on the graphite surface during graphite sliding against graphite and metal in air (Clark and

107

Lancaster 1963; Williams et al. 1997). Fatigue can arise due to the repeated insurgence of stresses at the interface between the asperities on the film and on the mating surface that lead to formation and propagation of cracks. Thus, even when the local stresses do not exceed the tensile strength of graphite, stress cycling could lead to fatigue-induced cracks, blistering and flaking. On the wear track, the number of cycles is in the order of 10^2-10^3, which is comparable to the number of cycles to failure for electrographite and natural graphite under a 50-100 MPa stress in (Clark and Lancaster 1963). In this study, OM of cleaved cross-sections of the wear tracks from HT and RT (images provided in the companion Data in Brief article) do not show cracks below the surface, as in the blistered electrographite samples attributed by (Clark and Lancaster 1963) to fatigue wear at RT. While no evidence of fatigue wear appears in this study, the possible RT trend of wear rate with number of rotational cycles on the wear track might merit consideration of fatigue failure of the tribo-film at RT. *Performing studies with different loads and number of cycles and constant sliding distance would make it possible to confirm or refute fatigue as an alternative mechanism for the fracture of the tribo-film.*

Abrasive wear occurs more evidently at HT than at RT, as observed in the wear marks. Abrasion grooves of 100-200 μm width are visible on both the RT and the HT wear spots. At RT they are only few microns deep, while at HT they are up to 50 μm deep. The width of the grooves is comparable to the platelet-like debris, suggesting that abrasion is due to ploughing of detached tribo-film fragments. From the profilometry of the HT wear marks, it is evident that the film is abraded by the wear debris, indicating that the debris is harder than the tribo-film, despite originating from it. This is compatible with observation of graphite anisotropy across crystallographic planes. As shown with nano-indentation tests on highly oriented pyrolytic graphite (HOPG) (Xiao et al. 2013), the hardness of graphite basal planes is 5 times as large as the hardness in the perpendicular direction. Hardness variability among crystallographic planes of ET-10 crystallites may be quantitatively different from HOPG, but the HOPG results suggest that if the basal plane of debris detached from the tribo-film impacts on the tribo-film at an angle, it could be able to plough through it, leading to an abrasion groove. As shown by Raman spectroscopy, the bottom of the abrasion grooves is characterized by nominal surface and there is no evidence of the nominal surface being cut by the debris, suggesting that the debris is less hard than the nominal surface. Therefore, *the deeper abrasion grooves at HT are attributed to the presence of a thicker and more extensive tribo-film*. Micro-indentation of tribo-film and of the debris from RT and HT and of nominal surface could be performed to verify this hardness assumption and confirm our assignment of tribo-film thickness based on the depth of the abrasion grooves.

4.1.3.2.3.2. *Chemical considerations*

Chemical interactions the tribo-film with the surface of the mating component can lead to adhesion wear of the tribo-film. The adhesion of the tribo-film could lead to a decrease of the film thickness and the appearance of local pits and tears, disrupting the continuity of the film. Due to the basal alignment of the tribo-film, the adhesion would be due to interaction of basal atoms, and not of edge atoms (as in the case of the nominal surface) and would therefore depend on the surface energy of the basal planes. As graphite temperature is increased, its out-of-plane lattice parameter *c* increases and the basal surface energy decreases. Based on the theoretical model developed in (Brennan 1952), (Walker et al. 1953a) estimates a linear dependence of basal surface energy with

temperature. Assuming this dependence, the basal surface energy at HT is approximately 5% less than at RT.[d]

The surface energy of the crystallite edges is responsible for the binding among the fractured crystallites and it is either constant with temperature (Abrahamson 1973) or possibly more reactive with temperature (Wu et al. 2018a). The temperature-dependence of the interaction energy of the basal planes and edge sites overall leads to *an increase in chemical anisotropy of graphite crystallites with temperature*. Thus, at HT there will be a higher driver for the formation of an aligned film, promoting a thicker and more continuous film (Figure 4.11).

4.1.3.2.3.3. *Temperature hysteresis*

Temperature-transient runs (Figure 4.3) show an increase in friction as the temperature is lowered, ultimately going back to the COF observed in other room temperature tests thus indicating that the mechanical damage from wear is superficial, also supported by no observable changes in XRD spectra upon wear, neither on the wear spot, not on the wear track (XRD results discussed in Data in Brief article (Vergari et al. 2023b)). The temperature-transient sequences also demonstrate that the film formed at high temperature is stable at the intermediate temperatures of 400 °C and 200 °C, for 100 m sliding distance, but degrades at room temperature. Conversely, COF measurements beginning at room temperature, and gradually increasing the temperature show hysteresis in the COF at the intermediate temperatures of 200 °C and 400 °C, for 100m sliding distance. This hysteresis causes more oscillation in the COF, and it causes a slightly higher average COF than in the temperature-decreasing sequence. This indicates that the film has some stability at these intermediate temperatures, but at these intermediate temperatures it cannot form independently of the starting condition of the wear spot, as it does at 600 °C. These observations from the temperature-transient sequences support the arguments made above that (1) *at high temperature the film is more likely to form due to the change in anisotropy of the crystallite reactivity* (i.e., edge reactivity vs. basal plane interaction energy), and (2) *at high temperature the film fractures less easily based on higher tensile strength of graphitic materials* with increased temperature.

4.1.4 Conclusion

This chapter presents and discusses the results of nuclear graphite tribology studies in argon gas, relevant to graphite-graphite friction in the PB-FHR nuclear reactor handling systems and in the cover space of the nuclear reactor core. Tests are performed at two temperatures (20 °C and 600 °C), and wear rates and coefficients of friction are reported. Friction and wear are lower at high temperature: the COF decreases by 40%, from 0.55(14) to 0.33(5), and the wear rate decreases by a factor of seven, from 0.4(3) to 0.06(3) μg/Nm, when the sliding temperature is changed from RT to 600 °C; the applied load is 50 N.

This result reconciles and explains the contradiction that previously existed in the literature about the effect of temperature on graphite-graphite friction in an inert environment. Different degassing strategies have been applied in high-temperature tribology studies for graphite (Table 4.6), and the presence of oxygen or water in the graphite at the time of testing can strongly influence the results. In our study, all graphite samples are degassed at 600 °C in an argon atmosphere for four hours to fully remove the adsorbed moisture and oxygen. This is shown by testing for thermal hysteresis that the decreased COF and wear rate at high temperature in our studies is not caused by oxygen

---

[d] Calculated using the contact-point temperatures achieved because of frictional heating.

or water. Future testing of could be performed via X-ray Photoelectron Spectroscopy (XPS) of the wear spot to quantify the C-O bond content (Barber et al. 1973; Hueso et al. 2007; Larciprete et al. 2012) on the HT versus RT wear spots.

The appearance of a carbon tribo-film on the surface of the sliding counterparts is identified by digital microscopy and SEM. Raman spectra indicate that the tribo-film is composed of crystallites with the same axial length of the reference crystallites but smaller basal size (approximately half). Polarized light microscopy indicates that the crystallites composing the tribo-film are aligned in a common direction. Lower COF and lower wear rates when the film is present can be explained by crystallite basal direction alignment that leads to reduced adhesion.

To further verify that the crystallites fracture perpendicularly to their basal planes, the wear marks could be probed with tests sensitive to the crystallite surface area or density of edge sites, such as BET (Contescu et al. 2012; Gallego et al. 2021a) or H_2 adsorption isotherms (Hoinkis 1991a; Lam et al. 2018; Wu et al. 2020a), or sampling the tribo-film and performing XRD on it. To further verify that the crystallites align with their basal planes facing the sliding interface, performing TEM (Wen et al. 2008; Zheng et al. 2014) of the film or O_2 adsorption isotherms (Walker et al. 1953b; Zarifyanz et al. 1967) is suggested, since oxygen adsorption would be specific to the density of surface-facing crystallite edges (unlike H_2, which is also sensitive to intra-crystallite reactive sites (Markin et al. 1997; Vergari and Scarlat 2021c)).

It is concluded that any structure modification at the wear spot is superficial (tens of microns), based on the absence of temperature hysteresis (Figure 4.3), the absence of changes in XRD at the wear marks and no structural damage on the cleaved cross-sections of the wear tracks as observed by OM (Vergari et al. 2023b). Thus, the temperature effect is strictly a consequence of the temperature-dependence of the mechanical and chemical properties of the graphite and the graphite tribo-film.

In summary, the following description for the tribo-film formation and destruction in inert argon atmosphere (Figure 4.11) is formulated based on SEM and OM microscopy, Raman spectroscopy, COF, wear rate and debris observations:

- As the graphite pebble and disk are put in relative motion, wear occurs by adhesion and third-body abrasion.
- Adhesion is due to the interaction of non-passivated dangling bonds on graphite crystallite edges at the sliding interface.
- The debris generated by tribo-film fracture remains entrapped between the sliding component, leading to three body abrasion causing matching grooves of up to 200 μm diameter on the pebble and the disk track.
- The crystallites involved in the wearing process fracture perpendicularly to their basal planes and align their basal planes to the sliding interface, forming a tribo-film of lower roughness and of expected lower hardness (Clark and Lancaster 1963) than the nominal surface.
- Due to the basal orientation of the crystallites of the tribo-film, the tribo-film is less prone to adhesion wear.
- The contact stresses on the tribo-film lead to tensile fracture at the asperity contact points.
- A thicker tribo-film is postulated to form at 600 °C (up to 50 μm) than at RT (up to 10 μm), based on appearance of deep abrasion grooves in the region covered by the tribo-film at HT and shallower grooves at RT when the film is patchy.

- At HT, the higher larger tensile strength, lower adhesion, and higher chemical anisotropy leads to the formation and maintenance of a uniform, oriented tribo-film.
- At RT, the film is less resistant to wear and is continuously fractured, leading to a patchy texture and slip-stick behavior in the COF.

4.1.5 Acknowledgement

4.2   Graphite Tribology in FLiBe

In the previous section, graphite tribology in argon is analyzed, and coefficients of friction (COFs) and wear rates (WRs) are quantified (Vergari et al. 2023a). To characterize pebble tribology in a PB-FHR, it is also necessary to predict wear and friction in the salt. Limited tribological and post-characterization data for graphite in salt are available in literature. A senior design project at UC Berkeley studied friction for graphite-graphite contacts in FLiNaK (Hong et al. 2009) using a two-ball-on-plate apparatus, yielding static and dynamic COF of 0.2 - 0.3. (He et al. 2023) used a pin-on-disk tribometer to measure WRs and COFs of graphite-316 stainless steel in FLiNaK and assess the effect of salt quantity, sliding speed, and temperature on lubrication. In this section, COFs and WRs for graphite-graphite sliding in FLiBe are reported for the first time in literature.

4.2.1   Methods

The experiments described in this summary are conducted using ET-10 and IG-11 graphite. ET-10 is a superfine grain graphite grade manufactured by Ibiden and selected by Kairos Power as reflector material for the KP-FHR design (Vergari et al. 2023a). IG-11 is a superfine grain graphite grade manufactured by Toyo Tanso and employed in HTR-PM (Guobin and Konishi 2014).

Tests are conducted in an argon glovebox (<10 ppm O2, <1 ppm H2O) using an Anton Paar Modular Compact Rheometer 702e (MCR702) rheometer in ball-on-three plates (BTP) configuration. In BTP tests, a shaft rotates over its axis while contacting three plates. A normal load up to 20N is applied on the shaft and a sensor measures the frictional force at the contact points. For each test presented in this summary, three graphite plates are employed, and a customized graphite shaft with a hemispherical cap is designed and manufactured. Prior to testing, samples are baked at 600°C for 4h to remove adsorbed moisture and oxygen.

Tests are performed in argon, to provide a benchmark against results obtained with a pin-on-disk (POD) configuration (Section 4.1), and in FLiBe. The salt used in this study originates from the same batch used in previous experiments by the same group. FLiBe preparation and purification are described in (Carotti et al. 2018; Kelleher et al. 2015; Vidrio et al. 2022).

Tests are performed at temperature between 500°C and 600°C, as measured by a type K thermocouple integrated in the MCR702 oven (less than 1°C variability). All tests described in this summary are conducted using 0.15 m/s velocity, 100 m sliding distance, and 20 N load. Velocity and sliding distance are chosen to replicate test parameters used in Section 4.1. The load used in this study is lower than the load used in Section 4.1 and corresponds to the maximum load admissible by the MCR702 instrument.

Post-characterization of the generated samples is performed inside the glovebox environment. Samples generated during salt-lubricated tests are removed from the test apparatus after tilting the sample holder and heating it to 600°C to let the salt drip out. In the test "Be600", sonication of the sample holder in 80°C water for 6 hours, was necessary to remove salt residue from the sample holder and extract the samples.

Imaging of the wear spots on the plates and wear track on the shaft is performed using a Nikon LV-150NL optical microscope under brightfield coaxial light and polarized light using a sensitive tint retardation plate. WR are estimated from the wear spot images, assuming no significant wear of the shafts, following the ASTM standard G99.17 "Standard test method for wear testing with a

Pin-on-Disk apparatus". Normalized wear rates (NWRs) are calculated by dividing WR by load and sliding distance. Roughness and surface profile measurements are performed using a Mahr SD26 profilometer with a 2 µm radius stylus tip. SEM/EDS characterization will be performed in the upcoming months.

4.2.2 Results

A complete list of the tests performed in this study is compiled in Table 4.7. Duplicate tests are conducted in argon and FLiBe to verify repeatability of the results. Tests in FLiBe are conducted at four different temperatures between 500 °C and 600 °C to investigate temperature dependence of friction and wear. Tests in FLiBe with added fluorides or metals are performed to explore the effect of salt composition on lubrication.

Table 4.7. Summary of tests. Tested materials: ET-10 vs ET-10; sliding distance: 100m; load: 20N; sliding speed: 0.15m/s unless specified differently.

Test ID	Environment	Temperature (°C)	Average COF	Steady State COF	Running-in Distance (m)	Normalized Wear Rate (µg/ Nm) [1]	Average roughness Ra (µm) [1]
A600#1	Ar	600	0.31(11)	0.2549(9)	10	0.034(6)	0.9(2)
A600#2			0.26(12)	0.127(2)	10	0.034(4)	0.9(1)
F500	FLiBe	500	0.25(4)	0.216(3)	14	0.0146(10)	1.1(2)
F550		550	0.19(12)	0.1154(9)	20	0.0141(14)	0.7(1)
F575		575	0.26(6)	0.245(3)	14	0.0197(14)	1.2(3)
F600#1		600	0.20(5)	0.1566(6)	10	0.0221(13)	1.3(2)
F600#2			0.20(6)	0.161(2)	10	0.0156(12)	1.3(3)
FMT[2]		500-550-600-550-500	0.25(5)-0.20(1)-0.19(1)-0.20(1)-0.21(1)	0.222(3)-0.194(1)-0.191(1)-0.192(1)-0.199(1)	20-5-10-10-20	N/A	N/A
AgF600	FLiBe + 1wt.% AgF	600	0.11(5)	0.0929(3)	10	0.0134(11)	1.3(3)
CrF$_2$600	FLiBe + 1wt.% CrF$_2$	600	0.41(17)	0.279(5)	40	0.11(3)	1.0(3)
Be600[3]	FLiBe + 1wt.% Be	600	0.05(3)	0.017(7)	50	0.010(-)	0.74(-)
ET-10 Reference Sample							1.4(3)
IG-11 Reference Sample							1.5
Notes : [1] wear rates and roughness averaged over the wear spots on the three plates. Only one wear spot is successfully imaged in test Be600. [2] sliding distance: 50m per segment (250m total). [3] tested materials: IG11 vs IG11							

4.2.2.1. Benchmarking: wear and friction in argon

Figure 4.14 displays the COFs for the tests performed at 600°C in Ar as a function of the sliding distance. Duplicate runs in argon show repeatability of the average COFs within 20%. One of the two argon runs shows a drop in the COF after ~40m of sliding. This leads to a difference in the steady-state COF (half than in the other run) but does not cause changes in wear. The cause of the change in COF mid-run remains unclear.
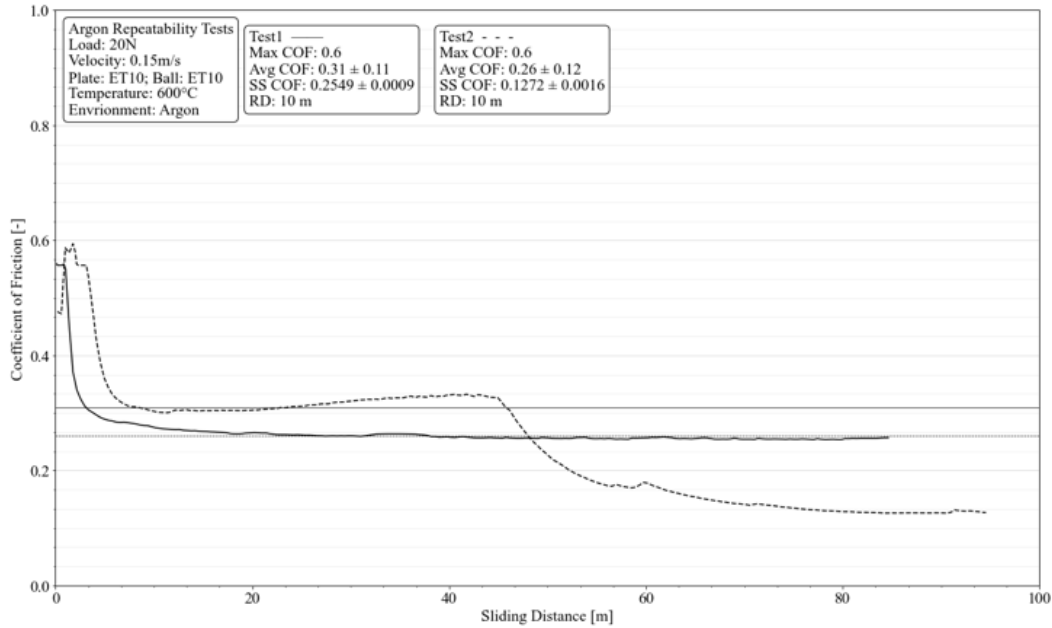
Figure 4.13: Coefficient of friction of the tests for ET-10 on ET-10 at 600 °C in Ar.

Tests in high temperature argon can be benchmarked against published results. Table 4.8 compares the tribology results obtained with the BTP setup and presented in this chapter with the results obtained with a POD setup and presented in Section 4.2. The tests show repeatability within one standard deviation in terms of average COF and max COF. This consistency confirms that BTP friction results can be compared with POD results.

The tests performed with the BTP tribometer achieve a 40% lower steady state COF and normalized wear rates. The differences in measured wear rates motivate an investigation of which of the two methodologies is more representative of friction and wear in a pebble-bed reactor.

Table 4.8 also shows that roughness of the wear spots generated with the BTP tribometer is on average three times larger than in wear spots generated with a POD setup. The discrepancy observed here is at least partly due to how roughness is measured. In Chapter 4.1, roughness is measured with a digital microscope over a 0.1 mm^2 spot area centered on the tribo-film; here, roughness is measured with a stylus over the entire wear spot diameter (~1 mm as shown in Figure 4.15). The larger trace length used in this chapter may comprise regions not covered by the film, thereby leading to a higher roughness.

Table 4.8: Benchmarking of tribology tests of ET-10 against ET-10 in argon at high temperature

Type of test	Load (N)	Speed (m/s)	Sliding distance (m)	Temperature (°C)	Avg COF	Max COF	Steady State COF	Running-in Distance (m)	Norm. Wear Rate (µg/Nm)	Ra Roughness Before (µm)	Ra Roughness After (µm)	Ref
POD	50	0.15	150	600(10)	0.35(3)	0.6	0.36(4)	15	0.104(11)	Measured on reference pin and disk	Measured on pin and disk for one test only	Ch. 4.1
				603(10)	0.31(3)	0.6	0.31(2)	20	0.030(1)			
				597(10)	0.35(7)	0.8	0.32(5)	20	0.063(4)			
				600(10)	0.32(4)	0.6	0.32(8)	20	0.051(5)			
Average for POD[1]					0.33(9)	0.6	0.33(10)	18	0.06(1)	1.2 – 1.9	0.3 -0.4	
BTP	20	0.15	100	600(1)	0.31(11)	0.6	0.2549(9)	10	0.034(6)	Measured on reference plate	0.9(2)	Ch. 4.2
				600(1)	0.26(12)	0.6	0.127(2)	10	0.034(4)		0.9(2)	
Average for BTP[1]					0.29(16)	0.6	0.191(2)	10	0.034(7)	1.4(3)	0.9(3)	

Note: [1] Standard deviation propagated in quadrature

4.2.2.2. *Wear and friction in FLiBe*

The COFs for two runs in FLiBe are shown in Figure 4.14. The tests show repeatability in COFs within 10% and in NWRs within 30%.
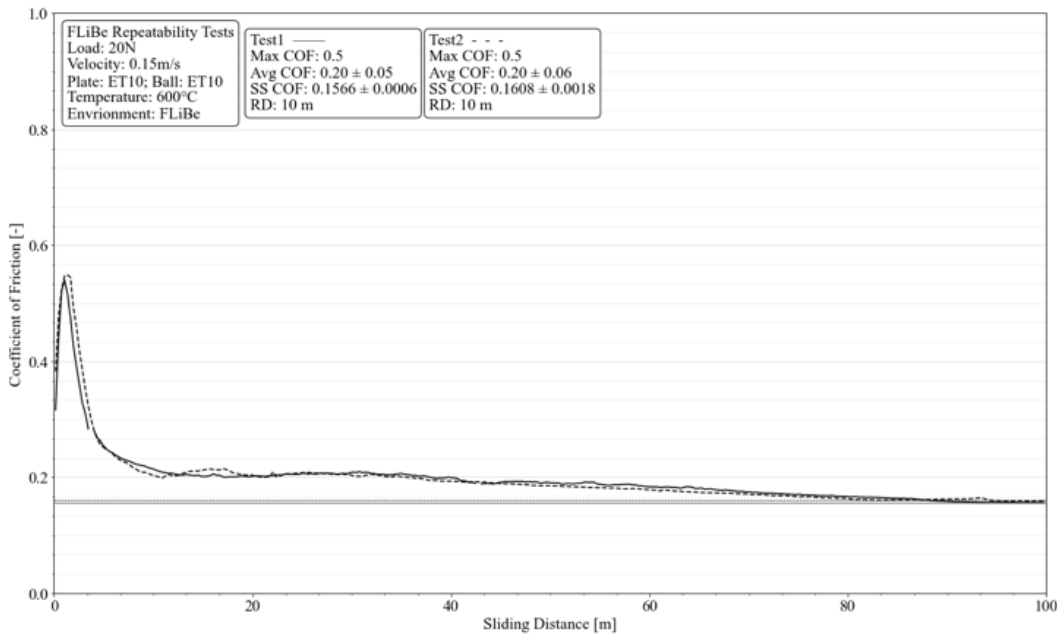
Figure 4.14: Coefficient of friction of the tests for ET-10 on ET-10 at 600 °C in FLiBe.

As observed from both couples of tests, addition of FLiBe leads to a decrease in both COFs and NWRs with respect to dry sliding conditions. The change in NWRs (decrease by a factor of 3) is more marked than the change in average and SS COFs, consistently to what is observed in previous graphite studies (Li and Sheehan 1980; Stansfield 1969; Vergari et al. 2023a).

Figure 4.15 shows the micrographs for the non-worn graphite surface, a wear spot generated in argon, a wear spot generated in FLiBe. The wear spot generated in argon appears bright under coaxial light, indicating the formation of a carbon film on its surface, consistently to what observed

in Section 4.1. The crystallites composing the film appear oriented in the same planar direction, as shown by polarized light microscopy. The wear spot generated in FLiBe appears brighter than the surrounding surface but less bright than the Ar wear spot, suggesting a less significant decrease in roughness compared to the sample tested in Ar, as confirmed by roughness measurements (Table 4.7). High magnification micrographs indicate a more discontinuous film than in the sample tested in argon at 600°C, with gaps of tens of microns (vs few microns in the sample tested in argon). These observations indicate that the formation of a self-lubricating film on graphite surface, described in Section 4.1 for dry-sliding in Ar at 600°C, is more favored in a dry sliding condition than in FLiBe-lubricated environments. SEM/EDS analysis will be performed to further analyze the texture and the composition of the surface of the wear spots.

Reference	FLiBe 500 °C	FLiBe 550 °C	FLiBe 575 °C	FLiBe 600 °C	Argon 600 °C

50X brightfield coaxial light

500X brightfield coaxial light

500X polarized light
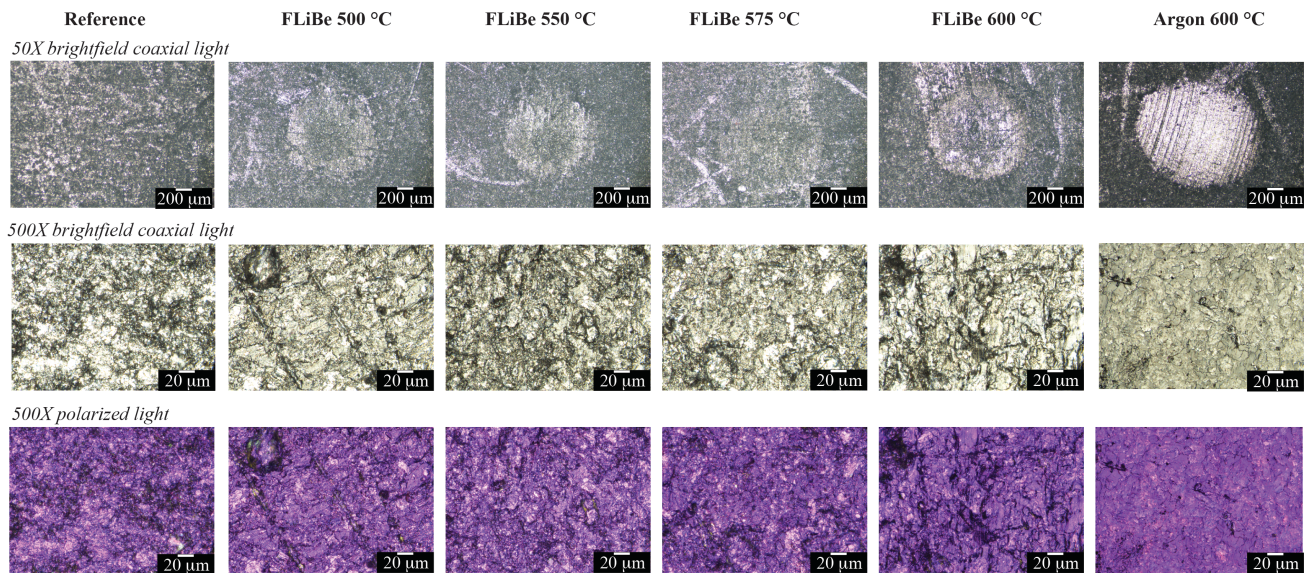
Figure 4.15. Optical micrographs of non-worn surface and wear spots generated in argon and FLiBe.

4.2.2.3. *Temperature dependence of friction and wear*

Figure 4.16 displays the COFs and the NWRs for the temperature-dependent tests conducted in FLiBe. The average COF is within one standard deviation at all temperatures, not suggesting a temperature dependence. NMR is largest at 575°C and 600°C, and lower at 500°C and 550°C, suggesting an increase with temperature.

116
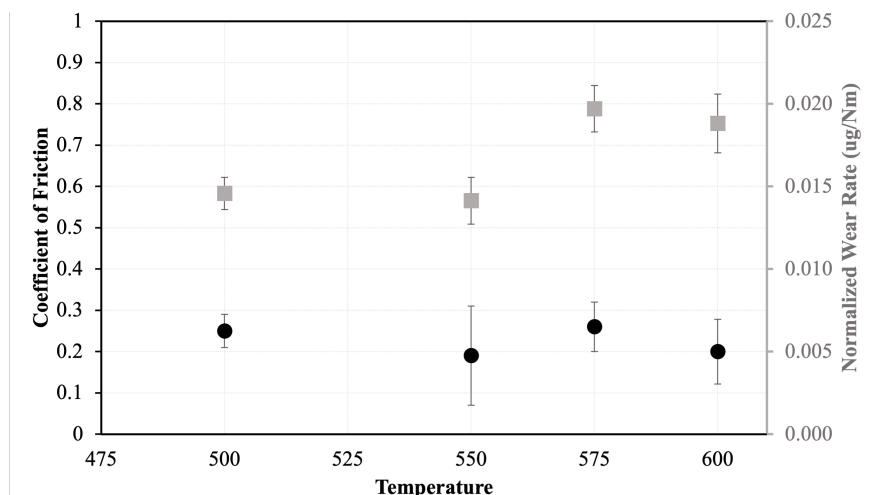
Figure 4.16. Coefficients of friction and NWR in temperature-dependent tests conducted in FLiBe.

Micrographs of the wear spots are shown in Figure 4.15. Polarized light indicates that while film formation occurs in all samples, the film features appear different with temperatures. The film is more discontinuous at lower temperatures, with visible gaps up to 100 µm in diameter and grooves. At temperatures 500-575°C, individual grains of 10-20 µm, can be observed composing the film. At 600 °C, the film appears composed of graphite domains of larger size, with less visible boundaries from one grain to another, closer to what is observed for the samples tested in argon. Further images of the film at 600 °C are included in the Mendeley Data repository linked in Supplementary Information.

To investigate reversibility of the damage caused by wear and friction, a set of samples is used for multiple consecutive runs at variable temperatures. Five tests (temperatures: 500°C – 550°C – 600°C – 550°C – 500°C) are performed to test the effect of temperature increase and decrease. As shown in Figure 4.17, COFs are similar across runs, with average by runs in the interval 0.19-0.25. Tests beyond the first one show lower running-in distances, suggesting that the surface polishing performed during the first test remains for the following ones. The test performed at 500°C at the end of the cooling sequence shows a COF lower than what is achieved at the same temperature at the beginning of the heating run and as a standalone test. Such COF is within one standard deviation of the previous tests at 550°C and 600°C, suggesting that the effects of wear remain during following runs, unlike what was observed in argon over the temperature interval 20°C – 600°C (Section 4.1).
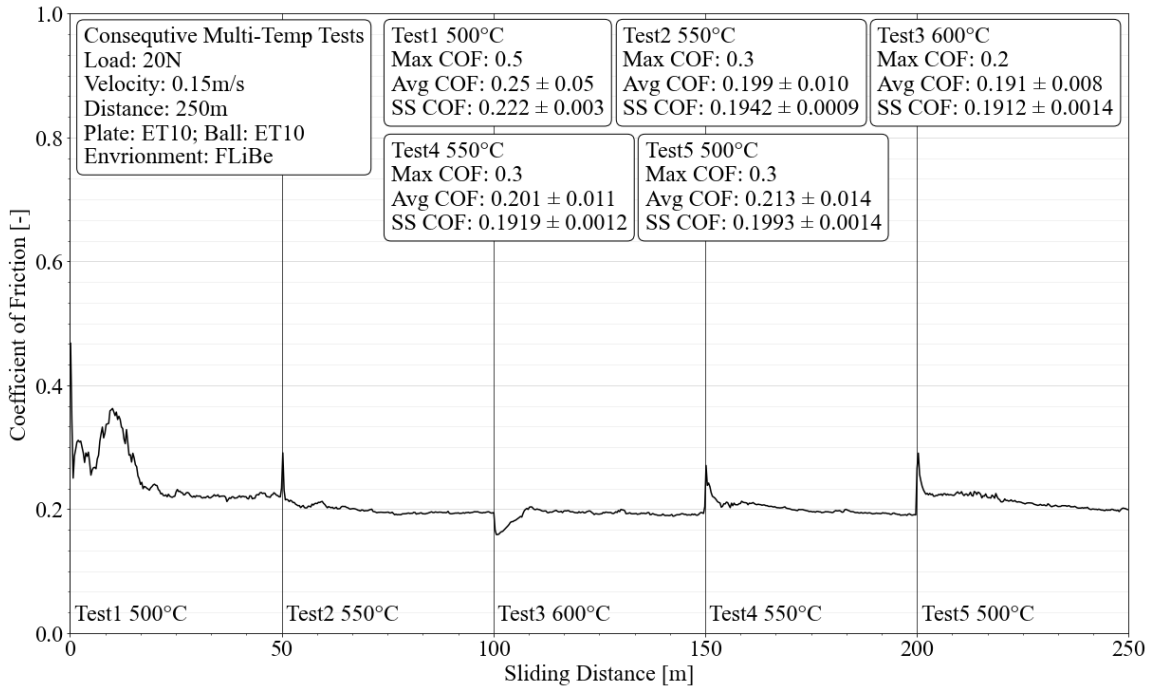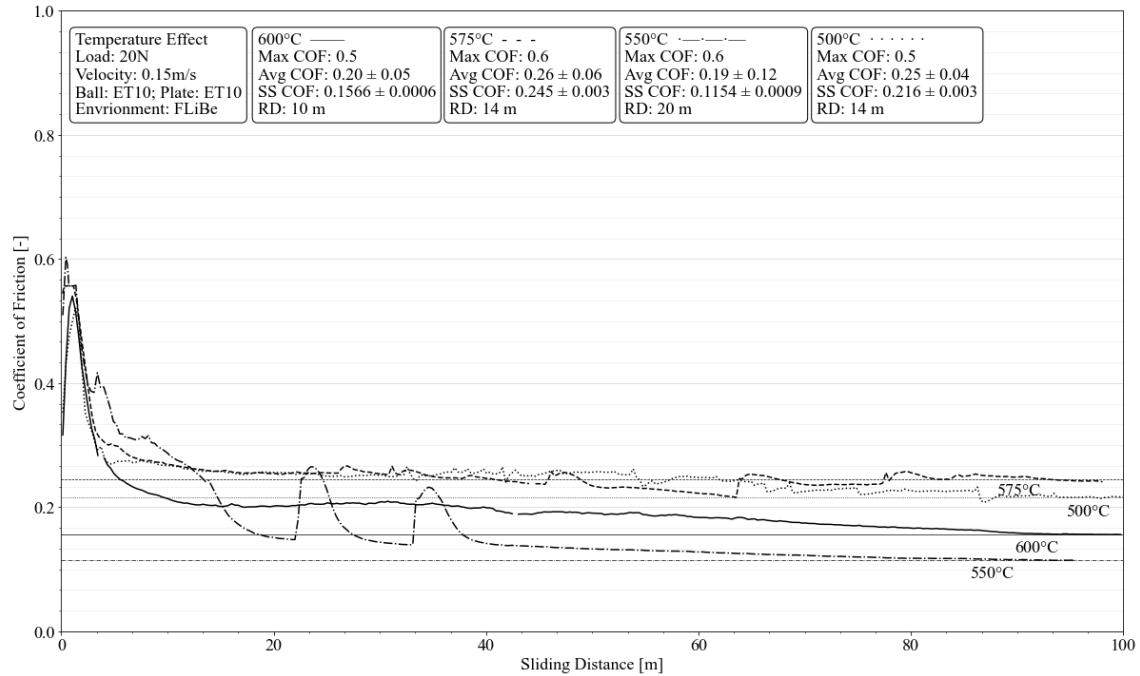
Figure 4.17: Coefficient of friction for ET-10 vs ET-10 in FLiBe at different temperatures. Top: Tests performed on individual sets of samples. Bottom: Tests run consecutively on the same set of samples

4.2.2.4. *Impacts of salt chemistry on friction and wear*

Figure 4.18 shows the COFs for tests conducted with variable salt composition. Both the COFs plotted in Figure 4.18 and the NWRs tabulated in Table 4.7 (which show the same trend as the COFs) suggest significant changes as a result of compositional changes.

118

The highest average COFs and NWRs are observed upon addition of 1 wt.% CrF_2 to FLiBe. Figure 4.18 shows that the COF undergoes a sudden increase to 0.5 after about 15m, to then decrease and stabilize around 0.3. Visual inspection of the samples post-run indicates that the salt was not covering the contact points by the end of the run and had creeped to the side of the plates. From the COF plot, it is deduced that the lack of salt coverage happened around 10-15m after the test onset, exposing the mating samples to dry contact. This contact leads to a COF around 0.5, which is consistent with values observed for graphite dry sliding in argon at room temperature, i.e., at conditions where a stable self-lubricating film does not form (Section 4.1). As high-temperature dry sliding continues, the film starts forming, leading to a decrease in COFs to values consistent with what is observed in the argon tests. Optical micrographs of the wear spot confirm that the film features are comparable with those observed in argon tests. In addition to this, micrographs also highlight the presence of a second phase, of brown/golden color, which is not observed in other samples. This phase could indicate precipitation of chromium metal or chromium carbides. EDS/XPS analysis will be performed to chemically identify this phase.

Lower wear and friction than in FLiBe are observed upon addition of 1 wt.% AgF. The test is characterized by a running-in distance comparable to the test in FLiBe, and lower average and SS COFs (approximately 2/3 of what is observed in FLiBe). NWRs decrease at the same rate. Micrographs of the wear spot indicate a non-round shape but a similar texture and coverage for the film. In literature, non-round wear spots have been associated to tribocorrosion (Zhu et al. 2021). XPS analysis will be performed to identify whether chemical lubrication mechanisms are responsible for the decrease of wear and friction observed here.
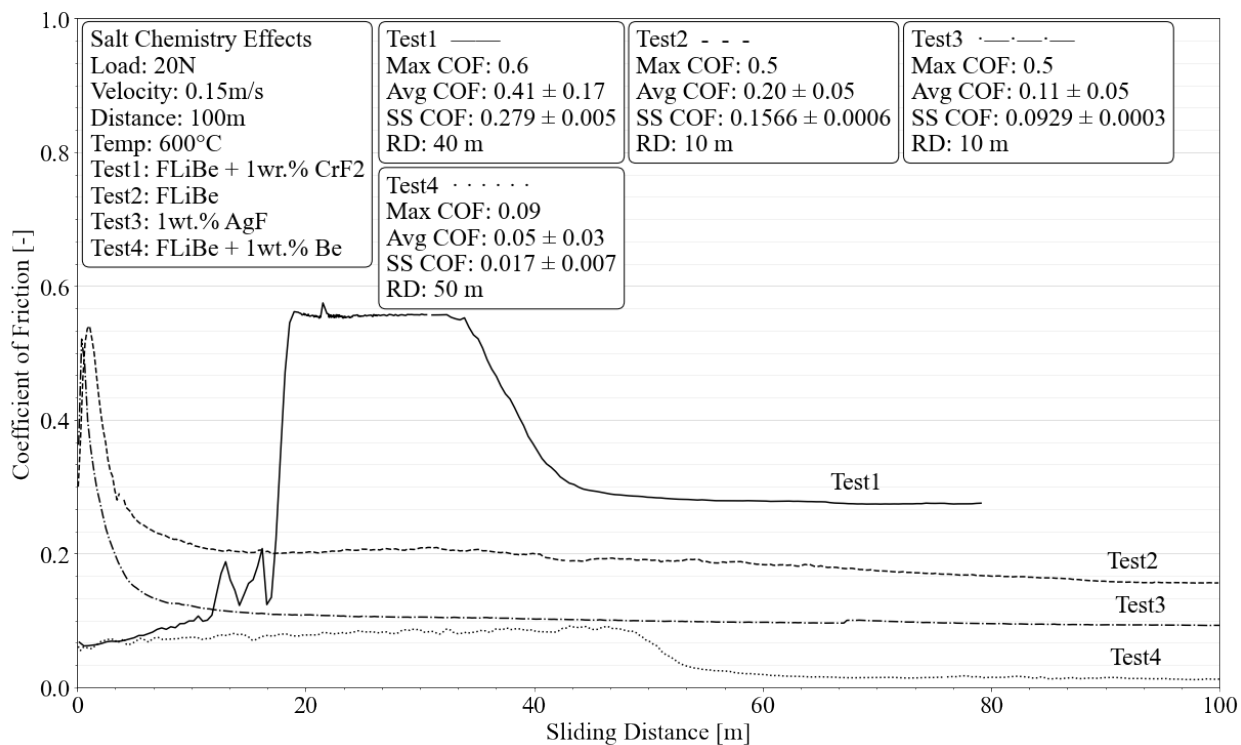
Figure 4.18: Coefficient of friction under variable FLiBe composition. Test details included in Table 4.7.

119

The lowest COFs and NWRs are observed upon addition of 1 wt.% Be(metal). Compared to the tests in FLiBe, this test yields a decrease in average COFs and NWRs by a factor of 4 and 2, respectively. In this test, the SS COF is achieved after approximately 50m of sliding and is lower than any other COF reported for graphite sliding in salt (He et al. 2023; Hong et al. 2009). Optical micrographs of the samples generated in this test reveal that the film observed in other tests is here absent. Salt residues stick to the wear spot (unlike all other samples) even after sonicating in 80°C water for 6 hours.

FLiBe	FLiBe + 1wt.% CrF$_2$	FLiBe + 1wt.% AgF	FLiBe + 1wt.% Be

50X brightfield coaxial light

500X brightfield coaxial light

500X polarized light
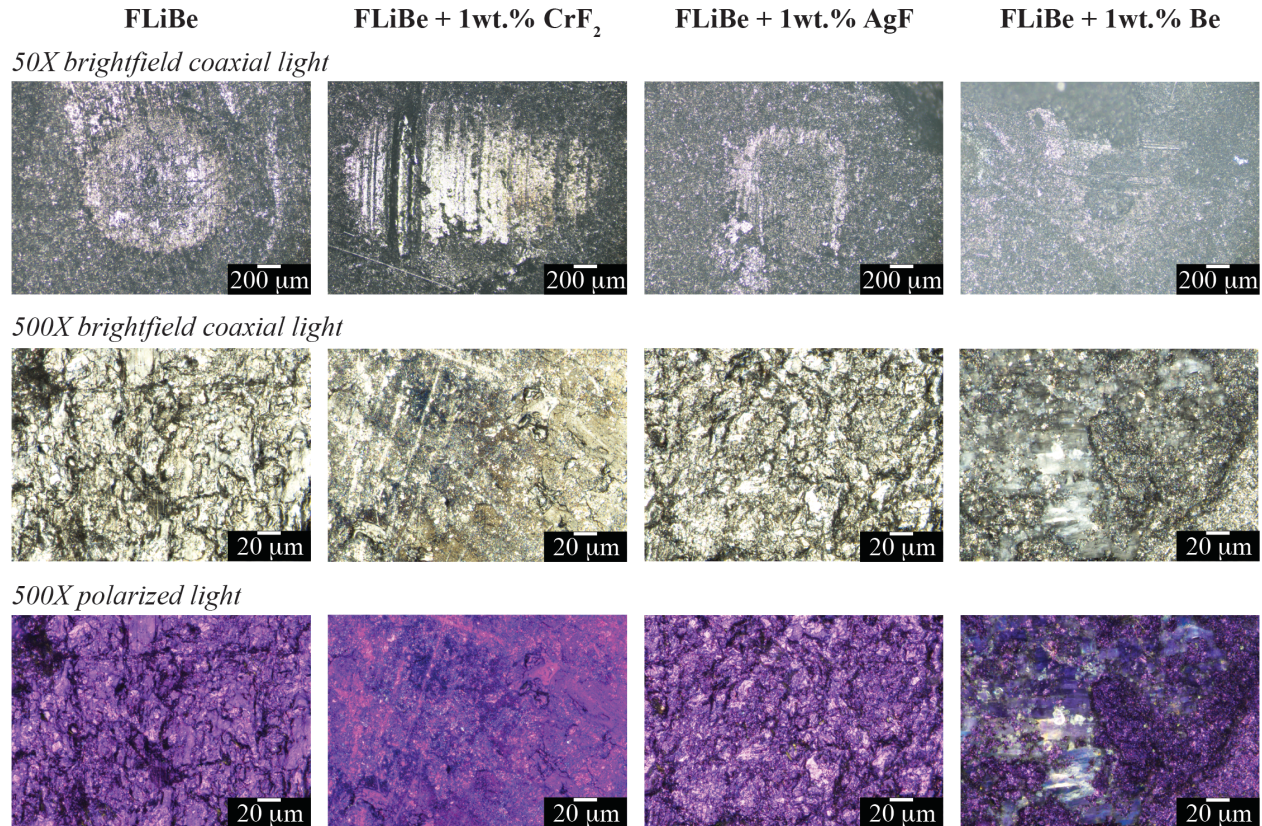
Figure 4.19: Optical micrographs of wear spots generated with variable salt composition

4.2.3   Discussion

Except for test in FLiBe + CrF$_2$, all tests in salt lead to a lower friction and wear than what is observed upon dry sliding in argon, suggesting that FLiBe is even more effective than graphite film formation. Using the Hamrock and Downson equation (Hamrock and Dowson 1981), one can calculate the thickness of the FLiBe film at the contact interface, compare it to the composite roughness, and identify the lubrication regime that is achieved with FLiBe. The parameters required for the calculations are included in Table 4.9. The minimum film thickness and minimum composite roughness are plotted in Figure 4.20. At any temperature, the film thickness is less than 1% of the minimum composite roughness, indicating that sliding with FLiBe happens in a boundary lubrication regime.

Table 4.9: Parameters used for calculation of lubrication regime

Parameter	Value	Reference
	Graphite Properties	
ET-10 elastic modulus at room temperature (E_{ET-10}^{RT})	10.9 GPa	Ibiden
IG-11 elastic modulus at room temperature (E_{IG-11}^{RT})	9.8 GPa	Toyo Tanso
Elastic modulus as a function of temperature (E^T)	$E^T = E^{RT}\left(1 + 0.2\dfrac{T(^\circ C) - 0}{1200}\right)$	(Malmstrom et al. 1951)
Poisson ratio	0.2	(He et al. 2023)
Minimum roughness σ_{min}	770 nm	Table 4.7
Minimum composite roughness σ_{min}^c	$\sigma_{min}^c = \sqrt{2\sigma_{min}^2} = 990\ nm$	(Hamrock and Dowson 1981)
	Salt Properties	
FLiBe viscosity	$0.000116\ e^{3755/(T(^\circ C)+273)}\ (Pa\ s)$	(Sohal et al. 2010)
Pressure-viscosity coefficient	Not available in literature, assumed 10 GPa⁻¹	(He et al. 2023)
Maximum film thickness	9.5 nm	Calculated as in (Hamrock and Dowson 1981)
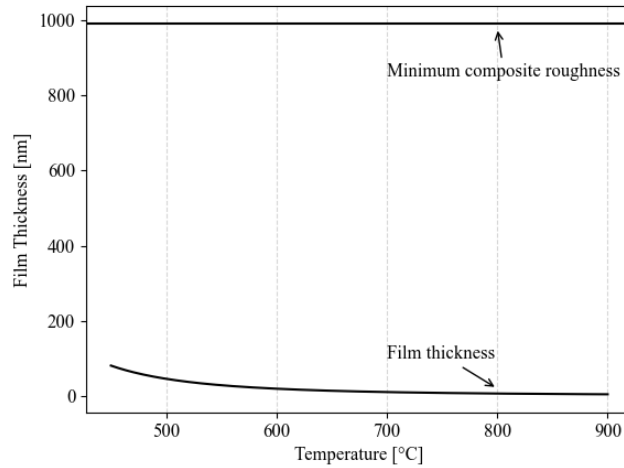
Figure 4.20: Comparison of FLiBe film thickness and roughness at the contact surface.

(Komvopoulos et al. 1985) indicates that, in boundary lubrication, the liquid film is effective in reducing adhesion forces between the mating surfaces (i.e., chemical contact), but is too thin to prevent abrasion (i.e., mechanical contact) caused by asperities. In graphite contacts, the main source of adhesion is the chemical interaction between dangling bonds at crystallite edges of the two mating surfaces. Tests of graphite dry sliding in argon at room temperature and high temperature show that graphite friction and wear is minimized when adhesion is limited (Section 4.1). In high temperature argon, graphite adhesion is minimized by the formation of a stable film of crystallites oriented in the basal direction (which is less chemical reactive than the crystallite edges) (Vergari et al. 2023a). The achievement of lower friction and wear in FLiBe than in argon suggests that FLiBe boundary lubrication is even more effective than graphite film formation in limiting the adhesion of carbon atoms at the crystallite edges.

The behavior observed in separate runs at different temperatures supports the hypothesis of FLiBe physically interposing between the mating surfaces. For runs F500-F600, wear is observed to increase in higher temperature tests (Table 4.7). Film thickness in boundary lubrication is temperature dependent. As calculated with the Hamrock and Downson equation (Hamrock and Dowson 1981), the salt film is 50% thicker at 500°C vs 600°C (7.6 nm vs 5.2 nm). The film thickness at 600°C may be insufficient to cover all asperities, leaving space for chemical interactions between the two graphite samples.

The liquid FLiBe film between the two surfaces might be effective in inhibiting adhesion not only because it is physically interposed between the two graphite surfaces, but also because it can chemically interact with graphite. In Chapter 2 of this thesis, evidence of chemical interactions between graphite and FLiBe upon long term exposure at high temperature is provided. The evidence collected in Chapter 2 suggests that upon exposure to liquid FLiBe, formation of covalent C-F bonds occurs at crystallite edges. Here, it is hypothesized that fluorination occurs during wear testing in FLiBe, and that it is effective in passivating carbon atoms at crystallite edges thereby preventing adhesion.

This hypothesis is supported by the behavior of the COF upon consecutive runs at different temperatures. Unlike what was observed upon Ar testing (Section 4.1), the COF shows hysteresis and does not return to the same value after a temperature cycle. If FLiBe lubrication was due purely to physical interposition between the surfaces, a return to the initial COF would be observed, as the film thickness would return to the initial value. This behavior may instead be indicative of irreversible changes to the surface of the sample, which support the hypothesis of a chemical reaction of the graphite with the salt. Studies in Table 2.8 show that the distribution of covalent and semi-ionic CF formed during fluorination is temperature dependent. It is possible that the two bond types have a different effect on lubrication, thereby inducing a temperature dependence once they are formed. Further investigation of the temperature effect is to be performed by means of isothermal tests at different loads. Increasing the load will allow to decrease the film thickness without changing temperature, allowing to decouple the effect of temperature-dependent chemical reactivity and film thickness. The observation of unchanged COFs and NWRs upon an increase of the load would suggest that chemical mechanisms are important for lubrication.

Under the hypothesis of a chemical lubrication mechanism, one might expect to see lower adhesion (i.e., lower COFs and NWRs) in conditions that maximize the chemical reactivity of the salt with the graphite. The salt chemical reactivity can be influenced by addition of metal fluorides that cause changes in the salt redox potential. For instance, one would expect to see a better lubrication upon addition of metal fluorides that cause an increase in the salt redox potential. This observation is aligned with what occurs upon addition of AgF to FLiBe, i.e., a decrease in wear and friction compared to tests performed in FLiBe. XPS characterization will help determine whether a higher degree of fluorination does correlate with reduced wear and friction.

The explanation provided above does not seem to correlate to what is observed upon addition of CrF_2 and Be. In the case of the test with FLiBe and CrF_2, an explanation is given in the previous section, where the increased wear and friction is attributed to the lack of salt at the contact interface. In the case of the test with FLiBe and Be, the difficulty in removing the samples from the sample holder and the observation of salt residues on the wear spot (not observed on other samples), seem to suggest that a different lubrication mechanism, which may be associated to salt wetting or

precipitation of Be metal on the sample surface, may be at play. Contact angle measurements and EDS/XPS analysis will be performed to investigate this further.

4.2.4   Conclusions

Quantifying friction and wear in pebble-pebble and pebble-structure contacts in PB-FHRs is necessary to predict pebble flow and degradation in the core. In this chapter, graphite-graphite tribology in molten fluoride salts is investigated, and, for the first time in literature, coefficients of friction and wear rates for graphite-graphite sliding in FLiBe are reported. The experiments discussed in this paper are performed using a ball-on-three-plates tribometer. The results are benchmarked against published data for graphite sliding in argon at high temperature design (Section 4.1). Repeatability tests are performed to verify consistency of coefficients of frictions and wear rates in both argon and FLiBe. Tests are performed as a function of temperature and salt composition to investigate the lubrication mechanisms. The results of the tribological tests indicate that FLiBe lubrication leads to a decrease of the coefficient of friction and of the wear rates compared to dry sliding in argon. Microstructural analysis shows that the formation of a self-lubricating film on graphite surface is favored in dry sliding condition and is less uniform in FLiBe. Temperature-dependent tests show uniform coefficients of friction in the interval $500°C - 600°C$, increase of wear with temperature, and hysteresis in the coefficient of friction upon temperature cycling. Salt composition-dependent tests show a decrease in friction and wear upon addition of AgF or Be. The combination of tribological and microstructural results suggest that an additional lubrication mechanism is at play upon addition of FLiBe. Calculating the salt film thickness indicates that tests are performed in the boundary lubrication regime. It is postulated that the FLiBe lubricates the graphite-graphite interface by interposing between the mating surfaces and passivating the carbon atoms at crystallite edges. Further testing at different load levels and chemical characterization of the wear spots by EDS, SEM, and contact angle studies is necessary to support the formulated hypothesis.

4.2.5   Acknowledgement

5 Tritium Uptake in Graphite

Tritium management is a priority in FHRs and MSRs, since substantial amounts of tritium are produced by neutron irradiation of the lithium and beryllium contained in the salts and tritium solubility in the salt is conventionally assumed to be limited. Graphite has shown to have a chemical affinity for tritium and has been proposed as a vector to remove tritium from PB-FHRs. This chapter focuses on tritium production and graphite-tritium interactions. Neutron activation reactions in FLiBe are modeled and tritium production rates are quantified. By reviewing the graphite-tritium interaction, the mechanisms for uptake and desorption relevant at reactor conditions are highlighted, and the effects of reactor phenomena are discussed. The findings are employed to develop an improved model for hydrogen uptake in graphite, which can be used to extract tritium transport parameters from experimental studies.

5.1   Neutron Activation of FLiBe, Tritium Production, and Redox Effects

Fusion and fission nuclear reactors that employ FLiBe as coolant or fuel solvent in the reactor core or in the blanket produce tritium primarily due to neutron activation of lithium and beryllium (Forsberg et al. 2017a). Tritium production, along with other activation reactions on all FLiBe constituents, is an oxidizing process that leads to corrosion of salt-facing metallic components, in the absence of redox control (Calderoni et al. 2008; Calderoni and Cabet 2012; Carotti et al. 2019; Petti et al. 2006; Zhang et al. 2018b). In addition to fission reactors employing mixtures including LiF and BeF$_2$ as fuel salts or coolants where the lithium is enriched in ^{7}Li, fusion power plants use FLiBe with lithium enriched in ^{6}Li as the tritium breeding blanket and heat transfer medium (Forsberg et al. 2020). Thus, it is of relevance to reactor designers and salt-irradiation experimentalists to have a methodology for quantifying the chemical effects that arise from neutron activation reactions on FLiBe.

Tritium production and all the other neutron activation reactions on Li, Be and F have chemical effects on the molten salt coolant by changing its redox potential and thus providing a continuous *corrosion driver* for metal components. In order to control degradation of metal components, *chemistry control* (i.e. redox control) must be employed to counteract the oxidizing (i.e. corrosive) effect of the neutron activation reactions (Zhang et al. 2018b). The oxidizing effect of activation reactions is acknowledged in literature reviews on molten salt corrosion (DeVan et al. 1995; Schmidt et al. 2021; Sridharan and Allen 2013) but it is not quantified. Furthermore, several computational studies on tritium production and activation reactions across reactors are available in literature (Bocci et al. 2020; Cisneros 2013a; Forsberg et al. 2018; Haubenreich 1971; Lyu et al. 2016; Mays et al. 1977; Moir et al. 1994; Phillips and Easterly 1981; Segantin et al. 2020b; Xie et al. 2018), but production rates of other hydrogen isotopes and oxygen isotopes in FLiBe have not yet been reported. Similarly, (Stempien et al. 2016) identifies an interplay between tritium production and redox control, but does quantify the oxidizing effect of tritium production.

The production rates and inventory build-up of all hydrogen isotopes and all other activation products (Fratoni and Greenspan 2011),(Cisneros 2013a) on FLiBe are analyzed here and the corresponding rates of corrosion product build-up are computed. The analyses in this chapter are performed for an FHR advanced fission reactor and an ARC fusion device, using the UC Berkeley Mark-I PB-FHR (Andreades et al. 2016) and the MIT ARC designs (Sorbom et al. 2015) as input parameters for these calculations. In addition to tritium production as an oxidizing process, Li

breeding from Be and O breeding from F are also quantified as not-negligible contributions to the oxidizing effects of neutron irradiation in FLiBe. Furthermore, the production rate of the oxide anion is quantified, compared to other environmental effects that can lead to the introduction of oxide impurities in the fluoride melt, and discussed in the context of oxoacidity Pourbaix diagrams for FLiBe and their impact on corrosion.

The results are applied to a redox control case-study and a prior irradiation-corrosion experiment. The impact on chemistry is quantified and quantitatively compared to other environmental effects with similar consequences on the salt chemistry. The effects of isotopic composition of lithium, operational time, reactor power, and primary salt inventory are then demonstrated. The results are normalized and generalized, making the data useful to the reactor chemist and designer concerned with corrosion and chemistry control and tritium management in FLiBe irradiated in fission and fusion reactors and to the designer of salt-irradiation experiments (Calderoni et al. 2008; Calderoni and Cabet 2012; Carotti et al. 2019; Edao et al. 2009; Petti et al. 2006; Schmidt et al. 2021; Suzuki et al. 1998; Terai et al. 1996, 2001; Zhang et al. 2018b).

5.1.1 Background

5.1.1.1. FLiBe Activation Reactions

Neutron irradiation of FLiBe produces tritium through neutron activation of its components (Table 1). The main pathway for tritium production is the (n,t) reaction on Li-6 (Equation 5.1 in Table 1). For this reason, FLiBe salt used in fission reactors is highly enriched in Li-7 to minimize tritium production, down to tens to hundreds of appm Li-6/(Li-6 + Li-7) at reactor startup (Andreades et al. 2016). Li-6 is continuously produced via a (n, α) reaction on Be-9 (Equation 5.2 in Table 5.1). As a result, Li-6 is not entirely depleted by the (n,t) reaction, and its concentration stabilizes to an equilibrium value over time. The time required to reach an equilibrium concentration depends on the reactor flux and the initial enrichment, as shown in Figure 5.2. Additional pathways to tritium production are the (n,t) reactions on F-19 and Be-9, as well as the $(n,n\,\alpha)$ reaction on Li-7 (Equations 5.3, 5.4, 5.5 in Table 5.1, respectively) . The latter reaction can occur only with fast neutrons and is listed here because it is particularly important for tritium breeding in fusion reactor blankets. As the reaction produces a neutron alongside the triton, it is effective in increasing tritium production without depleting the neutron flux in the blanket (Segantin et al. 2020b), but being an endothermic reaction, it does decrease the thermal energy output. The cross sections for the tritium-producing reactions are plotted as a function of energy in Figure 5.1 (ENDF-VIII.0 library is used for all cross sections in this thesis, unless specified otherwise).
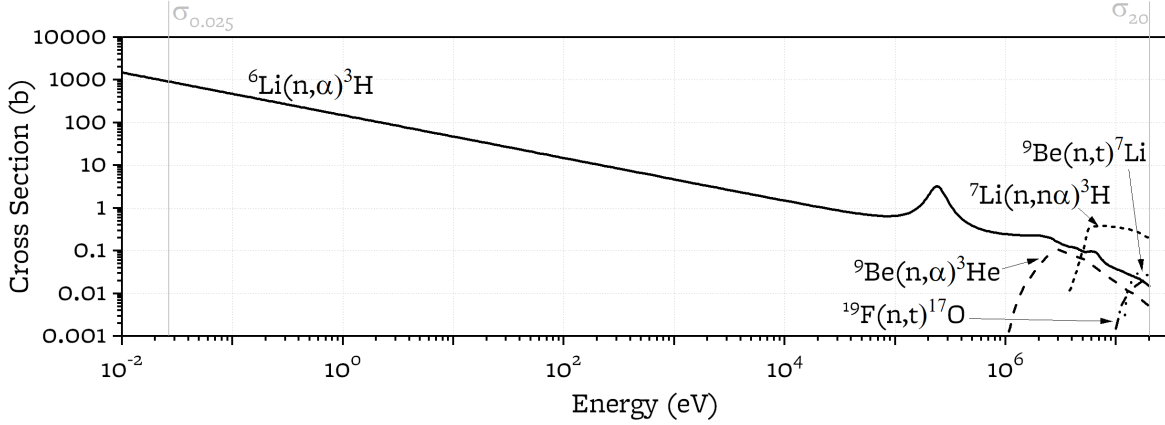
Figure 5.1: Cross section of tritium producing reactions. Li-7 cross-section from JEFF 3.1 library since not tabulated in ENDF VIII.0

Table 5.1: Neutron activation reactions (ordered by Q-value) in FLiBe and the corresponding decay chains.

Activation Reaction	Q-value (MeV)	Cross section at 0.025 eV $\sigma_{0.025}$ (b)	Cross section at 20 MeV σ_{20} (b)	Decay half-life $T_{1/2}$ (s)	Activation Reaction #
Tritium Production					
$^{6}_{3}Li(n,t)^{4}_{2}He$	4.8	946	0.015	-	5.1
$^{9}_{4}Be(n,\alpha)^{6}_{2}He \xrightarrow{\beta^-} {}^{6}_{3}Li$	-0.6	-	0.005	0.8	5.2
$^{7}_{3}Li(n,n\alpha)^{3}_{1}H$	-2.5	-	0.195	-	5.3
$^{19}_{9}F(n,t)\,^{17}_{8}O$	-7.6	-	0.024	-	5.4
$^{9}_{4}Be(n,t)\,^{7}_{3}Li$	-10.4	-	0.026	-	5.5
Protium Production					
$^{3}_{1}H \xrightarrow{\beta^-} {}^{3}_{2}He(n,p)^{3}_{1}H$	0.8	5349	0.082	-	5.6
$^{19}_{9}F(n,p)\,^{19}_{8}O \xrightarrow{\beta^-} {}^{19}_{9}F$	-4.0	-	0.010	26.5	5.7
$^{9}_{4}Be(n,p)\,^{9}_{3}Li \xrightarrow{\beta^-} {}^{9}_{4}Be$	-12.8	-	0.002	0.2	5.8
Deuterium Production					
$^{19}_{9}F(n,d)\,^{18}_{8}O$	-5.8	-	0.033	-	5.9
$^{7}_{3}Li(n,d)\,^{6}_{2}He \xrightarrow{\beta^-} {}^{6}_{3}Li$	-7.7	-	0.010	0.8	5.10
$^{9}_{4}Be(n,d)\,^{8}_{3}Li \xrightarrow{\beta^-} {}^{8}_{4}Be$	-14.7	-	0.012	0.8	5.11
Neon, Fluorine, Oxygen, Nitrogen and Carbon Production					
$^{19}_{9}F(n,\gamma)\,^{20}_{9}F \xrightarrow{\beta^-} {}^{20}_{10}Ne$	6.6	0.010	$8.8\ 10^{-6}$	11.2	5.12
$^{17}_{8}O(n,\alpha)\,^{14}_{6}C \xrightarrow{\beta^-} {}^{14}_{7}N$	1.8	0.236	0.130	$1.8\ 10^{11}$	5.13
$^{19}_{9}F\,(n,\alpha)\,^{16}_{7}N \xrightarrow{\beta^-} {}^{16}_{8}O$	-1.5	-	0.018	7.1	5.14
$^{16}_{8}O(n,n\alpha)\,^{12}_{6}C$	-7.2	-	0.246	-	5.15
$^{17}_{8}O(n,p)^{17}_{7}N \xrightarrow{\beta^-} {}^{17}_{8}O$	-7.9	-	0.064	4.2	5.16
$^{16}_{8}O(n,d)\,^{15}_{7}N$	-9.9	-	0.058	-	5.17
$^{18}_{8}O(n,t)\,^{16}_{7}N \xrightarrow{\beta^-} {}^{16}_{8}O$	-13.3	-	$1.1\ 10^{-5}$	7.1	5.18

The other isotopes of hydrogen, deuterium H-2 and protium H-1 are produced via *(n,d)* and *(n,p)* reactions on FLiBe constituents (reactions in Table 5.1). Reaction 5.6, the protium production via (n,p) on He-3 (produced from tritium decay) is generally neglected except where specified otherwise for the following reasons: FHRs are expected to employ tritium removal mechanisms (for example, tritium uptake in graphite (Forsberg et al. 2017b; Vergari and Scarlat 2021b, a; c)) and thus it is assumed that tritium does not decay in-core. In ARC, the He-3(n,p) reaction rate is negligible, relative to the F-19 (n,p) reaction rate[e] (Watson et al. 1962),(Carotti et al. 2021; Malinauskas and Richardson 1974) since helium has low solubility in the salt and would have a number density of 10^{-2} mol He/ m^3 FLiBe, compared to 10^5 mol F/m^3 FLiBe.

Other elements are also produced, via activation of the fluorine: several isotopes of neon, carbon, oxygen and nitrogen. Subsequently, the decay and activation of several of these activation products are responsible for the production of additional isotopes of these elements (Reactions 5.12-5.18 in Table 5.1).

5.1.1.1.1.   *The effects of activation reactions on redox state of the salt*

In the molten salt, the redox potential of the salt can change as a consequence of neutron activation and nuclear decay. Table 5.2 lists the redox effects of each of the transmutation reactions in FLiBe. For example, the neutron activation reaction 5.12 would lead to the chemical redox reaction 12 (Table 5.2). Fluorine in the salt is present in -1 valence state and neon is present in the oxidation state of 0. The production of neon from fluorine has a reducing effect on the salt because it makes electrons available for the reduction of other species. Most often, nuclear reactions have an oxidizing effect. Lithium breeding from beryllium (reactions 2 and 4 in Table 5.2) is an example, where beryllium has a +2 valence state and lithium has a +1 state. Similarly, tritium breeding from lithium has an oxidizing effect on the salt (reactions 1 and 5 in Table 5.2).

---

[e] Henry's constant for helium in FLiBe at 600ºC is (8.8)10^{-8} mol/cm^3-atm at 600°C (Carotti et al. 2021; Malinauskas and Richardson 1974), and at 1 atm partial pressure, this leads to 0.01 mol He/ m^3 FLiBe. Fluorine is present at a concentration of 4 mol F per mol FLiBe. Assuming that all fluorine is present as F-19, this corresponds to approximately 80,000 mol F/ m^3 FLiBe. Weighing these values by the ARC-averaged XS (Table 5.4; 0.7 for He-3, 0.009 for F-19), the p production from He-3 is 0.001% of p production from F-19, hence negligible.

Table 5.2. Redox consequences of neutron activation reactions in FLiBe and the corresponding decay chains.

Activation Reaction	Oxidation state of transmuting element	transmuted element	Redox Effect	Redox Reaction As a Consequence of Transmutation	Decay half-life $T_{1/2}$ (s)	Redox Reaction #
Tritium Production						
$^{6}_{3}Li(n,t)^{4}_{2}He$	+1	0	oxidizing	$Li^{+} + e^{-} \rightarrow He$	-	1
$^{9}_{4}Be(n,\alpha)^{6}_{2}He \xrightarrow{\beta^{-}} {}^{6}_{3}Li$	+2	+1	oxidizing	$Be^{2+} + e^{-} \rightarrow Li^{+}$	0.8	2
$^{7}_{3}Li(n,n\alpha)^{3}_{1}H$	+1	0	oxidizing	$2Li^{+} + 2e^{-} \rightarrow H_{2}$	-	3
$^{19}_{9}F(n,t)^{17}_{8}O$	-1	-2	reducing	$F^{-} + e^{-} \rightarrow O^{2-}$	-	4
$^{9}_{4}Be(n,t)^{7}_{3}Li$	+2	+1	oxidizing	$Be^{2+} + e^{-} \rightarrow Li^{+}$	-	5
Protium Production						
$^{3}_{1}H \xrightarrow{\beta^{-}} {}^{3}_{2}He(n,p)^{3}_{1}H$	0	0	neither	$H_{2} \rightarrow H_{2}$	-	6
$^{9}_{4}Be(n,p)^{9}_{3}Li \xrightarrow{\beta^{-}} {}^{9}_{4}Be$	+2	+2	neither	$Be^{2+} \rightarrow Be^{2+}$	0.2	7
$^{19}_{9}F(n,p)^{19}_{8}O \xrightarrow{\beta^{-}} {}^{19}_{9}F$	-1	-1	neither	$F^{-} \rightarrow F^{-}$	26.5	8
Deuterium Production						
$^{19}_{9}F(n,d)^{18}_{8}O$	-1	-2	reducing	$F^{-} + e^{-} \rightarrow O^{2-}$	-	9
$^{7}_{3}Li(n,d)^{6}_{2}He \xrightarrow{\beta^{-}} {}^{6}_{3}Li$	+1	+1	neither	$Li^{+} \rightarrow Li^{+}$	0.8	10
$^{9}_{4}Be(n,d)^{8}_{3}Li \xrightarrow{\beta^{-}} {}^{8}_{4}Be$	+2	+2	neither	$Be^{2+} \rightarrow Be^{2+}$	0.8	11
Neon, Fluorine, Oxygen, Nitrogen and Carbon Production						
$^{19}_{9}F(n,\gamma)^{20}_{9}F \xrightarrow{\beta^{-}} {}^{20}_{10}Ne$	-1	0	reducing	$F^{-} \rightarrow Ne + e^{-}$	11.2	12
$^{17}_{8}O(n,\alpha)^{14}_{6}C \xrightarrow{\beta^{-}} {}^{14}_{7}N$	-2	0	reducing	$O^{2-} \rightarrow C + 2e^{-}$	5700 years	13-1
	-2	-3	oxidizing	$O^{2-} + e^{-} \rightarrow N^{3-}$		13-2
$^{19}_{9}F(n,\alpha)^{16}_{7}N \xrightarrow{\beta^{-}} {}^{16}_{8}O$	-1	-2	oxidizing	$F^{-} + e^{-} \rightarrow O^{2-}$	7.1	14
$^{16}_{8}O(n,n\alpha)^{12}_{6}C$	-2	0	reducing	$O^{2-} \rightarrow C + 2e^{-}$	-	15
$^{17}_{8}O(n,p)^{17}_{7}N \xrightarrow{\beta^{-}} {}^{17}_{8}O$	-2	-2	neither	$O^{2-} \rightarrow O^{2-}$	4.2	16
$^{16}_{8}O(n,d)^{15}_{7}N$	-2	-3	oxidizing	$O^{2-} + e^{-} \rightarrow N^{3-}$	-	17
$^{18}_{8}O(n,t)^{16}_{7}N \xrightarrow{\beta^{-}} {}^{16}_{8}O$	-2	-2	neither	$O^{2-} \rightarrow O^{2-}$	7.1	18

The consequence of oxidizing activation reactions is that electrons need to be consumed from components dissolved in or in contact with the salt (i.e., oxidizing reactions need to occur). When the oxidized elements are metals from salt-facing metallic components, corrosion occurs:

$$0.5\,Cr \xrightarrow[\text{(oxidation)}]{\text{corrosion}} 0.5\,Cr^{2+} + e^{-} \quad \text{and} \quad 0.5\,Fe \xrightarrow[\text{(oxidation)}]{\text{corrosion}} 0.5\,Fe^{2+} + e^{-}$$
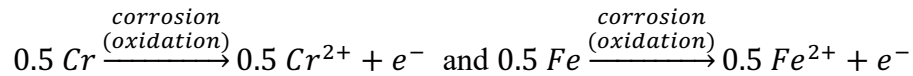
The overall reduction-oxidation reaction would be written as:

$$0.5Cr + Be^{2+} \xrightarrow[\text{and redox reaction}]{\text{transmutation}} 0.5Cr^{2+} + Li^{+}$$
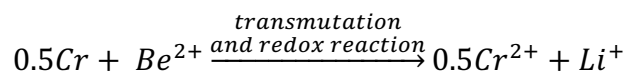
When instead the oxidized elements are redox control agents, these act as sacrificial elements that protect metallic components from corrosion:

128

$$U^{3+} \xrightarrow{oxidation} U^{4+} + e^-$$

$$Be \xrightarrow{oxidation} Be^{2+} + 2e^-$$
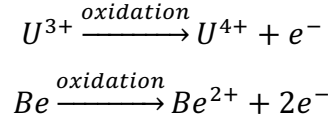
Conversely, the consequence of reducing activation reactions is that electrons are made available to ions dissolved in the salt:

$$0.5\ Cr^{2+} + e^- \xrightarrow{metal\ deposition} Cr$$

$$U^{4+} + e^- \xrightarrow{reduction} U^{3+}$$
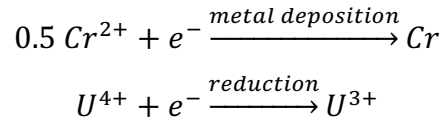
The oxidizing effect of activation reactions can have a *direct effect* on corrosion performance by *oxidation of structural metals*, and an *indirect effect* on corrosion performance by shifting of the redox potential, which in turn impacts the *rate of temperature-driven corrosion* in a non-isothermal flowing salt circuit, or similarly the rate of dissimilar-concentration-driven corrosion. Oxidation rate of chromium metal and beryllium metal will be used as proxies for rate of consumption of any other oxidizable element, such as Fe, Mn, Cu etc. Concentration of chromium fluoride in the salt will be used as a proxy for quantifying the redox potential drift; it can be converted to any other unit for redox potential, such as fluorine potential, electrochemical potential such as $E_{vs.F2/F-}$, concentration ratios such as x_{UF4}/x_{UF3}, or partial pressure ratios such as p_{H2}/p_{HF}.

5.1.1.1.2.   *Coupling between species valence states and evolution of redox potential*

For some elements, there are attainable redox potentials at which multiple valence states will coexist. In these cases, the final valence states of the activation product will depend on the redox potential in the salt. If the redox potential is controlled to a fixed value, then the relative amounts of each valence states can be computed from the law of mass action (i.e., from the chemical equilibrium constant). If the redox potential is not controlled, then activation reactions will shift the redox potential, and hence will shift the relative concentration of the two valence states. In this case a coupled calculation can be performed that computes the final redox potential in the melt and the relative amounts of valence states of all the species present in the melt.

For example, for the case of chromium oxidation by the oxidizing effect of tritium production the assumption of the predominant oxidation state of tritium being zero (H_2) and not +1 (H^+) needs to be verified for each specific concentration of Cr^{2+} in the salt, by considering the following chemical equilibrium reaction: $2H^+ + Cr \xleftrightarrow{equilibrium} H_2 + Cr^{2+}$. Assuming an upper bound of 750 appm Cr^{2+} in the salt and for simplicity a unitary activity of Cr metal and 1atm total pressure, the ratio of partial pressures p_{H2}/p_{HF} = 5000 (Olander 2002; Zhang et al. 2018b), so the tritium inventory *in the gas phase* that is in equilibrium with the salt is predominantly the oxidation state of zero ($^3H_2$).

To determine the relative inventory *in the salt* of the different valence states of tritium, the solubilities of ^3HF and $^3H_2$ in the salt must be known. H_2 and HF solubilities were measured by (Malinauskas and Richardson 1974) and (Field and Shaffer 1967), respectively. These values yield a ratio of $^3H_2$ to ^3HF solubilities in the salt of 0.0035 at 600 °C. From this, the ratio of tritium

concentrations in the salt is calculated to $x_{H2}/x_{HF} = (5000) \cdot 0.0035 = 18^f$. The solubility ratio could be even higher, as a recent electrochemical investigation of hydrogen in FLiBe upon addition of LiH in the salt reports a H_2 solubility four orders of magnitude larger that observed previously (Carotti et al. 2021). Based on these results, it is conventional to assume that tritium is predominantly in the oxidation state of zero for the dissolved tritium inventory *in the salt*. If the Cr^{2+} concentration is much above 750 appm (i.e., more oxidizing conditions), then a higher inventory of dissolved ^3HF will be present in the salt and the assumption of tritium existing entirely in the oxidation state of 0 will begin to introduce errors in the calculation of oxidative effects from tritium production that are higher than 5%. In this case, the simplifying assumption of an oxidation state of zero for tritium would need to be replaced by a coupled calculation between redox potential drift and tritium inventory in its two valence states.

5.1.2 Methodology

5.1.2.1. *Isotope Production*

The rates of change of tritium and other activation products are calculated by solving the ordinary differential equations (ODEs) corresponding to the balances of the nuclides. This strategy is equivalent to the solution of the Bateman equations (Bateman 1910) in conventional depletion codes, but is preferred to the use of a depletion codes because it permits to quantify the contribution of the individual terms to the production rates and identify the main contributors. In the balance for a given nuclide, source terms are associated to neutron activation and decay of other isotopes, while sink terms correspond to neutron induced reactions and decay of that nuclide.

The reaction rate for a given neutron activation reaction is computed as:

$$RR = N\bar{\sigma}\phi_{eq} \qquad\qquad 5.19$$

where N is the number of reacting isotopes in primary loop, ϕ_{eq} is the equilibrium neutron flux and $\bar{\sigma}$ is the one-group averaged reaction cross section. The equilibrium neutron flux and averaged cross sections for the FHR and the ARC blanket are computed using Serpent Monte Carlo (version 2.1.31, (Leppänen et al. 2015)). For the FHR, a Serpent model for the FHR cell at equilibrium from (Cisneros 2013a) is used and a power level of 236 MWth is considered. For ARC, a Serpent model is created from the simplified MCNP geometry of ARC included in (Segantin et al. 2020a) and a power level of 630 MWth is considered. For both reactors, neutron flux and cross sections are dependent on the composition and the geometry of the systems. The equilibrium fluxes are averaged across the geometries of the Serpent models and the cross-section are averaged over the neutron spectrum.

In the FHR, the coolant circulates in and out of the core, residing in irradiated areas only for a fraction of time in each loop, and spending a part of the looping time in regions that are not exposed to neutron flux. This aspect is accounted for by correcting the neutron flux with the ratio of the

---

[f] The Henry's law constants in FLiBe at 600 ºC are 2e-9 mol/mol-Pa for HF and 7e-12 mol/mol-Pa for H_2. Hence: $\frac{x_{H_2}}{x_{HF}} = 0.0035 \frac{p_{H_2}}{p_{HF}}$ at 600 ºC, where x_i is the molar ratio of species i in the FLiBe solvent, and p_i is the partial pressure of i in equilibrium with the salt.

volume of coolant in core and in the loop (Equation 5.20) [g]. A similar correction applies to ARC, as the FLiBe circulates between the heat exchanger and the blanket.

$$\bar{\phi}_{FHR} = \phi_{eq,FHR} \frac{V_{coolant}^{core}}{V_{coolant}^{loop}} , \bar{\phi}_{ARC} = \phi_{eq,ARC} \frac{V_{blanket}}{V_{blanket} + V_{hx}} \qquad 5.20$$

Each nuclide can be involved in distinct reactions involving other nuclides, resulting in an interdependent system of ODEs. In order to identify the most relevant source and sink terms, a depletion calculation is run with Origen (Rearden and Jessee 2016) using the effective cross sections calculated by Serpent, and all the terms contributing to less than 1% in the balance are not included in the ODEs. The resulting nuclide balances are in Equations 5.21-5.34. These balances have been obtained by integrating the ODEs to resolve the cross-dependencies.

The equation for tritium (Equation 5.21) adds the contribution of (n, t) reactions on Be and F to the equation used in (Cisneros 2013a) for the reactions on Li-6 and Li-7[h]. Tritium decay should be accounted for the purpose of tritium management but does contribute to the redox effects.

The equilibrium neutron flux and flux-averaged cross sections used in Equations 5.21-5.34 are dependent on the composition and the geometry of the systems. As a result, not only the values for the FHR and ARC (Table 5.3) are different, but also the values that would correspond to the same reactor but with two different equilibrium Li-6 enrichment of FLiBe would be different.

---

[g] This approach constitutes an approximation, as the downcomer and the reflector are outside of the core but are exposed to neutrons.

[h] The tritium production rate estimated here is 7% larger at BOL and 34% larger at equilibrium than the estimate in (Cisneros 2013) with 100 appm BOL Li-6 enrichment. The cause of the differences is the Li-6 (n,t) reaction rate, which is $6 \cdot 10^{18}$ 1/s in (Cisneros 2013) and $0.9 \cdot 10^{18}$ 1/s here, which may arise from using different cross-section libraries (ENDF-VII here, not reported in (Cisneros 2013)).

Table 5.3: Governing equations for activation calculations on FLiBe. Ordered in decreasing order of atomic and mass number

Hydrogen Isotopes

$$\frac{dN_{H3}}{dt} = \bar{\phi}\bar{\sigma}_{Li7}^{n\alpha}N_{Li7} + \bar{\phi}\bar{\sigma}_{Li6}^{t}\left(N_{Li6}^{0}\exp\left(-\bar{\phi}\bar{\sigma}_{Li6}^{abs}t\right) + \frac{\bar{\phi}\bar{\sigma}_{Be9}^{\alpha}N_{Be9}}{\bar{\phi}\bar{\sigma}_{Li6}^{abs}}\left(1 - \exp\left(-\bar{\phi}\bar{\sigma}_{Li6}^{abs}t\right)\right)\right) + \bar{\phi}\bar{\sigma}_{Be9}^{t}N_{Be9} + \bar{\phi}\bar{\sigma}_{F19}^{t}N_{F19} - \lambda N_{H3}$$

5.21

$$\frac{dN_{H2}}{dt} = \bar{\phi}\bar{\sigma}_{F19}^{d}N_{F19} + \bar{\phi}\bar{\sigma}_{Be9}^{d}N_{Be9} + \bar{\phi}\bar{\sigma}_{Li7}^{d}N_{Li7} - \bar{\phi}\bar{\sigma}_{H2}^{abs}N_{H2}$$

5.22

$$\frac{dN_{H1}}{dt} = \bar{\phi}\bar{\sigma}_{F19}^{p}N_{F19} + \bar{\phi}\bar{\sigma}_{Be9}^{p}N_{Be9} - \bar{\phi}\bar{\sigma}_{H1}^{abs}N_{H1}\left\{+\lambda_{H3}\bar{\phi}\bar{\sigma}_{He3}^{p}\left[\left(H_3(t)\circledast\exp\left(-\bar{\phi}\bar{\sigma}_{He3}^{p}t\right)\right)\right]\ \text{to include }\ ^3He\ \text{contribution}\right\}$$

5.23

Fluorine, Oxygen, Nitrogen, and Carbon Isotopes

$$\frac{dN_{F20}}{dt} = \bar{\phi}\bar{\sigma}_{F19}^{\gamma}N_{F19} - \lambda_{F20}N_{F20}$$

5.24

$$\frac{dN_{O19}}{dt} = \bar{\phi}\bar{\sigma}_{F19}^{p}N_{F19} - \lambda_{O19}N_{O19}$$

5.25

$$\frac{dN_{O18}}{dt} = \bar{\phi}\bar{\sigma}_{F19}^{d}N_{F19}$$

5.26

$$\frac{dN_{O17}}{dt} = \bar{\phi}\bar{\sigma}_{F19}^{t}N_{F19}$$

5.27

$$\frac{dN_{O16}}{dt} = \lambda_{N16}N_{N16}$$

5.28

$$\frac{dN_{N17}}{dt} = \bar{\phi}\bar{\sigma}_{O17}^{p}N_{O17} - \lambda_{N17}N_{N17}$$

5.29

$$\frac{dN_{N16}}{dt} = \bar{\phi}\bar{\sigma}_{F19}^{\alpha}N_{F19} - \lambda_{N16}N_{16}$$

5.30

$$\frac{dN_{N15}}{dt} = \bar{\phi}\bar{\sigma}_{O16}^{d}N_{O16} - \bar{\phi}\bar{\sigma}_{N15}^{abs}N_{N15}$$

5.31

$$\frac{dN_{N14}}{dt} = \lambda_{C14}N_{C14}$$

5.32

$$\frac{dN_{C14}}{dt} = \bar{\phi}\bar{\sigma}_{O17}^{\alpha}N_{O17} - \lambda_{C14}N_{C14}$$

5.33

$$\frac{dN_{C12}}{dt} = \bar{\phi}\bar{\sigma}_{O16}^{n\alpha}N_{O16} - \bar{\phi}\bar{\sigma}_{C12}^{abs}N_{C12}$$

5.34

Table 5.4: Input parameters for activation calculations on FLiBe. Ordered in decreasing order of atomic and mass number

Term	Symbol	Units	FHR	ARC
Volume of coolant in the core	$V_{coolant}^{core}$	m^3	7.20 (Andreades et al. 2014)	-
Volume of coolant in the loop	$V_{coolant}^{loop}$	m^3	46.82 (Andreades et al. 2014)	-
Volume of coolant in the blanket	$V_{blanket}$	m^3	-	241 (Sorbom et al. 2015)
Volume of coolant in the ARC heat exchanger	V_{hx}	m^3	-	241 (Sorbom et al. 2015)
Equilibrium neutron flux	ϕ_{eq}	n cm^{-2} s^{-1}	5.29 10^{14}	3.11 10^{13}
Volume-corrected neutron flux	$\bar{\phi}$	n cm^{-2} s^{-1}	8.13 10^{13}	3.11 10^{13}
Decay constant F-20	λ_{F20}	s^{-1}	0.06	0.06
(n, γ) cross section F-19	$\bar{\sigma}_{F19}^{\gamma}$	barn	1.35 10^{-3}	2.56 10^{-4}
(n, p) cross section F-19	$\bar{\sigma}_{F19}^{p}$	barn	5.77 10^{-5}	8.65 10^{-3}
(n, α) cross section F-19	$\bar{\sigma}_{F19}^{\alpha}$	barn	7.95 10^{-4}	2.28 10^{-2}
(n, d) cross section F-19	$\bar{\sigma}_{F19}^{d}$	barn	2.31 10^{-6}	5.92 10^{-3}
(n, t) cross section F-19	$\bar{\sigma}_{F19}^{t}$	barn	4.05 10^{-7}	3.16 10^{-3}
Decay constant O-19	λ_{O19}	s^{-1}	0.03	0.03
(n, p) cross section O-17	$\bar{\sigma}_{O17}^{p}$	barn	7.12 10^{-7}	9.18 10^{-3}
(n, α) cross section O-17	$\bar{\sigma}_{O17}^{\alpha}$	barn	3.64 10^{-2}	0.14
(n, d) cross section O-16	$\bar{\sigma}_{O16}^{d}$	barn	1.76 10^{-7}	3.68 10^{-3}
(n, α) cross section O-16	$\bar{\sigma}_{O16}^{n\alpha}$	barn	1.64 10^{-6}	5.64 10^{-2}
Decay constant N-17	λ_{N17}	s^{-1}	0.17	0.17
Decay constant N-16	λ_{N16}	s^{-1}	0.10	0.10
(n, abs) cross section N-15	$\bar{\sigma}_{N15}^{abs}$	barn	1.33 10^{-5}	3.32 10^{-2}
Decay constant C-14	λ_{C14}	s^{-1}	3.84 10^{-12}	3.84 10^{-12}
(n, abs) cross section C-12	$\bar{\sigma}_{C12}^{abs}$	barn	4.30 10^{-4}	2.88 10^{-2}
(n, p) cross section Be-9	$\bar{\sigma}_{Be9}^{p}$	barn	1.62 10^{-9}	0
(n, d) cross section Be-9	$\bar{\sigma}_{Be9}^{d}$	barn	3.95 10^{-9}	0
(n, t) cross section Be-9	$\bar{\sigma}_{Be9}^{t}$	barn	2.35 10^{-7}	4.59 10^{-3}
(n, α) cross section Be-9	$\bar{\sigma}_{Be9}^{\alpha}$	barn	2.59 10^{-3}	1.91 10^{-2}
$(n, n\alpha)$ cross section Li-7	$\bar{\sigma}_{Li7}^{n\alpha}$	barn	1.13 10^{-3}	0.19
(n, d) cross section Li-7	$\bar{\sigma}_{Li7}^{d}$	barn	2.96 10^{-7}	2.44 10^{-3}
(n, t) cross section Li-6	$\bar{\sigma}_{Li6}^{t}$	barn	98.33	0.26
(n, abs) cross section Li-6	$\bar{\sigma}_{Li6}^{abs}$	barn	98.34	0.27
(n, p) cross section He-3	$\bar{\sigma}_{He3}^{p}$	barn	554.43	0.70
Decay constant H-3	λ_{H3}	s^{-1}	1.78 10^{-9}	1.78 10^{-9}
(n, abs) cross section H-1	$\bar{\sigma}_{H1}^{abs}$	barn	3.46 10^{-2}	4.23 10^{-5}

In the FHR, the isotopes rates of change are shown as a function of time, starting with a FLiBe initial enrichment of 50 appm Li-6. In ARC, the FLiBe blanket could be a lifetime component, not undergoing re-plenishing during the reactor operation, or be re-plenished frequently to maintain constant Li-6 enrichment. Whether or not the blanket is replenished with Li-6 during operation will depend on the tritium burn fractions in the vacuum chamber and on the tritium breeding ratio target in the blanket (Abdou et al. 2021). Here, it is assumed that Li-6 replenishing maintains constant Li-6 enrichment. For ARC, isotopes rates of change are plotted as a function of Li-6 enrichment. In order to include the contribution of the decay of short living isotopes in ARC, the constant rates of change are calculated using t=1 day in Equations 5.21-5.34.

5.1.2.2. Redox change

The *oxidative effect of activation reactions* is quantified considering two representative oxidation reactions: pure beryllium metal (used for redox control) and pure chromium metal (a corrosion product of relevance to stainless steel alloys). Based on the rate of activation reactions on FLiBe in the FHR coolant, the corresponding rate of consumption of metals is computed by performing a balance of electrons (i.e., balance of charge). Table 5.5 provides the details of the calculations and the utility of each of the metrics employed.

Table 5.5. Metrics used for quantification of the oxidative effects of activation reactions, the utility of each of the metrics employed, and unit equivalences.

Metric for the oxidative effect of activation reactions	Of relevance to…	Calculation details	Units and unit conversions
Rate of beryllium oxidation $Be \rightarrow Be^{2+} + 2e^-$	Redox control	The rate of consumption of Be metal that would be necessary to maintain a constant redox potential.	mgBe/day per MWth (see other equivalent units in Table 5.7)
Rate of chromium oxidation $Cr \rightarrow Cr^{2+} + 2e^-$	Corrosion of metals and metal alloys	The rate of chromium oxidation is computed from the rate of "consumption of electrons" by the activation reactions, thus the equivalence between rate of oxidation of Cr and rate of oxidation of any other metal (e.g., Fe, Mn, Cu) can be done on the basis of a per mol of electrons consumed.	mgCr/day per m³ salt mgCr/day per MWth *1 mgBe/day = 52/9*2/2 = = 5.78 mgCr/day*
Chromium fluoride concentration in the salt $Cr + F_2 \rightarrow CrF_2(salt)$	Drift of redox potential in the absence of redox control	In the absence of redox control, as the concentration of corrosion products (e.g., CrF₂) increases in the melt, the redox potential of the salt drifts. The drift in redox potential is of importance to predicting the *rates of temperature-driven corrosion* in a salt loop; it can similarly impact corrosion driven by dissimilar-material or dissimilar species concentrations in a salt loop.	wppm = the mass ratio of the metal cation in a salt sample, $\frac{m_{Cr^{2+}}}{m_{FLiBe}}$ (this unit is commonly used for reporting salt elemental analysis (Carotti et al. 2018)). (see other equivalent redox units (Olander 2002; Zhang et al. 2018b) in Figure 5.9) *1 wppm Cr in FLiBe = 33/52 = = 0.63 appm Cr in FLiBe*

Full progression of the redox reactions to a single dominant valence state is assumed. The dominant valence states at redox potentials of engineering relevance are assumed to be H^o, Li^+, Be^{2+}, O^{2-}, Cr^{2+}, C^o and F^-. FHR oxidation rates are shown as a function of time and ARC rates are assumed constant with time and shown for various Li-6 enrichment levels.

5.1.3   Results: Activation Products in FLiBe

5.1.3.1.   Tritium production in the FHR and in ARC

Figure 5.2a (results calculated from Equation 5.21 in Table 5.3) shows the tritium production rate (in mol ^3H/day/ MWth) as a function of time, and its dependence on the isotopic composition of Li at the beginning of life of the coolant (BOL). For Li-6 enrichment (defined as mol Li-6 / (mol (Li-6 + Li-7)) on the order of tens to hundreds of appm (relevant to FHRs), the Mark-I PB-FHR

134

BOL tritium production rate is on the order of $10^{-4} - 10^{-3}$ mol/day/MWth[i]. The tritium production rates corresponding to different BOL enrichment levels converge to the same equilibrium value to approximately $2.7 \ 10^{-4}$ mol/day/MWth (assuming nominal salt inventory), after up to 50 years. The production rate at equilibrium is exclusively dependent on the ratio between the (n,α) cross section of Be-9 and the Li-6 absorption cross section (Fratoni and Greenspan 2011).

Figure 5.2b shows the Li-6 evolution with time. At equilibrium, the lithium enrichment converges to 13 appm. Because of the functional form of Equation 5.21, given two reactors with different BOL Li enrichments, the difference in years required to reach the equilibrium concentration is equal to the number of years that one of the two reactors would take to reach the BOL enrichment of the other one. Figure 5.2c shows that the tritium production rate scales linearly with lithium enrichment; the linear function for Mark-I PB-FHR (μmol H-3/day/MWth = 62.5 +5.45*(appm Li-6)) is valid for all other reactors with a similar neutron spectrum and hence similar averaged cross-sections for Li-7, Li-6, and Be-9.

---

[i] The concentration of Li-6 at equilibrium does not depend on the initial Li-6 enrichment. As a result, the same equilibrium flux and averaged cross-section can be assumed for multiple BOL Li isotopic compositions.
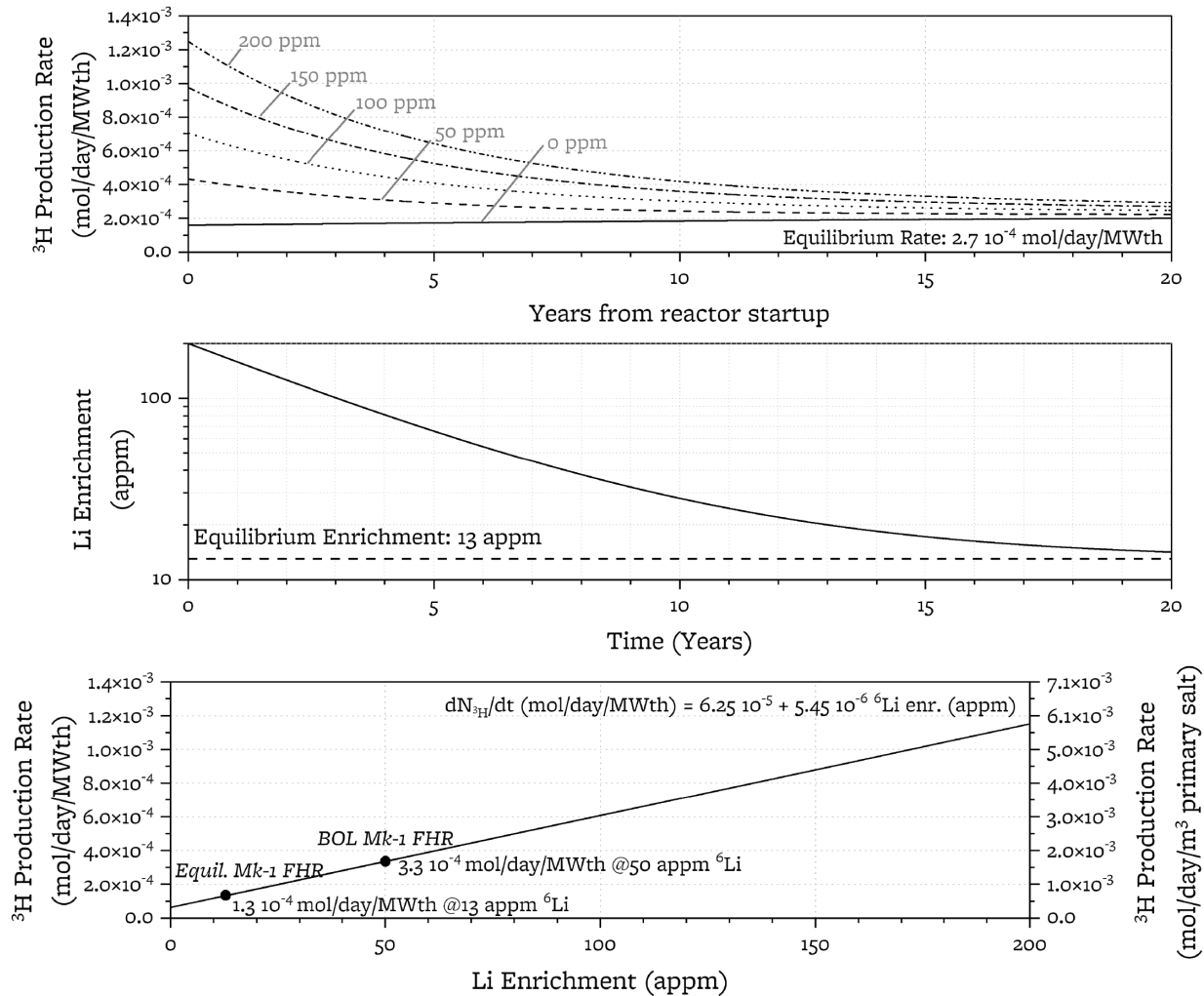
Figure 5.2: Tritium production rate in the Mark-I PB-FHR with variable initial Li-6 enrichment. (a) Production rates (in mol ^3H/day/MWth) with BOL Li-6 enrichment from 0 to 1000 appm. (b) Li-6 enrichment (appm) as a function of time. (c) H-3 production rate (mol ^3H/day/MWth) as a function of Li-6 enrichment (appm). 1 mol H-3/day = 28,950 Ci/day

The contribution of the different activation reactions to the tritium production rate is shown in Figure 5.3. For Mark-I PB-FHR, considering a nominal 50 appm Li-6 at BOL, 81% of total tritium production is due to the activation of the Li-6 in fresh FLiBe and 19% comes from the $(n, n\alpha)$ reaction on Li-7. As irradiation proceeds, the initial inventory of Li-6 is progressively consumed, and the tritium production is sustained by the Li-6 yielded by the (n, α) reaction on Be-9. At equilibrium, the two-step reaction on beryllium (Reactions 5.1, 5.2) is responsible for 53% of tritium production, the remainder being produced through Li-7 activation. It should be noted that the contribution from Li-7 appears to be constant with time because Li-7 depletion is negligible at the enrichment levels of interest for fission reactors (up to hundreds of appm of Li-6). At all times, tritium production from F-19 is negligible. For the ARC design at the nominal enrichment level of 90%, the main contributor to tritium production is Li-6, accounting for approximately 92% of the total production rate, followed by Li-7 (5%), F-19 (2%) and Be-9 (1%).

136
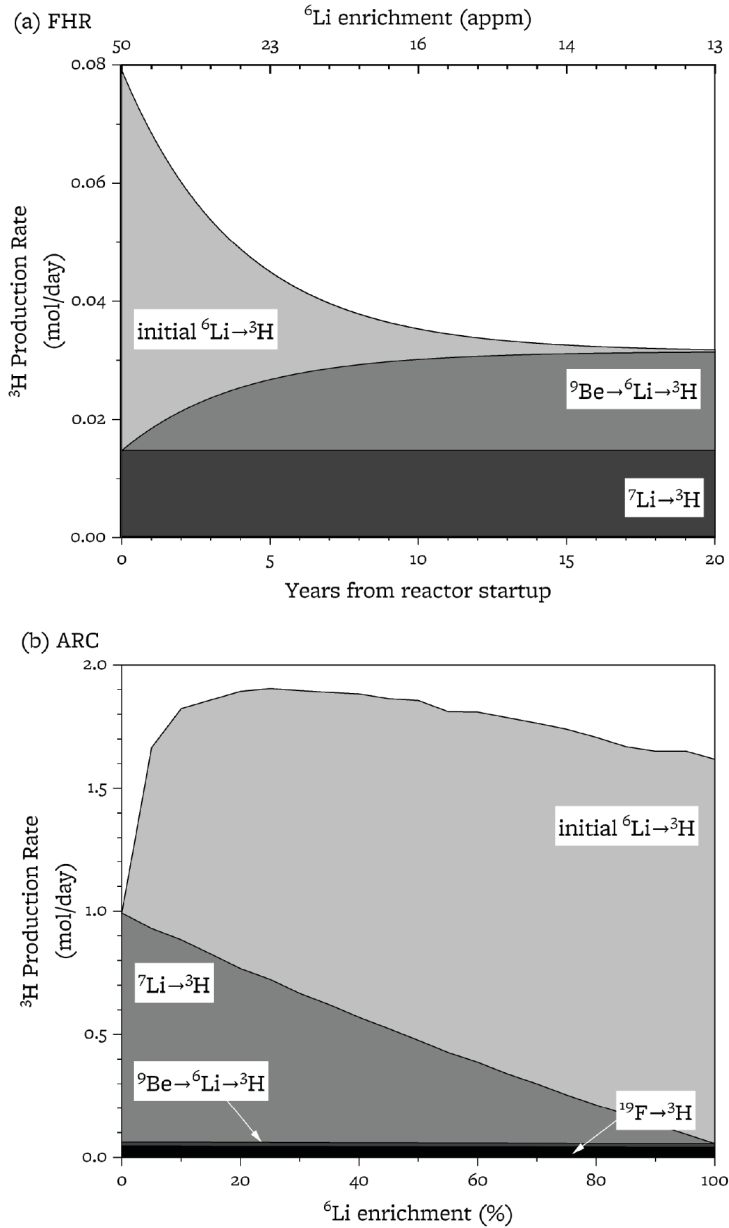
Figure 5.3: Contributions to the tritium production rate in FLiBe (in mol ^3H/ day). (a) Mark-I PB-FHR, 50 appm BOL Li-6. (b) ARC, variable FLiBe enrichment level. 1 mol H-3/day = 28,950 Ci/day

Assuming that the blanket salt is constantly replenished to ensure a constant Li-6 inventory (see Figure 5.10), tritium production rates are constant with time. While tritium production rates in ARC are constant with time, they depend on the target isotopic composition of lithium in the salt and the tritium production rates does not increase monotonically with the Li-6 enrichment. This effect, which was previously shown in (Jolodosky et al. 2016; Segantin et al. 2020a), is caused by the (n, nα) reaction on Li-7, which occurs with fast neutrons in FLiBe. This reaction has a lower average cross section than the reaction on Li-6 (Equation 5.1), but also produces another neutron. As a result, a high Li-6 enrichment reduces the frequency of the reaction on Li-7 and introduces a

137

penalty on the neutron flux. For the ARC design, the tritium production rate is optimized at an enrichment level of approximately 25 at. % (consistent with the results in (Segantin et al. 2020a))[j]. This enrichment level is significantly lower than the 90% Li-6 enrichment proposed in the early design stage (Sorbom et al. 2015). At 25 at. % Li-6, the contributors to H-3 production are Li-6 (60%) , followed by Li-7 (37%), F-19 (2%) and Be-9 (1%).

5.1.3.2.   *Comparison with tritium production in other reactors*

Table 5.6 compares tritium production rates of different types of reactors based on production rate per MWth. The volumetric tritium production rate in the salt is also reported since it is a useful parameter in calculations of mass transport of tritium. The Mark-I PB-FHR has a production rate two orders of magnitude larger than in current generation LWRs and about 5 times larger than a Pressurized Heavy Water Reactor (PHWR). ARC has a production rate approximately 20 times larger than the Mark-I PB-FHR at equilibrium.

In LWR and PHWR, tritium is mostly produced from the deuterated water (the moderator of PHWRs and naturally present in the light water of LWRs) and from neutron activation of the boric acid used for reactivity control in the coolant. In reactors containing graphite components, like HTGR and the Advanced Gas Reactor (AGR), tritium can be produced via neutron activation of the lithium impurities in graphite. This pathway exists also in FHRs and MSRs but is negligible in comparison to production in FLiBe. For example, taking the Mark-I PB-FHR as a reference and assuming 2 appm of Li (of natural isotopic enrichment) in graphite (the limit for nuclear graphite, according to current engineering standards (ASTM International, 2018)), approximately 2 mols of lithium are present across graphite pebbles. Using the fluxes and cross sections in Section 5.1.2, this would lead to a tritium production rate of 0.0006 mol/day for fresh graphite, i.e., about 2% of the production rate from FLiBe at equilibrium, hence negligible.

---

[j] While a Li-6 enrichment of 25 at.% maximizes tritium production, it may not optimize the energy output, as the reaction producing tritium from Li-7 is endothermic.

Table 5.6: Tritium production rates from different types of reactors (in decreasing order of Ci/GW/day), from computational studies.

	Thermal Power (MWth)	Salt Volume (m³ primary salt)	(m³ core salt)	H-3 Production Rate[i] (Ci/day) MWth[a]	(mol H-3/ day per m³ primary salt)	(mol H-3/ day per m³ core salt)[b]	Main sources of tritium in the coolant	Li-6 enrichment in salt	Refs. for tritium production rate
Molten Salt Reactors									
HYLIFE-II Fusion Blanket (Moir et al. 1994)	2500	1240 [b]	-	1,480	1.0×10^{-2}	-	${}_{3}^{6}Li(n,t){}_{2}^{4}He$ ${}_{3}^{7}Li(n,n\alpha){}_{1}^{3}H$	Natural (7.59 at% Li-6)	(Moir et al. 1994)
ARC Fusion Blanket (Sorbom et al. 2015)	630	482 [c]	241 [d]	74.1	3.4×10^{-3}	6.8×10^{-3}	${}_{3}^{6}Li(n,t){}_{2}^{4}He$ ${}_{3}^{7}Li(n,n\alpha){}_{1}^{3}H$	90 at% Li-6	This work
TMSR-LF1 (Lyu et al. 2016)	2	n.a.	0.18	12.0	n.a.	4.6×10^{-3}	${}_{4}^{9}Be(n,\alpha){}_{3}^{6}Li(n,t){}_{2}^{4}He$ ${}_{3}^{7}Li(n,n\alpha){}_{1}^{3}H$	500 appm Li-6	(Lyu et al. 2016)
Mark-I PB-FHR at BOL (Andreades et al. 2016)	236	46.8	7.2	9.7	1.7×10^{-3}	1.1×10^{-2}	${}_{3}^{6}Li(n,t){}_{2}^{4}He$	50 appm Li-6	This work
MSRE (Thoma 1971)	7.3	2.0	0.6	7.4 [e]	0.9×10^{-3}	3.1×10^{-3}	${}_{4}^{9}Be(n,\alpha){}_{3}^{6}Li(n,t){}_{2}^{4}He$ ${}_{3}^{7}Li(n,n\alpha){}_{1}^{3}H$	74 appm Li-6	(Mays et al. 1977)
Mark-I PB-FHR at Equilibrium (Andreades et al. 2016)	236	46.8	7.2	3.9	0.7×10^{-3}	4.3×10^{-3}	${}_{4}^{9}Be(n,\alpha){}_{3}^{6}Li(n,t){}_{2}^{4}He$ ${}_{3}^{7}Li(n,n\alpha){}_{1}^{3}H$	13 appm Li-6	This work
MSBR (Robertson 1971)	2250	48.7	30.4	1.1	0.2×10^{-3}	0.3×10^{-3}	${}_{4}^{9}Be(n,\alpha){}_{3}^{6}Li(n,t){}_{2}^{4}He$ ${}_{3}^{7}Li(n,n\alpha){}_{1}^{3}H$	50 appm Li-6 (initially)	(Mays et al. 1977)
Other Reactors									
PHWRs	Up to 3000	-	-	2.2	-	-	${}_{1}^{2}H(n,\gamma){}_{1}^{3}H$	-	(Gorman and Wong 1979; Phillips and Easterly 1981)
HTGRs	Variable	-	-	$6-8 \times 10^{-3}$	-	-	${}_{2}^{3}He(n,p){}_{1}^{3}H$ (He-3 content in the gas) ${}_{3}^{6}Li(n,t){}_{2}^{4}He$ (graphite Li impurity) ${}_{5}^{10}B(n,2\alpha){}_{1}^{3}H$ (graphite B impurity)	-	(Compere et al. 1974; Gainey 1976)
HTR-10	10	-	-	4.5×10^{-3} [f]	-	-	${}_{2}^{3}He(n,p){}_{1}^{3}H$ (He-3 content in the gas) ${}_{3}^{6}Li(n,t){}_{2}^{4}He$ (graphite Li impurity)	-	(Xu et al. 2017)
PWRs	Up to 4500	-	-	$6-8 \times 10^{-4}$ [g]	-	-	${}_{1}^{2}H(n,\gamma){}_{1}^{3}H$ ${}_{5}^{10}B(n,2\alpha){}_{1}^{3}H$	-	(Locante and Malinowski 1973; Phillips and Easterly 1981)
BWRs	Up to 4500	-	-	1×10^{-5} [h]	-	-	${}_{1}^{2}H(n,\gamma){}_{1}^{3}H$ ${}_{5}^{10}B(n,2\alpha){}_{1}^{3}H$	-	(Phillips and Easterly 1981; Smith and Gilbert 1973)

[a] 1 mol H-3/day = 28,950 Ci/day

[b] The volumetric tritium production rate in the salt is reported, since it is a useful parameter in calculations of mass transport of tritium.

[c] Salt volume in blanket tank

[d] Salt volume in blanket tank plus heat exchanger

[e] The MSRE has higher Li-6 enrichment than the Mark-I PB-FHR but a lower tritium production. This may be ascribed to the harder energy spectrum in the MSRE, leading to a lower average cross-section for the Li-6(n,t) reaction.

[f] Average production rate calculating dividing tritium inventory after 20 years by the time length

[g] Production rate in the coolant, not including production by ternary fission and activation of the fuel and the cladding. Total PWR production rate is approximately 1.7×10^{-2} *(Ci/day)/MWth* (Locante and Malinowski 1973; Phillips and Easterly 1981)

[h] Production rate in the coolant, not including production by ternary fission and activation of the fuel and the cladding. Total BWR production rate is approximately 2.4×10^{-2} *(Ci/day)/MWth* (Phillips and Easterly 1981; Smith and Gilbert 1973)

[i] As a point of comparison, natural tritium production in the upper atmosphere by fast neutrons from cosmic rays produce approximately 3,000 Ci/day from the N(n,t)C reaction (von Buttlar and Libby 1955).

5.1.3.3. *Experimental evidence of tritium release in molten salt system*

The production rates included in Table 5.6 are the results of computational studies, whose accuracies depend on the correctness of the assumptions in terms of fluxes, cross-sections, and initial concentration of the tritium sources. Computational estimates of tritium production can be (and often are) compared to experiments where tritium concentration in the coolants is measured. Not all the tritium produced in the coolant or moderator must remain in the primary loop, as a part of it can be absorbed elsewhere or released. As a result, such comparisons can only provide limited validation to the computational studies. Nonetheless, measured concentrations above the computed production rates may indicate errors in the inputs of computational studies, while similar orders of magnitude to the computed values may support the computational results.

For PWRs and BWRs, historical data indicate tritium releases from the coolant in amounts that are larger than the theoretical tritium production in the coolant. This discrepancy is caused by the diffusion into the primary loop of a fraction of the tritium produced by ternary fission in the fuel pellet (up to about 80%) (Phillips and Easterly 1981). In PHWRs, tritium is independently released from the coolant and the moderator. Analyses of the atmospherically released tritium have shown that most of the tritium is released from the coolant. This is explained by the higher diffusion coefficients and leakage rates in the coolant, which operates at larger pressure and temperature than the moderator. For HTGRs, (Xie et al. 2018) measured tritium activity in helium sampled from the primary loop of the HTR-10 and found a tritium concentration in the order of 5% of the computed value. This suggests either that the source term used in the calculation represents an overestimation of the actual value, or that tritium retention in graphite and other sinks is underestimated.

In molten salt systems, historical data about tritium production exist for the MSRE. The most recently calculated tritium production rate in the MSRE (74 ppm Li-6 at BOL) is 54 Ci/day (i.e., 1.9 mmol H-3/day) (Haubenreich 1971). Measured tritium content in the moderator graphite, in the off-gas systems, in the coolant radiator air and in the reactor cell atmosphere leads to an estimated tritium production rate of 43 Ci/day (1.9 mmol H-3/day), i.e., 80% of the computational prediction. The experimental estimates did not account for tritium retention in the components of the off-gas systems (i.e. charcoal beds, filters and particle traps) and in the oil residues, which may be responsible for the difference (Haubenreich 1971).

A more recent validation of tritium production calculations exists from the fluoride salt irradiation (FS) studies at the Massachusetts Institute of Technology Reactor (MITR). In the FS studies, a titanium capsule containing graphite crucibles filled with FLiBe (50 appm Li-6) was irradiated in the MITR. Tritium release in the off gas is measured in real time via a water bubbler, while tritium content in the samples is measured at the end of the experiment via thermal desorption spectroscopy (TDS). The off-gas tritium release rate accounts for 78% of the total production rate. TDS of the graphite samples yields a measure of tritium content per graphite surface area that is consistent with the 22% difference between the computational production rates and the off-gas release rates (Dolan et al. 2020, 2021b). (As a related discussion, the corrosion study performed in the FS-1 MITR salt capsule is further discussed as a case study in Section 5.1.4.3.)

Other experimental studies of tritium production from neutron irradiation of lithium-containing molten salts are available in literature, but such studies do not discuss the comparison of computed and experimental production rates (Edao et al. 2009; Petti et al. 2006; Suzuki et al. 1998; Terai et al. 1996, 2001).

5.1.3.4. *Production of all isotopes of hydrogen*

Because all isotopes of hydrogen have similar mass transport and chemical behavior, it is important to know if the production rates of H-1 and H-2 need also to be accounted for in engineering of tritium management systems for FHR and ARC. The results in Figure 5.4 show that H-1 and H-2 production rates can be neglected. In the Mark-I PB-FHR, if all produced tritium is assumed to be removed before it decays, tritium accounts for more than 98% of the total production rate of all hydrogen isotopes at BOL and 95% at equilibrium (Figure 5.4a). If tritium and its daughter nuclide He-3 are never removed from the core, the *(n,p)* reaction on He-3 causes a protium production rate larger than the tritium production rate, after 9 years of operation in FHR. The Mark-I PB-FHR will operate in the region between these two cases and its behavior could be approximated with the first case if the chemistry control system has the task of tritium removal.

In ARC at the 90% Li-6 nominal enrichment level, tritium accounts for about 90% of the produced hydrogen (Figure 5.4b). For ARC, continuous tritium removal and Li-6 replenishment for the blanket are assumed, as discussed in Section 5.1.2.1; therefore, the scenario with in-core tritium decay is not considered for ARC.
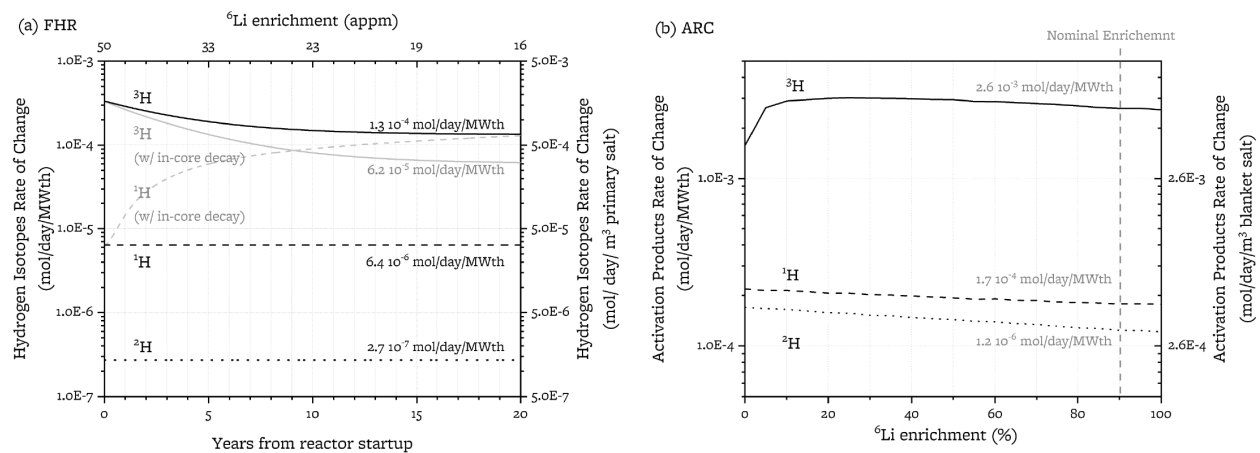
Figure 5.4: Production rates of all hydrogen isotopes. a) Mark-I PB-FHR, 50 appm BOL Li-6. b) ARC, 90 at. % BOL Li-6. The gray lines show the scenario that considers in-core decay of tritium in the Mark-I PB-FHR, which leads to H-1 production from He-3(n,p).

5.1.3.5. *Other FLiBe Activation Products*

The main activation product for FLiBe besides tritium is oxygen (see Figure 5.5). In Mark-I PB-FHR , the oxygen production rate is approximately 35% of the tritium production rate at BOL and

80% at equilibrium, and it is predominantly O-16. In ARC, the total oxygen production rate is 25% of the tritium production rate, with the 76% being O-16, the 19% being O-18 and the remainder O-17. The oxygen production rate in the FHR could suggest that a fraction of the produced tritium will be in the form of tritiated water. Nevertheless, the produced oxygen might also remain as a dissolved anion O^{2-}, produce a precipitated oxide (e.g., Cr_2O_3), or (if the redox potential is extremely oxidizing) be oxidized to O_2 gas, which in turn interacts with graphite or metals or is released into the cover gas.
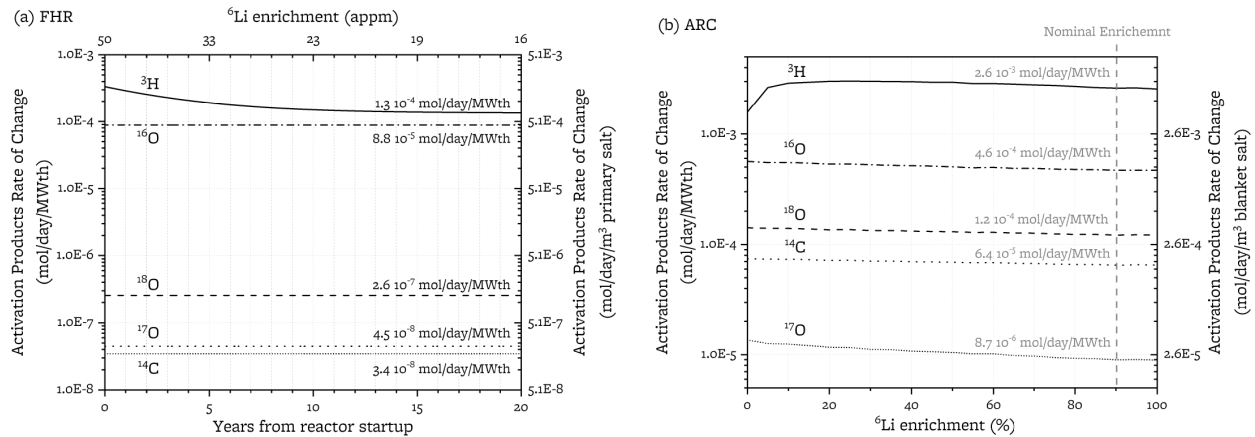
Figure 5.5: Rates of change of all activation products on FLiBe. Rate of F-20, O-19, N-14, N-15, N-16, N-17, and C-12 are below the lower limits of the figures. BOL Li-6 Enrichment: Mark-I PB-FHR 50 appm; ARC 90 at. %.

Carbon and nitrogen are also possible activation products of FLiBe. In the FHR, C and N production rates are negligible: carbon production rate is three orders of magnitude lower than oxygen production; nitrogen is more than ten orders of magnitude lower. In ARC, C-14 production about 2.4% of tritium production rate. This may suggest that a small fraction of the tritium may be present in the form of tritiated methane. The carbon produced in the salt could also speciate at carbonate anions in the salt, by complexing with O^{2-}, may interact with or deposit on the graphite and metal surfaces, or may produce other carbon products that are soluble or suspended in the salt. Nitrogen production rates remain negligible in ARC.

5.1.4 Discussion: Chemical effects of the activation reactions in FLiBe

5.1.4.1. *The oxidizing effects of neutron activation reactions on FLiBe*

The oxidizing effect of activation reactions in the salt has been qualitatively defined in (DeVan et al. 1995; Schmidt et al. 2021; Stempien et al. 2016) but never quantified. Here, the corrosion effect of the activation reactions is quantified in terms of rate of Cr oxidation or rate of sacrificial Be metal consumption. Figure 5.6 shows the oxidizing effect contributions of each of the activation reactions on FLiBe.

5.1.4.1.1. FHR

In an FHR at BOL and in absence of active chemistry control, Cr would be consumed at rate of 13 mg Cr/day/MWth, and the main sources of oxidative effects are:

- the production of H-3 from Li-6 and Li-7,
- the production of Li-6 from Be-9, and
- the production of O-16 from F-19.

At steady state isotopic composition of lithium, each of these four reactions contribute at a similar rate to the oxidizing effect. Thus, at 13 ppm Li-6, *the rate of tritium production accounts for only 50% of the total oxidative effects of activation reactions*, at the nominal BOL 50 ppm Li-6 it accounts for 70%; at natural Li isotopic abundance the tritium production would be the dominant oxidative activation reaction.

The progression rate of the corrosion front that corresponds to a given rate of Cr oxidation depends on the heat exchanger surface area relative to the rate of the activation reactions. For a 236 MWth FHR with 224 m^2 of heat exchanger surface area, the 13 mg Cr/day/MWth rate of Cr oxidation corresponds to a predicted corrosion front [k] that moves at rate of 4 um/year. This rate is comparable to the < 1 um/year corrosion rate in a non-isothermal FLiBe loop that is at the lowest possible redox potential set by beryllium metal (Keiser et al. 1979). Thus, depending on the heat exchanger surface area relative to the rate of the activation reactions, it is likely that the corrosion due to the oxidizing effects of FLiBe activation is negligible relative to the rate of corrosion driven by the temperature gradient in the flow loop (DT corrosion).

However, in the absence of redox control, the redox potential of the salt will drift as a consequence of the oxidizing effects of activation reactions on FLiBe, and the magnitude of the DT corrosion driver is in turn dependent on the redox potential as demonstrated in (Keiser et al. 1979). For example, for a loop at a redox potential that is unknow (as-received salt) but higher than that of Be metal, the DT corrosion rate was 8 um/year; with addition of Be metal to lower the redox potential, the corrosion rate was below 1 um/year. Thus, neutron activation reactions without redox control would lead to a drift in the redox potential and hence would lead to an increase in the DT corrosion rate in a salt loop. *For this indirect reason, redox control will still be necessary in an FHR, to counteract the oxidizing effects of the activation reactions that would otherwise aggravate DT corrosion.*

5.1.4.1.2. ARC

In ARC at the nominal enrichment and in absence of active chemistry control, Cr would be consumed at rate of 91 mg Cr/day/MWth and the main contributors to the oxidative effects are:

- oxidizing effect due to H-3 production from Li-7,
- oxidizing effect due to O-18 production from F-19, and
- counteracting reducing effect of C-14 production from O-17

---

[k] Assuming the corrosion front is a square wave that moves uniformly into the thickness of the salt-facing heat exchanger wall made of SS316 with a density of 8 g/cm3 and with 17 wt% Cr. This disregards diffusion-limited corrosion, which may lead to lower actual corrosion rate. This disregards grain-boundary attack, which may lead to a higher actual corrosion rate than a uniform Cr depletion front.

143

In ARC at the nominal enrichment (90% Li-6), the rate of tritium production accounts for 73% of the total oxidative effect (69% for tritium from Li-6, 4% for tritium from Li-7). At the lithium enrichment which optimizes tritium breeding (25% Li-6), tritium production accounts for 72% of the total oxidative effect of all activation reactions.

At 91 mg Cr/day/MWth, assuming about $1 m^2$ of heat exchanger surface area per MWth[1], ARC would experience a uniform corrosion front that moves at a rate of 25 um/year, which would be too high for engineering of metallic components. Thus, *in ARC the activation reactions of FLiBe will be a significant direct corrosion driver, requiring implementation of redox control.*
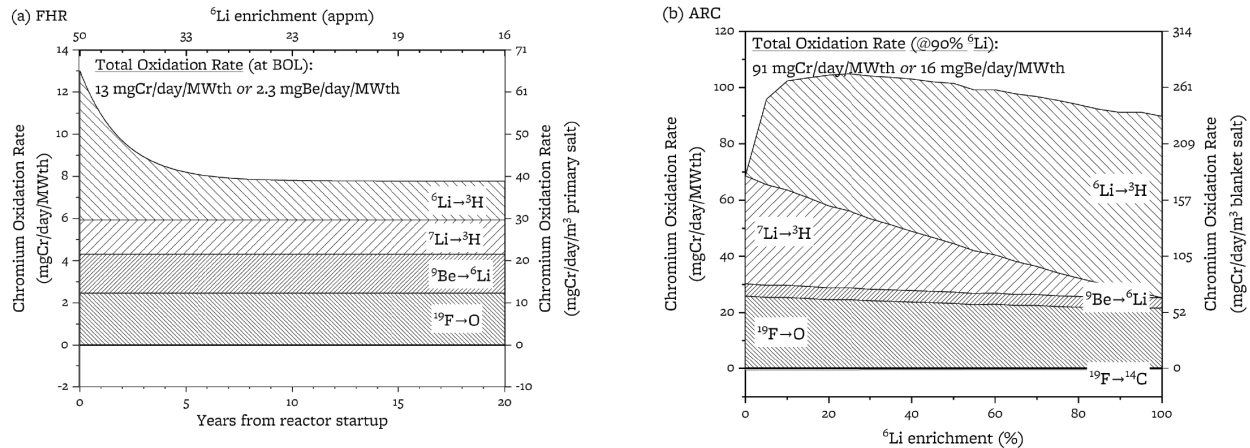
Figure 5.6. The oxidizing effects of transmutation reactions on FLiBe in the Mark-I PB-FHR and in ARC. Mark-I PB-FHR: BOL Li-6: 50 appm; Thermal power: 236 MWth; salt inventory: 46.8 m³ (Andreades et al. 2016). ARC: BOL Li-6: 90 at. %; Thermal power 630 MWth; total salt inventory: 482 m³ (Sorbom et al. 2015).

5.1.4.1.3. Comparison to other sources of oxidants

Table 5.7 provides several points of comparison for the oxidation rates computed here for the consequence of activation reactions on FLiBe: initial oxidants present in freshly loaded salt, air ingress, and introduction of a new heat exchanger with Cr_2O_3 oxides (i.e., Cr^{3+} oxidant) present on its metal surface. For freshly loaded FLiBe in an FHR, 2 mg Be/day/MWth for 300 MWth corresponds to 219 g Be consumed the first year. This would be equivalent to the amount of Be required to reduce an initial NiF_2 concentration in the salt (Ni2+ being an oxidant) of 15 wppm Ni, assuming 92 ton of salt in the primary circuit. Hydrofluorinated FLiBe has been measured at 22(5) wppm Ni (Carotti et al. 2018; Seifried et al. 2019); thus, the initial oxidants in the salt would be of a comparable order of magnitude as the tritium production in the first year.

The oxidizing effect of uranium fission in liquid fuel molten salt reactors is one order of magnitude higher than that of tritium production in a thermal reactor. If there is uranium present as an impurity in the unfueled coolant salt of FHR, the oxidizing effect of fission of tramp uranium will remain order of magnitude lower than that of tritium production, if tramp uranium is kept below 100 ppm concentration in the salt in an FHR. Hydrofluorinated FLiBe has been measured at 1.8(2) wppm

---

[1] Based on Mark-I PB-FHR, since the operational temperature of the FLiBe coolant are the same for ARC.

U (Carotti et al. 2018; Seifried et al. 2019); for this salt, the fission of tramp U would have a negligible oxidizing effect in an FHR, relative to the effects of the activation reactions on FLiBe.

For air ingress, an oxidizing effect of 2 mg Be/day/MW would correspond to an air ingress rate of 0.013 L STP air/day/MW (4L/day for 300 MWth). In the case of introduction of new metallic components, a heat exchanger of 224 m^2, with a thickness of 100 nm of Cr_2O_3 would introduce 1.5 mol of Cr^{3+}, which would lead to consumption of 21 g of Be, equivalent to 40 days of tritium production in a 236 MW reactor. Thus, the oxidizing effect of tritium production in the first year is more significant than the oxidants potentially introduced by initial presence of oxides on the surface of a new (not yet salt-flushed) metal heat exchanger and is equivalent to oxidation caused by air ingress at a rate of 4L/day.

Table 5.7. Oxidizing effects of activation reactions in fluoride salt reactors and equivalence to other oxidizing effects.

Point of comparison	Units	FHR @50 appm ^{6}Li [b]	FHR @13 appm ^{6}Li [b]	ARC [c]	MSRE ^{235}U fission [g,h]
Consumption of redox control agent	mgBe/day/MWth	2.2	1.4	16	20
	gBe/year/MWth	0.80	0.51	4	7.3
Inadvertent air ingress	L of STP dry air/day/MWth [a]	0.014	0.0090	0.11	0.13
Consumption of oxidants present in fresh FLiBe [e]	replenished hydrofluorinated FLiBe/year/MWth [f]	2.6%	1.6%		
	Time of transmutation reactions leading to an equivalent amount of oxidation	1.6 years	2.6 years	8 hours	40 minutes
Introduction of a new HX with 100 nm Cr_2O_3 on its surface [b, c, d]		40 days	63 days	42 hours	15 days

a: STP equivalent to 1 atm and 25 °C, 21% O2 and no H2O nor any other oxidizing gases
b: Thermal power output of 236 MW, FLiBe inventory of 92 tons, heat exchange surface of 224 m2. Assumed Cr2O3 thickness of 100 nm, and density of 5200 kg/m^3.
c: Thermal output of 630 MW and a salt inventory of 960 kg. A heat exchanger surface of 598 m2 is approximated using the ratio of thermal power to heat exchanger area in the Mark-I PB-FHR.
d: Thermal output of 7.3 MW, salt inventory of 1.2 kg salt, and a heat exchanger area of 23.6 m2. (Kedl and Mcglothlan 1968)
e: Assuming 22 wppm Ni as initial oxidizing impurities present in 92 ton of fresh salt (Carotti et al. 2018).
f: Reported as a % of the total hydrofluorinated salt inventory of 92 ton in an FHR primary circuit;
g: Assuming 3.2+ valence state of fission products (Lane et al. 1958 p. 591) and 4+ initial oxidation state of uranium since xU4+/xU3+ = 100 in an MSR (Baes 1974) and 0.78 MWd/ g of U-235 (Manson Benedict et al. 1981).
h: MSRE fuel composition: ~1 mol% UF$_4$ in LiF-BeF$_2$-ZrF$_4$.

5.1.4.1.4.   The impacts of total salt inventory and initial Li-6 inventory

The time evolution of the rate of oxidation reactions in an FHR depends on the initial Li-6 isotopic composition of the salt and on the total inventory of primary salt (Figure 5.7). A higher Li-6 isotopic composition leads to an initially higher oxidant production rate. A higher salt inventory leads to a higher initial inventory of Li-6, and hence a slower decrease with time of the oxidant production rate. In ARC, assuming constant Li-6 enrichment, the molar fraction of chromium in the salt increases linearly and reaches 1000 wppm after five years of operation. Overall, in both FHR and ARC, a higher salt inventory leads to a higher dilution of the corrosion products and of

the oxidants (both in FHR and in ARC). Hence, the redox potential (expressed here as the concentration of CrF_2 in the salt) *increases at a slower rate when the salt inventory is higher*.[m]
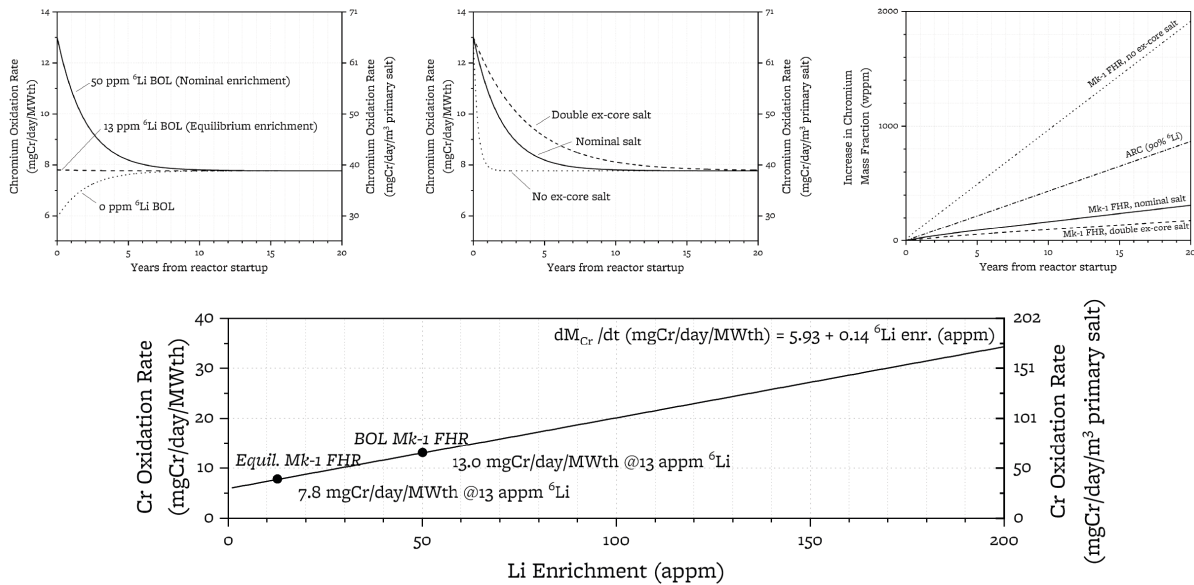
Figure 5.7. The effects of salt inventory and BOL lithium enrichment on redox potential. Mark-I PB-FHR: BOL Li-6: 50 appm; Thermal power: 236 MWth; salt inventory: 92 ton (Andreades et al. 2016). ARC blanket: Li-6: 90 at. %; Thermal power 630 MWth; total salt inventory: 948 ton (Sorbom et al. 2015).

5.1.4.2. *Oxide content and the effect of oxoacidity on corrosion*

Oxygen is produced from the activation reaction on F-19. In the Mark-I PB-FHR, oxygen is produced at a rate of $(8.8)10^{-5}$ mol O/ day/ MWth (Figure 5.5). Considering the nominal salt inventory of the FHR (92 ton), oxygen concentration in the salt would reach 30 wppm after 20 years of operation (Figure 5.8), if no oxygen control mechanism is in place (i.e. all produced O remains in the salt as a dissolved anion). As a point of comparison, the initial oxides on the metal surface area of the heat exchanger would lead to 0.4 wppm O in 92 ton of salt inventory[n]. Thus, *the oxygen production from activation reactions is more significant than the introduction of oxygen by unflushed metallic components*. Another point of comparison is the equivalent air ingress rate, which would be 1.2 L/day STP air (21% mol O_2 in dry air); thus, O production by activation is significant relative to an air ingress into the reactor cavity that would be expected to be below 1.2 L/day STP air (Table 5.8). In ARC, the oxygen production rate is $(5.9)~10^{-4}$ mol/day/MWth (Figure 5.5). Assuming no oxygen control mechanism, this production rate leads to an accumulation of about 2.5 wppm oxygen per year (Figure 5.8, Table 5.8), about twice as high as in the FHR.

Table 5.8. Comparisons of rates of introduction of oxygen in FHR and ARC from different

---

[m] In absence of ex-core salt, the chromium oxidation rate converges to equilibrium in less than two years. This is in line with (Fratoni and Greenspan 2011) that finds that Li-6 concentration in the Mark-I PB-FHR would reach equilibrium in 500 to 1000 days if no ex-core salt is present.

[n] 35.3 g O from 224 m2 for the surface area of the HX with 100 nm thickness of Cr2O3 on the surface of the metal with a density of 5g/cm3

146

	Units	FHR activation reactions @13 appm ^6Li	ARC activation reactions
FLiBe Activation reactions	(mgO/day/MWth)	1.4	9.4
Inadvertent air ingress	(L of STP dry air/day/MWth)	0.005	0.034
(equivalent air ingress of oxygen production from neutron activation)	(L of STP dry air/day)	1.2 (for 236 MWth)	22.1 (for 630 MWth)
Oxide possibly present on the surface of a new metallic heat exchanger (see Table 5.7 footnotes)	Equivalent duration of oxygen production from neutron activation	111 days	16 days
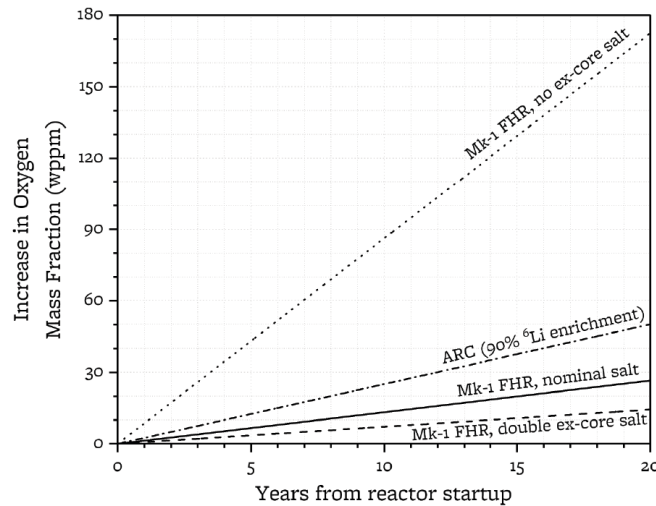
Figure 5.8. Oxygen build-up. Mark-I PB-FHR nominal salt inventory: 92 ton; power level: 236 MWth (Andreades et al. 2016).

The oxide content in the fluoride melt influences the oxoacidity of the melt and can consequently change the corrosion of metals in the salt, a concept commonly illustrated by Pourbaix diagrams for the constituents of metal alloys (Olander 2007). Figure 5.9 reproduces the pseudo-Pourbaix diagrams[o] reported by (Baes 1974) for the main constituents of stainless steel (Cr, Fe, Ni) in a LiF-BeF$_2$-ThF$_4$ salt. Solid oxide precipitates become thermodynamically stable in FLiBe when the oxide content is sufficiently high. Cr forms Cr$_2$O$_3$ when above 100 ppm O^{2-} in the salt, Ni forms NiO above 20 appm O^{2-} in the salt, and Fe forms Fe$_3$O$_4$ above 1000 appm O^{2-} in the salt. *Thus, in this particular salt (FLiBe+ThF₄), 100 ppm O^{2-} is the threshold beyond which Cr$_2$O$_3$ passivating oxide layers will begin to form on salt-facing surface.* Oxoacidity Pourbaix diagrams are not yet

---

[o] Pourbaix diagrams use acidity on the abscissa, but only measurements of total oxide content were experimentally available at the time of the generation of this diagram. Because total oxide content is not a direct measurement of oxoacidity, these diagrams are referred to as "pseudo-Pourbaix" diagrams.

available for FLiBe salt, which may behave differently in the absence of ThF₄, but the passivation of metal surface by chromium oxide layers in FLiBe has been reported at high oxide concentrations (Schmidt et al. 2021; Zhang et al. 2018b).
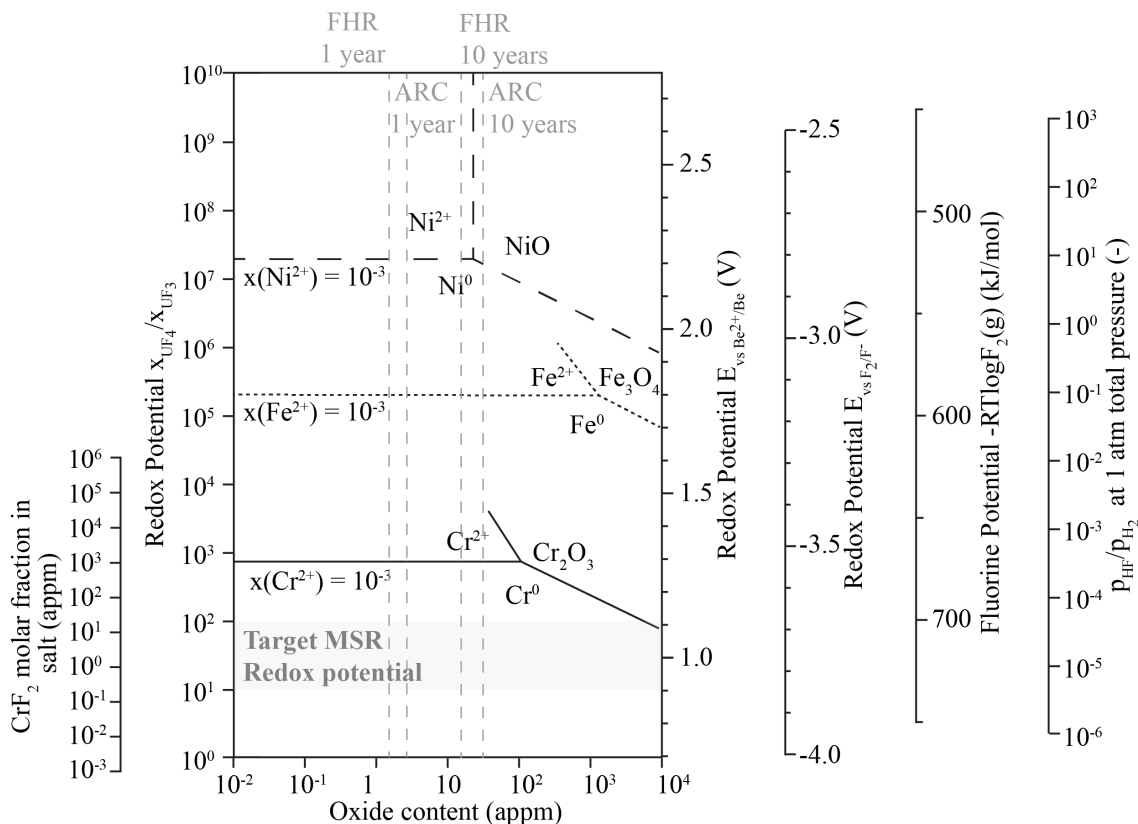
Conversions across the redox metrics using
$E^0_{U^{4+}/U^{3+}}$ = -1.15 V, $E^0_{Be^{2+}/Be}$ = -1.85 V, $E^0_{Cr^{2+}/Cr}$ = -0.49 V, $E^0_{F_2/F^-}$ = -2.87 V vs HF(g)/H₂(g) couple.
$\Delta G^°_{HF}$ = 279 kJ/mol, $\Delta G^°_{CrF_2}$ = -640 kJ/mol.

CrF₂ molar fraction calculated assuming x_{Cr}=0.07 in the metal in contact with the salt (nominal composition of Hastelloy N) and unity activity coefficients for Cr in the metal and CrF₂ in the salt.

Figure 5.9: Pseudo-Pourbaix diagram for structural materials in LiF-BeF₂-ThF₄ at 600°C, adapted from (Baes 1974). The optimal region for the redox potential is shown, as defined by (Baes 1974) for MSR operation. Vertical grey gridlines indicate structural metal oxide content in FHR (BOL 50 appm Li-6 enrichment) and ARC (90% Li-6 enrichment), as a consequence of build-up of oxygen from activation reactions on FLiBe. The inputs for the conversion between the two redox potential metrics are from (Baes 1974). Details on how to convert among different redox metrics are provided in (Olander 2002; Zhang et al. 2018b). Hastelloy N nominal composition is from (DeVan et al. 1995).The Excel spreadsheet used for the computation is provided in the Mendeley Data repository linked in Supplementary Information.

Assuming no oxygen removal and no external oxygen leaking into the system, FHR reaches 15 appm O²⁻ after 10 years of operation and 45 appm after 30 years of operation due to activation

148

reactions. Thus, an oxygen scavenger for the activation products might be warranted only upon long-term operation. If there is a driver for the oxidation of O^{2-} to $O_2(g)$, the graphite in FHR may be one of the sinks of the oxygen that is produced. ARC reaches 25 appm after 10 years of operation, thus either oxygen scavenging is implemented as part of chemistry control, or the redox control strategy relies on ensuring the stability of passive oxide layers in FLiBe. While passivating oxide layer for metals exposed to FLiBe fusion blanked has been proposed as a corrosion-control strategy (Nishimura et al. 2002; Terai et al. 1998, 2001; Tzvetkoff and Kolchakov 2004), it has been studied to a less extent than corrosion-control by redox control and oxygen-free salt (Schmidt et al. 2021; Zhang et al. 2018b).

5.1.4.3. *Case study: Redox control with addition of Be metal*

For active redox control with Be metal, FHR BOL would require 0.54 g Be/day (0.20 kg Be/yr) for the 236 MWth Mark-I PB-FHR to account for activation effects. The required Be addition would be higher if there is also oxygen or moisture ingress. Assuming a solubility of Be metal in FLiBe of 0.3 mol% (with M_{FLiBe} = 33 g/mol) (Hara et al. 2006; Simpson et al. 2006) and the FHR primary salt inventory of 92 ton, there can be an inventory of 75 kg of dissolved Be metal, which is sufficiently abundant to neutralize the effects of activation reactions on FLiBe for the entire reactor lifetime. *Otherwise stated, the Be that is needed for redox control of activation reactions has a 400-year residence time if Be metal is at its solubility limit in BOL FLiBe and is consumed at the rate dictated by the oxidation effect of activation reactions.* The amounts of Be metal added to the primary salt of an FHR for the purpose of redox control might need to be reduced to values lower than the solubility limits to prevent formation of beryllium carbides (Ferro et al. 2013; Porosnicu et al. 2011).

ARC would require 10 gBe/day (3.68 kg Be/yr) (Figure 5.6) to offset activation reactions. Assuming a solubility of Be metal in FLiBe of 0.3 mol% (Simpson et al. 2006) and the ARC salt inventory of 960 ton, there can be an inventory up to 790 kg of dissolved Be metal in the FLiBe inventory. *Otherwise stated, the Be that is needed for redox control of activation reactions has a 200-year residence time if Be metal is at its solubility limit in BOL FLiBe and is consumed at the rate dictated by the oxidation effect of activation reactions.*

Given the uncertainty in the solubility of Be metal in FLiBe, it might be the case that continuous addition of a redox control agent or sacrificial metal is necessary for the ARC blanket, which has a high volumetric tritium generation rate (7 mmol H-3/day/m^3 of salt inventory). LiF may need to be replenished at rate proportional to the Be redox agent consumption, to avoid changing the composition of the FLiBe towards higher BeF$_2$ molar ratios, which eventually will have a higher salt viscosity and higher vapor pressure (Abe et al. 1981; Olander et al. 2002). 4 kg Be/yr would require replenishing LiF at a rate of 22 kg LiF/yr. LiF replenishing is also needed for the second reason of replenishing the Li-6 isotope that is being consumed by tritium production reactions. Without LiF replenishing, Be metal addition would lead to a change in FLiBe composition of 0.02 mol% BeF$_2$ per year, so LiF replenishing to balance Be additions is negligible at these Be addition rates. Conversely, if Li-6 resupply is needed, depending on the enrichment in the LiF feed, BeF$_2$ additions may be needed to balance LiF additions.

Figure 5.10 gives an example of the *mass-balance calculations for redox control and Li-6 fueling of the tritium blanket*. If ARC operates at 90% Li-6, then 13.8 kg ^{6}LiF/yr, 0.7 kg ^{7}LiF/yr and 0.3 kg BeF$_2$ are consumed in ARC, as a consequence of 1.7 mol H-3/day production (Figure 5.3). In

order to maintain the 2LiF-BeF$_2$ stoichiometry and replenish the consumed fluorides, 14.5 kg/yr should be supplied as 95.4% Li-6 enriched LiF. A LiF replenishing rate is also needed for redox control via Be metal: 20.3 kg/yr should be supplied as 90% Li-6 enriched LiF for a redox supply of 3.7 kg Be/yr[p]. Figure 5.10 depicts the overall inlet and outlet streams for Li-6 replenishing and Be redox control for ARC operation at the nominal 90% Li-6 enrichment. Table 5.9 summarizes the streams for the two cases of 90% and 25% Li-6 enriched FLiBe.

The Mendeley Data repository linked in Supplementary Information includes a spreadsheet that can used for performing mass balance calculations for ARC fueling and redox control, such that the readers can design their own scenarios.

Table 5.9: Mass-flow balance in ARC for Li-6 makeup and redox control. Thermal power 630 MWth; total salt inventory: 482 m^3.

	Units	ARC @90 at.% Li-6 enrichment	ARC @25 at.% Li-6 enrichment
FLiBe Constituents Consumption for Tritium Production (Figure 5.3)			
Li6	mol/day	1.52	1.18
Li7	mol/day	0.08	0.66
Be	mol/day	0.01	0.02
F	mol/day	0.04	0.05
Consumption for Redox Control (Figure 5.6)			
Be	mgBe/day/MWth	15.78	18.15
Inlet Stream Composition			
LiF	kg/year	34.6	40.6
Li-6 enrichment	at. %	92.2	41.5
Be	kg/year	3.6	4.2
Outlet Stream Composition			
FLiBe	kg/year	38.7	45.1
Li-6 enrichment	at. %	90	25

---

[p] The O2- anion, which is the product of the F(n,t) reaction, is assumed to remain as a dissolved anion in the melt. Therefore, there is no need to make up for the lost F- anion unless oxide scavenging is implemented, in which case the rate of LiF replenishing, would need to match the rate of metal oxide removal.
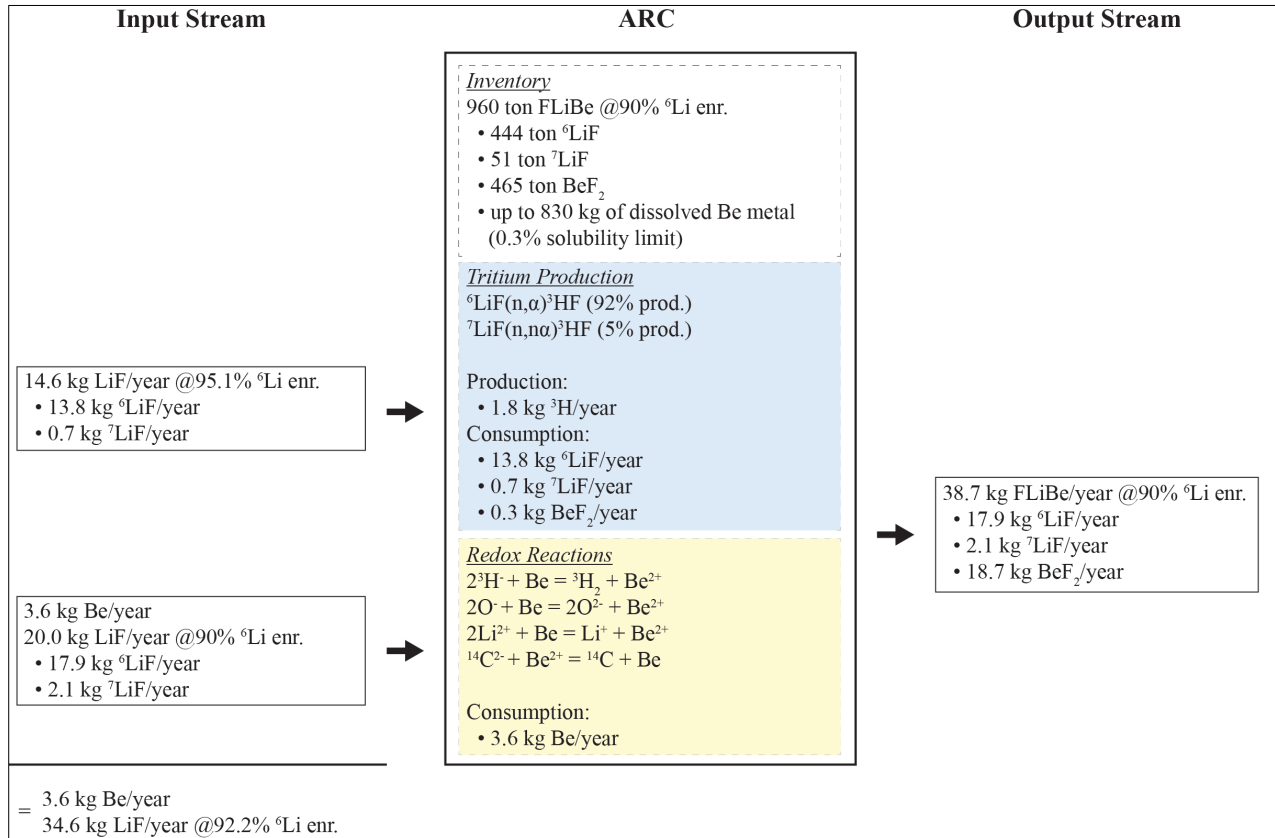
Figure 5.10: Mass-flow balance in ARC for 6-Li makeup and redox control. ARC: 90 at. % Li-6: Thermal power 630 MWth; total salt inventory: 482 m³ (Sorbom et al. 2015).

5.1.4.4.   *Case study: Corrosion-irradiation experiments*

Corrosion-irradiation studies (Schmidt et al. 2021) in molten salt are of interest because the simultaneous irradiation and corrosion of samples may lead to corrosion rates different from corrosion of previously irradiated samples. The limited data that exists on corrosion-irradiation in molten salts shows enhanced corrosion (Zheng et al. 2016), decreased corrosion (Ezell et al. 2020; Zhou et al. 2020) and no effect (Ezell et al. 2020). One of the challenges with corrosion-irradiation studies in molten salt is the difficulty of controlling for experimental artefacts that are specific to irradiation experiments and cannot otherwise be reproduced in out-of-pile experiments (Schmidt et al. 2021). One such effect can be the oxidizing effect of neutron activation reactions. This effect can be quantified by using the results provided in this study. *The calculation methodology for the use of these results in the prediction of corrosion rates directly caused by activation reactions on FLiBe is as follows:*

- The tritium production rate (Figure 5.2) and the relative contribution of tritium production to all oxidizing activation reactions (Figure 5.6) *provide* → the total mols of electrons involved in oxidizing reactions.

151

- The moles of electrons per oxidized metal atom (e.g., z = 2 for Cr oxidizing to Cr^{2+}) and the molecular weight of the oxidized metal (e.g., MW = 52 g/mol for Cr) $\xrightarrow{provide}$ the total mass of oxidized metal.

- The surface area of salt-facing metal $\xrightarrow{provides}$ the weight loss per surface area (mg/cm^2).

- The metal alloy density and the concentration of the of the oxidized metal in the metal alloy (in wt%) $\xrightarrow{provide}$ a bounding estimate for the depth of corrosion front progression (in um or um/year).

As a case study to demonstrate how the oxidizing effect of activation reactions can be quantified for irradiation-corrosion experiments, the conditions of the (Zheng et al. 2016) in-pile experiment are used.

Table 5.10 shows the comparison between the oxidative effect of all transmutation reactions on FLiBe and the difference between in-pile and out-of-pile corrosion rates for this experiment. In (Zheng et al. 2016), a graphite crucible contained six wells; each well was filled with MSRE-purified FLiBe (Kelleher et al. 2013) and contained two metal coupons. The crucible was exposed to neutron activation in the MIT reactor for 40 days. The tritium production rate was 0.5 mmol H-3/day (as predicted by neutronic calculations for a Li-6 enrichment of 50 ppm (Dolan et al. 2020)), with a total tritium production of 21 mmol over the 40-day experiment (3.5 mmol T per well) . The calculation methodology from Section 5.1.2 is applied to the MIT FS-1 capsule irradiation experiment (input deck available in the Mendeley Data repository linked in Supplementary Information)[q]. Matching the reported tritium inventory, the total oxidative effect is calculated to 2.7 mmol (0.14 mg) of Cr oxidized in each well due to the oxidizing effect of all the neutron activation reactions on FLiBe (Figure 5.6)[r]. To compare to the oxidative effect of activation reactions, this is corrected *for the total surface area of the salt-facing metals*, including both the metal coupons and the salt-facing surface of the metallic crucibles (for the wells in which metallic crucibles are used). The total additional amount of corrosion observed in-pile vs. out-of-pile was 8 mg. Thus, for this experiment, transmutation reactions can only explain 2% of the additional amount of corrosion observed in pile.

---

[q] Assuming the same reaction rates in the MIT FS-1 capsule as for the Mark-I PB-FHR (both being thermal spectrum reactors).

[r] At 50 ppm Li-6, 21 μmol of T produced would be accompanied by 6 μmol of O. As discussed in Section 5.1.1.1.1, each mole of produced tritium or oxygen consumes one mole of electrons, resulting in a total of 14 μmol of Cr oxidized to $^{Cr2+}$. Additionally, 2 μmol of Cr are oxidized due to the redox effect of the Be-Li transmutation. Assuming equal salt inventory in each of the six wells, this corresponds to 0.14 mg of Cr oxidized in each well.

Table 5.10. Evaluation of oxidative effects from transmutation in the capsule corrosion-irradiations by (Zheng et al. 2016).

Row #	Formula/Source		Units	Well #1	Well #2	Well #3	Well #4
		Coupons		316 SS		Hastelloy N	
(1)	(Zheng et al. 2016)			4.40	4.26	4.51	4.55
		Salt-facing crucible	metal surface area (cm^2)	Graphite	316 SS	Graphite	Nickel
(2)	(Zheng, Personal Communication 2021)			-	15.71	-	15.71
(3)	*(1)+(2)*	*All salt-facing metal*		*4.40*	*19.97*	*4.51*	*20.26*
(4)	(Zheng et al. 2016)	In-pile corrosion		2.09	0.51	0.42	0.26
(5)	(Zheng et al. 2016)	Out-of-pile corrosion	sample weight loss (mg/cm^2)	0.18	0.10	-0.17	0.13
(6)	*(4)-(5)*	*Difference between in-pile and out-of-pile*		*+1.91*	*+0.41*	*+0.59*	*+0.13*
(9)	*(6)*(3)*	*Difference between in-pile and out-of-pile*	weight loss from all salt-facing metal surfaces (mg)	*8.40*	*8.18*	*2.66*	*2.63*
(10)	(Dolan et al. 2020)	Li-6 enrichment	(appm ^{6}Li)	50			
(11)	*Figure 5.6*	Oxidative effect of tritium production / oxidative effect of all activation reactions on FLiBe		70%			
(12)	(Dolan et al. 2020)	Tritium Production	(μmol ^3H)	3.57			
(13)	½ *(12)/(11)	*Oxidative effect of all transmutation reactions on FliBe*	(μmol $Cr \rightarrow Cr^{2+}$)	2.68			
(14)	(52 g/mol)*(13)		*(mg Cr)*	*0.14*			
(15)	**(14)/(9)**	*Corrosion weight loss attributable to the oxidative effect of activation reactions*	*(Oxidative effect of transmutation)/(Difference between in-pile and out-of-pile)*	*2%*	*2%*	*5%*	*5%*

Remarkably, the total metal loss matches to within 3% between 8.40 mg in well #1 with SS316 coupons in a SS316 crucible and 8.18 mg in well #2 with SS316 coupons in a graphite crucible [s]. Since the salt inventory is the same in the two wells, this would indicate that sources of oxidants that scale with the amount of salt present could be the explanation for the difference between in-pile and out-of pile corrosion. The oxidative effect of transmutation reactions is one such effect.

---

[s] Similarly, the total weight loss matches to within 1% between well #3 and well #4 (the two wells with Hastelloy N/nickel); this amount does not match with the amount in wells #1 and #2, as would be expected if the source of oxidants scale with the amount of salt; however, the weight loss values for Hastelloy N are distorted by the fact that the dissimilar metal (nickel) used for the crucible leads to out-of-pile weight gain of the Hastelloy N coupons, thus masking some of the weight loss that may have occurred due to oxidation reactions.

Air ingress for a finite amount of time or other forms of salt contamination would also likely be identical among the wells of identical geometry and thermal history. For the MIT FS-1 corrosion-irradiation experiment neutron activation was not the dominant oxidizer.

Had the irradiated FLiBe contained natural Li isotopics (7.59 at% Li-6), the corrosion from neutron activation reactions would have been 18 mg/cm^2 in well #1 and 4 mg/mm^2 in well #2 (using Figure 5.7) - several times higher than what as observed here due to other oxidants present in the salt. It is also important to note that a smaller total surface area of the salt-facing metal (e.g., well #1 vs well #2) for the same total oxidative effect causes more pronounced corrosion when measured by mass loss or depth of corrosion. Thirdly, the total oxidative effect does not scale one-to-one with total tritium production rate since the oxidative contribution of tritium production to the total oxidative effect depends on the Li-6 isotopic composition (Figure 5.6); for example in FHR at 13 ppm Li-6, the rate of tritium production accounts for 50% of the total oxidative effects of activation reactions, and at 50 ppm Li-6 it accounts for 70% of it.

Thus, for design of salt-irradiation experiments investigating metal corrosion should account for:

(1a) lithium isotopic composition of the salt (Figure 5.2),

(1b) when relevant, the evolution of Li-6 isotopic composition with time (Figure 5.7)

(2a) all the activation reactions with redox contributions (Table 5.2, Figure 5.6 and Figure 5.7),

(2b) all other inventories or sources of oxidants, and

(3) the total surface area of the salt-facing metal.

For corrosion prediction in an FHR or ARC reactor, or in a flowing loop with neutron irradiation, the same (1)-(3) considerations apply, with the additional consideration of total salt inventory, which affects consideration (1b).

5.1.5 Conclusions

The oxidizing effect of activation reactions in the salt had been previously qualitatively defined in (DeVan et al. 1995; Schmidt et al. 2021; Stempien et al. 2016) but never quantified. Here, the corrosive effects of the activation reactions on FLiBe are quantified. The rates of change of *all of the activation products of FLiBe* are computed for an FHR advanced fission reactor and an ARC-class fusion reactor, using the UC Berkeley Mark-I PB-FHR (Andreades et al. 2016) and MIT ARC conceptual designs (Sorbom et al. 2015) as input parameters. The production rates of tritium and lithium (Figure 5.3), as well as oxygen and carbon (Figure 5.5) are quantified as a function of lithium enrichment of the salt, operational time and primary salt inventory (Figure 5.7). Deuterium and protium (Figure 5.4), nitrogen and neon activation products are computed to have negligible production rates. The impact of FLiBe activation reactions on the chemistry of the molten salt is quantified and compared to other environmental effects with similar consequences on the salt chemistry. The results are presented in a manner useful to the reactor chemist and the reactor designer concerned with corrosion control and chemistry control and tritium management for irradiated FLiBe salt in fission and fusion reactors and for salt-irradiation experiments. This study did not include the activation of dilute species inadvertently present in the salt, such as uranium or potassium or transition metals. The impact of impurities on the neutronic performance of FLiBe

has been previously studied by (Seifried et al. 2019), but the chemical and corrosion effects of the activation reactions of solutes in the salt remain topics of future study.

5.1.6 Acknowledgement

This chapter contains material included in the journal article *"The corrosion effects of neutron activation of 2LiF-BeF$_2$ (FLiBe)"* authored by L. Vergari, R.O. Scarlat, R.D. Hayes, M. Fratoni and published in *Nuclear Materials and Energy*. The co-authors of the original manuscript have been informed of the inclusion in this dissertation.

The authors contribution to the original manuscript are as follows:

LV: Methodology, Software, Formal analysis, Investigation, Data curation, Visualization, Writing - original draft, Writing – review & editing. **ROS**: Conceptualization, Methodology, Formal analysis, Investigation, Data curation, Visualization, Resources, Supervision, Writing - original draft, Writing – review & editing. **RDH**: Formal analysis, Investigation. **MF**: Resources, Supervision, Funding acquisition.

5.2   Thermodynamics of Hydrogen in Graphite at High Temperature

The dominant mechanism by which hydrogen isotopes interact with graphite depends on temperatures, pressures, microstructure, and chemical reactivity of the graphite. Many studies have investigated low temperature hydrogen uptake, relevant for hydrogen storage applications, and very high temperature hydrogen uptake into and release from graphite, for the purpose of tritium recycling and tritium management in nuclear fusion reactors. Few studies have been performed at the moderate temperatures of 500 °C – 800 °C, and the low partial pressures in the order of the tens of Pa. This regime is relevant to the management and removal of tritium produced in the core of fission reactors and in the blanket of fusion reactors that employ molten salts for cooling and tritium breeding. Even fewer studies have investigated the effects of pre-oxidation, neutron irradiation, and isotopics on hydrogen-graphite uptake and desorption at these conditions.

For hydrogen storage in carbon materials (activated carbon, porous carbon and carbon nanotubes), hydrogen adsorption has been studied at 77 K and room temperature with partial pressures in the order of the MPa (Fierro et al. 2010; Juan-Juan et al. 2010; Panella et al. 2005). The uptake is governed by physisorption of molecular hydrogen at the carbon surface (Panella et al. 2005). Physisorption at 77 K and hydrogen partial pressures of 1-8 MPa on activated carbon has been shown to yield hydrogen uptakes of 4% - 6% (Fierro et al. 2010; Juan-Juan et al. 2010; Panella et al. 2005).

In fusion research, graphite has been used as a plasma-facing material (Causey 1989; Miyahara and Tanabe 1988) in the Princeton TFTR, and, more recently, proposed as a material for divertor plates (Tanabe 2006), thanks to its low atomic number and resistance at high temperatures. In a fusion environment, the interaction takes place at temperatures up to 1200 °C with tritium partial pressures on the order of the Pa, and neutron irradiation and ion implantation at the graphite surface are highly relevant (Atsumi et al. 1988, 1992; Causey et al. 1986; Tanabe 2006; Wampler et al. 1990). At these conditions, the primary pathway for uptake of hydrogen isotopes is chemisorption, where the implanted hydrogen ions and dissociated hydrogen molecules form C-H chemical bonds with the graphite. Only few studies have investigated partial pressures in the order of Pa, due to the difficulty in measuring low concentrations of hydrogen, in the appm range (Hoinkis 1991b; c; Strehlow 1986; Thomas 1961). Even fewer studies have explored experimental conditions involving low partial pressures and neutron irradiation (Kwast et al. 1994).

Small quantities of tritium are produced in all types of fission reactors by ternary fission of the fuel and activation of boron and lithium used in the coolant for chemistry and reactivity control (e.g. 1.6 grams a year in a 1000 MWe PWR), but reactors that employ molten fluoride salts can produce up to thousand times as much, as discussed in Section 5.1. The continuously produced tritium needs to be separated from the salt for safe management or, as in the case of fusion reactors, for its re-use as fuel (Forsberg et al. 2020, 2017c; Yoshioka and Kinoshita 2017). The salt has relatively low solubility for H_2 (Field and Shaffer 1967; Malinauskas and Richardson 1974), and the partial pressure must be maintained on the order of a few to tens of Pa in order to prevent leakage of tritium through metallic components at the 500 °C – 800 °C operational temperature of

the salt[t]. Tritium at small partial pressures is also produced in gas-cooled reactors (Saeki 1981) and HTGRs (Xie et al. 2018), which use helium as a coolant. In these reactors, tritium is produced through neutron activation of ^{3}He and may leak from the core through the heat-exchanger tubes (Rohrig et al. 1976). Graphite, which is present in fission reactor cores as neutron moderator and reflector (gas-cooled reactors, HTGRs, FHRs, thermal-neutron spectrum MSRs) or as part of the fuel elements (HTGRs and PB-FHRs), is not a significant source of tritium production, as current engineering standards limit the concentration of lithium and boron impurities to less than 2 appm ASTM International, 2018)[u].

Graphite could act as a sink and a vector for tritium: it may uptake tritium produced in the core storing it until the end of life of the graphite component, and/or it can be a carrier for tritium out of the core where it is extracted from the graphite into another ultimate sink (Forsberg et al. 2017c; Lam 2017). The performance of graphite as vector for tritium removal depends on its uptake capacity, on the kinetics of uptake and desorption and on its release behavior. These aspects may be influenced by intrinsic graphite properties (e.g., crystallite size, degree of graphitization, porosity distribution) and by external phenomena (e.g., neutron irradiation, air oxidation, chemical attack of fluorine species). Developing a mechanistic understanding of hydrogen-graphite interaction would allow to optimize graphite manufacturing for tritium management, identify what parameters of graphite are appropriate predictors of its performance as a tritium vector, and predict how external phenomena influence the interaction.

This chapter seeks to highlight what can be inferred about the thermodynamics of hydrogen in graphite at moderate temperature and low hydrogen partial pressure – conditions which have not previously received as much attention. The relevant terminology pertaining to graphite microstructure and porosity is first introduced in the context of a brief background on graphite structure. The mechanisms and the thermodynamic data for each pathway and uptake site for hydrogen in graphite are discussed at length.

5.2.1 Hydrogen uptake in graphite: terminology

The term *uptake* is used to encompass all pathways that lead hydrogen in graphite and the term *desorption* to encompass all release pathways from graphite. The word *mechanism* is used to refer to the transport and reaction pathway to uptake into one particular type of site. In prior literature, the different pathways for hydrogen uptake by graphite have been given various names, depending on the sites that host hydrogen, or on the strength of the interaction. The term *adsorption* is generally used for those processes that increase the concentration of some species on the surface (Kolasinski 2012). Depending on the strength of the chemical bond that is formed, the process could be defined as *chemisorption* or *physisorption* (Lechner et al. 2018). In the context of hydrogen-graphite, the term *adsorption* has been used as a collective term for all paths (Deng et al. 2019), or to refer to the specific processes that lead to hydrogen bonding at reactive carbon sites

---

[t] Electrochemical measurements of hydrogen in FLiBe (using LiH as a hydrogen donor) in (Carotti et al. 2021) estimate H2 solubilities four orders of magnitude larger than what is reported by (Malinauskas and Richardson 1974). Higher hydrogen solubilities in the salt would lead to lower partial pressures in the cover gas.
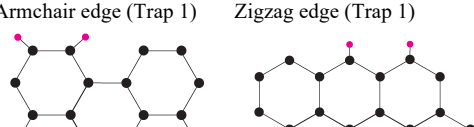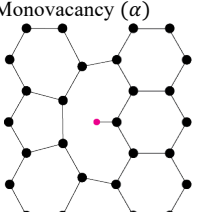
[u] Considering the Mark-I PB-FHR as a reference (Andreades et al. 2016), assuming 2 appm of natural Li, a flux of $3.4 \; 10^{14}$ n/cm^{2}s, an averaged cross section for tritium production from Li-6 of 148 b (Cisneros 2013) and a residence time of 1.4 years for FHR pebbles, the activation of Li would lead a tritium concentration ([H/C]) of around 0.01 appm. The production of tritium from boron is even lower, due to the lower cross section.
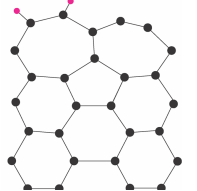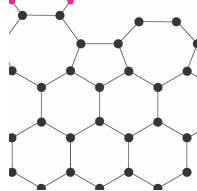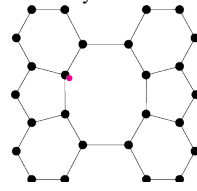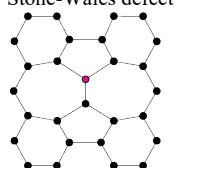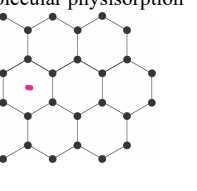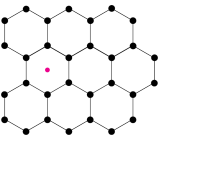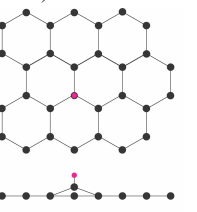
(introduced in Section 5.2.2) (Atsumi et al. 2013b; Hoinkis 1991a; Kanashenko 1996). In the latter sense, some studies have used the terms *retention* or *trapping* instead of *adsorption* (Atsumi 2003; Atsumi et al. 2009a, 2015). The term *absorption* is used for processes that increase the concentration of the species in the bulk. An example of an absorption process is what (Kanashenko 1996) defines "true solubility" of hydrogen in graphite, and corresponds to hydrogen forming a *solid solution* with carbon atoms on graphene basal planes   (Atsumi et al. 2013a; Kanashenko 1996).

5.2.2   Reactive carbon sites

Carbon atoms in a perfect basal plane are chemically inert; otherwise stated, it is not thermodynamically favorable to form C-H chemisorption bonds at these carbon sites. However, graphite possesses multiple types of RCS where adsorbates can bond. The carbon atoms that are chemically active and available for hydrogen chemisorption are those with unused valence orbitals or with unstable electron orbitals (Hoinkis 1991a). Uptake of hydrogen can take place on the different crystallite surfaces, at dislocation loops within the crystallite, and at point defects (isolated defects and clusters). Each of these uptake sites has a different enthalpy of uptake, as summarized in Table 5.11.

Table 5.11: Enthalpy of hydrogen uptake at different RCS. Entries are grouped by uptake site. Rows in each group are ordered by enthalpy of uptake.

Examples of hydrogen atoms at RCS. Carbon atoms in large black dots, hydrogen atoms in small magenta dots. Inspired by (Lechner et al. 2018).	Uptake site location *(name)*	Enthalpy of Uptake	Methodology	Source
		eV/H_2 (kJ/mole H)		
Non-reconstructed sites (incl. interstitial cluster loop edge) and monovacancies Armchair edge (Trap 1) Zigzag edge (Trap 1) Monovacancy (α) 	Non-reconstructed zigzag graphene edges *(Trap 1)*	−5.5 (−265)	AIMD	(Lechner et al. 2018)
	Non-reconstructed graphene edges *(Trap 1)*	−5.3 (−254)	AIMD	(Sha and Jackson 2004)
	Interstitial cluster loops edge *(Trap 1)*	−4.4 (−211)	Theoretical	(Kanashenko 1996)
	High Energy Trapping Site	−4.3 (−206)	D,T uptake on graphite samples	(Causey et al. 1986)
	Non-reconstructed armchair graphene edges	−4.2 (−203)	AIMD	(Lechner et al. 2018)
	Monovacancy	−3.8 (−183)[a]	AIMD	(Allouche and Ferro 2006)
	Monovacancy (α-vacancy and β-vacancy)	−3.8 (−183)[a]	AIMD	(Lechner et al. 2018)
	Non-reconstructed armchair graphene edges	−3.3 (−158)	AIMD	(Yang and Yang 2002)
	Non-reconstructed zigzag graphene edges	−2.9 (−139)	AIMD	(Yang and Yang 2002)

	Zigzag graphene edges with in-plane reconstruction *(Trap 2)*	−3.1 (−155)	AIMD	(Lechner et al. 2018)
Reconstructed sites and divacancies Reconstructed Armchair edge (Trap 2) Reconstructed Zigzag edge (Trap 2) Divacancy 	Armchair graphene edges with in-plane reconstruction *(Trap 2)*	−2.9 (−140)	AIMD	(Lechner et al. 2018)
	Graphene edges	−2.5 (−120)	D uptake on graphite samples	(Hoinkis 1991a)
	Graphene zigzag edges *(Trap 2)*	−2.3 (−110)	Theoretical	(Kanashenko 1996)
	Zigzag graphene edges with arch reconstruction	−1.2 (−58)	AIMD	(Lechner et al. 2018)
	Divacancy	−1.0 (−49)	AIMD	(Lechner et al. 2018)
	Armchair graphene edges with arch reconstruction	−0.8 (−39)	AIMD	(Lechner et al. 2018)
Stone-Wales defect and molecular physisorption on the basal plane Stone-Wales defect Molecular physisorption 	Stone-Wales defect	−0.5(−24)	AIMD	(Letardi et al. 2002)
	Molecular physisorption on basal plane	−0.05(−3)	AIMD	(Costanzo et al. 2012; Darvish Ganji et al. 2015; Rubeš et al. 2010)
	Monovacancy[a]	+0.1(+10)	AIMD	(Kanashenko 1996)
Atomic physisorption and chemisorption on basal plane Atomic physisorption Chemisorption on basal plane (with lifting of a C atom) 	Physisorption on basal plane *(True Solubility)*	+2.5 (+118)	Theoretical	(Kanashenko 1996)
	Chemisorption on basal plane lifting a carbon atom	+2.9(+140) and +3.3 (+159)	AIMD	(Lechner et al. 2018)
	Chemisorption on basal plane lifting a carbon atom	+2.9(+140)	AIMD	(Jeloaica and Sidis 1999)
	Physisorption on basal plane	+4.4 (+212)	AIMD	(Allouche et al. 2005; Bonfanti et al. 2007; Ferullo et al. 2010; Jeloaica and Sidis 1999)
	Physisorption on basal plane	+4.7 (+225)	AIMD	(Sha and Jackson 2004)

[a] The estimate in (Lechner et al. 2018) is based on the uptake of one hydrogen atom in the vacancy and in the reconstruction of neighboring C-C bonds. The estimate in (Kanashenko 1996) is based on the uptakes of two hydrogen atoms.

Early hydrogen uptake studies show that hydrogen chemisorbs on graphite edges with a positive binding energies but do not estimate the enthalpy of the reaction (Biederman et al. 1976; Strehlow 1986; Yang and Yang 1985). The first major theoretical study of graphite RCS was performed by

(Kanashenko 1996) and studied the hydrogen uptake reaction on graphite. The enthalpy of uptake $\Delta H_{chem,1}$ for such a reaction can be calculated as (Equation 5.35):

$$\Delta H_{chem,1} = E_{H-H} - 2E_{C-H} \qquad\qquad 5.35$$

where E_{H-H} is the bond energy of molecular hydrogen and E_{C-H} the C-H bond energy. Using E_{H-H} = 4.5 eV/H$_2$ (at 25 °C, 1 atm, (Luo 2007)) and the C-H bond energy in a benzene ring, $E_{C-H} = 4.45\ eV$ (at 25 °C, 1 atm, (Kanashenko 1996)), Kanashenko estimated that $\Delta H_1 = -4.4\ eV/H_2$.

The ΔH_1 theoretical prediction is in agreement with the experimental results from (Causey et al. 1986), where an enthalpy of $-4.3\ eV/H_2$ was estimated in a deuterium uptake experiment. Using a more recent estimate for the C-H bond energy in benzene (4.89 eV, at 25 °C, 1 atm, (Luo 2007)) yields an enthalpy uptake of -5.28 eV, suggesting that the benzene C-H bond might not be an appropriate model for the C-H bond in graphite.

According to (Kanashenko 1996), the benzene ring C-H energy cannot be used as a model for all uptake locations in graphite. The presence of dangling bonds along the surface edges of graphite crystallites allows contiguous atoms on the zigzag and armchair edges to interact with each other, forming a relaxed, more stable, surface than the C* site that would arise in benzene upon removal of a hydrogen atom. In such cases, the benzene C-H bond energy must be corrected by the relaxation energy to account for this improved stability of the RCS. (Kanashenko 1996) estimated that the relaxation energy is about 1.05 eV/ atom (for both zig zag and armchair graphene edges), leading to a reduction of the hydrogen uptake enthalpy as in Equation 5.36.

$$\Delta H_{chem,2} = \Delta H_{chem,1} - 2(-1.05\ eV) = -2.3\ eV/H_2. \qquad 5.36$$

Therefore, two distinct uptake enthalpies are defined, depending on whether carbon atoms have a benzene-like interaction with hydrogen or manifest the stabilizing tendency to interact with each other. Kanashenko denominated the former type of sites as *Trap 1* and the latter as *Trap 2*. *Trap 1* sites correspond to carbon atoms at the edge of interstitial loops between graphene planes, while *Trap 2* sites are represented by carbon atoms at carbon edges. For both sites, hydrogen uptake is an exothermic process. Atsumi has performed several thermal desorption experiments assuming the presence of both traps identified by Kanashenko, producing results that are compatible with the hypothesis of two types of trapping sites at the postulated uptake enthalpies (Atsumi et al. 2013b; Atsumi and Tauchi 2003).

More recently, several authors have used ab-initio modeling to study uptake of hydrogen on distinct crystallite surfaces, the armchair edge and the zigzag edge, either including or neglecting the effect of relaxation due to the reconstruction of dangling bonds (Diño et al. 2004; Lechner et al. 2018; Sha and Jackson 2004; Yang and Yang 2002). These studies show that *Trap 1* uptake enthalpy is compatible with carbon atoms on non-reconstructed armchair and zigzag edges, and that *Trap 2* sites are compatible with carbon atoms on both reconstructed armchair and zigzag edges.

An additional possibility for uptake is physisorption of hydrogen atoms and molecules on the basal plane. (Kanashenko 1996) defined the atomic physisorption as *true solubility* and estimated the reaction to be endothermic, with an enthalpy of $2.5\ eV/H_2$. Atsumi referred to this mechanism of uptake as a *solid solution* of hydrogen in graphite (Atsumi et al. 2013a). Ab-initio modeling by (Ferullo et al. 2010; Jeloaica and Sidis 1999; Sha and Jackson 2004) found atomic physisorption on the basal plane to be endothermic. Physisorption of the hydrogen molecule should be weakly

exothermic (Costanzo et al. 2012; Darvish Ganji et al. 2015; Rubeš et al. 2010). (Jeloaica and Sidis 1999; Lechner et al. 2018) found that hydrogen could chemisorb on the basal plane, lifting a carbon atom out of the graphene plane. The chemisorption on the basal plane is endothermic with calculated uptake enthalpies of 2.9-3.3 eV/H_2.

Hydrogen atoms may also uptake at lattice defects, and different types of point defects take place in graphite because of neutron irradiation. (Letardi et al. 2002) studied hydrogen uptake on Stone-Wales defects and calculated that the C-H binding energy at such defects is 2.5 eV/H_2. This would lead to an uptake enthalpy of -0.5 eV/H_2. In the event of irradiation with sufficiently energetic neutrons, interstitial-vacancy pairs are formed in graphite. A first study of uptake on vacancies was performed by (Kanashenko 1996) and estimated an enthalpy of uptake equal to 0.1 eV/H_2. On the contrary, (Lehtinen et al. 2004) calculated that hydrogen chemisorbs exothermically on monovacancies and divacancies. According to (Lechner et al. 2018), two types of monovacancies are possible in graphite: α-vacancies sitting on top of the carbon atom of the plane below and β-vacancies sitting on top of six-C ring of the underlying plane. The predicted uptake enthalpies for the two cases are very similar, approximately -3.8 eV/H_2. Moreover, Lechner estimated an enthalpy of uptake of -1.0 eV/H_2 for divacancies.

In conclusion, uptake of hydrogen in graphite is not characterized by a unique enthalpy, however, enthalpies are concentrated around certain values. In particular, monovacancies, interstitial loops, and non-reconstructed sites on armchair and zigzag edges have enthalpies around -4 eV/ H_2 (from -3.8 eV/ H_2 to -5.5 eV/ H_2, with the exception of (Yang and Yang 2002)); reconstructed sites and divacancies have enthalpies around -2 eV/ H_2 (from -3.3 eV/ H_2 to -0.8 eV/ H_2); molecular physisorption on the basal plane and uptake Stone-Wales defect sites have slightly negative enthalpies (above - 0.5 eV/ H_2). Chemisorption and atomic physisorption on the defect-free basal surface are endothermic processes. These uptake sites appear as multiple desorption peaks in thermal desorption spectra, discussed in detail in Section 5.2.7.

5.2.3   Uptake capacity across diverse graphite grades

In uptake experiments, the uptake capacity of hydrogen isotopes in graphite, i.e., the maximum hydrogen concentration that can be achieved in the experiment, is highly variable depending on the conditions at which the uptake experiments are performed, such as uptake temperature and pressure (i.e., partial pressure of the hydrogen isotope), duration of exposure, radiation field, and properties of the graphite. Measuring the uptake capacity of graphite exposed to hydrogen gas has been performed by many authors under a variety of conditions (Figure 5.11), yielding heterogeneous results (Table 5.12). It should be noted that the uptake capacities estimated in such studies may be different from the actual solubilities of the investigated graphite, as thermal equilibrium might not have been reached in some cases.

Table 5.12: High temperature uptake capacity for hydrogen isotopes in graphite (ordered by [H/C] values, which are also shown in Figure 5.11).

(a) Unirradiated graphite

Graphite Type	Uptake Temperature	Sample size	Partial Pressure	Duration of exposure	Fluence	Graphite Density	BET Surface Area	Isotope studied	Reported Total Porosity[a] α_T	H$_2$ in total porosity[b] [H/C]$_{pores}$	Total Hydrogen Uptake [H/C]	[H/C] normalized to BET Surface Area	Source number	Source
	(K)	(cm^3)	(Pa)	(h)	(n/m^2)	(g/cm^3)	(m^2/g)		(%)	(appm)	(appm)	(μmol/m^2)		
ISO-880U	1273	-	101,000	0.5-30	Unirradiated	1.90	1.3 [c]	H	14-18 [c]	9.8	640	41.0	[1]	(Atsumi et al. 1994)
POCO AXF-5Q	1273	-	101,000	0.5-30	Unirradiated	1.83	0.3 [c]	H	-	12.1	490	136.1	[1]	(Atsumi et al. 1994)
ISO-630U	1273	-	101,000	0.5-30	Unirradiated	1.82 [c]	0.8 [c]	H	12-14 [c]	12.5	390	40.6	[1]	(Atsumi et al. 1994)
S 1611	1123	-	0.1 to 10	10	Unirradiated	1.77	3.2	H, T	15.2	0.0	0.7 to 373	0.0 to 9.7	[2]	(Kwast et al. 1994)
T-6P	1273	-	101,000	0.5-30	Unirradiated	1.91 [c]	0.8 [c]	H	9 [c]	9.5	360	37.5	[1]	(Atsumi et al. 1994)
ISO-880U	973		60,000	5	Unirradiated	1.90 [c]	1.3 [c]	D	14-18 [c]	7.6	300	19.3	[3]	(Atsumi et al. 1988)
AX-650K	1273	-	101,000	0.5-30	Unirradiated	1.82 [c]	0.5 [c]	H	16-18 [c]	12.5	300	50.0	[1]	(Atsumi et al. 1994)
AX-750K	1273	-	101,000	0.5-30	Unirradiated	-	-	H	-	-	290	-	[1]	(Atsumi et al. 1994)
S 1611	673 -1323	-	80,000	10	Unirradiated	1.77	3.2	H, T	15.2	11.3 -21.3	14.4 to 277	0.4 to 7.2	[4]	(Kwast et al. 1996)
ISO-880U	1073		60,000	5	Unirradiated	1.90 [c]	1.3 [c]	D	14-18 [c]	6.9	260	16.7	[3]	(Atsumi et al. 1988)
AX-280K	1273	-	101,000	0.5-30	Unirradiated	1.77 [c]	0.6 [c]	H	16-18 [c]	14.2	260	36.1	[1]	(Atsumi et al. 1994)
ETP-10	1273	-	101,000	0.5-30	Unirradiated	1.75 [c]	0.4 [c]	H	13 [c]	15.0	230	47.9	[1]	(Atsumi et al. 1994)
ISO-880U	1173		60,000	5	Unirradiated	1.90 [c]	1.3 [c]	D	14-18 [c]	6.3	230	14.8	[3]	(Atsumi et al. 1988)
Nuclear Grade	1023	-	80	-	Unirradiated	-	3.0	H	-	-	228	6.3	[5]	(Thomas 1961)
ISO-880U	1273	-	10,000 to 48,000	0.5-30	Unirradiated	1.90 [c]	1.3 [c]	H	14-18 [c]	1.0 - 4.7	160 to 220	10.3 to 14.1	[6]	(Atsumi 2003)
IG-430U	1273	-	101,000	0.5-30	Unirradiated	1.82	-	H	-	12.5	213	-	[1]	(Atsumi et al. 1994)
ISO-880U	873		60,000	5	Unirradiated	1.90 [c]	1.3 [c]	D	14-18 [c]	8.5	190	12.2	[3]	(Atsumi et al. 1988)
A3	1173	1.57	164	80	Unirradiated	1.7	0.57	D	25	0.0	140	20.5	[7]	(Hoinkis 1991a)

Graphite Type	Uptake Temperature (K)	Sample size (cm³)	Partial Pressure (Pa)	Duration of exposure (h)	Fluence (n/m²)	Graphite Density [f] (g/cm³)	BET Surface Area [f] (m²/g)	Isotope studied	Reported Total Porosity [f] α_T (%)	H$_2$ in total porosity [b] [H/C]$_{pores}$ (appm)	Total Hydrogen Uptake [H/C] (appm)	Increase in [H/C] vs non-irradiated sample (-)	[H/C] normalized to BET Surface Area (μmol/m²)	Source number	Source
IG-110U	1273	-	10,1000	0.5-30	Unirradiated	1.77 [c]	0.6 [c]	H	11-12 [c]	14.2	138		19.2	[1]	(Atsumi et al. 1994)
A3	973	0.5	260 to 22,000	> 0.1	Unirradiated	1.7 [d]	0.57 [d]	H	-	0.1 to 4.8	10 to 124		1.5 to 18.0	[8]	(Wu et al. 2020a)
IG-110U	1273	-	3,600 to 40,000	0.5-30	Unirradiated	1.77 [c]	0.6 [c]	H	11-12 [c]	0.5 - 5.6	70 to 100		9.7 to 13.9	[9]	(Atsumi et al. 2011)
A3	1173	1.57	74	-	Unirradiated	1.7	0.57	D	25	0.0	78		11.4	[10]	(Hoinkis 1991b)
Nuclear TSP	1193	3.21	2,400	1	Unirradiated	1.7	0.30	H	25	0.4	64		17.8	[11]	(Redmond and Walker 1960)
RGT - Graphite	920-1150	0.49	100,000	6	Unirradiated	2.1	-	H	-	4.5	40-43		-	[12]	(Tazhibaeva et al. 1996)
IG-110U	1273	-	100,000	0.5-20	Unirradiated	1.77 [c]	0.6 [c]	H	11-12 [c]	1.4	42		5.8	[13]	(Atsumi and Iseki 2000)
IG-110U	973	0.5	260 to 22,000	> 0.1	Unirradiated	1.77 [c]	0.6 [c]	H	11-12 [c]	0.0 to 4.1	2 to 39		0.3 to 5.4	[8]	(Wu et al. 2020a)
ISO-880U	773		60,000	5	Unirradiated	1.90	1.3	D	14-18 [c]	9.6	30		1.9	[3]	(Atsumi et al. 1988)
IG-110U	623	0.10	-	1.5	Unirradiated	1.77	0.257	H	18	-	27.6		8.9	[14]	(Deng et al. 2019)
A3	1173	1.57	7.6	-	Unirradiated	1.70	0.57	D	25	0.0	24		3.5	[9]	(Hoinkis 1991b)
NG-CT-10	623	0.10	-	1.5	Unirradiated	1.90	0.238	H	14	-	16.4		5.7	[14]	(Deng et al. 2019)
POCO AXF-5Q	1473	0.59	0.66-66	1.5	Unirradiated	1.84	1	D	-	0.0	16		1.3	[15]	(Causey et al. 1986)
POCO AXF-5Q	1170	0.004	133	2	Unirradiated	1.83 [c]	-	D	-	0.0	14		-	[16]	(Markin et al. 1997)
HOPG	1273	0.20	13,300	40	Unirradiated	-	-	H	-	-	14		-	[17]	(Shirasu et al. 1993)
NBG-18	623	0.10	-	1.5	Unirradiated	1.85	0.192	H	12	-	9.6		4.2	[14]	(Deng et al. 2019)
A681 [e]	1023	1.00	0.14	4	Unirradiated	-	0.20	T	-	-	0.39		0.16	[18]	(Strehlow 1986)
POCO AXF-5Q [e]	1023	1.00	0.14	4	Unirradiated	1.83	0.25	T	-	0.0	0.11		0.04	[18]	(Strehlow 1986)
CBG [e]	1023	1.00	0.14	4	Unirradiated	-	0.27	T	-	-	0.03		0.01	[18]	(Strehlow 1986)

(a) Irradiated graphite

ISO-880U	1273	-	10,000	> 16	up to 3.9 10^{23}	1.90 [c]	1.3 [c]	H	14-18 [c]	1.0	up to 2.6 10^4	up to ×13	166.7	[19]	(Atsumi et al. 2009b)
IG-430U	1273	-	10,000	> 16	up to 5.4 10^{24}	1.82	-	H	-	1.2	up to 2.0 10^4	up to ×286	-	[19]	(Atsumi et al. 2009b)
IG-110U	1273	-	10,000	> 16	up to 1.9 10^{24}	1.77 [c]	0.6 [c]	H	11-12 [c]	1.4	up to 1.1 10^4	up to ×116	1527.8	[19]	(Atsumi et al. 2009b)
ETP-10	1273	-	up to 20,000	-	1.9 10^{24}	1.75 [c]	0.4 [c]	H	13 [c]	3.0	10^4	×44	2083.3	[20]	(Atsumi et al. 1992)
IG-430U	1273	-	up to 20,000	-	up to 5.4 10^{24}	1.82	-	H	-	2.5	up to 9 10^3	up to ×35	-	[20]	(Atsumi et al. 1992)
IG-110U	1273	-	up to 20,000	-	1.9 10^{24}	1.77 [c]	0.6 [c]	H	11-12 [c]	2.8	7 10^3	×44	972.2	[20]	(Atsumi et al. 1992)
S 1611	673-1573	-	10,000	10	1.4 10^{23}-1.4 10^{24}	1.77	3.2	H,T	15.2	0.0-2.7	62-1469	up to ×4	1.6	[2]	(Kwast et al. 1994)
S 1611	673-1023	-	80,000	10	1.4 10^{23}-1.4 10^{24}	1.77	3.2	H,T	15.2	14.0 - 21.3	179-1201	up to ×5	4.7 to 31.3	[4]	(Kwast et al. 1996)
T-6P	1273	-	10,000	> 5	3.9 10^{23}	1.91 [c]	0.8 [c]	H	9 [c]	0.9	1.1 10^3	up to ×28	114.6	[21]	(Atsumi et al. 2007)
IG-430U	1273	-	10,000	> 5	3.9 10^{23}	1.82	-	H	-	1.2	700	up to ×35	-	[21]	(Atsumi et al. 2007)
H451	1473	-	101,325	3	1.5 10^{22}	-	-	D	-	.	650	×33	-	[22]	(Wampler et al. 1990)
ISO-880U	1273	-	10,000	> 5	3.9 10^{23}	1.90 [c]	1.3 [c]	H	14-18 [c]	1.0	400	up to ×7	25.6	[21]	(Atsumi et al. 2007)
T-4MP	1273	-	10,000	> 5	3.9 10^{23}	1.78 [c]	0.4 [c]	H	15 [c]	1.4	300	up to ×14	62.5	[21]	(Atsumi et al. 2007)
IG-110U	1273	-	10,000	> 5	3.9 10^{23}	1.77 [c]	0.6 [c]	H	11-12 [c]	1.4	200	up to ×12	27.8	[21]	(Atsumi et al. 2007)
ETP-10	1273	-	10,000	> 5	3.9 10^{23}	1.75 [c]	0.4 [c]	H	13 [c]	1.5	200	up to ×6	41.7	[21]	(Atsumi et al. 2007)
RGT	920-1150	0.49	100,000	6	3.2 10^{22}	-	-	H	-	-	54.6-94.3	×2.2	-	[12]	(Tazhibaeva et al. 1996)

[a] See original sources for additional information on the techniques used; various techniques are used for determination of total porosity.

[b] Hydrogen uptake in closed porosity computed with the ideal gas law using uptake pressure and temperature and the reported density.

[c] From (Yamashina and Hino 1989)

[d] Using value from (Hoinkis 1991a)

[e] BET surface area, hydrogen uptake and hydrogen uptake specific to BET surface area averaged over samples of the same material in Table 2 from (Strehlow 1986)

[f] Graphite density, BET surface area and porosity of non-irradiated samples

Figure content (scatter plot data labels):

S 1611 / 1469 / [2]

POCO AXF-5Q / 16 / [15]   POCO AXF-5Q / 16 / [15]

IG-110U / 100 / [9]
IG-430U / 213 / [1]
IG-110U / 138 / [1]   H451 / 650 / [22]
IG-110U / 42 / [13]
AX-280K / 260 / [1]
AX-650K / 300 / [1]
ISO-880U / 640 / [1]   S 1611 / 232 / [4]

ISO-880U / 160 / [6]
ISO-880U / 400 / [1]   ISO-880U / 220 / [6]
T-6P / 1100 / [21]
IG-110U / 70 / [9]   HOPG / 14 / [18]   ISO-880U / 2600 / [1]   T-6P / 360 / [1]
ISO-880U / [19]

A3 / 78 / [10]   A3 / 140 / [7]
A3 / 24 / [10]   POCO AXF-5Q / 14 / [16]   TSP / 64 / [10]   ETP-10 / 10000 / [21]
ISO-880U / 230 / [3]   RGT / 43 / [12]
S 1611 / 0.7 / [2]   S 1611 / 373 / [2]   RGT / 94.3 / [12]

A681d / 0.39 / [18]   ISO-880U / 260 / [3]
POCO AXF-5Q / 0.11 / [18]   Nuclear Grade / 228 / [5]   S 1611 / 1201 / [4]
CBG / 0.03 / [18]   A3 / 10 / [8]   IG-110U / 39 / [8]   ISO-880U / 300 / [3]
IG-110U / 2 / [8]   A3 / 124 / [8]
RGT / 40 / [12]
RGT / 54.6 / [12]
ISO-880U / 190 / [3]

ISO-880U / 30 / [3]

S 1611 / 14.4 / [4]
S 1611 / 62 / [2]   S 1611 / 179 / [4]

Legend:
● Non-irradiated graphite
□ Irradiated graphite
[H/C] (appm)   Reference
POCO AXF-5Q / 16 / [15]
Graphite Grade

Axes: Uptake Temperature (K) vs Partial Pressure (Pa); right axis Uptake Temperature (°C)

Figure 5.11: High temperature uptake capacities for hydrogen isotopes in graphite. The references in square brackets corresponds to the studies cited in Table 5.12.

Multiple authors have highlighted correlations of hydrogen uptake with measurable characteristics of graphite, such as crystallite size, degree of graphitization, BET surface area and porosity. Table 5.13 summarizes these relationships; specific correlation equations are not provided in the original sources.

Table 5.13: Correlations of hydrogen uptake capacity with microstructural and porosity characteristics of graphite

Variable	Hydrogen uptake increases with….	Source
Crystallite Size (as determined by XRD)	lower crystallite size	(Atsumi et al. 1996; Orimo et al. 2001)
Degree of Graphitization (as determined by XRD)	lower degree of graphitization	(Atsumi et al. 1994, 1996; Saeki 1981)
Crystallite Edge Surface Area (as determined by XRD)	larger crystallite edge surface area	(Atsumi et al. 2011; Atsumi and Tauchi 2003)
Raman FWHM(D)	higher FWHM of D band in graphite Raman spectrum	(Wu et al. 2020a)
BET Surface Area	larger BET surface area	(Atsumi et al. 2011; Atsumi and Tauchi 2003; Causey et al. 2012; Wang et al. 2011)
Crystallite Edge Surface Area (as determined by XRD)	larger crystallite edge surface area (Hydrogen chemisorbed in Trap 1 and Trap 2)	(Atsumi et al. 2015)
BET Surface Area	larger BET surface area (Hydrogen chemisorbed in Trap 1 and Trap 2)	(Atsumi et al. 2015)
Surface Area of Pores with Diameter < 0.4 nm (as determined by BET)	larger surface area of pores with diameter < 0.4 nm	(Lam et al. 2018)

In summary, the hydrogen uptake experiments have provided highly scattered results depending on thermodynamic conditions (temperature and partial pressure) and external conditions (duration of exposure, presence of irradiation) (Table 5.12). It has also been postulated that hydrogen uptake capacity is correlated with measurable characteristics of the graphite such as degree of graphitization, BET surface area and crystallite size (Table 5.13).

165

5.2.4 Production and desorption of methane, water

It is possible, in principle, that hydrocarbon compounds and water formed from trace contaminant oxygen present in graphite are desorbed alongside with hydrogen gas, during thermal desorption experiments of hydrogen from graphite. Experimental data, summarized in Table 5.14, indicate that release of hydrocarbons or water spans from zero to ten mole % of the total release of hydrogen.

Table 5.14: Hydrocarbon and water desorption from graphite samples charged with hydrogen isotopes

Graphite	Degassing: Temperature / Pressure / Duration	Uptake Temperature	Partial Pressure [Isotope]	Duration of exposure	Fluence	Hydrogen compounds studied	Desorption Temperature Interval	Reported release and comments	Ref.
	(K)/(Pa)/(h)	(K)	(Pa)	(h)	(n/m^2)		(K)		
A3	1750/ 10^{-5}/Not reported	1173	74 [D$_2$]	80	-	Hydrocarbons	Up to 1973	No release. Detection limit is not reported.	(Hoinkis 1991b)
ISO-880U	1373/ 10^{-3}/2	973	60,000 [D$_2$]	5	-	CD$_4$	Up to 1373	Less than 0.1% of total deuterium content. Temperature of desorption not reported.	(Atsumi et al. 1988)
Nanostructured graphite	Not reported/ 10^{-4}/12	Room temperature	1,000,000 [H$_2$]	1-80h	-	CH$_4$ and C$_2$H$_6$	Up to 1200	Released around 700 K, in correspondence of H$_2$ desorption peak (1% of H$_2$ release). No release at the H$_2$ peak at 1100 K.	(Orimo et al. 2001)
RGT - Graphite	450/ 10^{-7}/ Not reported	920-1150	100,000 [H$_2$]	6	3.2 10^{22}	H$_2$O	Up to 1800	H$_2$O released up to 600 K (released amount not reported).	(Tazhibaeva et al. 1996)
						CO, CO$_2$, CH3, CH$_4$, C$_2$H$_x$, C$_3$H$_x$		Release up to 1200 K. 10% of hydrogen content released in the form of hydrocarbons.	
Pechiney Q1	No degassing (only sweeping with He)	423-673	Unspecified	Unspecified	1.66 10^{25} (thermal); 1.88 10^{23} (fast)	CH$_3$T	Up to 1623	Less than 0.4% of total tritium release. Temperature of desorption not reported.	(Saeki 1981)
						HTO		10% of tritium released as HTO. HTO is released at all temperatures and follows HT's desorption profile. Hence, it might not be desorbed from the sample but formed from the reaction of the released HT with molecular oxygen in proximity of the samples	

5.2.5 Hydrogen uptake pathways

When exposed to hydrogen gas, graphite can uptake hydrogen through multiple pathways at multiple uptake sites, characterized by different reaction energies, stoichiometry, uptake capacities, and kinetics. A summary of possible pathways in graphite is here provided, along with the relevant thermodynamic governing equations.

5.2.5.1. Uptake of gas in porosity

Gas molecules of hydrogen can be stored in the pore space of graphite. As discussed in Section 5.2.7.1, hydrogen molecules reach graphite pores through networks accessible from the surface or via molecular pore diffusion. Since hydrogen molecules are small and non-polar, hydrogen can be approximated as an ideal gas at the pressures and temperature of relevance here (<1 MPa H$_2$, < 1300 °C) with an error below 0.02% (calculated using the Lemmon equation for compressibility

(Lemmon et al. 2008)). Any gas-surface interactions effects are treated separately under *solid solution* uptake. Under this approximation, the molar fraction of hydrogen in the pores to carbon atoms $[H/C]_{pores}$ can be computed using the equation of state for ideal gases (Equation 5.37):

$$[H/C]_{pores} \text{ (appm)} = \frac{M_C \alpha}{\rho R T} P_{H_2(g)} \qquad 5.37$$

where M_C is the carbon molar mass (g/mol), R is the universal gas constant in J/mol·K, T is the temperature in K, ρ is the graphite bulk density in (g/m³), $P_{H_2(g)}$ the hydrogen partial pressure in Pa, and α is the relevant (open, closed, or total) sample porosity. The concentration of trapped hydrogen increases linearly with the partial pressure of hydrogen in the atmosphere to which graphite is exposed.

5.2.5.2. *Dissociative physisorption/ Solid solution uptake*

Atomic hydrogen can physisorb on the graphite basal plane, forming a solid solution with the graphite lattice (*Atomic physisorption* in Table 5.11). Defining $C^{\#}$ the basal plane carbon atoms, the process can be described by Reaction 5.38 and by the equilibrium constant K_{sol} in Equation 5.39:

$$2C^{\#} + H_2(g) \rightarrow 2\,C^{\#} - H \qquad 5.38$$

$$K_{sol} = \frac{[C^{\#} - H]^2}{[C^{\#}]^2\, P_{H_2(g)}} \qquad 5.39$$

In this case, hydrogen uptake follows Sievert's law, i.e., it is proportional to the square root of the hydrogen partial pressure. $[H/C]_{sol}$, the molar fraction of hydrogen in solid solution to total carbon atoms is computed by Equation 5.40.

$$[H/C]_{sol}(\text{appm}) = \sqrt{K_{sol}}\, [C^{\#}/C] \sqrt{P_{H_2(g)}} \qquad 5.40$$

where $[C^{\#}/C]$ is the molar fraction of basal plane carbon atoms in graphite (in appm) and K_{sol} is expressed in Pa⁻¹.

5.2.5.3. *Dissociative chemisorption*

Chemisorption is the formation of C-H chemical bonds and can occur at RCS such as dangling bonds at graphite edges or point defects (RCS are discussed in detail in Section 5.2.2 and outlined in Table 5.11). Compared to physisorption, the enthalpy of chemisorption is generally large, and this mechanism predominates at higher temperature. Defining with C* the trapping site, the chemisorption reaction can be written as in Equation 5.41 described by the equilibrium constant K_{chem} in Equation 5.42.

$$2C^{*} + H_2(g) \rightarrow 2\,C^{*} - H \qquad 5.41$$

$$K_{chem} = \frac{[C^{*} - H]^2}{[C^{*}]^2\, P_{H_2(g)}} \qquad 5.42$$

As the in the case of hydrogen in solid solution, the equilibrium reaction suggests the concentration of chemisorbed hydrogen to be proportional to the square root of the hydrogen partial pressure

(Atsumi et al. 1994). The equilibrium constant is expressed as a function of temperature as Equation 5.43:

$$K_{chem} = \exp\left(-\frac{\Delta H_{chem}}{k_b T}\right) \exp\left(\frac{\Delta S_{chem}}{k_b}\right) \qquad 5.43$$

where ΔH_{chem} and ΔS_{chem} are the enthalpy and entropy of reaction 5.41 and k_b is the Boltzmann's constant. The molar fraction of hydrogen chemisorbed in trapping sites to carbon atoms, $[H/C]_{chem}$, can then be computed as in Equation 5.44:

$$[H/C]_{chem}(\text{appm}) = [C^*/C] \left(K_{chem} P_{H_2(g)}\right)^{1/2} \qquad 5.44$$

where $[C^*/C]$ is the molar fraction of trapping sites in graphite (in appm) and K_{chem} is expressed in Pa^{-1}. According to Equation 5.42 and Equation 5.43, at constant temperature T, the occupancy $\epsilon \equiv \frac{[C^*-H]}{[C^*-H]+[C^*]}$ of the RCS C* follows a Langmuir isotherm (Equation 5.45):

$$\epsilon = \frac{1}{1 + \left(K_{chem} P_{H_2(g)}\right)^{-1/2}} \qquad 5.45$$

Alternatively, two hydrogen atoms might bind to the same carbon atom at a graphite edge (shown in the second graphene plane from the bottom in Figure 5.12 and described by Reaction 5.46, with the carbon atom hybridizing to sp^3 (Lechner et al. 2018).

$$C^* + H_2(g) \rightarrow C^* - H_2 \qquad 5.46$$

sp^3 hybridization allows for an uptake of up to three hydrogen atoms per carbon (Reaction 5.47). A *dangling carbon atom* is a carbon atom that is sp^3 hybridized and has one C-C bond; therefore, the dangling carbon atoms have three other bonds available to form C-H bonds. An example of a dangling carbon atom binding with three hydrogen atoms is shown in the bottom graphene plane of Figure 5.12.

$$C^* + 3/2\, H_2(g) \rightarrow C^* - H_3 \qquad 5.47$$
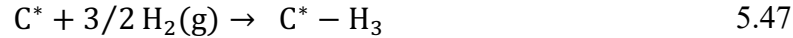
(Mandeltort et al. 2012) observed experimentally the reaction of the reaction of methyl (- CH$_3$) radicals with the basal plane of HOPG. The carbon atom in the methyl group is an example of *dangling carbon atom* . Another evidence of a dangling carbon atom bond with three hydrogen atoms is provided by hydrogen bombardment studies. (Vietzke et al. 1984) showed that bombarding graphite with hydrogen ions and atoms leads to the formation of the (-CH$_3$) radical group. Graphite may also present carboxyl (-COOH) groups as a result of oxidation (shown in second graphene plane from top in Figure 5.12) (Otake and Jenkins 1993). However, it is unlikely that the carboxyl group is converted to a methyl group by adsorbing hydrogen (Reaction 5.48), as the ΔG of the reaction is of approximately 350 kJ/mol in the interval of 0 °C to 1000 °C (Computed via HSC Chemistry v9.6.1).

$$-COOH + H_2 \rightarrow -CH_3 + O_2 \;;\;\; \Delta G > 0 \qquad 5.48$$

In summary, when exposed to hydrogen gas, graphite can uptake hydrogen through three different mechanisms: (a) uptake of gas in closed porosity; (b) physisorption/ solid solution on the graphite basal plane; (c) dissociative chemisorption at RCS. The stoichiometry of each uptake reaction determines the functional form of the dependence of occupancy on hydrogen partial pressure (e.g., linear, square root). The total uptake capacity will be a summation of hydrogen uptaken via each of these mechanisms:

$$[H/C] = [H/C]_{pores} + [H/C]_{sol} + [H/C]_{chem} \qquad\qquad 5.49$$

5.2.6 Models for hydrogen uptake capacities

The uptake capacities in Table 5.12 have been described by several authors using thermodynamic models based on single uptake pathways. (Shirasu et al. 1993) used physisorption to describe the overall uptake of hydrogen in graphite and estimated an enthalpy of solution ΔH_{uptake} for it. Their experiments indicate that the equilibrium concentration of hydrogen in graphite increased linearly with the square root pressure, closely following Sievert's law. Fitting the experimental results, they estimated different equilibrium constants across diverse graphite types (Equation 5.50):

$$ln\, K_{uptake} = -\frac{\Delta G_{uptake}}{RT} = (\Delta S_{uptake}/k_B) + \frac{(-\Delta H_{uptake}/k_b)}{T} \qquad\qquad 5.50$$

where k_b is the Boltzmann's constant, ΔG_{uptake}, ΔH_{uptake} and ΔS_{uptake} the Gibbs free energy, the enthalpy, and the entropy of uptake, respectively. Such values are reported in Table 5.15. ΔG_{uptake}, ΔH_{uptake} and ΔS_{uptake} in (Shirasu et al. 1993) refer to the overall uptake of hydrogen in graphite, and not to the uptake of hydrogen on a specific type of RCS. Since hydrogen is not only uptaken by highly energetic trapping sites but can also be physisorbed at lower enthalpies and trapped in closed porosity, the resulting ΔH_{uptake} is lower than the values listed in Table 5.11 for Trap 1 and Trap 2 sites.

Table 5.15: Thermodynamic coefficients based on the dependence on temperature of the equilibrium constant for hydrogen uptake in graphite. From (Shirasu et al. 1993)

Graphite	$\Delta S_{uptake}/k_b$ [a]	ΔH_{uptake}	Temperature range	Pressure range
	$(-/H_2)$	(eV/H_2)	(K)	(Pa)
IG-110	-29.0	-0.38	973-1273	$0 - (2)10^4$
POCO AXF-5Q	-31.2	-0.44	973-1273	$0 - (2)10^4$
ISO-880U	-31.6	-0.46	973-1173	$0 - (2)10^4$
ISO-880U	-37.0	-1.00	1173-1273	$0 - (2)10^4$
EK 98	-29.4	-0.28	973-1073	$0 - (2)10^4$
EK 98	-37.0	-0.98	1073-1273	$0 - (2)10^4$

[a] (Atsumi and Kondo 2018) used a value of $\Delta S_{sol}/k_b$ of -31.2 for uptake of a H_2 molecule (from (Speight 2005)).

In early studies, Atsumi et al. maintained that hydrogen uptake in graphite follows Sievert's law, and measured an enthalpy of solution of -0.4 eV/H_2 (Atsumi et al. 1988). Later on, in (Atsumi et al. 1994), the hypothesis that the square root dependence on pressure is always followed was rejected and, based on thermal desorption studies, a model involving multiple pathways for uptake is proposed. The proposed model converges to Sieverts' law at pressures below 30 kPa and temperatures between 973 K and 1323 K.

(Kanashenko 1996) found that Sieverts' law is followed at temperatures above 1273 K and for pressures from 2.5 kPa to 22.5 kPa but that at lower temperatures the uptake is almost independent on pressure due to saturation of uptake sites. The author attributed the difference to uptake kinetics, arguing that uptake in (Atsumi et al. 1994) was incomplete.

Another incongruence with Sieverts' law was found by (Kwast et al. 1996). In the study, the concentration of hydrogen in S 1611 graphite exposed to hydrogen gas at 80 kPa and temperatures between 673 K and 1323 K was shown to increase for loading temperature up to 1023 K and to

decrease only after that. However, the duration of exposure in (Kwast et al. 1996) was of 10 hours, which may have led to incomplete uptake at low temperatures.

In summary, modelling hydrogen uptake as simple physisorption yields inaccurate results at certain thermodynamic conditions, such as at very low (below 2 – 3 kPa) and very high (above 25 – 30 kPa) pressures (Atsumi et al. 1994; Kanashenko 1996). Thermal desorption experiments on hydrogen-loaded graphite are characterized by multiple desorption peaks, which hint at the presence of multiple mechanisms governing hydrogen-graphite interaction. To account for these deviations, models involving multiple uptake pathways were developed and are currently used to describe hydrogen-graphite interaction at high temperature and are further discussed in the following section.

5.2.7 Thermal desorption spectra

Thermal desorption spectroscopy (TDS) is an experimental technique that consists in heating a sample at a constant temperature ramp rate under vacuum and measuring the release of gas as a function of temperature. In hydrogen-graphite studies, TDS experiments are frequently performed in conjunction with uptake experiments. In the uptake experiment, a graphite sample is typically outgassed at high temperature and then exposed to hydrogen gas. The extent of hydrogen uptake and the distribution of hydrogen across RCS depend on the conditions of the sample (size, grade, pre-treatments) and on the conditions of uptake (temperature, hydrogen partial pressure and duration of exposure). After the uptake experiment is concluded, the samples are quenched to room temperature and placed in a vacuum (pressures below 10^{-4} Pa, typically). The thermal desorption experiment is then performed by applying a constant heating rate to the sample. Heating rates may vary from as little as 0.5 K/min to more than 6 K/min (Atsumi et al. 2013b). As the sample is heated up, the uptaken gas is progressively released. The plot of the current or the flow rate of gas release against temperature constitutes the thermal desorption spectrum.

Atsumi et al. has performed TDS experiments with hydrogen and deuterium on several graphite grades and carbon fiber composites previously charged at temperatures from 573 to 1323 K and hydrogen partial pressures from 83 Pa to 63.3 kPa. (Atsumi et al. 1988; Atsumi 2002a, 2003; Atsumi et al. 2011, 2013a; b; Atsumi and Kondo 2018). In the remainder of this section, the different hydrogen isotopes will be used interchangeably, and results for a specific isotope will be considered valid for the element in general. Of all carbon materials explored by Atsumi et al., isotropic graphite grades (e.g., IG-110, ISO-880, ISO-430, ISO-630) are the most interesting for application to fusion and fission nuclear reactors. Orimo et al. has also performed thermal desorption, up to 600K, of hydrogen and deuterium from nanostructured graphite milled for 80 hours and previously charged with a hydrogen partial pressure of 1.0 MPa (uptake temperature not reported) (Orimo et al. 2001).

Figure 5.12 shows an example deuterium TDS from ISO-880U graphite (Atsumi and Kondo 2018). TDS of hydrogen-charged isotropic graphite grades show four distinct peaks; the peaks are named Peak 1, Peak 2, Peak 4 and Peak 5 in order of increasing desorption temperature (Atsumi et al. 2013a). Each peak is attributed to a different desorption mode. Peak 1 is attributed to molecular desorption of H_2 from closed graphite pores. Peak 2 is attributed to desorption of hydrogen atoms dissolved as a solid solution on the basal planes of graphite (Atsumi et al. 2013b). Peak 4 is identified as de-trapping from reconstructed crystallite edge sites, which are named Trap 2. Peak 5 is identified as de-trapping from interstitial cluster loop edges (Atsumi and Kondo 2018) and non-reconstructed crystallite edge sites, which are named Trap 1. In between of Peak 2 and Peak

4, an additional peak (Peak 3) is present in the TDS of a few other carbonaceous materials, (Atsumi et al. 2015). Peak 3 has not been extensively discussed by Atsumi et al. Since the temperature at which it is observed changes sample by sample, it was speculated to be originated by desorption from smaller grains or from binder materials (Atsumi et al. 2015). The interpretation of the data from each of the TDS peaks is discussed in further detail in the subsequent sections.

Sources: [1] (Atsumi, 2003) [2] (Kanashenko,1996) [3] (Sha and Jackson, 2004) [4] (Lechner, Baranek and Vach, 2018) [5] (Causey, Baskes and Wilson, 1989) [6] (Hoinkis, 1991a) [7] (Atsumi and Kondo, 2018) [8] (Atsumi, Tanabe and Shikama, 2015)
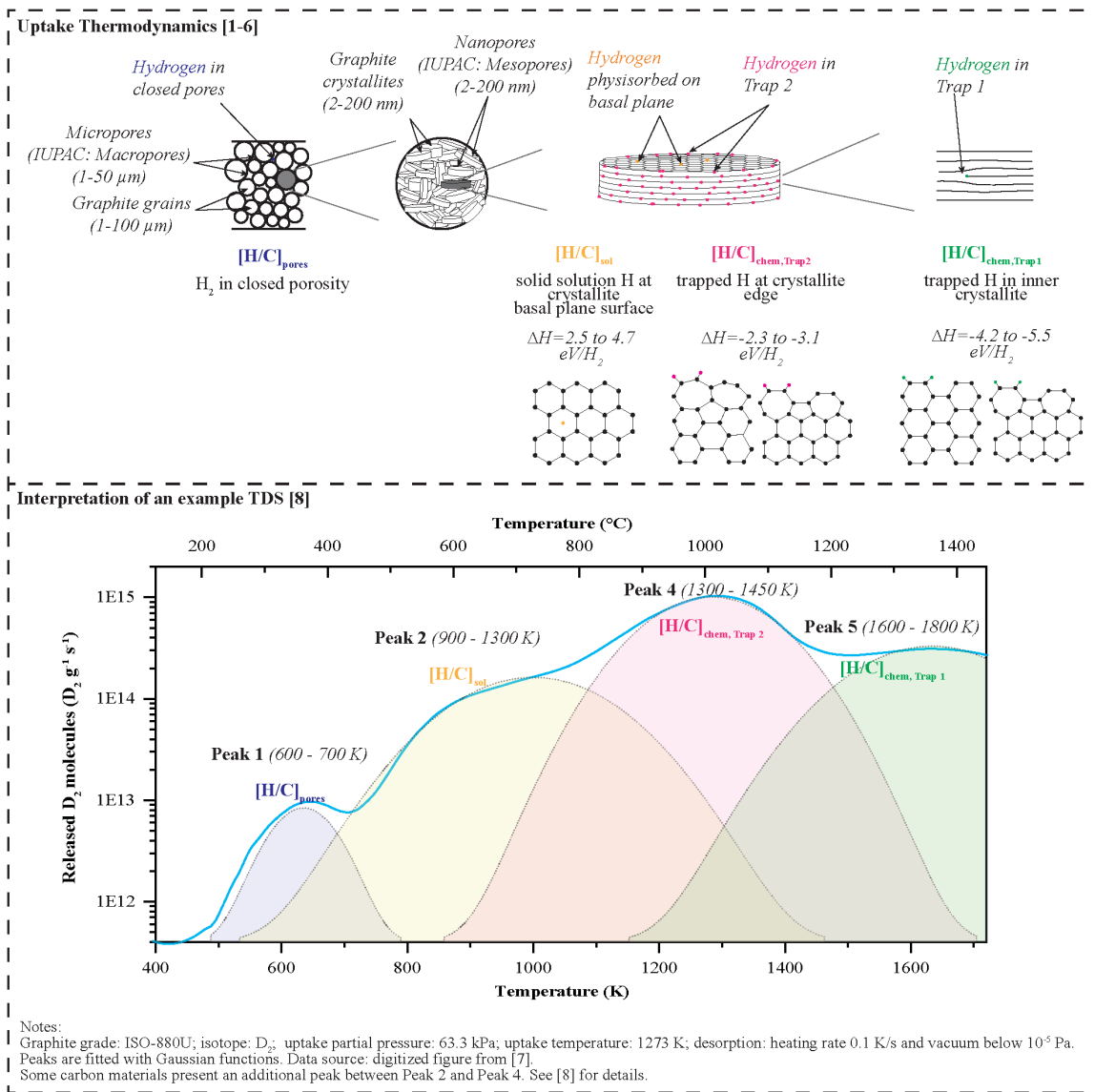
Figure 5.12: Pathways, sites, and uptake enthalpies for hydrogen uptake in graphite; from left to right: macroscopic scale to molecular scale. The interpretation of an example TDS is shown, as an experimental method that probes hydrogen distribution in different types of RCS.

5.2.7.1. Peak 1: desorption from closed pores

Peak 1 (600-700 K) corresponds to hydrogen molecules desorbing from closed porosity (Atsumi et al. 2013a), or small graphite pores (Orimo et al. 2001). Despite being inaccessible to gas at room

temperature, it has been observed that closed porosity can be accessed by gas at high temperature and pressure: (Hoinkis 1988) showed that He gas at 1073 K and 4 MPa can penetrate pores that were inaccessible at 300 K and 0.1 MPa. This phenomenon was attributed to the anisotropic thermal expansion of graphite grains and the elastic compression of the closed pores and the grains caused by the helium pressure. (Hoinkis 1988) argued that the effect could occur also at low pressures but experimental data at low pressures were not collected. The total pressures used in hydrogen uptake experiments are lower than the 4 MPa used in (Hoinkis 1988). For example, (Atsumi et al. 1988) employed total pressures of 5-95 kPa and (Hoinkis 1991a) employed a total pressure of 10 kPa. At these low pressures, it is not clear if this phenomenon takes place. Hydrogen molecules could, in fact, reach closed porosity via pore diffusion. TDS of graphite exposed to deuterium at (partial and total) pressures of 5-95 kPa and temperatures up to 900 °C showed that hydrogen leaves the closed porosity via pore diffusion at temperatures of 300-500 °C (Atsumi et al. 1988).

Peak 1 does not include the contribution of hydrogen uptaken in open porosity, as open porosity hydrogen would have degassed already at room temperature. The area of the peak (hence the amount of stored hydrogen) increases linearly with the uptake pressure (Figure 5.13(a)), as proposed in Equation 5.37. The area of the peak increases with a longer uptake time, until saturation. (Atsumi and Kondo 2018) reported that Peak 1 intensity and area do not vary with different uptake temperatures. This suggests that the uptake mechanism does not include a chemical bonding, which would exhibit an exponential dependence on uptake temperature. However, the inverse dependence of the peak area on the uptake temperature predicted by Equation 5.37 is not observed either. This suggests that the non-interacting ideal gas might not be the most accurate model for H_2 in the graphite pores, or that there are other mechanisms at play that are influenced by temperature and that counterbalance the $1/T$ dependence of the ideal gas law.

5.2.7.2. *Peak 2: desorption from basal plane/solid solution*

Peak 2 (900-1300 K) is ascribed to hydrogen atoms dissolved as solid solution in graphite (Atsumi et al. 2013a). The amount of deuterium gas released under this peak depends on the square root of the uptake pressure, indicating that hydrogen is uptaken in atomic form (Equation 5.38, Figure 5.13(b)). Increasing the uptake temperature causes a reduction of the area and the intensity of the peak, suggesting that the pathway involves a chemical bonding (Reaction 5.40) (Atsumi and Kondo 2018). Peak 2 is present also in the TDS of (Orimo et al. 2001), approximately at 700 °C. Orimo et al. attributed the peak to hydrogen/ deuterium chemically bond to graphite in atomic form. This uptake mechanism was termed differently by (Lechner et al. 2018) and (Kanashenko 1996), who referred to it as *true solubility* in the basal plane of graphite.

Another evidence of a desorption peak around 600 – 700 °C was provided by (Deng et al. 2019). (Deng et al. 2019) studied desorption of hydrogen from three grades of nuclear graphite (IG-110U, NBG-18 and NG-CT-10) charged at 350 °C. The desorption experiment was performed at temperatures below 700 °C. The authors did not provide a TDS in their research but observed that uptaken hydrogen could be divided in "weakly adsorbed hydrogen", which is desorbed with helium purging at room temperature and "strongly adsorbed hydrogen", which starts to desorb at T > 600 °C. Deng et al. showed that 14% to 71% of the strongly adsorbed hydrogen was desorbed at temperature between 600 °C and 700 °C (Peak 2). The percentage of hydrogen desorbed at T < 700 °C might be overestimated in the study, as degassing pre-uptake was performed at 1500 °C, which may not be high enough to remove all contained hydrogen.

172

5.2.7.3. Peak 4: desorption of Trap 2 chemisorbed hydrogen

The fourth peak in the TDS (*Peak 4,* 1300-1450 K) is attributed to release of hydrogen trapped in Trap 2 (Atsumi et al. 2013a; Atsumi and Kondo 2018) with an uptake enthalpy around -2 to -3 eV/ H_2 (Table 5.11). The area of the peak has a square root dependency on uptake pressure (Figure 5.13(c)), suggesting that hydrogen is uptaken in atomic form (Equation 5.41). The intensity and area of the peak decrease with higher uptake temperatures, confirming that hydrogen is involved in a chemical bond.

5.2.7.4. Peak 5: desorption of Trap 1 chemisorbed hydrogen

The highest temperature peak in the TDS (*Peak 5,* 1600-1800 K) is attributed to the release of hydrogen trapped in Trap 1 with an uptake enthalpy of -4.4 eV/ H_2 (Atsumi et al. 2013a; Atsumi and Kondo 2018). As discussed in Section 5.2.2, Trap 1 uptake enthalpy is compatible with non-reconstructed sites, of which interstitial cluster loop edges are an example. Peak 5 might then more generally correspond to hydrogen atoms in non-reconstructed sites, with uptake enthalpies around -4 to -5 eV/H_2.

As for Peak 3 and 4, the intensity and area of the peak decrease with higher uptake temperatures, indicating that hydrogen forms chemical bonds. Conversely, Peak 5 area shows no change with different uptake pressures (Figure 5.13(d)). The independence on uptake pressure was explained with a thermodynamic argument: Trap 1 uptake enthalpy is so high, that no equilibrium exists in the range of temperatures explored in uptake experiments (up to 1000 °C), and the uptake is a one-sided process, and not an equilibrium process (Atsumi and Kondo 2018).

A similar independency of hydrogen concentration from uptake pressure was reported by Causey (Causey 1989), for POCO graphite at an uptake temperature of 1473 K under various charging pressures. The results showed that deuterium uptake did not increase when changing the uptake pressure from 0.66 Pa to 66 Pa, suggesting that all Trap 1 sites are saturated at 1473 K regardless of the charging pressure. TDS show that all peaks except Peak 5 lie below 1473 K. This suggests that all traps apart from Trap 1 would be degassed at 1473 K, and therefore the independency of total hydrogen capacity with uptake pressure is coherent with the independency of Trap 1 concentration as showed by Atsumi.
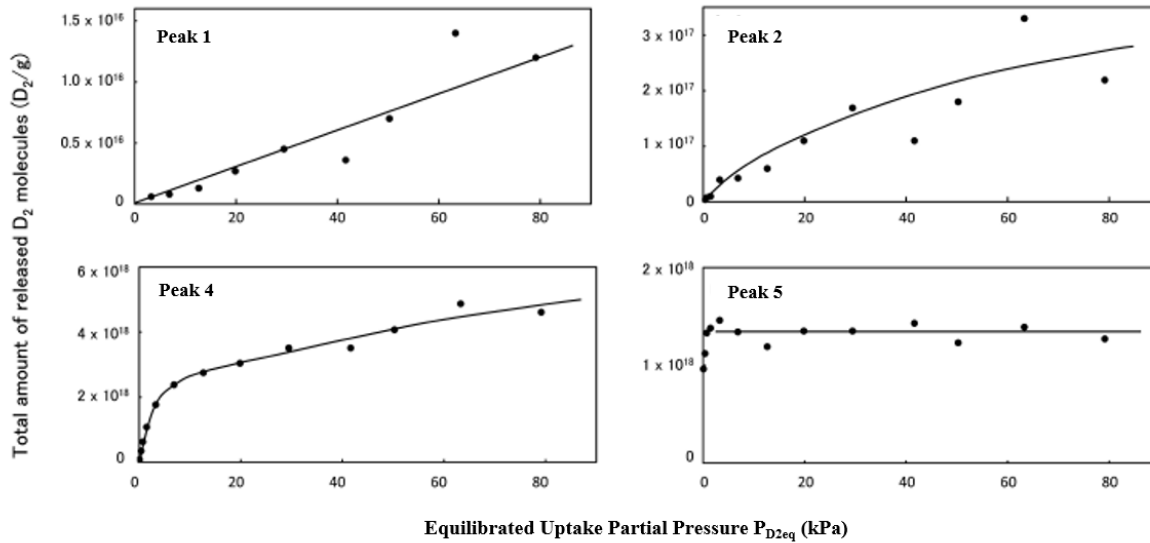
Figure 5.13: Amount of deuterium desorbed from each TDS peak as a function of uptake pressure. Graphite: ISO-880U, uptake temperature: 1273 K. Adapted from (Atsumi et al. 2013a).

In conclusion, thermal desorption of charged graphite samples is often employed as a technique to investigate the interaction of graphite and hydrogen. Thermal desorption spectra of graphite are characterized by four peaks: Peak 1 (600-700 K), associated to hydrogen gas stored in closed porosity; Peak 2 (900-1300 K), attributed to hydrogen dissolved as a solid solution; Peak 4 (1300-1450 K), associated to hydrogen chemisorbed in Trap 2, and Peak 5 (1600-1800 K), attributed to hydrogen chemisorbed in Trap 1. An additional peak (Peak 3) is present between of Peak 2 and Peak 4 in the TDS of a few carbonaceous materials other than graphite. Peak 3, whose temperature changes sample by sample, is attributed to desorption from smaller grains or from binder materials (Atsumi et al. 2015).

5.2.8   RCS distribution

After having described the different pathways and sites of hydrogen uptake, it is sought here to quantify the relative distribution of hydrogen among the different uptake sites. Such an analysis has been previously attempted by (Kanashenko 1996) (Table 5.16). When the occupancy of a trapping site becomes equal to one, the concentration of hydrogen chemisorbed in that trapping site is numerically equal to the concentration of that trapping site in graphite. According to the Langmuir isotherm (Equation 5.45), trapping site occupancies become close to unity at high uptake pressures and low uptake temperatures. Kanashenko used the experimental data (uptake pressures, uptake temperatures and hydrogen concentrations) from the hydrogen uptake experiments of (Causey 1989) and (Hoinkis 1991a) on POCO AXF-5Q graphite to extrapolate the concentration of Trap 1 and Trap 2 sites for POCO AXF-5Q graphite to 17 appm and 200 appm, respectively. Then, Kanashenko used the Langmuir isotherm (Equation 5.45) to predict the occupancy of the trapping sites and the concentration of hydrogen for the uptake conditions of (Causey 1989). Finally, the calculations were compared to the experimental results from (Causey 1989) for different temperatures showing a percentual deviation below 10% up to 1573 K.

Table 5.16: Deuterium concentration in trapping sites as a function of uptake temperature.

Graphite: POCO AXF-5Q, uptake pressure: 0.66 Pa. Experimental values from (Causey 1989) and calculated values from (Kanashenko 1996).

Uptake Temperature	[H/C]chem, Trap1 Calculated	[H/C]chem, Trap2 Calculated	[H/C] Calculated	[H/C] Experimental	Percentual deviation
(K)	(appm)	(appm)	(appm)	(appm)	(%)
1473	14.27	0.26	14.53	15	3.1
1573	10.59	0.14	10.73	11.5	6.7
1673	6.35	0.08	6.43	8	19.6
1773	3.31	0.05	3.36	6	44

The concentration of hydrogen in the different sites can also be estimated by comparing the area under each peak of the TDS. In Figure 5.14, this analysis is performed for two desorption spectra at two partial pressure (83 Pa and 63.3 kPa) and an uptake temperature of 1273 K. TDS at low uptake pressures are particularly relevant for tritium research in the fission reactor community as they are closer to the tritium uptake conditions in MSRs, FHRs and HTGRs. This desorption spectrum is compared to that for an uptake pressure of 63.3 kPa to show the marked differences in RCS distribution and to highlight that conclusions from uptake experiments with high partial pressure might not apply straightforwardly to low partial pressure applications. 83 Pa is the lowest uptake pressure at which a TDS is recorded in Atsumi et al.'s works. The relative areas are computed using Gaussian functions. This is an approximation, as the shapes of desorption peaks change depending on the pathway of desorption. At the low partial pressure (83 Pa), more than 99% of the uptaken hydrogen is chemisorbed, with only 0.1% retained in the closed porosity and 0.1% retained as a solid solution on the basal planes. At high partial pressure (63 kPa), 87% is chemisorbed, with 0.3% retained in the closed porosity and 12% retained as a solid solution on the basal planes. The low hydrogen content in pores indicates that neither *microporosity* nor *nanoporosity* are parameters of relevance to hydrogen uptake capacity in graphite, particularly at low partial pressure.

Since chemisorption dominates at the conditions of interest, further discussion is provided for the distribution of available RCS between Trap 2 sites and Trap 1 sites. At low partial pressure (83 Pa) 91% of the retained hydrogen is chemisorbed in Trap 1. At high partial pressure (63 kPa), only 25% of hydrogen is chemisorbed in Trap 1. Trap 2 sites can be used for reversible uptake of tritium in graphite. If degassing needs to be performed at temperatures below 1300 K, then Trap 1 sites primarily serve as a one-time, irreversible uptake of tritium. Degassing at temperatures around 1300 K the sample exposed to high partial pressure would be sufficient to desorb around 50% of the hydrogen content. On the other hand, degassing at the same temperature the sample exposed to low partial pressure would desorb less than 5% of the hydrogen inventory. In a technological application at these uptake conditions, a release of a large fraction of trapped hydrogen could be made possible only by degassing at temperatures above 1600 -1700 K.
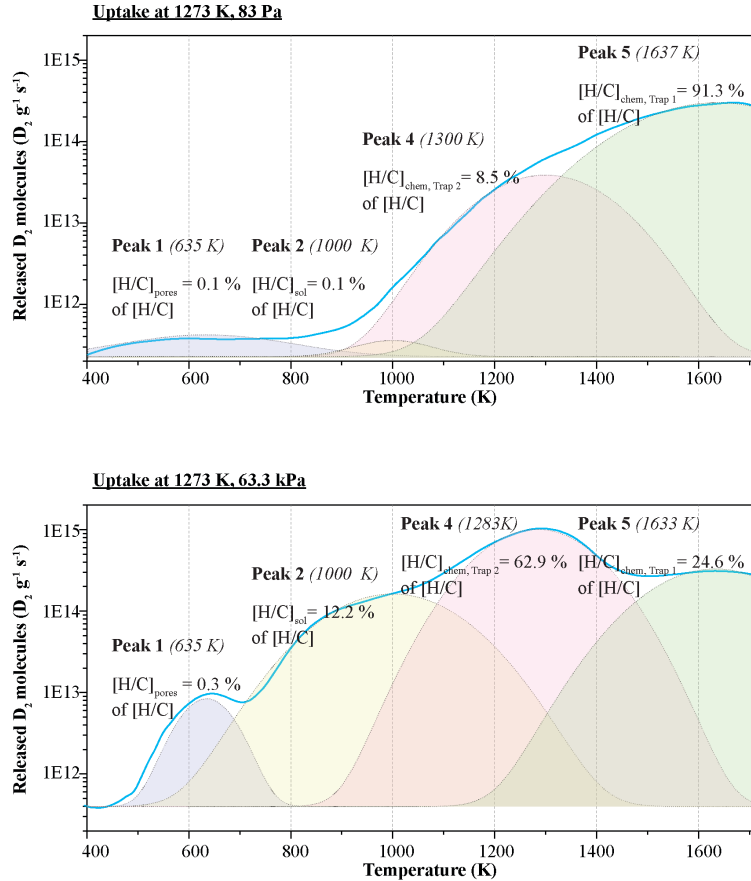
Figure 5.14: Peak decomposition of TDS from samples with uptake at two different partial pressures. Graphite grade: ISO-880U, isotope: D₂, uptake temperature: 1273 K, desorption: heating rate 0.1 K/s and vacuum below 10⁻⁵ Pa; peaks are fitted with Gaussian functions. Data source: digitized figures from (Atsumi and Kondo, 2018). Refer to Figure 5.12 for interpretation of the TDS peaks.

Table 5.17: Occupancy of Trap 1 and Trap 2 sites at different uptake pressures and temperatures. Calculations based on the Langmuir isotherm (Equation 5.45) with $\Delta H_{Trap1} = -4.4\ eV/H_2$, $\Delta H_{Trap2} = -2.3\ eV/H_2$ $\Delta S/k_b = -34.8$ /H₂ (Speight 2005)

	Occupancy of trapping sites			
	83 Pa, 1273K	63.3 kPa, 1273 K	20 Pa, 1273 K	20 Pa, 973 K
RCS Type	(%)	(%)	(%)	(%)
Trap 2	6.8	66.9	5.1	70.2
Trap 1	99.8	99.9	99.8	100.0

In MSRs, FHRs and HTGRs the low-partial-pressure and lower temperature conditions are most relevant to in-core conditions. The Mark-I PB-FHR (Andreades et al. 2016), for instance, is estimated to have tritium partial pressures up to 20 Pa (Stempien 2015) and temperatures of 500 - 800 °C in its core. TDS at these thermodynamic conditions is not currently available in literature. An extrapolation of available data to lower temperature has been performed (Table 5.17) using the Langmuir isotherm (Equation 5.45), the RCS enthalpies of reaction (compiled from prior literature

in Table 5.11), and the entropy of reaction. The Langmuir isotherm does not predict the available RCS population density, but it does predict change in occupancy of these sites with uptake temperature and pressure, allowing for extrapolation from available experimental data.

The Trap 2 occupancy at a low partial pressure (20 Pa) condition is predicted to be 5% at 1000 °C and 70% at 700 °C, thus the inventory of hydrogen in Trap 2 is expected to be about ten-fold at the reactor relevant uptake temperature of 700 °C and pressure of 20 Pa, as compared to the data at the lowest pressure available (83 Pa, 1000 °C). Trap 1 occupancy is very close to 100% both at 600 °C and 1000 °C, thus the inventory of hydrogen in Trap 1 is expected to be identical between the reactor relevant uptake temperature of 600 °C and the 1000 °C temperature at which data is available. Using the Langmuir isotherm (Equation 5.45), one finds that, due to the opposite effects of temperature and pressure in the isotherm, the occupancy of trapping sites caused by uptake at 973 K and 20 Pa is similar to those at 1273 K and 63.3 kPa (Table 5.17).

For PB-FHRs, it has been proposed to use fuel pebbles as vectors for tritium degassing (Forsberg et al. 2017c; Lam 2017). According to this strategy, the pebbles would uptake tritium while in-core and would then desorb it when degassed out-of-core. The desorption temperature and time at temperature must be chosen such that they are compatible with the structural integrity of the FHR fuel elements and reflectors. Using the temperatures and the area of the peaks in the TDS at 63.3 kPa, one finds that if the degassing temperature needs to remain below 1500 K, about 75 % of the tritium inventory will be degassed. In other words, at such degassing temperatures, the reversible tritium uptake capacity is 75% of the total uptake capacity. An option to increase tritium degassing may be to introduce a hydrogen partial pressure in core to dilute the tritium isotopes. Increasing the partial pressure of hydrogen isotopes during uptake, the relative fraction of hydrogen and tritium retained in Trap 2 sites would increase. The increase of the fraction of tritium and hydrogen retained in Trap 2 sites would make degassing at temperatures below 1500 K capable of desorbing amounts of trapped tritium and hydrogen larger than the base case. With this approach, the pebbles would contain a larger inventory of hydrogen isotopes at the end of degassing, but the inventory of tritium would be lower.

The distribution of hydrogen in Trap 1 and Trap 2 sites varies not only based on thermodynamic parameters, but also across graphite grades. For example, the ratio of Trap 2 to Trap 1 sites is estimated to be 10 for POCO AXF-5Q, 11.8 for TSP (Kanashenko 1996) and 4.3 for IG-430U (Atsumi et al. 2009a). The effect of irradiation and oxidation on Trap 1 and Trap 2 is discussed in Section 5.4, the isotopic effect is discussed in Section 5.2.9.

Other phenomena that relate to tritium removal from graphite are graphite oxidation with O_2 or H_2O (discussed in Section 5.4) and isotope exchange reactions between the tritium bound in graphite and the hydrogen in H_2 or H_2O. Once tritium-charged graphite is extracted from the core, if it is exposed to hydrogen gas or water vapor a replacement of some of the bound tritium with hydrogen will occur, leading to the formation of gaseous HT or HTO. Hydrogen isotope exchanges are not discussed further in this review; the interested reader is referred to (Brice et al. 1982; Junk and Catallo 1997; Nishikawa et al. 1995; Wilson and Hsu 1987).

In conclusion, the distribution of hydrogen across RCS is governed by thermodynamic parameters and can be estimated by analyzing TDS. At low partial pressures, in the Pa range, and high uptake temperatures, hydrogen is prevalently stored in Trap 1 sites. At higher pressures, in the kPa range, hydrogen chemisorption is predominant in Trap 2. The relative abundance of Trap 2 and Trap 1

sites varies with graphite grades and with environmental effects that can change the RCS in graphite.

5.2.9   Isotopic Effects

The term *isotopic effect* is used as an umbrella term to lump all differences in some molecular or atomic property caused by isotopic substitution (Wolfsberg 1969). Because tritium is radioactive, it is frequent in experimental studies to replace it with hydrogen or deuterium. Using these isotopes as surrogates introduces deviations on the thermodynamics of interactions.

The Gibbs free energy of the interaction with graphite depends on the isotopes. Even with a light element like hydrogen, in which the difference across the masses of the isotopes is in the order of magnitude of the mass itself, the variations in enthalpy are modest (Table 5.18). Differences in the entropy of the C-H bond formation are attributed to the rotational entropy of the hydrogen molecule and to the vibrational entropy of H in the carbon lattice. Atsumi, Hoinkis and Kanashenko used statistical mechanics to predict the entropic change ΔS_{chem} associated with the reaction in Equation 5.43. (Atsumi and Kondo 2018; Hoinkis 1991a) attributed the entropic change to the disappearance of the entropy of the gaseous hydrogen isotope molecule. (Kanashenko 1996) also included the appearance of the vibrational entropy of the hydrogen isotope atom in the graphite sample, as in Equation 5.51.

$$\exp\left(\frac{\Delta S_{chem}}{k_b}\right) = \exp\left(-\frac{7}{2}\right)\left(\frac{m_i k_b T}{2\pi\hbar^2}\right)^{-\frac{3}{2}} (k_b T)^{-1} \left(\frac{\theta_{rot,i}}{T}\right) \frac{\exp\left(2\frac{2\pi\hbar\nu}{k_b T} \frac{\exp\left(-\frac{2\pi\hbar\nu_i}{k_b T}\right)}{1-\exp\left(-\frac{2\pi\hbar\nu_i}{k_b T}\right)}\right)}{\left(1-\exp\left(-\frac{2\pi\hbar\nu_i}{k_b T}\right)\right)^2} \quad 5.51$$

where $\hbar$ is the reduced Planck's constant, m_i is the mass of the hydrogen isotope *(i=H,D,T)* , $\theta_{rot,i}$ is the characteristic temperature of rotation of the hydrogen isotope molecule and ν_i is the vibrational frequency of the hydrogen isotope.

It is to be noted that isotopic effects on carbon are not expected be impactful on the thermodynamics of the C-H interaction. Among carbon isotopes, the relative mass differences are much smaller than in the case of hydrogen isotopes, and the variations in enthalpy and in the vibrational entropy of H uptake in the carbon lattice could be expected to be negligible.

The enthalpy and entropy of uptake in Trap 1 and Trap 2 with the three isotopes can be computed using Equations 5.35, 5.36, and 5.41. Table 5.18 shows the results of this computation for the three isotopes, and the input values used for these calculations. Not all values are easily retrievable in chemical handbooks; those not available have been estimated with simplified reasoning detailed in the footnotes. Table 5.18 shows that enthalpies and entropies of uptake vary modestly (<10%) across the isotopes.

From the Gibbs free energy, the fraction of sites occupied, ϵ, at a partial pressure of 20 Pa and a given temperature is computed based on Equation 5.43 and 5.45 and shown in Table 5.18 and in the top row of Figure 5.15. For Trap 1, the most pronounced isotopic difference is in the range of 1200 to 1500 °C and above, where at any given temperature, T_2 has a lower occupancy by about 15% than H_2. Looking at the same data, but from the perspective of removing tritium from graphite by high-temperature degassing, a drop to 50% occupancy is achieved for T_2 at a temperature lower by 100 °C, compared to the case of H_2. Almost no difference (<1%) is predicted between D_2 and

T_2 for Trap 1 occupancy. For Trap 2, the most pronounced isotopic difference is in the range of 700 to 900 °C, where the occupancy by T_2 is lower by 13% than occupancy by H_2, at the same temperature. The maximum difference in occupancy between D_2 and T_2 is about 5%, in the same temperature range. The temperature leading to a 50% tritium occupancy of Trap 2 sites at thermodynamic equilibrium is about 40 °C lower than that which would be required with H_2. For both Trap 1 and Trap 2, the isotopic effects are more pronounced in moving from hydrogen to deuterium than from deuterium to tritium. This is partly due to the formulation of the entropy according to Equation 5.51; the asymptotic behavior in the limit for high temperatures shows that $\exp\left(\frac{\Delta S_{chem}}{k_b}\right) \sim \frac{T}{m^2}$.
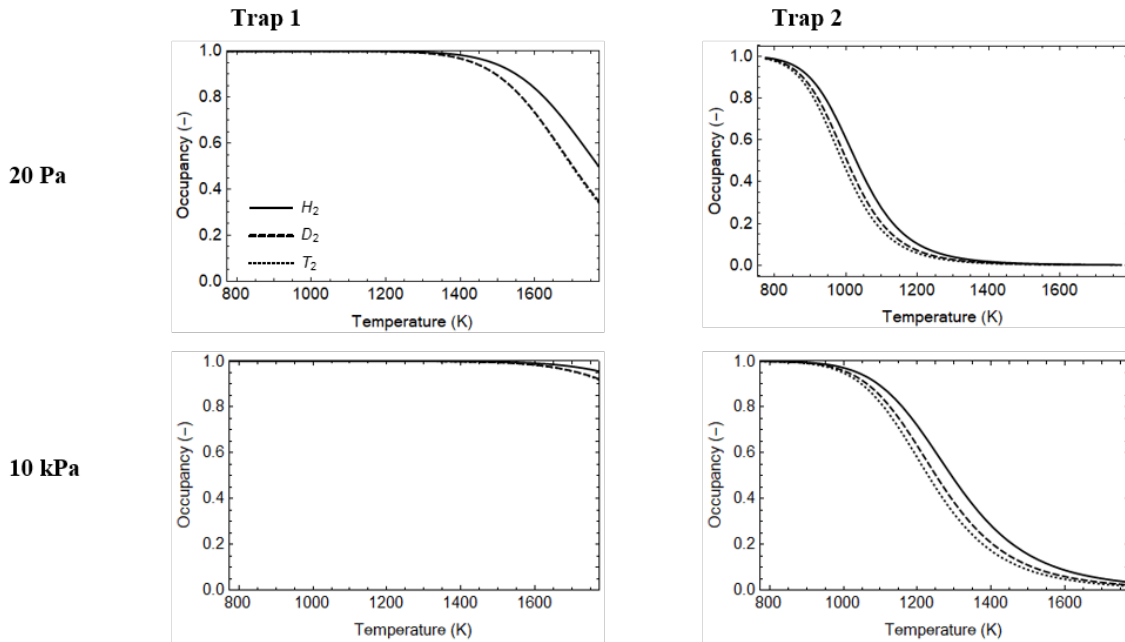
Figure 5.15: Occupancy of Trap 1 and Trap 2 as a function of temperature, under a partial pressure of 20 Pa (top row) and 10 kPa (bottom) of H_2, D_2 or T_2.

179

Table 5.18: Isotopic effects on the thermodynamic parameters of carbon-hydrogen interaction

Input Values		H	D	T
E_{H-H}	(eV/H$_2$)	4.52 (Luo 2007)	4.60 (Luo 2007)	4.59 (Kirk et al. 2007)
E_{C^*-H} (Trap 1)	(eV)	4.45 (Kanashenko 1996)	4.49[a]	4.53[a]
E_{C^*-H} with relaxation (Trap 2)	(eV)	3.51 (Luo 2007)	3.54 (Luo 2007)	3.58[a]
m_i	(g)	1.67 10^{-24}	3.34 10^{-24}	5.01 10^{-24}
ν_i [b]	(Hz)	8.7 10^{13}	6.2 10^{13}	5.0 10^{13}
$\theta_{rot,i}$	(K)	175 (Fast 1960)	87.5 (Fast 1960)	58.3[c]
Output Values				
$\Delta H_{chem,1}$	(eV/H$_2$)	-4.38	-4.38	-4.47
$\Delta H_{chem,2}$	(eV/H$_2$)	-2.42	-2.48	-2.51
$\Delta S_{chem}/k_b$ @ 773 K	(−)	-29.36	-30.98	-31.80
$\Delta S_{chem}/k_b$ @ 1073 K	(−)	-30.40	-31.80	-32.61
$\Delta G_{chem,1}$ @ 773 K	(eV)	-2.42	-2.32	-2.35
$\Delta G_{chem,2}$ @ 773 K	(eV)	-0.46	-0.42	-0.39
$\Delta G_{chem,1}$ @ 1073 K	(eV)	-1.57	-1.44	-1.45
$\Delta G_{chem,2}$ @ 1073 K	(eV)	0.39	0.46	0.51
ϵ_1 @ 773 K, 20 Pa	(%)	100.0	100.0	100.0
ϵ_2 @ 773 K, 20 Pa	(%)	99.3	99.0	98.8
ϵ_1 @ 1073 K, 20 Pa	(%)	100.0	100.0	100.0
ϵ_2 @ 1073 K, 20 Pa	(%)	34.8	26.5	22.5

[a] Assuming that the difference with C-H is limited to the vibrational zero-point energy using the stretching frequencies provided below, when not specified otherwise.

[b] Assuming a stretching frequency of 2900 cm^{-1} for C-H.

[c] Assuming $\frac{\theta_{rot,T_2}}{\theta_{rot,D_2}} = \frac{I(D_2)}{I(T_2)} = \frac{m_D}{m_T}$ where I is the moment of inertia.

The comparison of the Trap occupancies with the three isotopes provides guidance on the conditions at which hydrogen or deuterium can be used as surrogates of tritium in uptake experiments. At a pressure of 20 Pa, the errors that are introduced by replacing tritium with hydrogen are under 5% at all temperatures. This suggests that, at FHR conditions, tritium uptake can be predicted through deuterium uptake experiments with an accuracy of 95% of more. This is not the case for hydrogen: using hydrogen as a surrogate of tritium leads to an accurate (within 1% for temperatures below 1100 °C) estimation of Trap 1 occupation, but an overestimation in Trap 2 occupancies by up to 15%.

As shown in Table 5.12, only few uptake experiments are available at a partial pressure of tens of Pa, while most studies employ partial pressures of 1 – 100 kPa. The bottom row of Figure 5.15 shows the impact of isotopic effects at these pressures. The isotopic effects on Trap 1 occupancies are not pronounced (less than 4% at all temperature), while the effects on Trap 2 occupancies are of entity similar to the low pressure case and remain above 7% for temperatures up to 1200 °C. Overall, this suggests that among the hydrogen and deuterium experiments compiled in Table 5.12, those that suffer less from isotopic effects are a) those using deuterium (< 5% difference, at all pressures and temperatures) and b) those at low temperatures (approximately <1000 K if high pressure, <800 K if low pressure).

In summary, the Gibbs free energy, the enthalpy and entropy of hydrogen uptake in graphite vary across the isotopes (Table 5.18). For chemisorption in Trap 1 at FHR pressures, the most pronounced isotopic difference (15 % points drop in occupancy rate) is in the range of 1200 to 1500 °C and above, and the temperature leading to a 50% tritium occupancy of Trap 1 sites at thermodynamic equilibrium is about 100 °C lower for T_2 than for H_2. For chemisorption in Trap 2 at FHR pressures, the most pronounced isotopic difference (13 % points drop in occupancy rate) is in the range of 700 to 900 °C, and the 50% desorption temperature is 40 °C lower for T_2 than for H_2. The dominant driver of these differences is the entropy difference among H_2, D_2 and T_2, which scales with $1/m^2$. The isotopic effects on enthalpies of C-H bonds and H-H dissociation are also a small contributor.

5.2.10   Conclusion

This chapter seeks to describe what can be inferred about the mechanisms for uptake and desorption of hydrogen isotopes in graphite at moderate temperature (500 to 800 °C for uptake, < 1300 °C for desorption) and low hydrogen partial pressure (< 50 Pa) – conditions which have not previously received as much attention, and which are relevant to tritium management in FHRs, MSRs, HTGRs, and fusion systems. Low partial tritium pressures are particularly relevant to systems that employ molten salt as coolant, fuel, or tritium breeding blanket.

Prior studies have been conducted on a variety of graphite grades and a range of temperatures, pressures, and duration of uptake. The compilation of this data provides highly scattered results (Figure 5.11 and Table 5.12). Little to no data is available at the uptake conditions of interest in this thesis. In order to understand the relevance of this data to extrapolated conditions, an extensive discussion of the mechanisms of uptake is provided in this chapter. RCSs are identified in non-reconstructed crystallite edge sites, termed Trap 1, with uptake enthalpies around -4 to -5 eV/ H_2 and of reconstructed edge sites, termed Trap 2, with uptake enthalpies around -2 to -3 eV/ H_2 (Table 5.11).

TDS is introduced as a tool to quantify hydrogen desorption under each mechanism and TDS peak area decomposition is performed for two cases of low and high partial pressure (Figure 5.14). Since chemisorption is shown to dominate at the conditions of interest, further discussion is provided for the distribution of available RCS between Trap 2 type of RCS and Trap 1 type of RCS. Trap 2 sites can be used for reversible uptake of tritium in graphite. If degassing needs to be performed at temperatures below 1300 °C, then Trap 1 sites primarily serve as a one-time, irreversible uptake of tritium.

An extrapolation of this data to lower temperature is performed using the Langmuir isotherm (Equation 5.45), the RCS enthalpies of reaction (compiled from prior literature in Table 5.11), and the entropy of reaction (further described by Equation 5.51). The Langmuir isotherm does not predict the available RCS population density, but it does predict change in occupancy of these sites with uptake temperature and pressure, allowing for extrapolation from available experimental data.

The occupancy of Trap 2 sites is determined by the enthalpy and entropy of the chemisorption reaction with Trap 2. The isotopic effect on occupancy of Trap 2 sites is illustrated in Figure 5.15. The dominant driver of these deviations is the entropy difference among H_2, D_2 and T_2, which scales with the inverse of the squared mass. The differences across isotopes for the enthalpies of C-H bonds and H-H dissociation are also a small contributor. Enthalpy values from prior literature are compiled in Table 5.11 and Table 5.18, and entropy is described by Equation 5.51. For

chemisorption in Trap 2, the most pronounced isotopic difference (13 % points drop in occupancy rate) is in the range of 700 to 900 °C, and the 50% desorption temperature is 40 °C lower for T_2 than for H_2. Isotopic effects on Trap 1 are also relevant, lowering the desorption temperature for T_2 vs H_2 by about 100 °C.

There remain gaps in the available data and mechanistic understanding of hydrogen-graphite interaction at high temperature. Only few thermal desorption studies have been performed, and only limited combinations of uptake temperatures and have been explored. A TDS study of graphite with uptake temperatures in the range of 800 - 1000 K and as a function of partial pressure, including partial pressures of a few Pa, would provide confirmation of the extrapolated prediction on Trap 2/Trap 1 distribution performed in this study. A study comparing the TDS of identical graphite samples exposed to different irradiation conditions (non-irradiated, ion-irradiated, neutron-irradiated at low dpa and heavily irradiated) would be needed to confirm that irradiation effectively increases Trap 1 hydrogen capacity more than Trap 2, since this hypothesis has been formulated only based on the results of uptake studies. Lastly, scarce data is available for the graphite matrix material that comprises the fuel elements of PB-FHRs and HTGRs. Measurements of unirradiated matrix are needed to identify the population of Trap 1 and Trap 2 sites, and measurements as a function of dpa are needed to identify the evolution of the Trap 1 and Trap 2 sites with irradiation. Measurements on pre-oxidized matrix, with a variety of oxidizing gases, would similarly be necessary to identify the evolution with Trap 1 and Trap 2 with oxidation due to inadvertent air or steam ingress. Similarly, the effect of fluorination by molten fluoride salts on the evolution of Trap 1 and Trap 2 populations needs to be studied. The order of magnitude of the isotopic effects on hydrogen uptake and desorption is well-understood; verification of predicted isotopic effects would be of scientific interest, to verify the postulated isotopic effects on the enthalpy of chemisorption in Trap 1 and Trap 2.

5.2.11 Acknowledgements

5.3 Kinetics of Hydrogen in Graphite at High Temperature

In most experimental studies involving hydrogen uptake in carbon materials, the main goal has been to measure the *uptake capacity* of the carbon material, that is the maximum concentration of hydrogen that can be uptaken. Only some of these studies have investigated how the uptake process develops or its kinetics. A small number of them have explored the impact of pre-oxidation, neutron irradiation, and isotopic effects on these processes.

The performance of graphite as vector for tritium depends not only on its uptake capacity and thermodynamics, but also on the kinetics of uptake and of desorption and on its desorption behavior. Any theoretical prediction of hydrogen retention and distribution in graphite purely based on the thermodynamics of the carbon – hydrogen reaction bears the risk of being an overestimate of the engineering-relevant uptake capacity, because the thermodynamic equilibrium condition to which it applies may be reached after a long time or not reached at all. The purpose of this chapter is a review of the kinetics and mechanisms for uptake, transport, and desorption of hydrogen in graphite at high temperature.

5.3.1 Hydrogen penetration in the sample

Many uptake studies attempt to measure hydrogen uptake capacities at high temperature, which indicate the total amount of hydrogen in a sample. A few studies focus on how hydrogen distributes throughout the sample, and suggest that hydrogen concentration is not uniform, but is higher in the external layers and lower in the bulk. Table 5.19 compiles the available data for the ratio of the tritium concentration in the surface to the ratio of the tritium concentration in the bulk of the sample, *surface-to-bulk ratio*. The surface-to-bulk ratio varied across samples with oxidation, irradiation, and graphite type.

(Strehlow 1986) studied uptake of T_2 on graphite with and without simultaneous oxidation by steam. The experiments were conducted on three graphite grades (POCO, A681, CGB), at partial pressures of 0.14 Pa and a temperature of 1023 K. Tritium concentration was measured with increasing depth by analyzing 0.15 mm slices parallel to the tritium-exposed face. In all three samples, a tritium concentration gradient was observed, with tritium concentration in the first layer being larger than in the bulk. Similarly, a gradient of tritium concentration between the surface and the bulk of graphite was observed in the MSRE. In the MSRE, tritium was produced by neutron reactions with lithium and beryllium in the FLiBe fluoride salt fuel solvent and coolant; the tritium thus produced was in part uptaken by the CGB graphite moderator and POCO graphite samples (Compere et al. 1975). The graphite samples from the MSRE present a surface-to-bulk ratio much higher than the one observed by (Strehlow 1986) for T_2 uptake (Table 5.19).

Table 5.19: Surface-to-bulk ratio of tritium concentration in graphite samples

Graphite Type	Oxidation	Temperature of uptake / Pressure of uptake	Duration of exposure	BET Surface Area	Open Porosity	Thickness of outer layer/sample	Surface-to-bulk ratio	Source
		(K) / (Pa)		(m²/g)	(%)	(mm)	(-)	
A681	No			0.20	Not Reported		3.2	(Strehlow 1986)
	Yes			1.43			1.5	
	Yes			2.25			1.5	
POCO AXF-5Q	No	1023 / 0.14	4 h	0.21	16 (Lee et al. 2020)	0.15/10	10.7	
	No			0.28			14.8	
	Yes			0.72			3.9	
	Yes			0.76			3.9	
CGB	No			0.22	4 (Briggs 1964a)		26.3	
	No			0.32			37.7	
	Yes			2.31			5.1	
	Yes			2.68			4.0	
POCO AXF-5Q	No	~923 / Not reported	1786 h	Not Reported	16 (Lee et al. 2020)	1.6/50.8	450	(Compere et al. 1975)
CGB	No		~ 5 y	0.5	4 (Briggs 1964a)		200	

The presence of a gradient in tritium concentration may indicate either that tritium transport in the graphite is a rate-limiting step in the uptake of tritium within a graphite samples, or that the uptake capacity of the graphite at the surface of the sample is significantly higher than the graphite in the bulk of the sample. Furthermore, the presence of a steep tritium concentration gradient at the surface and a constant tritium concentration few mm into the sample is uncharacteristic of a transient diffusion profile, and may suggest a diffusion-trapping-detrapping mechanism for transport in the graphite; higher trapping-site density would lead to a lower effective diffusion coefficient, as discussed later in Section 5.3.2. Whether the effect is a consequence of spatial heterogeneity of uptake capacity or of spatial heterogeneity of effective diffusivity, both can be explained by a higher density of trapping sites at the sample surface. Under this hypothesis, surface-to-bulk ratios are expected to be higher in environments where the production of RCS is promoted. This would explain why the surface-to-bulk ratios are higher in the (Compere et al. 1975) where the graphite surface is exposed to molten fluoride salt and neutron irradiation than in (Strehlow 1986) where the graphite is as-manufactured.

The lower surface-to-bulk ratio observed by (Strehlow 1986) with oxidation may indicate, as postulated by (Strehlow 1986) in a different context and also by (Atsumi and Iseki 2000), that oxidation preferentially removes the more reactive carbon atoms, reducing the difference in reactive carbon site density between the surface and the bulk. Nonetheless, this change would be accompanied by a decrease of the uptake capacity, which does not occur upon graphite oxidation. The lower surface-to-bulk ratio can be explained with a change to graphite morphology as carbon atoms are removed, increasing hydrogen diffusion coefficient (further discussed in Section 5.4.2), and allowing more access to the bulk.

Similarly, (Dolan et al. 2020) demonstrates that tritium uptake in a salt-irradiation capsule leads to a tritium uptake in the graphite that scales with the surface area of the graphite that was exposed to the fluoride salt; this may be explained by creation of RCS as a consequence of graphite fluorination by the salt (Wu et al. 2018a). The high variability in surface-to-bulk ratio among the different types of graphite in (Strehlow 1986) indicates that the graphite manufacturing process also plays a role. In summary, exposure to molten fluoride salt and irradiation increase the surface-to-bulk ratio, oxidation decreases the surface-to-bulk ratio, and graphite grade matters. The higher density of RCS could be induced by interactions with the operational environment (e.g. oxidation, fluorination, irradiation, possibly friction and wear from pebble fuel movement), or by the manufacturing process (e.g. machining or polishing of sample surface, impregnation for graphite densification, specifics of the manufacturing process that might lead to heterogeneity) (Orimo et al. 2001; Shen et al. 1996).

Another hypothesis to explain the variability across graphite grades was formulated by (Causey 1989). Looking at the data from (Strehlow 1986), (Causey 1989) argued that the amount of tritium in the bulk is correlated with the open porosity in the sample. Graphite grades with abundant open porosity like POCO (16% open porosity, (Lee et al. 2020)) would then have a lower surface-to-bulk ratio than a graphite with little open porosity like CGB (4% open porosity, (Briggs 1964a)). This hypothesis is not verified in the MSRE, where the surface-to-bulk ratio is more in POCO is more than double in CGB. The hypothesis is not invalidated either, since the existence of longitudinal cracks where salt may have resided and transported tritium could explain a higher-than-expected bulk concentration in the CGB used in the MSRE. If one considers pore connectivity in graphite, several networks of pores exist within a graphite sample. A set of networks will communicate with the surface. In order to access the next set of pores into the depth of the graphite sample, which are closed porosity, diffusion is necessary. All the grains in contact with this next set of pore networks then have access to uptake of hydrogen. From there, further diffusion of network is needed to access further pore networks and so on. Therefore, if the (Causey 1989) hypothesis is valid, that open porosity explains the surface-to-bulk ratios, then the uptake of tritium into graphite is limited by transport to the closed porosity, as maintained also in (Hoinkis 1991a), and the diffusivity of hydrogen in graphite must be characterized in order to have a predictive model of hydrogen uptake in a macroscopic graphite sample.

5.3.2 Kinetics of Uptake

Table 5.20 compiles available data for overall diffusion coefficients in hydrogen uptake, measured by transient uptake experiments, and termed here *apparent diffusion coefficients*. In these experiments, degassed graphite samples are placed in a closed chamber filled with hydrogen atmosphere at the desired temperature and *initial* (partial) *pressure*. As hydrogen is uptaken in the sample, the pressure decreases. The pressure in the system is measured with a manometer and plotted against time. Eventually, the pressure stabilizes to the *equilibrium pressure*. The time to this condition is named *time to equilibrium. Uptake rates* and *apparent diffusion coefficients* can be computed through fitting of the pressure curves. In a diffusion-controlled process, the evolution of the hydrogen partial pressure in the chamber P_{H_2} can be described by Equation 5.52 (Atsumi et al. 1992) :

$$\frac{dP_{H_2}(t)}{dt} = \frac{S_0\sqrt{P(t)}}{V_0}\frac{6}{\pi^2}\frac{d}{dt}\sum_{n=0}^{\infty}\frac{1}{n^2}\exp(-n^2\pi^2\hat{D}\ t) \qquad \text{5.52}$$

where S_0 is the hydrogen uptake capacity (in atoms / m³) divided by the square root of the pressure, $\hat{D}$ is the uptake rate and V_0 is the volume of the chamber. As will be discussed later, pressure curves are fitted well by an inter-crystallite diffusion-controlled curve, suggesting that diffusion is the predominant process for hydrogen uptake. In an inter-crystallite diffusion-controlled process, the uptake rate $\hat{D}$ and the apparent diffusion coefficient $D_{H_2,app\ abs}$ are related as in Equation 5.53

$$\hat{D} = \frac{D_{H_2,app\ abs}}{r_{grain}^2} \qquad \text{5.53}$$

where r_{grain} is the radius of the graphite grain. As graphite grains have a distribution of size, the average radius is often used for computing the apparent diffusion coefficients.

Table 5.20: Apparent diffusion coefficients and uptake rates of hydrogen isotopes in graphite at high temperature, ordered by uptake rate.

(a) Unirradiated Graphite

Graphite	Hydrogen Isotope	Sample Thickness	Sample Volume	Reported Total Porosity[a] α_T	Temperature	Partial Pressure	Time to equilibrium	Uptake Rate $\widehat{D}$	Grain Radius (Yamashina and Hino 1989) r_{grain}	Apparent Diffusion Coefficient $D_{H_2,app\,abs}$	Inter-Crystallite Diffusion Coefficient [b] $D_{H_2,ic\,int}$	Source number	Source
		(cm)	(cm^3)	(%)	(K)	(Pa)	(h)	(s^{-1})	(μm)	(m^2 s^{-1})			
ISO-880U	H	2	3.2	14-18	1273	350	2.2	4 10^{-5} c	2.5	2.2 10^{-16}	2.2 10^{-16}	[1]	(Atsumi 2003)
ISO-880U	H	2	3.2	14-18	1273	38200	3.3	7 10^{-5} c	2.5	4.1 10^{-16}	4.1 10^{-16}	[1]	(Atsumi 2003)
Lorraine 5980PT	H	-	-	-	1273	10000	3.0	1 10^{-5}	-	-	-	[2]	(Atsumi and Iseki 2000)
IG-430U	H	-	-	-	1273	10000	-	4 10^{-5}	-	-	-	[2]	(Atsumi and Iseki 2000)
ETP-10	H	-	-	13	1273	10000	-	2 10^{-4}	20	6 10^{-14} c	6 10^{-14}	[2]	(Atsumi and Iseki 2000)
IG-110U	H	-	-	11-12	1273	10000	-	2.0 10^{-4}	7	1 10^{-14} c	1 10^{-14}	[2]	(Atsumi and Iseki 2000)
EK-98	H	-	-	-	1273	10000	-	5.0 10^{-5}	-	-	-	[2]	(Atsumi and Iseki 2000)
POCO AXF-5Q1	H	-	-	-	1273	10000	-	1.3 10^{-4}	5	3 10^{-15}	3 10^{-15}	[2]	(Atsumi and Iseki 2000)
ATJ	H	-	-	-	1273	10000	-	1.4 10^{-4}	-	-	-	[2]	(Atsumi and Iseki 2000)
ISO-880U	H	-	-	14-18	1273	10000	0.8	1.3 10^{-5}	2.5	8 10^{-17} c	8 10^{-17}	[2]	(Atsumi and Iseki 2000)
IG-110U	H	2	3.2	11-12	1073-1323	37000	-	1 10^{-5} – 1 10^{-4}	7	2 10^{-15} -2 10^{-14} c	2 10^{-15} -2 10^{-14}	[3]	(Atsumi 2002b)
IG-110U	H	2	3.2	11-12	1073-1323	270	-	1 10^{-7} – 9 10^{-6}	7	2 10^{-17} -2 10^{-15} c	2 10^{-17} -2 10^{-15}	[3]	(Atsumi 2002b)
IG-430U	H	2	3.2	-	1073-1323	37000	-	5 10^{-6} – 5 10^{-5}	-	-	-	[3]	(Atsumi 2002b)
IG-430U	H	2	3.2	-	1073-1323	310	-	2 10^{-7} – 3 10^{-6}	-	-	-	[3]	(Atsumi 2002b)
ISO-880U	H	2	3.2	14-18	1073-1323	36000	-	5 10^{-5} – 7 10^{-4}	2.5	8 10^{-14} -1 10^{-12} c	8 10^{-14} -1 10^{-12}	[3]	(Atsumi 2002b)
ISO-880U	H	-	-	14-18	973-1323	10000 d	-	2 10^{-5} - 5 10^{-4} c	2.5	1 10^{-16} - 3 10^{-15}	1 10^{-16} - 3 10^{-15}	[4]	(Atsumi et al. 2009a)
IG-430U	H	-	-	-	1123-1323	10000 d	-		-	1 10^{-16} - 3 10^{-15}	-	[4]	(Atsumi et al. 2009a)
ISO-880U	H	-	-	14-18	1073-1323	36000	-	2 10^{-3} – 2 10^{-2} c	2.5	1 10^{-14} -1 10^{-13} c	1 10^{-14} -1 10^{-13}	[3]	(Atsumi 2002b)
IG-110U	H	-	-	11-12	1273	17640	-	5 10^{-5} c	7	2.5 10^{-15}	2.5 10^{-15}	[5]	(Atsumi and Tauchi 2003)

187

Graphite	Hydrogen Isotope	Sample Thickness	Sample Volume	Reported Total Porosity	Temperature	Partial Pressure	Time to equilibrium	Uptake Rate $\hat{D}$	Grain Radius r_{grain}	Apparent Diffusion Coefficient	Inter-Crystallite Diffusion Coefficient	Source number	Source
IG-110U	H	-	-	11-12	1273	1150	-	$4\ 10^{-6\ c}$	7	$2.0\ 10^{-16}$	$2.0\ 10^{-16}$	[5]	(Atsumi and Tauchi 2003)
ISO-880U	H	-	-	14-18	1273	11300	2.5	$3\ 10^{-4\ c}$	2.5	$1.62\ 10^{-15}$	$1.62\ 10^{-15}$	[6]	(Atsumi et al. 2007)
IG-430U	H	-	-	-	1273	10400	-	-	-	$9\ 10^{-16}$	-	[7]	(Atsumi et al. 2009b)
IG-110U	H	-	-	11-12	1273	200-40000	-	$2\ 10^{-6} - 1\ 10^{-4\ c}$	7	$1\ 10^{-16} - 7\ 10^{-15}$	$1\ 10^{-16} - 7\ 10^{-15}$	[3]	(Atsumi 2002b)
S1611	T	-	-	15.2	1023	80000	-	-	-	-	-	[8]	(Kwast et al. 1996)
A3	D	1.57	0.5	25	1173	164	80	-	-	-	-	[9]	(Hoinkis 1991a)
POCO AXF-5Q1	D	0.06	0.04	-	1373-1473	66	1-20	-	5	-	-	[10]	(Causey 1989)

(b)   Irradiated Graphite

Graphite	Hydrogen Isotope	Sample Thickness	Sample Volume	Reported Total Porosity[a] α_T	Temperature	Partial Pressure	Neutron Fluence	Time to equilibrium	Uptake Rate $\hat{D}$	Grain Radius[e] r_{grain}	Apparent Diffusion Coefficient $D_{H_2,app\ abs}$	Inter-Crystallite Diffusion Coefficient[f] $D_{H_2,ic\ int}$	Source number	Source
		(cm)	(cm^3)	(%)	(K)	(Pa)	(n m^2)	(h)	(s^{-1})	(μm)	(m^2 s^{-1})			
ISO-880U	H	-	-	14-18	1273	11200	$3.9\ 10^{23}$	5.3	-	-	$3.13\ 10^{-16}$	$3.13\ 10^{-16}$	[6]	(Atsumi et al. 2007)
IG-430U	H	-	-	-	1273	10400	$3.9\ 10^{23}$/ $1.9\ 10^{24}$/ $5.4\ 10^{24}$	-	-	-	$3\ 10^{-17}$/ $2\ 10^{-17}$/ $6\ 10^{-17}$	-	[7]	(Atsumi et al. 2009b)
ISO-880U	H	-	-	14-18	1073-1323	10000 [d]	$3.9\ 10^{23}$	-	-	-	$2\ 10^{-17} - 8\ 10^{-16}$	$2\ 10^{-17} - 8\ 10^{-16}$	[7]	(Atsumi et al. 2009a)
IG-430U	H	-	-	-	1073-1323	10000 [d]	$3.9\ 10^{23}$	-	-	-	$5\ 10^{-19} - 3\ 10^{-17}$	-	[4]	(Atsumi et al. 2009a)

[a] See original sources for additional information on the techniques used; various techniques are used for determination of total porosity.

[b] Computed assuming $n_2 = 200$ appm and $\alpha_n = 1/2\ \alpha_T$

[c] Computed using Equation 5.52.

[d] Equilibrium pressure. Initial partial pressure not provided.

[e] Grain radius post-irradiation is not provided by any of the sources.

[f] Computed using Equations 5.53-5.56 and assuming $n_2 = 2000$ appm and $\alpha_n = 1/2\ \alpha_T$

Note: Data from (Atsumi et al. 1992) have not been included because temperature and pressure of the experiments are not specified in the original source

Apparent diffusion coefficients have been observed to depend on the uptake pressure (Atsumi 2002a), and significant variability is also observed with graphite type (Figure 5.16). In what follows, the transport mechanisms that lead to these dependences of diffusivity on partial pressure and graphite type are discussed. The distribution of hydrogen atoms and molecules across different uptake sites is the result of a multi-step hydrogen uptake and transport process (illustrated in Figure 5.12). Uptake sites are occupied progressively based on their location within the graphite, their enthalpy of uptake (Atsumi 2002a), and also based on transport within graphite and the kinetics of the uptake and desorption reactions.

Figure 5.16: Apparent diffusion coefficients from hydrogen uptake studies

Uptake Kinetics [1-7]

sample surface → open micro-porosity → closed micro-porosity **[H/C]pores** → nano-porosity, H_2 at crystallite surface → solid solution H at crystallite basal plane surface **[H/C]sol** → trapped H in inner crystallite **[H/C]chem,Trap1**

H_2 *permeation through open porosity*

H_2 *inter-granular diffusion*

H_2 *inter-crystallite diffusion*
E^{act} = 0.9 to 2.0 eV/H_2

H_2 *dissociation and reaction:*
physisorption on basal plane
ΔH=2.5 to 4.7 eV/H_2
or
trapping at crystallite edges
ΔH=-2.3 to -3.1 eV/H_2

[H/C]chem,Trap2 trapped H at crystallite edge

De-trapping and/or *dissociation and intra-crystallite diffusion*
E^{act} = 1.25 eV/H_2
Trapping at non reconstructed edges
ΔH=-4.2 to -5.5 eV/H_2

Notes:
Rate-limiting steps (RLS) are underlined
ΔS ~ 0.26 eV/K H_2 for hydrogen absorption at 500 - 800 °C
Trap 1 uptake is rate-limited by a first order kinetics (detrapping or dissociation), but the RLS has not yet been identified.

Desorption Kinetics [8-13]

sample surface ← open micro-porosity ← closed micro-porosity **[H/C]pores** ← nano-porosity, H_2 at crystallite surface ← solid solution H at crystallite basal plane surface **[H/C]sol**

Recombination
E^{act} = 2.5 or 2.17 eV/H_2

[H/C]chem,Trap2 trapped H at crystallite edge

[H/C]chem,Trap1 trapped H in inner crystallite

De-trapping
E^{act} = 6.93 or 4.8 eV/H_2

H_2 *permeation through open porosity*

H_2 *inter-granular diffusion*
E^{act} = 1.3 eV/H_2

H_2 *inter-crystallite diffusion*

H_2 *inter-crystallite diffusion (with trapping effects)* or *recombination*
E^{act} = 3.48 or 3.8 eV/H_2

Note:
Rate-limiting steps (RLS) are underlined

Interpretation of an example TDS

Peak 1 (600 - 700 K) Peak 2 (900 - 1300 K) Peak 4 (1300 - 1450 K) Peak 5 (1600 - 1800 K)

[H/C]pores
Uptake RLS = H_2 inter- granular diffusion
Desorption RLS = H_2 inter- granular diffusion

[H/C]sol
Uptake RLS = H_2 inter-crystallite diffusion
Desorption RLS = recombination

[H/C]chem, Trap 2
Uptake RLS = H inter-crystallite diffusion
Desorption RLS = H inter-crystallite diffusion (with trapping) or recombination

[H/C]chem, Trap 1
Uptake RLS = dissociation or detrapping
Desorption RLS = detrapping

Temperature (°C): 200, 400, 600, 800, 1000, 1200, 1400
Released D_2 molecules (D_2 g⁻¹ s⁻¹): 1E15, 1E14, 1E13, 1E12
Temperature (K): 400, 600, 800, 1000, 1200, 1400, 1600

Notes:
Graphite grade: ISO-880U; isotope: D_2; uptake pressure: 63.3 kPa; uptake temperature: 1273 K; desorption: heating rate 0.1 K/s and vacuum below 10^{-5} Pa. Peaks are fitted with Gaussian functions. Data source: digitized figure from [14].

Sources: [1] (Causey, Baskes and Wilson, 1986) [2] (Kanashenko,1996) [3] (Lechner, Baranek and Vach, 2018) [4] (Yang and Yang, 2002) [5] (Yamashina and Hino, 1989) [6] (Atsumi, 2002) [7] (Oriani, 1970) [8] (Ferullo et al., 2010) [9] (Dolan et al., 2020) [10] (Robell et al., 1964) [11] (Atsumi, 1989) [12] (Kissinger, 1957) [13] (Atsumi et al., 2013) [14] (Atsumi and Kondo, 2018)

Figure 5.17: Uptake and desorption mechanisms in graphite. From left to right: macroscopic scale to molecular scale. The interpretation of an example TDS is shown, as an experimental method that probes the RLS of uptake and desorption.

When the surface of a graphite sample is exposed to a hydrogen partial pressure, gas molecules penetrate the sample surface and reach the surface of grains by *permeation through the open porosity*. The diffusion of molecular hydrogen through the open pores is assumed to be rapid enough so that the partial pressure at the grain surface is the same to the pressure outside the sample (Atsumi and Iseki 2000). *Inter-granular diffusion* allows access of the H_2 molecules to the surface of the grains in the closed porosity. According to one of the earliest studies on hydrogen chemisorption in graphite (Hoinkis 1991a), hydrogen diffusion in closed porosity is the rate

190

limiting step in hydrogen uptake. The two paths for access of the closed porosity are inter-granular diffusion and inter-crystallite diffusion.

Within the graphite grain, hydrogen diffuses as a molecule via *inter-crystallite diffusion*, with a diffusion coefficient $D_{H_2,ic\ diff}$. The difference between the *inter-crystallite diffusion coefficients* and the *apparent diffusion coefficients* is explained by the trapping of hydrogen in Trap 2 sites, which involves dissociation of the molecules into atoms and formation of C-H bonds. For hydrogen uptake in steel, the effect of trapping sites on the apparent diffusivity is captured in the model of (Oriani 1970): diffusing atoms can be trapped in trapping sites along the diffusion path and trapped hydrogen is in equilibrium with un-trapped hydrogen at each point of the diffusion path. For inter-crystallite diffusion in graphite, trapped hydrogen is hydrogen in Trap 2 sites, and un-trapped hydrogen is molecular H_2 in the nano-porosity. Introducing ϵ_2 as the occupancy fraction of Trap 2 sites, n_2 as the number density of Trap 2 sites (sites per m^3) and $[H]_{nano}$ as the number density of hydrogen in nanoporosity (atoms per m^3), the apparent diffusion coefficient can be computed as in Equation 5.54:

$$D_{H_2,app\ abs} = \frac{D_{H_2,ic\ diff}}{1 + \frac{n_2 \epsilon_2}{[H]_{nano}}(1 - \epsilon_2)} \qquad 5.54$$

The concentration of hydrogen in nanoporosity can be computed using the ideal gas law (Equation 5.55):

$$[H]_{nano} = \frac{\alpha_n P_{H_2(g)} N_{Av}}{RT} \qquad 5.55$$

where α_n is the nanoporosity in the sample (in percent over sample volume), N_{Av} is the Avogadro number and R is the universal gas constant. As discussed in Section 5.2, Trap 2 occupancy follows a Langmuir isotherm (Equation 5.56):

$$\epsilon_2 = \frac{1}{1 + \left(K_{chem,2}P\right)^{-1/2}} \qquad 5.56$$

where $K_{chem,2}$ is the equilibrium constant of chemisorption in Trap 2, computed as in Equation 5.57 :

$$K_{chem,2} = \exp\left(-\frac{\Delta H_2}{k_b T}\right)\exp\left(\frac{\Delta S_{chem}}{k_b}\right) \qquad 5.57$$

where ΔH_2 is the enthalpy of adsorption in Trap 2, ΔS_{chem} is the entropy of adsorption and k_b is the Boltzmann's constant. Equations 5.54-5.57 describe the effect of one type of trapping sites (Trap 2) on apparent diffusion coefficients. Graphite crystallite surfaces present two uptake sites (physisorption and Trap 2) of similar locations within the graphite microstructure (i.e., at the surface of the crystallite). The formulation can be extended to consider more than one type of trapping site, either starting from Equation 5.54 or starting from the balance equations discussed in (Tsuchiya and Morita 1996).

As a result of Equations 5.54-5.57, the apparent diffusion coefficient depends on temperature, pressure, and density of Trap 2 trapping sites. The apparent diffusion coefficient converges to the inter-crystallite diffusion coefficient in case of no trapping sites and would degenerate to zero in the limit of an infinite amount of Trap 2 sites. To illustrate the effect of Trap 2 sites on the apparent

diffusion coefficient, Figure 5.18 plots the ratio of the apparent diffusion coefficient to the inter-crystallite diffusion coefficient at various pressures and two temperatures, for two values of n_2.

(Kanashenko 1996) estimated the concentration of Trap 2 sites in POCO AXF-5Q to 200 appm. This value and Equations 5.54-5.57 are used to estimate the inter-crystallite diffusion coefficients, which is reported in Table 5.20 alongside the apparent diffusion coefficient. Trap 2 number density n_2 varies across graphite grades and may vary across different types of grains within the same sample. Furthermore, as discussed in Section 5.4, neutron irradiation and pre-oxidation increase the number density of Trap 2 sites.
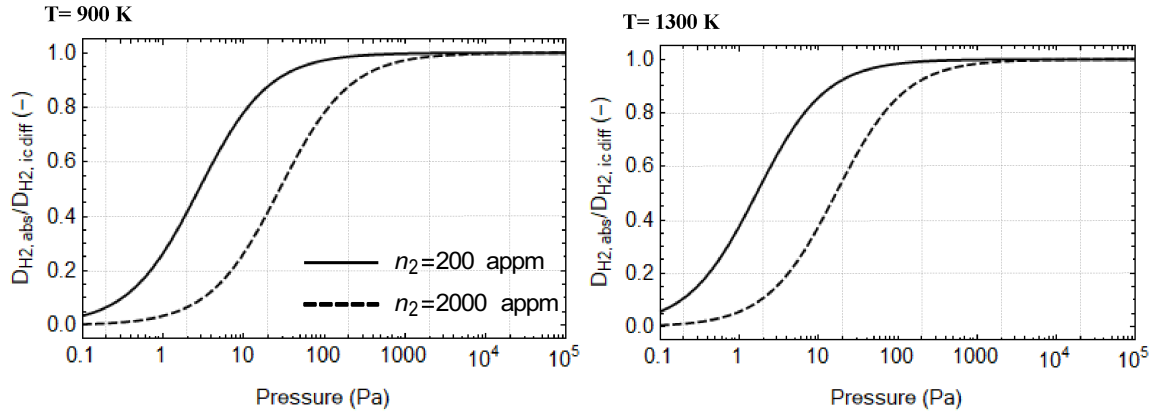

Figure 5.18: Ratio of the apparent diffusion coefficient to the inter-crystallite diffusion coefficient for two cases of Trap 2 density, as a function of partial pressure. Calculated from Equations 5.54 – 5.57.

Figure 5.18 shows that at high pressure or with a low density of trapping sites, the apparent diffusion coefficients converge to the inter-crystallite diffusion coefficients. For this reason, apparent and inter-crystallite diffusion coefficients of the experiments in Table 5.20 (all performed at pressures above 66 Pa) coincide. On the other hand, the difference between the apparent and inter-crystallite diffusion coefficient would be marked at low pressures, as in the FHR. In this case, assuming a partial pressure of 20 Pa and a temperature of 900 K, apparent diffusion coefficients would be 35% to 80% of the inter-crystallite diffusion coefficients otherwise measured at higher H_2 partial pressures.

The inter-crystallite diffusion coefficient $D_{H_2, ic\ diff}$ has an Arrhenius dependence on temperature (Equation 5.58) (Atsumi 2002a):

$$D_{H_2, ic\ diff}\left(\frac{m^2}{s}\right) = D_0 \exp\left(-\frac{E^{act}_{H_2, ic\ diff}}{k_b T}\right)$$

5.58

where T is in K , k_b i the Kevin-Boltzmann constant, D_0 depends on the type of graphite and $E^{act}_{H_2, ic\ diff}$ is the activation energy for inter-crystallite diffusion. The apparent diffusion coefficient has an additional dependence on temperature arising from the thermodynamics of trapping (Equations 5.54-5.57). Therefore, if trapping effects are important, the uptake rates and apparent diffusion coefficients should not follow a purely Arrhenius behavior. The deviation of the apparent diffusion coefficient from the Arrhenius behavior can be observed by plotting the ratio of the apparent and inter-crystallite diffusion coefficients as a function of temperature, for different pressure levels.

This is shown in Figure 5.19, for two values of the trapping site number density n_2 and for three levels of pressure. Figure 5.19 indicates that trapping effects are not effective at pressures of tens of kPa and become visible only for large Trap 2 number density and low pressure. At a pressure of 0.27 kPa and a number density of 200 appm (indicative of unirradiated graphite), the maximum predicted deviation is of about 5% at 1000 K. With a number density of 2000 appm (indicative of irradiated graphite), the maximum predicted deviation increases to about 20% at the same pressure and temperature. Based on Equations 5.54-5.57, at a pressure of 20 Pa, relevant for FHRs, the temperature dependence of the apparent diffusion coefficient deviates from the Arrhenius behavior by about 30% with a Trap 2 number density of 200 appm and by 80% with a density of 2000 appm.
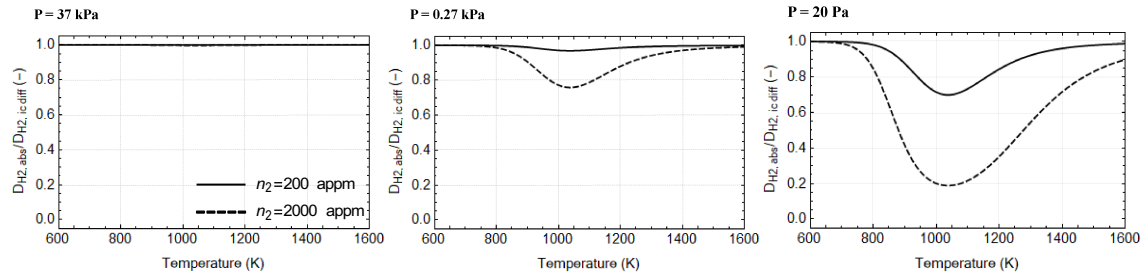

Figure 5.19: Ratio of the apparent diffusion coefficient to the inter-crystallite diffusion coefficient for two cases of Trap 2 density, as a function of uptake temperature. Calculated from Equations 5.54-5.57.

Apparent diffusion coefficient from uptake experiments on unirradiated graphite show little effect of the trapping sites. (Atsumi 2002b), for example, fitted the apparent diffusion coefficient with an exponential function of the temperature in the interval 1100 – 1300 K and at pressures between 0.027 kPa and 31 kPa (Figure 5.20). The fit seems reasonable for all datapoints except for IG-110U at 0.027 Pa. In this case, the apparent diffusion coefficient shows a marked decrease around 1200 K, coherently with Figure 5.19. As the fitting lines and the R^2 coefficient of the linear fit in Figure 5.20 are not available within the original source, this observation cannot be supported quantitatively.

If trapping effects are not impactful on the absorption rate, the only dependence on temperature appears in the Arrhenius relation for the inter-crystallite diffusion coefficient (Equation 5.58). This means that inter-crystallite diffusion activation energies $E_{H_2,ic\ diff}^{act}$ can be extracted from the logarithmic plots of the apparent diffusion coefficient (Table 5.21).
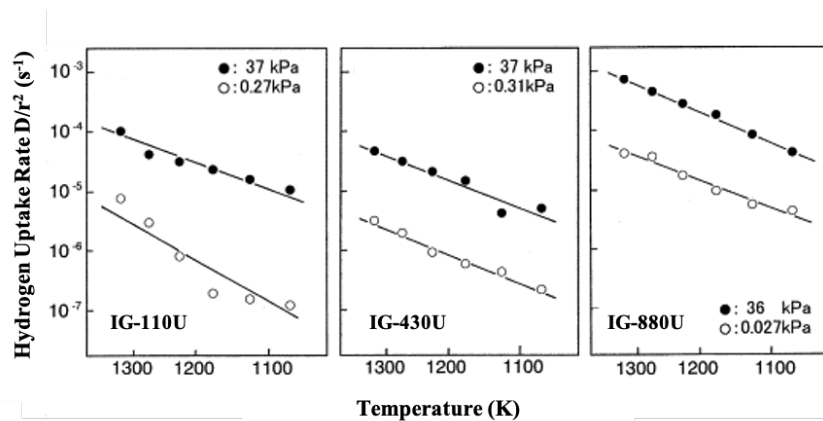

193

Table 5.21: Activation energy for hydrogen diffusion in graphite estimated from hydrogen uptake experiments

Graphite Type	Inter-crystallite diffusion activation energy $E_{H_2,ic\ diff}^{act}$	Temperature Range	Pressure	Hydrogen Isotope	Source
	(eV)	(K)	(Pa)		
POCO-AXF	0.9	573-773	Not Available (Exposure to plasma)	D, T	(Causey 1989)
ISO-880U	1.04	973-1323	10,000	H	(Atsumi et al. 2009a)
IG-110U, IG-430U, ISO-880U	1.3	1100-1300	27-37000	H	(Atsumi 2002a)
ISO-880U [a]	1.60	973-1323	10,000	H	(Atsumi et al. 2009a)
Platinized Carbon	1.7	573-665	40,000-80,000	H	(Robell et al. 1964a)
IG-430U [a]	1.92	973-1323	10,000	H	(Atsumi et al. 2009a)
IG-430U	1.99	973-1323	10,000	H	(Atsumi et al. 2009a)
[a] Irradiated at a fluence of $3.9\ 10^{19}$ n/cm^2					

As Trap 2 sites become more occupied and the chemisorption reaction approaches thermodynamic equilibrium, hydrogen atoms detrap from Trap 2 sites at the same rate at which they are trapped and recombine in molecules. The yet-to-be-trapped or detrapped H_2 molecules continue their diffusion along crystallite edges, as a sequence of trapping and detrapping. Ultimately, the molecule may dissociate at the crystallite surface and migrate inside the crystallites, diffusing between graphite lamella (*intra-crystallite diffusion)*, being ultimately bound to Trap 1 sites. Trapping in Trap 1 (Equation 5.59) has an equilibrium constant expressed in Equation 5.60.

$$2C_1^* + H_2(g) \rightarrow\ 2\ C_1^* - H \qquad\qquad 5.59$$

$$K_{chem,1} = \frac{[C_1^* - H]^2}{[C_1^*]^2 \cdot P_{H_2(g)}} = \exp\left(-\frac{\Delta H_1}{k_b T}\right)\exp\left(\frac{\Delta S_{chem}}{k_b}\right) \qquad 5.60$$

where C_1^* is the Trap 1 RCS and ΔH_1 is the enthalpy of adsorption in Trap 1. For practical applications, hydrogen does not detrap from Trap 1. The enthalpy of Trap 1 is large enough that, at the temperatures and pressures of interest, the equilibrium constant of the reaction in Equation 5.59 is very high, and the reaction rate of the inverse reaction is negligible.

Figure 5.21 shows a pressure curve for an uptake experiment that exhibits two regimes for the time-dependent uptake rate: a first regime that is *diffusion-controlled*, and a second regime that is

reaction-kinetics-controlled (Atsumi 2003). In the experiment with an initial hydrogen pressure of 38.2 kPa, the pressure evolution with time is fitted by the equation for transport by diffusion (Equation 5.52) only for an initial phase. At longer times, the decrease in the hydrogen partial pressure predicted by the diffusion-controlled curve is an underestimate of the experimental pressure decrease in the chamber. This second phase occurs as Trap 2 chemisorption approaches equilibrium and hydrogen starts to be trapped in Trap 1. In this second phase, the pressure decreases exponentially, hence following a first-order reaction kinetics. Both molecular dissociation and detrapping are first-ordered reactions, hence the reaction-kinetics-controlled process could be in principle attributed either to detrapping from Trap 2 sites or to a molecular dissociation at the surface of the crystallite. In a dissociation-controlled reaction, hydrogen pressure would evolve as in Equation 5.61:

$$\frac{dP_{H_2}}{dt} = \frac{RT}{V_0 N_{Av}} \frac{dN_{H_2}}{dt} = \frac{RT}{V_0 N_{Av}} k_{Diss} [H_2] \propto P_{H_2}(t) \qquad 5.61$$

where, in addition to the variables introduced earlier, N_{H_2} and $[H_2]$ are the number and concentration of hydrogen molecules in the chamber and k_{Diss} is the dissociation reaction constant.

In a detrapping-controlled process, the rate of detrapping atoms dN_T/dt is expressed as in Equation 5.62:

$$\frac{dN_T}{dt} = \mu N_T(t) \exp\left(-\frac{E_{dt}^{act}}{k_b T}\right) \qquad 5.62$$

where N_T is the number of trapped atoms, μ is a pre-exponential factor, and E_{dt}^{act} is the activation energy for detrapping. In steady state, assuming that hydrogen atoms are detrapped at an exponential rate, Trap 2 sites are filled by newly uptaken hydrogen atoms at the same rate. As a result, the decrease of hydrogen concentration in the chamber is exponential too. Assuming that the ideal gas law is valid for hydrogen in the chamber, also the hydrogen partial pressure will decrease exponentially (Equation 5.63).

$$\frac{dP_{H_2}}{dt} = \frac{RT}{V_0 N_{Av}} \frac{dN_{H_2}}{dt} \propto \frac{dN_T}{dt} \propto N_T(t) \qquad 5.63$$

Studying the reaction rate (computed from the pressure evolution with time in uptake experiments) at various temperatures (presumably in the 1100 K - 1300 K, but not reported in the article), (Atsumi 2003) estimated the activation energy of Trap 1 uptake to 1.25 eV/H_2. This value is considerably smaller than the enthalpy of detrapping from Trap 2 (2 to 3 eV/H_2). For this reason, (Atsumi 2003; Atsumi et al. 2011) hypothesized that that the process could be rate-limited by *surface dissociation*, instead of detrapping from Trap 2. Surface dissociation to a hypothetical free hydrogen atom requires an energy of 4.8 eV/H_2; however, as the state of hydrogen atoms diffusing intra-crystallite is different from free hydrogen atoms, the dissociation energy might be lower than 4.8 eV/H_2, and somewhere below 1.25 eV/H_2. Detrapping from Trap 2 starts at an energy level that is 2 to 3 eV/H_2 lower versus an H_2 molecule, which would make it not compatible with the 1.25 eV/H_2 activation energy measured experimentally. However, the two mechanisms might have different intermediate states, and if the intermediate state for H_2 dissociation is much harder to reach than the intermediate state for detrapping, then detrapping might in fact be associated with the 1.25 eV/H_2 activation energy. (Atsumi 2003) does not include details on how the activation

energy has been estimated from the data, and whether this result depends on pressure or varies across graphite grades.
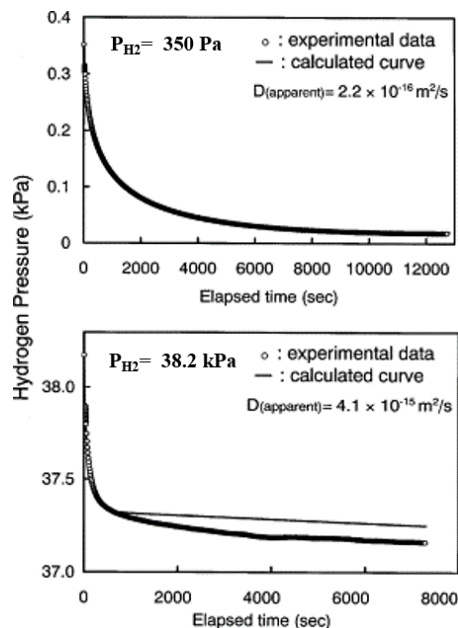

Figure 5.21: Hydrogen pressure change during hydrogen uptake on graphite compared to calculations based on inter-crystallite diffusion controlled-uptake, at different partial pressures. Sample: ISO-880U. Uptake Temperature: 1273 K (Atsumi 2003).

This regime of reaction kinetics-limited transport leading to Trap 1 uptake is not seen when the initial pressure of the uptake experiment is at the lower value of 350 Pa. In this case, the time-dependent pressure curve is fitted accurately by an inter-crystallite diffusion-controlled curve. (Atsumi 2003) argued that at this low pressure the occupancy of Trap 2 sites was insufficient to cause their detrapping and the trapping of the Trap 1 sites. In agreement with this hypothesis, a 5% Trap 2 occupancy is calculated using the Langmuir isotherm at 350 Pa, 1273 K and Trap 2 enthalpy of -2.4 eV/H_2 (Section 5.2). This result suggests hydrogen needs to be previously trapped in Trap 2 sites to be able to access Trap 1 sites and points towards a detrapping rather than a molecular dissociation mechanism. The missing information to elucidate the nature of the transport mechanism in the reaction kinetics-limited regime is the energy level of a dissociated hydrogen atom that is diffusing intra-crystallite; no prior studies have estimated this energy level. Neither have there been prior studies that quantify the reaction constant or activation energy for trapping in Trap 1, or the diffusion coefficient or its activation energy for intra-crystallite diffusion; therefore, it remains an assumption that the rate-limiting step of Trap 1 uptake mechanism is either detrapping or dissociation, and not intra-crystallite diffusion or trapping in Trap 1.

In summary, hydrogen uptake in graphite occurs via a multi-step process (illustrated in Figure 5.12). When graphite is exposed to a hydrogen partial pressure, by permeation through the open porosity, gas molecules penetrate the sample surface and reach the surface of grains that outline the open porosity networks. *Inter-granular diffusion* and *inter-crystallite diffusion* allow access of the H_2 molecules to the surface of the grains in the closed porosity. Within the graphite grain, hydrogen continues to diffuse as a molecule via *inter-crystallite diffusion* (a *diffusion-controlled* process) and as an atom via *intra-crystallite* diffusion (a *reaction-kinetics-controlled* process). The inter-crystallite diffusion process is slowed down by trapping-detrapping at Trap 2 sites; this effect

196

is quantified by the ratio of the apparent diffusivity to the inter-crystallite diffusivity, which is dependent on temperature, pressure, and abundance of Trap 2 sites in the graphite; the activation energy for the inter-crystallite diffusion is 0.9 to 1.7 eV/H_2. The intra-crystallite diffusion takes place with hydrogen atoms dissociated and not yet trapped or detrapped from Trap 2 sites. Once dissociated or detrapped, the atoms migrate inside the crystallites, diffuse between graphite basal planes, and are finally trapped by Trap 1 sites. The reaction-kinetics-controlled process is attributed either to molecular dissociation or to detrapping from Trap 2; the activation energy is 1.25 eV/H_2. The enthalpy of Trap 1 is large enough that, at the temperatures and pressures of interest for fission and fusion applications, the equilibrium constant of the trapping reaction is very high, and the reaction rate of the inverse reaction is negligible.

For PB-FHRs, it has been proposed to use fuel pebbles as vectors for tritium degassing (Forsberg et al. 2017c; Lam 2017). According to this strategy, the pebbles would uptake tritium while in core and would then desorb it when degassed out of core. As shown in Table 5.20, the time required to reach thermodynamic equilibrium spans from less than one hour to eighty hours, for sample thicknesses on the order of cm.

Estimates of apparent diffusion coefficients are not available at low partial pressures, such as 20 Pa. Extrapolating the trapping effects at this pressures, apparent diffusion coefficients are postulated to be 35% to 80% of the inter-crystallite diffusion coefficients otherwise measured at higher H_2 partial pressures. As a result, the time required to reach thermodynamic equilibrium in tritium uptake at FHR conditions may be longer than that of studies at higher pressures. Comparing this time window to the length of stay of fuel pebbles in the PB-FHR core could support a preliminary estimation of whether the pebbles will be capable of uptaking the amount of tritium predicted by thermodynamics before they are withdrawn and, potentially, degassed.

5.3.3 Kinetics of desorption studied via thermal desorption spectra (TDS)

Hydrogen desorption occurs via different mechanisms depending on the site at which hydrogen is retained within the graphite sample (i.e., confined in molecular form in the pores, physisorbed/dissolved on the basal planes, chemisorbed on trapping sites). Each of the desorption mechanism has a different kinetics, influenced by a different rate-limiting step (RLS). Thermal desorption is an experimental method that can probe the RLS of uptake and desorption. Figure 5.12 shows the interpretation of an example TDS, and each of the TDS peaks is discussed in detail in the subsequent sections, in terms of kinetics and transport.

5.3.3.1. Peak 1: desorption from closed pores

Molecular hydrogen confined in closed pores is desorbed through *inter-granular diffusion* (Atsumi et al. 2013a). This is confirmed by the effect of shorter uptake times on the temperature of Peak 1 in the TDS. As shown in (Atsumi et al. 2013a), a shorter uptake time leads to a downshift of Peak 1 temperature in TDS. In a diffusion-controlled process, an insufficient charge of the sample produces higher concentration of gas close to the sample surface. As a result, gas molecules start to be desorbed sooner during desorption, and the TDS peak is shifted to a lower temperature. The diffusion scale is the thickness of the sample. To access the closed pores, hydrogen diffuses by inter-granular diffusion, moving across the different pore networks. During desorption, it is evident that the rate-limiting diffusion is at the sample scale because the Peak 1 intensity is impacted by the sample thickness. The diffusion coefficient $D_{H_2, ig\ diff}$ for the inter-granular diffusion of hydrogen molecules can be modeled with an Arrhenius equation (Equation 5.58), with an

activation energy of 1.3 eV/H₂ (Atsumi et al. 1988). The desorption rate dN_1/dt can be modeled by Equation 5.64,

$$\frac{dN_1}{dt} = -N_{0,1} \frac{8}{\pi^2} \frac{d}{dt} \sum_{n=0}^{\infty} \frac{1}{(2n+1)^2} \exp\left(-\frac{(2n+1)^2 \pi^2}{r_{sample}^2} D_{H_2,ig\ diff}\, t\right) \qquad 5.64$$

where $N_{0,1}$ is the number of confined molecules and r_{sample} is the thickness of the sample (Atsumi 1989). As discussed in Section 5.3.2 for hydrogen uptake, inter-granular diffusion allows access of the H₂ molecules to the surface of the grains in the closed porosity. Inter-granular diffusion coefficients and their corresponding activation energies have not been estimated in any hydrogen uptake study. However, as the diffusion mechanism should occur equivalently in uptake and desorption, estimates performed by (Atsumi et al. 1988) might apply to the uptake step as well.

5.3.3.2.   *Peak 2: desorption from basal plane/solid solution*

Hydrogen dissolved as a solid solution on graphite basal plane desorbs through a recombination-controlled process (Atsumi et al. 2013a). This conclusion is supported by Peak 2 temperature decreasing at increasing uptake pressures. In fact, if the process is rate-limited by recombination, the desorption occurs faster in case of a larger concentration of hydrogen atoms able to recombine, which is obtained with a higher uptake pressure (Atsumi et al. 2015). The desorption rate dN_2/dt with a recombination-controlled process is described by Equation 5.65 (Atsumi 1989).

$$\frac{dN_2}{dt} = \mu_2 N_2^2(t) \exp\left(-\frac{E_{H,rec}^{act}}{k_b T}\right) \qquad 5.65$$

where μ_2 is a pre-exponential factor, depending on sample specifics, and $E_{H,rec}^{act}$ is the recombination activation energy. In these studies, the activation energy for the process was not estimated. Estimates of the activation energy were instead provided by (Orimo et al. 2001) (2.5 eV/H₂ using TDS of milled graphite) and (Deng et al. 2019) (2.17 eV/H₂ by means of density functional theory (DFT) calculations).

5.3.3.3.   *Peak 4: desorption of Trap 2 chemisorbed hydrogen*

According to (Atsumi et al. 2013a), hydrogen trapped in Trap 2 sites is desorbed through *inter-crystallite diffusion*. As in the case of Peak 1, evidence for a diffusion process is given by the decrease of the peak temperature in the TDS with shorter uptake times. Unlike Peak 1 desorption, the diffusion scale for Peak 4 is the graphite grain.

The activation energy of the process was derived using the Kissinger method (Kissinger 1957). In this method, a thermal desorption experiment is performed several times with different values of the heating rate β. Changes to the heating rate produce shifts in the temperature of thermal desorption peaks T_m (for example, in (Atsumi et al. 2013b), Peak 4 temperature increases by 80 °C when the heating rate is increased from 0.0083 K/s to 0.1 K/s). (Kissinger 1957) showed that a plot of $1/T_m$ versus $\log \beta/T_m^2$ yields straight lines, and that activation energies can be estimated through the slope of the lines. Using this method, the activation energy of the process was estimated to 3.48 eV/H₂. This activation energy is more than double the activation energy for inter-crystallite diffusion estimated for H₂ uptake (Atsumi 2002b). The difference was explained by trapping effects, hypothesizing that hydrogen diffuses in atomic form and is subjected to a

sequence of trapping and detrapping from the crystallite edges that slows it down. The atomic desorption rate dN_4/dt can be modeled through Equation 5.66 (Atsumi 1989).

$$\frac{dN_4}{dt} = -N_{0,4} \frac{6}{\pi^2} \frac{d}{dt} \sum_{n=1}^{\infty} \frac{1}{n^2} \exp\left(-\frac{n^2\pi^2}{r_{grain}^2} D_{H,ic\ diff} t \right) \qquad 5.66$$

where $N_{0,4}$ is the number of hydrogen atoms trapped in Trap 2 sites, r is the radius of the grain and $D_{H,ic\ diff}$ is the trapping-influenced inter-crystallite diffusion coefficient (which follows an Arrhenius equation with activation energy of 3.48 eV/H$_2$).

The activation energy found by (Atsumi et al. 2013a) agrees with the value found by (Hoinkis 1991b) in deuterium desorption experiments. In (Hoinkis 1991b), A3 graphite was charged at 900°C with a D$_2$ partial pressure of 74 Pa. Deuterium desorption was studied at temperatures below 1700°C. Two main desorption peaks, Peak 4 (1150°C) and Peak 5 (1500°C) were individuated. The first was attributed to a recombination-controlled desorption mechanism with an activation energy of 3.8 eV/H$_2$.

5.3.3.4. *Peak 5: desorption of Trap 1 chemisorbed hydrogen*

Hydrogen desorbs from Trap 1 sites through a detrapping-controlled process, according to (Atsumi et al. 2013a). Despite Peak 5 desorption temperature decreases with shorter uptake times, (Atsumi et al. 2013a) argued that hydrogen diffusion within the grain and within the crystallite diffusion are rapid above 1400 K, and therefore that the desorption is not rate-limited by diffusion (this was the original attribution by (Hoinkis 1991b), with an activation energy of 4.8 eV/H$_2$). Hence, detrapping was regarded as the RLS. A detrapping-controlled process would lead to a desorption peak narrower than Peak 5, if with a single-valued uptake enthalpy for Trap 1. Hence, (Atsumi et al. 2013a) hypothesized a continuum distribution of uptake enthalpies between 4.0 and 4.9 eV/H$_2$ to reproduce the shape of the experimental desorption peak. This hypothesis is supported by the variability of the uptake enthalpies in non-reconstructed reactive sites in the -4 to -5 eV/H$_2$ window (Section 5.2).

The desorption rate dN_5/dt is modeled through Equation 5.67, valid for detrapping-controlled processes (Atsumi 1989).

$$\frac{dN_5}{dt} = \mu_5 N_5(t) \exp\left(-\frac{E_{H,dt}^{act}}{k_b T} \right) \qquad 5.67$$

where μ_5 is a pre-exponential factor, depending on sample specifics, and $E_{H,dt}^{act}$ is the detrapping desorption process activation energy. Using Kissinger's plots, the activation energy was estimated to 6.93 eV/H$_2$. The value might not be accurate since Peak 5 does not have a sharply defined peak temperature to use in Kissinger's plot (Atsumi et al. 2013a, 2015; Atsumi and Kondo 2018).

In summary, hydrogen desorption occurs through different modes depending on the way hydrogen is retained within the graphite sample (Table 5.22). Molecular hydrogen confined in closed pores (Peak 1) is desorbed through a diffusion-controlled process (Atsumi 1989). Hydrogen dissolved as a solid solution on graphite basal plane (Peak 2) desorbs through a recombination-controlled process (Atsumi 1989). Hydrogen trapped in Trap 2 sites (Peak 4) is desorbed through an inter-crystallite diffusion-controlled (Atsumi et al. 2013a) or a recombination-controlled process (Hoinkis 1991b). Finally, desorption of hydrogen trapped in Trap 1 sites (Peak 5) takes place

through a detrapping-controlled (Atsumi et al. 2013a) or a diffusion-controlled process (Hoinkis 1991b). Table 5.22 compiles the activation energies for each of these RLS relevant to desorption.

Table 5.22: Attribution of uptake and desorption mechanisms and features of each TDS peak

		Peak 1	Peak 2	Peak 4	Peak 5
Desorption Peak Temperature (Atsumi et al. 2013a)	(K)	600-700	900-1300	1300-1450	1600-1800
Dependence of Peak Area on Charging Pressure (Atsumi et al. 2013a)		Linear dependence	Square root dependence	Square root dependence with a knee	Independent
Dependence of Peak Temperature on Charging Pressure (Atsumi et al. 2013a)		Independent	Decrease with increasing pressure	Independent	Independent
Dependence of Peak Temperature on Time of Uptake (Atsumi and Kondo 2018)		Increase with increasing time	Independent	Increase with increasing time	Increase with increasing time
Dependence of Peak Intensity and Area on Uptake Temperature		Independent	Decrease with increasing temperature	Decrease with increasing temperature	Decrease with increasing temperature
Uptake mechanism (Atsumi et al. 2013a)		H_2 in closed porosity	Solid solution on the basal plane	Chemisorption in Trap 2	Chemisorption in Trap 1
Uptake enthalpy	(eV/H_2)			-2.6	-4.4
Desorption RLS (Atsumi et al. 2013a)		Inter-Granular Diffusion	Recombination	Inter-Crystallite Diffusion with trapping effects (or Recombination (Hoinkis 1991b))	Detrapping (Hoinkis 1991b))
Activation energy of desorption RLS mechanism	(eV/H_2)	0.9 (Causey 1989) or 1.3 (Atsumi et al. 1988) or 1.7 (Robell et al. 1964b)	2.5 (Orimo et al. 2001) or 2.17 (Deng et al. 2019)	3.48 (Atsumi et al. 2015) or 3.8 (Hoinkis 1991b)	6.93 (Atsumi et al. 2015) or 4.8 (Hoinkis 1991b)

5.3.4 Kinetics of desorption at constant temperature

In thermal desorption experiments, hydrogen-loaded graphite samples are heated with a constant temperature ramp rate. This condition happens rarely for degassing in technological applications. More frequently, the samples are heated to a given temperature which is kept constant for the duration of the degassing. An experimental approach in which a pre-charged graphite sample is maintained at high temperature and the desorption of hydrogen is monitored is more representative of these applications. This approach allows to assess the fraction of hydrogen evolved with time and was followed by (Redmond and Walker 1960). TSP nuclear graphite was charged with hydrogen at partial pressures of 2.4 kPa and temperatures of 1193 – 1768 K for the duration of the uptake. Then, the graphite samples were heated at temperatures between 1318 – 1538 K and the desorption of hydrogen was monitored (Redmond and Walker 1960). Hydrogen desorption curves were plotted against the logarithm of time (Elovich plots), obtaining linear curves at each desorption temperature (Fig. 2 in (Redmond and Walker 1960)).

In their analysis, the energy of activation for desorption depends on the surface coverage ϕ. In adsorption isotherms, the surface coverage represents the number of adsorbed molecules on a surface divided by the number of adsorbate molecules in a filled monolayer required for saturation (IUPAC 1997). In (Redmond and Walker 1960), ϕ is rather intended as the ratio of hydrogen not yet desorbed and still in the sample to the total amount of uptaken hydrogen at equilibrium with

the hydrogen partial pressure used for charging the sample. The activation energy E^{act} was modelled as a linearly decreasing function of the surface coverage (Equation 5.68).

$$E^{act} = E^{act}_{\phi=0} - C_0 \phi \qquad\qquad 5.68$$

where $E^{act}_{\phi=0}$ is the activation energy at the end of the desorption, i.e., at zero coverage and C_0 is a constant. For TSP graphite, $E^{act}_{\phi=0}$ was estimated to 5.9 eV/H_2 and C_0 to 1.8 eV/H_2. As a result, the activation energy spans from 4.1 eV/H_2 at the beginning of the desorption to 5.9 eV/H_2 at the end. The magnitude of the activation energy is comparable the values estimated by (Hoinkis 1991b) and (Atsumi et al. 2013b) for hydrogen desorption from Trap 1 and Trap 2 sites. The increase in the desorption activation energy with decreasing coverage hints that hydrogen retained in less energetic reactive sites (i.e., hydrogen in pores, physisorbed and in Trap 2) is desorbed earlier (i.e., at higher coverage ratio) than hydrogen in deeper trapping sites, i.e., Trap 1 (which would desorb at a lower coverage ratio).

Hydrogen desorption curves were normalized to the total volume of desorbed hydrogen and were fitted by Equation 5.69:

$$F(t) = 1 - \phi = 1 + \frac{RT}{C_0}\ln t - \frac{RT}{C_0}\ln\frac{RT}{C_0 C_1} \qquad\qquad 5.69$$

where F is the fraction of hydrogen desorbed after an interval of time t at a temperature T and C_1 is a constant.

Other authors have explored hydrogen desorption at constant temperature and have modelled the overall desorption as a diffusion process, estimating single-valued apparent activation energies. These activation energies are collected in Table 5.21. In a diffusion process, hydrogen desorption is proportional to the square root of time, rather than to the logarithm of time (Saeki 1985). However, none of the studies on unirradiated graphite includes a plot of hydrogen desorption against time. Such plots are included in two studies on irradiated graphite (Malka et al. 1980b; Rohrig et al. 1976), and will be discussed in the next section.

Table 5.23: Activation energy for hydrogen diffusion in graphite estimated from hydrogen desorption experiments

Graphite Type	Apparent diffusion activation energy	Desorption Temperature Range	Uptake Pressure	Hydrogen Isotope	Source
	(eV)	(K)	(Pa)		
Pyrolytic Carbon	2.6 - 2.7	973-1223	Not available (Exposure to ions)	D, H	(Saeki 1985)
AL2-500, AS1-500, Matrix Graphite [a]	2.78	973-1673	Not reported	T	(Rohrig et al. 1976)
A3 [b]	3.8	973-1223	Not reported	T	(Malka et al. 1980b)
Pyrolytic Carbon	4.3	1430-1730	Not available (Exposure to ions)	T	(Causey et al. 1979)
TSP	4.1 – 5.9	1318 – 1538	2400	H	(Redmond and Walker 1960)
[a] AS1-500 irradiated at a fluence of 1.6 10^{20} n/cm^{-2}, AL2-500 irradiated at a fluence of 7.7 10^{21} n/cm^{-2}, Matrix Graphite irradiated at a fluence of 2.5 10^{20} n/cm^{-2}					
[b] Irradiated at a fluence of 2.3 10^{20} n/cm^{-2}					

Degassing of tritium-loaded PB-FHR pebbles is one example of a technological application involving constant-temperature desorption of hydrogen from graphite. During their irradiation, PB-FHR pebbles alternate periods in core with periods out-of-core. A pass through the core requires about 60 days, and PB-FHR pebbles spend 4 days in the defueling chute between two passes. Tritium degassing may take place during some or all of these out-of-core periods or at the end of the pebble irradiation. If degassing is expected to take place during the out-of-core periods, these periods should be long enough to allow for the desired fractional desorption of tritium. Assuming a linear increase of the activation energy with coverage, (Redmond and Walker 1960) estimated that hydrogen/tritium desorption at constant temperature occurs at an exponential rate. Assuming a degassing temperature of 1150 °C and extrapolating from (Redmond and Walker 1960), about 100 hours would be required for a tritium fractional desorption of 80%.This interval is comparable to the time spent by the pebbles in the defueling chute.

5.3.5 Isotopic Effects

Because tritium is radioactive, it is frequent in experimental studies to replace it with hydrogen or deuterium, and to assume that the results are unchanged.

Changes in the uptake and desorption behavior across the isotopes may be due to isotopic effects on the diffusivities or on the activation energy of hydrogen diffusion. According to classical diffusion theory, the diffusivity coefficients of isotopes in metals scale with the inverse of the square root of the mass of the isotopes, as in Equation 5.70 (Wert and Zener 1949):

$$\frac{D_{0,H}}{D_{0,T}} = \sqrt{\frac{m_T}{m_H}} \tag{5.70}$$

Equation 5.70 predicts a 1.4 diffusivity ratio for hydrogen vs. deuterium, 1.7 for hydrogen vs. tritium, and 1.2 for deuterium vs. tritium. In many hydrogen-metal systems, deviations from this relation have been observed experimentally. Experimental results indicate that Equation 5.70 might be accurate only at elevated temperatures (above 200°C), and that it tends to underestimate the isotopic effects for BCC metals and to overestimate them for FCC metals (Völkl and Alefeld 1978). In graphite, computational and experimental studies suggest that some deviation from Equation 5.70 occur even at elevated temperatures. Using Kinetic Monte Carlo and Molecular Dynamics, (Warrier et al. 2004) showed that hydrogen diffusion in graphite takes place by two mechanisms: a jump mechanism that shows $1/\sqrt{m}$ dependence and a jump mechanism that is independent of the mass of the isotope and depends only on the phonon frequency of the graphite; at 700°C, they computed a ratio of 1.2 for T vs H and 1.1 for D vs H diffusivity in a graphite crystallite, and higher ratios at lower temperatures. (Atsumi and Iseki 2000) studied the uptake behavior of hydrogen and deuterium in IG-110U graphite under an uptake pressure of 10 kPa and estimated a ratio of 1.33 between the diffusivities of the isotopes at 1273 K. (Nishikawa et al. 1995) studied deuterium and hydrogen diffusion in desorption experiments with ATX-20U graphite and estimated a ratio of 1.7 between their diffusivities (for temperatures in the interval 973-1273 K). Neither (Nishikawa et al. 1995) nor (Atsumi and Iseki 2000) provided error bars in their data.

On the contrary, the activation energy of diffusion, in both uptake and desorption processes, does not appear to demonstrate isotopic effects. Ref. (Atsumi and Iseki 2000) estimated an activation energy of diffusion of 1.58 eV for hydrogen uptake and 1.64 eV for deuterium (6% deviation). The uncertainty associated with the estimation was not reported, and therefore the difference in the

activation energies may be artificial. (Nishikawa et al. 1995) estimated the desorption energy of both hydrogen and deuterium to 1.05 eV (error bars on these values are not reported); these results were obtained by fitting the desorption curves of hydrogen and deuterium from pre-charged ATX-20U graphite to a model of diffusion-controlled desorption. (H.D. Rohrig et al. 1975) plotted thermal desorption spectra of hydrogen and tritium from graphite matrix and individuated three peaks in the interval 200°C – 1000°C: Peak 1,2 and 4. Peak 1 and Peak 4 are controlled by diffusion, and Peak 2 is controlled by recombination. As each peak occurs approximately at the same temperature for both isotopes, the activation energies for diffusion and recombination process appear to be approximately the same between tritium and hydrogen (Fig. 4 in (H.D. Rohrig et al. 1975)). The resolution of the thermal desorption spectra (~100 °C) is too low to allow for a more precise comparison.

The lack of isotopic effects on the activation energy of recombination-controlled desorption is confirmed by (Ashida et al. 1984). (Ashida et al. 1984) studied thermal desorption of hydrogen, deuterium, and tritium from ion-implanted pyrolytic graphite. They individuated three peaks in the desorption spectra, approximately at the same temperature for the three isotopes. Among these, Peak 2 was located around 650°C and was attributed to a recombination-controlled desorption process. The same desorption activation energy (1.91 eV) was estimated for all three isotopes. For recombination-controlled desorption, (Ashida et al. 1984) observed that the pre-exponential factor in Equation 5.65 is proportional to *1/m*; the ratio of the desorption frequencies was measured at H_2:D_2:T_2= 3:1.5:1. This result is in opposition to the theoretical model developed by (Baskes 1980) for recombination-controlled desorption from metals, according to which the desorption rate is proportional to $1/\sqrt{m}$.

An isotopic-dependence of the activation energy was observed only in the case of ion-implanted isotopes; for example, (Zecho et al. 2002) studied low temperature (T < 700K) thermal desorption from HOPG graphite implanted with hydrogen and deuterium atoms and the desorption of H chemisorbed on the basal plane (with puckering of a carbon atom out of the surface) had an activation energy of 0.95 eV for D and 0.6 eV for H.

In conclusion, the kinetics of uptake and desorption are susceptible to isotopic effects on the pre-exponential factor, but not on the activation energy. According to classical diffusion theory, the diffusivity coefficients of isotopes in metals scale with the inverse of the square root of the mass of the isotopes. Computational and experimental studies suggest that isotopic effect for hydrogen diffusion in graphite may be either more or less pronounced than the inverse square root relation. Desorption frequencies of recombination-controlled processes were shown to be proportional to *1/m,* in disagreement with theoretical predictions for metals showing a $1/\sqrt{m}$ dependency (Ashida et al. 1984; Zecho et al. 2002). Activation energies of diffusion-controlled processes and recombination process were shown to be generally insensitive to isotopic effects (Atsumi and Iseki 2000), (Nishikawa et al. 1995). Only desorption of ion-implanted hydrogen isotopes showed a difference in activation energy between hydrogen and deuterium (Zecho et al. 2002).

5.3.6   Conclusion

For tritium management in PB-FHRs, it has been proposed to use fuel pebbles as vectors for tritium degassing (Forsberg et al. 2017c; Lam 2017). According to this strategy, the pebbles would uptake tritium while in core and would then desorb it when degassed out of core. Any theoretical prediction of hydrogen retention and distribution in graphite based entirely on the thermodynamics of the C-H reactions bears the risk of being an overestimate in the case of uptake and an

underestimate in the case of desorption, because the thermodynamic equilibrium condition to which it applies may be reached after a long time or not reached at all. The purpose of this chapter is a review of the kinetics of uptake, transport, and desorption of hydrogen in graphite at high temperature and to briefly discuss the applicability of the reviewed concepts to FHR conditions: <20 Pa partial pressures, 500-700 °C uptake temperature, <1600 °C desorption temperature, in-core neutron irradiation above 1 dpa, in-core residence time of 100s days, and pebble lifetime on the order of a year.

A review of uptaken hydrogen distribution within a sample shows that the distribution is not spatially uniform, with hydrogen concentration in the external surface up to 450 times larger than in the bulk (Table 5.19). A higher density of RCS at the sample surface could be induced by interactions with the operational environment (e.g. oxidation, fluorination, irradiation, possibly friction and wear from pebble fuel movement), or by the manufacturing process (e.g. machining or polishing of sample surface, impregnation for graphite densification, specifics of the manufacturing process that might lead to heterogeneity) (Orimo et al. 2001; Shen et al. 1996). Further investigation of the surface/bulk differences could involve testing hydrogen uptake on a cleaved graphite surface.

Available literature on hydrogen uptake rates is compiled in Table 5.20 and Figure 5.16 and the multi-step process through which uptake take place is described in Figure 5.12. Hydrogen desorption has a different rate-limiting step (RLS) and hence different kinetics, depending on how the hydrogen is retained in the graphite (Table 5.22 and Figure 5.12). Table 5.22 compiles activation energies from experiments of hydrogen desorption at constant temperature.

Isotopic effects on the kinetics of uptake and desorption have been shown by computational and experimental studies to deviate from the classical diffusion theory, in which the diffusivity coefficients of isotopes in metals scale with the inverse of the square root of the mass of the isotopes. Desorption frequencies of recombination-controlled processes were shown to be proportional to $1/m$. (Ashida et al. 1984; Zecho et al. 2002). Activation energies of diffusion-controlled processes and recombination process were shown to be generally insensitive to isotopic effects (Atsumi and Iseki 2000), (Nishikawa et al. 1995).

As shown in Table 5.20 for sample thicknesses on the order of cm, the time required to reach thermodynamic equilibrium spans from less than one hour to eighty hours. Estimates of apparent diffusion coefficients are not available at low partial pressures, such as 20 Pa. Extrapolating the trapping effects at these pressures, apparent diffusion coefficients are postulated to be 35% to 80% of the inter-crystallite diffusion coefficients otherwise measured at higher H_2 partial pressures. As a result, the time required to reach thermodynamic equilibrium for tritium uptake at FHR conditions may be longer than that of studies at higher pressures and may exceed the pebble residence time in core. The reduction of uptake rates with irradiation could also decrease the effectiveness of pebbles as a vector for removal of tritium in PB-FHRs. Assuming that the time to thermodynamic equilibrium increases by a factor of 40 with irradiation, then it could take more than 1000 days for the pebbles to reach its hydrogen uptake capacity.

Constant-temperature desorption of hydrogen from graphite is relevant for degassing of tritium-loaded PB-FHR pebbles. Tritium degassing may take place in-between consecutive irradiation of the pebbles or after the pebbles are ultimately discharged. If degassing is expected to take place in-between irradiation periods, these periods should be long enough to allow for the desired fractional desorption of tritium. Using the exponential relation from (Redmond and Walker 1960)

with a degassing temperature of 1150 °C, about 100 hours would be required for a tritium fractional desorption of 80%. This interval is comparable to the time spent by the pebbles in the defueling chute. Using the square-root relation developed by (H.D. Rohrig et al. 1975) with a degassing temperature of 1100 °C, the estimated degassing time would increase to around 11,000 hours (1.25 years, making full degassing during the out-of-core passes impractical, but degassing before spent fuel disposal still feasible). Nevertheless, as the uptake capacity of irradiated graphite is high and hydrogen uptake in-core in the irradiated graphite is kinetically limited, partial tritium removal during recirculation passes may be acceptable.

Numerous gaps prevent from a full description of hydrogen uptake and desorption behavior. Experimental gaps are particularly concentrated around pressure, temperature, irradiation, and oxidation conditions of great interest for FHRs operations and accident scenarios. Hydrogen uptake experiments seem to suggest that uptake occurs in a two-stage process, but the kinetics and rate-limiting steps are far from being convincingly explained. The interpretation of TDS is not univocal; authors have attributed some of the desorption peaks (e.g., Peak 4 and Peak 5) to different RLS and have estimated alternative desorption activation energies. It is not clear whether RLS and activation energies are the same across grades or are influenced by microstructure. It is not clear whether irradiation causes changes to the RLS and diffusion activation energies. Estimates of apparent diffusion coefficients at low partial pressures, such as 20 Pa, are not available. In this review, apparent diffusion coefficients are extrapolated at these pressures using a model developed for interstitial diffusion in metal. The validity of this model for hydrogen diffusion in graphite needs to be verified experimentally with uptake studies at low pressures. Constant-temperature hydrogen desorption have been described with exponential and square-root time evolutions. Such attributions are derived from few experimental results and lead to opposite theoretical conclusions (variable vs constant activation energies) and to significant variability in predictions for desorption time longer than one hour. In the future, producing a wide database of desorption experiments, under variable experimental conditions (uptake and desorption temperature, uptake pressure, graphite grade, oxidation, and irradiation conditions) could support mechanistic models to identify the appropriate desorption behavior and would increase the accuracy for long desorption time extrapolations. Lastly, studies on the isotopic effects on kinetics are limited to diffusion-controlled and recombination-controlled processes. Investigating the effects on detrapping-controlled processes would be relevant for FHR designers, as about 25% of tritium in an FHR would desorb from Trap 1 with a detrapping-controlled process.

5.3.7 Acknowledgement

5.4 Effects of Neutron Irradiation, Graphite Oxidation, and Chemical Environment on Tritium Uptake and Desorption

5.4.1 Effects of Neutron Irradiation

Graphite in a fission reactor is exposed to neutron irradiation. The intensity of the irradiation received by components depends on their location within the core, their residence time in the core and on the neutron spectrum of the reactor. Two metrics are used to quantify the irradiation level of materials, *neutron fluence* and *displacement-per-atom* (dpa). The former represents the integral of the neutron flux over the irradiation time; the latter is the average number of displacements of each lattice atom. The two metrics are correlated, and the proportionality coefficient depends on the material type and the neutron spectrum. For graphite in a pebble bed reactor, 1 dpa corresponds to a fluence of $0.78 \cdot 10^{21}$ n/cm^2 of neutrons above 0.1 MeV (Windes et al. 2007).

5.4.1.1. *Graphite changes with irradiation*

Irradiation introduces point defects and dimensional changes in graphite. Lattice carbon atoms displaced by impinging neutrons tend to coalesce and form clusters the graphene planes in the crystallite. In turn, the vacancies left behind by the displaced atoms tend to coalesce on the basal planes. These mechanisms introduce a growth of the crystallite in the direction perpendicular to the basal plane (*c* direction) and a shrinkage parallel to the basal plane (*a* direction). In irradiation early-phases, the growth in the perpendicular direction is absorbed by the sealing of pre-existing cracks, and the only macroscopically visible effect is a volume shrinkage (*pre-turnaround*). As irradiation continues, sealing of cracks is not sufficient to accommodate the growth in the *c* direction, so that the new porosity is created, and the shrinkage rate is first balanced (*turnaround*) and then overcome by the expansion (*post-turnaround*). The dpa for turnaround changes across graphite grades and is lower for higher temperature. In the case of IG-110 graphite, turnaround is reached with 15 dpa at 600°C (Ishiyama et al. 1996).

5.4.1.2. *Impact on uptake capacities*

All hydrogen uptake experiments on irradiated graphite have shown an increase in uptake capacity with irradiation. The increase seems to be variable depending on the graphite grades, with increases that span from 2x in RGT graphite (Tazhibaeva et al. 1996) to 286x in IG-430U (Atsumi et al. 2009a). (Atsumi et al. 2009a) shows that the capacity begins to increase with irradiation of less than 0.01 dpa and grows monotonically with irradiation.

Irradiation temperature has an effect on the increase in uptake capacities. (Atsumi et al. 2007) measured hydrogen uptake capacities at 1273K and 10 kPa for six graphite grades irradiated at 416-456 K and 541-582 K with 0.05 dpa. For all grades, the increase in capacities was more pronounced when irradiated at the low temperature. The extent of this difference varied across grades, from a minimum of 5% in IG-110 to a maximum around 500% in IG-430U. The effect had also been captured by (Kwast et al. 1996), which shows uptake capacities (at 850°C, 80 kPa, S-1611 graphite) to be 13% larger in samples irradiated at 400°C than in samples irradiated at 600°C (0.1 dpa). The limited increase in uptake capacities at higher temperature was attributed to a partial annealing of the uptake sites created by irradiation (Atsumi et al. 2007). Most of the uptake data on irradiated graphite are available at temperatures of 900-1100 °C (Figure 5.11), while the FHR operates at 600-800°C (Andreades et al. 2016). Therefore, this dependence on temperature

suggests that the effects in the FHR may be more pronounced than those reported in literature. Also, since uptake capacities increase monotonically with fluence, it is expected that the increase in uptake capacities will occur more rapidly in reactors with higher neutron flux (e.g. the FHR, whose flux is ten times higher than in a LWR (Cisneros 2013b)). However, no uptake studies have compared samples exposed to the same fluence but different fluxes.

The effect of irradiation on uptake capacities is beneficial for the purpose of tritium management in the FHR. The increase in uptake capacities could allow the irradiated graphite components to uptake more of the tritium produced in the core than fresh, unirradiated graphite. Based on the increase in uptake capacities of Figure 5.11 for unirradiated graphite, FHR uptake capacities are expected to be at least of 260 appm and possibly up to two orders of magnitude larger. This prediction strongly suggests that the fuel elements will be capable of uptaking all produced tritium.

The increase in uptake capacities is attributed to an increase in the number of Trap 1 and/or Trap 2 sites (Atsumi and Tauchi 2003). The number densities of the two trapping sites, $[C_2^*]$ and $[C_1^*]$, do not increase in the same way with irradiation. (Atsumi et al. 2009a) shows that, in all graphite grades, Trap 2 sites number density increases more than Trap 1 up to doses of about one-hundredth of a dpa. For higher doses, Trap 1 sites number density increases more. In IG-430 loaded at 1273 K and 10 kPa, the ratio of uptake capacity in Trap 2 to Trap 1 is around 10 at 0.006 dpa and decreases to less than 1 at 0.47 dpa (Figure 5.22).

In PB-FHRs, graphite elements are subjected to a dose in the order of 3-5 dpa (Andreades et al. 2016; Young et al. 2015). Despite hydrogen uptake studies for this dose level are not available, the trend suggests that Trap 1 sites outnumber Trap 2 sites. At the low partial pressures of the FHR, hydrogen is predominantly uptaken in Trap 1 sites. As a result of these two effects, more than 50% of the tritium uptaken in core will reside in Trap 1 sites. This could be not beneficial for the purpose of tritium management; because hydrogen in Trap 1 cannot be effectively degassed at temperatures below 1300°C, the amount of tritium *irreversibly* trapped in the fuel element would increase.
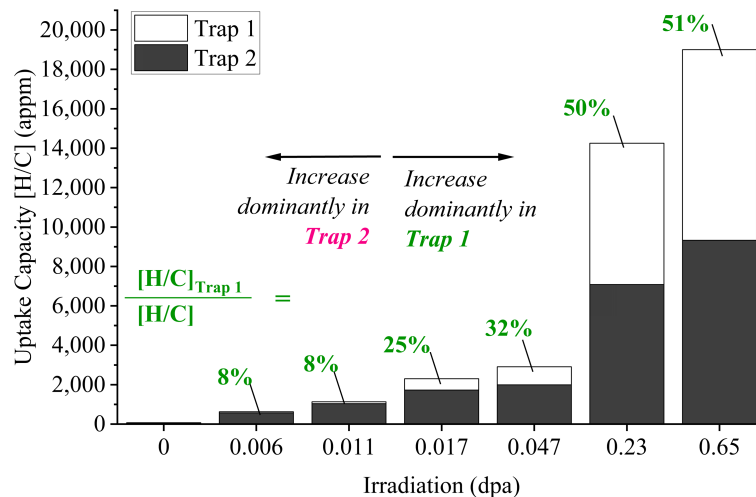
Sample: IG-430U. Uptake Temperature: 1273 K. Partial Pressure: 10 kPa.

Figure 5.22: Hydrogen concentration in neutron irradiated graphite, by trapping site. Percentages represent fraction of hydrogen in Trap 1. Original from (Atsumi et al. 2009a).

The production of Trap 2 sites with irradiation is due to the increase in crystallite edge surface area. X-Ray diffraction (Atsumi et al. 1996) and Raman spectroscopy (Krishna et al. 2015) of irradiated graphite indicate shrinking of the crystallites, which can be related to an increase of the number of edge sites (i.e. of Trap 2). As Trap 1 sites are associated to non-reconstructed edges, which can form when interstitial coalesce in clusters, their increase occurs only when enough interstitials have been produced and coalesced.

Conversely, in two constant-temperature desorption studies of irradiated graphite ((H.D. Rohrig et al. 1975): desorption temperatures of 850°C – 1100°C, 5.8 dpa; (Malka et al. 1980a): desorption temperatures of 700°C -1000°C, 0.2 dpa [v]) hydrogen desorption was fitted with the square-root of time, rather than the logarithmic fitting developed by (Redmond and Walker 1960). The square-root dependence would suggest that the hydrogen desorption is dominated by diffusion, rather than de-trapping. Since chemisorbed hydrogen is released via a diffusion-controlled process only when trapped in Trap 2 sites (Atsumi et al. 2013a), this evidence would indicate that irradiation has caused a larger relative increase in Trap 2, in opposition with Figure 5.22. Further studies on evolution of $[C_2^*]$ and $[C_1^*]$ with irradiation are needed in order to elucidate the relative importance of Trap 2 and Trap 1 in graphite irradiated to FHR dpa levels.

5.4.1.3. *Impact on uptake kinetics*

Hydrogen uptake rates in irradiated graphite are much slower than those in absence of irradiation. As for uptake capacities, the drop in uptake rates and apparent diffusion coefficient is not uniform across graphite grades (spans from -50% in ISO-880U (Atsumi et al. 2009b) to -97% in IG-430U (Atsumi et al. 2009a)). As in the case of uptake capacities, the effect appears even with irradiation of less than 0.1 dpa. Unlike uptake capacities, however, the effect decreases at irradiation of more than 0.1 dpa, even though uptake rates continue to remain about one order of magnitude less than in the unirradiated case (Figure 5.23).

---

[v] dpa calculated from fluences using a conversion factor dpa/fluence of 3.83 10^{-11} dpa m[2] (Campbell et al. 2016)
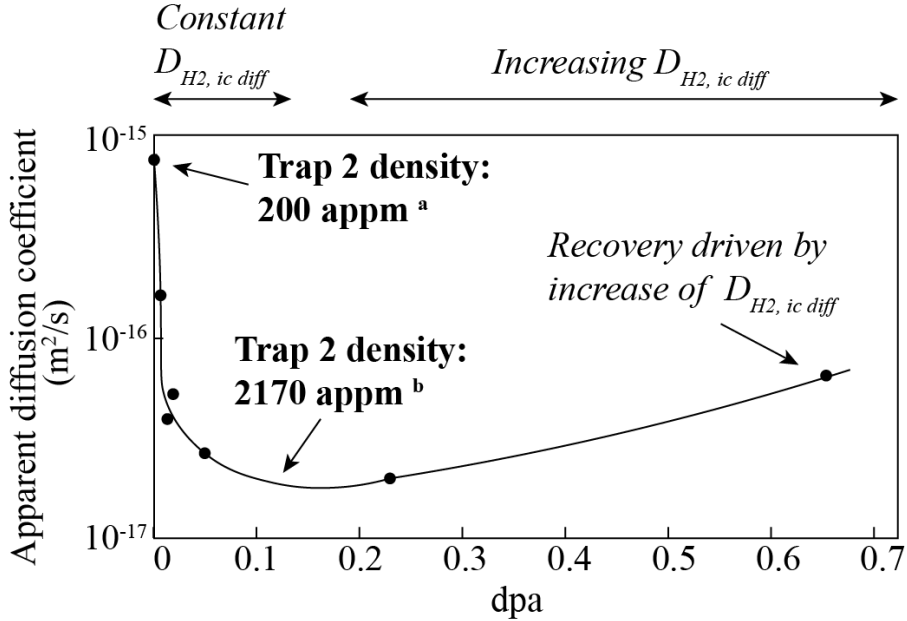
Sample: IG-430U. Uptake temperature: 1273 K. Uptake partial pressure: 10 kPa. Original data from (Atsumi et al., 2009)

[a] Assumed based on (Kanashenko et al., 1986).

[b] Calculated using $[C_2^*/C] = 200$ appm, $\Delta H_{Trap2} = -2.5$ eV/H_2, $\Delta S/k_b = -34.8/H_2$, $\rho = 1.82$ g/cm^3, assuming $\alpha = 15\%$ and $\alpha_n = 8\%$.

Figure 5.23: Apparent diffusion coefficient and Trap 2 number density in irradiated graphite. Original data from (Atsumi et al. 2009b). Trap 2 number density calculated using assumptions based on (Kanashenko 1996; Yamashina and Hino 1989)

The sudden decrease of uptake rates with irradiation can be ascribed to trapping effects. As described in Section 5.3, the ratio of the apparent diffusion coefficient to the inter-crystallite diffusion coefficient is a function of the number density of Trap 2 sites. The partial recovery of the uptake rate at higher doses has not been explained univocally, yet. According to (Atsumi et al. 2009a), it could be due to a combination of three factors: (1) Trap 2 sites become saturated with trapped hydrogen atoms and the trapping effect during diffusion becomes less pronounced. (2) The size of crystallites reduces, leading to an increase in the intra-crystallite diffusion rate. (3) Micro-cracks are formed via irradiation, so that the connectivity of the open porosity is larger and inter-granular diffusion occurs through shorter paths.

In (Tazhibaeva et al. 1996), the TDS of unirradiated graphite is compared with the TDS of graphite irradiated in argon and then charged with hydrogen and the TDS of graphite irradiated in hydrogen. At all desorption temperatures, and especially in the region of Peak 4, the sample irradiated in argon has lower desorption rates than the sample irradiated in hydrogen. This could be caused by a partial annealing of the sample exposed to hydrogen after irradiation, which would reduce the number of trapping sites available for chemisorption. Alternatively, it could be explained by kinetics, assuming higher uptake rates in the sample simultaneously exposed to neutrons and hydrogen, resulting from a less pronounced trapping effect.

The decrease in uptake rates with irradiation is particularly relevant at the FHR low pressure. Assuming a partial pressure of 10 Pa, a temperature of 900 K and neglecting the partial recovery

of the uptake rate, a tenfold increase in trapping sites would lead to a decrease of the uptake rate by more than 50%. Using the uptake rate calculated with Equation 5.54 – 5.58 and the inter-crystallite diffusion coefficient from (Atsumi and Iseki 2000) as a reference for unirradiated Mark-I PB-FHR graphite, the uptake rate in irradiated graphite would be lower than 2×10^{-9} 1/s, i.e., less than one thirtieth of the minimum value estimated for unirradiated graphite. This would need to be verified by kinetics experiment at FHR conditions. Other factors that have not been explored yet and would require experimental study are the dependence on irradiation temperature and on the intensity of the neutron flux. If these factors have an impact on the change in kinetics, tritium may be absorbed at different rates in various regions of the core.

5.4.1.4. *Summary of irradiation effects*

Neutron irradiation introduces changes in both the thermodynamics and the kinetics of the hydrogen-graphite interaction. The dimensional changes and the creation of defects in graphite microstructure cause an increase in hydrogen trapping sites, which translates in uptake capacities increased by as much as two orders of magnitude. The effect is maximized at low irradiation temperature and partially mitigated by higher temperatures. At FHR conditions, uptake capacities of irradiated graphite are expected to be more than twenty times larger than those required to uptake all tritium produced during the permanence of the fuel elements in the core.

Irradiation produces both Trap 2 and Trap 1 sites. The former are mostly produced in the early phases of irradiation (dose < 0.01 dpa), while the latter are predominantly produced at larger doses and outnumber Trap 2 sites. This effect is detrimental for tritium sequestration in the FHR, since tritium in Trap 1 can be desorbed only if degassing above 1300 °C.

The increase in trapping sites also causes a reduction in the uptake rates. This is more pronounced at low fluences, when mostly Trap 2 sites are produced, and partially recovered at higher fluences. The decrease of uptake rates becomes of particular importance at low pressures. At the FHR pressure, a tenfold increase in trap site number density would lead to a decrease of the ratio of apparent diffusion coefficient and the inter-crystallite diffusion coefficient by more than 50%. The resulting absorption rate would not allow PB-FHR fuel pebbles to uptake most of the in-core tritium during their permanence. Limited evidence of the impact of irradiation on desorption behavior is available in literature. The only available TDS study hints that the desorption behavior may change depending on whether irradiation and hydrogen exposure occur simultaneously or not (Tazhibaeva et al. 1996). Constant-temperature desorption studies suggest that the time-profile of desorption may be different for irradiated and unirradiated graphite.

5.4.2   Effects of oxidation

In normal FHR and MSR operations, graphite is not exposed to air or oxygen. However, graphite may enter in contact with air in an accident sequence that involves air ingress in the core or because of accidents in the fuel handling system. In this chapter, the shorthand notation *oxidized graphite* refers to graphite that has been previously attacked with an oxidizing gas. This should not be confused with graphite oxides, which are out of the scope of this work.

5.4.2.1. *Graphite changes with oxidation*

Graphite oxidation occurs when graphite is exposed to air at sufficiently high temperatures. At low temperatures (T < 400°C – 500°C), the reaction rates of the oxidation reactions (which is expressed

here as the grams of graphite reacting per second) are small (e.g. less than 5 $\mu g/s$ for IG-110 at 500°C), and graphite does not undergo changes even under a prolonged exposure (Xiaowei et al. 2004). At higher temperatures, reaction rates become larger and the oxidation reaction occurs under different kinetic regimes depending on the temperature (Contescu et al. 2008; Velasquez et al. 1978).

The main effect of oxidation on graphite is a weight loss due to the formation of CO and CO_2 from carbon atoms reacting with oxygen. The gasification of carbon atoms leads to the creation of new porosity and to the formation of pores networks that make closed porosity accessible to fluids. The new porosity is created both at the nano-scale and at the micron-scale, and is accompanied by an increase in the BET surface area (Contescu et al. 2012; Wang et al. 2012). The extent of weight loss, the degree of microstructural change and the thickness of the region where oxidation occurs depend on the graphite grade and on temperature. The interested reader may refer to (Chi and Kim 2008; Contescu et al. 2012) for a comparison across graphite grades and (Xiaowei et al. 2004) for a comparison across temperatures.

5.4.2.2. *Impact on uptake capacities*

Graphite oxidation leads to the creation of new crystallite surface and, consequently, new Trap 2 sites. The newly formed Trap 2 sites are competitively occupied by oxygen atoms, oxidation products (CO, CO_2) and hydrogen atoms. The newly created sites are more favorably occupied by oxygen than hydrogen, as the Gibbs free energies of formation of carbon-oxygen bonds are lower than those of carbon-hydrogen bonds at all temperature. However, unoccupied Trap 2 sites are available to hydrogen and the increase of the Trap 2 number density is associated to an increase in uptake capacity. Since Peak 5 of graphite TDS does not change upon oxidation of the samples, Trap 1 sites are not accessible to air and their hydrogen capacity remains unaltered in oxidation events (Markin et al. 1997).

The degree of increase in hydrogen capacity varies across studies. In (Strehlow 1986), simultaneous oxidation with steam and exposure to tritium gas at 1023 K and 0.14 Pa leads to an increase in uptake capacity ranging from a factor 2 to a factor 76. In (Atsumi and Iseki 2000), hydrogen uptake capacity (at 1273 K, 10 kPa) of samples previously oxidized with steam at 973 K for 2 hours increase only by few percentual points, and only when the oxidation products have been outgassed at high temperature (Figure 5.24).

Multiple experimental parameters are different in (Strehlow 1986) and (Atsumi and Iseki 2000) and thus indicate that enhancement of hydrogen uptake capacity upon gas oxidation is sensitive to some of these environmental conditions. The longer duration of oxidation in (Strehlow 1986) (4h vs 2h) may explain the larger uptake capacity increase because a longer exposure could have led to larger changes in porosity and available crystallite surface. Another experimental difference is the order of oxidation and exposure to hydrogen (simultaneous in (Strehlow 1986), oxidation before hydrogen exposure in (Atsumi and Iseki 2000)). With oxidation and exposure to hydrogen occurring simultaneously in (Strehlow 1986), oxygen and oxidation products may compete with hydrogen for uptake sites. Conversely, since the samples in (Atsumi and Iseki 2000) are exposed to hydrogen only after oxidation and degassing have ended, all oxidation-created trapping sites are available to hydrogen. However, since the data indicate a larger increase in uptake rates in (Strehlow 1986), this effect seems to be less relevant than the duration of oxidation. Finally, the two studies differ on the total hydrogen pressure (0.14 Pa in (Strehlow 1986) vs 10 kPa in (Atsumi and Iseki 2000)). This difference may have an impact on the increase of uptake rates with oxidation,

but this cannot be postulated in absence of a study that probes specifically for it (for example by studying uptake rates at different hydrogen pressure in samples that have been oxidized for the same amount of time).
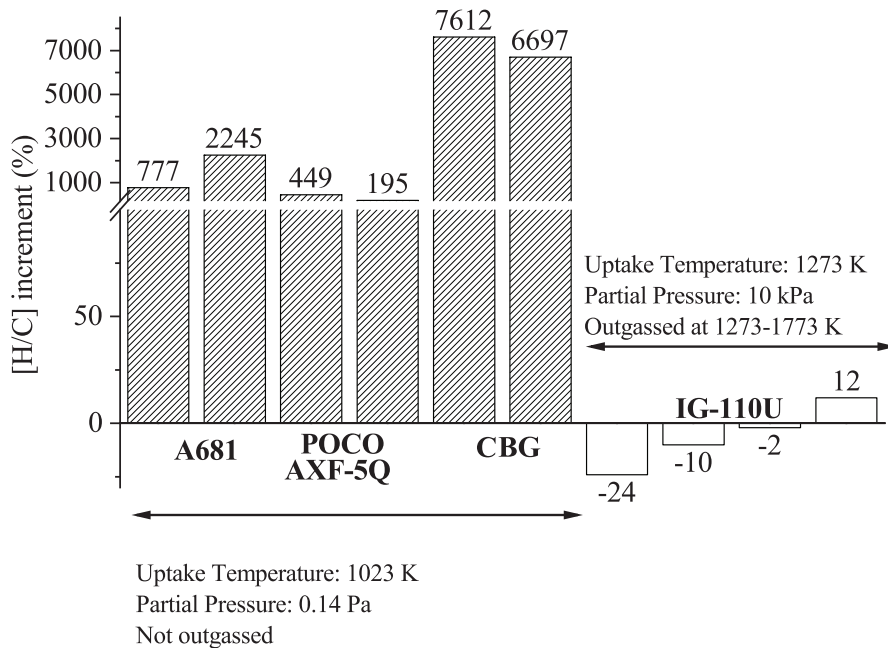

Figure 5.24: Change in [H/C] uptake capacity in samples pre-oxidized with steam. Original data from (Strehlow 1986) and (Atsumi and Iseki 2000).

5.4.2.3. *Impact on uptake kinetics*

Hydrogen uptake rates are higher for graphite that has been previously attacked by an oxidizing gas. (Atsumi and Iseki 2000) shows an increase in the uptake rates by a factor of 3 and more. The increase is less pronounced when graphite is outgassed at high temperature (Atsumi and Iseki 2000).

The increase in uptake rates with oxidation may be at least in part responsible of the difference in the results between (Strehlow 1986) and (Atsumi and Iseki 2000). In (Strehlow 1986), both oxidized and non-oxidized samples are exposed to tritium for 4 h. At a tritium partial pressure of 0.14 Pa, this time might not be enough to reach thermodynamic equilibrium in the non-oxidized samples. Instead, it could be sufficient for the oxidized samples, due to the increase in the oxidation rates. This effect should not occur in (Atsumi and Iseki 2000), because of the higher partial pressure (10 kPa) and the longer exposure to hydrogen (30 h).

Both irradiation and oxidation lead to an increase in the number densities of trapping sites but only in the case of irradiation does this also lead to a decrease in the kinetics of hydrogen uptake. This suggests that oxidation introduces additional changes to graphite that cause an overall increase in uptake rates. Three explanations for the increase in the uptake rates are postulated in (Atsumi and Iseki 2000): (a) a change in the path of diffusing hydrogen molecules; (b) the occupation of Trap 2 sites by oxygen atoms; (c) the removal of some of the existing Trap 2 sites. Option (a) seems realistic: oxidation leads to the formation of pore networks through which hydrogen can more rapidly diffuse. The other options are more controversial. In (Atsumi and Iseki 2000), uptake rates increase even after graphite is outgassed at higher temperature, i.e. after oxygen atoms have been

removed and the overall number of Trap 2 sites available to hydrogen chemisorption is increased. At low uptake pressures, this increase should lead to a decrease in the uptake rates, rather than an increase. This does not manifest in (Atsumi and Iseki 2000) due to the high partial pressure (10 kPa), but could manifest at FHR pressures.

5.4.2.4. *Summary of oxidation effects*

Oxidation of graphite by air or steam produces new Trap 2 sites available for hydrogen chemisorption. As a result, hydrogen uptake capacities increase in graphite previously attacked by an oxidizing gas. The formation of new porosity leads to increased hydrogen uptake rates. At pressures of tens to hundreds of Pa, this increase might be partially counteracted by an increased trapping effect (from Trap 2 sites created by oxidation) on the apparent diffusivity of hydrogen in graphite. The impact of oxidation on uptake capacities and kinetics may vary depending on the specific oxidizing gas (steam, air, O_2, or CO_2); data is only available on graphite oxidation by steam and air.

5.4.3 Effects Of Fluorination

Thermodynamic calculations of the graphite-fluoride salt system suggest that the chemical reduction of fluoride salts by graphite has a positive Gibbs free energy, i.e., is not thermodynamically favorable. Nevertheless, experimental studies of graphite in fluoride salts indicate that graphite fluorinates upon exposure to FLiNaK (Yang et al. 2012) and FLiBe (Wu et al. 2018a). The opposition between thermodynamic calculations and experimental studies is resolved by hypothesizing that not all carbon atoms, but only graphite reactive sites (including hydrogen uptake sites) are involved in the reaction.

5.4.3.1. *Fluorination of graphite*

As fluorides react with graphite, uptake sites otherwise available to hydrogen might be occupied by reaction products. An evidence of this behavior is seen in (Yang et al. 2012). In this study, IG-110 graphite is immersed in FLiNaK at 500°C for 16 hours. Pre-exposure X-ray uptake near-edge structure (XANES) and X-ray diffraction (XRD) of graphite indicate pre-existing C-H bonds in the sample. Post-exposure XANES and XRD data show that a part of the C-H bonds is replaced by C-F bonds. The results of (Yang et al. 2012) would suggest that graphite fluorination decreases the hydrogen uptake capacity.

Fluorination could also create new reactive sites available for hydrogen uptake. Section 2 shows that exposure of IG-110 graphite to FLiBe at 700°C for 240h leads to the formation of C-F bonds and an increase in the number of available RCS. The increase in available RCS could be evidence of the formation of additional number of new types of defects in graphite, which may be available for hydrogen chemisorption. No experiments exist to-date for graphite characterization by XPS, Raman, XRD nor XANES post exposure to both hydrogen and molten fluoride salt.

5.4.3.2. *Impact on uptake capacity*

Data from the MSRE suggest that exposure to fluorination leads to an overall increase in hydrogen uptake. In (Compere et al. 1975), graphite samples of two grades (POCO AXF-5Q and CGB) that resided in the MSRE core for up to 5 years are analyzed for tritium concentration. For both grades, tritium concentration in the outermost layer of the sample (1.6 mm thick) is found to be more than

two orders of magnitude larger than concentration in the bulk. This gradient of concentration is 5 to 30 times as large as that for graphite of the same grades not exposed to salt (Strehlow 1986). The enhanced tritium concentration at the surface indicates a larger abundance of uptake sites on the surface of graphite, which was in contact with molten salts. It is reasonable to assume that the increase in trapping site number density may be ascribed, at least in part, to the fluorination of graphite (Compere et al. 1975). A similar hypotheses can be formulated to explain the results of (Dolan et al. 2020), in which IG-110 crucibles containing FLiBe were irradiated with neutrons for 1000 hours and absorbed the tritium produced by activation of the salt. Tritium concentration in graphite was found to scale with the surface area of graphite exposed to the salt. This can be explained by the formation of new tritium uptake sites in the region in contact with the salt.

While these studies seem to suggest an overall increase in uptake capacities, it remains unclear how the extent of this increase changes across graphite grades and temperatures.

5.4.3.3.   *Impact on kinetics*

Experimental studies that assess hydrogen uptake capacities in fluorinated graphite are not available. The formation of C-F bonds upon exposure to the salt and the creation of new defects with fluorination have opposite effects on hydrogen uptake rates. In fact, the former would decrease the trapping effect on diffusion, whereas the latter would decrease it, respectively increasing and decreasing uptake rates. The evidence of larger uptake capacities with fluorination leads us to hypothesize that the creation of new uptake sites prevails over the consumption of existing ones. Under this hypothesis, hydrogen uptake rates would be decreased. Direct measurements of hydrogen diffusion coefficients before and after fluorination are required to test this hypothesis.

5.4.3.4.   *Summary of fluorination effects*

In summary, the exposure of graphite to fluoride salts at high temperatures leads to the formation of C-F bonds and leads to an increase in available reactive sites. Experimental studies show that hydrogen uptake capacities increase at salt-facing graphite surfaces, suggesting that creation of new sites prevails over occupation of the existing ones. Accordingly, uptake rates are expected to be decreased by exposure to fluoride salts.

5.4.4   Conclusion

The uptake capacity extrapolated using relationships valid for unirradiated graphite is about ten times larger than the estimated minimum uptake capacity required in the Mark-I PB-FHR. The estimated uptake rate is more than one order of magnitude lower than the minimum for the Mark-I PB-FHR. However, these estimates need to be corrected to account for the effect of neutron irradiation, oxidation, and reactions with fluoride salts, which may occur in the FHR.

Neutron irradiation increases uptake capacities by up to two orders of magnitude due to the production of Trap 2 and Trap 1 sites (Figure 5.22). Trap 2 sites are mostly produced in the early phases of irradiation (dose < 0.01 dpa), while Trap 1 sites are predominantly produced at larger doses. The increase in Trap 2 sites causes a reduction in the uptake rates by one-two orders of magnitude. Uptake rates are partially recovered at fluences of 0.1 dpa and beyond, as a result of crystallite shrinking or formation of new porosity (Figure 5.23). The decrease of uptake rates is particularly sensible at pressures of tens to hundreds of Pa, where a tenfold increase in trapping

site number can decrease the apparent diffusion coefficient by more than 50%. Limited evidence of the impact of irradiation on desorption behavior is available in literature. The decreased uptake rates of irradiated graphite may preclude the use of graphite pebbles as a tritium getter in PB-FHR cores.

Oxidation of graphite by air or steam produces new Trap 2 sites but does not affect Trap 1 sites. In addition to increasing hydrogen uptake capacities, oxidation also causes higher hydrogen uptake rates due to the formation of new porosity. At low pressures, this increase might be partially counteracted by an increased trapping effect in diffusion. This does not manifest in (Atsumi and Iseki 2000) due to the high partial pressure (10 kPa), but could manifest at FHR pressures. Low pressure uptake experiments on graphite previously exposed to an oxidizer would help understand if oxidation might be a technique helpful to increase in-core tritium uptake rates.

The reaction of graphite with fluoride salts leads to the formation of C-F bonds and increases available reactive sites. Accordingly, uptake rates are expected to be decreased upon exposure to fluoride salts. Experimental measurements of uptake rates are required to validate this hypothesis and account for the effect of graphite fluorination in tritium uptake predictions.

A complete understanding of the effects of reactor phenomena on hydrogen-graphite thermodynamics and kinetics has not been achieved yet. Examples of experiments that should be prioritized in order to address these gaps are: (a) measurements of hydrogen uptake rates in irradiated graphite at various pressure levels to disentangle changes in the apparent diffusion coefficient from changes in the inter-crystallite diffusion coefficient; (b) measurements of hydrogen uptake capacities for graphite irradiated at high doses (> 5 dpa), representative of PB-FHR fuel pebbles; (c) Direct measurements of hydrogen diffusion coefficients before and after fluorination. This set of experiments targeted at FHR conditions will support a quantitative assessment of the effectiveness of graphite as a tritium getter in FHRs.

5.4.5 Acknowledgement

5.5 Modeling Tritium Transport in Graphite: A Genetic Algorithm, Diffusion-with-Trapping Model for Hydrogen Uptake and Transport

Hydrogen uptake studies have been performed at hydrogen partial pressures of tens to hundreds of kPa, which are not representative of uptake conditions in a fission reactor and fusion blanket. Developing hydrogen uptake models that account for the different mechanisms of hydrogen uptake is necessary to extract hydrogen transport parameters and extrapolate uptake behavior to low pressures.

A kinetics model for hydrogen transport in graphite was originally developed by (Morita and Muto 1992) to study hydrogen re-emission from ion-implanted graphite. The model was developed from hydrogen diffusion-with-trapping models for metals (McNabb and Foster 1963; Oriani 1970) and later used by (Atsumi 2002b) and.(Dolan et al. 2021a) to describe hydrogen diffusion in graphite exposed to a hydrogen gas atmosphere. The model used by (Morita and Muto 1992) was developed before (Kanashenko 1996) proposed two types of hydrogen trapping sites in graphite, with different concentrations and energies for each (Section 5.2), and therefore comprehends only one type of sites. As such, it cannot be used to estimate the density of the two population of trapping sites. Knowledge of the density of both trapping sites is important to evaluate graphite performance as a reversible tritium getter, as the temperature required to desorb tritium varies across trapping sites and only one type sites may be accessible at temperature compatibles to the fuel pebbles.

In this chapter, the first model in the literature for hydrogen uptake and transport in graphite that considers both types of trapping sites is developed. The new model is implemented with a finite-difference discretization scheme and used in conjunction to a generic algorithm to fit hydrogen uptake data from hydrogen adsorption experiments to extract transport parameters such as diffusion coefficients and trapping site density and energy.

5.5.1 Modeling

5.5.1.1. *Diffusion-with-trapping model*

Given a graphite sample, its hydrogen content can be expressed in terms of the hydrogen-to-carbon ratio [H/C] (Equation 5.71):

$$\left[\frac{H}{C}\right] = \frac{Number\ of\ hydrogen\ atoms\ in\ the\ sample}{Number\ of\ carbon\ atoms\ in\ the\ sample} \qquad 5.71$$

Graphite exposed to hydrogen gas can uptake hydrogen through multiple mechanisms. Depending on the mechanism, hydrogen will be uptaken in the closed pores and within the grain, at three different types of uptake sites, basal planes, Trap 2 sites (reconstructed crystallite edges) and Trap 1 sites (unconstructed crystallite edges). At FHR conditions (temperatures in the order of 500-800°C and hydrogen partial pressures up to a few tens of Pa), almost all uptaken hydrogen is chemisorbed in Trap 1 and Trap 2 sites (Section 5.2). The total amount of hydrogen that can be hosted in Trap 1 and Trap 2 sites (i.e., the uptake capacities of Trap 1 and Trap 2 sites) can be calculated from thermodynamic considerations. However, this value only rarely coincides with the hydrogen molar fractions measured in adsorption experiments, because these occur over a finite time interval, such that thermodynamic equilibrium is not achieved. In these cases, the hydrogen-to-carbon ratio is influenced by kinetics.

Uptake of hydrogen in graphite occurs as a multi-step process (Section 5.3). When a graphite sample is exposed to a hydrogen gas partial pressure, hydrogen molecules can penetrate the sample surface, permeate in the open porosity among the grains, and diffuse in the closed porosity via *inter-grain diffusion*. (Atsumi and Iseki 2000) assumed that permeation of molecular hydrogen through the open and closed pores among the grains is rapid so that the partial pressure at the grain surface is the same as the pressure outside the sample and hence the inter-grain diffusion is not rate-limiting can be neglected. This assumption is verified in the model by (Dolan et al. 2021a) for the uptake data of (Causey 1989). Once hydrogen molecules reach the surface of the grains, they can diffuse within the grain, across the crystallites (*inter-crystallite diffusion*). As hydrogen diffuses, some of the molecules reach Trap 2 sites where they dissociate into atoms that are chemisorbed by the sites (*trapping step)*. As these trapping sites become progressively full, some of the trapped atoms are released by the trapping sites *(detrapping step)* and continue diffusing across the crystallites and inside the crystallite, where they could be trapped from Trap 1 sites. The overall process can be modelled as a multi-scale diffusion-with-trapping process. A previous mathematical formulation of the process was developed in (Atsumi 2002b; Dolan et al. 2021a; Morita and Muto 1992), with the simplifying assumption of a single type of trapping site (Trap 2). In this work, the constitutive equations are modified to account for two types of reversible trapping sites: Trap 2 sites (reconstructed crystallite edges), and Trap 1 sites (unreconstructed crystallite edges).

The hydrogen-to-carbon-ratio is calculated from hydrogen in the pores, calculated using the ideal gas law, plus hydrogen diffusing in the grains, calculated by volume-averaging the molar fractions of freely diffusing hydrogen (modeled as a function of space and time) and trapped hydrogen. The molar fraction of trapped hydrogen is separated in two contributions for the two types of sites and factored in terms of the number and occupancy of the trapping sites.

$$\left[\frac{H}{C}\right] = \left[\frac{H}{C}\right]_{pores} + \left[\frac{H}{C}\right]_{grain} = 2\frac{M_C \alpha P_{H_2(g)}}{\rho\, R\, T} + \frac{1}{V_{grain}}\int_{V_{grain}} (H_D(\vec{r},t) + \phi_1 e_1(\vec{r},t) + \phi_2 e_2(\vec{r},t)\ dV) \tag{5.72}$$

In Equation 5.72, $\left[\frac{H}{C}\right]_{pores}$ and $\left[\frac{H}{C}\right]_{grain}$ are normalized to the number of carbon atoms in the sample, $P_{H_2(g)}$ is the hydrogen pressure in the pores (assumed constant across the pores (Atsumi and Iseki 2000; Dolan et al. 2021a)), T is the temperature, M_C is carbon molar mass, R is the universal gas constant, α_C is the volume fraction of the closed pores (11.5% for IG-110 (Wu et al. 2020a)), ρ is the density of graphite, V_{grain} is the grain volume assumed uniform across the sample, H_D is the molar fraction of hydrogen atoms freely diffusing in the grain, ϕ_1 and ϕ_2 are the number densities of the two types of trapping sites, and e_1 and e_2 are their occupancies. In this work, ϕ_1 and ϕ_2 are assumed to be uniformly distributed across the grain and constant in time, while e_1 and e_2 are modeled as time- and space-dependent.

The molar fraction of hydrogen atoms H_D diffusing (not trapped) in the grain is described by the solution to a diffusion-with-trapping equation (Equation 5.73) (Iino 1986; Pound 1989):

$$\frac{\partial H_D(\vec{r},t)}{\partial t} = D_{inter}\nabla^2 H_D(\vec{r},t) - \phi_1\frac{\partial e_1(\vec{r},t)}{\partial t} - \phi_2\frac{\partial e_2(\vec{r},t)}{\partial t} \tag{5.73}$$

where $D_{intercryst}$ is the inter-crystallite diffusion coefficient. Modeling the trapping sites as reversible sites (i.e., allowing for hydrogen desorption), their occupancies are described by Equation 5.74 (Iino 1986; Pound 1989):

$$\frac{\partial e_i(\vec{r},t)}{\partial t} = k_i^T H_D(\vec{r},t)[1 - e_1(\vec{r},t)] - k_i^{DT} e_i(\vec{r},t) \quad i = 1,2$$

5.74

Where $k_1^T, k_2^T, k_1^{DT}, k_2^{DT}$ are the trapping and detrapping rate constants for the two types of trapping sites. The trapping and detrapping rate constants are calculated according to Equations 5.75-5.77. The formulation extends to Trap 1 and Trap 2 sites the formulation used by (Dolan et al. 2021a) for Trap 2 sites only, following the methodology described in (Longhurst et al. 1992) for the generic diffusion-with-trapping problem.

$$k_1^T = k_2^T = \frac{D_{intercryst}}{a^2 N_c}$$

5.75

$$k_1^{DT} = v_0 e^{\frac{-E_1}{2k_b T}}$$

5.76

$$k_2^{DT} = v_0 e^{\frac{-E_2}{2k_b T}}$$

5.77

The trapping rate constants are assumed equal to each other and are computed from the inter-crystallite diffusion coefficient. Detrapping is modeled as an Arrhenius process, with different activation energies, E_1 and E_2. For unit consistency between activation energies of detrapping and enthalpies of trapping, E_1 and E_2 are normalized to the two atoms of the hydrogen molecule, i.e., expressed in units of eV/H_2. Table 5.24 lists all the parameters used in the system of Equations 5.73 – 5.78.

Table 5.24. Parameters of the diffusion-with-trapping model (Equations 5.73 – 5.79)

Variable	Meaning	Units	Type
H	Molar fraction of hydrogen in graphite	appm	Dependent Variable
t	Time coordinate	s	Independent Variable
$\vec{r}$	Radial coordinate of the grain (modeled as a sphere)	m	Independent Variable
k_1^T, k_2^T	Trapping rate constants	1/s	Fitting Parameter
k_1^{DT}, k_2^{DT}	Detrapping rate constants	1/s	Fitting Parameter
K_S	Sievert constant for dissociative adsorption	mol/cm^3 1/Pa$^{1/2}$	Fitting Parameter
$D_{intercryst}$	Inter-crystallite diffusion coefficient	m^2/s	Fitting Parameter
ϕ_1	Number density of Trap 1 sites	appm	Fitting Parameter
ϕ_2	Number density of Trap 2 sites	appm	Fitting Parameter
E_1	Trap 1 sites detrapping activation energy (normalized per two H atoms)	eV/H$_2$	Fitting Parameter
E_2	Trap 2 sites detrapping activation energy (normalized per two H atoms)	eV/H$_2$	Fitting Parameter
T	Temperature	K	Input Parameter
$P_{H_2(g)}$	Partial pressure of hydrogen	Pa	Input Parameter
α	Porosity fraction	%	Input Parameter
a	Crystallite parameter	2.46 10^{-10} m	Input Parameter (Bernal 1924)
k_b	Boltzmann constant	8.617 10^{-5} eV/K	Constant
ρ	Graphite theoretical density	2.26 g/cm^3	Input Parameter (Bernal 1924)
M_c	Molar mass of carbon	12.01 g/mol	Input Parameter
N_c	Molar density of carbon atoms in the grains ^{w}; $N_c = 10^6 \rho / M_c$	188160 mol C/m^3	Input Parameter
v_0	Debye frequency	10^{13} s^{-1}	Input Parameter (Dolan et al. 2021a)
$H_{surface}$	Molar fraction of hydrogen at the grain surface	appm	Boundary Condition

Solution of the system of partial differential equations (PDEs) in Equations 5.73-5.74 requires initial and boundary conditions, which depend on the specific process being simulated. In this work, the model is used to simulate adsorption isotherms at different pressures. In these experiments, a sample is exposed to increasingly larger partial pressures of hydrogen gas, with every step lasting a constant or variable duration (usually the time required for the pressure to equilibrate).

For the first adsorption step, the initial condition is set by assuming no pre-existing hydrogen in graphite. For the following adsorption steps, the initial condition is chosen as the ending hydrogen distribution from the previous step. In all adsorption steps, the boundary conditions are expressed in terms of the hydrogen pressure at the surface of the grain, according to Equation 5.78.

---

^{w} Using the theoretical density instead of the bulk density in the calculation of N_C assumes that the all the porosity is at the intergranular scale, i.e., intragranular porosity is negligible.

$$H_{surface} = K_S \sqrt{P_{H_2(g)}}$$
<div align="right">5.78</div>

Where $H_{surface}$ is the mole fraction of hydrogen atoms at the surface, K_S is the dissociative Sievert constant for hydrogen in graphite, and $P_{H_2(g)}$ is the hydrogen pressure outside the sample (which coincides with the pressure at the grain surface(Atsumi and Iseki 2000; Dolan et al. 2021a)).

5.5.1.2.   *Time and space discretization*

The system of PDEs in in Equations 5.73 and 5.74 is solved numerically using finite differences, following the approach by (Dolan 2020) and expanding to two types of trapping sites. Time discretization is performed using forward differences; space discretization is performed with central finite differences in spherical coordinates (Crank 1975). The adsorption time is divided in N_t time steps of size *dt* and the radius is divided in *Ns* segments of size *dr*. At time instant *i*, a vector of unknowns $\underline{\Psi^i}$ is defined as follows.

$$\underline{\Psi^i} = \begin{bmatrix} H_0^i & H_1^i & \cdots & H_j^i & \cdots & H_{N_s}^i & e_{1,0}^i & e_{1,1}^i & \cdots & e_{1,j}^i & \cdots & e_{1,N_s}^i & e_{2,0}^i & e_{2,1}^i & \cdots & e_{2,j}^i & \cdots & e_{2,N_s}^i \end{bmatrix}^T$$
<div align="right">5.79</div>

At the time step *i+1*, the vector of unknown is calculated from the vector at time step *i* according to Equation 5.80.

$$\underline{\Psi^{i+1}} = A^i \underline{\Psi^i}$$
<div align="right">5.80</div>

Where A^i is a *Ns* by *Ns* matrix whose elements (for $2 \leq j \leq Ns$) are defined as in Equations 5.81 – 5.89.

$$A^i[j, j-1] = \frac{dt \, D_{inter}}{j \, dr^2} (j - 1)$$
<div align="right">5.81</div>

$$A^i[j, j] = 1 - \frac{2dt \, D_{inter}}{j \, dr^2} - \phi_1 k_1^T \left(1 - e_{1,j}^i\right) - \phi_2 k_2^T \left(1 - e_{2,j}^i\right)$$
<div align="right">5.82</div>

$$A^i[j, j+1] = \frac{dt \, D_{inter}}{j \, dr^2} (j + 1)$$
<div align="right">5.83</div>

$$A^i[j, j + N_s] = \phi_1 k_1^{DT}$$
<div align="right">5.84</div>

$$A^i[j, j + 2N_s] = \phi_2 k_2^{DT}$$
<div align="right">5.85</div>

$$A^i[N_s + j, j] = k_1^T \left(1 - e_{1,j}^i\right)$$
<div align="right">5.86</div>

$$A^i[N_s + j, N_s + j] = k_1^{DT}$$
<div align="right">5.87</div>

$$A^i[2N_s + j, j] = k_2^T \left(1 - e_{2,j}^i\right)$$
<div align="right">5.88</div>

$$A^i[2N_s + j, 2N_s + j] = k_2^{DT}$$
<div align="right">5.89</div>

The reflecting boundary condition at the center of the grain is enforced as in Equations 5.90-5.92.

$$A^i[1, :] = A^i[2, :]$$
<div align="right">5.90</div>

$$A^i[N_s + 1, :] = A^i[N_s + 2, :]$$
<div align="right">5.91</div>

$$A^i[2N_s + 1, :] = A^i[2N_s + 2, :]$$
<div align="right">5.92</div>

The boundary condition at the surface of the grain is enforced as in Equations 5.93 and 5.94:

$$H_{N_s}^i = H_{surface} \qquad\qquad\qquad 5.93$$

$$A^i[N_s, j] = \delta_{N_s, j} \qquad\qquad\qquad 5.94$$

After solving Equation 5.80, the molar fraction of hydrogen diffusing in the grain, trapped in Trap 1 sites, and trapped in Trap 2 sites is calculated as an average of the values in each radial cell (weighted by the volume of each cell).

5.5.1.3. *Genetic algorithm*

In this study, the mathematical model developed in the previous sections is used to simulate hydrogen an adsorption isotherm experiment. In order to build the matrix A, it is necessary to know the graphite parameters listed in Equations 5.81-5.89, such as trapping site densities, Trap 2 detrapping energy, and hydrogen diffusion coefficients. However, these parameters vary across graphite grades and have not been defined univocally in literature. For example, estimates for inter-crystallite diffusion coefficients span 3 orders of magnitude across graphite grades (Section 5.3) and estimates for intra-crystallite diffusion coefficients are available only for graphite implanted with hydrogen ions (Morita et al. 1989) or atoms (Tanabe and Watanabe 1991) . Therefore, to use this model in a predictive fashion for a specific graphite grade, it is first necessary to fit the model to existing experimental data for that grade and find the unknown diffusion parameters. Here, a genetic algorithm is used to fit the diffusion-with-trapping model described above to adsorption isotherm data for IG-110 graphite (Wu et al. 2020a).

A genetic algorithm is a search algorithm based off the concept of natural selection (Michalewicz 1996). An outline of this process is described below:

- A population of N_g gene sets (sets of parameters) is initialized using initial guesses and introducing some randomness.
- The equation with unknown parameters (Equation 5.82, in this case) is solved N_g times, using the different gene sets.
- The N_g solutions are compared to the experimental data, and the prediction errors are computed.
- The fitness of each member of the population is determined based on how small the corresponding prediction error is.
- The top M gene sets are selected based off fitness; these are the ones that will be used to create the new population.
- New N_g -M gene sets are created by taking a randomly weighted average of the values of the fittest gene sets. The stochastic nature of the population generation process prevents the genetic algorithm from getting stuck in local minima during optimization.
- Repeat from step 2 until the fittest members of the population achieve an acceptable prediction error.

A gene set consists of the following parameters: K_S, $D_{intercryst}$, ϕ_1, ϕ_2, E_1, and E_2. Fitness is measured through the mean absolute percentage error (MAPE) (Equation 5.95):

$$MAPE = \frac{1}{n}\sum_{i=1}^{n}\left|\frac{Y_i - \hat{Y}_i}{Y_i}\right| \qquad\qquad\qquad 5.95$$

where Y_i is the actual value of H for data point i, $\hat{Y}_i$ is the predicted value of H for data point i, and n is the number of data points. The initial guesses for the genetic parameters are sampled from a

uniform distribution with user defined minimum and maximum bounds, listed in Table 5.25. At each iteration of the genetic algorithm, new gene sets whose parameters fall out of the bounds are resampled to increase convergence speed.

Table 5.25: Lower and upper bounds for generation of genetic algorithm parameters

Variable	Type of Sampling	Lower Bound for Acceptance	Upper Bound for Acceptance	Motivation
K_S	Uniform (sampling bounds= 0.1 mol/m³Pa$^{1/2}$, 1 mol/m³Pa$^{1/2}$)	N/A	N/A	Uniform sampling with bounds including the values compiled in (Dolan 2020) for five graphite grades at 700 °C.
$D_{intercryst}$	Normal (mu = 5 10^{-19} m²/s, std = 4 10^{-19} m²/s)	N/A	N/A	Sampling mean based on input parameter of (Dolan et al. 2021a) and large standard deviation to allow for excursions, no physical bounds
ϕ_1	Normal (mu = 20 appm, std = 10 appm)	0 appm	N/A	Sampling mean based on input parameter of (Kanashenko 1996) and large standard deviations to allow for excursions. Lower bound to 0
ϕ_2	Normal (mu = 200 appm, std = 100 appm)	0 appm	N/A	Sampling mean based on input parameter of (Kanashenko 1996) and large standard deviations to allow for excursions. Lower bound to 0
E_1	Uniform (sampling bounds: 8, 11 eV/H$_2$)	8 eV	N/A	Uniform sampling across the bounds. Higher bound constraining E_1 to be smaller than enthalpy of adsorption in Trap 1 sites + dissociation energy of hydrogen molecule (max 11 eV/H$_2$) (Figure 5.30). Lower bound constraining $E_1 > E_2$
E_2	Uniform (sampling bounds: 6, 8 eV)	N/A	8 eV	Uniform sampling across the bounds. Higher bound constraining E_2 to be smaller than enthalpy of adsorption in Trap 2 sites + dissociation energy of hydrogen molecule (max 8 eV/H$_2$) (Figure 5.30).

To provide a statistical distribution of the estimates of each the fitting parameter, 100 runs of the genetic algorithm are run, each with 500 iterations and randomly generated initial guesses. For each trial, the 10 best performing gene sets are saved and plotted.

5.5.2   Results

5.5.2.1.   *Application to IG-110 adsorption isotherms*

The model developed in this work is applied to adsorption isotherms for IG-110 measured in (Wu et al. 2020a). Hydrogen in the pores is calculated using the gas law (Equation 5.72) using a total porosity volume fraction of 11.5% and a density of 1.7 g/cm³ for IG-110 (Yamashina and Hino 1989).

The IG-110 grains are modeled as 10 μm spheres. Uptake and diffusion parameters (i.e., diffusion coefficients and trapping sites density and energy) are then extracted using a genetic algorithm. The genetic algorithm is run with N = 100 gene sets and M=10. The finite difference simulation is run with three different timestep intervals to test sensitivity of the model to this parameter. Figure 5.25 shows how the MAPE of the simulations evolve as a function of the number of iterations. After 500 iterations of the algorithm, the best gene set of the model has a fitting accuracy of approximately 97% (3.4% MAPE), and that the MAPE is comparable across timesteps. For all time-steps, the MAPE converges to values within 10% of the final MAPE before 150 iterations.
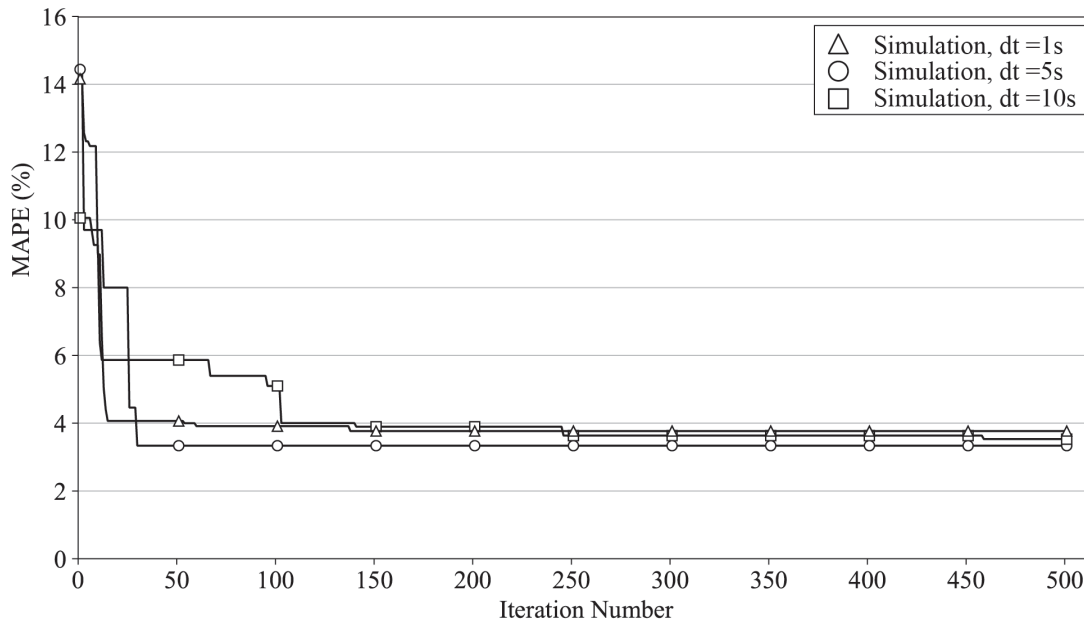
Notes:
Finite differences parameters: time-step: 1,5, 10s; mesh cell size: 1 μm.
Genetic algorithm parameters: number of gene sets: 100; number of gene sets kept after each iteration: 10.

Figure 5.25. MAPE evolution by genetic algorithm iteration.

Figure 5.26 shows the experimental hydrogen-to-carbon ratios, the simulation results, and their residuals as a function of adsorption pressure, as calculated with 500 iterations of the genetic algorithm.
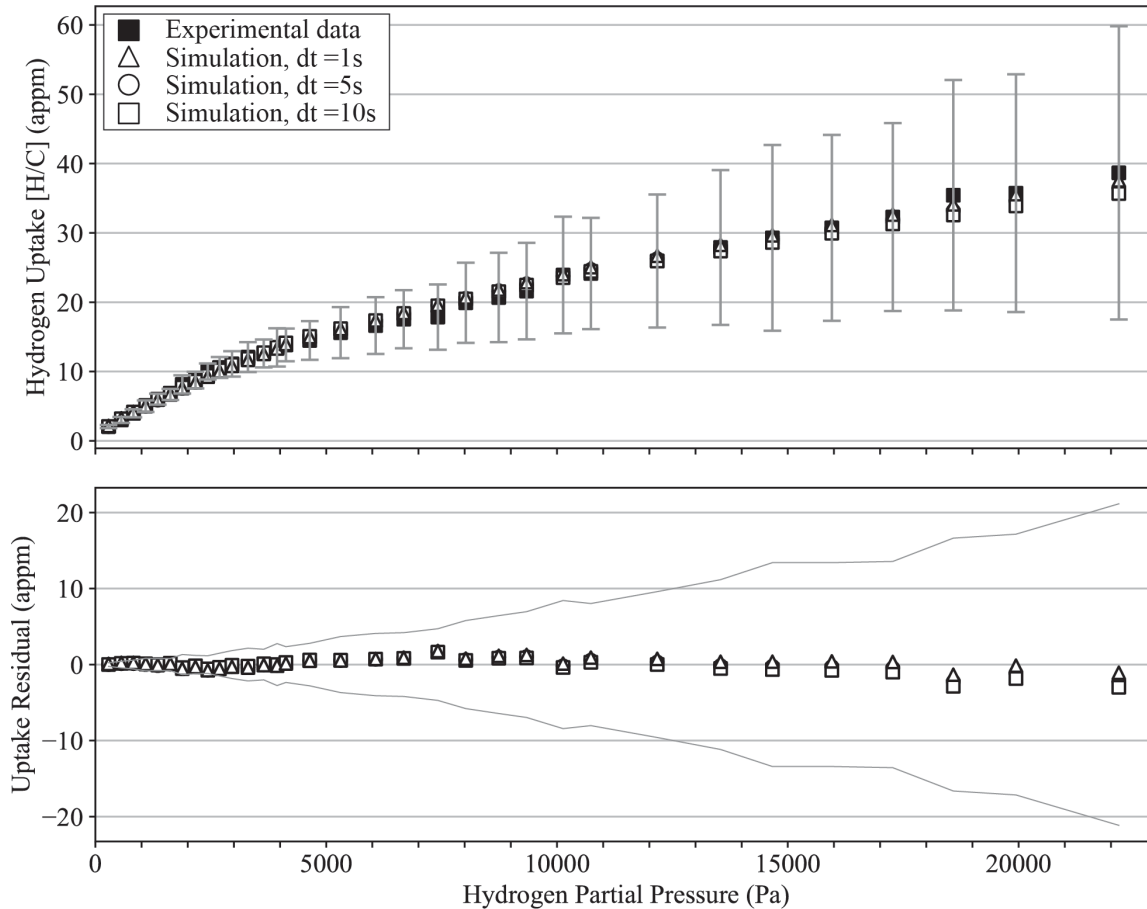
Notes:
Uncertainty on experimental data represented as an error band when plotting residual residuals.
Finite differences parameters: time-step: 1,5, 10s; mesh cell size: 1 μm.
Genetic algorithm parameters: number of iterations: 500; number of gene sets: 100; number of gene sets kept after each iteration: 10.

Figure 5.26. Experimental hydrogen uptake on IG-110 graphite, simulation results and residuals.

As seen in Figure 5.26, residuals are always below 3 appm in absolute value at each pressure level for all tested timesteps (up to 8% error in [H/C]) and do not indicate a systematic over- or underprediction of the experimental data. Simulations with a smaller time-step predict a higher [H/C] than simulations with a longer time-step at every pressure.

Figure 5.27 shows the distribution of hydrogen across uptake sites at each adsorption pressure, simulated with dt=5s timestep. At every pressure level, most hydrogen is found diffusing in the grain and trapped in Trap 2 sites. In the same figure, the actual occupancies of Trap 1 and Trap 2 sites calculated with the diffusion-with-trapping model are compared with the occupancies predicted by thermodynamics, using Equations 5.43, 5.45, and 5.53 with the deuterium trapping enthalpy and entropy tabulated in Table 5.18. The comparison suggests that at all adsorption pressures, hydrogen uptake is kinetically limited: a longer adsorption time would be required to achieve hydrogen uptake capacity at the corresponding temperature and pressure.

Figure 5.27: Distribution of hydrogen across uptake sites and trapping site occupancies.

To provide a statistical distribution of the estimates of each of the parameters that enter the diffusion model, 50 trials of the genetic algorithm (based on the boundary condition of Equation 5.81) are run, each with 500 iterations and randomly generated initial guesses. After completion, all gene sets achieving an error within 10% of the best MAPE of Figure 5.25 (423 gene sets) are selected and used to determine the mean and standard deviation of each parameter, which are displayed in Table 5.26 and compared to estimates available in literature. Due to the insensitivity of the model to the timestep duration, all simulations in the rest of the paper are run with dt=5s.

Table 5.26. Mean and standard deviation of the genetic algorithm parameters. Comparison

Parameter	Estimate	Values available in literature
K_{S1} (mol/m^{3}Pa$^{1/2}$)	0.127(4)	0.2-0.9. Compiled in (Dolan 2020).
$D_{intercryst}$ (m^2/s)	$4.8(1.6)10^{-20}$	4 10^{-22} – 10^{-19}. Compiled in (Dolan 2020) and in Section 5.3
ϕ_1 (appm)	30(24)	$\phi_1 \sim$ 17-20 appm and $\phi_1 \sim$ 64-228 appm in previous estimates (Table 5.28) but $\phi_1 + \phi_2$ could be above 600 appm based on hydrogen uptake results (Section 5.2)
ϕ_2 (appm)	766(266)	
E_1 (eV/H$_2$)	9.5(8)	Expected in 8.7 eV/H2 – 10.0 eV/H2 if physisorption enthalpy for atomic H is negligible. Lower otherwise (Section 5.2)
E_2 (eV/H$_2$)	6.4(2)	Expected in 6.7 eV/H2 – 7.6 eV/H2 if physisorption enthalpy for atomic H is negligible. Lower otherwise (Section 5.2)
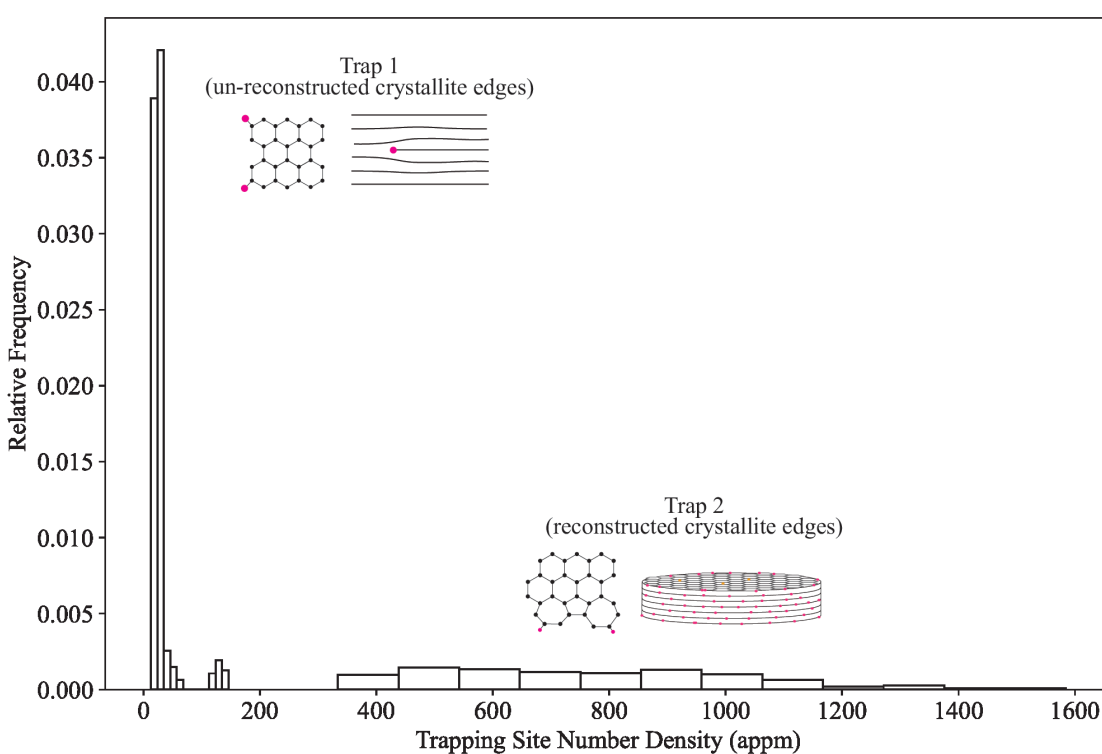
Notes:
Finite differences parameters: time-step: 5s; mesh cell size: 1 μm.
Genetic algorithm parameters: number of trials: 50; number of iterations: 500 number of gene sets: 100;
number of gene sets kept after each iteration: 10.

Figure 5.28. Distribution of Trap 1 and Trap 2 number density from the genetic algorithm runs.

Figure 5.28 displays the distribution of the estimates for number density of trapping sites for Trap 1 and Trap 2. The distribution of estimates for Trap 1 is narrow but bimodal, with the most likely value in the bin 15-20 appm. The distribution for Trap 2 is less peaked (266 appm s.d.). This could indicate that the model is more sensitive to Trap 1 than to Trap 2, as variance of the latter has a lower effect to the model error.

5.5.2.2. *Benchmark on temperature-dependent uptake data*

In Section 5.5.2.1, the diffusion-with-trapping model is used on constant-temperature, pressure-dependent uptake data. Here, the model is fitted on temperature-dependent data from (Causey et al. 1986), which has been used as a benchmark by previous diffusion models (Dolan et al. 2021a). In (Causey et al. 1986), POCO AXF-5Q graphite is exposed to a deuterium partial pressure of 0.66 Pa for 1.5 hours at each temperature step (in the range 973 K – 1773K). Figure 5.29 shows that the model develop in this work is able to fit the experimental data from (Causey et al. 1986) (using the parameters in Table 5.27 both at low temperatures and high temperatures).
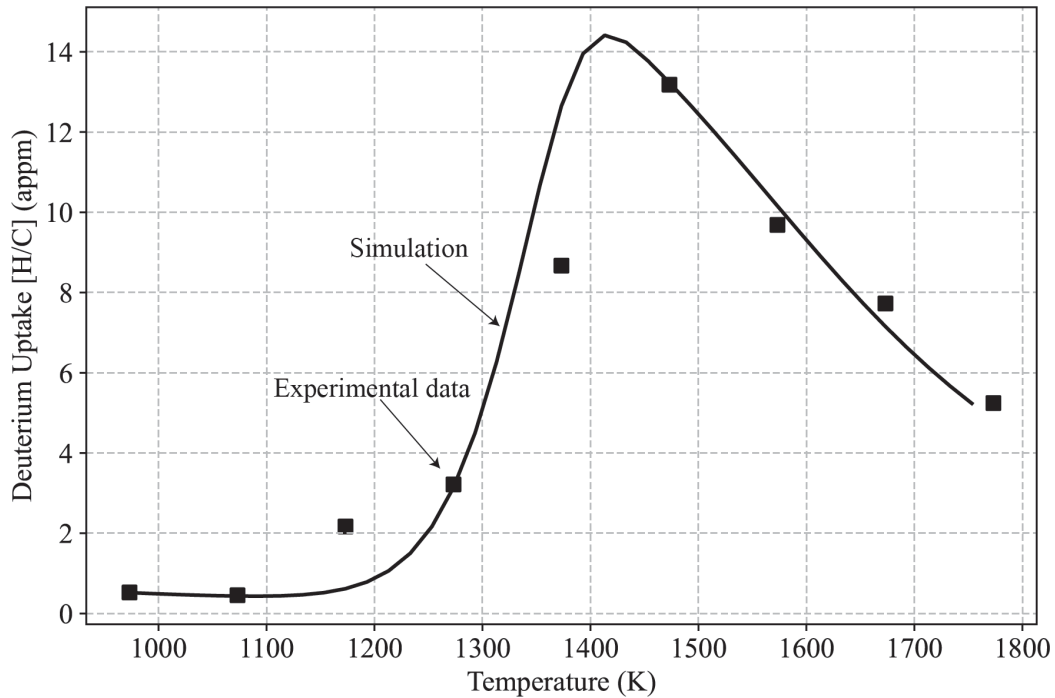
Notes:
Experimental parameters from (Causey et al., 1986): graphite grade: POCO AXF-5Q; partial pressure: 0.66 Pa; uptake time: 5400 seconds per point.
Finite differences parameters: time-step: 5s; mesh cell size: 5 μm.

Figure 5.29: Experimental data (from [35) and simulated profile for temperature-dependent deuterium uptake data on POCO AXF-5Q

Table 5.27. Simulation parameters for temperature-dependent deuterium uptake data on POCO AXF-5Q from (Causey et al. 1986).

Parameter	Value	Discussion
K_{S1} (1/Pa$^{1/2}$)	$6.0 \cdot 10^{-4} \exp\left(-0.19 \frac{eV}{k_b T}\right)$	Functional form from (Atsumi et al. 1988). Pre-exponential factor and activation energy fitted on experimental data.
$D_{intercryst}$ (cm^2/s)	$2.0 \exp\left(-3.35 \frac{eV}{k_b T}\right)$	Functional form from (Causey 1989). Pre-exponential factor and activation energy fitted on experimental data.
ϕ_1 (appm)	70	Fitted on experimental data
ϕ_2 (appm)	200	Estimated by (Kanashenko 1996) for TSP graphite and assumed representative of POCO AXF-5Q.
E_1 (eV/H$_2$)	9.95	Fitted on experimental data (constrained in the interval of Table 5.26)
E_2 (eV/H$_2$)	6.4	Fitted on experimental data (constrained in the interval of Table 5.26)

In this fit, the detrapping activation energies are constrained to the intervals identified in Table 5.26, since they are not expected to vary across graphite grades. Using Equations 5.43, 5.45, and 5.53 with the deuterium trapping enthalpy and entropy tabulated in Table 5.18, one finds that the thermodynamic occupancy of Trap 2 sites is approximately 22% at 973 K, 6% at 1073 K, and less than 2% at all other temperatures. A low occupancy of Trap 2 sites suggests that the fit would be insensitive to the number density of Trap 2 sites, ϕ_2. For this reason, ϕ_2 is not used as a fitting parameter but is assumed to 200 appm, which was previously estimated by (Kanashenko 1996) for TSP graphite.

5.5.3   Discussion

In this thesis, a diffusion-with-trapping model is developed to describe hydrogen uptake into and kinetics in graphite. While this approach has been already used in the previous literature, this is the first paper that considers two distinct types of trapping sites in the model. Previous works by (Dolan et al. 2021a), (Atsumi 2002b), (Morita and Muto 1992) include trapping in and detrapping from Trap 2 sites in the kinetics model, but do not define a second trapping site (Trap 1). The model developed here includes both Trap 1 and Trap 2 sites. This explicit definition of the two types of trapping sites allows to estimate trapping site densities and desorption activation energies for both Trap 1 and Trap 2, instead of an overall trapping site density and an averaged desorption energy, as discussed in Section 5.5.3.1.

5.5.3.1.   *Comparison of transport parameters with published literature*

The trapping site densities estimated for IG-110 through the fitting of the adsorption isotherms in (Wu et al. 2020a) is in the same order of magnitude of the estimates available in literature for other grades of nuclear graphite and graphite matrix (Table 5.28) and to hydrogen molar fractions measured in uptake experiments (Section 5.2).

Table 5.28: Comparison of trapping site densities with literature

Source	Type of Estimate	Graphite Type	Experimental Conditions	Trap 1 (appm)	Trap 2 (appm)	Comment
This paper	Kinetic fitting to adsorption isotherm	IG-110	Hydrogen adsorption isotherms at 700 °C and 300 Pa – 22 kPa. Each pressure step has a duration of 5 min or more (Wu et al. 2020a).	30 ± 24	766 ± 266	Kinetic modelling including two types of trapping sites.
(Hoinkis 1991a)	Thermodynamic fitting to adsorption isotherms	A3	Deuterium adsorption isotherms at 800 °C and 1 Pa – 130 Pa.	Not estimated because not included in the model	140	Thermodynamic modelling of dissociative adsorption isotherm. Trap 2 density estimate is a lower bound, as it is calculated concentration from hydrogen concentration limit at high pressure, but temperature dependence is not considered.
		TSP	Hydrogen adsorption isotherms at 920°C, and at 13 Pa - 133 kPa. (Redmond and Walker 1960).		64	
		Reactor grade graphite (no additional information provided)	Hydrogen adsorption isotherms at 600°C, 700°C, 750°C, and 1 Pa – 4 kPa (Thomas 1961).		228	
(Causey 1989)	Thermodynamic fitting to temperature-dependent solubility data	POCO AXF-5Q	Tritium uptake at 1100 °C and 0.66 Pa for 80 hours.	17	Not estimated because data collected at high temperature for which Trap 2 occupancy is negligible	Fitting performed using the DIFFUSE code (M. I. Baskes 1980), assuming one type of trapping sites.
(Kanashenko 1996)	Thermodynamic fitting to adsorption isotherms at multiple temperatures	TSP	Hydrogen adsorption isotherms at 920°C, 1085°C, 1335°C, and 1495°C with pressures in range 13 Pa - 133 kPa (Redmond and Walker 1960).	20	200	Thermodynamic modelling of dissociative adsorption isotherm. Time-dependent processes are not considered.

The application of the diffusion-with-trapping model to adsorption isotherms allows to estimate the energy of the trapping sites, in addition to the trapping site densities. Both types of trapping sites are modeled as reversible sites, and their de-trapping energies, defined as the energy barrier that the hydrogen atom must overcome to be de-trapped, are estimated through the optimization. Fitting with the IG-110 adsorption isotherms yields an energy of 9.5 ±0.8 eV/H_2 for Trap 1 sites and 6.4 ±0.2 eV/H_2 for Trap 2 sites. A summary of the energetic levels involved in hydrogen

uptake, discussed in Section 5.2, is shown in Figure 5.30. As shown in Figure 5.30, estimating Trap 1 and Trap 2 detrapping energies allows to estimate an upper bound to the enthalpy of solution of atomic hydrogen, i.e., the difference in energy between non-adsorbed and adsorbed dissociated, to 1.3 eV/H$_2$.
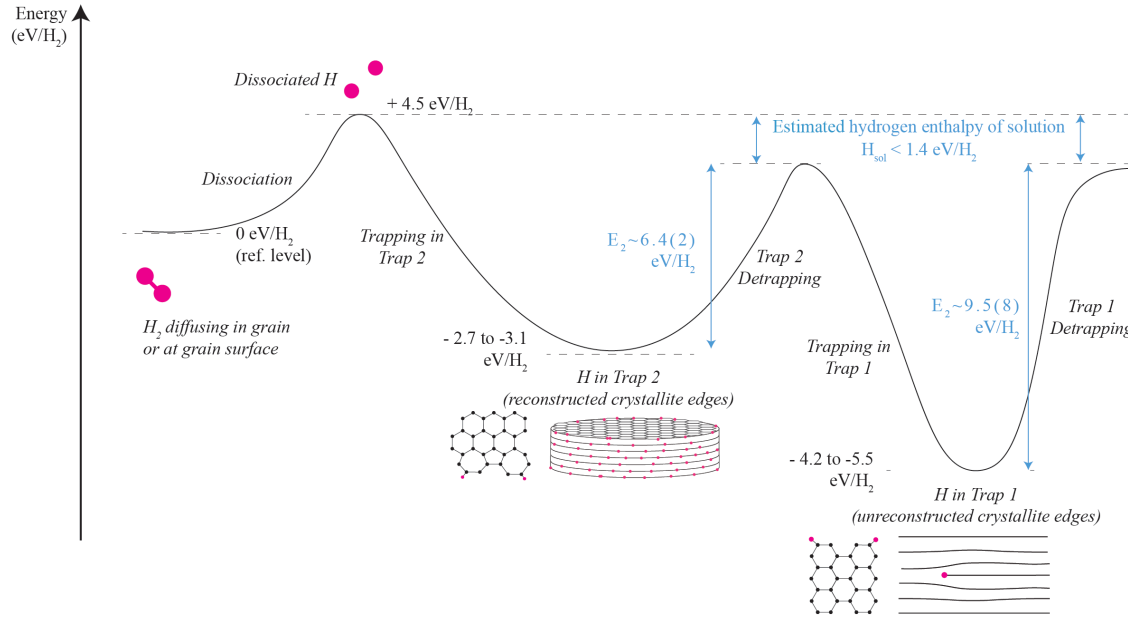
Notes:
Carbon atoms in black, hydrogen atoms in magenta. Not drawn to scale.
Trap 1 and Trap 2 sites illustration and all energy levels in **black** are from (Vergari and Scarlat, 2021).
Energy levels in **blue** are estimated in this work.

Figure 5.30: Energy levels for hydrogen uptake in graphite.

Another transport parameter obtained by fitting the model to the adsorption isotherms in (Wu et al. 2020a) is hydrogen inter-crystallite diffusion coefficient. The diffusion coefficient is estimated to $4.8(1.6)10^{-20} m^2/s$, which is within in the range of published apparent diffusion coefficients determined from transient uptake experiments at this temperature (compiled in Table 5.20).

5.5.3.2. *Model assumptions and limitations*

One of the main assumptions of the model presented in this work is that hydrogen molecules can penetrate the sample surface, permeate its open porosity, and diffuse into the closed porosity sufficiently fast that the partial pressure at the grain surface is the same as the pressure outside the sample and the inter-grain diffusion can be neglected. This assumption was originally made in (Atsumi and Iseki 2000) and was shown to not impact modeling results in (Dolan et al. 2021a) for the uptake data of (Causey 1989), which is used as a benchmark. A second assumption in this model is that hydrogen diffuses in the grain as an atom, i.e., that hydrogen dissociation occurs at the grain boundary. As discussed in Section 5.3, both dissociated (i.e., atomic) and non-dissociated (i.e., molecular) hydrogen diffuses in the grain, depending on whether it has been already trapped and detrapped by the trapping site. Similarly, different diffusion coefficients may apply depending on whether hydrogen is diffusing in the proximities of Trap 2 sites (i.e., reconstructed crystallite edges) or Trap 1 sites (i.e., unreconstructed crystallite edges). To limit the parameters in the genetic algorithm in an effort to limit modeling bias, a single diffusion coefficient is used for hydrogen diffusion in the grain.

5.5.4 Conclusion

Most of the uptake studies available in literature are performed at high hydrogen partial pressures (kPa - MPa range), which are not representative of the hydrogen pressures in reactors (few Pa to tens of Pa). Developing hydrogen uptake models that account for the different mechanisms of hydrogen uptake is necessary to extract hydrogen transport parameters and extrapolate uptake behavior to low pressures.

In this work, the first model for hydrogen uptake and transport in graphite that considers the two types of hydrogen trapping sites in graphite as distinct components is developed. Hydrogen transport is modeled as a diffusion-with-trapping process. Using a genetic algorithm, this model is fitted to adsorption isotherm data for IG-110 graphite (Wu et al. 2020a) to extract Trap 1 and Trap 2 number density, Trap 1 and Trap 2 detrapping energies, and inter-crystallite diffusion coefficient for this graphite grade (Table 5.26 and Figure 5.28). The trapping site densities estimated in this work are of comparable magnitude to the densities estimated in previous works by means of thermodynamic analysis of uptake experiments (Table 5.28). The detrapping energies are lower than the difference between the energy of hydrogen in trapping sites and non-trapped, dissociated hydrogen (Figure 5.30) and allow to estimate an upper bound for hydrogen enthalpy of solution. The inter-crystallite diffusion coefficient is within the range of previous estimates for the multiple graphite grades at the same temperature.

The model and the genetic algorithm presented in this work are made available in the Mendeley Data repository linked in Supplementary Information with the intent to provide a tool for extracting transport parameters from hydrogen uptake and desorption studies. As a next step, this model will be used to model hydrogen uptake in PB-FHRs. The author encourages the application of the model in this article to adsorption isotherms at other temperatures to estimate temperature-dependent parameters in diffusion coefficients and Sievert's constants. As a further validation of the model, the authors suggest comparing the model results with the trapping site distribution estimated via thermal desorption spectroscopy experiments.

5.5.5 Acknowledgement

6 Conclusion

The scope of this dissertation is to investigate physical and chemical mechanisms of interactions of fluoride salts with graphite and assess their impact on graphite engineering during reactor operation and waste management. This investigation is organized in four chapters, with the first two chapters focusing on the interactions, and the last two chapters presenting two topics of engineering relevance for graphite is a salt-containing reactor.

In **Chapter 2**, the chemical and microstructural changes that occur to nuclear graphite upon exposure to FLiBe salt for 240h at 700 °C are studied, investigating both samples exposed to the liquid FLiBe, and samples exposed to the cover gas above molten salt. Characterization of the samples is performed using SEM/EDS, surface XPS, depth profiling XPS, and Raman spectroscopy, and prior GDMS depth profiling data is re-analyzed. This chapter advances the understanding of FLiBe-graphite interactions in MSRs and FHRs by providing evidence of graphite fluorination upon exposure to the salt and to the cover gas and identifying presence of both semi-ionic and covalent C-F bonds formation. It also concludes that C-F bonds form by different mechanisms in the liquid phase than in the cover gas of the molten salt. Further studies are needed to establish the relationships among chemical and surface microstructural modifications in graphite upon exposure to molten salt and the cover gas above it and to develop a mechanistic description for the formation of covalent and semi-ionic C-F with exposure to salt and to the cover-gas above the salt. ^{19}F NMR has been successfully used to distinguish semi-ionic and covalent C-F bonds in highly fluorinated carbon materials and is proposed as a technique to validate the observation of this study. Adsorption isotherms with gas able to probe different reactive sites (N_2, O_2, H_2) are also proposed as a strategy to identify the location of the C-F bonds in the graphite structure.

In **Chapter 3**, salt wetting and infiltration data on graphite are reviewed to conclude that few graphite grades would satisfy the 4 vol % limit set in the MSRE and even fewer would satisfy the 0.5 vol % design target (Briggs 1964b p. 255). This finding indicates that most graphite grades would be unsuitable for MSRs but not necessarily for FHRs, for which infiltration limits have not been defined. To define infiltration limits for FHRs, it is necessary to evaluate the effect of salt infiltration on graphite properties and quantify its impact on reactor safety and graphite waste management. To this scope a series of suggested experiments is suggested to quantify the implications of salt infiltration on graphite thermo-mechanical properties and performance in safety transients. Prioritized experiments would include measuring heat conductivity and heat transfer resistance of salt-exposed and infiltrated pebbles, measuring strength of infiltrated graphite with thermal cycling, and simulating operational transients using infiltrated graphite. In **Chapter 3**, it is also observed that salt infiltration in graphite is impacted by salt chemistry and graphite conditions, yielding scattered results across studies. To better understand what parameters impact infiltration, a method to predict salt infiltration behavior from a graphite of known porosity distribution based on the sessile drop method is discussed. This approach is applied on FLiNaK and allows measuring contact angle variability as function of graphite surface finish and salt composition, thereby improving the infiltration prediction from literature. Further work will involve applying the approach to FLiBe and examining the effect of reducing agents, oxides, and hydroxides on wetting behavior.

In **Chapter 4**, graphite-graphite tribology in argon and molten fluoride salts is investigated. The mechanisms of lubrication in these two environments are identified. Coefficients of friction and wear rates for graphite-graphite sliding in FLiBe are reported for the first time in literature. Based on the wear and friction results from argon tests at room temperature and 600°C, and microstructural characterization via microscopy and Raman spectroscopy, it is postulated that graphite self-lubricates at high temperature through the formation of a film of aligned fractured crystallites. Further tests involving atomic force microscopy, adsorption isotherms with N_2, O_2, and H_2 are proposed to verify the mechanism. Tribology testing in FLiBe indicates that FLiBe lubrication leads to a decrease of the coefficient of friction and of the wear rates compared to dry sliding in argon. The combination of tribological and microstructural results suggests that a lubrication mechanism alternative to film-formation is at play upon addition of FLiBe. Calculating the salt film thickness indicates that tests are performed in the boundary lubrication regime. It is postulated that the FLiBe lubricates the graphite-graphite interface by passivating the carbon atoms at crystallite edges. Further testing at different load levels and chemical characterization of the wear spots by EDS, SEM, and contact angle studies is proposed to verify the formulated hypothesis.

In **Chapter 5,** the tritium-graphite interaction is discussed. Using the Mark-I PB-FHR and the ARC breeding blanket as case studies, rates of change of tritium and other activation products of FLiBe are calculated and the corrosive effects of the activation reactions on FLiBe are quantified. The calculated tritium production rates are three to four orders of magnitude greater than in light water reactors, indicating that tritium management is important for reactors employing molten salts. As shown in the MSRE, a significant fraction of the tritium produced during operation may end up in graphite components. To better characterize the process by which graphite uptakes tritium, available literature on thermodynamics and kinetics of the hydrogen-graphite interaction at conditions of relevance for salt-containing reactor is reviewed. Extrapolating from available data, the prevailing mechanisms of uptake and desorption at the condition of interest are identified, and the effectiveness of using graphite as a tritium vector is assessed. It is observed that the uptake capacities of the graphite employed in FHRs would be sufficient to trap all produced tritium, but the process may be limited by uptake kinetics. It is also observed that irradiation and chemical reactions may impact the distribution of tritium across reactive sites, impacting the amount of tritium that could be desorbed upon high temperature degassing out of the core. Across the chapters, gaps in the available data are identified to generate a prioritized list of experiments that would improve the mechanistic understanding of hydrogen-graphite interaction at high temperature and reduce the uncertainty in predictions. Prioritized experiments include measurements of hydrogen uptake rates and capacities for graphite irradiated at high dpa (> 5 dpa), representative of PB-FHR fuel pebbles, and direct measurements of hydrogen diffusion coefficients before and after fluorination. The findings from the literature review are used to inform a computational model for hydrogen isotopes uptake and transport in graphite. This model improves on the state of the art by separately considering two types of hydrogen trapping sites in graphite. Using a genetic algorithm, this model is fitted to adsorption isotherm data for IG-110 graphite to extract trapping sites number densities and detrapping energies. The model and the genetic algorithm presented in this work are made available as in the Mendeley Data repository linked in Supplementary Information with the intent to provide a tool for extracting transport parameters from hydrogen uptake and desorption studies.

In conclusion, this dissertation characterizes graphite behavior in reactors that employ fluoride salts, by focusing on graphite-graphite interactions (tribology in argon), graphite-salt interactions (fluorination, infiltration, and tribology in FLiBe), and graphite-salt-tritium interactions (tritium

uptake and transport). The experiments conducted in this work indicate that the presence of the salt impacts the engineering performance of graphite in the reactor in multiple ways, from providing increased lubrication to changing graphite surface chemistry. Additional areas where the salt could have an effect include evolution of oxidation and graphite reactive sites upon neutron irradiation, in the presence of salt-exposure. Exploration of these areas is recommended as a further development. This dissertation also indicates that the graphite-FLiBe interactions bear significance for graphite management after discharge from the reactor, and leaves open questions associated to radiolysis of fluorine residuals and oxidation. Follow-up efforts on graphite characterization after discharge and decontamination will be instrumental to define a roadmap for management of graphite waste forms from salt reactors.

7 Supplementary Information

7.1 Data Availability

All supplementary material and raw data are available at the Mendeley Data repository:

Vergari, Lorenzo (2023), "Chemistry and Physics of Graphite in Fluoride Salt Reactors - Ph.D. Dissertation Data", Mendeley Data, V1, doi: 10.17632/ng4yw2scgf.1

7.2 Supplementary Information for Chapter 2

Figure 7.1 displays EDS point spectra collected on selected features on the surface of the liquid-FLiBe exposed sample.
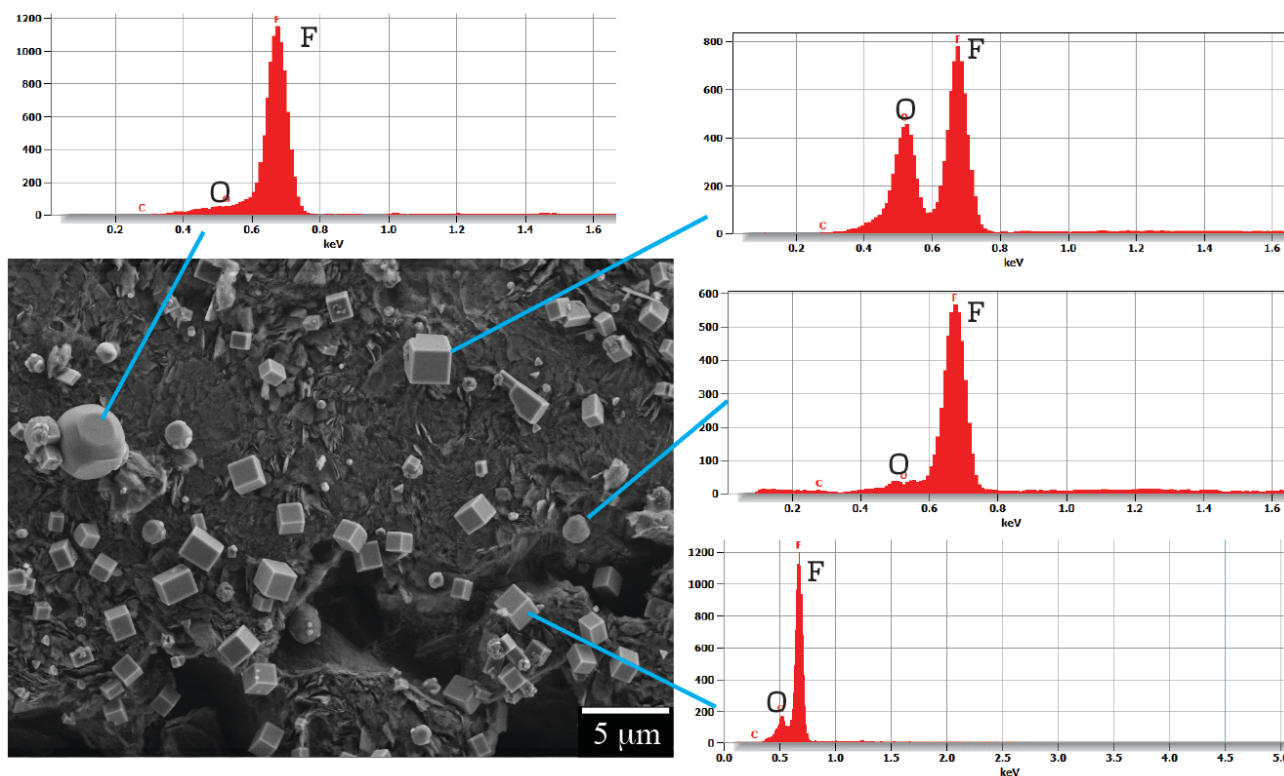
Figure 7.1: EDS point spectra of the surface of the liquid-FLiBe exposed sample. Collected using a Zeiss LEO 1530 at an accelerating voltage of 10 kV

7.3   Supplementary Information for Chapter 3
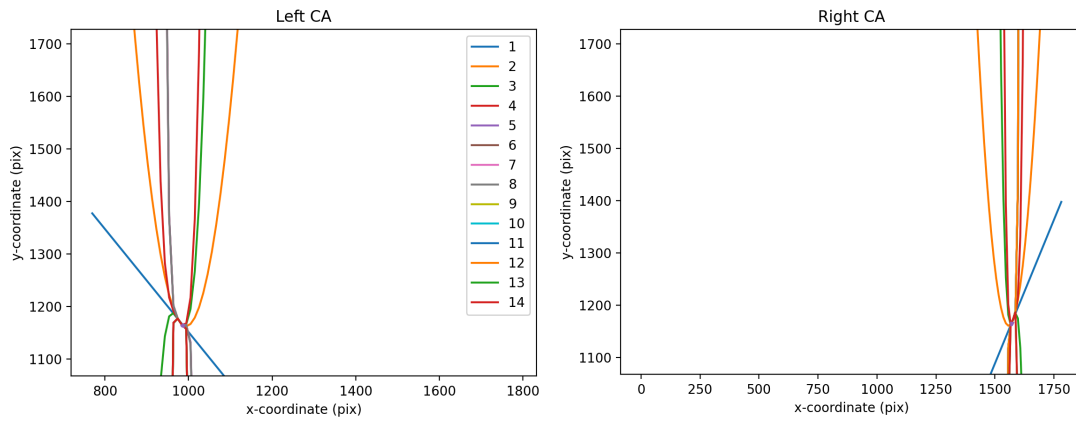
Figure 7.2: Fitting of n-th degree polynomials on the left and right droplet contact points (GUI-generated image).
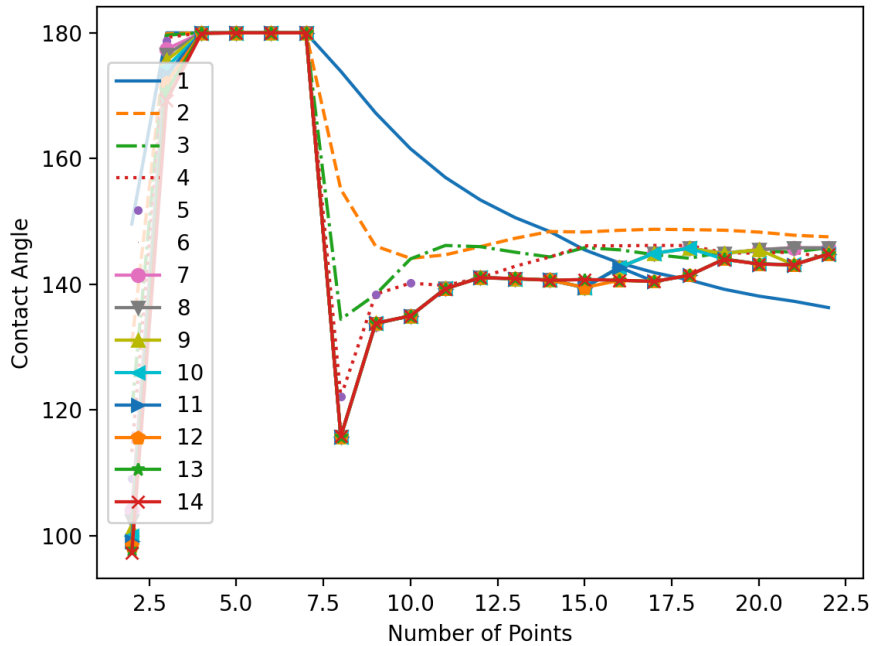
Figure 7.3: Variability of measured contact angle with respect to number of points for droplet-surface slope calculation and polynomial order (GUI-generated image).

7.4   Supplementary Information for Chapter 4
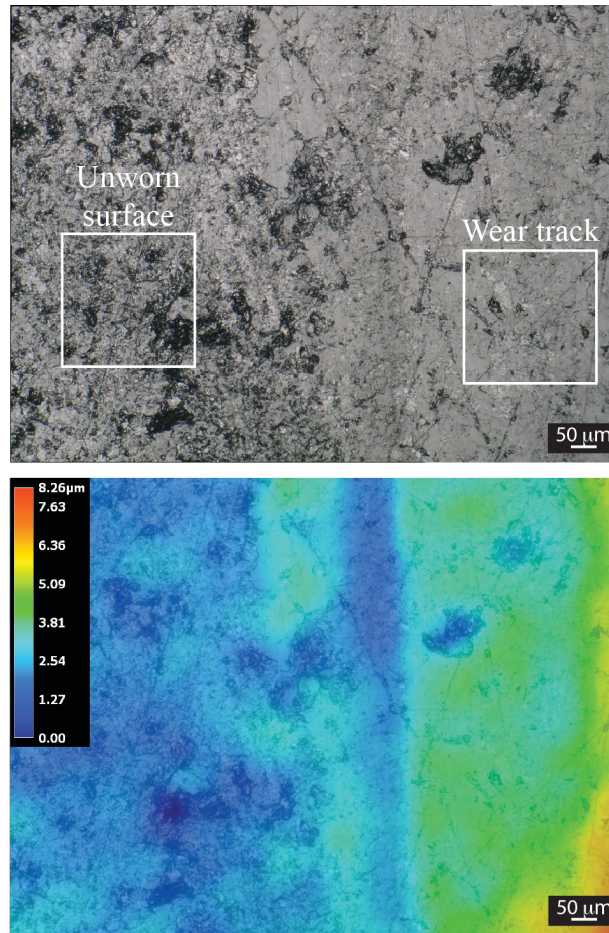
Figure 7.4: Digital microscopy (top) and profilometry (bottom) of the wear disk in proximity of the wear track WT4, showing that the wear track is deposited on top of the disk surface.
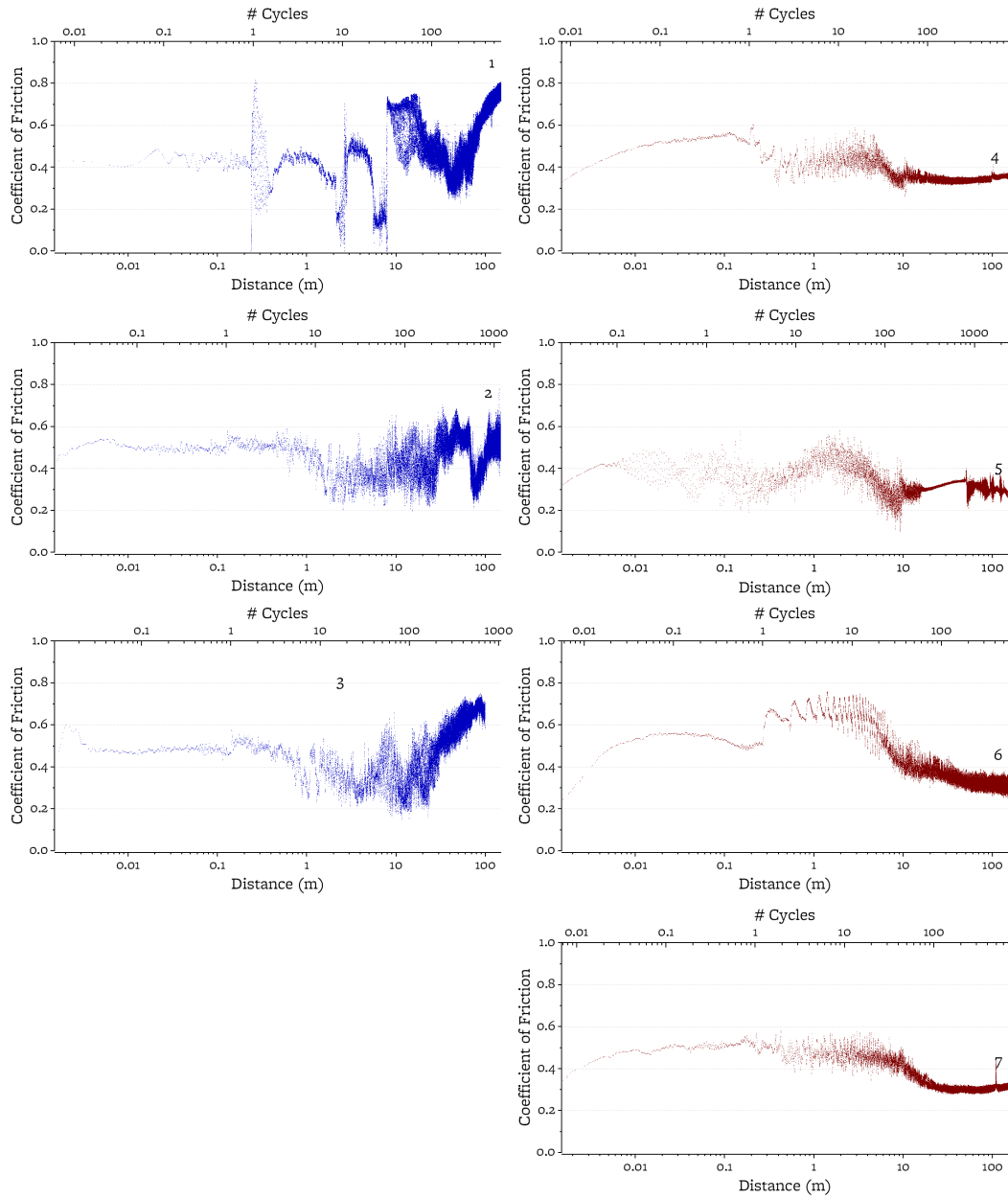
Figure 7.5: Coefficient of friction as function of sliding distance and disk rotational cycles, in logarithmic scale. Left column: RT. Right-column: HT.

8 References

Abdou, M., M. Riva, A. Ying, C. Day, A. Loarte, L. R. Baylor, P. Humrickhouse, T. F. Fuerst, and S. Cho. 2021. "Physics and technology considerations for the deuterium-tritium fuel cycle and conditions for tritium fuel self sufficiency." *Nucl. Fusion*.

Abe, Y., O. Kosugiyama, and A. Nagashima. 1981. "Viscosity of LiF-BeF 2 eutectic mixture (XBeF2= 0.328) and LiF single salt at elevated temperatures." *J. Nucl. Mater.*, 99: 173–183. https://doi.org/10.1016/0022-3115(81)90186-0.

Abrahamson, J. 1973. "The surface energies of graphite." *Carbon*, 11 (4): 337–362. https://doi.org/10.1016/0008-6223(73)90075-4.

Albers, T. L. 2009. "High-temperature properties of nuclear graphite." *J. Eng. Gas Turbines Power*, 131 (6). https://doi.org/10.1115/1.3093995/474602.

Allouche, A., and Y. Ferro. 2006. "Dissociative adsorption of small molecules at vacancies on the graphite (0 0 0 1) surface." *Carbon*, 44 (15): 3320–3327. https://doi.org/10.1016/j.carbon.2006.06.014.

Allouche, A., Y. Ferro, T. Angot, C. Thomas, and J. M. Layet. 2005. "Hydrogen adsorption on graphite (0001) surface: A combined spectroscopy-density-functional-theory study." *J. Chem. Phys.*, 123 (12): 124701. https://doi.org/10.1063/1.2043008.

Ambrosek, J., M. Anderson, K. Sridharan, and T. Allen. 2009. "Current status of knowledge of the fluoride salt (FLiNaK) heat transfer." *Nucl. Technol.*, 165 (2): 166–173.. https://doi.org/10.13182/NT165-166.

Ammar, M. R., N. Galy, J. N. Rouzaud, N. Toulhoat, C. E. Vaudey, P. Simon, and N. Moncoffre. 2015. "Characterizing various types of defects in nuclear graphite using Raman scattering: Heat treatment, ion irradiation and polishing." *Carbon*, 95: 364–373. https://doi.org/10.1016/j.carbon.2015.07.095.

Andreades, C., A. Cisneros, J. K. Choi, A. Chong, M. Fratoni, S. Hong, L. Huddar, K. Huff, D. Krumwiede, M. Laufer, M. Munk, R. Scarlat, N. Zweibaum, E. Greenspan, and P. Peterson. 2014. *Technical Description of the "Mark 1" Pebble-Bed Fluoride-Salt-Cooled High-Temperature Reactor (PB-FHR) Power Plant*. UC Berkeley

Andreades, C., A. T. Cisneros, J. K. Choi, A. Y. K. Chong, M. Fratoni, S. Hong, L. R. Huddar, K. D. Huff, J. Kendrick, D. L. Krumwiede, M. R. Laufer, M. Munk, R. O. Scarlat, N. Zweibaum, E. Greenspan, X. Wang, and P. Peterson. 2016. "Design Summary of the Mark-I Pebble-Bed, Fluoride Salt-Cooled, High-Temperature Reactor Commercial Power Plant." *Nucl. Technol.*, 195 (September): 223–238. https://doi.org/10.13182/NT16-2.

Arifvianto, B., Suyitno, M. Mahardika, P. Dewo, P. T. Iswanto, and U. A. Salim. 2011. "Effect of surface mechanical attrition treatment (SMAT) on microhardness, surface roughness and wettability of AISI 316L." *Mater. Chem. Phys.*, 125 (3): 418–426. https://doi.org/10.1016/j.matchemphys.2010.10.038.

Arun Prakash, A., P. Chaudhuri, S. Khirwadkar, N. Chauhan, P. M. Raole, D. Chenna Reddy, and Y. C. Saxena. 2008. "On residual gas analysis during high temperature baking of graphite tiles." *J. Phys. Conf. Ser.*, 114 (1): 012063. IOP Publishing. https://doi.org/10.1088/1742-6596/114/1/012063.

Asakuma, Y., M. Asada, Y. Kanazawa, and T. Yamamoto. 2016. "Thermal analysis with contact resistance of packed bed by a homogenization method." *Powder Technol.*, 291: 46–51. https://doi.org/10.1016/j.powtec.2015.12.006.

Asanov, I. P., V. M. Paasonen, L. N. Mazalov, and A. S. Nazarov. 1998. "X-ray photoelectron study of fluorinated graphite intercalation compounds." *J. Struct. Chem.*, 39 (6): 928–932.. https://doi.org/10.1007/BF02903607.

Ashida, K., K. Ichimura, M. Matsuyama, and K. Watanabe. 1984. "Thermal desorption of hydrogen, deuterium and tritium from pyrolytic graphite." *J. Nucl. Mater.*, 128–129 (C): 792–797. https://doi.org/10.1016/0022-3115(84)90459-8.

ASTM International 2018. *Graphite Standard Specification for Isotropic and Near-isotropic Nuclear Graphites*.

ASTM International. 2016. *Standard Guide for Impregnation of Graphite with Molten Salt*.

ASTM International. 2017. *Standard Test Method for Wear Testing with a Pin-on-Disk Apparatus*.

Atsumi, H. 1989. "Graphite surface erosion by ion irradiation and releasing behavior of deuterium and helium from graphite." Ph.D. Thesis.

Atsumi, H. 2002a. "Mechanism of hydrogen trapping and transport in carbon materials." *Phys. Scr. T*, 103: 77–80. https://doi.org/10.1238/physica.topical.103a00077.

Atsumi, H. 2002b. "Hydrogen bulk retention in graphite and kinetics of diffusion." *J. Nucl. Mater.*, 307–311: 1466–1470. https://doi.org/10.1016/S0022-3115(02)01069-3.

Atsumi, H. 2003. "Hydrogen retention in graphite and carbon materials under a fusion reactor environment." *J. Nucl. Mater.*, 313–316: 543–547. https://doi.org/10.1016/S0022-3115(02)01464-2.

Atsumi, H., and M. Iseki. 2000. "Hydrogen absorption process into graphite and carbon materials." *J. Nucl. Mater.*, 283–287 (PART II): 1053–1056. https://doi.org/10.1016/S0022-3115(00)00094-5.

Atsumi, H., M. Iseki, and T. Shikama. 1992. "Hydrogen solubility and diffusivity in neutron-irradiated graphite." *J. Nucl. Mater.*, 191–194: 368–372. https://doi.org/10.1016/S0022-3115(09)80068-8.

Atsumi, H., M. Iseki, and T. Shikama. 1994. "Trapping and detrapping of hydrogen in carbon-based materials exposed to hydrogen gas." *J. Nucl. Mater.*, 212–215 (PART B): 1478–1482. https://doi.org/10.1016/0022-3115(94)91073-1.

Atsumi, H., M. Iseki, and T. Shikama. 1996. "Hydrogen behavior in carbon-based materials and its neutron irradiation effect." *J. Nucl. Mater.*, 233–237: 1128–1132. https://doi.org/10.1016/0022-3115(95)00180-8.

Atsumi, H., and Y. Kondo. 2018. "Retention and release of hydrogen isotopes in carbon materials priorly charged in gas phase." *Fusion Eng. Des.*, 131 (April): 49–53. https://doi.org/10.1016/j.fusengdes.2018.04.039.

Atsumi, H., A. Muhaimin, T. Tanabe, and T. Shikama. 2009a. "Hydrogen trapping in neutron-irradiated graphite." *J. Nucl. Mater.*, 386–388: 379–382. https://doi.org/10.1016/j.jnucmat.2008.12.135.

Atsumi, H., N. Shibata, T. Tanabe, and T. Shikama. 2007. "Hydrogen absorption into neutron-irradiated graphite and estimation of the trapping effect." *Phys Scr*, 128: 72–75. https://doi.org/10.1088/0031-8949/2007/T128/014.

Atsumi, H., Y. Takemura, T. Konishi, T. Tanabe, and T. Shikama. 2013a. "Thermal desorption of hydrogen from carbon and graphite at elevated temperatures." *J. Nucl. Mater.*, 438: S963–S966. https://doi.org/10.1016/j.jnucmat.2013.01.209.

Atsumi, H., Y. Takemura, T. Miyabe, T. Konishi, T. Tanabe, and T. Shikama. 2013b. "Desorption of hydrogen trapped in carbon and graphite." *J. Nucl. Mater.*, 442 (1-3 SUPPL.1): S746–S750. https://doi.org/10.1016/j.jnucmat.2013.03.041.

Atsumi, H., T. Tanabe, and T. Shikama. 2009b. "Bulk hydrogen retention in neutron-irradiated graphite at elevated temperatures." *J. Nucl. Mater.*, 390–391 (1): 581–584. https://doi.org/10.1016/j.jnucmat.2009.01.112.

Atsumi, H., T. Tanabe, and T. Shikama. 2011. "Hydrogen behavior in carbon and graphite before and after neutron irradiation – Trapping, diffusion and the simulation of bulk retention–." *J. Nucl. Mater.*, 417 (1–3): 633–636. https://doi.org/10.1016/j.jnucmat.2010.12.100.

Atsumi, H., T. Tanabe, and T. Shikama. 2015. "Trapping state of hydrogen isotopes in carbon and graphite investigated by thermal desorption spectrometry." *Fusion Sci. Technol.*, 67 (2): 245–249. https://doi.org/10.13182/FST14-T2.

Atsumi, H., and K. Tauchi. 2003. "Hydrogen absorption and transport in graphite materials." *J. Alloys Compd.*, 705–709.

Atsumi, H., S. Tokura, and M. Miyake. 1988. "Absorption and desorption of deuterium on graphite at elevated temperatures." *J. Nucl. Mater.*, 155–157 (PART 1): 241–245. https://doi.org/10.1016/0022-3115(88)90247-4.

Awasthi, A., Y. J. Bhatt, and S. P. Garg. 1996. "Measurement of contact angle in systems involving liquid metals." *Meas. Sci. Technol.*, 7 (5): 753. https://doi.org/10.1088/0957-0233/7/5/005.

Baes, C. F. 1974. "The chemistry and thermodynamics of molten salt reactor fuels." *J. Nucl. Mater.*, 51 (1): 149–162. https://doi.org/10.1016/0022-3115(74)90124-X.

Baker, D. J., and J. B. Morris. 1971. "Structural damage in graphite occurring during pore size measurements by high pressure mercury." *Carbon*, 9 (5): 687–690. https://doi.org/10.1016/0008-6223(71)90092-3.

Barber, M., E. L. Evans, and J. M. Thomas. 1973. "Oxygen chemisorption on the basal faces of graphite: an XPS study." *Chem. Phys. Lett.*, 18 (3): 423–425. https://doi.org/10.1016/0009-2614(73)80208-8.

Barinov, A., O. B. Malcioğlu, S. Fabris, T. Sun, L. Gregoratti, M. Dalmiglio, and M. Kiskinova. 2009. "Initial Stages of Oxidation on Graphitic Surfaces: Photoemission Study and Density Functional Theory Calculations." *J. Phys. Chem. C*, 113 (21): 9009–9013.https://doi.org/10.1021/jp902051d.

Baskes, M. I. 1980. "A calculation of the surface recombination rate constant for hydrogen isotopes on metals." *J. Nucl. Mater.*, 92 (2–3): 318–324. https://doi.org/10.1016/0022-3115(80)90117-8.

Bateman, H. 1910. "The solution of a system of differential equation soccuring in the theory of radio-active transformations." *Proc. Camb. Philos. Soc. Math. Phys. Sci.*, 11 (February): 423–427.

Beamson, G., and D. Briggs. 1992. *High resolution XPS of organic polymers: The Scienta ESCA 300 database*. *John Wiley Sons*.

Bernal, J. D. 1924. "The structure of graphite." *Proc. R. Soc. Lond. Ser. Contain. Pap. Math. Phys. Character*, 106 (740): 749–773. https://doi.org/10.1098/rspa.1924.0101.

Berthier, Y., L. Vincent, and M. Godet. 1989. "Fretting fatigue and fretting wear." *Tribol. Int.*, 22 (4): 235–242. https://doi.org/10.1016/0301-679X(89)90081-9.

Biederman, D. L., A. J. Miles, F. J. Vastola, and P. L. Walker. 1976. "Carbon-carbon dioxide reaction: Kinetics at low pressures and hydrogen inhibition." *Carbon*, 14 (6): 351–356. https://doi.org/10.1016/0008-6223(76)90009-9.

Blau, P. J., and R. L. Martin. 1994. "Friction and wear of carbon-graphite materials against metal and ceramic counterfaces." *Tribol. Int.*, 27 (6): 413–422. https://doi.org/10.1016/0301-679X(94)90018-3.

Blume, R., D. Rosenthal, J. P. Tessonnier, H. Li, A. Knop-Gericke, and R. Schlögl. 2015. "Characterizing Graphitic Carbon with X-ray Photoelectron Spectroscopy: A Step-by-Step Approach." *ChemCatChem*, 7 (18): 2871–2881. https://doi.org/10.1002/cctc.201500344.

Blyth, R. I. R., H. Buqa, F. P. Netzer, M. G. Ramsey, J. O. Besenhard, P. Golob, and M. Winter. 2000. "XPS studies of graphite electrode materials for lithium ion batteries." *Appl. Surf. Sci.*, 167 (1): 99–106. https://doi.org/10.1016/S0169-4332(00)00525-0.

Bocci, B., Z. Hartwig, S. Segantin, R. Testoni, D. Whyte, and M. Zucchetti. 2020. "ARC reactor materials: Activation analysis and optimization." *Fusion Eng. Des.*, 154: 111539. https://doi.org/10.1016/j.fusengdes.2020.111539.

Bonal, J.-P., A. Kohyama, J. van der Laan, and L. L. Snead. 2009. "Graphite, Ceramics, and Ceramic Composites for High-Temperature Nuclear Power Systems." *MRS Bull.*, 34 (1): 28–34. https://doi.org/10.1557/mrs2009.9.

Bonfanti, M., R. Martinazzo, G. F. Tantardini, and A. Ponti. 2007. "Physisorption and diffusion of hydrogen atoms on graphite from correlated calculations on the H-coronene model system." *J. Phys. Chem. C*, 111 (16): 5825–5829. https://doi.org/10.1021/jp070616b.

Bowden, F. P., D. Tabor, and F. Palmer. 1951. "The Friction and Lubrication of Solids." *Am. J. Phys.*, 19 (7): 428–429. https://doi.org/10.1119/1.1933017.

Bowden, F., and J. Young. 1951. "Friction of diamond, graphite, and carbon and the influence of surface films." *Proc. R. Soc. Lond. Ser. Math. Phys. Sci.*, 208 (1095): 444–455. https://doi.org/10.1098/rspa.1951.0173.

Brennan, R. O. 1952. "The interlayer binding in graphite." *J. Chem. Phys.*, 20 (1): 40–48. https://doi.org/10.1063/1.1700193.

Brice, D. K., B. L. Doyle, and W. R. Wampler. 1982. "Extended local mixing model for hydrogen retention and isotope exchange." *J. Nucl. Mater.*, 111–112 (C): 598–605. https://doi.org/10.1016/0022-3115(82)90273-2.

Briggs, R. B. 1964. *Molten Salt Reactor Program Semi-annual Progress Report for Period Ending July 31,1964*. ORNL-TM 3812, Oak Ridge, TN (United Staes).

Briggs, R. B., W. H. Cook, and A. Taboada. 1963. *Modifications to Specifications for MSRE Graphite*. CF-63-2-18. Oak Ridge, TN (United States).

Bueno, H. 2005. "The critical surface tension of 316L stainless steel." M.S. Thesis. San Jose State University.

Burchell, T., R. Bratton, and W. Windes. 2007. *NGNP Graphite Selection and Acquisition Strategy*. ORNL-TM-2007/153. Oak Ridge, TN (United States).

Burchell, T. D. 1997. "Radiation effects in graphite and carbon-based materials." *MRS Bull.*, 22 (4): 29–35. https://doi.org/10.1557/S0883769400033005.

Burchell, T. D., and L. L. Snead. 2007. "The effect of neutron irradiation damage on the properties of grade NBG-10 graphite." *J. Nucl. Mater.*, 371 (1–3): 18–27. https://doi.org/10.1016/j.jnucmat.2007.05.021.

von Buttlar, H., and W. F. Libby. 1955. "Natural distribution of cosmic-ray produced tritium. II." *J. Inorg. Nucl. Chem.*, 1 (1–2): 75–91.. https://doi.org/10.1016/0022-1902(55)80070-X.

Calderoni, P., and C. Cabet. 2012. "Corrosion issues in molten salt reactor (MSR) systems." *Nucl. Corros. Sci. Eng.*, 842–865.

Calderoni, P., P. Sharpe, M. Hara, and Y. Oya. 2008. "Measurement of tritium permeation in flibe (2LiF-BeF2)." *Fusion Eng. Des.*, 83 (7–9): 1331–1334. https://doi.org/10.1016/j.fusengdes.2008.05.016.

Campbell, A. A., Y. Katoh, M. A. Snead, and K. Takizawa. 2016. "Property changes of G347A graphite due to neutron irradiation." *Carbon*, 109: 860–873. https://doi.org/10.1016/j.carbon.2016.08.042.

Cançado, L. G., K. Takai, T. Enoki, M. Endo, Y. A. Kim, H. Mizusaki, N. L. Speziali, A. Jorio, and M. A. Pimenta. 2008. "Measuring the degree of stacking order in graphite by Raman spectroscopy." *Carbon*, 46 (2): 272–275. https://doi.org/10.1016/j.carbon.2007.11.015.

Carotti, F., B. Goh, M. Shafer, and R. O. Scarlat. 2018. "Datasets for elemental composition of 2LiF-BeF2 (FLiBe) salt purified by hydro-fluorination, analyzed by inductively coupled plasma mass spectrometry (ICP-MS) using two digestion methods." *Data Brief*, 21: 1612–1617. https://doi.org/10.1016/j.dib.2018.09.053.

Carotti, F., E. Liu, D. D. Macdonald, and R. O. Scarlat. 2021. "An electrochemical study of hydrogen in molten 2LiF-BeF2 (FLiBe) with addition of LiH." *Electrochimica Acta*, 2 (367): 137114. https://doi.org/10.1016/j.electacta.2020.137114.

Carotti, F., H. Wu, and R. O. Scarlat. 2019. *Characterization of Tritium Transport in Molten 2LiF-BeF 2 Salt and Graphite by Electrochemistry Techniques*. Transactions of the American Nuclear Society.

Causey, R. A. 1989. "The interaction of tritium with graphite and its impact on tokamak operations." *J. Nucl. Mater.*, 162–164 (C): 151–161. https://doi.org/10.1016/0022-3115(89)90265-1.

Causey, R. A., M. I. Baskes, and K. L. Wilson. 1986. "The retention of deuterium and tritium in POCO AXF-5Q graphite." *J. Vac. Sci. Technol. Vac. Surf. Films*, 4 (3): 1189–1192. https://doi.org/10.1116/1.573392.

Causey, R. A., T. S. Elleman, and K. Verghese. 1979. "Hydrogen diffusion and solubility in pyrolytic carbon." *Carbon*, 17 (4): 323–328. https://doi.org/10.1016/0008-6223(79)90003-4.

Causey, R. A., R. A. Karnesky, and C. San Marchi. 2012. "Tritium barriers and tritium diffusion in fusion reactors." *Compr. Nucl. Mater.*, 511–549.

C.D. Wagner, W.M. Riggs, L.E. Davis, J.F. Moulder, G. E. M. 1995. "Handbook of X Ray Photoelectron Spectroscopy_ A Reference Book of Standard Spectra data for use in X-ray Photoelectron spectroscopy." *Perkin-Elmer Corp.*

Challen, J. M., P. L. B. Oxley, and B. S. Hockenhull. 1986. "Prediction of Archard's wear coefficient for metallic sliding friction assuming a low cycle fatigue wear mechanism." *Wear*, 111 (3): 275–288. https://doi.org/10.1016/0043-1648(86)90188-2.

Chau, T. T., W. J. Bruckard, P. T. L. Koh, and A. V. Nguyen. 2009. "A review of factors that affect contact angle and implications for flotation practice." *Adv. Colloid Interface Sci.*, 150 (2): 106–115. https://doi.org/10.1016/j.cis.2009.07.003.

Chi, S. H., and G. C. Kim. 2008. "Comparison of the oxidation rate and degree of graphitization of selected IG and NBG nuclear graphite grades." *J. Nucl. Mater.*, 381 (1–2): 9–14. https://doi.org/10.1016/j.jnucmat.2008.07.027.

Chimezie, U., and A. Srinivas Gurram. 2016. "Wetting properties of stainless steel surfaces." Ph.D. Thesis. Hogskolan i Halmstad

Chingas, G. C., J. Milliken, H. A. Resing, and T. Tsang. 1985. "Graphite-AsF5 intercalation kinetics and diffusion by NMR imaging." *Synth. Met.*, Proceedings of The International Symposium on Graphite Intercalation Compounds, 12 (1): 131–136. https://doi.org/10.1016/0379-6779(85)90099-2.

Choi, W. K., B. J. Kim, E. S. Kim, S. H. Chi, and S. J. Park. 2011. "Oxidation behavior of IG and NBG nuclear graphites." *Nucl. Eng. Des.*, 241 (1): 82–87. https://doi.org/10.1016/j.nucengdes.2010.10.007.

Cisneros, A. 2013. "Pebble Bed Reactors Design Optimization Methods and their Application to the Pebble Bed Fluoride Salt Cooled High Temperature Reactor." Ph.D. Thesis. UC Berkeley.

Clark, D. T., W. J. Feast, D. Kilcast, and W. K. R. Musgrave. 1973. "Applications Of Esca To Polymer Chemistry - 3. Structures And Bonding In Homopolymers Of Ethylene And The Fluoroethylenes And Determination Of The Compositions Of Fluoro Copolymers." *J Polym Sci Part -1 Polym Chem*, 11 (2): 389–411., Ltd. https://doi.org/10.1002/pol.1973.170110207.

Clark, W. T., and J. K. Lancaster. 1963. "Breakdown and surface fatigue of carbons during repeated sliding." *Wear*, 6 (6): 467–482. https://doi.org/10.1016/0043-1648(63)90282-5.

Compagnini, G., O. Puglisi, and G. Foti. 1997. "Raman spectra of virgin and damaged graphite edge planes." *Carbon*, 35 (12): 1793–1797. https://doi.org/10.1016/S0008-6223(97)00141-3.

Compere, E., S. Freid, and C. Nestor. 1974. *Distribution and release of tritium in high-temperature gas-cooled reactors as a function of design, operational, and material parameters, ORNL-TM-4303*, Oak Ridge, TN (United States)

Compere, E., S. Kirslis, E. Bohlmann, and F. Blankenship. 1975. *Fission Product Behavior in the Molten Salt Reactor Experiment.* ORNL-4865. Oak Ridge, TN (United States)

Contescu, C. I., J. D. Arregui-Mena, A. A. Campbell, P. D. Edmondson, N. C. Gallego, K. Takizawa, and Y. Katoh. 2019. "Development of mesopores in superfine grain graphite neutron-irradiated at high fluence." *Carbon*, 141: 663–675. https://doi.org/10.1016/j.carbon.2018.08.039.

Contescu, C. I., S. Azad, D. Miller, M. J. Lance, F. S. Baker, and T. D. Burchell. 2008. "Practical aspects for characterizing air oxidation of graphite." *J. Nucl. Mater.*, 381 (1–2): 15–24. https://doi.org/10.1016/j.jnucmat.2008.07.020.

Contescu, C. I., T. Guldan, P. Wang, and T. D. Burchell. 2012. "The effect of microstructure on air oxidation resistance of nuclear graphite." *Carbon*, 50 (9): 3354–3366. https://doi.org/10.1016/j.carbon.2012.01.040.

Contescu, C. I., and R. W. Mee. 2016. *Status of Chronic Oxidation Studies of Graphite*. ORNL/TM-2016/195. Oak Ridge, TN (United States).

Contescu, C. I., R. W. Mee, J. Lee, J. D. Arregui-Mena, N. C. Gallego, T. D. Burchell, J. J. Kane, and W. E. Windes. 2018. "Beyond the classical kinetic model for chronic graphite oxidation by moisture in high temperature gas-cooled reactors." *Carbon*, 127: 158–169. https://doi.org/10.1016/j.carbon.2017.11.001.

Contescu, C. I., R. W. Mee, P. Wang, A. V. Romanova, and T. D. Burchell. 2014. "Oxidation of PCEA nuclear graphite by low water concentrations in helium." *J. Nucl. Mater.*, 453 (1–3): 225–232. https://doi.org/10.1016/j.jnucmat.2014.07.009.

Costanzo, F., P. L. Silvestrelli, and F. Ancilotto. 2012. "Physisorption, diffusion, and chemisorption pathways of H 2 molecule on graphene and on (2,2) carbon nanotube by first principles calculations." *J. Chem. Theory Comput.*, 8 (4): 1288–1294. https://doi.org/10.1021/ct300143a.

Crank, J. 1975. *The Mathematics of Diffusion*. Oxford: Clarendon Press.

Crassous, I., H. Groult, F. Lantelme, D. Devilliers, A. Tressaud, C. Labrug??re, M. Dubois, C. Belhomme, A. Colisson, and B. Morel. 2009. "Study of the fluorination of carbon anode in molten KF-2HF by XPS and NMR investigations." *J. Fluor. Chem.*, 130 (12): 1080–1085. https://doi.org/10.1016/j.jfluchem.2009.07.022.

Cui, Z., N. Khosla, T. Lai, J. Narayan, and A. Manthiram. 2023. "Laser-Assisted Surface Lithium Fluoride Decoration of a Cobalt-Free High-Voltage Spinel LiNi0.5Mn1.5O4 Cathode for Long-Life Lithium-Ion Batteries." *ACS Appl. Mater. Interfaces*, 15 (1): 1247–1255. https://doi.org/10.1021/acsami.2c18918.

Darapaneni, P., A. U. Mane, Z. D. Hood, and J. W. Elam. 2022. "Removal of Surface Carbonate from Lithium-Ion Battery Cathode Materials via Vapor-Phase Fluorination." *ACS Appl. Energy Mater.*, 5 (8): 9870–9876.. https://doi.org/10.1021/acsaem.2c01205.

Darvish Ganji, M., S. M. Hosseini-Khah, and Z. Amini-Tabar. 2015. "Theoretical insight into hydrogen adsorption onto graphene: A first-principles B3LYP-D3 study." *Phys. Chem. Chem. Phys.*, 17 (4): 2504–2511. https://doi.org/10.1039/c4cp04399e.

Deacon, R., and J. Goodman. 1958. "Lubrication by lamellar solids." *Proc. R. Soc. Lond. Ser. Math. Phys. Sci.*, 243 (1235): 464–482. https://doi.org/10.1098/rspa.1958.0013.

Delmore, A. R., W. Derdeyn, R. Gakhar, and M. Raluca O. Scarlat (Univ. Wisconsin. 2018. "Wetting of Graphite by Molten Fluoride Salts: Initial Experiments." *Transactions*, 118 (1): 121–124. American Nuclear Society.

Deng, K., M. Zhang, X. Wu, Q. Zhang, G. Yang, Z. Ma, F. Wei, G. Wang, and W. Liu. 2019. "Adsorption and Desorption of Tritium in Nuclear Graphite at 700°C: A Gas Chromatographic Study Using Hydrogen." *Nucl. Technol.*. https://doi.org/10.1080/00295450.2019.1590076.

DeVan, J. H., J. R. DiStefano, W. P. Eatherly, J. R. Keiser, and R. L. Klueh. 1995. "Materials considerations for molten salt accelerator-based plutonium conversion systems." *AIP Conf. Proc.*, 476–487..

Díaz, J., G. Paolicelli, S. Ferrer, and F. Comin. 1996. "Separation of the sp3 and sp2 components in the C1s photoemission spectra of amorphous carbon films." *Phys. Rev. B*, 54 (11): 8064–8069. https://doi.org/10.1103/PhysRevB.54.8064.

Dickinson, J. M., and J. W. Shore. 1968. "Observations concerning the determination of porosities in graphites." *Carbon*, 6 (6): 937–941. https://doi.org/10.1016/0008-6223(68)90077-8.

Diño, W. A., Y. Miura, H. Nakanishi, H. Kasai, T. Sugimoto, and T. Kondo. 2004. "H2 dissociative adsorption at the armchair edges of graphite." *Solid State Commun.*, 132 (10): 713–718. https://doi.org/10.1016/j.ssc.2004.08.043.

Dolan, K., S. Huang, M. Hackett, and L. W. Hu. 2021a. "Modeling Tritium Retention in Graphite for Fluoride-Salt-Cooled High-Temperature Reactors." *Nucl. Technol.*, 207 (10): 1578–1598. https://doi.org/10.1080/00295450.2020.1829428.

Dolan, K. P. 2020. "Tritium Retention in Nuclear Graphite, System-Level Transport, and Management Strategies for the Fluoride-Salt-Cooled High-Temperature Reactor." PhD Thesis. Massachusetts Institute of Technology.

Dolan, K., G. Zheng, D. Carpenter, S. Huang, and L. W. Hu. 2020. "Tritium Content and Chemical Form in Nuclear Graphite from Molten Fluoride Salt Irradiations." *Fusion Sci. Technol.*, 76 (4): 398–403. https://doi.org/10.1080/15361055.2020.1712993.

Dolan, K., G. Zheng, K. Sun, D. Carpenter, and L. wen Hu. 2021b. "Tritium generation, release, and retention from in-core fluoride salt irradiations." *Prog. Nucl. Energy*, 131: 103576. https://doi.org/10.1016/j.pnucene.2020.103576.

Drelich, J. 1997. "The Effect of Drop (Bubble) Size on Contact Angle at Solid Surfaces." *J. Adhes.*, 63 (1–3): 31–51. https://doi.org/10.1080/00218469708015212.

Drelich, J., J. D. Miller, and R. J. Good. 1996. "The Effect of Drop (Bubble) Size on Advancing and Receding Contact Angles for Heterogeneous and Rough Solid Surfaces as Observed with Sessile-Drop and Captive-Bubble Techniques." *J. Colloid Interface Sci.*, 179 (1): 37–50. https://doi.org/10.1006/jcis.1996.0186.

Drelich, J., J. D. Miller, and J. Hupka. 1993. "The Effect of Drop Size on Contact Angle over a Wide Range of Drop Volumes." *J. Colloid Interface Sci.*, 155 (2): 379–385. https://doi.org/10.1006/jcis.1993.1050.

Dunks, G. B., D. Stelman, and S. J. Yosim. 1980. "Graphite oxidation in molten sodium carbonate." *Carbon*, 18 (5): 365–370. https://doi.org/10.1016/0008-6223(80)90008-1.

Dunks, G. B., D. Stelman, and S. J. Yosim. 1982. "Graphite Oxidation in Sodium Carbonate/Sodium Sulfate Melts." *Inorg. Chem.*, 21 (1): 108–114. https://doi.org/10.1021/ic00131a021.

Ebnesajjad, S. 2011. "Surface tension and its measurement." *Handb. Adhes. Surf. Prep.*, 21–30. William Andrew Publishing.

Edao, Y., S. Fukada, H. Noguchi, and A. Sagara. 2009. "Tritium release from neutron-irradiated fube purged out by Ar-H2 or Ar at controlled temperature." *Fusion Sci. Technol.*, 55 (2): 140–151. https://doi.org/10.13182/FST09-A4067.

Engineering ToolBox. 2003. "Solids, Liquids and Gases - Thermal Conductivities." https://www.engineeringtoolbox.com/thermal-conductivity-d_429.html.

Eustathopoulos, N., N. Sobczak, A. Passerone, and K. Nogi. 2005. "Measurement of contact angle and work of adhesion at high temperature." *J. Mater. Sci.*, 2271–2280.

Ezell, N. D. B., S. S. Raiman, J. M. Kurley, and J. McDuffee. 2020. "Neutron irradiation of alloy N and 316L stainless steel in contact with a molten chloride salt." *Nucl. Eng. Technol.*, 53, 3. https://doi.org/10.1016/j.net.2020.07.042.

Fast, J. 1960. "Entropie: die Bedeutung des Entropiebegriffes und seine Anwendung in Wissenschaft und Technik." Technische Bibliothek

Ferrari, A., and J. Robertson. 2000. "Interpretation of Raman spectra of disordered and amorphous carbon." *Phys. Rev. B*, 61 (20): 14095. https://doi.org/10.1103/PhysRevB.61.14095.

Ferro, Y., A. Allouche, and C. Linsmeier. 2013. "Absorption and diffusion of beryllium in graphite, beryllium carbide formation investigated by density functional theory." *J. Appl. Phys.*, 113 (21): 213514. https://doi.org/10.1063/1.4809552.

Ferullo, R. M., N. F. Domancich, and N. J. Castellani. 2010. "On the performance of van der Waals corrected-density functional theory in describing the atomic hydrogen physisorption on

graphite." *Chem. Phys. Lett.*, 500 (4–6): 283–286. https://doi.org/10.1016/j.cplett.2010.10.027.

Fieberg, C., and R. Kneer. 2008. "Determination of thermal contact resistance from transient temperature measurements." *Int. J. Heat Mass Transf.*, 51 (5–6): 1017–1023. https://doi.org/10.1016/j.ijheatmasstransfer.2007.05.004.

Field, P. E., and J. H. Shaffer. 1967. "The solubilities of hydrogen fluoride and deuterium fluoride in molten fluorides." *J. Phys. Chem.*, 71 (10): 3218–3222. https://doi.org/10.1021/j100869a013.

Fierro, V., A. Szczurek, C. Zlotea, J. F. Marêché, M. T. Izquierdo, A. Albiniak, M. Latroche, G. Furdin, and A. Celzard. 2010. "Experimental evidence of an upper limit for hydrogen storage at 77 K on activated carbons." *Carbon*, 48 (7): 1902–1911. https://doi.org/10.1016/j.carbon.2010.01.052.

Forsberg, C., and P. F. Peterson. 2015. "Spent nuclear fuel and graphite management for salt-cooled reactors: Storage, safeguards, and repository disposal." *Nucl. Technol.*, 191 (2): 113–121. https://doi.org/10.13182/NT14-88.

Forsberg, C. W., D. M. Carpenter, D. G. Whyte, R. Scarlat, and L. Wei. 2017a. "Tritium control and capture in salt-cooled fission and fusion reactors." *Fusion Sci. Technol.*, 71 (4): 584–589. https://doi.org/10.1080/15361055.2017.1289450.

Forsberg, C. W., S. Lam, D. M. Carpenter, D. G. Whyte, R. Scarlat, C. Contescu, L. Wei, J. Stempien, and E. Blandford. 2017b. "Tritium control and capture in salt-cooled fission and fusion reactors: Status, challenges, and path forward." *Nucl. Technol.*, 197 (2): 119–139. https://doi.org/10.13182/NT16-101.

Forsberg, C. W., P. F. Peterson, and P. S. Pickard. 2003. "Molten-salt-cooled advanced high-temperature reactor for production of hydrogen and electricity." *Nucl. Technol.*, 144 (3): 289–302. https://doi.org/10.13182/NT03-1.

Forsberg, C. W., P. F. Peterson, K. Sridharan, L. Hu, M. Fratoni, and A. K. Prinja. 2018. *Integrated FHR technology development: Tritium management, materials testing, salt chemistry control, thermal hydraulics and neutronics, associated benchmarking and commercial basis*. Idaho Falls, ID (United States).

Forsberg, C., G. Zheng, R. G. Ballinger, and S. T. Lam. 2020. "Fusion Blankets and Fluoride-Salt-Cooled High-Temperature Reactors with Flibe Salt Coolant: Common Challenges, Tritium Control, and Opportunities for Synergistic Development Strategies Between Fission, Fusion, and Solar Salt Technologies." *Nucl. Technol.*, 206 (11): 1778–1801. https://doi.org/10.1080/00295450.2019.1691400.

Fratoni, M., and E. Greenspan. 2011. "Neutronic Feasibility Assessment of Liquid Salt-Cooled Pebble Bed Reactors." *Nucl. Sci. Eng.*, 168 (1): 1–22.. https://doi.org/10.13182/NSE10-38.

Gainey, B. W. 1976. *A Review of Tritium Behavior in HTGR Systems, GA-A13461*. San Diego, CA (United States)

Gallagher, R. C., C. Agca, N. Russell, J. W. McMurray, and N. D. Bull Ezell. 2022. "Assessment of Molten Eutectic LiF-NaF-KF Density through Experimental Determination and Semiempirical Modeling." *J. Chem. Eng. Data*, 67 (6): 1406–1414. https://doi.org/10.1021/acs.jced.2c00081.

Gallego, N. C., J. D. Arregui-Mena, and C. I. Contescu. 2021a. "Probing basal planes and edge sites in polygranular nuclear graphite by gas adsorption: Estimation of active surface area." *Carbon*, 179: 633–645. https://doi.org/10.1016/J.CARBON.2021.04.044.

Gallego, N. C., C. I. Contescu, and J. Keiser. 2020. *Progress Report on Graphite-Salt Intrusion Studies*. ORNL/TM-2020/1621, Oak Ridge, TN (United States).

Gallego, N. C., C. I. Contescu, J. R. Keiser, J. Qu, X. He, and K. Myhre. 2021b. *Progress Report on Graphite-Salt Interaction Studies (FY21)*. ORNL/TM-2021/2247, Oak Ridge, TN (United States).

Ghasemi, H., and C. A. Ward. 2010. "Sessile-Water-Droplet Contact Angle Dependence on Adsorption at the Solid−Liquid Interface." *J. Phys. Chem. C*, 114 (11): 5088–5100. https://doi.org/10.1021/jp911259n.

Gong, L., Y. Wang, X. Cheng, R. Zhang, and H. Zhang. 2014. "A novel effective medium theory for modelling the thermal conductivity of porous materials." *Int. J. Heat Mass Transf.*, 68: 295–298. https://doi.org/10.1016/j.ijheatmasstransfer.2013.09.043.

Good, R. J., and M. N. Koo. 1979. "The effect of drop size on contact angle." *J. Colloid Interface Sci.*, 71 (2): 283–292. https://doi.org/10.1016/0021-9797(79)90239-X.

Gorman, D., and K. Y. Wong. 1979. "Environmental aspects of tritium from CANDU station releases." *Int. Symp. Behav. Tritium Environ.*, 622–623.

Greenwood, J. A., and J. H. Tripp. 1970. "The Contact of Two Nominally Flat Rough Surfaces." *Proc. Inst. Mech. Eng.*, 185 (1): 625–633. https://doi.org/10.1243/PIME_PROC_1970_185_069_02.

Grimes, W. R. 1964. *Reactor Chemistry Division Annual Progress Report for Period Ending January 31, 1964*. ORNL-3591. Oak Ridge, TN (United States)

Guobin, Z., and T. Konishi. 2014. "Relationship between the Toyo Tanso Group and HTR-PM." *HTR-2014*. Weihai (China).

Gupta, V., T. Nakajima, Y. Ohzawa, and B. Žemva. 2003. "A study on the formation mechanism of graphite fluorides by Raman spectroscopy." *J. Fluor. Chem.*, 120 (2): 143–150. https://doi.org/10.1016/S0022-1139(02)00323-8.

Haag, G., D. Mindermann, G. Wilhelmi, H. Persicke, and W. Ulsamer. 1990. "Development of reactor graphite." *J. Nucl. Mater.*, 171 (1): 41–48. https://doi.org/10.1016/0022-3115(90)90345-N.

Hacker, P. J., G. B. Neighbour, and B. McEnaney. 2000. "Coefficient of thermal expansion of nuclear graphite with increasing thermal oxidation." *J. Phys. Appl. Phys.*, 33 (8): 991–998. https://doi.org/10.1088/0022-3727/33/8/316.

Hamrock, B. J., and D. Dowson. 1981. "Ball bearing lubrication: The elastohydrodynamics of elliptical contacts." Wiley.

Hamwi, A., M. Daoud, and J. C. Cousseins. 1988. "Graphite fluorides prepared at room temperature 1. Synthesis and characterization." *Synth. Met.*, 26 (1): 89–98. https://doi.org/10.1016/0379-6779(88)90338-4.

Hara, M., Y. Hatano, M. F. Simpson, G. R. Smolik, J. P. Sharp, Y. Oya, K. Okuno, M. Nishikawa, T. Terai, S. Tanaka, R. A. Anderl, D. A. Petti, and D. K. Sze. 2006. "Interactions between molten Flibe and metallic Be." *Fusion Eng. Des.*, 561–566.

Haubenreich, P. N. 1971. *A Review of Production and Observed Distribution of Tritium in the MSRE in Light of Recent Findings*.

Haubenreich, P. N., and J. R. Engel. 1970. "Experience with the Molten-Salt Reactor Experiment." *Nucl. Appl. Technol.*, 8 (2): 118–136. https://doi.org/10.13182/NT8-2-118. CF-71-8-34. Oak Ridge, TN (United States)

Haverkamp, R. G. 2012. "An XPS study of the fluorination of carbon anodes in molten NaF–AlF3–CaF2." *J. Mater. Sci.*, 47 (3): 1262–1267. https://doi.org/10.1007/s10853-011-5772-5.

H.D. Rohrig, P. G. Fischer, and R. Hecker. 1975. "Tritium Balance in High-Temperature Gas-Cooled Reactors." *J. Am. Ceram. Soc.*, 59 (7): 316–320.

He, X., C. Kumara, D. Sulejmanovic, J. R. Keiser, N. Gallego, and J. Qu. 2023. "Tribocorrosion of stainless steel sliding against graphite in FLiNaK molten salt." *Wear*, 204706. https://doi.org/10.1016/J.WEAR.2023.204706.

He, X., J. Song, J. Tan, B. Zhang, H. Xia, Z. He, X. Zhou, M. Zhao, X. Liu, L. Xu, and S. Bai. 2014a. "SiC coating: An alternative for the protection of nuclear graphite from liquid fluoride salt." *J. Nucl. Mater.*, 448 (1–3): 1–3. https://doi.org/10.1016/j.jnucmat.2014.01.034.

He, X., J. Song, L. Xu, J. Tan, H. Xia, B. Zhang, Z. He, L. Gao, X. Zhou, M. Zhao, Z. Zhu, and S. Bai. 2013. "Protection of nuclear graphite toward liquid fluoride salt by isotropic pyrolytic carbon coating." *J. Nucl. Mater.* 442 (1-3): 306-308. https://doi.org/10.1016/j.jnucmat.2013.09.015

He, Z., L. Gao, W. Qi, B. Zhang, X. Wang, J. Song, X. He, C. Zhang, H. Tang, R. Holmes, H. Xia, and X. Zhou. 2015a. "Molten FLiNaK salt infiltration into degassed nuclear graphite under inert gas pressure." *Carbon*, 84: 511–518. https://doi.org/10.1016/j.carbon.2014.12.044.

He, Z., L. Gao, X. Wang, B. Zhang, W. Qi, J. Song, X. He, C. Zhang, H. Tang, H. Xia, and X. Zhou. 2014b. "Improvement of stacking order in graphite by molten fluoride salt infiltration." *Carbon*, 72: 304–311. https://doi.org/10.1016/j.carbon.2014.02.010.

He, Z., P. Lian, Y. Song, Z. Liu, J. Song, J. Zhang, X. Ren, J. Feng, X. Yan, Q. Guo, and W. Liu. 2018. "Protecting nuclear graphite from liquid fluoride salt and oxidation by SiC coating derived from polycarbosilane." *J. Eur. Ceram. Soc.*, 38 (2): 453–462. https://doi.org/10.1016/j.jeurceramsoc.2017.09.031.

Hertz, H. 1899. *The principles of mechanics presented in a new form*. Macmillan. London (United Kingdom)

Hirohata, Y., M. Okita, T. Hino, and T. Yamashina. 1994. "Desorption behavior for H2O from isotropic graphite dipped in water." *Carbon*, 32 (2): 369–372. https://doi.org/10.1016/0008-6223(94)90208-9.

Hiruta, M., G. Johnson, M. Rostamian, G. P. Potirniche, A. M. Ougouag, M. Bertino, L. Franzel, and A. Tokuhiro. 2013. "Computational and experimental prediction of dust production in pebble bed reactors, Part II." *Nucl. Eng. Des.*, 263: 509–514. https://doi.org/10.1016/j.nucengdes.2013.04.032.

Hoinkis, E. 1988. "The volume of small micropores in unmodified, oxidized or irradiated graphitic matrix." *Stud. Surf. Sci. Catal.*, 193–202. https://doi.org/10.1016/S0167-2991(09)60743-6

Hoinkis, E. 1991a. "The chemisorption of hydrogen on porous graphites at low pressure and at elevated temperature." *J. Nucl. Mater.*, 182 (C): 93–106. https://doi.org/10.1016/0022-3115(91)90418-7.

Hoinkis, E. 1991b. "Thermodesorption of deuterium from a porous graphitic carbon." *J. Nucl. Mater.*, 183 (1–2): 9–18. https://doi.org/10.1016/0022-3115(91)90465-J.

Hoinkis, E., W. P. Eatherly, P. Krautwasser, and E. Robens. 1986. "Corrosion- and irradiation-induced porosity changes of a nuclear graphitic material." *J. Nucl. Mater.*, 141–143 (PART 1): 87–95. https://doi.org/10.1016/S0022-3115(86)80015-0.

Hong, R., S. Huber, K. Lee, P. Purcell, S. Margossian, and J. Seelig. 2009. *Reactor Safety and Mechanical Design for the Annular Pebble-Bed Advanced High Temperature Reactor*. Senior Design Project. UC Berkeley.

Huang, Q., and H. Tang. 2018. "Great structural stability of irradiated graphite after testing in molten Li2BeF4 salt." *Nucl. Instrum. Methods Phys. Res. Sect. B Beam Interact. Mater. At.*, 436: 40–44. https://doi.org/10.1016/j.nimb.2018.08.049.

Huang, Q., H. Tang, Y. Liu, X. H. Long, P. Liu, X. L. Wang, Q. T. Lei, Q. Deng, and Y. Q. Wang. 2019. "Pore structure evolution of IG-110 graphite during argon ion irradiation at 600 °C." *J. Mater. Sci.*, 54 (8): 6098–6110. https://doi.org/10.1007/s10853-019-03329-7.

Hueso, J. L., J. P. Espinós, A. Caballero, J. Cotrino, and A. R. González-Elipe. 2007. "XPS investigation of the reaction of carbon with NO, O2, N2 and H2O plasmas." *Carbon*, 45 (1): 89–96. https://doi.org/10.1016/J.CARBON.2006.07.021.

Hutzler, S., J. C. F. Ryan-Purcell, F. F. Dunne, and D. Weaire. 2018. "A simple formula for the estimation of surface tension from two length measurements for a sessile or pendant drop." *Philos. Mag. Lett.*, 98 (1): 9–16. https://doi.org/10.1080/09500839.2018.1434320.

Iino, M. 1986. "more generalized analysis of hydrogen trapping." *Perspect Hydrog. Met*, 403–411. https://doi.org/10.1016/b978-0-08-034813-1.50060-7.

Ishiyama, S., T. D. Burchell, J. P. Strizak, and M. Eto. 1996. "The effect of high fluence neutron irradiation on the properties of a fine-grained isotropic nuclear graphite." *J. Nucl. Mater.*, 230 (1): 1–7. https://doi.org/10.1016/0022-3115(96)00005-0.

IUPAC. 1997. *Compendium of Chemical Terminology*. (A. D. McNaught and A. Wilkinson, eds.). Oxford: Blackwell Scientific Publications.

Jackson, S. T., and R. G. Nuzzo. 1995. "Determining hybridization differences for amorphous carbon from the XPS C 1s envelope." *Appl. Surf. Sci.*, 90 (2): 195–203. https://doi.org/10.1016/0169-4332(95)00079-8.

Jeloaica, L., and V. Sidis. 1999. "DFT investigation of the adsorption of atomic hydrogen on a cluster-model graphite surface." *Chem. Phys. Lett.*, 300 (1–2): 157–162. https://doi.org/10.1016/S0009-2614(98)01337-2.

Jolodosky, A., K. Kramer, W. Meier, J. DeMuth, S. Reyes, and M. Fratoni. 2016. "Neutronics and activation analysis of lithium-based ternary alloys in IFE blankets." *Fusion Eng. Des.*, 107: 1–12. https://doi.org/10.1016/j.fusengdes.2016.03.071.

Jones, K. L., G. M. Laudone, and G. P. Matthews. 2018. "A multi-technique experimental and modelling study of the porous structure of IG-110 and IG-430 nuclear graphite." *Carbon*, 128: 1–11. https://doi.org/10.1016/j.carbon.2017.11.076.

Jones, K. L., G. P. Matthews, and G. M. Laudone. 2020. "The effect of irradiation and radiolytic oxidation on the porous space of Gilsocarbon nuclear graphite measured with mercury porosimetry and helium pycnometry." *Carbon*, 158: 256–266. https://doi.org/10.1016/j.carbon.2019.11.084.

Juan-Juan, J., J. P. Marco-Lozar, F. Suárez-García, D. Cazorla-Amorós, and A. Linares-Solano. 2010. "A comparison of hydrogen storage in activated carbons and a metal-organic framework (MOF-5)." *Carbon*, 48 (10): 2906–2909. https://doi.org/10.1016/j.carbon.2010.04.025.

Junk, T., and W. J. Catallo. 1997. "Hydrogen isotope exchange reactions involving C-H (D, T) bonds." *Chem. Soc. Rev.*, 26 (5): 404–406. Royal Society of Chemistry. https://doi.org/10.1039/cs9972600401.

Kairos Power LLC. 2018. *Design Overview for the Kairos Power Fluoride Salt-Cooled, High Temperature Reactor*. Alameda, CA (United States)

Kanashenko, S. L. 1996. "Hydrogen adsorption on and solubility in graphites." *J. Nucl. Mater.*, 233–237 (PART II): 1207–1212. https://doi.org/10.1016/S0022-3115(96)00067-0.

Kane, J. J., C. I. Contescu, R. E. Smith, G. Strydom, and W. E. Windes. 2017. "Understanding the reaction of nuclear graphite with molecular oxygen: Kinetics, transport, and structural evolution." *J. Nucl. Mater.* 493: 343-367. https://doi.org/10.1016/j.jnucmat.2017.06.001

Kasten, P. R. 1969. *Graphite behavior and its effects on msbr performance*. ORNL TM-2136. Oak Ridge, TN (United States).

Kedl, R. J., and C. K. Mcglothlan. 1968. *The primary heat exchanger f o r the Molten-Salt Reactor Experiment*. ORNL TM-2098. Oak Ridge, TN (United States).

Keiser, J. R., J. H. DeVan, and E. J. Lawrence. 1979. "Compatibility of molten salts with type 316 stainless steel and lithium." *J. Nucl. Mater.*, 85–86 (PART 1): 295–298. https://doi.org/10.1016/0022-3115(79)90505-1.

Kelleher, B. 2013. "Purification and Chemical Control of Molten Li 2 BeF 4 Salts for a Fluoride Salt Cooled Reactor." Ph.D. Thesis. UW Madison

Kelleher, B. C., K. P. Dolan, P. Brooks, M. H. Anderson, and K. Sridharan. 2015. "Batch-scale hydrofluorination of 7Li2BeF4 to support molten salt reactor development." *J. Nucl. Eng. Radiat. Sci.*, 1 (4).. https://doi.org/10.1115/1.4030963.

Kelleher, B., G. Zheng, M. Anderson, K. Sridharan, and G. Cao. 2013. "Purification of non uranium bearing fluoride salts for nuclear applications." *Trans. Am. Nucl. Soc.*, 1079–1081.

Kelly, B. 1981. *Physics of graphite*. Applied Science Publisher. London (United Kingdom)

Kemball, C. 1946. "On the surface tension of mercury." *Trans. Faraday Soc.*, 42 (0): 526–537. https://doi.org/10.1039/TF9464200526.

Kim, D., N. M. Pugno, and S. Ryu. 2016. "Wetting theory for small droplets on textured solid surfaces." *Sci. Rep.*, 6 (1): 37813. https://doi.org/10.1038/srep37813.

Kirk, R., D. F. Othmer, D. Grayson, and D. Eckroth. 2007. "Encyclopedia of Chemical Technology, 5th Edition". Wiley

Kissinger, H. E. 1957. "Reaction Kinetics in Differential Thermal Analysis." *Anal. Chem.*, 29 (11): 1702–1706. https://doi.org/10.1021/ac60131a045.

Kolasinski, K. W. 2012. *Surface Science: Foundations of Catalysis and Nanoscience. Surf. Sci. Found. Catal. Nanosci. Third Ed.* Wiley. Hoboken, NJ (United States)

Komvopoulos, K., N. Saka, and N. P. Suh. 1985. "The Mechanism of Friction in Boundary Lubrication." *J. Tribol.*, 107 (4): 452–462. https://doi.org/10.1115/1.3261108.

König, U., and W. Keck. 1983. "Contact Angles Between III–V Melts and Several Substrates." *J. Electrochem. Soc.*, 130 (3): 685. https://doi.org/10.1149/1.2119782.

Krawietz, T. R., and J. F. Haw. 1998. "Characterization of poly(carbon monofluoride) by 19 F and 19 F to 13 C cross polarization MAS NMR spectroscopy." *Chem. Commun.*, 0 (19): 2151–2152. https://doi.org/10.1039/A803252A.

Krishna, R., A. N. Jones, L. McDermott, and B. J. Marsden. 2015. "Neutron irradiation damage of nuclear graphite studied by high-resolution transmission electron microscopy and Raman spectroscopy." *J. Nucl. Mater.*, 467: 557–565. https://doi.org/10.1016/j.jnucmat.2015.10.027.

Kwast, H., H. Werle, M. Glugla, C. H. Wu, and G. Federici. 1994. "The effect of neutron irradiation on the trapping of tritium in carbon-based materials." *J. Nucl. Mater.*, 212–215: 1472–1477. https://doi.org/10.1016/0022-3115(94)91072-3.

Kwast, H., H. Werle, and C. H. Wu. 1996. "Tritium retention in neutron-irradiated carbon-based materials and beryllium." *Phys. Scr. T*, 64: 41–47. https://doi.org/10.1088/0031-8949/1996/t64/006.

Lam, S. T. 2017. "Managing Tritium Inventory and Release with Carbon Materials in a Fluoride Salt-Cooled High-Temperature Reactor." M.S. Thesis. Massachusetts Institute of Technology.

Lam, S. T., R. Ballinger, and C. Forsberg. 2018. "Modeling and predicting total hydrogen adsorption in nanoporous carbon materials for advanced nuclear systems." *J. Nucl. Mater.*, 511: 328–340. https://doi.org/10.1016/j.jnucmat.2018.09.009.

Lancaster, J. K. 1990. "A review of the influence of environmental humidity and water on friction, lubrication and wear." *Tribol. Int.*, 23 (6): 371–389. https://doi.org/10.1016/0301-679X(90)90053-R.

Lancaster, J. K., and J. R. Pritchard. 1981. "The influence of environment and pressure on the transition to dusting wear of graphite." *J. Phys. Appl. Phys.*, 14 (4): 747–762. https://doi.org/10.1088/0022-3727/14/4/027.

Lane, J. A., H. G. MacPherson, and F. Maslan. 1958. *Fluid fuel reactors.* Addison-Wesley Publishing Company. Reading, MA (United States)

Langford, L., N. Winner, A. Hwang, H. Williams, L. Vergari, R. O. Scarlat, and M. Asta. 2022. "Constant-Potential Molecular Dynamics Simulations of Molten Salt Double Layers for FLiBe and FLiNaK." *J. Chem. Phys.*, 157 (9): 094705. https://doi.org/10.1063/5.0097697.

Larciprete, R., S. Gardonio, L. Petaccia, and S. Lizzit. 2009. "Atomic oxygen functionalization of double walled C nanotubes." *Carbon*, 47 (11): 2579–2589. https://doi.org/10.1016/j.carbon.2009.05.008.

Larciprete, R., P. Lacovig, S. Gardonio, A. Baraldi, and S. Lizzit. 2012. "Atomic Oxygen on Graphite: Chemical Characterization and Thermal Reduction." *J. Phys. Chem. C*, 116 (18): 9900–9908. https://doi.org/10.1021/jp2098153.

Lascovich, J. C., R. Giorgi, and S. Scaglione. 1991. "Evaluation of the sp2/sp3 ratio in amorphous carbon structure by XPS and XAES." *Appl. Surf. Sci.*, 47 (1): 17–21. https://doi.org/10.1016/0169-4332(91)90098-5.

Lechner, C., P. Baranek, and H. Vach. 2018. "Adsorption of atomic hydrogen on defect sites of graphite: Influence of surface reconstruction and irradiation damage." *Carbon*, 127: 437–448. https://doi.org/10.1016/j.carbon.2017.09.095.

Lee, J. J., J. D. Arregui-Mena, C. I. Contescu, T. D. Burchell, Y. Katoh, and S. K. Loyalka. 2020. "Protection of graphite from salt and gas permeation in molten salt reactors." *J. Nucl. Mater.*, 534. https://doi.org/10.1016/j.jnucmat.2020.152119.

Lee, J. J., T. K. Ghosh, and S. K. Loyalka. 2014. "Oxidation rate of nuclear-grade graphite IG-110 in the kinetic regime for VHTR air ingress accident scenarios." *J. Nucl. Mater.*, 446 (1–3): 38–48. https://doi.org/10.1016/j.jnucmat.2013.11.032.

Lehtinen, P. O., A. S. Foster, Y. Ma, A. V. Krasheninnikov, and R. M. Nieminen. 2004. "Irradiation-induced magnetism in graphite: A density functional study." *Phys. Rev. Lett.*, 93 (18): 187202. https://doi.org/10.1103/PhysRevLett.93.187202.

Lei, Q., Z. He, W. Qi, H. Tang, J. Zeng, Q. Deng, C. Zhang, N. Guo, H. Zhang, Y. Zhang, H. Shen, and X. Zhou. 2019. "Irradiation-induced mixing of Na and K in graphite in molten salt reactor: An estimation based on ion beam irradiation." *Nucl. Instrum. Methods Phys. Res. Sect. B Beam Interact. Mater. At.*, 450: 100–107. https://doi.org/10.1016/j.nimb.2018.08.018.

Lemmon, E. W., M. L. Huber, and J. W. Leachman. 2008. "Revised standardized equation for hydrogen gas densities for fuel consumption applications." *J. Res. Natl. Inst. Stand. Technol.*, 113 (6): 341–350. National Institute of Standards and Technology. https://doi.org/10.6028/jres.113.028.

Leppänen, J., M. Pusa, T. Viitanen, V. Valtavirta, and T. Kaltiaisenaho. 2015. "The Serpent Monte Carlo code: Status, development and applications in 2013." *Ann. Nucl. Energy*, 82: 142–150. https://doi.org/10.1016/j.anucene.2014.08.024.

Lesiak, B., L. Kövér, J. Tóth, J. Zemek, P. Jiricek, A. Kromka, and N. Rangam. 2018. "C sp 2 /sp 3 hybridisations in carbon nanomaterials – XPS and (X)AES study." *Appl. Surf. Sci.*, 452: 223–231. https://doi.org/10.1016/J.APSUSC.2018.04.269.

Letardi, S., M. Celino, F. Cleri, and V. Rosato. 2002. "Atomic hydrogen adsorption on a Stone-Wales defect in graphite." *Surf. Sci.*, 496 (1–2): 33–38. https://doi.org/10.1016/S0039-6028(01)01437-6.

Leung, T. Y., W. F. Man, P. K. Lim, W. C. Chan, F. Gaspari, and S. Zukotynski. 1999. "Determination of the sp3/sp2 ratio of a-C:H by XPS and XAES." *J. Non-Cryst. Solids*, 254 (1–3): 156–160. https://doi.org/10.1016/S0022-3093(99)00388-9.

Li, C. C., and J. E. Sheehan. 1980. *Friction and wear studies of graphite and a carbon-carbon composite in air and in helium*. General Atomic Co., San Diego, CA (USA).

Li, C. C., and J. E. Sheehan. 1981. "Friction and wear studies of graphite and a carbon-carbon composite in air and in helium." *Wear Mater. Int. Conf. Wear Mater.*, 525–533.

Li, D. 2017. *Friction, Lubrication, and Wear Technology. Frict. Lubr. Wear Technol.*, (G. E. Totten, ed.). ASM International.

Li, K., K. Shen, Z.-H. Huang, W. Shen, G. Yang, J. Yang, and F. Kang. 2016. "Wettability of natural microcrystalline graphite filler with pitch in isotropic graphite preparation." *Fuel*, 180: 743–748. https://doi.org/10.1016/j.fuel.2016.04.091.

Li, Z. Q., C. J. Lu, Z. P. Xia, Y. Zhou, and Z. Luo. 2007. "X-ray diffraction patterns of graphite and turbostratic carbon." *Carbon*, 45 (8): 1686–1695. https://doi.org/10.1016/j.carbon.2007.03.038.

Lian, P., J. Song, Z. Liu, J. Zhang, Y. Zhao, Y. Gao, Z. Tao, Z. He, L. Gao, H. Xia, Q. Guo, P. Huai, and X. Zhou. 2016. "Preparation of ultrafine-grain graphite by liquid dispersion technique for inhibiting the liquid fluoride salt infiltration." *Carbon*, 102: 208–215. https://doi.org/10.1016/j.carbon.2016.02.018.

Liu, Y., Y. Song, H. Ai, M. Shen, H. Liu, S. Zhao, Y. Liu, Z. Fei, X. Fu, and J. Cheng. 2020. "Corrosion of Cr in molten salts with different fluoroacidity in the presence of CrF3." *Corros. Sci.*, 169: 108636. https://doi.org/10.1016/j.corsci.2020.108636.

Locante, J., and D. Malinowski. 1973. "Tritium in pressurized water reactors." *Tritium*, 45–57.

Longhurst, G. R., D. F. Holland, J. L. Jones, and B. J. Merrill. 1992. "TMAP4 User's Manual." Idaho Falls, ID (United States)

Luo, X., X. Li, and S. Yu. 2010. "Nuclear graphite friction properties and the influence of friction properties on the pebble bed." *Nucl. Eng. Des.*, 240 (10): 2674–2681. https://doi.org/10.1016/j.nucengdes.2010.07.030.

Luo, X., J. C. Robin, and S. Yu. 2005a. "Comparison of oxidation behaviors of different grades of nuclear graphite." *Nucl. Sci. Eng.*, 151 (1): 121–127. https://doi.org/10.13182/NSE05-A2534.

Luo, X., S. Yu, X. Sheng, and S. He. 2005. "Temperature effect on IG-11 graphite wear performance." *Nucl. Eng. Des.*, 235 (21): 2261–2274. https://doi.org/10.1016/j.nucengdes.2005.05.001.

Luo, X., L. Zhang, and S. Yu. 2004. "The wear properties of nuclear grade graphite IG-11 under different loads." *Int. J. Nucl. Energy Sci. Technol.*, 1 (1): 33–43. https://doi.org/10.1504/IJNEST.2004.005272.

Luo, Y. R. 2007. *Comprehensive handbook of chemical bond energies*. Taylor and Francis

Lyu, X. W., X. Bin Xia, Z. H. Zhang, J. Cai, and C. Q. Chen. 2016. "Analysis of tritium production in a 2 MW liquid-fueled molten salt experimental reactor and its environmental impact." *Nucl. Sci. Tech.*, 27 (4). https://doi.org/10.1007/s41365-016-0100-z.

Macpherson, H. G. 1958. *Molten salt reactor program quarterly progress report for Period Ending October 31, 1958*. ORNL-2626. Oak Ridge, TN (United States)

MacPherson, H. G. 1985. "molten salt reactor adventure." *Nucl. Sci. Eng.*, 90 (4): 374–380. https://doi.org/10.13182/NSE90-374.

Malinauskas, A. P., and D. M. Richardson. 1974. "The Solubilities of Hydrogen, Deuterium, and Helium in Molten Li2BeF4." *Ind. Eng. Chem. Fundam.*, 13 (3): 242–245. https://doi.org/10.1021/i160051a015.

Malka, V., H. D. Rohrig, and R. Hecker. 1980a. "Tritium Technology in Fission, Fusion, and Isotope Application." *Radiat. Therm. Environ. Pollut. Eff. LIVING Org. Biol. Mater.*, 102.

Malka, V., H. Röhrig, and R. Hecker. 1980b. "Investigations on sorption and diffusion of tritium in HTGR-graphite." *Int. J. Appl. Radiat. Isot.*, 31 (8): 469. https://doi.org/10.1016/0020-708x(80)90253-7.

Mallouk, T., B. L. Hawkins, M. P. Conrad, K. Zilm, G. E. Maciel, N. Bartlett, R. J. Gillespie, and P. Day. 1997. "Raman, infrared and n.m.r. studies of the graphite hydrofluorides CxF1-δ(HF)δ(2 ≤ x ≤ 5)." *Philos. Trans. R. Soc. Lond. Ser. Math. Phys. Sci.*, 314 (1528): 179–187. https://doi.org/10.1098/rsta.1985.0017.

Malmstrom, C., R. Keen, and L. Green. 1951. "Some mechanical properties of graphite at elevated temperatures." *J. Appl. Phys.*, 22 (5): 593–600. https://doi.org/10.1063/1.1700013.

Mandeltort, L., P. Choudhury, J. K. Johnson, and J. T. Yates. 2012. "Methyl radical reactivity on the basal plane of graphite." *J. Phys. Chem. C*, 116 (34): 18347–18357. https://doi.org/10.1021/jp3063367.

Manson B., T. Pigford, and H.W. Levi. 1981. *Nuclear Chemical Engineering, Second Edition*. McGraw-Hill Education.

Markin, A. V., A. E. Gorodetsky, and A. P. Zakharov. 1997. "Effect of oxidation on thermal desorption of deuterium sorbed in graphite." *J. Nucl. Mater.*, 248: 34–37. https://doi.org/10.1016/S0022-3115(97)00205-5.

Marsden, B. J., G. N. Hall, and A. N. Jones. 2020. "Graphite in Gas-Cooled Reactors." *Compr. Nucl. Mater.*, 357–421.

Marsden, B. J., M. Haverty, W. Bodel, G. N. Hall, A. N. Jones, P. M. Mummery, and M. Treifi. 2016. "Dimensional change, irradiation creep and thermal/mechanical property changes in nuclear graphite" *International Materials Reviews,* 61(3). https://doi.org/10.1080/09506608.2015.1136460.

Maslova, O. A., M. R. Ammar, G. Guimbretière, J. N. Rouzaud, and P. Simon. 2012. "Determination of crystallite size in polished graphitized carbon by Raman spectroscopy." *Phys. Rev. B - Condens. Matter Mater. Phys.*, 86 (13). https://doi.org/10.1103/PhysRevB.86.134205.

Matsuo, H. 1980. "The effect of porosity on the thermal conductivity of nuclear graphite." *J. Nucl. Mater.*, 89 (1): 9–12. https://doi.org/10.1016/0022-3115(80)90003-3.

Mays, G. T., A. N. Smith, and J. R. Engel. 1977. *Distribution and Behavior of Tritium in the Coolant-Salt Technology Facility*. ORNL/TM-5759. Oak Ridge, TN (United States)

Mays, T. J. 2007. "A new classification of pore sizes." *Stud. Surf. Sci. Catal.*, 57–62. https://doi.org/10.1016/S0167-2991(07)80009-7

McKee, D. W., and D. Chatterji. 1975. "The catalytic behavior of alkali metal carbonates and oxides in graphite oxidation reactions." *Carbon*, 13 (5): 381–390. https://doi.org/10.1016/0008-6223(75)90006-8.

McNabb, A., and P. K. Foster. 1963. "A New Analysis of the Diffusion of Hydrogen in Iron and Ferritic Steels." *Trans. Metall. Soc. AIME*, 227 (3): 618.

Michalewicz, Z. 1996. "Evolutionary algorithms for constrained parameter optimization problems." *Evol. Comput.*, 4 (1): 1–32. https://doi.org/10.1162/evco.1996.4.1.1.

Mironov, B. E., A. V. K. Westwood, A. J. Scott, R. Brydson, and A. N. Jones. 2012. "Structure of different grades of nuclear graphite." *J. Phys. Conf. Ser.*, 012017.

Miyahara, A., and T. Tanabe. 1988. "Graphite as plasma facing material." *J. Nucl. Mater.*, 155–157 (PART 1): 49–57. https://doi.org/10.1016/0022-3115(88)90226-7.

Mizokawa, Y., T. Miyasato, S. Nakamura, K. M. Geib, and C. W. Wilmsen. 1987. "Comparison of the CKLL first-derivative auger spectra from XPS and AES using diamond, graphite, SiC and diamond-like-carbon films." *Surf. Sci.*, 182 (3): 431–438. https://doi.org/10.1016/0039-6028(87)90011-2.

Moir, R. W., R. L. Bieri, X. M. Chen, T. J. Dolan, M. A. Hoffman, P. A. House, R. L. Leber, J. D. Lee, Y. T. Lee, J. C. Liu, G. R. Longhurst, W. R. Meier, P. F. Peterson, R. W. Petzoldt, and V. E. Schrock. 1994. "HYLIFE-II: A molten-salt inertial fusion energy power plant design - final report." *Fusion Technol.*, 25 (1): 5–25. Taylor & Francis. https://doi.org/10.13182/FST94-A30234.

Morel, C. F. 1966. "Apparatus for contact angle measurements between molten salts and solids and surface tensions of molten salts at high temperatures." *J. Sci. Instrum.*, 43 (9): 647–648. https://doi.org/10.1088/0950-7671/43/9/308.

Morita, K., and Y. Muto. 1992. "Isotopic effect in thermal re-emission of hydrogen from graphite at elevated temperatures." *J. Nucl. Mater.*, 196–198 (C): 963–966. https://doi.org/10.1016/S0022-3115(06)80176-5.

Morita, K., K. Ohtsuka, and Y. Hasebe. 1989. "Dynamic measurements of depth profiles of hydrogen implanted into graphite at elevated temperatures." *J. Nucl. Mater.*, 162–164 (C): 990–996. https://doi.org/10.1016/0022-3115(89)90398-X.

Mulder, E. J., and W. A. Boyes. 2020. "Neutronics characteristics of a 165 MWth Xe-100 reactor." *Nucl. Eng. Des.*, 357: 110415. https://doi.org/10.1016/J.NUCENGDES.2019.110415.

Murch, G. E., and R. J. Thorn. 1980. "Relation between orbital binding energies and ionicities in alkali and alkaline earth flourides." *J. Phys. Chem. Solids*, 41 (7): 785–791. https://doi.org/10.1016/0022-3697(80)90088-8.

Mysels, K. J. 1990. "The maximum bubble pressure method of measuring surface tension, revisited." *Colloids Surf.*, 43 (2): 241–262. https://doi.org/10.1016/0166-6622(90)80291-B.

Nakajima, T. 2001. *Fluorine-Carbon and Fluoride-Carbon Materials: Chemistry, Physics, and Applications*. CRC Press.

Nakajima, T., M. Koh, R. N. Singh, and M. Shimada. 1999. "Electrochemical behavior of surface-fluorinated graphite." *Electrochimica Acta*, 44 (17): 2879–2888. https://doi.org/10.1016/S0013-4686(99)00048-1.

Nakajima, T., A. Mabuchi, and R. Hagiwara. 1988a. "A new structure model of graphite oxide." *Carbon*, 26 (3): 357–361. https://doi.org/10.1016/0008-6223(88)90227-8.

Nakajima, T., A. Mabuchi, R. Hagiwara, N. Watanabe, and F. Nakamura. 1988b. "Discharge Characteristics of Graphite Fluoride Prepared via Graphite Oxide." *J. Electrochem. Soc.*, 135 (2): 273. https://doi.org/10.1149/1.2095600.

Nakajima, T., and Y. Matsuo. 1994. "Formation process and structure of graphite oxide." *Carbon*, 32 (3): 469–475. https://doi.org/10.1016/0008-6223(94)90168-6.

Nakamura, K., M. Fujitsuka, and M. Kitajima. 1990. "Disorder-induced line broadening in first-order Raman scattering from graphite." *Phys. Rev. B*, 41 (17): 12260–12263. https://doi.org/10.1103/PhysRevB.41.12260.

Nansé, G., E. Papirer, P. Fioux, F. Moguet, and a. Tressaud. 1997. "Fluorination of carbon blacks: An X-ray photoelectron spectroscopy study: I. A literature review of XPS studies of fluorinated carbons. XPS investigation of some reference compounds." *Carbon*, 35 (2): 175–194. https://doi.org/10.1016/S0008-6223(96)00095-4.

Nishikawa, M., N. Nakashio, T. Takeishi, S. Matsunaga, and K. Kuroki. 1995. "Sorption behavior of tritium to isotropic graphite." *Fusion Technol.*, 28 (3 pt 2): 1233–1238. https://doi.org/10.13182/fst28-1233.

Nishimura, H., T. Terai, M. Yamawaki, S. Tanaka, A. Sagara, and O. Motojima. 2002. "Compatibility of ferritic steels with Li2BeF4 molten salt breeder." *J. Nucl. Mater.*, 307–311 (2 SUPPL.): 1355–1359. https://doi.org/10.1016/S0022-3115(02)01123-6.

Niwase, K., T. Tanaka, Y. Kakimoto, I. KN, and S. PH. 1995. "Raman spectra of graphite and diamond mechanically milled with agate or stainless steel ball-mill." *Mater. Trans. JIM*, 36 (2): 282–288.

Olander, D. 2002. "Redox condition in molten fluoride salts: Definition and control." *J. Nucl. Mater.*, 300 (2–3): 270–272. https://doi.org/10.1016/S0022-3115(01)00742-5.

Olander, D. 2007. "General Thermodynamics." CRC Press.

Olander, D. R., G. T. Fukuda, and C. F. Baes. 2002. "Equilibrium Pressures over BeF 2 /LiF(Flibe) Molten Mixtures." *Fusion Sci. Technol.*, 41 (2): 141–150. https://doi.org/10.13182/fst02-a208.

Olasov, L. R., F. W. Zeng, J. B. Spicer, N. C. Gallego, and C. I. Contescu. 2019. "Modeling the effects of oxidation-induced porosity on the elastic moduli of nuclear graphites." *Carbon*, 141: 304–315. https://doi.org/10.1016/j.carbon.2018.09.051.

Oriani, R. A. 1970. "The diffusion and trapping of hydrogen in steel." *Acta Metall.*, 18 (1): 147–157. https://doi.org/10.1016/0001-6160(70)90078-7.

Orimo, S., T. Matsushima, H. Fujii, T. Fukunaga, and G. Majer. 2001. "Hydrogen desorption property of mechanically prepared nanostructured graphite." *J. Appl. Phys.*, 90 (3): 1545–1549. https://doi.org/10.1063/1.1385362.

Otake, Y., and R. G. Jenkins. 1993. "Characterization of oxygen-containing surface complexes created on a microporous carbon by air and nitric acid treatment." *Carbon*, 31 (1): 109–121. https://doi.org/10.1016/0008-6223(93)90163-5.

Pan, Z., and R. T. Yang. 1992. "Strongly Bonded Oxygen in Graphite: Detection by High-Temperature TPD and Characterization." *Ind. Eng. Chem. Res.*, 31 (12): 2675–2680. https://doi.org/10.1021/ie00012a008.

Panella, B., M. Hirscher, and S. Roth. 2005. "Hydrogen adsorption in different carbon nanostructures." *Carbon*, 43 (10): 2209–2214. https://doi.org/10.1016/j.carbon.2005.03.037.

Panich, M., A. I. Shames, and T. Nakajima. 2001. "On paramagnetism in ¯uorinated graphite: EPR and solid state NMR study." *J. Phys. Chem. Solids*, 8.

Pappano, P. J., T. D. Burchell, J. D. Hunn, and M. P. Trammell. 2008. "A novel approach to fabricating fuel compacts for the next generation nuclear plant (NGNP)." *J. Nucl. Mater.*, 381 (1–2): 25–38. https://doi.org/10.1016/j.jnucmat.2008.07.032.

Petti, D. A., G. R. Smolik, M. F. Simpson, J. P. Sharpe, R. A. Anderl, S. Fukada, Y. Hatano, M. Hara, Y. Oya, T. Terai, D. K. Sze, and S. Tanaka. 2006. "JUPITER-II molten salt Flibe research: An update on tritium, mobilization and redox chemistry experiments." *Fusion Eng. Des.*, 81 (8-14 PART B): 1439–1449. https://doi.org/10.1016/j.fusengdes.2005.08.101.

Philipps, V., K. Flaskamp, and E. Vietzke. 1982. "Enhancement of the sputtering yield of pyrolytic graphite at elevated temperatures." *J. Nucl. Mater.*, 111–112: 781–784. https://doi.org/10.1016/0022-3115(82)90305-1.

Phillips, J. E., and C. E. Easterly. 1981. "Sources of tritium." *Nucl. Saf.*, 612–626.

Pimenta, M. A., G. Dresselhaus, M. S. Dresselhaus, L. G. Cançado, A. Jorio, and R. Saito. 2007. "Studying disorder in graphite-based systems by Raman spectroscopy." *Phys. Chem. Chem. Phys.*, 9 (11): 1276–1291. https://doi.org/10.1039/b613962k.

Ponter, A. B., and A. P. Boyes. 1972. "The Relation between Contact Angle and Drop Size for Water at its Boiling Point for a Pressure Range 50–760 Torr." *Can. J. Chem.*, 50 (15): 2419–2422. https://doi.org/10.1139/v72-388.

Popov, V. L. 2017. *Contact mechanics and friction: Physical principles and applications, second edition*. Springer Berlin Heidelberg (Germany).

Porosnicu, C., A. Anghel, K. Sugiyama, K. Krieger, J. Roth, and C. P. Lungu. 2011. "Influence of beryllium carbide formation on deuterium retention and release." *J. Nucl. Mater.*, Proceedings of the 19th International Conference on Plasma-Surface Interactions in Controlled Fusion, 415 (1, Supplement): S713–S716. https://doi.org/10.1016/j.jnucmat.2010.12.238.

Pound, B. G. 1989. "Application of a diffusion/trapping model for hydrogen ingress in high-strength alloys." *Corrosion*, 45 (1): 18–25. https://doi.org/10.5006/1.3577881.

Prajitno, D. H., A. Maulana, and D. G. Syarif. 2016. "Effect of Surface Roughness on Contact Angle Measurement of Nanofluid on Surface of Stainless Steel 304 by Sessile Drop Method." *J. Phys. Conf. Ser.*, 739 (1): 012029. https://doi.org/10.1088/1742-6596/739/1/012029.

Rabinowicz, E., L. A. Dunn, and P. G. Russell. 1961. "A study of abrasive wear under three-body conditions." *Wear*, 4 (5): 345–355. https://doi.org/10.1016/0043-1648(61)90002-3.

Ragan, S., and H. Marsh. 1983. "Science and technology of graphite manufacture." *J. Mater. Sci.*

Rearden, B., and M. Jessee. 2016. "SCALE code system.". ORNL/TM-2005/39. Oak Ridge, TN (United States).

Redmond, J. P., and P. L. Walker. 1960. "Hydrogen sorption on graphite at elevated temperatures." *J. Phys. Chem.*, 64 (9): 1093–1099. https://doi.org/10.1021/j100838a002.

Rideal, E. K. 1931. "The physics and chemistry of surfaces." *J. Chem. Educ.*

Rietsch, J. C., P. Brender, J. Dentzer, R. Gadiou, L. Vidal, and C. Vix-Guterl. 2013. "Evidence of water chemisorption during graphite friction under moist conditions." *Carbon*, 55: 90–97. https://doi.org/10.1016/j.carbon.2012.12.013.

Riley, B. J., J. Mcfarlane, G. D. Delcul, J. D. Vienna, C. I. Contescu, L. M. Hay,) A V Savino, and H. E. Adkins. 2018. *Identification of Potential Waste Processing and Waste Form Options for Molten Salt Reactors.* ORNL/LTR-2018/907. Oak Ridge, TN (United States).

Robell, A. J., E. V. Ballou, and M. Boudart. 1964. "Surface diffusion of hydrogen on carbon." *J. Phys. Chem.*, 68 (10): 2748–2753. https://doi.org/10.1021/j100792a003.

Robert, F., D. Paulmier, H. Zaïdi, and E. Schouller. 1995. "Combined influence of an inert gas environment and a mechanical action on a graphite surface." *Wear*, 181–183 (PART 2): 687–690. https://doi.org/10.1016/0043-1648(95)90185-X.

Robertson, R. C. 1971. *Conceptual design study of a single-fluid molten-salt breeder.* ORNL - 4541. Oak Ridge, TN (United States).

Robinson, J. T., J. S. Burgess, C. E. Junkermeier, S. C. Badescu, T. L. Reinecke, F. K. Perkins, M. K. Zalalutdniov, J. W. Baldwin, J. C. Culbertson, P. E. Sheehan, and E. S. Snow. 2010. "Properties of fluorinated graphene films." *Nano Lett.*, 10 (8): 3001–3005. . https://doi.org/10.1021/NL101437P/SUPPL_FILE/NL101437P_SI_001.PDF.

Rohrig, H. D., P. G. Fischer, and R. Hecker. 1976. "Tritium Balance in High-Temperature Gas-Cooled Reactors." *J. Am. Ceram. Soc.*, 59 (7–8): 316–320.

Rosenthal, M. W., and R. B. Briggs. 1968. *Molten Salt Reactor Program Semi-Annual Progress Report*. ORNL 4254. Oak Ridge, TN (United States).

Rosenthal, M. W., P. N. Haubenrich, and R. Briggs. 1972. *The Development Status of Molten-Salt Breeder Reactors*. ORNL-4812. Oak Ridge, TN (United Staes)

Rubeš, M., J. Kysilka, P. Nachtigall, and O. Bludský. 2010. "DFT/CC investigation of physical adsorption on a graphite (0001) surface." *Phys. Chem. Chem. Phys.*, 12 (24): 6438–6444. https://doi.org/10.1039/c001155j.

Rycroft, C. H., G. S. Grest, J. W. Landry, and M. Z. Bazant. 2006. "Analysis of granular flow in a pebble-bed nuclear reactor." *Phys. Rev. E - Stat. Nonlinear Soft Matter Phys.*, 74 (2). https://doi.org/10.1103/PHYSREVE.74.021306.

Saeki, M. 1981. "Release behavior of tritium from graphite heavily irradiated by neutrons." *J. Nucl. Mater.*, 99 (00642): 100–106.

Saeki, M. 1985. "Effects of pyrolytic carbon structure on diffusivity of tritium." *J. Nucl. Mater.*, 131 (1): 32–36. https://doi.org/10.1016/0022-3115(85)90421-0.

Sangiorgi, R., G. Caracciolo, and A. Passerone. 1982. "Factors limiting the accuracy of measurements of surface tension by the sessile drop method." *J. Mater. Sci.*, 17 (10): 2895–2901. https://doi.org/10.1007/BF00644667.

Sato, Y., K. Itoh, R. Hagiwara, T. Fukunaga, and Y. Ito. 2004. "On the so-called 'semi-ionic' C-F bond character in fluorine-GIC." *Carbon*, 42 (15): 3243–3249. https://doi.org/10.1016/j.carbon.2004.08.012.

Savage, R. H. 1948. "Graphite lubrication." *J. Appl. Phys.*, 19 (1): 1–10. https://doi.org/10.1063/1.1697867.

Scarlat, R., and C. Andreades. 2017. *Solid fuel, salt-cooled reactors. Molten Salt React. Thorium Energy*. Elsevier.

Scharf, T. W., and I. L. Singer. 2003. "Thickness of diamond-like carbon coatings quantified with Raman spectroscopy." *Thin Solid Films*, 440 (1–2): 138–144. https://doi.org/10.1016/S0040-6090(03)00703-X.

Schmidt, F., P. Hosemann, R. O. Scarlat, D. K. Schreiber, J. R. Scully, and B. P. Uberuaga. 2021. "Effects of Radiation-Induced Defects on Corrosion." *Annu. Rev. Mater. Res.*, 51 (1): 293–328. https://doi.org/10.1146/annurev-matsci-080819-123403.

Segantin, S., R. Testoni, Z. Hartwig, D. Whyte, and M. Zucchetti. 2020a. "Optimization of tritium breeding ratio in ARC reactor." *Fusion Eng. Des.*, 154: 111531. https://doi.org/10.1016/J.FUSENGDES.2020.111531.

Segantin, S., R. Testoni, and M. Zucchetti. 2020b. "Neutronic comparison of liquid breeders for ARC-like reactor blankets." *Fusion Eng. Des.*, 160 (September): 112013. https://doi.org/10.1016/j.fusengdes.2020.112013.

Seifried, J. E., R. O. Scarlat, P. F. Peterson, and E. Greenspan. 2019. "A general approach for determination of acceptable FLiBe impurity concentrations in Fluoride-Salt Cooled High Temperature Reactors (FHRs)." *Nucl. Eng. Des.*, 343 (January): 85–95. https://doi.org/10.1016/j.nucengdes.2018.09.038.

Serp, J., M. Allibert, O. Beneš, S. Delpech, O. Feynberg, V. Ghetta, D. Heuer, D. Holcomb, V. Ignatiev, J. L. Kloosterman, L. Luzzi, E. Merle-Lucotte, J. Uhlíř, R. Yoshioka, and D. Zhimin. 2014. "The molten salt reactor (MSR) in generation IV: Overview and

perspectives." *Prog. Nucl. Energy*, 77: 308–319. https://doi.org/10.1016/j.pnucene.2014.02.014.

Sha, X., and B. Jackson. 2004. "The Location of Adsorbed Hydrogen in Graphite Nanostructures." *J. Am. Chem. Soc.*, 126 (40): 13095–13099.. https://doi.org/10.1021/ja0472836.

Shen, K., K. Xu, S. Yu, and F. Kang. 2021. "The optical texture of PGA, Gilsocarbon, NBG-18, and IG-110 nuclear graphite." *J. Nucl. Mater.*, 552: 153013. https://doi.org/10.1016/j.jnucmat.2021.153013.

Shen, T. D., W. Q. Ge, K. Y. Wang, M. X. Quan, J. T. Wang, W. D. Wei, and C. C. Koch. 1996. "Structural Disorder and Phase Transformation in Graphite Produced by Ball Milling." *Nanostructured Mater.*, 7 (4): 393–399. https://doi.org/10.1016/0965-9773(96)00010-4.

Shinotsuka, H., S. Tanuma, C. J. Powell, and D. R. Penn. 2015. "Calculations of electron inelastic mean free paths. X. Data for 41 elemental solids over the 50eV to 200keV range with the relativistic full Penn algorithm." *Surf. Interface Anal.*, 47 (9): 871–888. https://doi.org/10.1002/sia.5789.

Shirasu, Y., S. Yamanaka, and M. Miyake. 1993. "Thermodynamic analysis of hydrogen solubility in graphite." *J. Nucl. Mater.*, 200 (2): 218–222. https://doi.org/10.1016/0022-3115(93)90332-S.

Simpson, M. F., G. R. Smolik, J. P. Sharpe, R. A. Anderl, D. A. Petti, Y. Hatano, M. Hara, Y. Oya, S. Fukada, S. Tanaka, T. Terai, and D. K. Sze. 2006. "Quantitative measurement of beryllium-controlled redox of hydrogen fluoride in molten Flibe." *Fusion Eng. Des.*, 81 (1–7): 541–547. https://doi.org/10.1016/J.FUSENGDES.2005.08.031.

Smith, A. L., E. Capelli, R. J. M. Konings, and A. E. Gheribi. 2020. "A new approach for coupled modelling of the structural and thermo-physical properties of molten salts. Case of a polymeric liquid LiF-BeF2." *J. Mol. Liq.*, 299: 112165. https://doi.org/10.1016/j.molliq.2019.112165.

Smith, J., and R. Gilbert. 1973. "Tritium experience in boiling water reactors." *Tritium*, 57–68.

Sohal, M. S., M. A. Ebner, P. Sabharwall, and P. Sharpe. 2010. *Engineering Database of Liquid Salt Thermophysical and Thermochemical Properties*. Idaho National Lab. (INL), Idaho Falls, ID (United States).

Song, J., Y. Zhao, J. Zhang, X. He, B. Zhang, P. Lian, Z. Liu, D. Zhang, Z. He, L. Gao, H. Xia, X. Zhou, P. Huai, Q. Guo, and L. Liu. 2014. "Preparation of binderless nanopore-isotropic graphite for inhibiting the liquid fluoride salt and Xe135 penetration for molten salt nuclear reactor." *Carbon*, 79 (1): 36–45. Elsevier Ltd. https://doi.org/10.1016/j.carbon.2014.07.022.

Sorbom, B. N., J. Ball, T. R. Palmer, F. J. Mangiarotti, J. M. Sierchio, P. Bonoli, C. Kasten, D. A. Sutherland, H. S. Barnard, C. B. Haakonsen, J. Goh, C. Sung, and D. G. Whyte. 2015. "ARC: A compact, high-field, fusion nuclear science facility and demonstration power

plant with demountable magnets." *Fusion Eng. Des.*, 100: 378–405. https://doi.org/10.1016/j.fusengdes.2015.07.008.

Speight, J. 2005. *Lange's Handbook of Chemistry. N. Y. NY McGraw Hill.*

Spreadborough, J. 1962. "The frictional behaviour of graphite." *Wear*, 5 (1): 18–30. https://doi.org/10.1016/0043-1648(62)90177-1.

Sridharan, K., and T. R. Allen. 2013. "Corrosion in Molten Salts." *Molten Salts Chem.*, 241–267.

Standring, J. 1966. "Calculation of the graphite weight-loss in civil magnox and advanced gas-cooled reactors." *J. Nucl. Energy Parts AB React. Sci. Technol.*, 20 (3): 201–217. Pergamon. https://doi.org/10.1016/0368-3230(66)90169-8.

Stansfield, O. M. 1969. "Friction and Wear of Graphite in Dry Helium at 25, 400, and 800°C." *Nucl. Appl.*, 6 (4): 313–320. https://doi.org/10.13182/nt69-a28339.

Stelman, D. 1976. "Air Oxidation of Graphite in Molten Salts." *ECS Proc. Vol.*, 1976–6 (1): 299–314. https://doi.org/10.1149/197606.0299pv.

Stempflé, P., G. Castelein, and M. Brendlé. 2002. "Influence of environment on the size of the elemental wear debris of graphite." *Tribol. Ser.*, 40: 295–304. https://doi.org/10.1016/s0167-8922(02)80033-5.

Stempflé, P., and J. Von Stebut. 2006. "Nano-mechanical behaviour of the 3rd body generated in dry friction - Feedback effect of the 3rd body and influence of the surrounding environment on the tribology of graphite." *Wear*, 260 (6): 601–614. https://doi.org/10.1016/j.wear.2005.03.021.

Stempien, J. D. 2015. "Tritium Transport, Corrosion, and Fuel Performance Modeling in the FHR." Ph.D. Thesis. Massachusetts Institute of Technology.

Stempien, J. D., R. G. Ballinger, and C. W. Forsberg. 2016. "An integrated model of tritium transport and corrosion in Fluoride Salt-Cooled High-Temperature Reactors (FHRs) – Part I: Theory and benchmarking." *Nucl. Eng. Des.*, 310: 258–272. https://doi.org/10.1016/j.nucengdes.2016.10.051.

Stepanov, V. P. 2018. "Wetting of a Charged Surface of Glassy Carbon by Molten Alkali-Metal Chlorides." *Russ. J. Phys. Chem. A*, 92 (3): 570–574. https://doi.org/10.1134/S0036024418030287.

Strehlow, R. A. 1986. "Chemisorption of tritium on graphites at elevated temperatures." *J. Vac. Sci. Technol. Vac. Surf. Films*, 4 (3): 1183–1185. https://doi.org/10.1116/1.573434.

Sun, Q., W. Peng, S. Yu, and K. Wang. 2020. "A review of HTGR graphite dust transport research." *Nucl. Eng. Des.*, 360 (December 2019): 110477. https://doi.org/10.1016/j.nucengdes.2019.110477.

Suzuki, A., T. Terai, and S. Tanaka. 1998. "Mechanism on change of tritium species in Li2BeF4 molten salt breeder under neutron irradiation at elevated temperature." *Fusion Technol.*, 34 (3 pt 2): 526–530. https://doi.org/10.13182/FST98-A11963666.

Tanabe, T. 2006. "On the possibility of ITER starting with full carbon." *Fusion Eng. Des.*, 139–147. https://doi.org/10.1016/j.fusengdes.2005.08.083

Tanabe, T., and Y. Watanabe. 1991. "Hydrogen behavior in graphite at elevated temperatures." *J. Nucl. Mater.*, 179–181 (PART 1): 231–234. https://doi.org/10.1016/0022-3115(91)90068-I.

Tang, H., W. Qi, Z. He, H. Xia, Q. Huang, C. Zhang, X. Wang, J. Song, P. Huai, and X. Zhou. 2017. "Infiltration of graphite by molten 2LiF–BeF2 salt." *J. Mater. Sci.*, 52 (19): 11346–11359. https://doi.org/10.1007/s10853-017-1310-4.

Taylor, R., R. G. Brown, K. Gilchrist, E. Hall, A. T. Hodds, B. T. Kelly, and F. Morris. 1967. "The mechanical properties of reactor graphite." *Carbon*, 5 (5): 519–531. https://doi.org/10.1016/0008-6223(67)90029-2.

Tazhibaeva, I. L., A. K. Klepikov, V. P. Shestakov, O. G. Romanenko, E. V. Chikhray, E. A. Kenzhin, Y. S. Cherepnin, L. N. Tikhomirov, and V. A. Zverev. 1996. "Hydrogen release of reactor irradiated RGT-graphite." *J. Nucl. Mater.*, 233–237 (PART II): 1198–1201. https://doi.org/10.1016/S0022-3115(96)00069-4.

Telling, R. H., and M. I. Heggie. 2007. "Radiation defects in graphite." *Philos. Mag.*, 87 (31): 4797–4846. https://doi.org/10.1080/14786430701210023.

Terai, T., Y. Hosoya, S. Tanaka, A. Sagara, and O. Motojima. 1998. "Compatibility of structural materials with Li2BeF4 molten salt breeder." *J. Nucl. Mater.*, 258–263 (PART 1 A): 513–518. https://doi.org/10.1016/S0022-3115(98)00371-7.

Terai, T., A. Suzuki, and S. Tanaka. 1996. "In-Situ Tritium Release Experiment from Molten Li 2 Bef 4 Salt Under Neutron Irradiation at Elevated Temperatures (Intrexflibe), Fusion Technology." *Fusion Technol.,* 30 (3): 911–915. https://doi.org/10.13182/FST96-A11963054.

Terai, T., A. Suzuki, and S. Tanaka. 2001. "Tritium release from Li2BeF4 molten salt breeder under neutron irradiation at elevated temperature." *Fusion Technol.*, 39 (2): 768–772. https://doi.org/10.13182/FST01-A11963331.

Theodosiou, A., B. F. Spencer, J. Counsell, and A. N. Jones. 2020. "An XPS/UPS study of the surface/near-surface bonding in nuclear grade graphites: A comparison of monatomic and cluster depth-profiling techniques." *Appl. Surf. Sci.*, 508: 144764. https://doi.org/10.1016/j.apsusc.2019.144764.

Thoma, R. E. 1971. *Chemical Aspects of MSRE Operations*. ORNL-4658. Oak Ridge, TN (United States)

Thomas, W. J. 1961. "The adsorption of hydrogen at graphite." *J. Chim. Phys.*, 58: 61–69. https://doi.org/10.1051/jcp/1961580061.

Tian, L., W. Huang, F. Jiang, H. Zheng, T. Zhu, C. She, X. Wang, D. Long, Y. Gong, G. Wu, and Q. Li. 2017. "Electrochemical Behavior of Graphite Anode in LiF-NaF-KF Eutectic with YF 3." *Electrochimica Acta*, 225: 392–398. https://doi.org/10.1016/j.electacta.2016.12.165.

Toth, L. M., and L. K. Felker. 1990. "Fluorine generation by gamma radiolysis of a fluoride salt mixture." *Radiat. Eff. Defects Solids*, 112 (4): 201–210. https://doi.org/10.1080/10420159008213046.

Touhara, H., K. Kadono, Y. Fujii, and N. Watanabe. 1987. "On the Structure of Graphite Fluoride." *ZAAC - J. Inorg. Gen. Chem.*, 544 (1): 7–20. John Wiley & Sons, Ltd. https://doi.org/10.1002/zaac.19875440102.

Touhara, H., and F. Okino. 2000. "Property control of carbon materials by fluorination." *Carbon*, 38 (2): 241–267. https://doi.org/10.1016/S0008-6223(99)00140-2.

Tressaud, A., F. Moguet, S. Flandrois, M. Chambon, C. Guimon, G. Nanse, E. Papirer, V. Gupta, and O. P. Bahl. 1996. "On the nature of C-F bonds in various fluorinated carbon materials: XPS and TEM investigations." *J. Phys. Chem. Solids*.

Tsuchiya, B., and K. Morita. 1996. "Retention of H and D in graphite by simultaneous H+ and D+ ion implantation." *J. Nucl. Mater.*, 227 (3): 195–202. https://doi.org/10.1016/0022-3115(95)00126-3.

Tuinstra, F., and J. L. Koenig. 1970. "Raman Spectrum of Graphite." *J. Chem. Phys.*, 53 (3): 1126–1130. AIP Publishing. https://doi.org/10.1063/1.1674108.

Tzvetkoff, T., and J. Kolchakov. 2004. "Mechanism of growth, composition and structure of oxide films formed on ferrous alloys in molten salt electrolytes—a review." *Mater. Chem. Phys.*, 87 (1): 201–211. Elsevier. https://doi.org/10.1016/J.MATCHEMPHYS.2004.05.039.

Ul-Hamid, A. 2018. *A Beginners' Guide to Scanning Electron Microscopy*. Springer International Publishing.

Vacik, J., H. Naramoto, J. Cervena, V. Hnatowicz, I. Peka, and D. Fink. 2001. "Absorption of molten fluoride salts in glassy carbon, pyrographite and Hastelloy B." *J. Nucl. Mater.*, 289 (3): 308–314. https://doi.org/10.1016/S0022-3115(01)00419-6.

Varma, V., D. Holcomb, F. Peretz, E. Bradley, and D. Ilas. 2012. "AHTR mechanical, structural, and neutronic preconceptual design." ORNL/TM-2012/320. Oak Ridge, TN (United States).

Velasquez, C., G. Hightower, and R. Burnette. 1978. "Oxidation of H-451 graphite by steam. Part I. Reaction kinetics." GA-A-14951. General Atomics. San Diego, CA (United States).

Vergari, L., and M. Fratoni. 2021. "Spent fuel management strategies for fluoride-cooled pebble bed reactors." *Nucl. Eng. Des.*, 378: 111189. https://doi.org/10.1016/J.NUCENGDES.2021.111189.

Vergari, L., M. Nelson, A. Droster, C. Contescu, N. Gallego, and R. O. Scarlat. 2022a. "Infiltration of molten fluoride salts in graphite: Phenomenology and engineering considerations for reactor operations and waste disposal." *J. Nucl. Mater.*, 572: 154058. https://doi.org/10.1016/j.jnucmat.2022.154058.

Vergari, L., J. Quincey, G. Meric de Bellefon, T. Merriman, M. Hackett, and R. O. Scarlat. 2023a. "Self-lubrication of nuclear graphite in argon at high temperature." *Tribol. Int.*, 177: 107946. https://doi.org/10.1016/j.triboint.2022.107946.

Vergari, L., J. Quincey, G. Meric de Bellefon, and R. O. Scarlat. 2023b. "Microstructural characterization data for nuclear graphite samples generated during tribology testing in argon." *Data Brief*, 47: 108796. https://doi.org/10.1016/j.dib.2022.108796.

Vergari, L., and R. O. Scarlat. 2021a. "Kinetics and transport of hydrogen in graphite at high temperature and the effects of oxidation, irradiation and isotopics." *J. Nucl. Mater.* https://doi.org/10.1016/j.jnucmat.2021.153142.

Vergari, L., and R. O. Scarlat. 2021b. "The impact of neutron irradiation, graphite oxidation and fluorination on tritium uptake into and desorption from graphite in molten salt environments." *Fusion Eng. Des.*, 168: 112627. https://doi.org/10.1016/j.fusengdes.2021.112627.

Vergari, L., and R. O. Scarlat. 2021c. "Thermodynamics of hydrogen in graphite at high temperature and the effects of oxidation, irradiation and isotopics." *J. Nucl. Mater.*, 552. https://doi.org/10.1016/j.jnucmat.2021.152797.

Vergari, L., R. O. Scarlat, R. D. Hayes, and M. Fratoni. 2022b. "The corrosion effects of neutron activation of 2LiF-BeF2 (FLiBe)." *Nucl. Mater. Energy.*, 34, 101289. https://doi.org/10.1016/j.nme.2022.101289

Vidrio, R. 2019. "Density Measurement Of Molten FLiBe." M.S. Thesis. UW Madison

Vidrio, R., S. Mastromarino, E. Still, L. Chapdelaine, and R. O. Scarlat. 2022. "Density and Thermal Expansivity of Molten 2LiF-BeF2 (FLiBe): Measurements and Uncertainty Quantification." *J. Chem. Eng. Data*. https://doi.org/10.1021/acs.jced.2c00212.

Vietzke, E., K. Flaskamp, and V. Philipps. 1984. "Differences in the CH3 and CH4 formation from graphite under bombardment with hydrogen ions and hydrogen atoms/argon ions." *J. Nucl. Mater.*, 128–129 (C): 545–550. https://doi.org/10.1016/0022-3115(84)90408-2.

Völkl, J., and G. Alefeld. 1978. "Diffusion of hydrogen in metals." 321–348. Springer, Berlin (Germany).

Walker, P. L., H. A. McKinstry, and C. C. Wright. 1953. "X-Ray Diffraction Studies of a Graphitized Carbon - Changes in Interlayer Spacing and Binding Energy with Temperature." *Ind. Eng. Chem.*, 45 (8): 1711–1715. https://doi.org/10.1021/ie50524a033.

Wampler, W. R., B. L. Doyle, R. A. Causey, and K. Wilson. 1990. "Trapping of deuterium at damage in graphite." *J. Nucl. Mater.*, 176–177 (C): 983–986. https://doi.org/10.1016/0022-3115(90)90178-P.

Wang, H., L. Xu, Y. Zhong, X. Li, H. Tang, F. Zhang, X. Yang, J. Lin, Z. Zhu, Y. You, J. Lu, and L. Zhu. 2020. "Mesocarbon microbead densified matrix graphite A3-3 for fuel elements in molten salt reactors." *Nucl. Eng. Technol.* https://doi.org/10.1016/j.net.2020.10.018.

Wang, L., H. Liu, Z. Pang, and X. Lv. 2016. "Overall heat transfer coefficient with considering thermal contact resistance in thermal recovery wells." *Int. J. Heat Mass Transf.*, 103: 486–500. https://doi.org/10.1016/j.ijheatmasstransfer.2016.07.050.

Wang, L., N. R. Stuckert, and R. T. Yang. 2011. "Unique hydrogen adsorption properties of graphene." *AIChE J.*, 57 (10): 2902–2908. https://doi.org/10.1002/aic.12470.

Wang, P., C. I. Contescu, S. Yu, and T. D. Burchell. 2012. "Pore structure development in oxidized IG-110 nuclear graphite." *J. Nucl. Mater.*, 430 (1–3): 229–238. https://doi.org/10.1016/j.jnucmat.2012.07.015.

Warrier, M., R. Schneider, E. Salonen, and K. Nordlund. 2004. "Multi-scale modeling of hydrogen isotope diffusion in graphite." *Contrib. Plasma Phys.*, 307–310. J

Washburn, E. W. 1921. "The dynamics of capillary flow." *Phys. Rev.*, 17 (3): 273–283. https://doi.org/10.1103/PhysRev.17.273.

Watson, G. M., R. B. Evans, W. R. Grimes, and N. V. Smith. 1962. "Solubility of Noble Gases in Molten Fluorides. In LiF-BeF2." *J. Chem. Eng. Data*, 7 (2): 285–287. https://doi.org/10.1021/je60013a038.

Welham, N. J., V. Berbenni, and P. G. Chapman. 2003. "Effect of extended ball milling on graphite." *J. Alloys Compd.*, 349 (1): 255–263. https://doi.org/10.1016/S0925-8388(02)00880-0.

Wen, K., J. Marrow, and B. Marsden. 2008. "Microcracks in nuclear graphite and highly oriented pyrolytic graphite (HOPG)." *J. Nucl. Mater.*, 381 (1–2): 199–203. North-Holland. https://doi.org/10.1016/j.jnucmat.2008.07.012.

Wert, C., and C. Zener. 1949. "Interstitial atomic diffusion coefficients." *Phys. Rev.*, 76 (8): 1169–1175. https://doi.org/10.1103/PhysRev.76.1169.

Williams, D. F., L. M. Toth, and K. T. Clarno. 2006. *Assessment of Candidate Molten Salt Coolants for the Advanced High-Temperature Reactor (AHTR)*. ORNL-TM-200669. Oak Ridge, TN (United States)

Williams, J. A., J. H. Morris, and A. Ball. 1997. "The effect of transfer layers on the surface contact and wear of carbon-graphite materials." *Tribol. Int.*, 30 (9): 663–676. https://doi.org/10.1016/S0301-679X(97)00034-0.

Williamson, J. A., and J. B. P. Greenwood. 1966. "Contact of nominally flat surfaces." *Proc. R. Soc. Lond. Ser. Math. Phys. Sci.*, 295 (1442): 300–319. https://doi.org/10.1098/rspa.1966.0242.

Wilson, K. L., and W. L. Hsu. 1987. "Hydrogen recycling properties of graphite." *J. Nucl. Mater.*, 145–147 (C): 121–130. https://doi.org/10.1016/0022-3115(87)90317-5.

Windes, W., T. Burchell, and R. Bratton. 2007. *Graphite Technology Development Plan*. INL/EXT-07-13165. Idaho Falls, ID (United States).

Windes, W., G. Strydom, R. Smith, and J. Kane. 2014. *Role of Nuclear Grade Graphite in Controlling Oxidation in Modular HTGRs*. INL/EXT-14-31720. Idaho Falls, ID (United States).

Wolfsberg, M. 1969. "Isotope Effects." *Annu. Rev. Phys. Chem.*, 20 (1): 449–478. https://doi.org/10.1146/annurev.pc.20.100169.002313.

Worthington, A. M. 1881. "II. On pendent drops." *Proc. R. Soc. Lond.*, 32 (212–215): 362–377.. https://doi.org/10.1098/rspl.1881.0032.

Wu, H. 2019. "Understanding Tritium Transport Behavior in Fluoride-salt and Graphite System." Ph.D. Thesis. UW Madison.

Wu, H., F. Carotti, R. Gakhar, N. Patel, and R. O. Scarlat. 2018a. "Fluorination of nuclear graphite IG-110 in molten 2LiF-BeF2 (FLiBe) salt at 700 $^{\circ}$C." *J. Fluor. Chem.*, 211: 159–170. https://doi.org/10.1016/j.jfluchem.2018.04.001.

Wu, H., F. Carotti, R. Gakhar, and R. Scarlat. 2018b. "Spectroscopy (Raman, XPS, and GDMS) and XRD analysis for studying the interaction between nuclear grade graphite and molten 2LiF-BeF 2 (FLiBe) at 700 °C Q2." *Data Brief*, 20: 1816–1821. https://doi.org/10.1016/j.dib.2018.08.079.

Wu, H., R. Gakhar, A. Chen, S. Lam, C. P. Marshall, and R. O. Scarlat. 2020a. "Comparative analysis of microstructure and reactive sites for nuclear graphite IG-110 and graphite matrix A3." *J. Nucl. Mater.*, 528: 151802. https://doi.org/10.1016/j.jnucmat.2019.151802.

Wu, H., R. Gakhar, A. Chen, Z. Zhou, and R. O. Scarlat. 2020b. "Data analysis for characterization of IG110 and A3 by X-Ray diffraction and Raman spectroscopy." *Data Brief*, 32. https://doi.org/10.1016/j.dib.2020.106193.

Xiao, J., L. Zhang, K. Zhou, J. Li, X. Xie, and Z. Li. 2013. "Anisotropic friction behaviour of highly oriented pyrolytic graphite." *Carbon*, 65: 53–62. https://doi.org/10.1016/j.carbon.2013.07.101.

Xiaowei, L., R. Jean-Charles, and Y. Suyuan. 2004. "Effect of temperature on graphite oxidation behavior." *Nucl. Eng. Des.*, 227 (3): 273–280. https://doi.org/10.1016/j.nucengdes.2003.11.004.

Xiaowei, L., Y. Suyuan, S. Xuanyu, and H. Shuyan. 2006. "The influence of roughness on tribological properties of nuclear grade graphite." *J. Nucl. Mater.*, 350 (1): 74–82. https://doi.org/10.1016/j.jnucmat.2005.11.013.

Xie, F., J. Cao, X. Feng, J. Tong, Y. Dong, Z. Zhang, and R. O. Scarlat. 2018. "Study of tritium in the primary loop of HTR-10: Experiment and theoretical calculations." *Prog. Nucl. Energy*, 105 (January): 99–105. https://doi.org/10.1016/j.pnucene.2017.12.018.

Xu, Y., H. Li, F. Xie, J. Cao, and J. Tong. 2017. "Source Term Analysis of Tritium in HTR-10." *Fusion Sci. Technol.*, 71 (4): 671–678. https://doi.org/10.1080/15361055.2017.1290949.

Yajima, K., H. Moriyama, J. Oishi, and Y. Tominaga. 1982. "Surface tension of lithium fluoride and beryllium fluoride binary melt." *J. Phys. Chem.*, 86 (21): 4193–4196. https://doi.org/10.1021/J100218A021.

Yamashina, T., and T. Hino. 1989. "Overall evaluation study for isotropic graphite as fusion first wall material in japan." *J. Nucl. Mater.*, 162–164 (C): 841–850. https://doi.org/10.1016/0022-3115(89)90372-3.

Yang, F. H., and R. T. Yang. 2002. "Ab initio molecular orbital study of adsorption of atomic hydrogen on graphite:" *Carbon*, 40 (3): 437–444. https://doi.org/10.1016/S0008-6223(01)00199-3.

Yang, R. T., and K. L. Yang. 1985. "Kinetics and mechanisms of the carbon-steam reaction on the monolayer and multilayer edges of graphite." *Carbon*, 23 (5): 537–547. https://doi.org/10.1016/0008-6223(85)90090-9.

Yang, X., S. Feng, X. Zhou, H. Xu, and T. K. Sham. 2012. "Interaction between nuclear graphite and molten fluoride salts: A synchrotron radiation study of the substitution of graphitic hydrogen by fluoride ion." *J. Phys. Chem. A*, 116 (3): 985–989. https://doi.org/10.1021/jp208990y.

Yang, Y., Z. Wang, R. Zhou, H. Guo, and X. Li. 2016. "Effects of lithium fluoride coating on the performance of nano-silicon as anode material for lithium-ion batteries." *Mater. Lett.*, 184: 65–68. https://doi.org/10.1016/j.matlet.2016.08.006.

Yen, B. K. 1995. "Roles of oxygen in lubrication and wear of graphite in ″dusting″ and ambient conditions." *J. Mater. Sci. Lett.*, 14 (21): 1481–1483. https://doi.org/10.1007/BF00633136.

Yen, B. K. 1996. "Influence of water vapor and oxygen on the tribology of carbon materials with sp2 valence configuration." *Wear*, 192 (1–2): 208–215. https://doi.org/10.1016/0043-1648(95)06807-4.

Yen, B. K., T. Ishihara, and I. Yamamoto. 1997. "Influence of environment and temperature on 'dusting' wear transitions of carbon-carbon composites." *J. Mater. Sci.*, 32 (3): 681–686. https://doi.org/10.1023/A:1018539819346.

Yen, B. K., B. E. Schwickert, and M. F. Toney. 2004. "Origin of low-friction behavior in graphite investigated by surface x-ray diffraction." *Appl. Phys. Lett.*, 84 (23): 4702–4704. https://doi.org/10.1063/1.1760597.

Yeo, S., J. Yun, S. Kim, M. S. Cho, and Y. W. Lee. 2018. "Fabrication methods and anisotropic properties of graphite matrix compacts for use in HTGR." *J. Nucl. Mater.*, 499: 383–393. https://doi.org/10.1016/j.jnucmat.2017.11.055.

Yin, H., P. Zhang, X. An, J. Cheng, X. Li, S. Wu, X. Wu, W. Liu, and L. Xie. 2018. "Thermodynamic modeling of LiF-NaF-KF-CrF3 system." *J. Fluor. Chem.*, 209: 6–13. https://doi.org/10.1016/j.jfluchem.2018.02.005.

Yoshioka, R., and M. Kinoshita. 2017. "Liquid fuel, thermal neutron spectrum reactors." *Molten Salt React. Thorium Energy*, 281–373. Elsevier.

Young, M., H. Wu, and R. Scarlat. 2015. "Characterization of tritium transport in the flibe-graphite system, for in-situ tritium absorption by the fuel elements of the fluoride-salt-cooled high-temperature reactor (FHR)." *Int. Top. Meet. Nucl. React. Therm. Hydraul. 2015 NURETH 2015*, 4972–4986.

Young, T. 1802. "II. The Bakerian Lecture. On the theory of light and colours." *Philos. Trans. R. Soc. Lond.*, 92: 12–48. https://doi.org/10.1098/rstl.1802.0004.

Yumitori, S. 2000. "Correlation of C1s chemical state intensities with the O1s intensity in the XPS analysis of anodically oxidized glass-like carbon samples." *J. Mater. Sci.*, 35 (1): 139–146. https://doi.org/10.1023/A:1004761103919.

Yun, S.-M., J.-W. Kim, M.-J. Jung, Y.-C. Nho, P.-H. Kang, and Y.-S. Lee. 2007. "An XPS Study of Oxyfluorinated Multiwalled Carbon Nano Tubes." *Carbon Lett.*, 8 (4): 292–298. https://doi.org/10.5714/cl.2007.8.4.292.

Zaidi, H., A. Mezin, M. Nivoit, and J. Lepage. 1989. "The influence of the environment on the friction and wear of graphitic carbons. I. Action of atomic hydrogen." *Appl. Surf. Sci.*, 40 (1–2): 103–114. https://doi.org/10.1016/0169-4332(89)90164-5.

Zaidi, H., D. Paulmier, A. Jeanmaire, and H. Nery. 1991. "Behaviour of graphite in friction under various environments. Connection with the surface reactivity." *Surf. Sci.*, 251–252 (C): 778–781. https://doi.org/10.1016/0039-6028(91)91097-H.

Zaidi, H., D. Paulmier, and J. Lepage. 1990. "The influence of the environment on the friction and wear of graphitic carbons. II. Gas coverage of wear debris." *Appl. Surf. Sci.*, 44 (3): 221–233. https://doi.org/10.1016/0169-4332(90)90053-3.

Zaidi, H., F. Robert, and D. Paulmier. 1995. "Influence of adsorbed gases on the surface energy of graphite: consequences on the friction behaviour." *Thin Solid Films*, 264 (1): 46–51. https://doi.org/10.1016/0040-6090(95)06606-3.

Zakharova, V. V., A. A. Ryzhov, and V. A. Volkovich. 2020. "Electrochemistry of iron, nickel and chromium in LiF–NaF–KF (FLiNaK) eutectic melt: A cyclic voltammetry study." *AIP Conf. Proc.*, 2313 (1): 050039. https://doi.org/10.1063/5.0032424.

Zarifyanz, Y. A., V. F. Kiselev, N. N. Lezhnev, and O. V. Nikitina. 1967. "Interaction of graphite fresh surface with different gases and vapours." *Carbon*, 5 (2): 127–135. Pergamon. https://doi.org/10.1016/0008-6223(67)90066-8.

Zecho, T., A. Güttler, X. Sha, B. Jackson, and J. Küppers. 2002. "Adsorption of hydrogen and deuterium atoms on the (0001) graphite surface." *J. Chem. Phys.*, 117 (18): 8486–8492. American Institute of PhysicsAIP. https://doi.org/10.1063/1.1511729.

Zemann, J. 1965. "Crystal structures, 2 nd edition. Vol. 1 by R. W. G. Wyckoff ." *Acta Crystallogr.*, 18 (1): 139–139.. https://doi.org/10.1107/s0365110x65000361.

Zhang, C., Z. He, Y. Gao, H. Tang, W. Qi, J. Song, and X. Zhou. 2018a. "The effect of molten FLiNaK salt infiltration on the strength of graphite." *J. Nucl. Mater.*, 512: 37–45. https://doi.org/10.1016/j.jnucmat.2018.09.051.

Zhang, J., C. W. Forsberg, M. F. Simpson, S. Guo, S. T. Lam, R. O. Scarlat, F. Carotti, K. J. Chan, P. M. Singh, W. Doniger, K. Sridharan, and J. R. Keiser. 2018b. "Redox potential control in molten salt systems for corrosion mitigation." *Corros. Sci.*, 144: 44–53. Elsevier. https://doi.org/10.1016/j.corsci.2018.08.035.

Zhang, R., C. Zheng, C. Chen, B. Lv, G. Gao, Z. Yang, Y. Yang, and F. Zhang. 2021. "Study on fatigue wear competition mechanism and microstructure evolution on the surface of a bainitic steel rail." *Wear*, 482–483: 203978. https://doi.org/10.1016/j.wear.2021.203978.

Zhang, W., B. Zhang, J. Song, W. Qi, X. He, Z. Liu, P. Lian, Z. He, L. Gao, H. Xia, X. Liu, X. Zhou, L. Sun, and X. Wu. 2016. "Microstructure and molten salt impregnation characteristics of a micro-fine grain graphite for use in molten salt reactors." *New Carbon Mater.*, 31 (6): 585–593. https://doi.org/10.1016/S1872-5805(16)60034-3.

Zhang, W., H. Zhu, Z. Gao, T. Wang, Wendurina, G. Xu, S.-X. Hu, X. Chen, B. Liu, and Y. Tang. 2023. "Carbonate of strontium anchored at the edge of graphite." *Nucl. Mater. Energy*, 35: 101448. https://doi.org/10.1016/J.NME.2023.101448.

Zhang, Z., Z. Wu, D. Wang, Y. Xu, Y. Sun, F. Li, and Y. Dong. 2009. "Current status and technical description of Chinese 2 × 250 MWth HTR-PM demonstration plant." *Nucl. Eng. Des.*, 239 (7): 1212–1219. https://doi.org/10.1016/J.NUCENGDES.2009.02.023.

Zheng, G., D. Carpenter, L. Hu, and K. Sridharan. 2016. "High Temperature Corrosion of Structural Alloys in Molten Li2BeF4 (FLiBe) Salt." *Am. Ceram. Soc. Adv. Mater. Sci. Environ. Energy Technol. V*, 9: 93–101.

Zheng, G., P. Xu, K. Sridharan, and T. Allen. 2014. "Characterization of structural defects in nuclear graphite IG-110 and NBG-18." *J. Nucl. Mater.*, 446 (1–3): 193–199. https://doi.org/10.1016/j.jnucmat.2013.12.013.

Zhong, Y., J. Zhang, J. Lin, L. Xu, F. Zhang, H. Xu, Y. Chen, H. Jiang, Z. Li, Z. Zhu, and Q. Guo. 2017. "Mesocarbon microbead based graphite for spherical fuel element to inhibit the infiltration of liquid fluoride salt in molten salt reactor." *J. Nucl. Mater.*, 490: 34–40. https://doi.org/10.1016/j.jnucmat.2017.04.003.

Zhou, S., S. D. Sherpa, D. W. Hess, and A. Bongiorno. 2014. "Chemical Bonding of Partially Fluorinated Graphene." *J. Phys. Chem. C*, 118 (45): 26402–26408. https://doi.org/10.1021/jp508965q.

Zhou, W., Y. Yang, G. Zheng, K. B. Woller, P. W. Stahle, A. M. Minor, and M. P. Short. 2020. "Proton irradiation-decelerated intergranular corrosion of Ni-Cr alloys in molten salt." *Nat. Commun.*, 11 (1). https://doi.org/10.1038/s41467-020-17244-y.

Zhou, X. W., Y. P. Tang, Z. M. Lu, J. Zhang, and B. Liu. 2017. "Nuclear graphite for high temperature gas-cooled reactors." *Xinxing Tan CailiaoNew Carbon Mater.*

Zhu, X., B. Dang, F. Li, D. Wei, P. Zhang, and S. Li. 2021. "Tribocorrosion behavior of Nb coating deposited by double-glow plasma alloying." *Mater. Res. Express*, 8 (1): 016411. https://doi.org/10.1088/2053-1591/abdc39.

Ziesing, G. 1953. "The Determination of Surface Tension by Sessile Drop Measurements, with Application to Mercury." *Aust. J. Phys.*, 6 (1): 86. https://doi.org/10.1071/PH530086.

Zisman, W. A. 1964. "Relation of the Equilibrium Contact Angle to Liquid and Solid Constitution." *Contact Angle Wettability Adhes.*, Advances in Chemistry, 1–51.